

# **NMR Spectroscopy: New Methods and Applications**



# NMR Spectroscopy: New Methods and Applications

George C. Levy, EDITOR  
*Syracuse University*

Based on a symposium jointly  
sponsored by the Divisions  
of Analytical, Organic,  
and Physical Chemistry  
at the 181st Meeting  
of the American Chemical Society,  
Atlanta, Georgia,  
March 29–April 3, 1981.

A C S   S Y M P O S I U M   S E R I E S **191**

**AMERICAN CHEMICAL SOCIETY**  
**WASHINGTON, D. C.      1982**



**Library of Congress Cataloging in Publication Data**

NMR spectroscopy.

(ACS symposium series, ISSN 0097-6156; 191)

"Based on a symposium jointly sponsored by the Division[s] of Analytical, Organic, and Physical Chemistry at the 181st meeting of the American Chemical Society, Atlanta, Ga., March 29–April 3, 1981."

Includes index.

1. Nuclear magnetic resonance spectroscopy—Congresses.

I. Levy, George C. II. American Chemical Society. Division of Analytical Chemistry. III. American Chemical Society. Division of Organic Chemistry. IV. American Chemical Society. Division of Physical Chemistry. V. Title: NMR spectroscopy. VI. Series.

QD96.N8N59 1982 543.0877 82-11458

ISBN 0-8412-0723-2

ACSMC8 191

1-388

1982

Copyright © 1982

American Chemical Society

All Rights Reserved. The appearance of the code at the bottom of the first page of each article in this volume indicates the copyright owner's consent that reprographic copies of the article may be made for personal or internal use or for the personal or internal use of specific clients. This consent is given on the condition, however, that the copier pay the stated per copy fee through the Copyright Clearance Center, Inc. for copying beyond that permitted by Sections 107 or 108 of the U.S. Copyright Law. This consent does not extend to copying or transmission by any means—graphic or electronic—for any other purpose, such as for general distribution, for advertising or promotional purposes, for creating new collective work, for resale, or for information storage and retrieval systems. The copying fee for each chapter is indicated in the code at the bottom of the first page of the chapter.

The citation of trade names and/or names of manufacturers in this publication is not to be construed as an endorsement or as approval by ACS of the commercial products or services referenced herein; nor should the mere reference herein to any drawing, specification, chemical process, or other data be regarded as a license or as a conveyance of any right or permission, to the holder, reader, or any other person or corporation, to manufacture, reproduce, use, or sell any patented invention or copyrighted work that may in any way be related thereto.

PRINTED IN THE UNITED STATES OF AMERICA

**American Chemical  
Society Library**

1155 16th St. N. W.

In NMR Spectroscopy: New Methods and Applications; Levy, G.;  
ACS Symposium Series 191, American Chemical Society, Washington, DC, 1982.

Washington, D. C. 20036

# ACS Symposium Series

**M. Joan Comstock, *Series Editor***

## *Advisory Board*

David L. Allara

Robert Baker

Donald D. Dollberg

Robert E. Feeney

Brian M. Harney

W. Jeffrey Howe

James D. Idol, Jr.

Herbert D. Kaesz

Marvin Margoshes

Robert Ory

Leon Petrakis

Theodore Provder

Charles N. Satterfield

Dennis Schuetzle

Davis L. Temple, Jr.

Gunter Zweig

# FOREWORD

The ACS SYMPOSIUM SERIES was founded in 1974 to provide a medium for publishing symposia quickly in book form. The format of the Series parallels that of the continuing ADVANCES IN CHEMISTRY SERIES except that in order to save time the papers are not typeset but are reproduced as they are submitted by the authors in camera-ready form. Papers are reviewed under the supervision of the Editors with the assistance of the Series Advisory Board and are selected to maintain the integrity of the symposia; however, verbatim reproductions of previously published papers are not accepted. Both reviews and reports of research are acceptable since symposia may embrace both types of presentation.

## PREFACE

**T**HE PAST TEN YEARS HAVE SEEN PHENOMENAL DEVELOPMENTS in the methodology and application of nuclear magnetic resonance (NMR) to chemistry and biophysics. The introduction of Fourier transform NMR instrumentation was quickly followed by major extensions in instrumental capabilities. As a result, the two chief characteristics of NMR spectra, sensitivity and resolution, underwent radical improvements. Applications once essentially restricted to a few nuclei became established broadly across the entire periodic table. Carbon-13 NMR spectroscopy studies of very complex systems—including proteins, nucleic acids, and crystalline and amorphous solids—are now common. Other inventions, like multi-dimensional FT NMR, NMR imaging, and multiple quantum NMR spectroscopy, encourage future developments.

These chapters describe many current advances in NMR spectroscopy. Most are reports based on lectures given in April 1981. The Editor would like to thank all of the authors for their exciting presentations.

GEORGE C. LEVY  
Syracuse University  
Syracuse, New York

February 1, 1982

## Introduction

GEORGE C. LEVY and DAVID J. CRAIK

Syracuse University, Department of Chemistry, Syracuse, NY 13210

Nuclear Magnetic Resonance (NMR) Spectroscopy has developed into an ever expanding and exciting research discipline. Early in its 35 year history, NMR spectroscopy was adapted from sole use by physicists, who had first discovered it, to the realm of chemists who saw the potential of the so-called "chemical shift" phenomenon as a structural probe. This first useful parameter has now been supplemented by many other experimentally accessible quantities, as well as a labyrinth of new applications and methods. In this monograph, we hope to outline some of these new and exciting developments in NMR spectroscopy. Most of the chapters are based on symposium lectures given at the 181st National Meeting of The American Chemical Society, in Atlanta Georgia, March, 1981. Several additional manuscripts were solicited from leading NMR spectroscopists.

In broad terms, most new applications of NMR in recent years have derived from parallel improvements in instrumentation and methods. The instrumental improvements may be categorized as follows:

1. The development and use of spectrometers operating at higher magnetic fields, in some cases with large and versatile probe (sample) geometries.
2. The development of multi-nuclear spectrometers.
3. Improved spectrometer design for Fourier Transform techniques; higher sensitivity for proton ( $^1\text{H}$ ) NMR and all other nuclei.
4. Advances in computer capabilities.

Magnetic field strength. Since the early 1970's there has been increasing use of superconducting solenoid based systems which are capable of extremely high magnetic fields. The highest fields in use today (11.7-14.4 Tesla) correspond to proton NMR frequencies of 500-600 MHz. The development of wide-bore superconducting magnets also represents a significant instrumental improvement that has made possible many new applications. The first important benefit is an increased sample

0097-6156/82/0191-0001\$06.00/0  
© 1982 American Chemical Society



volume and thus increased sensitivity: the larger the number of nuclei within the receiver coil the stronger the signal. Secondly, a larger probe volume allows more flexibility with respect to the nature and geometry of the experiment. For example, it is now possible to place organs or even living animals into the probe of a high resolution magnet.

Multi-nuclear NMR. It was of course no accident that the earliest nuclei studied by NMR were those with the highest susceptibility to detection. NMR studies of less accessible nuclei awaited improvements in instrument sensitivity, and it was not until the 1970's that multi-nuclear spectrometers dramatically expanded the range of potential applications of NMR spectroscopy. NMR is no longer only associated with a few nuclei such as  $^1\text{H}$ ,  $^{13}\text{C}$  and  $^{19}\text{F}$ , but has also been applied to many others, including  $^2\text{H}$ ,  $^{15}\text{N}$ ,  $^{17}\text{O}$ ,  $^{23}\text{Na}$ ,  $^{113}\text{Cd}$ ,  $^{193}\text{Pt}$  to name a few.

Fourier Transform NMR. Another critical development has been improved spectrometer design for Fourier Transform NMR. The technique of pulsed Fourier transform NMR was commercialized around 1970 and brought an immediate 10-15 fold increase in sensitivity for  $^{13}\text{C}$  NMR (as well as a smaller factor observed for  $^1\text{H}$  NMR). It is less well known, but during the last 10 years, improvements in spectrometer design (e.g. optimization of receiver coil and electronic circuits for pulsed operation) have produced an additional order of magnitude gain in sensitivity, essentially matching the initial advantage of FT NMR.

Computer developments. Increased computer capabilities have also greatly contributed to new applications. The modern NMR computer system and software can control complicated multipulse experiments where many factors such as delay times, decoupler levels, pulse widths or rf phase may be varied systematically. In fact, virtually all spectrometer functions are now set under computer control.

The second factor responsible for many recent applications is that of conceptually new NMR methods. Some of these are listed below:

1. Two-dimensional Fourier Transform NMR.
2. High resolution NMR in solids.
3. New kinds of pulse sequences.
4. Chemically Induced Dynamic Nuclear Polarization (CIDNP)
5. Multiple Quantum NMR.
6. NMR imaging.

This general breakdown represents a somewhat arbitrary division of subjects and techniques. In fact, there is a great deal of overlap among the various categories, as will be seen from the discussion below, and from the remaining chapters of this monograph.

Two-dimensional FT NMR spectroscopy. The exciting new techniques of 2D FT NMR spectroscopy are currently being applied to a variety of chemical and biological problems. 2D FT NMR involves the collection of data as a function of two independent

time domains,  $t_1$  and  $t_2$  followed by a double Fourier transformation. The resultant 2D spectrum contains one intensity axis and two frequency axes. A large variety of 2D experiments are possible, depending on the perturbations (e.g. frequency or phase of rf irradiation, decoupler level, etc.) that are applied to the nuclear spins during the intervals  $t_1$  and  $t_2$ .

Most but not all applications of 2D correlated spectroscopy to date have involved  $^{13}\text{C}$  and  $^1\text{H}$  studies. A 2D spectrum in which one axis represents  $^{13}\text{C}$  chemical shifts and the other  $^1\text{H}$  chemical shifts yields cross peaks only for coupled nuclei (i.e. there is a degree of correlation between the  $^{13}\text{C}$  and  $^1\text{H}$  spectra). This information often allows complete assignments to be made in the individual  $^{13}\text{C}$  or  $^1\text{H}$  spectra of complex organic molecules.

While 2D correlated spectroscopy provides information which is not directly obtainable from a 1D experiment, another class of 2D experiments, collectively called 2D resolved spectroscopy, simplifies complex spectra by spreading the lines in a 1D spectrum into a second dimension. Typical spreading parameters include scalar couplings, dipolar couplings, or chemical shifts. When scalar coupling constants are used as the spreading parameter the technique is called J-resolved 2D spectroscopy, and chemical shift and coupling information can be effectively separated. This is a very powerful and important feature of 2D FT NMR spectroscopy, as it is often very difficult to obtain coupling constants from normal (1D) spectra of complex molecular systems because of the overlap of many multiplets. Spreading the overlapping peaks in complex  $^1\text{H}$  spectrum into a second dimension often greatly simplifies spectra and allows complete peak assignments to be made. Using appropriate projections in this type of J-resolved 2D proton spectrum it is in fact possible to produce a simulated broadband homonuclear decoupled proton spectrum.

NMR spectroscopy of solid samples. The development of methodology to obtain high resolution spectra of solids has greatly enhanced the range of potential NMR applications, particularly for studies of low natural abundance nuclei such as  $^{13}\text{C}$ . Under the normal conditions used to obtain  $^{13}\text{C}$  NMR spectra of liquids, a solid sample would yield only an extremely broad featureless spectrum. A large contribution to the broadening arises from static dipolar interactions.  $^{13}\text{C}$  spectra of solids obtained using high power proton irradiation (often termed dipolar decoupling) can have much of the initial broadening removed, but still may have linewidths of 5-10 KHz or more. This broadening is due to chemical shift anisotropy. The observed broad envelope is a result of contributions from the many individual chemical shifts of nuclei in molecules oriented differently within the sample. The anisotropy can be effectively removed if the sample is spun rapidly at an angle of  $54.7^\circ$  (the magic angle) with respect to the external magnetic field.

Using the techniques of dipolar decoupling and magic angle spinning it is possible to produce spectra in solids having nearly the same resolution as is obtained in liquids. However, the low natural abundance of  $^{13}\text{C}$  nuclei, and their longer spin lattice relaxation times ( $T_1$ s) in solids compared with liquids severely limits the signal-to-noise ratio that can be obtained in a given time for a solid sample. This sensitivity problem can be overcome using the technique of cross polarization (CP), which not only brings about an increase in sensitivity by allowing the magnetization from the abundant  $^1\text{H}$  nuclear spins to be transferred (cross polarized) to the dilute  $^{13}\text{C}$  nuclei, but also allows signal accumulation to be repeated at intervals related to the shorter  $^1\text{H}$  relaxation times rather than the longer  $^{13}\text{C}$  relaxation times. In fact, it is also usual to perform the unrelated MAS experiment in conjunction with cross polarization (these are specified as CPMAS experiments). Figure 1(1) demonstrates the remarkable resolution obtained in a state-of-the-art  $^{13}\text{C}$  CPMAS spectrum of solid reserpine.

Multi-pulse techniques. Today, the simple repetitive single pulse FT NMR experiment has been augmented by pulse schemes designed to probe different parameters or phenomena or to improve sensitivity. One new sequence, which is currently gaining widespread application has been given the acronym INEPT (Insensitive Nuclei Enhanced by Polarization Transfer).(2) It provides significant signal enhancements, particularly for nuclei such as  $^{15}\text{N}$  or  $^{29}\text{Si}$  but also provides a means of determining signal multiplicity in proton decoupled  $^{13}\text{C}$  spectra.

Chemically Induced Dynamic Nuclear Polarization (CIDNP). This term has been used to describe the enhancement of nuclear spin polarization observed in the NMR spectra of compounds undergoing radical reactions. Some exciting applications are described in Chapter X.

Multiple quantum NMR The signals observed in normal NMR spectra arise from transitions which obey the selection rule  $\Delta m = \pm 1$  ( $m$  is the total magnetic quantum number of the spin system). Using special pulse techniques it is possible to excite multiple quantum "coherences" between states where  $m = \pm 2, 3$  etc. Although not directly observable these coherences can be converted, using special pulse techniques, into signals which can be detected. In the last few years, studies of multiple quantum transitions(3) have been carried out in liquids, liquid crystals and solids, and promise to provide much information on molecular structures, conformations and correlated motions. Specifically, the relative simplicity of multiple quantum spectra greatly aids in structural determinations of molecules aligned in liquid crystals. In addition, relaxation measurements obtained from multiple quantum spectra are particularly valuable in determining complex anisotropic or correlated molecular motions. Multiple quantum methods also promise to be extremely useful for assignment purposes. For example, it has been recently shown(4)

that a combination of the powerful methods of 2D spectroscopy and double quantum NMR allows  $^{13}\text{C}$ - $^{13}\text{C}$  coupling constants to be readily measured and assigned in natural abundance samples. Using this coupling information it is possible to systematically build up a picture of the connectivity of carbon atoms in a molecule and hence readily determine the entire structure of the carbon skeleton.

NMR imaging. This describes a class of experiments in which NMR signals are used to obtain information having spatial significance. Most imaging experiments involve the detection of proton signals, although some experiments have been done using other highly sensitive nuclei such as  $^{19}\text{F}$ . The instruments used in these experiments may be quite different from standard high resolution NMR spectrometers, but they operate on the same principle: nuclei having a magnetic moment absorb rf energy at a frequency directly proportional to the local external magnetic field. In the imaging technique of zeugmatography, developed by Lauterbur(5) a field gradient is superimposed on the main field so that different parts of the sample experience different magnetic fields and hence resonate at different frequencies. The resultant NMR signals provide a linear profile of the distribution of magnetic nuclei across the sample, and when further scans are taken, using gradients in different directions, it is possible to reconstruct a two or three dimensional image of the sample. Recent developments in field gradient and other imaging methods are discussed in some detail in a recent review by Hoult,(6) Methods which do not utilize a static linear field gradient, for example the "field focussing" technique of Damadian(7) are also in current use. In this technique and in related methods it is possible to shape the magnetic field in such a manner as to focus on specific volumes within the sample.

#### LITERATURE CITED

1. Levy, G. C.; Lichter, R. L.; Nelson, G. L. Carbon-13 Nuclear Magnetic Resonance Spectroscopy, (2nd edition) Chapter 10, Wiley, New York 1980.
2. a) Morris, G. A.; Freeman, R. J. Amer. Chem. Soc., 1979, **101**, 760; b) Barum, D. P.; Ernst, R. R. J. Magn. Reson., 1980, **39**, 163; c) Doddrell, D. M.; Pegg, D. T. J. Amer. Chem. Soc., 1980, **102**, 6390.
3. Vega, S.; Pines, A. J. Chem. Phys., 1977, **66**, 5624; Wokaun, A.; Ernst, R. R. Chem. Phys. Lett., 1977, **52**, 407.
4. Bax, A.; Freeman, R.; Frenkiel, T. A.; Levitt, M. H. J. Magn. Reson., 1981, **43**, 478.
5. Lauterbur, P. C. Nature, 1973, **242**, 190.
6. Hoult, D. I. in "Magnetic Resonance in Biology", Ed. J.S. Cohen, Vol.1, Chapter 2, Wiley, New York 1980.
7. Damadian, R. L.; Minkov, L.; Goldsmith, M.; Koutcher, J. Naturwiss., 1978, **65**, 250.

RECEIVED February 1, 1982.

# Ultra High-Field NMR

FELIX W. WEHRLI

Bruker Instruments, Inc., Billerica, MA 01821

The viability of NMR spectroscopy as an analytical tool is largely owed to the on-going development of superconducting magnet technology which has led to magnetic fields of up to 11.7 T with field decay rates of better than two parts in  $10^8$ . A major breakthrough was the combined utilization of multifilamentary NbTi and Nb<sub>3</sub>Sn superconductors together with jointing technologies providing solenoids with very small residual resistance. Paralleling these efforts were improvements in probe technology resulting in detection sensitivities that are one order of magnitude better than those achievable at electromagnet fields. The resolving power of such a spectrometer permits analysis of the proton spectra of very large bio-molecules while much simplifying the multiplet structure in the spectra of complex organic molecules. It is further shown that increased chemical shift dispersion greatly enhances the utility of magnetic resonance of other nuclei such as <sup>13</sup>C, deuterium, and many of the quadrupolar metal resonances with inherently broad lines.

Nuclear magnetic resonance spectroscopy first aroused the chemist's interest when the discovery was made that the exact nuclear precession frequency is dependent upon the chemical environment of the nucleus. The displacement of the resonance frequency relative to an arbitrary standard is commonly referred to as chemical shift. Without this property, NMR would be without practical utility to the chemist as an analytical tool and it would probably long be extinct.

Since the chemical shift is dictated by field-induced paramagnetic and diamagnetic circulation of electrons, its quantity is dependent upon the external magnetic field or, more accurately, proportional to the latter. With the displacements being of the order of a few parts per million or often only a fraction of a part per million, it is essential to conduct the experiments at a sufficiently high field in order to resolve resonances of various nuclei pertaining to a molecule.

0097-6156/82/0191-0007\$06.75/0  
© 1982 American Chemical Society

Another motivation to increase the magnetic field is detection sensitivity. NMR happens to be an intrinsically insensitive spectroscopic method, being orders of magnitude less sensitive than such methods as optical or mass spectroscopy.

When NMR was first commercialized in 1953 in the form of a 30 MHz instrument, it was barely possible to resolve the three proton resonances pertaining to ethyl alcohol, not even to mention spin-spin coupling. It was therefore immediately recognized that in order to become a viable technique, the resolving power of the instruments had to be augmented in terms of both magnet resolution and magnetic field strength. The early HR-30 pioneered by Varian was therefore rapidly superseded by a 40 MHz instrument. Within five years the spectrometer frequency was doubled to 60 MHz, at which stage the population of instruments rapidly increased, although the technique remained the privilege of few research laboratories.

Broader use of NMR started in 1962 with the introduction of the popular A-60, an instrument that was easy to use, reliable and which served the scientific community for more than a decade.

With the development and introduction of the HR-100 in 1962, NMR received a further impetus. The real breakthrough, however, was achieved by departing from the classical electromagnet in 1964, although the latter succeeded in maintaining its role and will probably not phase out before the mid-80's. Since saturation of iron, which is used as the core of electromagnets, occurs between 2.0 - 2.3 T, other avenues had to be explored to increase the crucial magnetic field. The clue was superconducting technology, known for some time but not realized in the form of a high-resolution magnet before 1964. With the introduction of the HR-200 during that year, shortly later followed by the HR-220, a new dimension of NMR was opened up. For the first time it became possible to study high-molecular-weight synthetic and biological molecules in solution, allowing the characterization of these complex systems by separating some of the closely spaced resonances which cannot be resolved at lower field strength.

In spite of this remarkable achievement, superconducting spectrometers initially failed to become widely popular and they remained the exclusivity of a few high-powered research laboratories. There are a variety of reasons for the slow start of superconducting NMR. One of the key obstacles, which prevented entry of such systems into the analytical lab, was the high purchase price, but more importantly, the exorbitant operating costs associated with the boil-off of liquid helium and nitrogen which, typically, had to be replenished within a few days. Moreover, these instruments required skillful operators. Remarkably, however, superconducting magnets, even in those days, were not inferior in reliability to their iron counterparts and those early systems were put out of operation primarily because their utilization was no longer economically viable.

The necessity for improved helium economy led to a new genera-

tion of superconducting magnets during the early 70's, which were fitted with more efficient cryostats, therefore prolonging helium and nitrogen hold time. Today's cryostats typically boil-off 10-20 cc of helium per hour resulting in an annual helium cost of less than \$1,000 (cf. Table I).

Table I: Typical annual helium consumption and associated cost for a superconducting magnet system between 1967 and 1980. Underlying assumption: typical refill volume = 30 liters; average price per liter = \$5.00.

YEAR	REFILL INTERVAL	ANNUAL HE COST (\$)
1967	3 Days	18,000
1971	1 Week	7,500
1975	3 Weeks	2,600
1980	2-3 Months	900

With the introduction of Bruker's HX-270 in 1971, field strength received another boost. At the same time it was recognized that high magnetic fields are desirable and often critical for the successful observation of a number of heteronuclei. Superconducting instruments therefore became multinuclear, although they were still equipped with fixed-frequency transmitters and fixed-tuned probes. Within only a few years, field strength was further increased to 300 MHz in 1973, 360 MHz in 1974, and finally 400 MHz in 1978. The latter two represent another milestone since fields beyond 300 MHz proton frequency require radically different magnet technology.

In 1979, another significant jump was made to 500 MHz proton frequency, concurrently with the introduction of a new generation of spectrometer consoles. This culminated in the WM-500 spectrometer (1), the highest-field commercial NMR spectrometer built so far. It should not go unmentioned that during the same year researchers at the Carnegie-Mellon Institute in Pittsburgh succeeded in taking into operation a 600 MHz spectrometer (2) which, however, differs in one important aspect; its field is not persistent, i.e., the magnet has to be continuously energized to compensate for field decay.

The evolution of magnetic field strength in commercial NMR spectrometers over the past 15 years is illustrated by the chart in Figure 1.

### Magnet Technology

In order to appreciate the problems behind the development of the past ten years it may be appropriate to briefly review the principles and characteristics of superconductors.

The materials which have the magnificent property of carrying current resistance-free have one element in common: they do so only at cryogenic temperatures. Table II lists the characteristics of a few commercial superconductors.

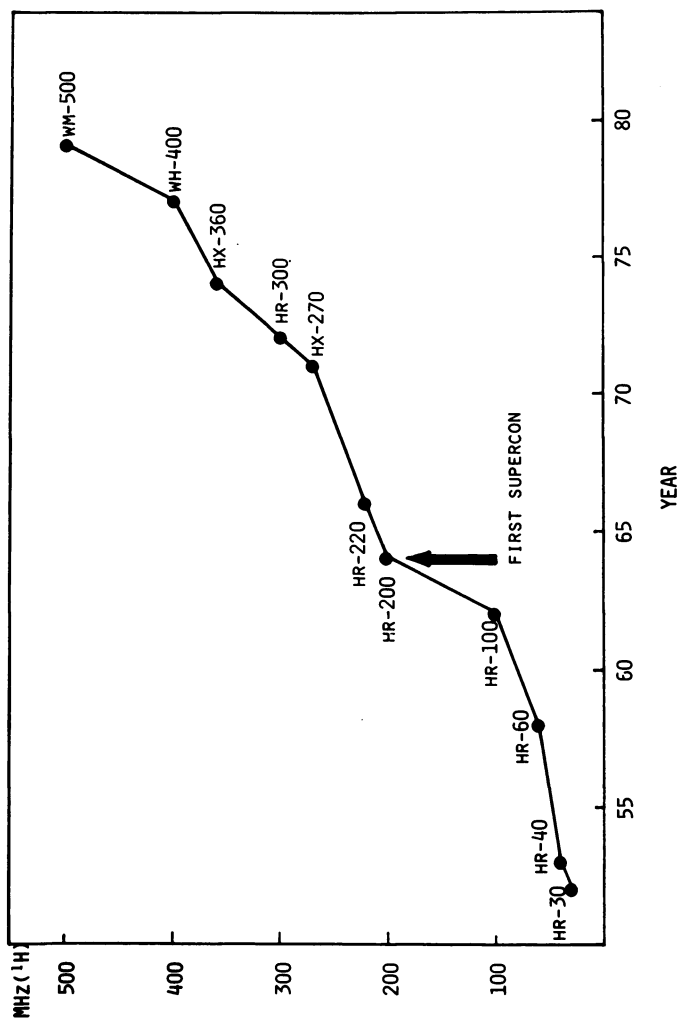


Figure 1. Evolution of magnetic field strength (in units of the proton magnetic resonance frequency) of commercial NMR spectrometers 1953-80. Model designations: HR (Varian), HX, WH, and WM (Bruker).



Table II: Characteristics of some common superconductors

MATERIAL	CRITICAL TEMPERATURE	CRITICAL FIELD at 0°K	CRITICAL FIELD at 4.2°K
NbTi	10.6 °K	17.6 T	11.8 T
Nb <sub>3</sub> Sn	18.05°K	35.0 T	20.0 T
V <sub>3</sub> Ga	14.5 °K	50.0 T	21.1 T

So far, two possible routes for very high field magnets have been pursued (3):

(1) Nb<sub>3</sub>Sn Ribbon

The strength of this approach is its provision of the highest current densities. This advantage, however, is outweighed by a number of serious limitations:

(a) The diamagnetic currents generated at the surface of the conductor lead to an unstable operating condition with unpredictable field/current ratios and high residual fields.

(b) The pancake construction causes a discontinuous current path and thus higher-order field gradients that cannot easily be shimmed out.

(c) Joining the tape rings is made by using soldered resistive joints precluding persistent operation. In practice this means that the current leads cannot be removed, causing high consumption of liquid helium.

(2) Multifilament Nb<sub>3</sub>Sn

Filamentary Nb<sub>3</sub>Sn wire produces high homogeneity and low remanence. The smaller number of joints can be made with very low resistance ( $10^{-7}$  -  $10^{-13}$  ohms)(3), thus providing persistent operation and consequently little helium loss.

Nb<sub>3</sub>Sn filament conductors are generally fabricated by means of a solid-state diffusion process (4). In this the niobium rods are placed into a bronze matrix and jointly extruded. Once the final dimension is attained, the wire is subjected to heat treatment upon which tin selectively diffuses from the copper-tin matrix into niobium. This process is often executed after solenoid winding since the heat-treated wire can only to a limited extent be mechanically deformed.

The most commonly used superconductor is NbTi, an alloy, which is relatively ductile, and which can be extruded into wire in a relatively straightforward manner. Its theoretical critical field at the temperature of liquid helium is 11.8 T.

A more powerful superconductor is Nb<sub>3</sub>Sn, which is superconduc-

tive below 18°K with a critical field of 20 T at the temperature of liquid helium at ambient pressure. Another superconductor which so far has played only an insignificant role in superconducting magnet technology is V<sub>3</sub>Ga. The latter two have in common that they are intermetallic compounds that are both extremely brittle and therefore most difficult to process.

An important criterion of a superconductor is its critical current density, i.e., the limiting value of transport current density. Generally this quantity is found to decrease monotonically with increasing field strength. However, even when operating below the critical current, local disturbances of various kinds may prevent a stable operating condition. It is therefore essential that the conductor be stabilized. Basically this is achieved by embedding the superconductor in a high-conductivity substrate material (typically copper). The effect is threefold: heat generated from local disturbances is dissipated to the helium and the matrix material acts both as a current bypass and for the attenuation of flux penetration. A critical requirement of a supercon magnet is field persistence, i.e., the extent of decay in field per hour. Using special jointing techniques, persistencies of 2 parts in 10<sup>8</sup> per hour have been reached routinely and even values up to 1 in 10<sup>10</sup> (0.05 proton Hz/hour) were attained (5).

If a magnet fails to operate in the persistent mode, it is resistive in either the coil itself, or in the so-called joints, i.e., those critical interfaces where two wires join each other. Joint technology, in particular where Nb<sub>3</sub>Sn is concerned, is probably the most tightly kept secret of magnet manufacturers. Oxford Instruments, Ltd., which currently manufactures the highest field super-homogeneous superconducting magnet operating in the persistent mode, undoubtedly owes its lead to precisely this expertise. The 500 MHz ethyl benzene spectrum in Figure 2, recorded over a 30 minutes period in the absence of field lock illustrates the remarkable stability of this magnet (6).

For the construction of persistent-mode multifilament magnets above 9.2 T a design strategy has been adopted in which a background field of ca. 8 T is generated by means of an outer solenoid consisting of NbTi multifilament wire, wound on an aluminum former and potted in a binding matrix to prevent wire movement. Inside this coil a Nb<sub>3</sub>Sn insert coil is placed that is run in series with the outer solenoid.

Another major challenge in supercon magnet technology is achievement of field uniformity. It should for example be borne in mind that in order to obtain a given line width at 500 MHz requires a 5 times better field homogeneity than at 100 MHz spectrometer frequency. Realization of say 0.1 Hz proton resolution, a value which has been achieved and surpassed, therefore demands the utmost in terms of workmanship and quality of material. This concerns, among other factors, constancy of wire diameter and uniformity of winding. In spite of these precautions, such ambitious objectives necessitate various forms of field corrections, whose detailed discussion however, would break the scope of this article.

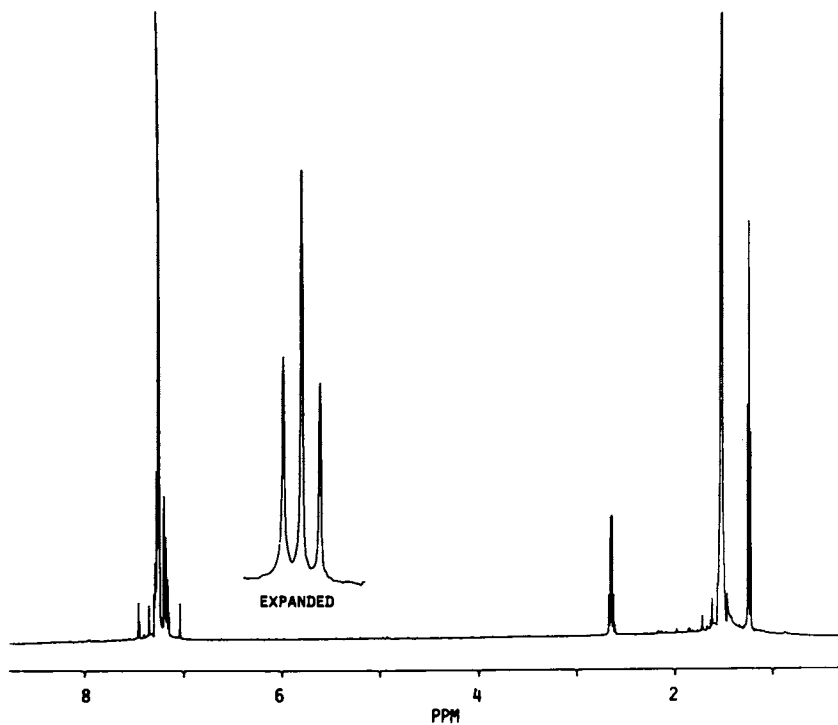


*Figure 2. A 500-MHz proton spectrum of 0.01% ethylbenzene standard, recorded over a 30 min total accumulation time in the absence of field/frequency lock. Inset shows expanded methyl triplet (6).*

The resolution and line shape test spectra in Figures 3a and b obtained at 500 MHz demonstrate that a level of performance has become feasible that until recently was unachievable even at a considerably lower field. Obtainment of this degree of field uniformity is crucial, however, if the benefit of enhanced shift separation is to be fully exploited.

#### Instrumental Requirements at Very High Field

The magnet, though the heart of the spectrometer, is not the only component that puts higher demands on its performance. A particular challenge, for example, is probe technology, both in terms of observation and decoupling, since at 500 MHz one approaches the frequency range which is midway between radio frequencies and microwaves. This led to hybrid cavity resonators which have successfully been used for both proton observation and proton heteronuclear broadband decoupling. Outstanding sensitivity can be obtained by this approach. The S/N ratio of 20:1 on 0.01% ethyl benzene, recently achieved on a WM-500 spectrometer, is nearly two orders of magnitude better than that of a 1970 vintage electromagnet system, thus providing access to experiments on either extremely small sample quantities (submicrogram) or at very low concentrations ( $10^{-5}$  -  $10^{-6}$  molar).

A number of additional requirements are related to the increased spectral windows demanding faster ADC's, larger data memories and disk storage capacities and, in order to ensure uniform excitation across the full spectrum, increased pulse power. A 200 ppm  $^{19}\text{F}$  spectrum, for example, at 11.7 T is nearly 100 KHz wide, thus requiring sampling at 200 KHz. The achievable resolution under such circumstances is almost certainly not limited by magnet homogeneity but rather by data memory. From the data in Table III, it can be inferred that at 11.7 T a 250 ppm  $^{13}\text{C}$  spectrum requires at least 128 K of data memory in order to obtain a digital resolution of .5 Hz. Although the cost of computer memory has steadily decreased over the past years, it may be of benefit to enhance digital resolution in other ways than by adding memory chips. This can, for example, be realized by storing the acquired data points onto disk during the dwell time, i.e., the interval between two digitizer samples. This so-called virtual memory capability allows one to acquire very large data tables and its only limitation lies in spectral width since the maximum rate at which data can be sampled and stored is dictated by the disc transfer rate. For a modern high-speed disc drive, transfer rates are such that in the disc acquisition mode spectral widths of typically 50 KHz have become feasible, which is adequate for most high-resolution applications. The potential of this approach is exemplified by the ultra-high-resolution spectrum of ethyl benzene in Figure 4 obtained by disk acquisition of 256 K data points (6). In this remarkable spectrum almost all of the aromatic protons are completely separated, showing long-range couplings between methylene and ring protons.

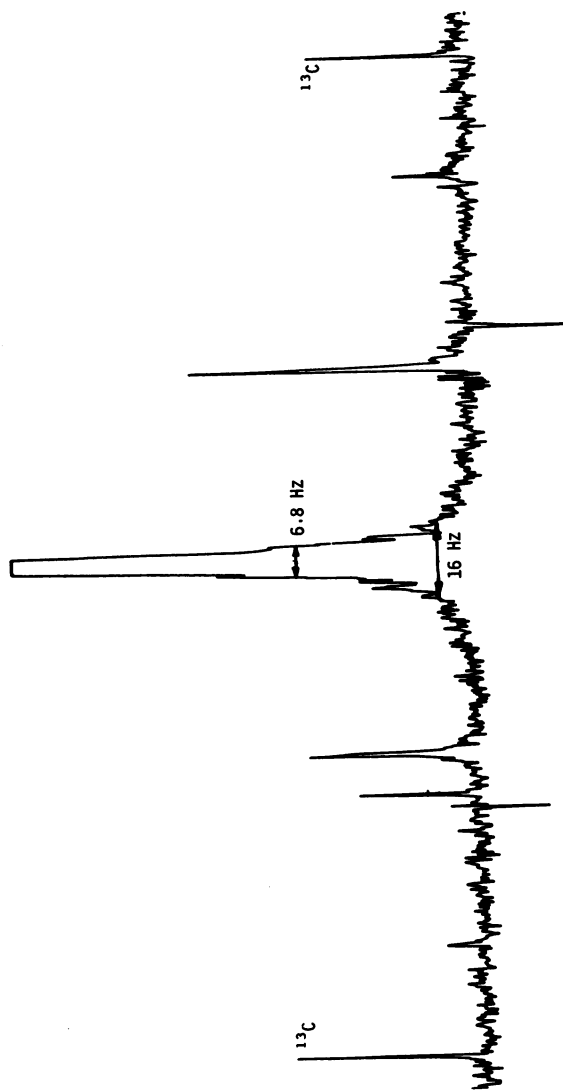


Figure 3a. A 500-MHz lineshape test showing chloroform line width at a height of  $^{13}\text{C}$  satellites and at a height 1/5 thereof. Recorded on a 5-mm o.d. sample.

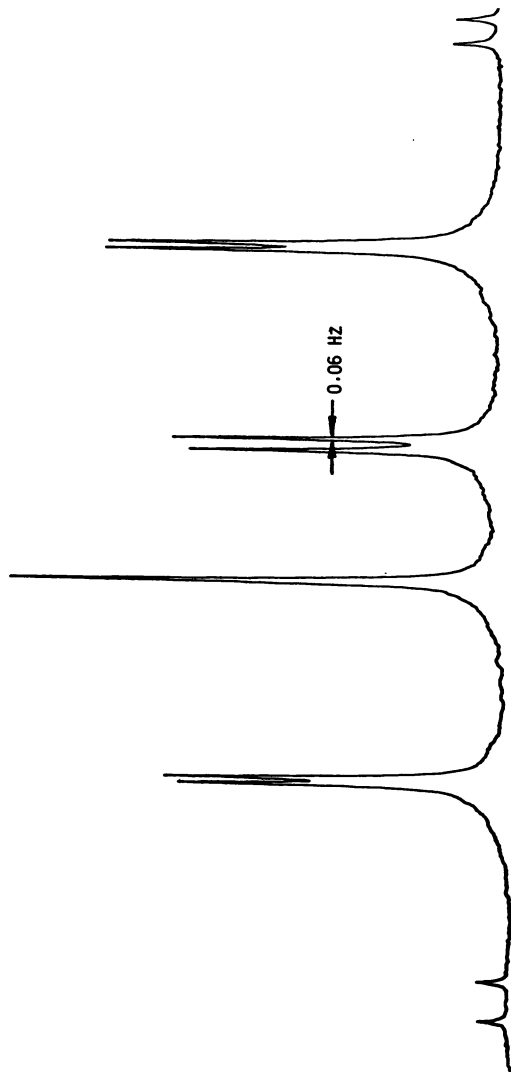
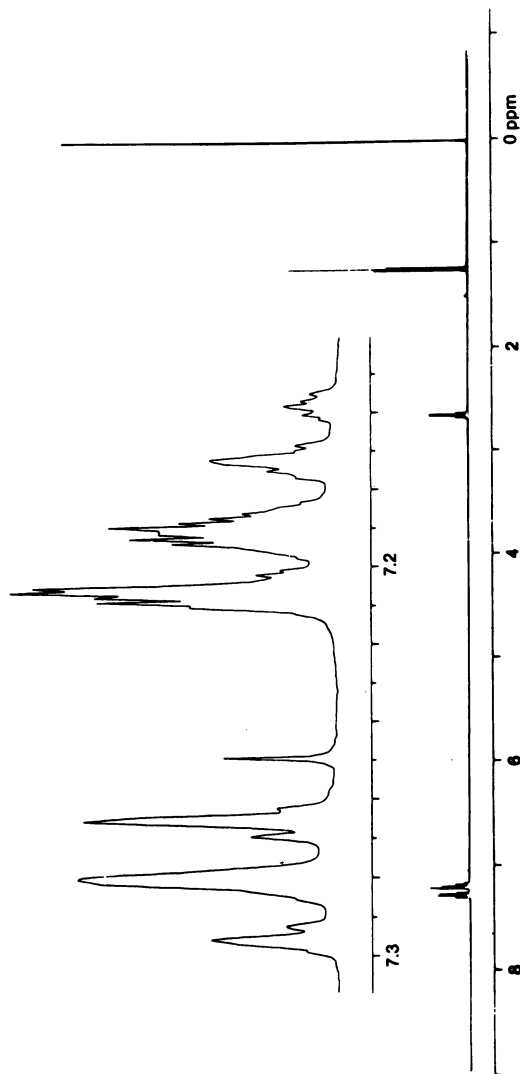
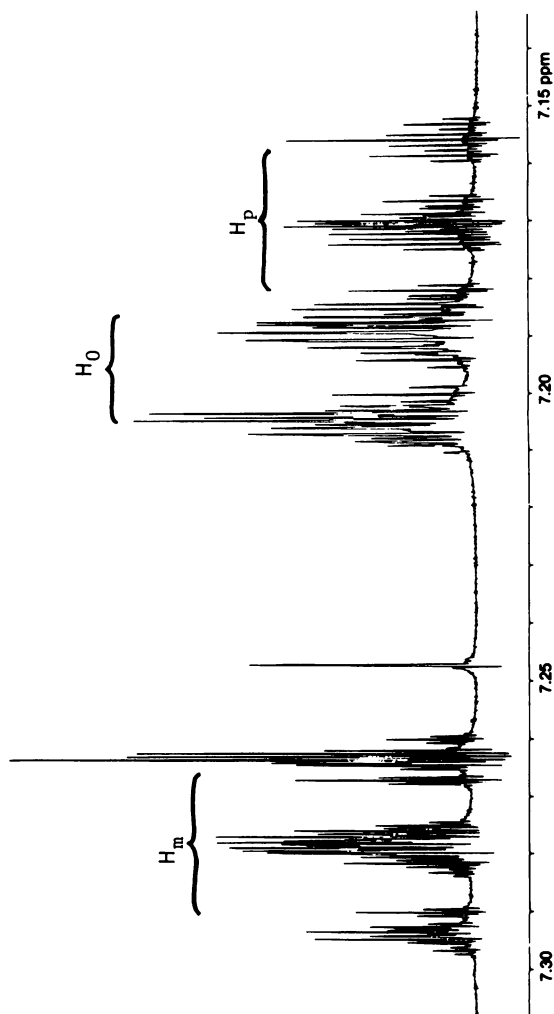


Figure 3b. A 500-MHz resolution test showing the high-frequency half of the o-dichlorobenzene signal. Recorded on a 5-mm o.d. sample.



*Figure 4a. A 500-MHz proton NMR spectrum of 1% ethylbenzene obtained by in-core acquisition and transformation of 32 K data points without further data manipulation. Inset shows expansion of aromatic region.*



*Figure 4b. Aromatic portion of the spectrum of the same sample recorded by disk acquisition and transformation of 128 K data points using a total of 48 K hardware memory. Resolution was further enhanced by Lorentz-Gauss transformation (6).*



Table III: Data memory requirements for a digital resolution of 0.5 Hz across a 250 ppm  $^{13}\text{C}$  spectrum at different spectrometer frequencies.

FIELD (T)	$^1\text{H}$ FREQUENCY (MHz)	MEMORY CAPACITY (K WORDS)
2.3	100	32
5.7	250	64
11.7	500	128

The transformation time of such large data sets becomes of the order of minutes, eventually invoking hardwired Fourier transform processors. Although currently not in use on any commercial NMR spectrometers, array processors are expected to supersede Fourier transformation by software over the next few years.

Concomitant with the increased data size, the memory requirements for permanent storage will render it necessary to expand the storage capacity of backup stores. Disk storage capacities of over 100 M-byte, as they have become available in the form for example of the CDC 9730 Series, are a true necessity in many high-field NMR applications. Memory requirements are particularly severe in two-dimensional spectroscopy such as the 2D-J experiments where spectral arrays are obtained in which spin-spin coupling is separated from chemical shielding. A 10 ppm  $\times$  50 Hz 2D spectrum with a digital resolution of 2 Hz on the  $\delta$  axis and 0.2 Hz on the J axis, for example, corresponds to a 4 M-word data matrix.

An additional consequence of the widened spectral windows at high spectrometer field is the requirement for enhanced pulse power. In order to assure uniform excitation across the full spectral width the rf pulses have to be sufficiently short. This is particularly critical to achieve with high-Q multinuclear probes, and a fully satisfactory solution to this problem has at this time not been found. In Figure 5 the transmitter rf amplitude distribution for a 25 microsecond pulse is illustrated for a 250 ppm  $^{13}\text{C}$  spectrum at three different field strengths, showing only minimal droop across the spectrum at 2.3 T but a considerable fall-off at 11.7 T. In practice, this problem is alleviated since relaxation often demands pulse flip angles that are considerably less than 90°. Moreover, it turns out that the fall-off of rf amplitude is largely offset by the increased effective rf field that exists at frequencies more remote from the carrier.

### Typical Applications

Clearly the greatest benefits of very high magnetic field are expected in proton spectroscopy of large biological molecules such as peptides, proteins, nucleic acids, etc. Organic chemists however, who have struggled with the analysis of proton spectra of natural products and their synthetic analogs will agree that the spectra of rather low-molecular weight molecules (MW 200-500) may be entirely

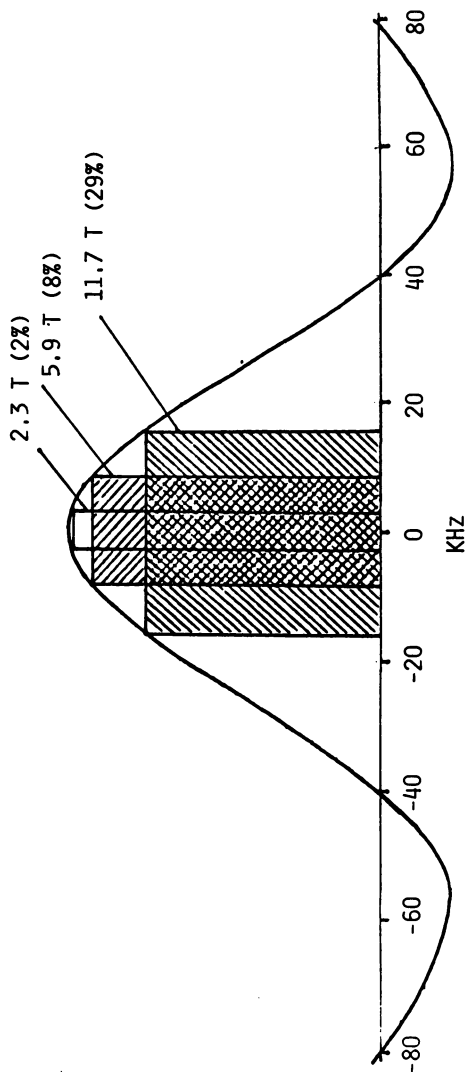


Figure 5. RF amplitude distribution across a 250-ppm  $^{13}\text{C}$  NMR spectral window for a 25- $\mu\text{s}$  excitation pulse at three different magnetic field strengths. Percentage numbers indicate total variation of amplitude.

uninterpretable unless nature has blessed them with at least one or several electronegative substituents or multiple bonds. In this unfortunate but rather common situation two dozen magnetically nonequivalent protons may typically be squeezed in the region between 1 and 2.5 ppm. Not only are such spectra highly second order, but worse, their individual multiplets are mutually overlapping. The expert NMR spectroscopist rapidly concludes in such a situation that any further effort is a waste of time. Figure 6 illustrates the power of 500 MHz  $^1\text{H}$  NMR of a medium-sized molecule (7). Among the 18 magnetically nonequivalent groups of protons in guajol (MW=222), 16 give rise to separated multiplets in spite of their total resonance range of only 1.6 ppm. Figure 6b shows the expanded spectrum following a Lorentz-Gauss transformation of the free induction decay, allowing extraction of three and more different spin-spin coupling constants per multiplet. The highest field proton, for example, shows coupling constants of 13.5 Hz (geminal), 10 Hz (vicinal axial-axial) and 5 Hz (vicinal axial-equatorial). Assuming the C-4 substituent to be equatorially disposed, this proton has to be assigned to either H(2)<sub>ax</sub> or H(3)<sub>ax</sub> since the multiplicity pattern shows two equal equatorial interactions and one each of the axial-axial and geminal type. Since assignment of H(1) is straightforward, a single double resonance experiment would eliminate this ambiguity and at the same time corroborate the stereochemistry at C(1) or C(4).

Among the many applications of the technique,  $^{13}\text{C}$  NMR has been found to be the method of choice for the characterization of synthetic polymers such as sequence analysis, end group determination and elucidation of stereoregularity in vinyl polymers. In a vinyl polymer, for example, the CH shielding in the  $-\text{CHX}-\text{CH}_2-$  repeating unit depends upon the configuration of the asymmetric carbon of its neighbors and nearest neighbors. If only nearest neighbors can be distinguished, triad splittings are observed, according to the stereochemical dispositions mm (meso meso), mr, rm (meso racemic or its indistinguishable racemic meso) and rr. If next nearest interactions can be differentiated, so-called pentad splittings result (maximum 10). Increased field clearly augments the capability of resolving this fine structure and the spectrum of atactic poly(vinyl chloride) in 1,4-dioxane in Figure 7 (8) shows evidence of heptad fine structure, i.e., lines resulting from contributions of repeating units in third position relative to the carbon observed. In this case, 16 out of the theoretical 36 observationally different heptads could be fully resolved.

Another nucleus of considerable analytical potential is deuterium, whose observation at natural abundance has been demonstrated earlier (9) but whose practicality has so far been severely limited due to its low NMR receptivity and also because of its more than six times smaller chemical shift range relative to the proton. These limitations are largely overcome at high magnetic field as illustrated by the natural-abundance deuterium spectra of camphor in Figure 8.

By lining up the proton-decoupled deuterium spectrum with the

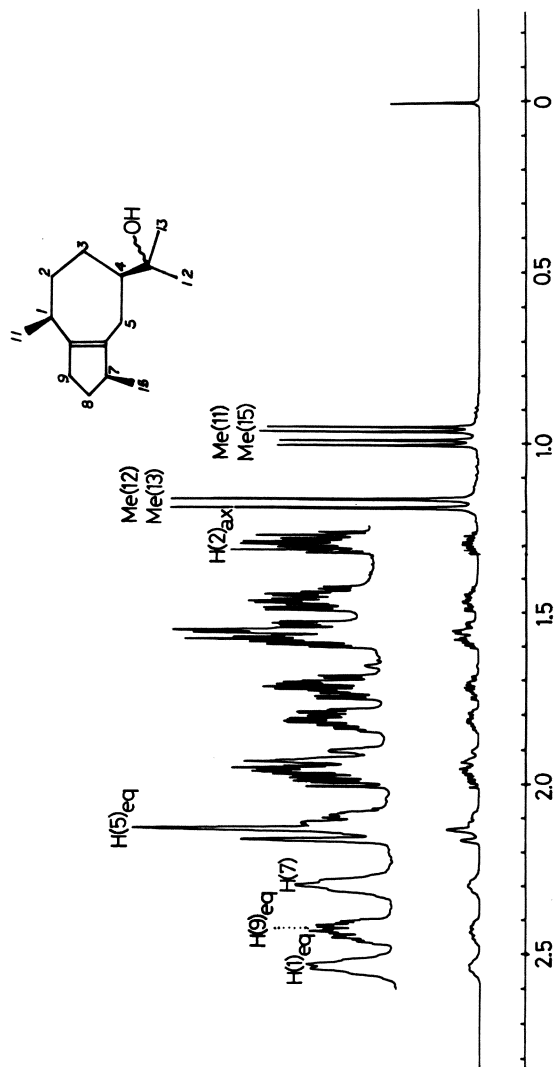


Figure 6a. A 500-MHz  $^1\text{H}$  full spectrum of guaiol with partial assignments. Resolution in this spectrum was further enhanced by a Lorentz-Gauss transformation of the free induction decay (F).

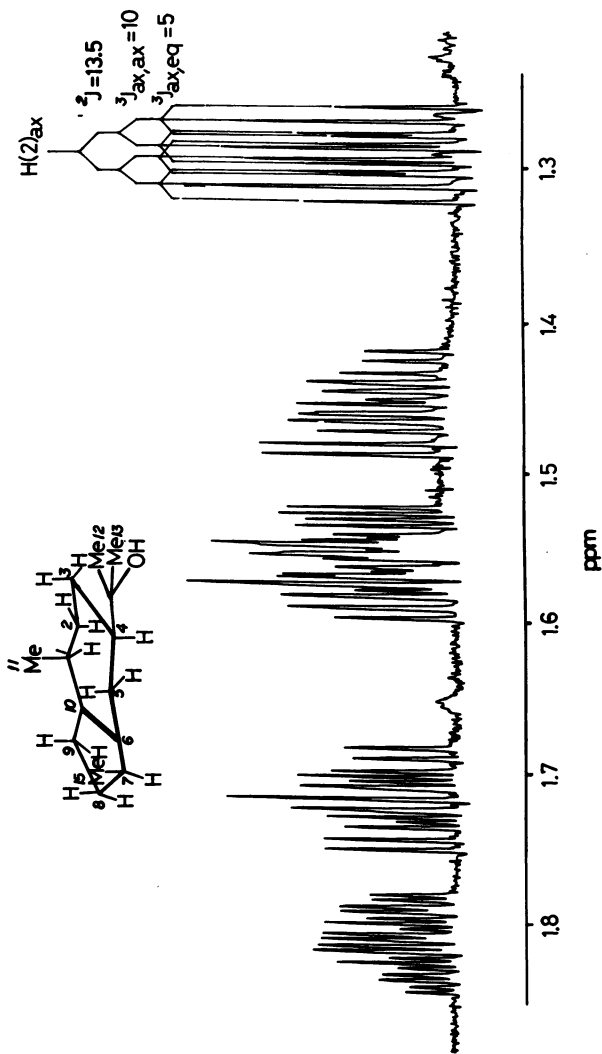


Figure 6b. 500-MHz  $^1\text{H}$  spectrum of guaijol with partial assignments. Region between 1.3 and 1.8 ppm expanded. Resolution in this spectrum was further enhanced by a Lorentz-Gauss transformation of the free induction of decay (7).

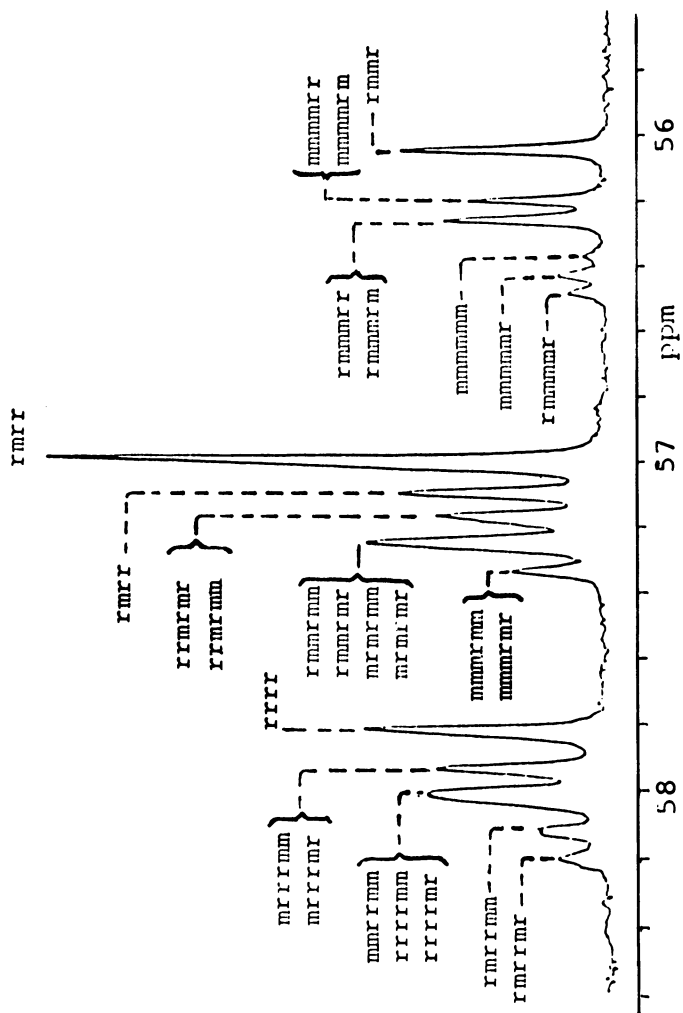


Figure 7. A 125.8-MHz  $^{13}\text{C}$  NMR spectrum of the methane carbon region in polyvinyl chloride, 10% in 1,4-dioxane- $d_8$  at 370 K. Configurational assignments are based on the relative triad intensities assuming Bernoullian statistics (8).

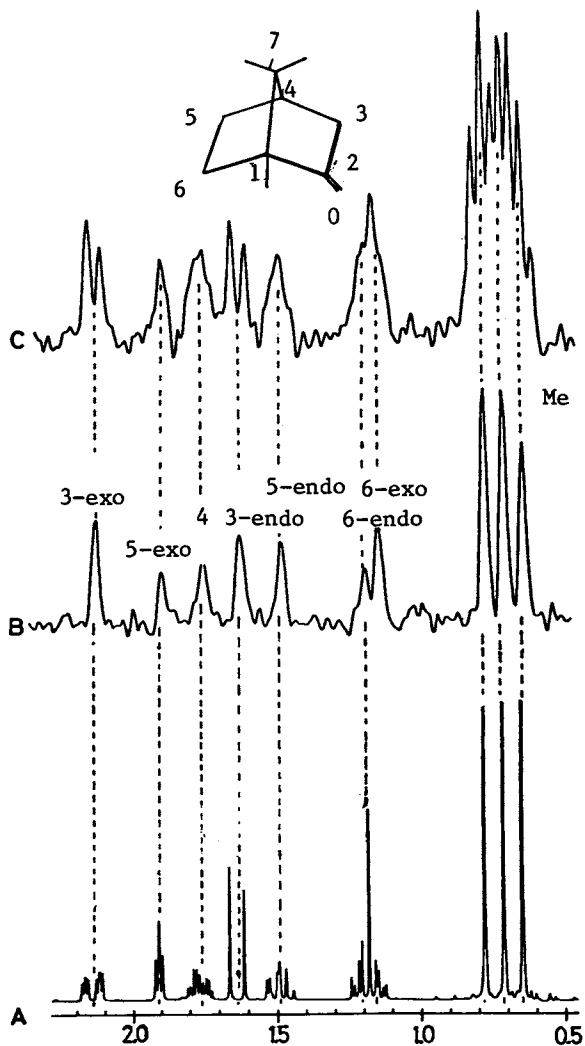


Figure 8. A, A 360-MHz proton NMR spectrum of camphor, 2 M in deuteriochloroform; B and C, A 55-MHz natural-abundance  $^2\text{H}$  NMR spectrum of the same sample with (B), and without (C) proton broadband decoupling.

respective proton spectrum on the same ppm scale (Figures 8a and b) the 1:1 correspondence of the two spectra becomes apparent. High-resolution deuterium NMR spectra may therefore be drawn upon to establish chemical shifts in complex proton spectra to provide a set of starting parameters for computer-aided spectral analysis.

Further diagnostic information may be derived from the proton-coupled deuterium spectrum as illustrated in Figure 8c showing multiplets due to geminal  $^2\text{H}$ - $^1\text{H}$  coupling; for example triplets for methyl groups and doublets for the signals due to the isolated hydrogens  $\text{H}(2)_{\text{eq}}$  and  $\text{H}(2)_{\text{ax}}$ . Other multiplets remain unresolved since the geminal couplings are obscured by vicinal and long-range coupling.

As quadrupole relaxation dominates deuterium relaxation, high-resolution  $^2\text{H}$  NMR in liquids will be confined to small and medium-sized molecules where relaxation broadening is moderate. Assuming for example a correlation time of  $10^{-11}$  sec as it is typical of a molecule of MW ~ 250, a natural  $^2\text{H}$  line width of 1.5 Hz results based upon a quadrupole coupling constant of 180 kHz.

A somewhat esoteric application of deuterium NMR, which is totally outside the realm of the possible at low field concerns the determination of the anisotropy of the diamagnetic susceptibility. This experiment, first suggested by Dutch workers MacLean and Lohman, (10) is based upon the fact that the static quadrupole splitting may not be totally averaged due to partial alignment of the molecule at high magnetic field strength. While dipolar splittings are too small to be retained during motional averaging, the quadrupolar interaction is large enough to be detectable at fields above ca. 9.2 T. Field strength is critical since the splittings are proportional to the square of the magnetic field. Figure 9 shows the resolution-enhanced 77 MHz (11.7 T) deuterium spectrum of nitrobenzene displaying quadrupole splittings for all three magnetically nonequivalent deuterons (11).

There are many more nuclei whose potential cannot be exploited unless the chemical shifts are dispersed beyond the line widths. This holds true for the great deal of quadrupolar nuclei which constitute the bulk of the magnetic nuclei in the Periodic Table and which play an important role in inorganic chemistry.

The utility of high magnetic field in this area may be illustrated with an example from inorganic solution chemistry, related to some recent work in this laboratory directed toward the characterization of the solution species formed upon dissolving the aluminum halides in polar organic solvents (12).

While, for a long time, it was assumed that in polar solvents the dimeric  $\text{Al}_2\text{Cl}_6$  breaks up into  $\text{AlCl}_4^-$  and  $\text{AlS}_6^{3+}$  ( $\text{S}$  = acetonitrile), this view was recently challenged (13) as a result of the  $^{27}\text{Al}$  spectra which suggest the existence of mixed species  $[\text{AlCl}_n\text{S}_{6-n}]^{3-n}$ . However, conclusive evidence was only provided by experiments at high field. Figure 10 shows a stacked plot of 93.7 MHz  $^{27}\text{Al}$  NMR spectra of  $\text{AlCl}_3$  in acetonitrile recorded at different solute concentrations. These signals are due to above-mentioned hexacoordinated solvate/counterion complexes which could be identified on the basis of characteristic chemical shifts and predictable



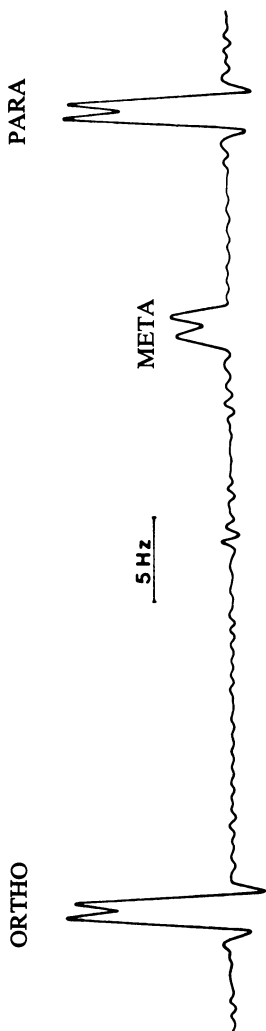


Figure 9. A 76.8-MHz resolution-enhanced deuterium NMR spectrum of neat nitrobenzene showing quadrupole splittings due to partial alignment resulting from anisotropy of diamagnetic susceptibility. (Reproduced, with permission, from Ref. 11. Copyright 1981, Academic Press.)

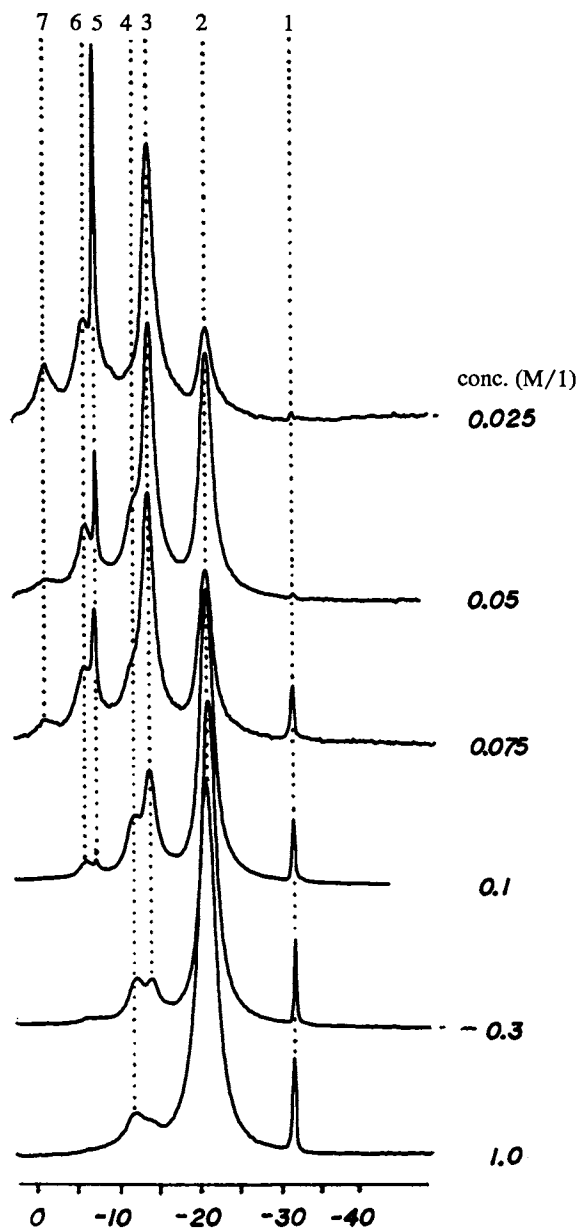


Figure 10. High-field  $^{27}\text{Al}$  NMR spectra of aluminum chloride in acetonitrile solution showing the resonance region of hexacoordinated Al. Peak designations: 1,  $\text{Al}(\text{CH}_3\text{CN})_6^{3+}$ ; 2,  $[\text{AlCl}(\text{CH}_3\text{CN})_5]^{2+}$ ; 3, *cis*- $[\text{AlCl}_2(\text{CH}_3\text{CN})_4]^+$ ; 4, *trans*- $[\text{AlCl}_2(\text{CH}_3\text{CN})_4]^+$ ; 5, *cis*- $\text{AlCl}_3(\text{CH}_3\text{CN})_3$ ; 6, *trans*- $\text{AlCl}_3(\text{CH}_3\text{CN})_3$ , and 7, *cis/trans*- $[\text{AlCl}_4(\text{CH}_3\text{CN})_2]^-$ . (Reproduced, with permission, from Ref. 12. Copyright 1981, Academic Press.)

quadrupole relaxation rates. The closely spaced line pairs 3/4 and 5/6, for example, reflect the effect of *cis/trans* isomerism in  $[\text{AlCl}_2\text{S}_4]^+$  and  $\text{AlCl}_3\text{S}_3$  which would clearly be unresolvable if the field strength were halved.

In conclusion, it may be stated that NMR at very high field has given the technique an unprecedented impetus. As a consequence of the enhanced shift separation the spectral information content has been greatly increased, opening up a range of new experiments. Together with the concomitant sensitivity increase this will have a significant impact on a variety of research areas, notably molecular biology, macromolecular chemistry, but also organic and inorganic chemistry in general.

#### LITERATURE CITED

1. Bruker Report 3/1979.
2. 600 MHz Symposium at Carnegie-Mellon Institute, 1979.
3. McDonald, P. & Proctor, W., Proceedings of the Eighth International Cryogenic Engineering Conference, 1980, p. 509.
4. Kwasnitza, K., Narlikar, A.V., Nissen, H.U., & Salate, D., Cryogenics 20, 715, 1980.
5. Hull, W. E., personal communication.
6. Hull, W. E., personal communication.
7. Formacek, V., personal communication.
8. Elgert, K.F., Kosfeld, R., & Hull, W.E., personal communication.
9. Shoolery, J.N., Varian Application Topic, 1977, p. 7-14.
10. Lohman, J.A.B., & MacLean, C., Chem. Phys., 1978, 35, p. 269; 1979, 43, 144.
11. Lohman, J.A.B., MacLean, C., J. Magn. Res., 1981, 42, p.5.
12. Wehrli, F.W. & Wehrli, S.L., J. Magn. Res., 1981, 44.
13. Akitt, J.W. & Duncan, R.H., J. Magn. Res., 1977, 25, 391.

RECEIVED February 2, 1982.

## NMR Spectroscopy at 600 MHz

A. A. BOTHNER-BY and J. DADOK

Carnegie-Mellon University, Department of Chemistry, Pittsburgh, PA 15213

In December 1979, the NMR Facility for Biomedical Studies formally opened service on the 600 MHz NMR spectrometer assembled there, and the intervening year has seen a variety of applications to structure made possible by the high magnetic field (14.1 Tesla) employed.

The first advantage which comes to mind when considering the use of high magnetic fields for NMR is the increased spectral dispersion which results, and the possibility of separating and observing signals from complex molecules which are not resolved at lower fields. This advantage is well understood and widely appreciated, and only a few illustrative examples will be given here.

An example of the degree of complexity which can be sorted out is Palytoxin, a water-soluble toxin obtained from marine coelenterates of the genus Palythoa. The molecular formula of the compound is  $C_{129}H_{221}N_5O_{54}$ . The complete gross structure for Palytoxin has been elucidated by R. E. Moore and G. Bartolini of the University of Hawaii and reported in a recent communication (1). The structural elucidation involved extensive proton spectroscopy at 600 MHz, together with homonuclear decoupling, to establish the sequence and stereochemistry in degradation fragments as well as the entire molecule. The structure deduced is displayed in Figure 1, with the spectrum of the intact toxin shown beneath. An expanded view of a portion of this spectrum is displayed in Figure 2. The structure of an N-terminal degradation product and its spectrum is displayed in Figure 3.

A second example illustrating the greater dispersion at high field is bradykinin, a nonapeptide with sequence arg-pro-pro-glyphe-ser-pro-phe-arg. The spectrum of this peptide and of a number of analogs has been investigated in a collaborative effort with Dr. G. Fisher of the University of Miami. The spectrum with assignments is shown in Figure 4. The separate observation of  $\beta$  protons from each of the three proline residues has made it possible, for example, to determine the degree of puckering and preference for Ramachandran A or B forms in proline rings. Analysis of coupling constants in the side chains, amide proton

0097-6156/82/0191-0031\$06.00/0

© 1982 American Chemical Society

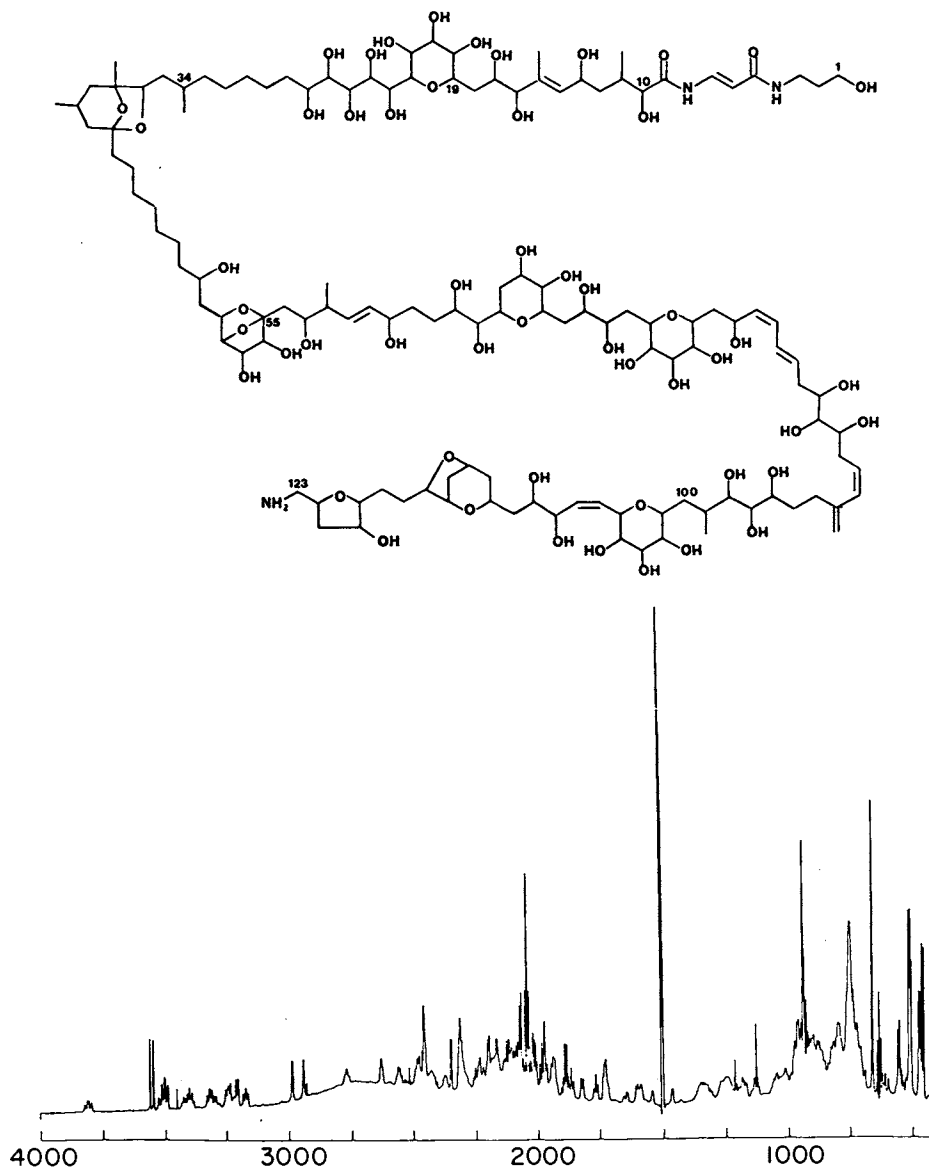


*Figure 1. A 600-MHz high resolution spectrum of palytoxin, a marine toxin isolated from a species of Palythoa. The gross structure deduced for the toxin also is shown.*

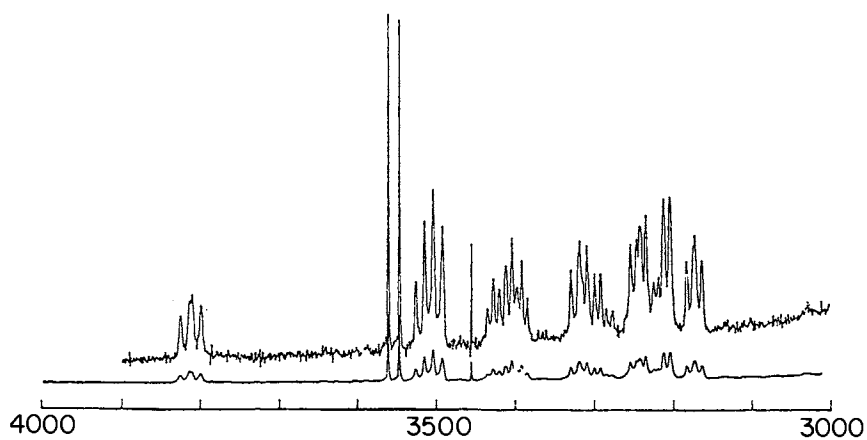


*Figure 2. Expanded view of a small region of the spectrum of palytoxin shown in Figure 1.*



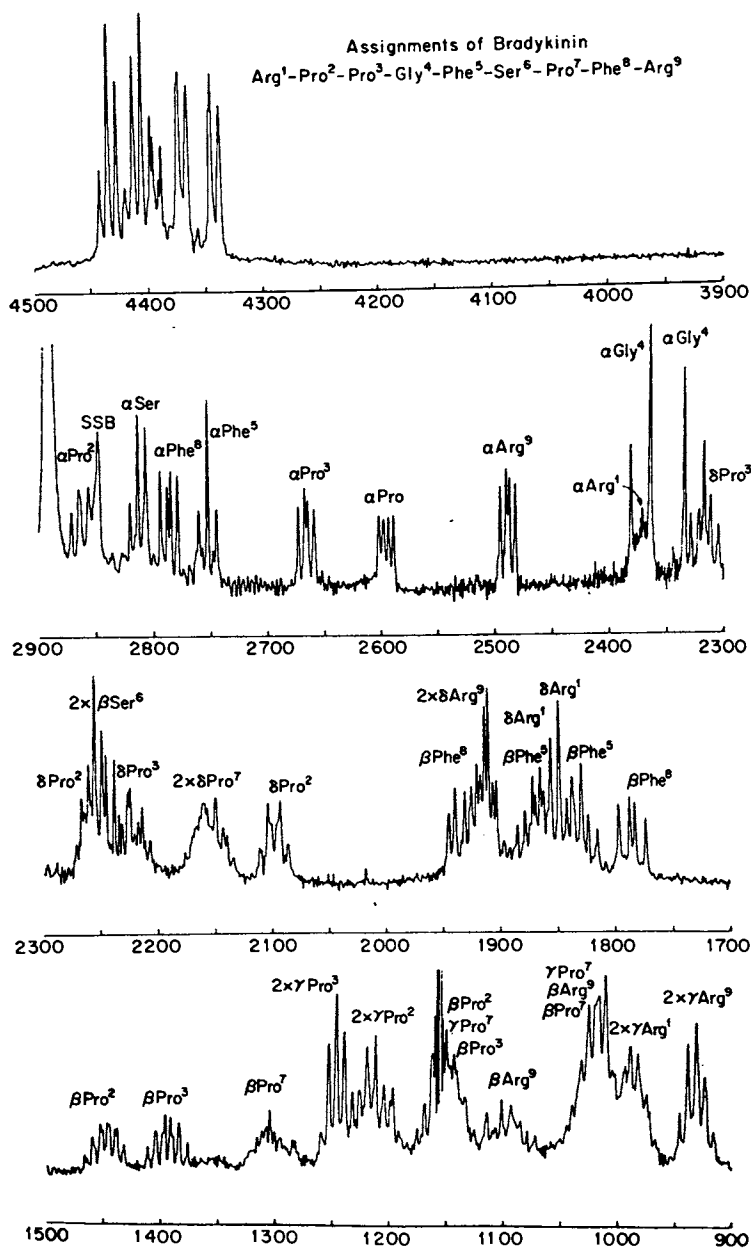


Figure 4. A 600-MHz spectrum of bradykinin in  $D_2O$  solution.



shifts, pH titration, use of paramagnetic shift and broadening reagents, and other standard NMR techniques have been applied to demonstrate that bradykinin is a rapidly interconverting mixture of many conformers, with no highly preferred conformation in solution, but that complexes are formed with lipids, particularly at pro<sup>7</sup> and phe<sup>8</sup> which impose some conformational restraint on the molecule (2).

Other classes of compounds for which the extra resolving power at high field has been useful include DNA restriction fragments (investigated by T. A. Early, D. R. Kearns, W. Hiller and R. D. Wells (3)); alkaloids (S. Danishefsky (4)), and sugars (5).

A second advantage of higher fields is that rapid chemical exchange processes (for example between conformational states) are more readily apparent. Line broadening in the rapid exchange limit is given by:

$$\Delta\nu_{1/2} = \pi p_A^2 p_B^2 (\nu_A - \nu_B)^2 \tau$$

where  $\Delta\nu_{1/2}$  is the increased line width,  $p_A$  and  $p_B$  are the fractions of the two conformers,  $(\nu_A - \nu_B)$  the chemical shift in frequency units between nuclei in the two conformers, and  $\tau$  the average residence time in one conformer. Increasing the field by a factor of ten will increase the line broadening by a factor of one hundred; rapid exchange processes which cause a broadening of 0.1 Hz at 60 MHz and might escape notice, will cause a broadening of 10 Hz at 600 MHz and will be very noticeable.

Thus Professor J. Glasel (6) noted that the 600 MHz spectrum of morphine at physiological pH was broad (Figure 5), (although the low field spectrum appeared normal). This suggested a conformational equilibrium (axial-N-methyl  $\rightleftharpoons$  equatorial N-methyl). The conclusion was confirmed by observing the spectrum at pH 1.5, which slowed the interconversion and gave a sharp spectrum showing signals from each conformer. The intensities were in the ratio 1:5, indicating an energy difference of only about 1 Kcal/mole, although earlier calculations (7) had predicted the N-equatorial conformer to be more stable by about 6 Kcal/mole. The interesting question arises as to which conformer is bound in the receptor site, and the role of the lone pair in binding.

The availability of higher fields also opens the door to the observation of features in the NMR spectrum which depend quadratically on the field strength. In particular, the field is sufficiently strong so that even relatively small diamagnetic and paramagnetic molecules with anisotropic magnetic susceptibilities are significantly oriented, and the ordering produces observable effects in the spectrum. Such effects have been observed in the past with molecules in macroscopic crystals which are either physically oriented, or are oriented by the field, (8) or by observing the spectra of the molecules dissolved in liquid crystals (in which the liquid crystal domains are oriented by the field), (9) or by the application of a strong electric field to solutions of polar molecules (10).

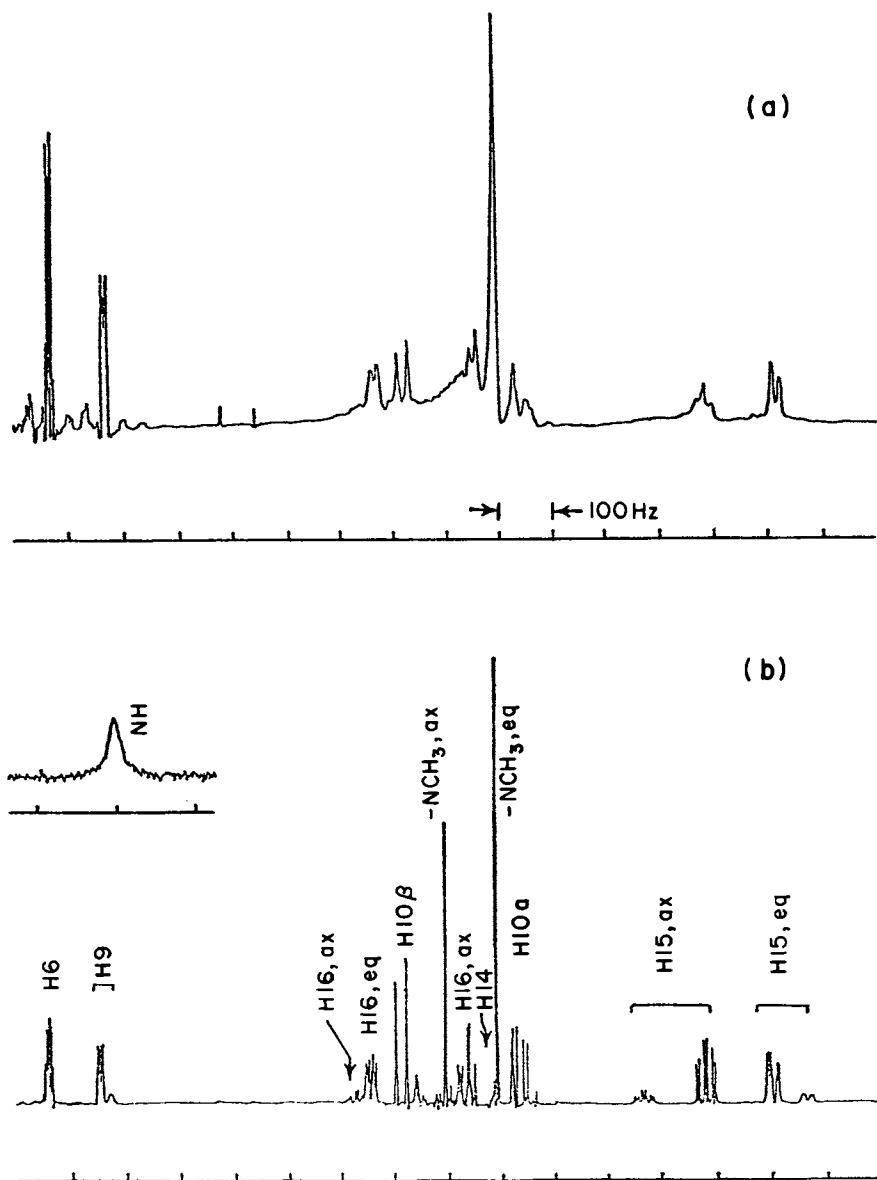


Figure 5. Spectra of morphine at neutral and low pH demonstrating the occurrence of exchange phenomena at neutral pH (a) and slow interconversion of axial and equatorial N-methyl isomers at low pH (b).

Following the treatment of Lohman and MacLean, (11) the ordering of the molecule may be described in terms of two ordering parameters  $S$  and  $K$ , which are defined by the relations

$$S = \langle 3/2 \cos^2 \theta - 1/2 \rangle$$

$$K = \langle \sin^2 \theta \cos 2 \varphi \rangle$$

The angular brackets denote an expectation or time-averaged value, and  $\theta$  and  $\varphi$  are the polar angles giving the direction of the static magnetic field in the molecule-fixed coordinate frame  $x, y, z$ . These axes are chosen to be the principal axes of the magnetic susceptibility tensor of the molecule.

The energy of the molecule in a magnetic field is given by the expression

$$E = -1/2 H \cdot \underline{\chi} \cdot H$$

The ordering parameters  $S$  and  $K$  may be calculated assuming a Boltzmann distribution, and are then given by

$$S = \Delta \chi H^2 / 15kT$$

$$K = \Delta_{\perp} \chi H^2 / 15kT$$

where  $\Delta \chi$  the susceptibility anisotropy is given by  $\chi_{zz} - 1/2 (\chi_{xx} + \chi_{yy})$ , and  $\Delta_{\perp} \chi$  the susceptibility asymmetry is given by  $\chi_{xx} - \chi_{yy}$ .

For aromatic molecules,  $\Delta \chi$  amounts to about  $1 \times 10^{-28} \text{ cm}^3/\text{mol}$  per benzene ring (12), while  $\Delta_{\perp} \chi$  is expected to be an order of magnitude smaller, so the ordering parameter  $S$  for benzene at room temperature and 141 kilogauss is expected to be about  $3 \times 10^{-6}$ .

The parameter  $S$  for paramagnetic molecules is given by

$$S = 1/15 \left( \frac{\Delta \mu H}{kT} \right)^2$$

Substituting typical values of  $\Delta \mu$ , the parameter is found to be only one to two orders of magnitude larger than those of aromatic compounds.

The occurrence of this ordering can be detected in several ways using magnetic techniques. In the case of quadrupolar nuclei, such as deuterium, the ordering will give rise to a quadrupole splitting of the deuterium signal, as is well known from experiments with liquid crystals (13). The observation of large splittings in a small paramagnetic molecule arising from this origin have been reported by P. J. Domaille (14), and an example showing such splittings is given in Figure 6.

The observation of deuterium quadrupole splittings in the deuterium spectra of deuterated aromatic compounds has also been reported in a series of articles by Lohman and Maclean (11, 15, 16).

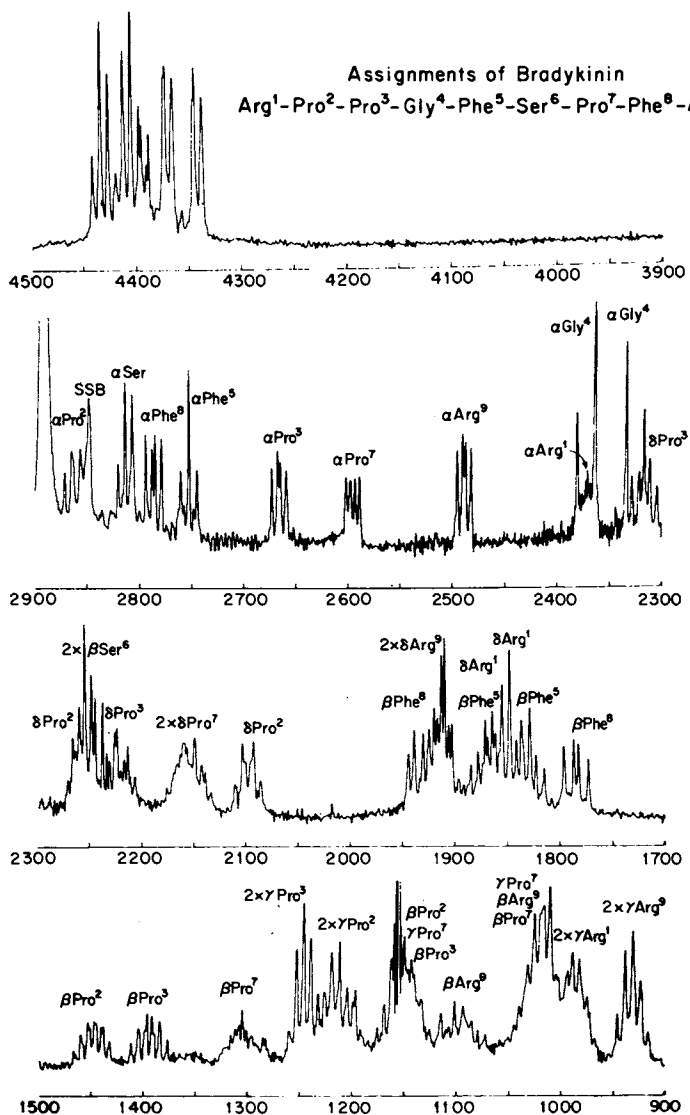


Figure 6. Observation of quadrupole splittings in the 92.1-MHz  $^2\text{H}$  spectrum of deuterated bis[*tolyl-tris(pyrazolyl)borato*]cobalt(II).

The magnitude of the observed splitting is given by

$$\delta\nu = \frac{3}{2} \left( \frac{e^2 q Q}{h} \right) (c_1 S + \frac{3}{4} c_2 K)$$

where

$$c_1 = \frac{1}{2} \{3l^2 - 1\}$$

$$c_2 = \{m^2 - n^2\}$$

and  $l, m, n$  are the direction cosines for the principal axis of the electric field gradient (taken to be coincident with the direction of the C-D bond) and the molecule-fixed coordinate axes. Figure 7 shows several spectra with the splittings well resolved. Since the size of the quadrupole coupling constant for deuterons attached to an aromatic ring is quite constant, this provides an independent method for determining the ordering and hence the susceptibility anisotropy and asymmetry of aromatic (and anti-aromatic) compounds).

Two nuclei separated by distance  $r$  interact via their magnetic dipoles, with

$$E = \frac{\gamma_1 \gamma_2 h}{r^3} \langle 3 \cos^2 \theta - 1 \rangle$$

when  $\theta$  is the angle between the internuclear axis and the static field. For randomly tumbling molecules  $\langle 3 \cos^2 \theta - 1 \rangle = 0$ , but preferential orientation of the molecule will cause this averaging to be incomplete, and dipolar splittings may become evident in the spectrum.

The first observation of such a splitting in a paramagnetic molecule has been made in collaboration with Dr. P. J. Domaille: the spectrum illustrating this is shown in Figure 8. The para methyl group is rigidly held in this molecule with the axis of maximum susceptibility along the three-fold axis of the methyl group. Consequently, an orientation is preferred in which the interproton axes are perpendicular to the field. The magnitude of the splitting is given by,

$$\mathfrak{J}_{DHH} = \frac{-3\gamma_H^2 h}{4\pi r_{HH}^3} S_0 \Gamma_0$$

where  $\Gamma_0 = \frac{1}{2} \{3 \cos^2 \psi - 1\}$ ,  $\psi$  being  $90^\circ$ , as stated above.  $K$  is zero by symmetry. From the known anisotropy in the susceptibility and the standard geometry of methyl groups, the splitting is predicted to be 15 Hz. The observed splitting is 16 Hz.

The observation of a direct dipolar contribution to the splitting of a methylene group in a diamagnetic molecule is shown in Figure 8. A sample of methyl pyropheophorbide a (Figure 9) was kindly supplied by Dr. J. J. Katz of Argonne National Laboratory. This compound is a chlorin, and is expected to have a large diamagnetic anisotropy. In addition, ring V of the chlorin

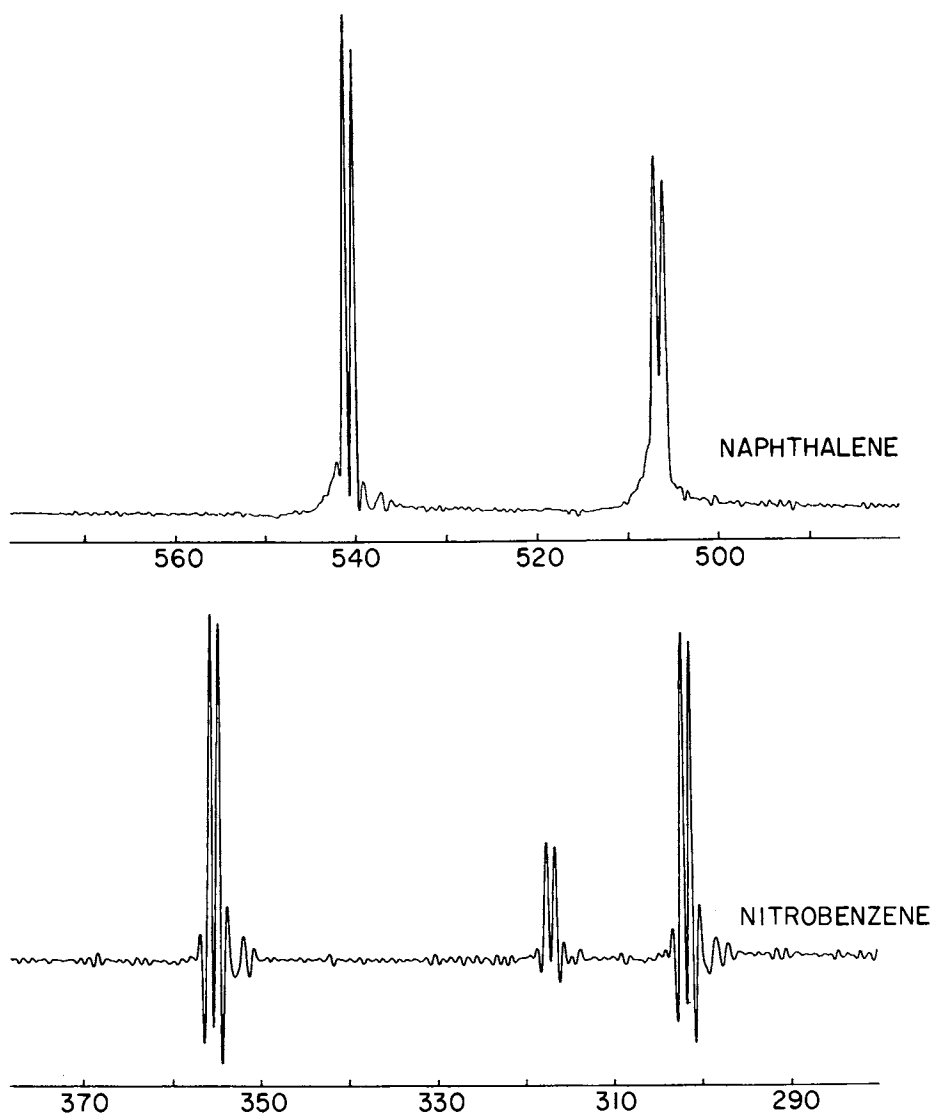


*Figure 7. A 92.1-MHz  $^2\text{H}$  spectra of perdeuterated naphthalene and nitrobenzene, illustrating quadrupole splitting arising from molecular orientation. A resolution enhancement filter was applied.*

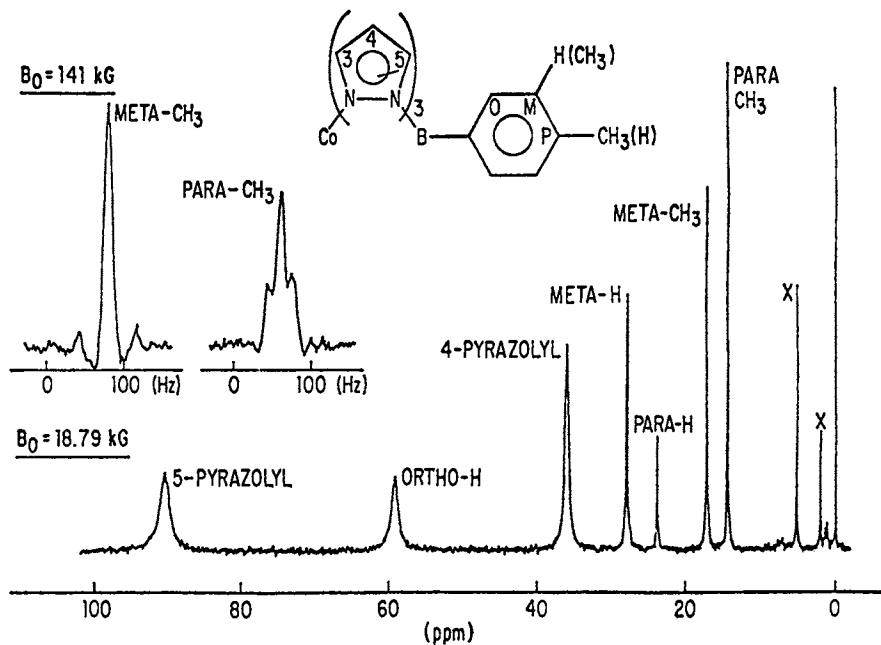


Figure 8. Observation of direct dipolar splitting in the signals from the p-methyl group of protio-bis[tolyl-tris(pyrazolyl)borato]cobalt(II). No splitting is observed in the signal from the m-methyl group because rotation about the  $\text{CH}_3$  axis, which is inclined at  $60^\circ$  to the axis of largest susceptibility, averages the interaction to near zero.

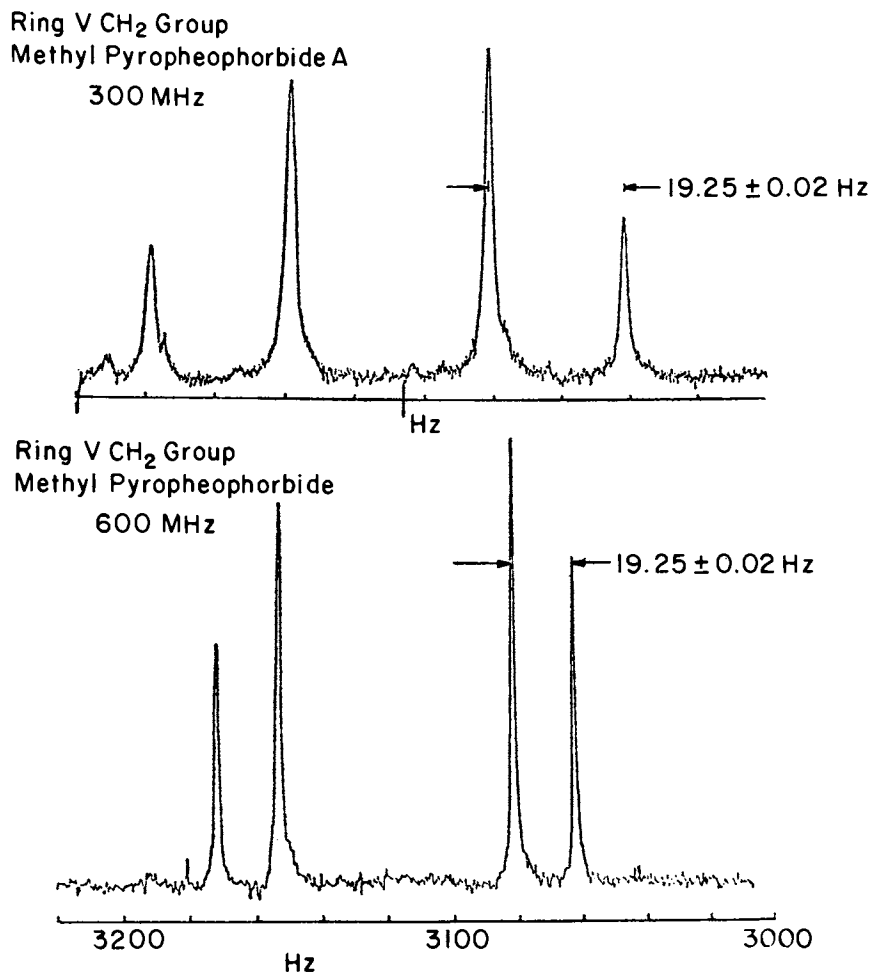


Figure 9. AB spectra of methyl pyropheophorbide a ring V CH<sub>2</sub> group. Splittings observed at 300 and 600 MHz are  $-19.92$  and  $-19.25$  Hz, respectively.



contains a CH<sub>2</sub> group held so that the internuclear axis is parallel to the axis of maximum diamagnetic susceptibility. Thus the action of a strong field will be to orient the molecule so that the HH internuclear axis lies perpendicular to the static field.

In this case the protons are non-equivalent, because of the neighboring dihydropyrrole ring. The protons thus give rise to an AB quartet. However, the observed splitting is the sum of the ordinary scalar spin-spin coupling and the direct dipolar interaction, and is therefore field dependent, showing the value -19.92 Hz at 300 MHz and -19.25 Hz at 600 MHz. The effective J is thus field dependent and is given by

$$J_{\text{obs}} = -20.2 + 0.005 H_0^2$$

with H<sub>0</sub>, the static field strength given in Teslas. The positive sign of the quadratic term is in accord with the geometry assumed above. If the protons are separated by 1.78<sup>o</sup> Å, as expected, the Δχ for the chlorin ring system is deduced to be -15.8 x 10<sup>-28</sup> cm<sup>3</sup>/molecule.

It is interesting to note that the orientation parameters S and K depend on the molecular susceptibility tensor, and the attachment of even rather extensive arrays of isotropic structure to an anisotropic group should not diminish the orientation. Thus myoglobin is expected to be about equally as oriented as heme, and the observation of orientation effects in remote parts of the molecule yielding geometric information, is an interesting possibility.

#### Acknowledgements

The work reported here was performed at the NMR Facility for Biomedical Studies, and supported, in part, by NIH grant RR00292 .

#### Literature Cited

1. Moore, R. E.; Bartolini, G. J. Am. Chem. Soc. 1981, 103, 2491.
2. Denys, L. A. "Magnetic Resonance Studies on the Conformational Diversity of Bradykinin at 600 MHz"; Thesis, Carnegie-Mellon University, Pittsburgh, PA; May, 1981.
3. Early, T. A.; Kearns, D. R.; Hiller, W.; Wells, R. D. Biochemistry 1981, 20, 3756.
4. Danishefsky, S.; Vaughan, K.; Gadwood, R. L.; Tsuzuki, K.; J. Am. Chem. Soc. 1980, 102, 4262.
5. Work in press: D. Horton; R. Barker.
6. Glasel, J.; University of Connecticut Health Center, Farmington, CT; private communication.
7. Loew, G. H.; Berkowitz, D. J. J. Med. Chem. 1975, 18, 656.
8. Oldfield, E.; Rothgeb, T. M. J. Am. Chem. Soc. 1980, 102, 3635.

9. Diehl, P.; Khetrepal, C. L. "NMR Basic Principles and Progress"; 1969, 1, 1.
10. Hilbers, C. W.; MacLean, C. Mol. Phys. 1969, 16, 275.
11. Lohman, J. A. B.; MacLean, C. Chem. Phys. 1978, 35, 269.
12. Bothner-By, A. A.; Pople, J. A. Ann. Rev. Phy. Chem. 1965, 16, 43.
13. Emsley, J. W.; Lindon, J. C. "NMR Spectroscopy Using Liquid Crystal Solvents"; Pergamon Press, Oxford 1978.
14. Domaille, P. J. J. Am. Chem. Soc. 1980, 102, 5392.
15. Lohman, J. A. B.; MacLean, C. Chem. Phys. Letters 1978, 58, 483.
16. Lohman, J. A. B.; MacLean, C. Mol. Phys. 1979, 38, 1255.

RECEIVED February 8, 1982.

# The Information Content of Two-Dimensional Fourier Spectroscopy

R. R. ERNST

Eidgenössische Technische Hochschule, Laboratorium für Physikalische Chemie,  
8092 Zürich, Switzerland

This brief essay discusses two-dimensional (2D) spectroscopy (1-6) with regard to its information content. In particular, we would like to elaborate those occasions where the use of 2D spectroscopy in place of one-dimensional (1D) Fourier spectroscopy is justified by the increase of available information.

The fundamentals for such a comparison of 1D and 2D spectroscopy are quite simple and straightforward. In 1D spectroscopy, a signal is represented as a function  $S(\omega)$  of a single frequency variable. The frequency  $\omega$  is a numerical coordinate which measures one particular feature, like the local magnetic field sensed through the chemical shielding, or the local electric field gradient through the nuclear quadrupole interaction. The single intensity  $S(\omega)$  represents a measure for the probability density of occurrence of the value  $\omega$ . It measures, for example, the number of nuclei experiencing a certain local magnetic field. A system is fully describable by a 1D spectrum only when its Hamiltonian  $H$  contains separate terms for each nucleus, each being characterized by a single parameter  $p_k$  (like the chemical shift or the quadrupolar coupling constant),

$$H = \sum_{k=1}^N H_k(p_k)$$

We have to impose the additional restriction that each term  $H_k(p_k)$  leads to a unique transition frequency.

As soon as the nuclei experience simultaneously different types of interactions or when pair interactions occur, a 1D spectrum becomes ambiguous, and it is no longer possible to uniquely relate apparent features to inherent parameter values. The most well known ambiguous situation is high-resolution spectroscopy in liquid phase where simultaneously chemical shielding and spin-spin couplings are active, leading to chemically shifted multiplets which may possibly seriously overlap. An unequivocal analysis of such a spectrum is no longer

American Chemical Society Library  
0097-6186/86 \$06.00/0  
© 1982 American Chemical Society

1155 16th St. N. W.

In NMR Spectroscopy: New Methods and Applications; Levy, G.;  
ACS Symposium Series 2003; American Chemical Society: Washington, DC, 1982.

possible. Three chemically shifted lines of equal separation and relative intensities 1, 2, 1 may, for example, be misinterpreted as a spin-spin coupling triplet.

In such a situation, an extension to 2D spectroscopy is in order. A 2D spectrum  $S(\omega_1, \omega_2)$  is capable of representing simultaneously two independent features without leading to any ambiguity, for example representing multiplet splittings along  $\omega_1$  which are shifted by the pertinent chemical shifts in the  $\omega_2$  direction. Such a representation is realized in 2D J-resolved proton spectroscopy (7).

In general, 2D spectroscopy is required to remove ambiguities whenever the Hamiltonian contains two different kinds of terms involving the same nuclear spins  $I_k$ , with the two sets of parameters  $p_k$  and  $q_k$ ,

$$H = \sum_{k=1}^N H_k^{(1)}(p_k) + \sum_{k=1}^N H_k^{(2)}(q_k)$$

or when in addition to linear terms, bilinear terms are present, involving spins  $I_k$  and  $I_\ell$ ,

$$H = \sum_{k=1}^N H_k^{(1)}(p_k) + \sum_{k < \ell} H_{k\ell}^{(2)}(q_k)$$

By a properly designed experiment, the two kinds of interactions can then be displayed independently along the two frequency axes.

Let us briefly mention the most important 2D spectroscopy techniques which conform to the principle of separation of different interactions in two dimensions:

- (a) 2D shift-resolved carbon-13 spectroscopy in liquid phase (3) was one of the first realizations of the 2D spectroscopy principle. It resolves overlapping multiplets caused by the  $^{13}\text{C}$ -H interaction by the  $^{13}\text{C}$  chemical shift. In a modification of this technique,  $^{13}\text{C}$  shifts and  $^{13}\text{C}$ - $^1\text{H}$  multiplets are completely separated in two dimensions (5,8).
- (b) Separated local field  $^{13}\text{C}$  spectroscopy (4) applies the same principle to solids where the dipolar multiplets can be resolved by the  $^{13}\text{C}$  chemical shielding. It can be applied to single crystals (4,9), powders (10,11) and to liquid crystals (12) (see Fig. 1).
- (c) 2D J-resolved proton spectroscopy (7) attempts the separation of homonuclear J multiplets and of chemical shifts. Its utility is restricted to weakly coupled spin systems at sufficiently high magnetic field strengths. It has been applied

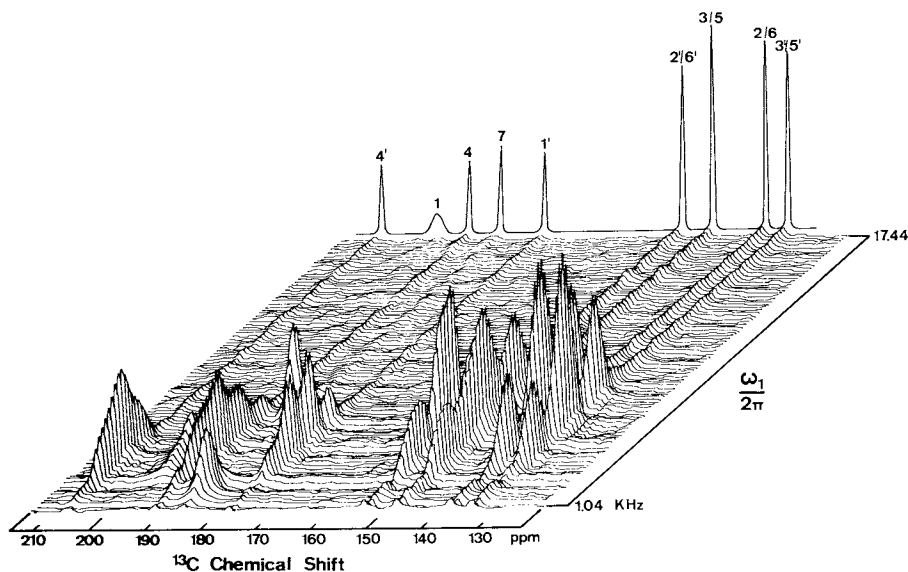


Figure 1. Aromatic part of the phase-sensitive 2D resolved dipolar  $^{13}\text{C}$  spectrum of the liquid crystal 4'-methoxybenzylidene-4-n-butylaniline (MBBA) in the nematic phase. The spread in the  $\omega_1$ -direction is governed by the proton-carbon dipolar couplings (+ carbon chemical shifts) while the spread along the horizontal axis is determined by the carbon chemical shifts, exclusively. The corresponding proton-decoupled 1D spectrum is sketched at the top of the 2D spectrum for clarification. Projection of the 2D spectrum onto the  $\omega_1$  axis would reproduce the proton-coupled 1D  $^{13}\text{C}$  spectrum. For each of 64 different values of  $t_1$ , 20 FID's represented by 1024 data points were co-added. The FID's were cosineapodized before 2D Fourier transformation (based on a zero-filled  $256 \times 2048$ ) data matrix. Conditions:  $24^\circ\text{C}$ ; carbon resonance frequency, 25 MHz; proton rf field strength, 13 G; Hartmann-Hahn contact time, 1.5 ms. Such a 2D spectrum provides information on molecular geometry and partial orientation based on resolved  $^{13}\text{C}$ -H dipolar couplings. (Reproduced, with permission, from Ref. 12. Copyright 1979, Taylor & Francis, Ltd.)

primarily for the elucidation of protein spectra (13,14)(see Fig. 2).

There is a second reason for the introduction of 2D spectroscopy. Pair interactions like the scalar spin-spin coupling or the dipole-dipole interaction can not be represented appropriately in a single frequency dimension even in the absence of further interactions. Pair interactions, leading to a network of couplings, immediately call for a representation by an interaction matrix or by a 2D correlation map (1,2). The two frequency coordinates  $\omega_1$  and  $\omega_2$  represent here parameters of single-spin interactions which are employed to label the various spins or the various transitions. The chemical shielding is of particular utility, in this respect. However, it is also possible to use the quadrupolar interaction as a nuclear label. The presence and the strength of cross-peaks in such a 2D correlated spectrum is then a measure for the strength of the various pair interactions.

A 2D correlation map may represent the interactions within a set of nuclei, leading to an auto-correlation map, or between two disjoint sets in the form of a cross-correlation map. We would like to mention four important applications of 2D correlated spectroscopy.

- (a) 2D auto-correlation spectroscopy (1,2), proposed in the very first mentioning of the "2D idea" by Jeener (1), has found widespread application for the analysis of proton coupling networks in particular in proteins to determine the protons belonging to the same amino acid residue (15-17)(see Fig. 3).
- (b) A very recent application utilizes natural abundance  $^{13}\text{C}$ - $^{13}\text{C}$  couplings for the elucidation of connectivity in carbon networks in organic molecules (19,20).
- (c) 2D cross-correlation spectroscopy has found application in the form of chemical shift correlation maps (21-24) for the study of proton-carbon connectivity in organic molecules.
- (d) 2D spectroscopy can also be used to determine from powder spectra the orientation of interaction tensors in the molecular frame by correlating chemical shielding (or quadrupolar interaction) tensors with dipolar coupling tensors (11,25)(see Fig. 4). 2D resolution in the sense of separated local field spectroscopy provides in this case the required correlation information.

So far, only coherent interactions, which can be represented in the Hamiltonian, have been considered. There are, however, also incoherent pair interactions, in particular in the form of dipolar cross-relaxation and of chemical exchange processes.

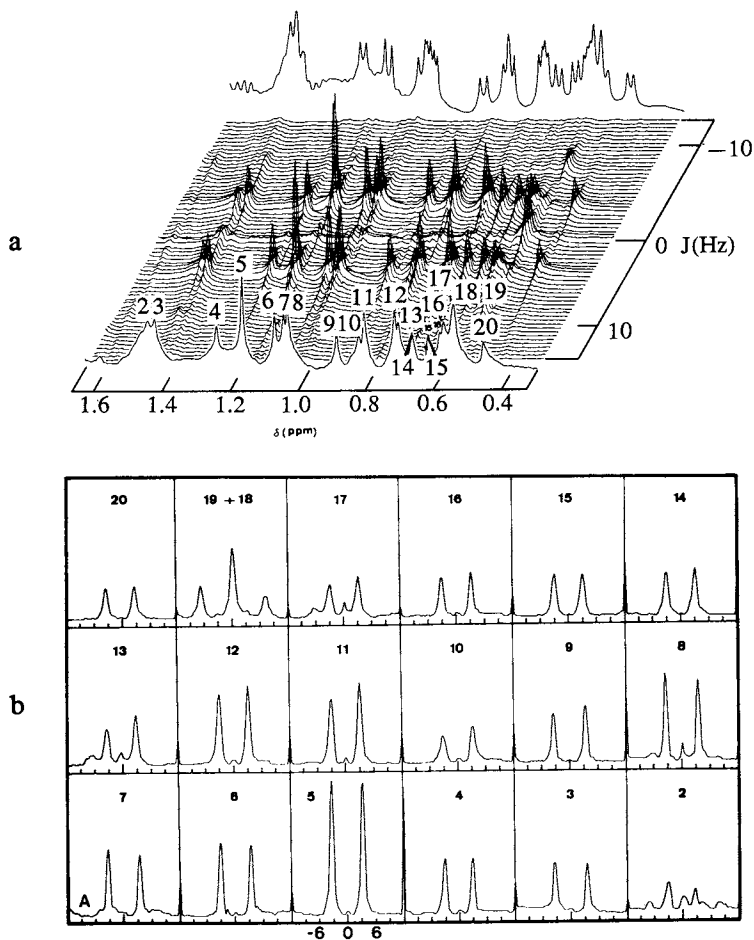


**Figure 2.** 2D J-resolved proton spectrum of the protein bovine pancreatic trypsin inhibitor (BPTI). *a*, High-field region from 0.4–1.6 ppm, which contains the resonances of 19 methyl groups of the 360-MHz  $^1\text{H}$  NMR spectra of a 0.01 M solution of BPTI in  $\text{D}_2\text{O}$  at pH 4.5,  $60^\circ\text{C}$ . Prior to the Fourier transformation, the 2D data set was weighted in the  $t_1$  and  $t_2$  directions by weighting functions  $\cos[(t_x/2T_2)\pi]\exp(t_x/0.4T_x)$ , with  $x = 1, 2$ ;  $T_1 = 2.46$  s, and  $T_2 = 1.23$  s are the maximum acquisition times in the  $t_1$  and  $t_2$  domains. The 2D J-resolved spectrum was computed from  $64 \times 8192$  data points and is presented as a  $(J, \delta)$  spectrum; the top trace shows the conventional 1D spectrum; the bottom trace shows the projection of the 2D spectrum with  $\phi = \pi/4$ . *b*, Presentation of the 2D J-resolved  $^1\text{H}$  spectrum (*a*) by cross sections. The resolved multiplets of 19 methyl protons are shown. The 2D resolved spectrum allows the analysis of otherwise overlapping multiplets, the accurate measurement of coupling constants, and the assignment of the resonances. (Reproduced, with permission, from Ref. 14. Copyright 1978, Academic Press.)

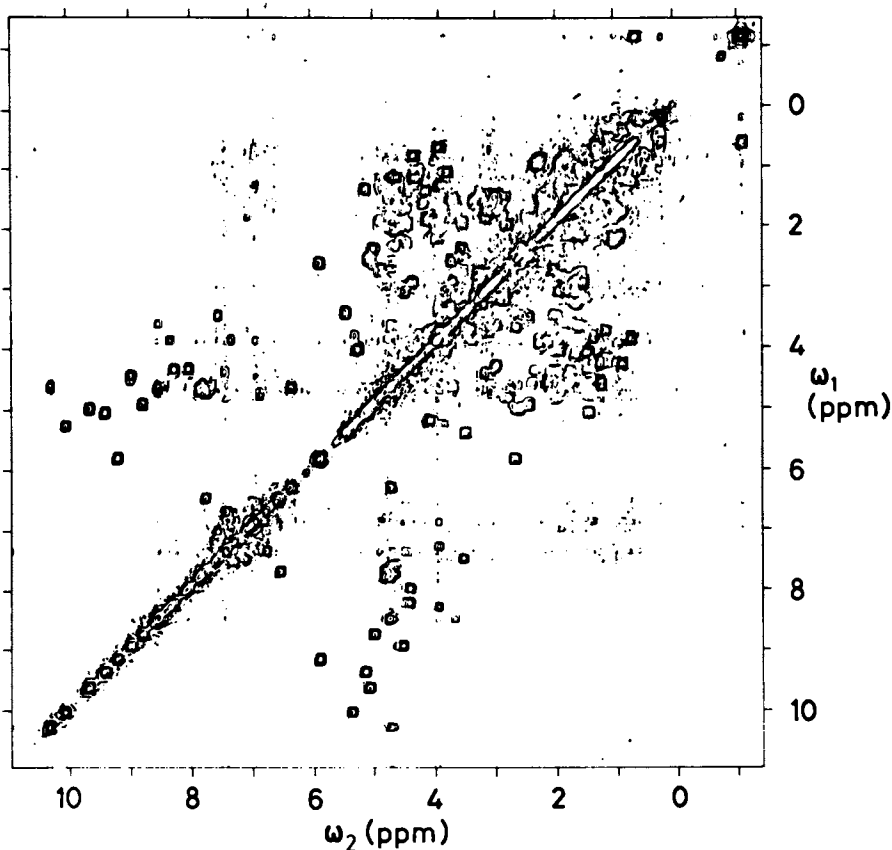


*Figure 3. 2D correlated (COSY)  $^1\text{H}$  spectrum of a 0.01 M  $\text{D}_2\text{O}$  solution of *Dendroaspis polylepis polylepis* (black mamba) inhibitor K, pD 3.4, recorded at 25°C on a Bruker HX 360 spectrometer equipped with an Aspect 2000 data system. The spectrum was recorded with quadrature detection in ca. 22 h. The spectral width is 4464.3 Hz, the data set consists of  $1024 \times 1024$  points. The spectral resolution was improved by multiplication of the free induction decays with a phase-shifted sine-squared bell in the  $t_2$ -direction and by a phase-shifted sine bell in the  $t_1$ -direction. The spectrum after symmetrization is shown. The 2D correlated spectrum visualizes the J-coupling connectivities and allows the assignment of resonances to individual amino acid residues. (Reproduced, with permission, from Ref. 18. Copyright 1981, Academic Press.)*



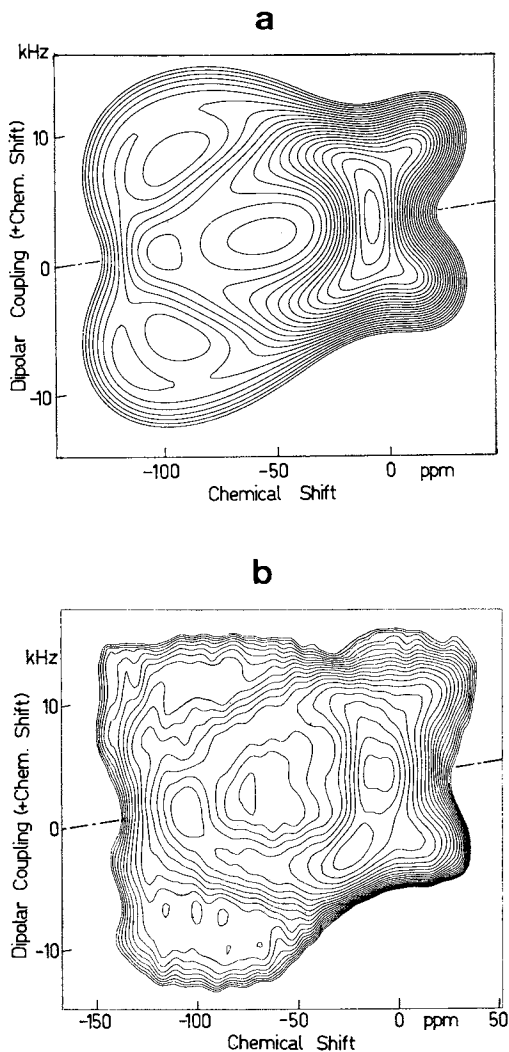


**Figure 4.** Correlation of the  $^{13}\text{C}$  chemical shielding and C-H dipolar coupling tensors of the formate group of 50%  $^{13}\text{C}$ -enriched methyl formate powder. *a*, Computer calculated 2D spectrum for  $\alpha = 33^\circ$  and  $\beta = 85^\circ$ . *b*, Experimental spectrum recorded at 25-MHz  $^{13}\text{C}$  resonance and 90 K. The 2D spectrum permits the determination of the relative orientation of two molecular interaction tensors without the need of growing single crystals. (Reproduced, with permission, from Ref. 11. Copyright 1980, American Institute of Physics.)

They also lead to an interaction network which is best represented by a 2D exchange matrix (26-28). The two frequency coordinates signify origin and destination of the magnetization exchange processes while the peak intensities measure the exchange taking place in a fixed time  $\tau_m$ .

For a detailed comprehension of the exchange dynamics it is necessary to study the exchange as a function of the exchange time  $\tau_m$ . This naturally leads to a 3D experiment where two frequency dimensions are required to represent origin and destination while the third (time) dimension represents the exchange dynamics (29).

2D exchange spectroscopy has found two relevant applications:

- (a) 2D chemical exchange spectroscopy permits the investigation of slow exchange processes in complicated chemical exchange networks (26,27). Proton (26,27) and carbon-13 (30) spectroscopy are useful in this respect (see Fig. 5).
- (b) 2D NOE spectroscopy (28,31,32,17) has attained extraordinary importance for the determination of the tertiary structure of biological macromolecules through the  $1/r^6$  dependence of the nuclear Overhauser effect on the internuclear separation (see Fig. 6).

In view of the presented reasons in favor of 2D spectroscopy, it is astonishing that until quite recently all NMR information has been obtained exclusively from 1D spectra. Indeed, all the interactions and effects mentioned above are reflected also in features of 1D spectra. The problems of ambiguity encountered in 1D spectroscopy can best be appreciated by considering a 1D spectrum as a projection of a 2D spectrum onto one of the frequency axes. However, the ambiguity problems of 1D spectroscopy can often be solved uniquely based on previous knowledge of the investigated system or by the intuition of an experienced spectroscopist. For example, overlapping multiplet patterns are often easily recognized, and exchange-broadened lines are properly interpreted.

In addition, there are numerous specialized techniques which booster 1D spectroscopy in ambiguous situations or when the straight 1D spectrum does not contain at all the desired information. To name the most important techniques only, we mention spin tickling, spin decoupling, scaling, selective magnetization transfer, nuclear Overhauser effects, and spin echo experiments. Most of these experiments can be considered as specialized variants of more general 2D experiments. For example, the selective magnetization transfer experiments, introduced by Forsen and Hoffman (33), measure single rows of the 2D exchange matrix mentioned above by labeling the magnetization of one particular nucleus and following its exchange to other spectral positions.

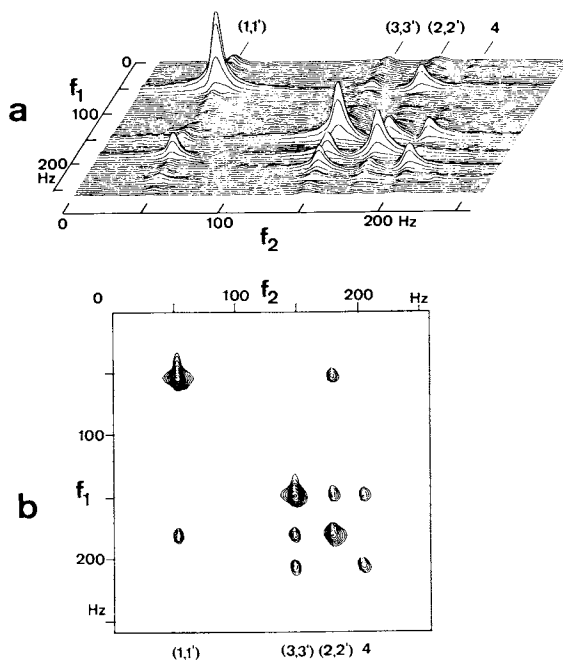


Figure 5. a, 2D exchange spectrum of heptamethylbenzenonium ion in 9.4 M  $H_2SO_4$ , obtained by a 2D Fourier transformation from 64 free induction decays with  $t_1$  values ranging from 0 to 142 ms, and with  $\tau_m = 280$  ms (60-MHz proton resonance on a modified Varian DA60 spectrometer, 40°C sample temperature). b, Contour plot based on the same data as used for Figure 5a. Off-diagonal peaks indicate slow intramolecular exchange between the four nonequivalent groups of protons labeled 1 to 4. (Reproduced, with permission, from Ref. 26. Copyright 1979, American Institute of Physics.)

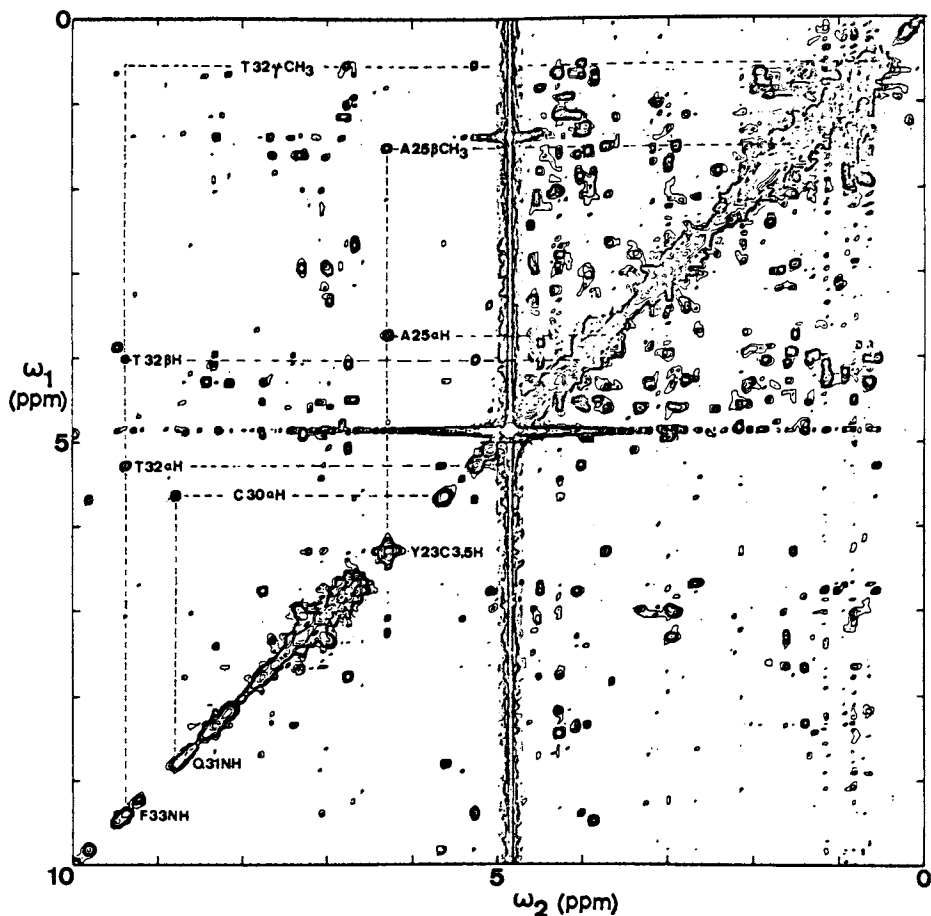
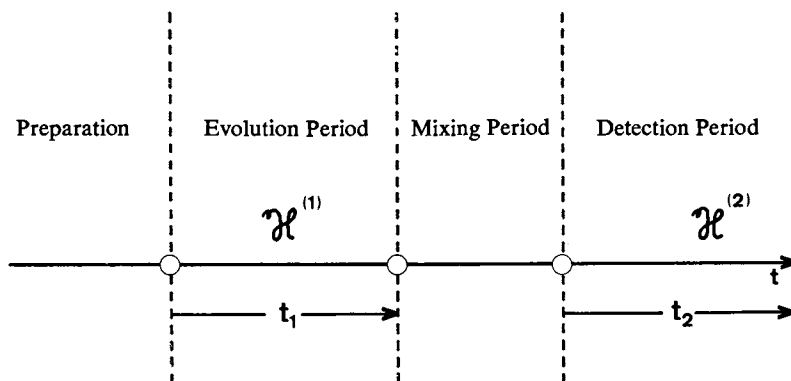


Figure 6. Contour plot of a proton 2D NOE spectrum at 360 MHz of the basic pancreatic trypsin inhibitor. The protein concentration was 0.02 M; solvent,  $^2\text{H}_2\text{O}$ ;  $p^2\text{H}$ , 3.8; and  $18^\circ\text{C}$ . The spectral width was 4000 Hz. 512 data points were used in each dimension. 56 transients were accumulated for each value of  $\tau_1$ . The mixing time,  $\tau_m$ , was 100 ms. The total accumulation time was 18 h. The absolute value spectrum obtained after digital filtering in both dimensions with a shifted sine bell is shown. Cross-relaxation connectivities for selected amino acid residues are indicated by the broken lines. Some selected peaks connected by NOE's are identified by the one-letter symbol for amino acids (A, alanine; T, threonine; C, cysteine; Q, glutamine; F, phenylalanine; and Y, tyrosine), the position in the amino acid sequence, and the type of protons observed. Such 2D NOE spectra are of decisive importance for the determination of the three-dimensional structure of biopolymers in solution. (Reproduced, with permission, from Ref. 31. Copyright 1980, Academic Press.)

These considerations somewhat reduce the glamour of 2D spectroscopy. Indeed, no information has yet been mentioned which could not be extracted by suitably modified 1D experiments. However, 2D spectroscopy techniques have the great advantage of being completely universal and require no previous knowledge on the system to be investigated. They serve primarily survey purposes, but may equally well be used for detail studies. They exhibit their favorable properties best when applied to particularly intricate situations. The most spectacular demonstrations of their power have certainly been provided by applications to the elucidation of protein structure (13-17,31,32). Here, they are unrivalled with regard to ease of usage and to the plentiful content of information.

We should, finally, mention also the possibility to indirectly detect resonance by 2D experiments. A 2D experiment invariably involves two variable time periods (2)(see Fig. 7). During the initial "evolution period" the  $\omega_1$ -information is acquired by the nuclear spins and "stored" in the form of phase or amplitude information which is read out and recorded during the detection period together with the  $\omega_2$ -information. The indirect detection of the  $\omega_1$ -information permits the study of otherwise inaccessible properties. This feature can be utilized to indirectly observe resonance of low sensitivity nuclei (21) and of forbidden transitions (2,34,35), i.e. multiple quantum transitions and combination lines. In this respect 2D spectroscopy really provides novel information. In particular zero quantum transitions, i.e. transition between energy levels of equal magnetic quantum number had never been observed before (35)(see Fig. 8).

In summary, 2D spectroscopy can provide new information. However, its main features are the capability to eliminate ambiguities from 1D spectra by separation of independent features in two dimensions and the possibility to correlate features based on coupling networks or on magnetization exchange networks. 2D spectroscopy is a universal technique, being applicable in a great variety of situations without previous knowledge on the investigated system. It delivers a maximum of information in a comparably short performance time. Its main field of application is the elucidation of the structure of complex molecules and the study of complicated exchange networks. 2D spectroscopy embraces a new powerful class of spectroscopic techniques which do not replace but supplement and generalize the well-known 1D techniques.



*Figure 7. Schematic representation of a general 2D experiment consisting of four phases: preparation, evolution, mixing, and detection periods of which evolution and detection periods contain the two time variables  $t_1$  and  $t_2$ , respectively.*

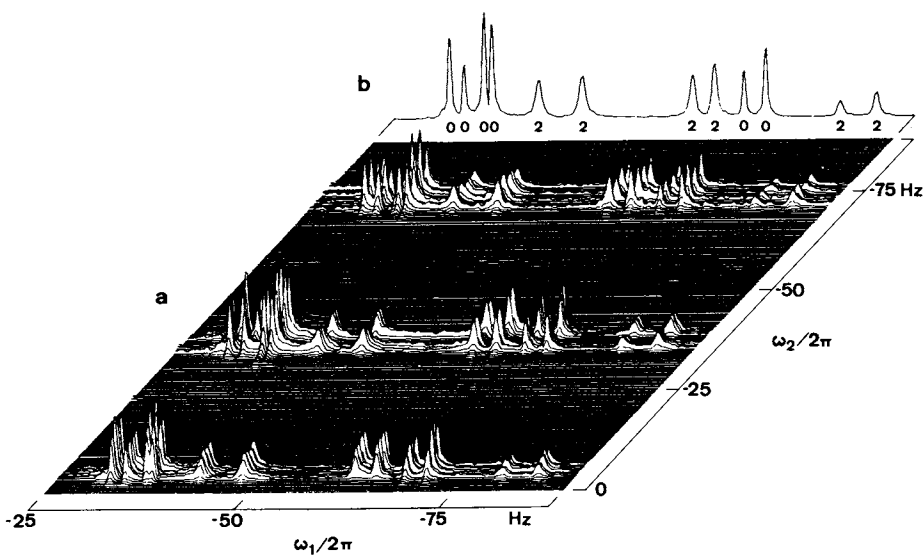


*Figure 8. Zero quantum and double quantum transitions in the AMX system of 2-furancarboxylic acid methyl ester. a, 2D spectrum. b, Projection of the 2D spectrum onto the  $\omega_1$  axis. ZQT's and 2QT's are labeled by 0 and 2, respectively. The middle doublet of 2QT's has been folded at the Nyquist frequency,  $-88.2$  Hz. Otherwise forbidden zero quantum and double quantum transitions provide connectivity information valuable for the analysis and assignment of spectra, and relaxation information useful for the study of molecular motional processes. (Reproduced, with permission, from Ref. 35. Copyright 1977, North-Holland Publishing Company.)*

ACKNOWLEDGEMENTS

Partial support by the Swiss National Science Foundation is acknowledged. The author is indebted to Dr. G. Bodenhausen for constructive comments and to Miss I. Müller for editorial support.

LITERATURE CITED

1. Jeener, I. Ampere International Summer School Basko Polje, Yugoslavia, 1971.
2. Aue, W. P.; Bartholdi, E.; Ernst, R. R. J. Chem. Phys. 1976, **64**, 2229.
3. Müller, L.; Kumar, A.; Ernst, R. R. J. Chem. Phys. 1975, **63**, 5490.
4. Hester, R. K.; Ackerman, J. L.; Neff, B. L.; Waugh, J. S. Phys. Rev. Lett. 1976, **36**, 1081.
5. Bodenhausen, G.; Freeman, R.; Turner, D. L. J. Chem. Phys. 1976, **65**, 839.
6. Freeman, R.; Morris, G. A. Bull. Magn. Reson. 1979, **1**, 5.
7. Aue, W. P.; Karhan, J.; Ernst, R. R. J. Chem. Phys. 1976, **64**, 4226.
8. Müller, L.; Kumar, A.; Ernst, R. R. J. Magn. Reson. 1977, **25**, 383.
9. Rybaczewski, E. F.; Neff, B. L.; Waugh, J. S.; Sherfinski, J. S. J. Chem. Phys. 1977, **67**, 1231.
10. Opella, S. J.; Waugh, J. S. J. Chem. Phys. 1977, **66**, 4919.
11. Linder, M.; Höhener, A.; Ernst, R. R. J. Chem. Phys. 1980, **73**, 4959.
12. Höhener, A.; Müller, L.; Ernst, R. R. Mol. Phys. 1979, **38**, 909.
13. Nagayama, K.; Wüthrich, K.; Bachmann, P.; Ernst, R. R. Biochem. Biophys. Res. Commun. 1977, **78**, 99.
14. Nagayama, K.; Bachmann, P.; Wüthrich, K.; Ernst, R. R. J. Magn. Reson. 1978, **31**, 133.
15. Nagayama, K.; Wüthrich, K.; Ernst, R. R. Biochem. Biophys. Res. Commun. 1979, **90**, 305.
16. Nagayama, K.; Kumar, A.; Wüthrich, K.; Ernst, R. R. J. Magn. Reson. 1980, **40**, 321.
17. Nagayama, K.; Wüthrich, K. Eur. J. Biochem. 1981, **114**, 365; Wagner, G.; Kumar, A.; Wüthrich, K. Eur. J. Biochem. 1981, **114**, 375.
18. Baumann, R.; Wider, G.; Ernst, R. R.; Wüthrich, K. J. Magn. Reson., in press.
19. Bax, A.; Freeman, R.; Frenkiel, T. A. J. Amer. Chem. Soc. 1981, **103**, 2102.
20. Bax, A.; Freeman, R.; Frenkiel, T. A.; Levitt, M. H. J. Magn. Reson. 1981, **43**, 478.
21. Maudsley, A. A.; Ernst, R. R. Chem. Phys. Lett. 1977, **50**, 368.



22. Maudsley, A. A.; Kumar, A.; Ernst, R. R. J. Magn. Reson. 1977, 28, 463.
23. Bodenhausen, G.; Freeman, R. J. Magn. Reson. 1977, 28, 47.
24. Freeman, R.; Morris, G. A. J. Chem. Soc. Chem. Comm. 1978, 684.
25. Vaughan, R. W. Ann. Rev. Phys. Chem. 1978, 29, 397.
26. Jeener, J.; Meier, B. H.; Bachmann, P.; Ernst, R. R. J. Chem. Phys. 1979, 71, 4546.
27. Meier, B. H.; Ernst, R. R. J. Amer. Chem. Soc. 1979, 101, 6441.
28. Macura, S.; Ernst, R. R. Mol. Phys. 1980, 41, 95.
29. Bodenhausen, G.; Ernst, R. R. submitted for publication.
30. Huang, Y.; Macura, S.; Ernst, R. R. J. Amer. Chem. Soc., in press.
31. Kumar, A.; Ernst, R. R.; Wüthrich, K. Biochem. Biophys. Res. Commun. 1980, 95, 1.
32. Baumann, R.; Kumar, A.; Ernst, R. R.; Wüthrich, K. J. Magn. Reson. 1981, 44, 76.
33. Forsen, S.; Hoffman, R. A. J. Chem. Phys. 1963, 39, 2892, J. Chem. Phys. 1964, 40, 1189; Hoffman, R. A.; Forsen, S. J. Chem. Phys. 1966, 45, 2049.
34. Vega, S.; Shattuck, T. W.; Pines, A. Phys. Rev. Lett. 1976, 37, 43.
35. Wokaun, A.; Ernst, R. R. Chem. Phys. Lett. 1977, 52, 407.

RECEIVED December 17, 1981.

## Quadrupolar Metallic Nuclei

### <sup>23</sup>Na NMR Studies of Cation Binding by Natural and Synthetic Ionophores

PIERRE LASZLO

Institut de Chimie et de Biochemie (B6), Université de Liège,  
Sart-Tilman par 4000 Liège, Belgium

It is an interesting coincidence that the advent of Fourier-transform NMR, by opening the whole periodic table for investigation, has been contemporary with a major surge of interest in organometallic chemistry and in the closely related field of bio-inorganic chemistry. As a consequence, dozens of metallic nucleides, starting with those having the most favorable magnetic properties, have served as structural and/or dynamic probes. Rather than providing here a wide - encompassing survey of multi-nuclear NMR, we have opted for a different presentation: sodium-23 nuclear magnetic resonance will provide in this chapter a case study, as it were, for the use of such a metallic nucleus. In many respects, it will be illustrative both of the problems encountered with, and of the information derivable from, the nuclear magnetic resonance of quadrupolar nuclei.

This chapter summarizes the types of information to be derived from application of sodium-23 nmr to the study of synthetic and natural cation binders. Its scope won't be limited to the binding of Na<sup>+</sup>: due to the high sensitivity of <sup>23</sup>Na, the binding of other singly- and multiply-charged cations can also be studied, from competition experiments. We shall present both thermodynamic results (binding constants) and kinetic results (rate constants for binding and release), emphasizing somewhat work from the author's laboratory. An historical comment is appropriate at this point.

The work of our Liège group reported herein had small beginnings and a rather inauspicious start. Little did we imagine that, a mere four years after the beginning of our sodium-23 work, we would have completed studies of sodium binding and release by numerous biomolecular hosts, including simple sugars, more complex polysaccharides, nucleotides, antibiotics, and cation-binding proteins. If this review starts on such an historical note, it is because our experience could be taken as

0097-6156/82/0191-0063\$10.00/0  
© 1982 American Chemical Society

fairly representative of that of many other members of the nmr community who, in the early or middle 1970s, broke with the tradition of spin 1/2 nuclei, and rekindled the brushfire, enthusiastically lit in the late 1950s by the R.E. Richards' group in Oxford, by renewing the exploration of quadrupolar nuclei. The Richards' group had broken the ground and, perforce, did not go much further than establishing the potential of the nmr quadrupolar nuclei for answering questions about solvation or coordination. The appearance, in the late 1960s and early 1970s, of the new generation of instruments with fast Fourier transform added a new potential: that of exploring, at low enough concentrations, binding of quadrupolar ions by biological molecules.

At the onset of our sodium-23 work, we stayed away from such studies, however unduly restricting ourselves to what appeared as much simpler applications to problems of ion pairing and solvation from inorganic and organic chemistry. Our timidity towards large, fat, albeit attractive, biomolecules found support in reports that univalent ions, such as the sodium cation, did take only very weakly to them, and did not stay very long in the bound state. A single sentence will serve to convey the stale flavor of the field at the time: "Because of short lifetimes of the macromolecular complexes of sodium, the relaxation rate of  $^{23}\text{Na}$  cannot be used in studies of macromolecular dynamics in solution". Since the prediction has been ridiculed by the success of precisely such studies, its author is better left nameless!

### Theoretical Background: Dual Relaxation of a Spin 3/2 Particle

The detailed and precise understanding of relaxation of a spin 3/2 system assumes great importance for two reasons: (i) spin 3/2 nucleides include some of the most important species for bio-inorganic, inorganic and organometallic chemistry:  $^7\text{Li}$ ,  $^{23}\text{Na}$ ,  $^{39}\text{K}$ ,  $^{87}\text{Rb}$  among the alkali metals;  $^{35}\text{Cl}$ ,  $^{37}\text{Cl}$ ,  $^{79}\text{Br}$ ,  $^{81}\text{Br}$  among the halogens; and miscellaneous nuclei, such as  $^9\text{Be}$ ,  $^{11}\text{B}$ ,  $^{63}\text{Cu}$ ,  $^{65}\text{Cu}$ , etc.; (ii) the overall spin quantum number for the three protons of a methyl group is also 3/2. Hence, both types of systems can be analyzed in like manner.

Hubbard (1) pointed out in 1970 that the lineshape for a spin 3/2 resonance should consist of  $I + 1/2 = 2$  superimposed Lorentzians. Their widths are obtainable in closed form, because in the  $I = 3/2$  case, it is possible to solve analytically the set of  $I + 1/2$  linearly coupled equations which describe the time evolution for the two distinct  $\pm 3/2 \rightarrow \pm 1/2$  and  $+ 1/2 \rightarrow - 1/2$  transitions (2). The latter transition remains narrow even under slow reorientation, because its width is at most second order with respect to the quadrupolar interaction (slow relaxation) (3). This line, with 40% of the total intensity, is superimposed on the much broader resonance (fast relaxation, 60% of the total

intensity) for the  $\pm 3/2 \pm 1/2$  transition. Under extreme narrowing conditions, both these lines merge into a single resonance centered at the unperturbed frequency(1-3),

In short and to quote Werbelow(4) : "the total magnetization is correctly described as a composite of two irreducible submagnetizations, one transforming as an  $I = 3/2$  momentum and one (doubly degenerate) transforming as an  $I = 1/2$  momentum. In the simplest approximation, each submagnetization is characterized by an intrinsic relaxation rate. A relatively weak virtual cross relaxation renders the time evolution of each of these submagnetizations biexponential (...) If the doublet and quartet transitions are coincident in frequency, the observable lineshape is described as a sum of two superimposed Lorentzians, unequal in both width and intensity". The doublet and quartet transitions are indeed coincident in frequency in all of the applications to be covered in this article.

The linewidth of the fast relaxation transition is of the form(1-3) :

$$\frac{1}{\pi T_2} = \frac{\pi}{5} \left( \frac{e^2 q Q}{h} \right)^2 \tau_c / (1 + \omega^2 \tau_c^2)$$

with a maximum when  $\omega \tau_c \sim 1$ . There is also a shift from the unperturbed frequency of magnitude :

$$\left( \frac{e^2 q Q}{h} \right)^2 \tau_c^{-1} (\omega^2 \tau_c^2) / (1 + \omega^2 \tau_c^2)$$

This shift is important only when  $\omega \tau_c > 1$ , and it vanishes in the extreme narrowing limit  $\omega \tau_c \ll 1$ . These equations are valid under the condition :

$$\left( \frac{e^2 q Q}{h} \right)^2 \tau_c \ll 1$$

The linewidth of the slow relaxation transition is of the form (1-3) :

$$\frac{1}{\pi T_2} = \frac{\pi}{5} \left( \frac{e^2 q Q}{h} \right)^2 \tau_c [(1 + 4 \omega^2 \tau_c^2)^{-1} + (1 + \omega^2 \tau_c^2)^{-1}]$$

Bull (5) has extended these equations to include the effect of chemical exchange between two states, a free (F) and a

bound state (B), with a residence time  $\tau_B$  in the bound state. The transverse relaxation rate is given, under a series of simplifying assumptions by :

$$\frac{1}{T_2} = \frac{1 - p_B}{T_{2F}} + p_B \left[ \frac{0.6}{T_{2B} + \tau_B} + \frac{0.4}{T_{2B} + \tau_B} \right]$$

Because the fast and slow relaxation components do not depend upon the same spectral densities :  $J(0)$  and  $J(\omega)$  versus  $J(\omega)$  and  $J(2\omega)$  respectively, they change in unlike manner with the observing Larmor frequency . For sodium-23, when the correlation time  $\tau_C$  in the bound state exceeds ca. 5 ns the observed resonance acquires enough non-Lorentzian character that it is feasible to deconvolute reliably the lineshape into its two Lorentzian components. Then the most accurate method is to perform another deconvolution at a widely different Larmor frequency  $\omega'$ . For instance, the slow relaxation rate  $\frac{1}{T_2}$  varies by about 700% between observing frequencies of 23.81 and 62.86 MHz for long  $\tau_C$  values ( $> 5$  ns)(6).

This is equivalent to a determination of the important parameters  $\chi = (e^2qQ/h)$  and  $\tau_C$ , since once the individual linewidths for the narrow and for the broad components are obtained, their ratio at a given  $\omega$  value is a function only of the correlation time  $\tau_C$ . This procedure of deconvoluting the experimental lineshape is the most reliable access to  $\chi$  and  $\tau_C$ , as compared to analysis of a biexponential decay of the longitudinal magnetization ( $T_1$  determination) with an 80% - 20% contribution from the fast and slow relaxations, respectively. It need not involve the full digitization of the actual lineshape : a simplified procedure, based upon two linewidth measurements at 1/2 and 1/8 of the total height, gives equally good results, and can be programmed on a manual calculator (6).

Let us mention finally, as a close to this section, that the longitudinal relaxation times for the two coincident components of the proton signal of a methyl group, attached to a slowly reorienting molecule, have been determined by direct observation of their null points in the recovery after a  $180^\circ$  pulse (7).

### Experimental Procedure and Data Analysis

Sensitivity, Concentrations, Viscosity Corrections. At constant field,  $^{23}\text{Na}$  is 525 times more receptive than the widely used  $^{13}\text{C}$  nucleus : because of the combination of a greater natural abundance (100% versus 1.1%) and of a higher constant field sensitivity relative to an equal number of protons ( $9.25 \times 10^{-2}$  versus  $1.59 \times 10^{-2}$ ). In the absence of a biomolecular receptor,  $^{23}\text{Na}$  linewidths are small, about 5-10 Hz for dilute ( $10^{-3}$ - $10^{-1}$  M) aqueous solutions of NaCl. However, binding by a

macromolecular host increases the linewidth considerably, into the kHz range. Since such linewidths (or, equivalently, relaxation rates) can be measured to  $\pm 5-10\%$ , this affords a nice handle for studying attachment of  $\text{Na}^+$  to biomolecular receptors. The high sensitivity of the  $^{23}\text{Na}$  nucleus makes it possible to routinely use centimolar and millimolar solutions. A typical useful concentration range for study of ionophores is  $10^{-3}\text{M}-10^{-1}\text{M}$ . The upper limit is approximately the physiological sodium concentration in the blood! One measures the enhancement of the longitudinal and of the transverse relaxation rates with increased concentration of the ionophoric host. Results are normalized to unit viscosity; even though this procedure is not adhered to by all the authors, indications abound that relaxation rates do follow closely viscosity changes. Even in aqueous solutions, for which one would expect perhaps the greatest deviations from Debye-Stokes-Einstein behavior, the ca. 20% increase of the relaxation rate from  $\text{H}_2\text{O}$  to  $\text{D}_2\text{O}$  simply matches the increase in solvent viscosity (8).

Derivation of Stoichiometry and of Binding Constants. Consider the simple binding equilibrium:  $\text{I} + n\text{M} \rightleftharpoons \text{complex}$   
(ionophore) (metallic ion)

If a large excess of M is used, so that the mole fraction in the free state  $p_F$  greatly exceeds that in the bound state  $p_B$  ( $p_F \gg p_B$ ), and under fast chemical exchange between the free and the bound states, the Swift and Connick treatment (9) leads to:

$$S = \Delta\nu_{1/2}/\Delta\nu_{1/2}^B = \frac{n[\text{I}]_t}{K_D + [\text{M}]_t}$$

$\Delta\nu_{1/2}$  is the observed line broadening, or relaxation rate enhancement,  $\Delta\nu_{1/2}^B$  is the limiting value in the complex;  $[\text{I}]_t$  and  $[\text{M}]_t$  are the total ionophore and metallic ion concentrations respectively; and  $K_D$  is the dissociation constant for the complex.

A plot of  $1/\Delta\nu_{1/2}$  versus  $[\text{M}]_t$  will be linear, with a slope inversely proportional to  $[\text{I}]_t$ , the intercept with the  $[\text{M}]_t$  axis is  $-K_D$ . A number of authors have used such graphical solutions (9-11).

A crucial and vexing problem is the accuracy of the resulting parameters. My remarks will be confined to the case of 1:1 stoichiometry ( $n = 1$ ), since the set-up of the experiment and the data sampling should ideally be adapted to the case at hand. A 1:1 stoichiometry corresponds to a linear increase of  $\Delta\nu_{1/2}$  with  $[\text{I}]_t$ . The saturation fraction  $S$  asymptotically approaches unity as the molar ratio  $[\text{M}]_t/[\text{I}]_t$  (or  $M/I$ , for a shorthand) becomes infinitely large. In that region of saturation curve ( $S$  versus  $M/I$ ),  $S$  varies little, and the  $\Delta\nu_{1/2}$  variations lack

accuracy. At small S values, S is linear with M/I, *i.e.* the saturation curve provides only limited information. Hence, the greatest accuracy in determination of  $K_D$  and  $\Delta\nu_{1/2}^B$  attaches itself to the intermediate region, that of greatest curvature, for saturation fractions S between about 0.2 and 0.8 (12).

In practice, correspondingly, one should ideally follow the observable as a function of the mole ratio M/I in the whole range between values of *ca.* 0.5 and 1.5 (13-14). How many experimental points N does one need in that range? With  $n = 1$ , the number  $\pi$  of parameters to be determined is  $\pi = 2(\Delta\nu_{1/2}^B$  and  $K_D$ ). While in principle,  $N = \pi + 1$  should be sufficient, in practice N is best taken as 2 to  $3\pi$ . We find it advisable to obtain a minimum of  $N = 7$  data points for characterization of a 1:1 complex. Rather than a graphic procedure, we use multi-parameter fitting to an algebraic equation. The 1:1 stoichiometry thus corresponds to solving a second-degree equation of the type ( $K$  is a stability constant):

$$[\text{Na}^+]_F = \frac{1}{2K} \left\{ -K[\text{I}]_t + K[\text{Na}^+]_t \right. \\ \left. - 1 + \sqrt{-(K[\text{I}]_t - K[\text{Na}^+]_t + 1)^2 + 4K[\text{Na}^+]_t} \right\}$$

Starting with trial values, an iterative scheme (Newton-Rafson, Newton-Gauss, or other more or less equivalent algorithms) is best used for the solution.

In our experience, for problems with  $\pi > 3$ , *i.e.* those which cannot be described by a simple 1:1 equilibrium, Simplex procedures (13a) work reasonably well for the complex task of multiparameter fitting to the data.

Derivation of Rate Constants for Binding and Release. There are two kinds of favorable situations. Chemical exchange between the free and the bound states affects the observed relaxation whenever the rate of chemical exchange is of the same order of magnitude as the relaxation rates. The kinetics of  $\text{Na}^+$  exchange were first studied by Schchori *et al.* upon the example of the dibenzo-18-crown-6 complex (15,16). They observed virtually no chemical shift difference between the free and the complexed ion, so that the following simplified equations hold:

$$k_F = \tau_F^{-1} = \frac{(R_B - R)(R - R_F)p_B}{(\bar{R} - R)}$$

with  $\bar{R} = p_F R_F + p_B R_B$ .

In these expressions,  $\tau_F$  is the lifetime of  $\text{Na}^+$  in the free state,  $R$  is the observed relaxation rate - either longitudinal ( $T_1$  measurement) or transverse (linewidth measurement), for the signal corresponding to the free ion; the subscripts F and B refer to the free and the bound states, respectively.

In the presence of a substantial chemical shift difference between the free and the bound states, fast exchange corresponds to:

$$\bar{R}_1 = p_F R_{1,F} + p_B R_{1,B}$$

$$\bar{R}_2 = p_F R_{2,F} + p_B R_{2,B} + p_F p_B \tau_{ex} \Delta\omega^2$$

with :  $\tau_{ex} = \frac{p_B}{k_+} = \frac{p_F}{k_-}$

and :  $\Delta\omega = \Delta\omega_B - \Delta\omega_F$

These equations are used in the region of intermediate exchange rates. In the fast exchange limit,  $R \rightarrow \bar{R}$ ; whereas, in the slow exchange limit,  $R \rightarrow R_F$ , since free sodium ions are in large excess ( $p_F \gg p_B$ ). In essence, one is looking only at the resonance for free sodium ions broadened by exchange with the underlying signal for bound sodium ions, whose intensity is too low to be directly detected. A number of studies have used this formalism (15-19).

Another kinetic range is accessible with  $^{23}\text{Na}$  NMR. Following an original idea of Henry Eyring (20), the correlation time for molecular reorientation of the complex  $(\tau_R)_B$  can be used as an internal clock against which to measure the lifetime  $\tau_B$  in the bound state. When chemical exchange is fast with respect to molecular rotation ( $k_+, k_- \gg k_F, k_B$ ):

$$T_i = p_B T_{i,B} + p_F T_{i,F} \quad ; \quad i = 1, 2$$

When chemical exchange is slow with respect to molecular rotation (but it can be quite fast with respect to the NMR relaxation rates):

$$R_i = p_B R_{i,B} + p_F R_{i,F} \quad ; \quad i = 1, 2$$



We are assuming here the absence of any line broadening arising from chemical shift differences between the free and the bound states.

This method for studying very fast kinetics with rate constants typically in the range  $10^6$ - $10^9$  s<sup>-1</sup>, has been reviewed elsewhere (21).

### Application to Structure Reactivity Correlations

Many useful reactions are conducted with salt reagents in low-dielectric organic solvents. It is well known that in these solvents, such as dioxane or tetrahydrofuran (THF), organolithium and organosodium reagents can be aggregated rather extensively. The availability of new reagents, such as the sodium ferrates, for instance the Collman salt  $\text{Na}_2\text{Fe}(\text{CO})_4$  (22), with their high nucleophilicity, makes it even more important to fully characterize the species present in solution.

<sup>23</sup>Na NMR has a great potential for solving such questions for the organosodium and organometallic sodium species. Study of the change in chemical shift and linewidth with concentration of the reagent present alone in solution provides the mean aggregation number, together with the limiting values for these observables in the pure aggregates. More important yet is a study of the solutions containing jointly the substrate and the reagent, under conditions of solvent, concentration, and temperature as close as possible to reaction conditions. The conjunction of classical chemical kinetics (and the resulting reactivity data) with <sup>23</sup>Na NMR spectroscopy (providing not only structural information, but also the relative concentrations of the coexisting species) can be a very powerful tool.

We have looked for instance at the alkylation by ethyl iodide of ambident anions, such as ethyl acetylacetae, in THF solution (23). In this solvent, a prior variable concentration study points for sodium ethylacetylacetae to a mean aggregation number of two (dimers). It is to be expected for the predominant structure of this species to have Na<sup>+</sup> ions chelated by the two oxygen atoms of the β-dicarbonyl ambident anion. Hence, increasing the average Na<sup>+</sup>-anion distance, by complexation of the sodium cation with a crown ether or with a cryptand, ought to boost the reactivity of the anion towards C<sub>2</sub>H<sub>5</sub>I alkylation. Indeed, the observed rate constant increases considerably in the presence of the 15-crown-5 or the (2.2.1) cryptand, both selective for Na<sup>+</sup> ions. The spectroscopic data (linewidths) show that at least four coexisting species are to be taken into consideration. These four entities are the following :



$E^-Na^+$	(monomers)
$(E^-Na^+)_2C$	(crowned dimers)
$E^-Na^+C$	(crowned monomers)

The spectral analysis provides an estimate of the relative concentrations for each value of the  $[E^-Na^+]/[C]$  ratio, where  $E^-Na^+$  is the enolate salt, and C is the specific complexant (either crown ether or cryptand).

Comparison of the resultant concentrations with the chemical rate data indicated that the latter,  $E^-Na^+C$ , is the single kinetically-active species under the conditions of our experiments; the NMR results also ruled out the intervention of loose  $E^-||Na^+$  or dissociated  $E^-$ ,  $Na^+$  ion pairs, which could have been guessed naively to be responsible for the reactivity enhancement in the presence of the crown ethers and cryptands.

Such results exemplify the analytic use of NMR of a quadrupolar nucleus. It is not mandatory to be able to make a detailed interpretation of the NMR parameters, chemical shifts and linewidths, for each of the chemical species in the solution to which the quadrupolar nucleus can attach itself. If these NMR parameters differ sufficiently between these various species, relative concentrations can be obtained and such information can be quite valuable. Regarding the structure of the ion pairs themselves, at present  $^{23}Na$  NMR is restricted to distinguishing between tight, loose or dissociated ion pairs, which it can do rather reliably (24). But obviously, it is to be complemented by  $^1H$  and  $^{13}C$  NMR if information about the geometry and the electron distribution in the anion is desired (25-27).

#### Site Binding or Atmospheric Condensation by Polyelectrolytes

According to a number of authors (28-31), the interaction of cations such as  $Na^+$  with a poly-anion in water can occur under two different modes: either a true contact ion pair is formed, as dictated by the mass action law and so that the two hydration shells are perturbed; or the sodium cation, as the hexaquo species, is attracted into the electrostatic potential in the vicinity of the charged counter-ion: it is like a free ion in every respect except for being constrained not to diffuse outside of a certain volume surrounding the polyelectrolyte. The former interaction type is called site binding. The latter, which is reminiscent of formation of a loose, solvent-separated, ion pair is referred to as atmospheric condensation. (Figures 1-2).

The driving force for atmospheric condensation can be visualized as the instability in solution of a polyelectrolyte in which charged groups are structurally constrained at a too small mutual spacing along a chain: some of the counter-ions will

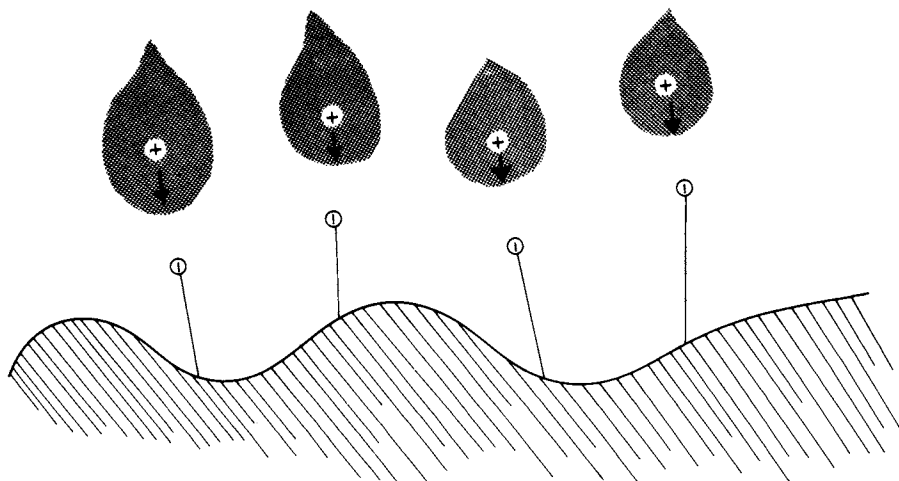


Figure 1. Schematic illustration of site binding.

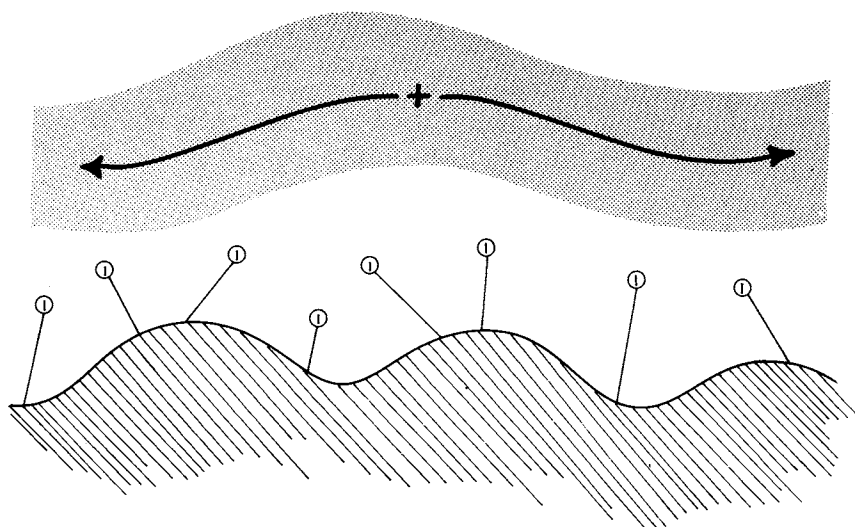


Figure 2. Schematic illustration of atmospheric condensation. Positive counterions flow freely around the surface of the polyelectrolyte, constrained into a shell by the electrostatic potential around the charged macromolecule.

condense in order to decrease the electrostatic repulsion, thus bringing back the value of  $\xi$ , a reduced linear charge density, to a critical value : for univalent counter-ions, such as  $\text{Na}^+$ ,  $\xi_c = 1$ . The corresponding critical distance is given by  $d_c = e^2/\epsilon K T$ , where  $e$  is the electronic charge,  $\epsilon$  the dielectric constant of the solvent,  $K$  the Boltzmann constant, and  $T$  the absolute temperature. In water, at  $25^\circ\text{C}$ ,  $d_c = 7.1 \text{ \AA}$ . The reduced linear charge density  $\xi$  is simply the ratio of the mean distance between adjacent charges on the polyelectrolyte, projected onto the cylindrical axis of the polyanion, to  $d_c$ .

Various treatments of atmospheric condensation have been offered. The simplest approximation, that of Manning (31), is to consider that the charge fraction  $f$  (i.e., the ratio of the number of non neutralized negative charges to the total number of negative charges along the poly-anion) is given by the following relations:

$$f = (\xi)^{-1} \quad \text{whenever } \xi > 1$$

$$f = 1 \quad \text{whenever } \xi < 1$$

where the dimensionless parameter  $\xi = -e^2/ K T b$  depends upon the average linear charge spacing  $b$  of the poly-anion, bearing univalent charged groups. What these relations describe is condensation of  $\text{Na}^+$  ions into the atmosphere around the polyanion as soon as the parameter  $\xi$  reaches unity.

For instance, the system consisting of polyacrylic acid in the presence of  $\text{Na}^+$  is such that condensation, absent at  $\xi = 0.8$ , does occur at  $\xi = 1.1$  (32,33). When  $\text{NaCl}$  is added to a solution of the tetramethylammonium (TMA) salt of polyacrylic acid, the relaxation rate  $R$  of  $^{23}\text{Na}$  is a fast decreasing function of the  $[\text{Na}^+]/[\text{TMA}]$  ratio, which demonstrates the heterogeneity in the physical states of condensed counter ions (34).

The Glycosaminoglycans. An important category of biological polyelectrolytes, the glycosaminoglycans, includes biopolymers (formerly named mucopolysaccharides) which occur at neuronal synapses, in the extracellular volume of connective tissues, etc. Accumulation of these substances in the nervous tissues, including the central nervous system, of young animals, prevents normal transmission of the nervous impulse, and is termed mucopolysaccharidosis. This disease is very severe and rather widespread, which underlines the importance of a better knowledge, at the molecular level, of mucopolysaccharides.

A  $^{23}\text{Na}$  NMR study has been performed on chondroitin sulfate and dermatan sulfate, which have one ionizable group, alternatively  $-\text{OSO}_3^-$  and  $-\text{COO}^-$  on each monosaccharide unit; and on hyaluronic acid, with a  $-\text{COO}^-$  group on every second monosaccharide unit (35). The relaxation rate  $R_2$  increases with

the degree of neutralization  $\alpha$  as a sigmoidal change. The results were analyzed in greater detail for dermatan-4-sulfate (35), indicating a gradual increase of the correlation time  $\tau_c$  with the addition of HCl, bringing about a reduction of the degree of neutralization  $\alpha$  of the poly-electrolyte. The product  $p_B \cdot \chi^2$  can also be determined, where  $p_B$  is the mole fraction of bound  $\text{Na}^+$  ions, and  $\chi$  the quadrupolar coupling constant in the bound state, from comparison of the longitudinal  $R_1$  and transverse  $R_2$  relaxation rates: it undergoes a sharp increase in the range  $\alpha = 0.6 - 0.9$  (35). In this range,  $\chi$  is essentially independent of  $\alpha$ , with a value of about 0.15 MHz, which is consistent only with a full hydration shell, and therefore with atmospheric condensation rather than site binding.

Conversely, when we studied sodium heparinate, we found that site binding is the predominant mode of interaction (36,37): the quadrupolar coupling constant characteristic of the bound  $\text{Na}^+$  was estimated at 1.2 MHz, consistent with chelation of  $\text{Na}^+$  by carboxyl groups on two monosaccharide units separated by a third one. Furthermore, one could analyze using the mass-action formulation competition experiments to provide the following sequence of binding strength by heparin:  $\text{Ca}^{++} > \text{Mg}^{++} \gg \text{Na}^+, \text{K}^+ > \text{Li}^+ \gg \text{N}(\text{CH}_3)_4$ .

Interaction with DNA. The interaction of the univalent  $\text{Na}^+$  ions with DNA has also been described in terms of either specific binding to the negatively charged phosphate groups, or formation of a positively-charged atmosphere around the regularly spaced phosphate groups. A variety of methods had been applied to the problem, prior to the use of sodium-23 NMR, and did not give an unambiguous answer (38-41). The matter is important, and could be of biological importance because of the high physiological concentration of the  $\text{Na}^+$  ions.

Reuben, Shporer and Gabbay (42) made the pioneering application of  $^{23}\text{Na}$  (and  $^{87}\text{Rb}$ ) NMR to this question. They measured longitudinal relaxation rates of NaCl (1M), in the presence of DNA (91.6 nM), at three distinct frequencies: 4.3, 8.15, and 15.7 MHz. This yields a correlation time  $\tau_c = 5.5$  ns. A variable concentration experiment gave a limiting relaxation rate in the bound state of 170Hz which, taken together with the value of  $\tau_c$ , translates into a very small value of 0.1 MHz for the quadrupolar coupling constant. By reference, the quadrupolar coupling constant for the hexaquo  $\text{Na}^+$  ion is ca. 0.5 MHz.

When Reuben, Shporer, and Gabbay (42) analyzed their results with a mass action law model, the resultant quadrupolar coupling constant had this absurdly low value: which led these authors (42) to reject a site-binding model.

Thus, these authors (42) were led to conclude that, to a large extent (> 99%),  $\text{Na}^+$  ions merely condense in the atmosphere surrounding the charged macromolecule, due to electrostatic interaction rather than the more specific chemical ion pair

formation. The earlier results of James and Noggle (43) on soluble RNA also fitted the same description.

These conclusions were put on a firmer basis by Anderson, Record and Hart (44) in a cogent piece of work, on the cation-DNA interactions, studied by sodium-23 NMR. They find, in the high salt range of the titrations, with sodium-to-phosphate ratios above 2, a linear dependence of the linewidth at half-height  $\Delta\nu_{1/2}$  with  $[P]/[Na]$ . This result is consistent with the condensation model, only if the fraction  $r$  of polyanionic charge on DNA neutralized by sodium association is a constant.

In order to determine the value of this constant  $r$ , it is mandatory to analyze the non-linear, low salt region of the titration curves, when  $Na^+$  is not the only ion associated with the nucleic acid. The competing cations chosen were tetrabutyl- and tetraethylammonium, so that they would have much lower affinity than sodium for DNA, yet display similar electrostatic interactions: *i.e.* they should be capable of condensation only. Fitting of the titration curves revealed that the relative affinities of  $Na^+$ ,  $(C_2H_5)_4N^+$ , and  $(C_4H_9)_4N^+$  for DNA are approximately in the ratio 20 : 5 : 1. The  $r$  values are in the range 0.6 - 1.0 for the tetraethyl- $Na^+$  and 0.65 - 0.85 for the tetrabutyl- $Na^+$  system. These compare quite well with the theoretical value  $r = 0.76$  based upon the linear charge density on DNA, from phosphate charges 1.7 Å apart from one another (as projected onto the helical axis). The limiting relaxation rate of bound sodium is  $180 \pm 10$  Hz, in good agreement with the value reported in the earlier study (42). But the main conclusion from this precise determination of the type of interaction present between  $Na^+$  and DNA is to exclude a mass action model.

Binding to Phosphatidylserine Vesicles. As in the case of DNA (see preceding section), an early study had concluded that  $Na^+$  cations bind weakly to phosphatidylserine vesicles, from  $^{23}Na$  NMR relaxation measurements (45). More recently, this question has been carefully reexamined by two groups in Buffalo, working in collaboration (46,47). The initial finding, of moderately strong sodium binding ( $K = 0.8 M^{-1}$  versus 4 and  $35 M^{-1}$  for  $Mg^{++}$  and  $Ca^{++}$ , respectively) (46), has been fully confirmed by a recent detailed investigation of the  $^{23}Na$  relaxation rate enhancements of  $Na^+$  in presence of competing cations (47).

The two limiting cases are again specific binding and atmospheric condensation. Specific binding, as exemplified by the divalent cations  $Ca^{++}$  and  $Mg^{++}$ , implies entrapment within a Stern layer and attachment to a specific group, such as carboxylate or phosphate. Atmospheric condensation refers to the presence of the fully hydrated ion in a diffuse double layer or in a Gouy-Chapman shell.

The relaxation rate enhancements for  $Na^+$  in the presence of phosphatidylserine vesicles are moderate (a maximum of 40 Hz), and the motional narrowing condition prevails: the magnetization

decay curves remain monoexponential (47). The authors analyze their data with a simplified two-sites model, in which  $\text{Na}^+$  ions are either free or bound to the external surface of the vesicles (the contribution from  $\text{Na}^+$  ions inside the vesicles is minor, and can safely be neglected). Data analysis confirms the value for the binding constant:  $K_{\text{Na}} \approx 0.8 \text{ M}^{-1}$ . Partial displacement of  $\text{Na}^+$  ions occurs upon competition with  $\text{Ca}^{++}$  or  $\text{Mg}^{++}$  ions. Tetraethylammonium ions have much less influence: they do not compete for a phosphatidylserine binding site with the  $\text{Na}^+$  ions; their presence in the double layer only alters the surface potential of the vesicles. As a result, the fraction  $p_B$  of bound  $\text{Na}^+$  decreases by about 10% when 0.1 M  $(\text{C}_2\text{H}_5)_4\text{N}^+$  is added to a 0.1 M  $\text{Na}^+$  solution, holding a suspension of the sonicated phosphatidylserine vesicles. By comparison, 22% of the phosphatidylserine charges are associated with  $\text{Na}^+$  and 53% are neutralized by  $\text{Ca}^{++}$  when 0.5 mM  $\text{Ca}^{++}$  is added to a 0.1 M  $\text{Na}^+$  solution containing the vesicles (47).

The somewhat low value of the limiting relaxation rate  $R_B$  for the bound state (260 Hz) is a little intriguing: it may correspond to the sodium cation retaining its full hydration shell in the bound state; and/or to a rather short correlation time in this bound state (47). Both these criteria evoke atmospheric condensation rather than true site binding. These phosphatidylserine vesicles appear to this writer as an intermediate case between the two extremes of site binding and of atmospheric condensation.

### Results for Ionophore Antibiotics

Quite a number of antibiotics are effective because of their cation-binding ability. Some of them are also efficient ion-carriers across membranes. Their study has focussed on the ion-binding properties, both in terms of thermodynamics and in terms of kinetics; and on transport of cations. Three levels of complexity can be distinguished: as a first step, the work is performed in homogeneous media, simulating the membrane environment; as a second step, membrane models are used; the third step being the study of real membranes. By and large, only exploratory studies have been performed, and they have gone not much further than the second step just defined, because of the complexity of most biological systems, with the possible exception of erythrocyte ghosts.

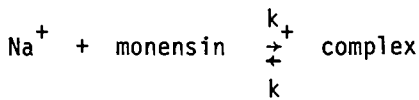
Numerous  $^1\text{H}$  and  $^{13}\text{C}$  NMR studies of ion-ionophore interactions have been performed. They serve to determine the nature of the atoms coordinated to the cation in the ionophore, and to monitor the conformational changes undergone by the ionophore upon ion capture.

Tetracycline inhibits the growth of bacteria by blocking protein synthesis at the ribosomes. We have performed a study of the thermodynamics of cation binding by tetracycline in aqueous

solution, at pH 2.3 and 8.6, using sodium-23 nuclear magnetic resonance (48). Its high sensitivity allowed the binding constants of other univalent cations to be determined through competition experiments. At pH 8.6, complexation follows the sequence:  $\text{Li}^+ > \text{Na}^+, \text{Cs}^+ > \text{K}^+ > \text{Rb}^+$ . The dissociation constants  $K_d$  for 1:1 complexes between tetracycline and the univalent alkali metal cations are of the order of 50 mM. With this knowledge, it is possible to determine the nature of the tetracycline species which attaches itself to the bacterial ribosome. Given the cytoplasmic concentrations of various cations, if each of the following species would be present alone it would partially neutralize tetracycline to the extent of:  $\text{Mg}^{++} = 71\%$ ;  $\text{Na}^+ = 14\%$ ;  $\text{K}^+ = 53\%$ . In the extracellular fluid, the figures are:  $\text{Mg}^{++} = 75\%$ ;  $\text{Ca}^{++} = 75\%$ ;  $\text{Zn}^{++} = 75\%$ ;  $\text{Na}^+ = 65\%$ . This serves to show that univalent cations have far from negligible effects compared to divalent ions. Also, the antibiotic is close to being fully neutralized by metal cations when it binds to the ribosome. Hence, it is likely that it bonds unto lipophilic membrane sites, rather than in the more polar environment at the interface with the solvent (48).

Another antibiotic ionophore, lasalocid (X-537 A) is a member of the family of linear carboxylic polyethers, capable of pseudo-cyclization around the cation. We have elected to study it, because of its remarkable avidity for binding numerous entities. Not only does it complex and transport a wide variety of ions: alkali and alkaline earth, rare earth, transition metal ions. It has similar action on biogenic amines. Furthermore, it also stimulates thromboxane or prostaglandin synthesis, and thus affects calcium metabolism. Through direct observation of the sodium ion, we have demonstrated competitive binding of  $\text{Na}^+$  and biogenic amines by lasalocid (49). We chose to study this competition in a binary mixture of methanol and *n*-hexane (71:29 v/v) in order to mimic the lipid membrane-aqueous solution interface. These conditions are such that only 1:1 complexes form. The stability constants of the complexes are ( $M^{-1}$ ): 500 towards  $\text{Na}^+$ , 260 towards 3-hydroxytyramine, 280 with L-norepinephrine, and 450 with serotonin bimalate (49).

Monensin is another member of this family of carboxylic polyether ionophores. The kinetics of sodium binding ( $k_+$ ) and release ( $k_-$ ) by the monensin ionophore in methanol have been determined by  $^{23}\text{Na}$  NMR spectroscopy (18). The exchange between free and bound  $\text{Na}^+$  ions is adequately described by the equation:



At 25°C, the rate constant corresponding to this first-order dissociative mechanism is  $k_- = 63 \text{ s}^{-1}$ , corresponding from the independently-determined value of the equilibrium constant, to  $k_+$



=  $6.3 \cdot 10^7 \text{ M}^{-1} \text{ s}^{-1}$ . The activation parameters descriptive of the release of  $\text{Na}^+$  ions from the complex are  $\Delta H_a^\ddagger = 10.3 \text{ kcal.mol}^{-1}$ , and  $\Delta S_a^\ddagger = -15.8 \text{ cal.mol}^{-1} \cdot \text{K}^{-1}$ . The latter value, when compared to those for reference compounds, indicates that the monensin anion does not undergo a conformational change prior to interaction with the sodium (18).

Besides carrier antibiotics, there are also antibiotics which effect transport because they form channels within the cellular membranes. Such is the case of gramicidin A, a linear pentadecapeptide, with regular alternation of L and D aminoacid residues: formyl-L-Val-Gly-L-Ala-D-Leu-L-Ala-D-Val-L-Val-D-Val-(L-Trp-D-Leu)<sub>3</sub>-L-Trp-ethanolamide. Ionic permeability conferred on membranes by gramicidin doping occurs through association of gramicidin molecules into head-to-head dimers, which form channels responsible for the transport process. According to a sophisticated mathematical analysis of conductance data, two kinds of sites are associated with each gramicidin A channel: outer sites, at the entrance to the channel; and inner sites, to which univalent ions can migrate only by overcoming an energy barrier, and which are also significantly higher in potential energy. We decided to test this proposal of a duality of sites by having a direct look, using sodium-23 NMR (50). Indeed, in ethanol-water mixtures (90 : 10) the gramicidin dimer binds  $\text{Na}^+$  cations at well-defined sites ( $\chi$  has the high value of 1.7 MHz, consistent only with partial desolvation of the bound cation), with a binding constant  $K = 4 \text{ M}^{-1}$ . By comparison, the sodium binding constant inferred from the fitting of conductance data in symmetrical single salt solutions is  $K = 2.9 \text{ M}^{-1}$ , in nice agreement. The rate constants for binding and release are  $k_+ < 2.2 \cdot 10^9 \text{ M}^{-1} \text{ s}^{-1}$ , and  $k_- < 5.5 \cdot 10^8 \text{ s}^{-1}$ , respectively. The high value of  $k_+$  close to the diffusion-control limit, points to the outer sites as the  $\text{Na}^+$ -binding sites (50).

Almost simultaneous with our work, the group headed by Dan Urry, which has been responsible for many elegant studies of the gramicidin A properties, showed with the help of  $^{23}\text{Na}$  NMR that gramicidin channels can pack themselves into micelles formed by lysolecithin (51). Gramicidin is incorporated into the hydrophobic core of the micelle. The temperature dependence of the sodium-23 linewidth defines an exchange process with an activation energy of  $6.8 \text{ kcal.mol}^{-1}$  which is essentially the same as the activation energy earlier reported for transport through the channel in lecithin bilayer studies, and the sodium exchange process is blocked by ions ( $\text{Ag}^+$ ,  $\text{Tl}^+$ ) which are also known to block sodium transport through the channel (51).

It now remains to determine the binding constants, and the attendant kinetic parameters, for  $\text{Na}^+$  interacting with the inner and outer sites of gramicidin channels incorporated in membranes, or in membrane models. We fully expect our conclusions on the binding by the outer sites, as obtained in solution, to be transferable to the real membrane environment with only minor

adjustment. It would be nice, though, to have an accurate determination by  $^{23}\text{Na}$  NMR of the binding characteristics to the inner sites too.

### Cation-Binding Muscular Proteins

**Calciproteins:** this term has become recognized for the manifold of proteins which bind and store calcium ions.  $\text{Ca}^{++}$  ions are important because they serve as second messengers: their binding by proteins such as calmodulin is a chemical signal for the occurrence of such important biological events as muscular contraction, hormonal action, blood clotting, self-assembly of microtubules, production of neurotransmitters, and intercellular communication.

The calciproteins we have investigated: parvalbumins, troponin C, calmodulin, are closely inter-related. Parvalbumins are ubiquitous substances, found mostly in the muscles of vertebrates. From their sequence of amino acids, their evolution is inferred. The ancestor of the present-day parvalbumins would appear to have consisted of two helices joined at a single calcium-binding site. Gene fusion and duplication occurred twice, and produced a I-II-III-IV sequence. The evolutionary loss of region I was accompanied by the disappearance of the calcium-binding ability of region II (52,53). Thus, the present parvalbumins II-III-IV have six helical portions, labelled as A-F, and they bind only two calcium cations, one at the C/D and one at the E/F junction (54). Parvalbumins are structurally related to the light chains of myosin (55). They resemble and can substitute for the calcium-dependent regulator of cyclic nucleotide phosphodiesterase: for instance, carp parvalbumin activates rat brain phosphodiesterase in a  $\text{Ca}^{++}$ -dependent manner (55). Troponin-C has a I-II-III-IV sequence (using the same notation) of four homologous regions, which are structurally very similar to each of the three regions of parvalbumins (56-58). Skeletal muscle troponin C has thus retained four  $\text{Ca}^{++}$ -binding sites. Calmodulin has a molecular weight (ca.18,000) and constitution very similar to those of troponin C, with the four homologous regions I-II-III-IV. However, there is marked functional difference: while the binding of  $\text{Ca}^{++}$  ions onto troponin C initiates muscular contraction, calmodulin is a regulatory protein. Troponin C is one of the three components of troponin, which is present in vertebrate muscles. Troponin-T interacts with another protein, tropomyosin. Troponin-I inhibits actomyosin in ATPase activity. And, in the presence of  $\text{Ca}^{++}$ , troponin-C prevents this inhibition by troponin-I.

The accurately-determined structure of parvalbumin (59) will serve to describe this family of calciproteins. These are globular proteins, with an ellipsoidal shape: the long axis of 36 Å and the short axis of 30 Å define the overall shape, which includes a hydrophobic core approximately 14 x 18 Å (59), (Figure 3)

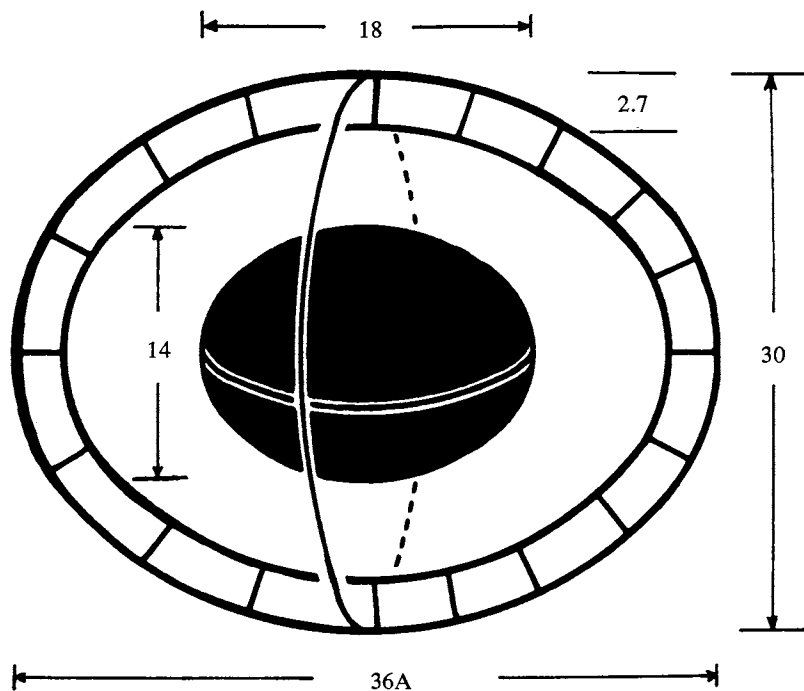


*Figure 3. The muscle calcium binding protein molecule has the general shape of a prolate ellipsoid of revolution (59). The shell, 2.7-Å thick, contains those atoms, exclusive of hydrogen, that would be exposed to the solvent were there no surface indentations. The oblate ellipsoid hydrocarbon core consists of side chains of phenylalanine, leucine, isoleucine, and valine.*

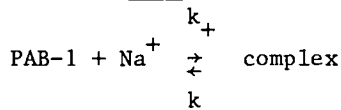
The two calcium-binding sites are located outside of this core, and close to the molecular surface: at the junction of the C and D helices, and at the junction of the E and F helices. (Figure 4)

Notice that because of the gene duplication, these two isomorphous moieties are related to one another as a pair of right hands (59), (Figure 4)

Calmodulin is held to be the ancestor protein for troponin-C, parvalbumin, and the light chains of myosin. It is homologous with troponin-C, and its I-II-III-IV structure holds four calcium-binding sites which are but weakly differentiated.

The ionic radii of  $\text{Ca}^{++}$  and  $\text{Na}^+$  ions are very similar: 1:00 versus 0.95 Å, respectively, for hexacoordinate ions. Both these cations have hydration numbers of 6. Thus, and since direct observation of  $\text{Ca}^{++}$  ions is impeded by the high price and poor magnetic properties of calcium-43, we decided to use  $\text{Na}^+$  ions as iso-steric probes into the structure of calcium-binding sites. However, on the basis of electrostatics alone, the binding energy for  $\text{Ca}^{++}$  is twice that for  $\text{Na}^+$ . Hence, the strategy of prior removing a portion of the calcium ions from the calciproteins. Then, we explore, taking full advantage of the high sensitivity of sodium-23 NMR, the deserted calcium-binding sites, using sodium ions.

For instance, it is possible to remove selectively and reversibly a single calcium ion from pike or carp parvalbumin with EGTA (60-61). The resulting single calcium protein (PAB-1) retains most of the conformational integrity of the native protein (PAB-2), as seen for instance from the helical content deduced from chiroptical properties or from  $^1\text{H}$  and  $^{13}\text{C}$  NMR parameters (60). Binding of sodium ions into the vacant EF calcium-binding site (Fig. 5) is demonstrated by the linear increase of the  $^{23}\text{Na}$  transverse relaxation rate with concentration of PAB-1. By (Figure 5) contrast, the linewidth shows no change upon admixture of the sodium chloride aqueous solutions with PAB-2 (62). As a check, introduction of  $\text{CaCl}_2$  displaces  $\text{Na}^+$  ions from their binding site on PAB-1: the  $\text{Ca}^{++}/\text{Na}^+$  competition can be followed from the return of the  $^{23}\text{Na}$  relaxation rate from a relatively high value ( $\sim 300 \text{ s}^{-1}$ ) to the low value ( $\sim 40 \text{ s}^{-1}$ ) characteristic of free sodium ions in the solution, as  $\text{Ca}^{++}$  ions are added (62-64). Furthermore, the correlation time  $\tau_c$  for the bound  $\text{Na}^+$  is similar to the reorientational correlation time  $\tau_R$  for the protein host as measured by  $^{13}\text{C}$   $T_1$  determinations (62). For the equilibrium:



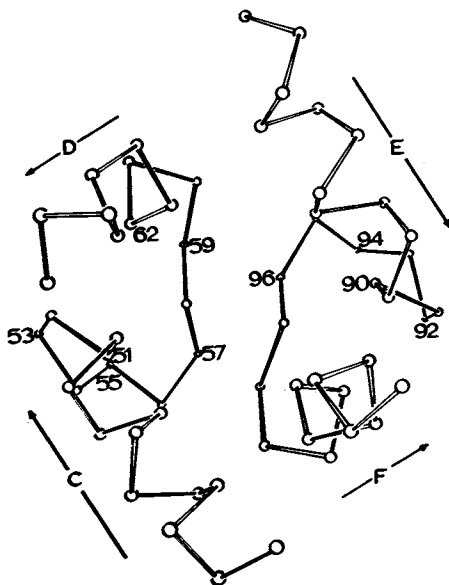


Figure 4. Helix C, the CD binding loop, and helix D are related to the EF regions by an approximate twofold axis (59). The CD and EF regions can be symbolized by a pair of right hands. Helix C (and helix E) runs from the tip to the base of the forefinger. The flexed middle finger corresponds to the CD (and EF) calcium binding loop. Helix D (and helix F) runs to the end of the thumb.

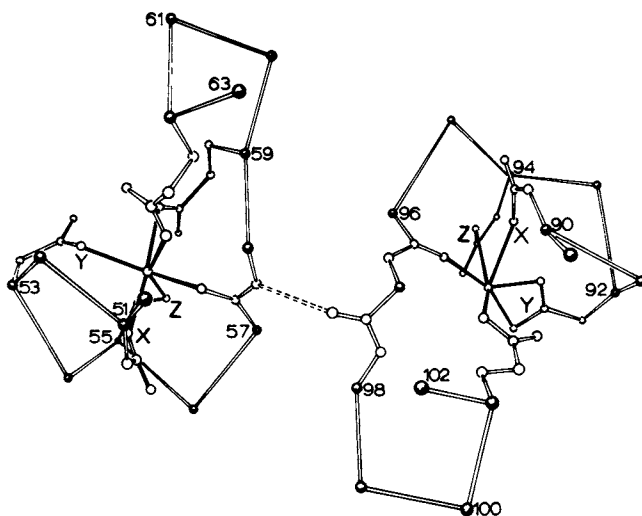


Figure 5. The CD and EF calcium binding loops are viewed, as in Figure 4, down the twofold axis. Individual side-chain atoms that coordinate the two calcium ions are drawn. The CD  $\text{Ca}^{++}$  ion is octahedrally coordinated by a side-chain oxygen of Asp-51, Asp-53, Ser-55, Glu-59, and Glu-101 and by the carbonyl oxygen of Lys-96, plus a water molecule at the X vertex.

we have derived (63) the rate constants for binding and release (see section 3.3):

$$k_+ = 0.6 \times 10^9 \text{ M}^{-1} \text{ s}^{-1}$$
$$k_- = 2 \times 10^7 \text{ s}^{-1}.$$

Interestingly, sodium-binding and calcium-binding differ mostly, not in the binding step (both bind at a rate close to the diffusion limit), but in the release step, with calcium release several orders of magnitude below sodium release:  $10 - 10^2 \text{ s}^{-1}$  versus  $2 \times 10^7 \text{ s}^{-1}$  (63). Hence, the thermodynamic preference of parvalbumins for calcium over sodium, which is related to the difference in the mode of binding of the two metals, calcium binding as a close to fully dehydrated ion, while sodium binds as a close to fully hydrated ion ( $\text{Ca}^{++}$ , 1  $\text{H}_2\text{O}$  against  $\text{Na}^+$ , 4-5  $\text{H}_2\text{O}$ ) (63). In this study of  $\text{Na}^+$  binding to a protein (PAB-1) near to the native state and renatured upon calcium addition, we find moderately strong binding of  $\text{Na}^+$  ( $K = 30 \text{ M}^{-1}$  at  $25^\circ\text{C}$ ) and we find  $\text{Na}^+/\text{Ca}^{++}$  competitive binding (62-64).

Sodium-23 NMR was also used as an indicator of sodium binding to troponin C (65). Two of the four calcium-binding sites can bind either  $\text{Ca}^{++}$  or  $\text{Mg}^{++}$ , and show a high affinity for  $\text{Ca}^{++}$  ( $K = 2 \cdot 10^7 \text{ M}^{-1}$ ) at low  $\text{Mg}^{++}$  concentrations, whereas the other two sites are  $\text{Ca}^{++}$ -specific and have a lower affinity for this cation ( $K = 10^5 \text{ M}^{-1}$ ) (66-67). These two classes of sites appear to be involved in different functions: binding of  $\text{Ca}^{++}$  to the high affinity sites effects a conformational change into the suitable configuration (68), whereas the low affinity  $\text{Ca}^{++}$ -specific sites control the interaction between actin and myosin in the muscle (66, 67, 69-72). Digestion by the proteolytic enzyme trypsin leads to the cleavage of the peptide bonds involving Arg-8, Lys-84, and Lys-88. Two main fragments are isolated (73-75): TR-1 (residues 9-84) contains the two  $\text{Ca}^{++}$ -binding sites I and II of low affinity; TR-2 (residues 89-159) carries the two high affinity  $\text{Ca}^{++}$  binding sites III and IV. Cyanogen bromide digestion of troponin-C yields the peptide CB-9 which contains residues 84-134, including the region responsible for troponin I binding and the high affinity site III (75-76) (Figure 6) (68).

The  $^{23}\text{Na}$  NMR results show competitive  $\text{Na}^+/\text{Ca}^{++}$  binding, below one calcium per molecule, with the low affinity sites I and II of TR-1 and troponin C (65). At low calcium content, sodium ions bind to TR-2 and to troponin-C non-competitively with  $\text{Ca}^{++}$  ions. Binding of  $\text{Ca}^{++}$  ions to the high affinity sites III and IV allosterically affects the binding of the  $\text{Na}^+$  ions: even when sites I and II located on TR-1, or sites I-IV of troponin-C, are saturated with  $\text{Ca}^{++}$  ions,  $\text{Na}^+$  ions continue to bind weakly at secondary binding sites (65). Quantitative analysis of the data

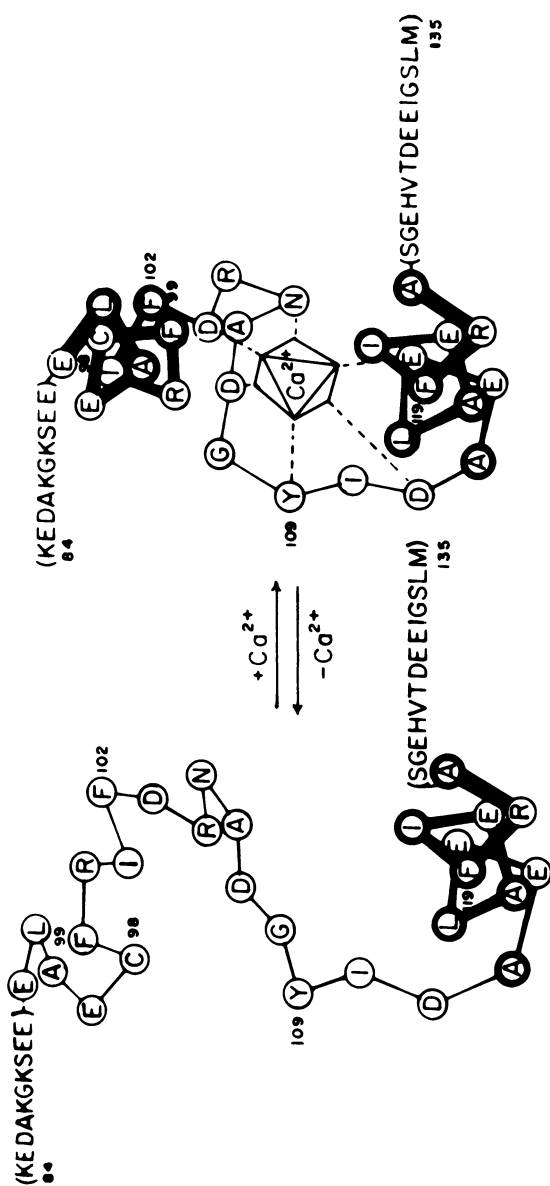


Figure 6. Schematic representation of the conformational change induced by  $\text{Ca}^{2+}$  in the CB-9 fragment of troponin-C (68).

yields  $K_{Na} = 10^2 M^{-1}$  and  $K_{Ca} = 5 \times 10^5 M^{-1}$  for sites I and II of TR-1. The binding constants  $K_{Na}$  for sites I and II of troponin-C itself are ca.  $100 M^{-1}$  (at  $6^\circ C$ ).

We have studied in like manner the interaction of  $Na^+$  ions with partly decalcified calmodulin, and with its tryptic fragments TR-1 and TR-2 (77). The observations are qualitatively similar to those obtained with the weak affinity sites of troponin-C: there is competitive  $Na^+/Ca^{++}$  binding. The correlation times for sodium bound to the protein ( $M = 18,000$ ) are closely similar for troponin-C (9.2 ns) (65) and for the homologous calmodulin (9.1 ns) (77). Like troponin-C, calmodulin retains some structure even at low calcium levels (78). While with troponin C and its tryptic fragment TR-1 sodium could bind also to secondary sites, in calmodulin displacement of  $Na^+$  ions from their binding sites by  $Ca^{++}$  ions is complete, and generates only free sodium ions: there are no secondary sites available for  $Na^+$  binding (77). We have also studied the influence of  $Mg^{++}$  ions, starting with the protein almost completely decalcified:  $Mg^{++}$  binding is weaker than  $Ca^{++}$  binding up to ratios of  $Mg^{++}$  ions to calmodulin close to 10. Likewise with the two tryptic fragments TR-1 and TR-2. But conformational changes occur upon addition of  $Mg^{++}$ , as compared to  $Ca^{++}$  (78-80): they are similar to those caused by  $Na^+$  ions.

Sodium and calcium binding to Panulirus interruptus hemocyanin has also been studied by  $^{23}Na$  NMR (81): this is a much larger protein than those just discussed, consisting of six subunits having each a molecular weight of 75,000 and one oxygen-binding site. From the observed changes of the  $^{23}Na$  relaxation parameters as a function of  $Ca^{++}$  concentration, 3-5  $Ca^{++}$  ions are needed to displace sodium ions from high affinity sites. There are at least 6-10 such high-affinity sites per hemocyanin subunit (81). Binding of oxygen affects that of sodium ions: addition of oxygen to a solution of deoxyhemocyanin produces an increase in the  $^{23}Na$  linewidth: for instance, in the absence of  $Ca^{++}$  ions, the oxy and deoxy forms correspond to enhancements of the fast-relaxation components of 102 and 90 Hz, respectively (81). This is in agreement with oxygen equilibrium measurements, which indicate stronger binding of  $Na^+$  ions to the oxy than to the deoxy form of the protein.

#### Structures Maintained by $Na^+$ Binding: The 5'-GMP Supramolecular Assembly

Alone among the nucleotides, guanosine monophosphate (GMP) is capable of self-ordering (82). We have been interested in the aggregates formed by the 5'-isomer, in aqueous solution, at pHs close to neutrality: there has been speculation that these self-ordered structures could have played an important pre-biotic role (83-85), and it is unlikely that the primeval ocean would have had a pH markedly different from that prevailing nowadays, i.e. in the pH range 7.8 - 8.4 (86-88).



The transition of the disodium salt  $5'-\text{GMP}^{2-}$ ,  $2 \text{Na}^+$  from the disordered monomeric state to the ordered  $n$ -mer can be brought about, either by lowering the temperature at constant concentration, or by increasing the concentration at constant temperature. It is a quite sharp transition, with a "melting" range of some  $15^\circ$  (89-90). The phenomenon was discovered in 1972 with the help of infrared spectroscopy (89). Later, the same group used  $^1\text{H}$  NMR to find that the aggregates are highly rigid (91): there are non-equivalent sites so that, for instance, the H-8 resonance splits into four lines at 273 K. The two outer lines, 1.3 ppm apart, are still separated to the same extent at 307 K: energy barriers of at least  $15 \text{ kcal.mol}^{-1}$  prevent fast exchange of monomer nucleotides between sites (91).  $^{31}\text{P}$  NMR for the phosphate groups yields similar results (92). By correlating information from  $^1\text{H}$  and  $^{31}\text{P}$  NMR, it can be shown (93) that the system consists of at least three types of structures: a regular, ordered structure containing two different but equally populated types of  $^1\text{H}$ -8 and  $^{31}\text{P}$  environments (A); another regular, ordered structure containing a single type of  $^1\text{H}$ -8 and  $^{31}\text{P}$  environment (B); and more mobile structures corresponding to the time-averaging of two or more classes of  $^1\text{H}$ -8 protons and  $^{31}\text{P}$  nuclei in rapid chemical exchange (C).

The X-ray structures of the aggregates formed by  $5'$ -GMP at slightly basic pHs (8.2) point to the presence of planar tetrameric arrangements of the guanine bases, centrosymmetric, and held together by eight hydrogen bonds. These tetramers stack into a right-handed helix, each tetramer being rotated by  $30^\circ$  with respect to its neighbors (94). The soluble aggregates formed in neutral solution at concentrations between 0.5 and 1 M thus appear to be built from the stacking of tetrameric units (94).

We have investigated the role of alkali metal cations in the build-up of these structures, using  $^7\text{Li}$  (95),  $^{23}\text{Na}$  (90,93,96-101),  $^{39}\text{K}$  (96,97) and  $^{87}\text{Rb}$  (95,97) NMR. The latter three techniques are well suited for this study (lithium ions do not nucleate the self-ordering of  $5'$ -GMP), and can also be used to follow the disorder-order transition.

For instance, abrupt changes occur in the  $^{23}\text{Na}$  resonance position and linewidth with a decrease in temperature or an increase in concentration of  $5'$ -GMP,  $\text{Na}_2$  (90,93,96-101). A more subtle change affects the lineshape: as aggregation sets in, it becomes markedly non-Lorentzian, thus proving that a fraction of the sodium ions are bound to very slowly reorienting  $n$ -mers, characterized by correlation times greater than about 5 ns. ( $1 \text{ ns} = 10^{-9} \text{ s}$ )(100).

The pronounced upfield chemical shift of the  $^{23}\text{Na}$  resonance (the observed line shifting by about 15 ppm, while the limiting chemical shift in the pure aggregates is greater by one order of magnitude) is attributed to inclusion of the  $\text{Na}^+$  cation in the central cavity of the hydrogen-bonded tetramers, which has about

the right size to accommodate it (96). Not only can these core sites host  $\text{Na}^+$  ions, they can also interact with other alkali metal ions (96,102), with a selectivity sequence:  $\text{K}^+ > \text{Rb}^+, \text{Na}^+ \gg \text{Li}^+, \text{Cs}^+$ . Since potassium ions bind more strongly at these core sites than sodium ions, it would be expected that all the manifestations from binding to the ordered structures would be reduced in the sodium NMR spectra, in the presence of competing potassium ions: one ought to find a  $^{23}\text{Na}$  resonance resembling more, in width and in position, that of the free  $\text{Na}^+$  ions in the solution. Surprisingly, the converse obtains: in the presence of competing potassium ions, one observes a further broadening of the  $^{23}\text{Na}$  line. There is increased binding of sodium ions to ordered structures; to the extent that potassium ions nucleate the self-assembly process at concentrations (0.1 M) at which there is very little aggregation in their absence. What is implied by this finding of  $\text{K}^+-\text{Na}^+$  synergism is the existence of alternate sites than the core sites, to which the  $\text{Na}^+$  ions can attach themselves: these are the doubly charged phosphate groups on the periphery of the aggregates, at the interface with the solvent.

Thus, the self-ordered structures that form in the joint presence of  $\text{Na}^+$  and  $\text{K}^+$  ions have a duality of sites: inner sites, which are potassium ion-selective; and outer sites, which turn out to be sodium ion-selective (97). A chemical equilibrium model leads to the conclusion that the main structure formed under such conditions consists of a dimer of tetramers of 5'-GMP, having one potassium ion sandwiched-in between the planes of the two tetramers, and with four sodium ions trapped on the outer sites constituted by the charged phosphate groups and/or the hydroxyl oxygens from the sugar (97). These supramolecular assemblies are maintained not only by hydrogen-bonding of the guanines into tetrameric arrays. Ion binding also contributes to the stability of these self-ordered structures. This can be shown by focussing on the approximate residence time  $\tau_B \sim 30$  ns for  $\text{Na}^+$  ions in the bound state on the ordered structures, which can be extracted from analysis of the non-Lorentzian lineshape. This value is consistent neither with an ion pairing to a single phosphate - dissociation mechanism for chemical exchange which would lead to a  $\tau_B$  value in the  $10^{-9}$ - $10^{-12}$  s range. Nor can it be reconciled with a monomer-n-me 5'-GMP exchange: the above-quoted 15 kcal.mol $^{-1}$  energy barrier translates into a  $\tau_B > 1.7 \times 10^{-2}$  s. The observed  $\tau_B$  value, which corresponds to an independently determined  $\Delta G^0 \sim 3$  kcal.mol $^{-1}$  at 273 K that has to be overcome for sodium ions to escape from the bound to the free state, is consistent only with sodium binding by several chemical groups: several phosphate groups, or a coalition of oxygen and nitrogen atoms from phosphate groups, the ribose sugar, and the guanine base are all involved in the formation of the sodium binding sites. Sodium cation binding contributes directly to the buildup of ordered structures which, for 5'-GMP,  $\text{Na}_2$  in the absence of

potassium ions, appear to be constituted predominantly of octamers (corresponding presumably to species of type A) coexisting with hexadecamers (the B type species) (93).

Our initial impetus for using  $^{23}\text{Na}$  NMR to study the complex self-assembly of 5'-GMP was the fact, already mentioned in the previous sections, that binding of even a few percent of the  $\text{Na}^+$  ions to a slowly reorienting macromolecule or molecular assembly will show up through an enhancement of the quadrupolar relaxation rate. This rather typical feature of quadrupolar ions allows, in straightforward cases when 1:1 ion pairs are the only significant species, for the determination of binding constants. Even in the absence of such simple 1:1 stoichiometry, as exemplified by the 5'-GMP system, there is a wealth of information to be garnered from the use of  $^{23}\text{Na}$  NMR. Such information, which complements that obtained by the resonance of covalent nuclei from the anion - such as  $^1\text{H}$ ,  $^{13}\text{C}$ , and  $^{31}\text{P}$  in the case of 5'-GMP $^{2-}$  - is both thermodynamic and kinetic; furthermore, it can uniquely characterize the intervention of the quadrupolar ion in the structure-forming that is thus being looked at directly.

### $^{23}\text{Na}$ NMR of Whole Tissue

The culmination of applications of  $^{23}\text{Na}$  NMR to the study of the binding of  $\text{Na}^+$  by biomolecules is clearly the determination of the mobility of the  $\text{Na}^+$  cation in cell and in whole organs. This potential was grasped quite early. Unfortunately, an error in interpretation marred the results, and further study became necessary.

Following the erroneous analysis by Freeman Cope (103-106) and a whole bandwagon (107-110), of  $^{23}\text{Na}$  NMR signals in whole tissue as due to strong immobilization of a substantial fraction (~ 60%) of the  $\text{Na}^+$  ions, the observations were convincingly attributed to the quadrupolar interactions, as described in Section 2, Monoi (111-112) reinterpreted the experimental results by the coexistence of two states of  $^{23}\text{Na}$  in such systems. The first state, in the liquid phase of tissue, is characterized by a single  $T_2$  and a single Larmor frequency (state A). The second state, attributed to membrane-bound sodium ions, thus has to be described with two different  $T_2$  values and/or more than one Larmor frequency in the first order perturbation effect (state B). Under moderately fast A  $\rightleftharpoons$  B exchange, the resulting lineshape consists of two Lorentzian components centered at the same frequency, but having different  $T_2$  values. When the fast relaxation  $T_2$  is sufficiently short, only the narrower component, with 40% of the total intensity, is seen (112). The observations agree with these theoretical predictions. For instance, if erythrocyte ghosts are present at sufficient concentration (above 1%), the  $^{23}\text{Na}$  resonance intensity is depressed: to 73% in the presence of 5 M erythrocyte ghosts (113); and the whole signal is restored at 100% its intensity in the presence of guanidinium

ions (113) which presumably denature the sodium-binding membrane components. Likewise, mitochondrial, heavy and light microsomal fractions of rat liver homogenate also lower the  $^{23}\text{Na}$  resonance intensity (113). Hence it is tempting to identify state B with  $\text{Na}^+$  ions paired to the head groups of phospholipids on either side of the cellular membranes (113).

Using halophilic-halotolerant bacteria  $B_{aI}$  isolated from the Dead Sea, Goldberg and Gilboa (114) went one step further in the analysis: there are two types of intracellular bound sodium, a fraction B which exchanges with the extracellular sodium A, and a fraction C which is bound but which does not exchange with the extracellular sodium. The exchanging fraction B is characterized by a correlation time  $\tau_c = 5.5 \times 10^{-7}$  s, while the lifetime of sodium at site B is  $\tau_B = 6 \times 10^{-4}$  s.

Chang and Woessner, using the spin-echo technique, made  $T_1$  and  $T_2$  measurements on skeletal muscle (115). While the  $T_1$  curve is close to a single exponential decay, the  $T_2$  curve can be fitted with a double exponential function. The fast and slow (f,s) components have  $T_2$  values of 16 and 1.6 ms, respectively, for fresh muscle. The  $T_1$  value for the same sample is 18 ms. Hence,  $T_{1f} = T_{1s}$ ;  $T_{2f} < T_{2s}$ ; and  $T_{2s} \approx T_1$ . The reader will recall (Section 2) that  $T_{1s}$  depends upon the spectral density at twice the Larmor frequency,  $T_{1f}$  depends on  $J(\omega_0)$ ; whereas  $T_{2f}$  depends upon spectral densities at zero and at Larmor frequency; and  $T_{2s}$  depends upon the sum  $J(\omega_0) + J(2\omega_0)$ . Thus, the experimental results obtained by Chang and Woessner imply that  $J(0) \gg J(\omega_0) \approx J(2\omega_0)$ . This last equality, in turn, indicates that  $\omega_0 \tau_c \ll 1$ . The former inequality  $J(0) \gg J(\omega_0)$  conversely implies that  $\omega_0 \tau_c > 1$ . Therefore the autocorrelation function consists of at least two exponential decay curves with differing correlation times:  $\omega_0 \tau_{c1} \ll 1 < \omega_0 \tau_{c2}$ . Since the Larmor frequency  $\omega_0$  in these experiments is 26.5 MHz,  $\tau_{c1} \ll 10^{-8}$  s: it must correspond to free sodium ions with their usual correlation time  $\tau_c \approx 10^{-11}$  s. Whereas  $\tau_{c2}$  is estimated as less than  $10^{-5}$  s from the fact that the fast  $T_2$  component is an exponential. The resulting quadrupolar coupling constants are  $\chi = 1.25$  MHz for the "free" sodium ions, and  $\chi < 0.17$  MHz for "bound" sodium ions. The low value of the quadrupolar coupling constant for these suggests atmospheric condensation around charged macromolecules. Following the Berendsen-Edzes proposal (116) that a long  $\tau_{c2}$  as found here ( $10^{-5} < \tau_{c2} < 10^{-8}$  s) reflects the time needed for a  $\text{Na}^+$  ion to diffuse out of a region inside the cell characterized by some macromolecular ordering, Chang and Woessner make an estimate of the size of these regions: from 80 to 2450 Å (these values correspond to the lower and upper limit of  $\tau_{c2}$  respectively). The vast majority of sodium ions (90%) are in this "bound" state, in the intracellular compartment, where they are absorbed or condensed to the charged sites of biomacromolecules, as water-separated ion pairs, at an anion-cation distance which could be as low as 4.5 Å. The

correlation time  $\tau_{c2} = 10^{-5} - 10^{-8}$  s agrees with that found by Goldberg and Gilboa (114)  $\tau_c = 5.5 \times 10^{-7}$  s for the bound exchanging intracellular sodium in halotolerant bacteria.

### Concluding Remarks

This review has been centered on the studies performed in the author's laboratory during the last few years. "Nobody can ever speak for anybody but himself-and even then in doubt and great confusion"(117). Despite such bias, it should be apparent that  $^{23}\text{Na}$  NMR is applicable to a great variety of systems. It provides invaluable information about stoichiometry of complex formation; about the mode of attachment, site-binding or atmospheric condensation; about thermodynamic binding constants; about rate constants for binding and release by bio-macromolecules. Sodium-23 NMR thus is complementary to the NMR of covalent nuclei such as  $^1\text{H}$ ,  $^{13}\text{C}$ , and  $^{31}\text{P}$ . It allows also, through competition experiments, for the indirect determination of the binding constants for more poorly endowed quadrupolar ions,  $^{39}\text{K}$ ,  $^{43}\text{Ca}$  being examples.

The future development of the field stretches in several directions: metabolic studies, in which  $^{23}\text{Na}$  NMR will usefully complement  $^1\text{H}$ ,  $^{13}\text{C}$ , and  $^{31}\text{P}$  NMR (one thinks primarily of the nerve impulse, and of active transport across membranes, in this respect); NMR imaging, also in conjunction with use of the  $^1\text{H}$  and  $^{31}\text{P}$  nuclei. But simple model systems will continue to be important, so that we gain a better understanding of the factors determining the magnitudes of chemical shifts and of quadrupolar coupling constants.

### ACKNOWLEDGEMENTS

My coworkers, listed in the references, formed an enthusiastic and efficient team, with much spirit and good humor: I owe them a very large debt indeed. I am also pleased to express my thanks to Fonds de la Recherche Fondamentale Collective, Brussels for their support of our program of study "Binding of ions by organic and biomolecules".

### LITERATURE CITED

1. Hubbard, P. S. J. Chem. Phys., 1976, **53**, 985.
2. Rubinstein, M.; Baram, A.; Luz, Z. Mol. Phys., 1971, **20**, 67.

3. Baram, A.; Luz, Z.; Alexander, S. *J. Chem. Phys.* 1973, 58.
4. Werbelow, L. G. *J. Magn. Res.* 1979, 34, 439.
5. Bull, T. E. *J. Magn. Res.* 1972, 8, 344.
6. Delville, A.; Detellier, C.; Laszlo, P. *J. Magn. Res.* 1979, 34 301.
7. Haslinger, E.; Lynden-Bell, R. M. *J. Magn. Res.* 1978, 31, 33.
8. Holz, M. *J. Chem. Soc. Faraday Trans I.* 1978, 74, 644.
9. Swift, T. J.; Connick, R. E. *J. Chem. Phys.* 1962, 37, 307.
10. Lanir, A.; Navon, G. *Biochemistry*, 1971, 10, 1024.
11. Eady, R. R.; Smith, B. E.; Cook, K. A.; Postgate, J. R. *Biochem. J.* 1972, 128, 655.
12. Deranleau, A. *J. Am. Chem. Soc.* 1969, 91, 4044, 4050.
13. Reuben, J. *J. Am. Chem. Soc.* 1973, 95, 3534.
- 13a. Deming, S. N.; Morgan, S. S. *Anal. Chem.* 1973, 45, 278A-282A.
14. Lenkinski, R. E.; Elgavish, G. A.; Reuben, J. *J. Magn. Res.* 1978, 32, 367.
15. Schchori, E.; Jagur-Godzinski, J.; Luz, Z.; Shporer, M. *J. Am. Chem. Soc.* 1971, 93, 7133.
16. Schchori, E.; Jagur-Grodzinski, J.; Shporer, M. *J. Am. Chem. Soc.* 1873M 95, 3842.
17. Shporer, M.; Zemel, H.; Luz, Z. *FEBS Letters*, 1974, 40, 357.
18. Degani, H. *Biophys. Chem.* 1977, 6, 345.
19. Bouquant, J.; Delville, A.; Grandjean, J.; Laszlo, P. *J. Am. Chem. Soc.* 1982, 104, 0000.
20. Eyring, H. *J. Chem. Phys.* 1936, 4, 283.
21. Laszlo, P. in *Progress in NMR Spectroscopy*, J. W. Emsley, J. Feeney and L. H. Sutcliffe, Eds. Pergamon Press, Oxford, 1980.
22. Collman, J. P. *Accounts Chem. Res.* 1975, 8, 342.
23. Cornelius, A.; Laszlo, P.; Cambillau, C. *J. Chem. Res.* (S), 1978, 462; (M) 1978, 5457.
24. Laszlo, P. *Angew. Chem.* 1978, 90, 271; *Angew. Chem. Int. Ed. Engl.* 1978, 17, 254.
25. Raban, M.; Noe, E. A.; Yamamoto, G. *J. Am. Chem. Soc.* 1977, 99, 6527.
26. Raban, M.; Haritos, D. *J. Chem. Soc. Chem. Comm.* 1978, 965.
27. O'Brien, D. H.; Russell, C. R.; Hart, A. J. *J. Am. Chem. Soc.* 1979, 101, 633.
28. Zana, R.; Tondre, C. *Biophys. Chem.* 1974, 1, 367.
29. Spegt, P.; Weill, G. *Biophys. Chem.* 1976, 4, 143.
30. Karenzi, P. C.; Meurer, B.; Spegt, P. Weill, G. *Biophys. Chem.* 1979, 9, 181.
31. Manning, G. S. *Accounts Chem. Res.* 1979, 12, 443.
32. van der Klink, J. J.; Zuiderweg, L. H.; Leyte, J. C. *J. Chem. Phys.* 1974, 60, 2391.
33. Manning, G. S. *J. Chem. Phys.* 1975, 62, 749.

34. Meurer, B.; Spegt, P.; Weill, G. Chem. Phys. Lett. 1978, **60**, 55.
35. Gustavsson, H.; Siegel, G.; Lindman B.; Fransson, L. A. FEBS Letters. 1978, **86**, 127.
36. Herwats, L.; Laszlo, P.; Genard, P. Nouveau J. Chim. 1977, **1**, 173.
37. Herwats, L. these de doctorat, University de Liege, 1978.
38. Eisenberg, H. in Basic Principles in Nucleic Acid Chemistry, P.O.P. Ts'0, Ed., Academic Press, New York, vol. 2, 1974, pp. 171-263.
39. Felsenfeld, G.; Miles, H, T, Ann. Rev. Biochem. 1967, **36**, 407-448.
40. Izatt, R. M.; Christensen, J. J.; Rytting, J. H. Chem. Rev. 1971, **71**, 439-481.
41. von Hippel, P. H.; McGhee, J. D. Ann. Rev. Biochem. 1972, **41**, 231-300.
42. Reuben, J.; Shporer, M.; Gabbay, E. J. Proc. Nat. Acad. Sci. USA. 1975 **72**, 245.
43. James, T. L.; Noggle, J. H. Proc. Nat. Acad. Sci. USA. 1969, **62**, 644.
44. Anderson, C. F.; Record, Jr., M. T.; Hart, P. A. Biophys. Chem. 1978, **7**, 301.
45. James, T. L.; Noggle, J. H. Anal. Biochem. 1972, **49**, 208.
46. Newton, C.; Pangborn, W.; Nir, S.; Paphadjopoulos, D. Biochim. Biophys. Acta. 1978, **506**, 281.
47. Kurland, R.; Newton, C.; Nir, S.; Papahadjopoulos, D. Biochim. Biophys. Acta. 1979, **551**, 137.
48. Coibion, C.; Laszlo, P. Biochem. Pharmacol. 1979, **28**, 1367.
49. Grandjean, J.; Laszlo, P. Angew. Chem. Int. Ed. Engl. 1979, **18**, 153.
50. Cornelis, A.; Laszlo, P. Biochemistry. 1979, **10**, 2004.
51. Urry, D. W.; Spisni, A.; Kahled, M. A. Biochem. Biophys. Res. Comm. 1979, **88**, 940.
52. Weeds, A. G.; McLachlan, A. D. Nature. 1974, **252**, 646.
53. Goodman, M.; Pechere, J. C. J. Mol. Evol. 1977, **9**, 131.
54. Moews, P. C.; Kretsinger, R. H. J. Mol. Biol. 1975, **91**, 229.
55. Potter, J. D.; Dedman, J. R.; Means, A. R. J. Biol. Chem. **252**, 5609.
56. Collins, J. H.; Potter, J. D.; Horn, M. J.; Wilshire, G.; Jackman, N. FEBS Letters. 1973, **36**, 268.
57. Collins, J. H. Biochem. Biophys. Res. Comm. 1974, **58**, 301.
58. Collins, J. H.; Potter, J. D.; Horn, M. J.; Wilshire, G.; Jackman, N. in Calcium Binding Proteins, W. Drabikowski, H. Strzelecka-Golaszewska, and E. Carafoli, Eds., Elsevier, Amsterdam, 1973, pp. 51-64.
59. Kretsinger, R. H.; Nockolds, C. E. J. Biol. Chem. 1973, **248**, 3313.

60. Donato, Jr., H.; Martin, R. B. Biochemistry, 1974, **13**, 4575.
61. Closset, J.; Gerday, Ch. Biochem. Biophys. Acta, 1975, **405**, 228.
62. Grandjean, J.; Laszlo, P.; Gerday, Ch. FEBS Letters, 1977, **81**, 376.
63. Grandjean, J.; Laszlo, P. in Protons and Ions Involved in Fast Dynamic Phenomena, P. Laszlo, ed., Elsevier, Amsterdam, 1978, pp. 373-380.
64. Gerday, Ch.; Grandjean, J.; Laszlo, P. FEBS Letters, 1979, **105**, 384.
65. Delville, A.; Grandjean, J.; Laszlo, P.; Gerday, Ch.; Grabarek, Z.; Drabikowski, W. Eur. J. Biochem... 1980, **105**, 289.
66. Potter, J. D.; Gergely, J. J. Biol. Chem. 1975, **250**, 4628.
67. Potter, J. D.; Seidel, J. C.; Leavis, P.; Lehrer, S. S.; Gergely, J. J. Biol. Chem. 1976, **251**, 7551.
68. Nagy, B.; Potter, J. D.; Gergely, J. J. Biol. Chem. 1978, **253**, 5971.
69. Bremel, R. D.; Weber, A. Nature New Biol. 1972, **238**, 97.
70. Potter, J. D.; Hsu, F. J.; Powmall, H. J. J. Biol. Chem. 1977, **252**, 2452.
71. Levine, B. A.; Mercola, D.; Coffman, D.; Thornton, J. M. J. Mol. Biol. 1977, **115**, 743.
72. Seamon, K. B.; Hartshorne, D. J.; Bothner-By, A. A. Biochemistry, **16**, 1977, 4039.
73. Leavis, P. C.; Rosenfeld, S. S.; Gergely, J.; Grabarek, Z.; Drabikowski, W.; J. Biol. Chem. 1978, **253**, 5452.
74. Drabikowski, W.; Grabarek, Z.; Barylko, B. Biochem. Biophys. Acta, 1977, **490**, 216.
75. Weeks, R. A.; Perry, S. V. Biochem. J. 1978, **173**, 449.
76. Weeks, R. A.; Perry, S. V.; Biochem. Soc. Trans. 1977, **5**, 1391.
77. Delville, A.; Grandjean, J.; Laszlo, P.; Gerday, Ch.; Brzeska, H.; Drabikowski, W. Eur. J. Biochem. in press.
78. Seamon, K. Biochem. Biophys. Res. Comm. 1979, **86**, 1256.
79. Walsh, M.; Oikawa, K.; Kay, C. M. Can. J. Biochem. 1979, **57**, 267.
80. Richman, P. G.; Klee, C. B. J. Biol. Chem. 1979, **254**, 5372.
81. Norne, J. E.; Gustavsson, H.; Forsen, S.; Chiancone, E.; Kuiper, H. A.; Antonini, E. Eur. J. Biochem. 1979, **98**, 591.
82. Guschlbauer, W.; Chantot, J. F. in Proceedings of the International Conference held in Dymaczewo near Poznan, 13-17.9.76, Poznan, pp. 96-114.
83. Sulston, J. E.; Lohrmann, R.; Orgel, L. E.; Miles, H. T. Proc. Nat. Acad. Sci. USA, 1960, **69**, 409.
84. Weimann, B. J.; Lohrmann, R.; Orgel, L. E. II Schneider-Bernloehr, and J. E. Sulston, Science, 1968, **161**, 387.
85. Orgel, L. E. J. Mol. Biol. 1968, **38**, 381.



86. Jukes, T. H.; Holmquist, R.; Moise, H. Science, 1975, **189**, 50.
87. Mackenzie, F. T. in Chemical Oceanography, 2nd ed., vol. 1., J. P. Riley and G. Skirrow, Eds., Academic Press, London, 1975, p. 309.
88. Burton, J. D. Chem. Inc. (London), 1977, p. 550.
89. Miles, H. T.; Frazier, J. Biochem. Biophys. Res. Comm., 1972, **49**, 199.
90. Paris, A. these de doctorat, Universite de liege, 1978.
91. Pinnavaia, T. J.; Miles, H. T.; Becker, E. J. J. Am. Chem. Soc., 1975, **97**, 7198.
92. Borzo, M.; Laszlo, P. Compt. Rend. Ac. Sci. Paris, 1978, **287C**, 475.
93. Borzo, M.; Detellier, C.; Laszlo, P.; Paris, A. J. Am. Chem. Soc., 1980 **102**, 1124.
94. Zimmerman, S. B. J. Mol. Biol., 1976, **106**, 663.
95. Rinaldi, P.; Laszlo, P. unpublished observations.
96. Detellier, C.; Paris, A.; Laszlo, P. Compt. Rend. Ac. Sci. Paris, 1978, **286D**, 781.
97. Detellier, C.; Laszlo, P. J. Am. Chem. Soc., 1980, **102**, 1135.
98. Paris, A.; Laszlo, P. in Magnetic Resonance in Colloid and Interface Science, H. A. Resing and C. G. Wade, Eds., A.C.S. Symposium Series, American Chemical Society, Washington, 1976, **no. 34**, p. 418.
99. Paris, A.; Laszlo, P. Compt. Rend. Ac. Sci. Paris, 1978, **286O**, 717.
100. Delville, A.; Detellier, C.; Laszlo, P. J. Magn. Resonance, 1979, **34**, 301.
101. Detellier, C.; Laszlo, P. Helv. Chim. Acta., 1979, **62**, 1559.
102. Pinnavaia, T. J.; Marshall, C. L.; Mettler, C. M.; Fisk, C. L.; Miles, H. T.; Becker, E. D. J. Am. Chem. Soc., 1978, **100**, 3625.
103. Cope, F. W. Proc. Natl. Acad. Sci. Usa, 1965, **54**, 225.
104. Cope, F. W. J. Gen. Physiol., 1967, **50**, 1353.
105. Cope, F. W. Physiol. Chem. Phys., 1970, **2**, 545.
106. Ling, G. N.; Cope, F. W. Science, 1969, **163**, 1335.
107. Czeisler, J. L.; Fritz, Jr., O. G.; Swift, T. J. Biophys. J., 1970, **10**, 260.
108. Rotunno, C. A.; Kowalewski, V.; Cereiido, M. Biochim. Biophys. Acta, 1967, **135**, 170.
109. Martinez, D.; Silvindi, A. A.; Stokes, R. M. Biophys. J., 1969, **9**, 1256.
110. Reisin, I. L.; Rotunno, C. A.; Corchs, L.; Kowalewski, V.; Cereiido, M. Physiol. Chem. Phys., 1970, **2**, 171.
111. Monoi, H. Biophys. J., 1974, **14**, 645.
112. Monoi, H. Biophys. J., 1974, **14**, 653.
113. Monoi, H.; Katsukura, Y. Biophys. J., 1976, **16**, 979.
114. Goldberg, M.; Gilboa, H. Biochim. Biophys. Acta, 1978, **538**, 268.

115. Chang, D. C.; Woessner, D. E. **J. Magn. Resonance**, 1978, **30**, 185.
116. Berendsen, H. J. C.; Edzes, H. T. **Ann. N.Y. Acad. Sci.**, 1973, **204**, 459.
117. Ewart, G. **No Fool Like an Old Fool**, Gollancz, London, 1976, p. 71.

RECEIVED November 17, 1981.

# Deuterium NMR Spectroscopy

IAN C. P. SMITH and HENRY H. MANTSCH

National Research Council of Canada, Ottawa, Canada, K1A 0R6

The enormous utility of  $^2\text{H}$  NMR was pointed out very early by Diehl and Leipert (1). Due in part to lack of instrumentation, a considerable lag occurred in realizing this potential. However, with the advent of Fourier transform spectrometers, a great surge of activity ensued. In 1977 we attempted a comprehensive review of the literature on  $^2\text{H}$  NMR (2). The activity since then has been so great as to make impossible a thorough discussion of all reports. Instead we shall make extensive reference to our earlier review, and present some of the highlights of applications over the past four years.

## Magnetic Properties of Deuterium

The fundamental properties of the  $^2\text{H}$  nucleus are listed in Table I. The low magnetogyric ratio of  $^2\text{H}$  leads to a somewhat low detection sensitivity, but this presents very little problem for a modern spectrometer. It also scales all couplings between  $^2\text{H}$  and other nuclei to 15% of the corresponding values for protons, as we have discussed in detail earlier (2). The low natural abundance of  $^2\text{H}$  is an advantage, since labeling to 100% is relatively simple, and the negligible background signals at natural abundance will not complicate the overall spectrum.

The main novelty of  $^2\text{H}$  for high resolution NMR practitioners is the spin of 1. A feature of nuclei with  $I > 1/2$  is an unsymmetrical charge distribution in the nucleus, Figure 1, and therefore an electrical quadrupole moment,  $Q$ . This moment can interact with the charge distribution about the nucleus and thus affect the energies of the nuclear spin states, Figure 2. The magnitude of the interaction depends upon the second derivative of the electric potential at the nucleus,  $q_{\alpha\beta}$ , and on the direction of the magnetic field with respect to the principal axes of the tensor  $q_{\alpha\beta}$ . The energy of this interaction is given by the quadrupole coupling tensor,  $e^2q_{\alpha\beta}Q/h$ . Note that if the  $q_{\alpha\beta}$  are zero, there is no interaction and the nuclear spin energy levels are unaffected. This can arise in situations of high

0097-6156/82/0191-0097\$06.25/0

© 1982 American Chemical Society

Table I

## Properties of the Deuteron

Natural Abundance	0.015%
Resonance Frequency at 2.3487 T	15.351 MHz
Spin	1
Sensitivity <sup>1</sup> relative to <sup>1</sup> H	0.965%
Receptivity <sup>2</sup>	1.45 x 10 <sup>-6</sup> %
Quadrupole moment (x10 <sup>28</sup> m <sup>2</sup> )	2.73 x 10 <sup>-3</sup>

---

<sup>1</sup>For equal numbers of nuclei.

<sup>2</sup>Sensitivity relative to that of <sup>1</sup>H, at natural abundance.

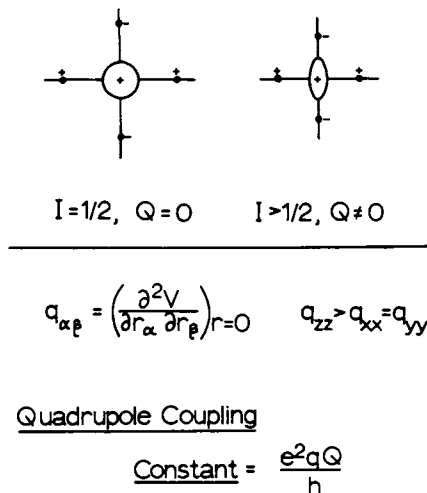


Figure 1. Representation of the properties of a nonquadrupolar and a quadrupolar nucleus. The charges around the nucleus represent those of its molecular environment. The electric field gradient tensor,  $q_{\alpha\beta}$ , is expressed in the coordinate system of the molecule. Usually, the z-axis lies along the carbon-deuterium bond;  $e$  is the charge on the electron,  $h$  is Planck's constant, and  $Q$  is the quadrupole moment. For axial symmetry, only  $q_{zz}$  is required to express the quadrupole coupling constant.

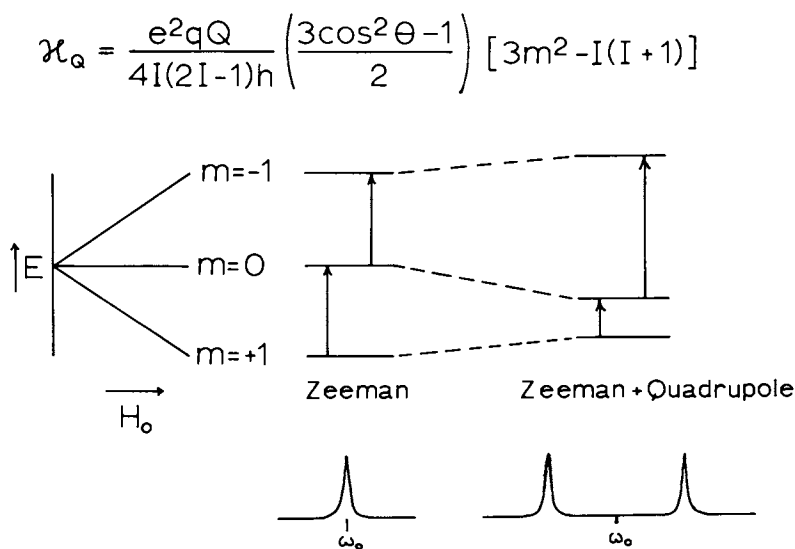


Figure 2. Effect of the quadrupole interaction on the Zeeman energy levels of an  $I = 1$  nucleus with axial symmetry.  $I$  is the total spin,  $m$  its component, and  $\theta$  is the angle between the applied magnetic field and the principal (z) axis of the quadrupole splitting tensor.

symmetry, which are rare for deuterium. However, quite commonly the tensor  $q_{\alpha\beta}$  is axially-symmetric, i.e.  $q_{xx} = q_{yy}$ . In this case only  $q_{zz}$  need be considered, and the subscripts are often neglected in formulation of the quadrupole coupling constant, Figure 1. Deviations from axial symmetry are expressed in terms of the asymmetry parameter,  $\eta = (q_{xx} - q_{yy})/q_{zz}$ . For deuterium in  $sp^3$  bonds to carbon, the asymmetry parameter is usually negligible, and the quadrupole coupling constant varies between 160 and 190 kHz, depending upon the nature of the other substituents on the carbon atom (2).

Figure 2 shows the effect of a finite quadrupole coupling constant (in the case of axial symmetry), on the Zeeman levels of deuterium. For an immobilized species, two transitions of unequal energy are allowed, their energy differences depending upon the magnitude of the quadrupole coupling constant and the angle  $\theta$  between the magnetic field and the z-axis of the electric field gradient tensor  $q_{\alpha\beta}$ , usually the direction of the carbon-deuterium bond.

In solution, where molecular reorientation is rapid relative to the reciprocal of the quadrupole coupling constant, these effects are averaged and only a single transition at the frequency of the isotropic situation,  $\omega_0$ , is observed. The modulation of the quadrupole interaction by molecular reorientation manifests itself in the relaxation behaviour of  $^2H$ , providing the dominant mechanism (2). In liquid crystals or biomembranes, where rapid motion occurs with limited amplitude within a large, slowly tumbling superstructure, partial averaging of quadrupole splitting takes place, the resultant splitting being a measure of the degree of molecular ordering within the superstructure (2,3).

### High Resolution Deuterium NMR

High resolution  $^2H$  NMR is extremely useful in studies of small molecules in solution (2). The chemical shifts of  $^2H$  are the same in parts per million as those of  $^1H$ ; the separations in frequency units are correspondingly less than those of  $^1H$  by the quotient of the magnetogyric ratios,  $\gamma_{^2H}/\gamma_{^1H} = 0.154$ . The reduced couplings to  $^1H$  afford an enormous simplification of the spectra, and these can be removed by broad band decoupling.

Figure 3 shows the  $^1H$ -coupled and -decoupled  $^2H$  NMR spectra of a mixture of solvents, taken at natural abundance of  $^2H$  (4). The only couplings that usually appear in the  $^2H$  spectra are those of geminal hydrogens, as seen in the expansion of the acetone resonances (starred region of the left of Figure 3). In very complex proton systems, the ability to obtain chemical shifts from NMR spectra of  $^2H$  at natural abundance, without resort to spectral simulation, is a powerful first step towards understanding the  $^1H$  spectra (2).

There are circumstances where knowing the chemical shifts in

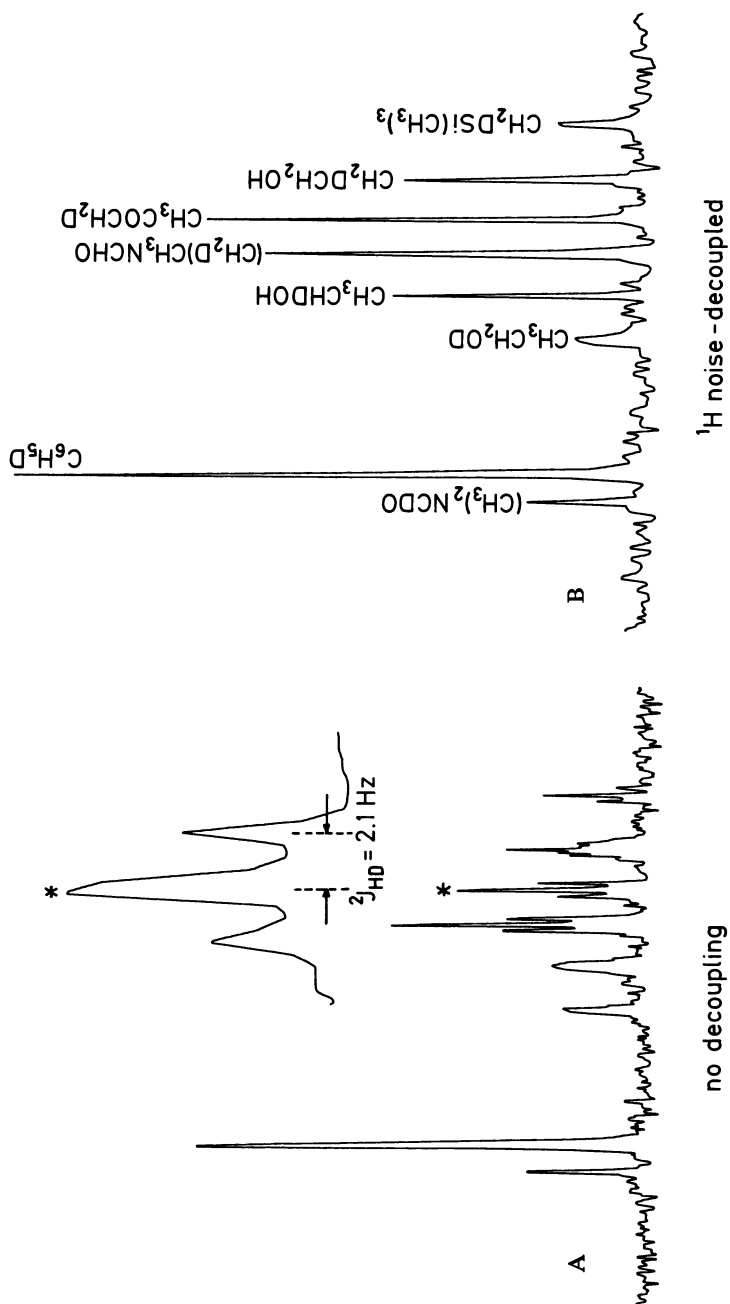


Figure 3. NMR spectra (15.4 MHz) of  $^2\text{H}$  at natural abundance for a mixture of common solvents, as indicated from left to right: dimethylformamide (amide), benzene, ethanol (hydroxyl), ethanol (methylene), dimethylformamide (methyl), acetone, ethanol (methyl), tetramethylsilane. The  $D$  in each formula is to emphasize that for a molecular species containing  $^2\text{H}$  at natural abundance all other hydrogen is  $^1\text{H}$ . Key: A, proton-coupled; B, proton-decoupled. (From Ref. 4.)

$^1\text{H}$  spectra is not sufficient for assignment of resonances. An example is the  $^1\text{H}$  NMR spectrum of nicotine, Figure 4. In this case specific labeling with deuterium allowed both measurement of chemical shifts and assignments for the methylene groups at positions 3',4', and 5' (5). Note the considerably greater widths of the  $^2\text{H}$  resonances relative to their  $^1\text{H}$  counterparts; this is due to the efficient quadrupolar relaxation mechanism of  $^2\text{H}$ , which is approximately 20 times more effective than that of  $^1\text{H}$  in a geminal pair of hydrogen.

An obvious application of high resolution deuterium NMR is to study reaction mechanisms involving hydrogen. Rather than following the disappearance of one of many  $^1\text{H}$  resonances due to incorporation of deuterium, it is much more convenient to observe the appearing deuterium resonances directly, as only the incorporated deuterium atoms are observed. Furthermore, the deuterium resonances yield very accurate integrated intensities as there is no significant nuclear Overhauser effect to accompany proton decoupling. A number of such kinetic studies, involving both slow and fast exchange processes have been described in reference (2).

A more recent demonstration of the usefulness of high resolution deuterium NMR as an analytical technique is illustrated in Figure 5. Here deuterium resonances were used to characterize the radical- and cation-derived products obtained by anodic oxidation of the [2,2- $\text{d}_2$ ] butyrate ion (6). The assignment of these resonances was made on the basis of the 1:1 relationship between the chemical shifts of  $^1\text{H}$  and  $^2\text{H}$ , and the deuterium label distribution was determined from the proton noise-decoupled  $^2\text{H}$  NMR spectra. As can be seen from Figure 5, propene was labeled in the terminal olefinic carbon but not in the central olefinic carbon atom, while propane turned out to be deuterium-labeled exclusively at  $\text{C}_1$ .

Further information may be extracted from the analysis of the fine structure of proton-coupled high resolution deuterium spectra. Thus, the proton-coupled deuterium spectrum of the methyl group of propene appears as a doublet of doublets (see inset to Figure 5), indicating that the position must be doubly deuterated.

Another recent application of high resolution  $^2\text{H}$  NMR was to study the reaction mechanism of the solvolysis of norbornen-2-yl derivatives (7). The acetolysis of the mono-deuterium compound 1, [2-d] *exo*-5-norbornen-2-yl brosylate, for instance led to the products 2 to 5. The deuterium label distribution of these products was determined unambiguously (Figure 6) and thus allowed the elimination of a previously proposed mechanism which required the intervention of asymmetrical homoallylic cation intermediates.

In a pioneering experiment Cox and Styles (8) have applied high resolution deuterium NMR towards biochemical imaging by generating  $^2\text{H}$  NMR spectra collected from localized regions, that is from volume elements, small compared with the NMR coil.



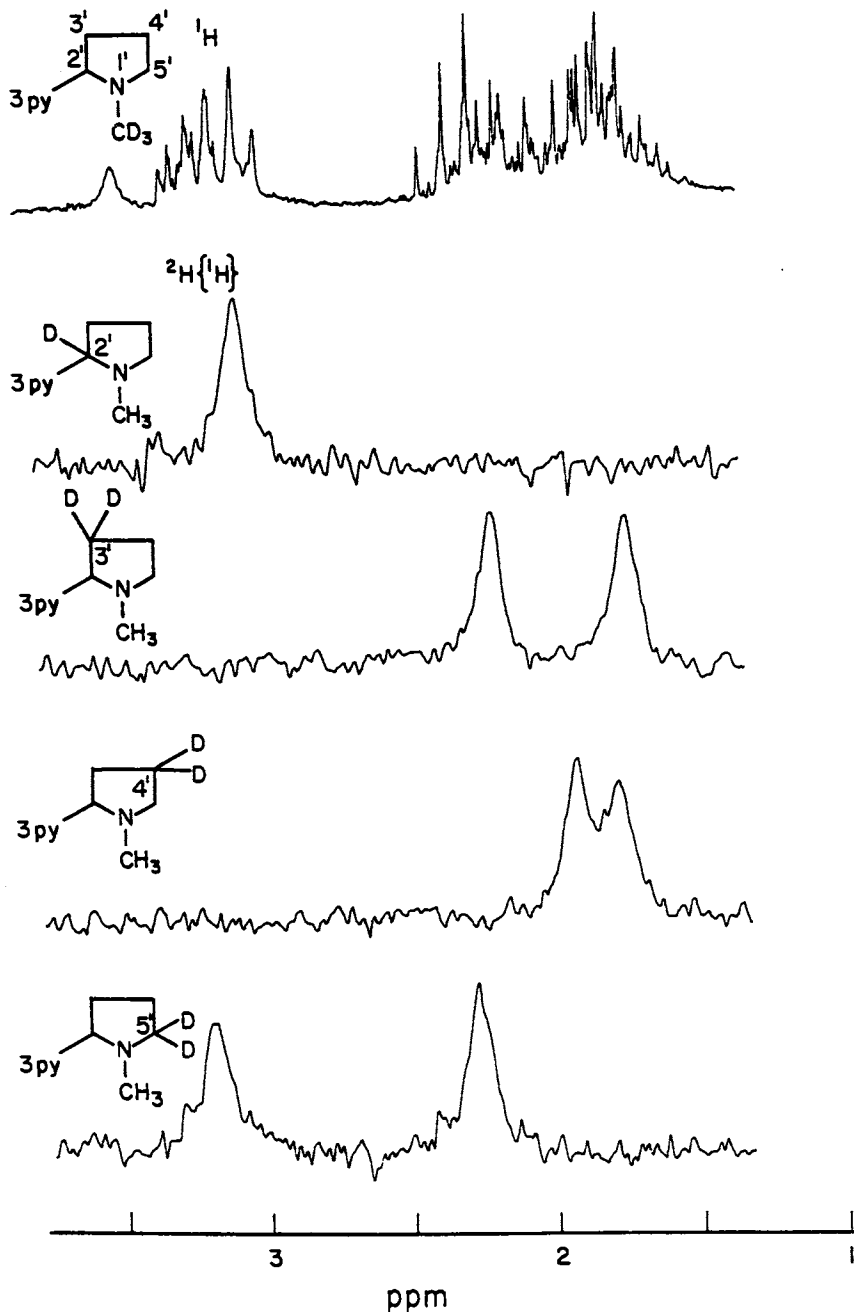


Figure 4. NMR spectra of nicotine and specifically deuterated derivatives: top,  $^1\text{H}$  at 100 MHz; others,  $^2\text{H}$  at 15.4 MHz. (Reproduced from Ref. 5. Copyright 1978, American Chemical Society.)

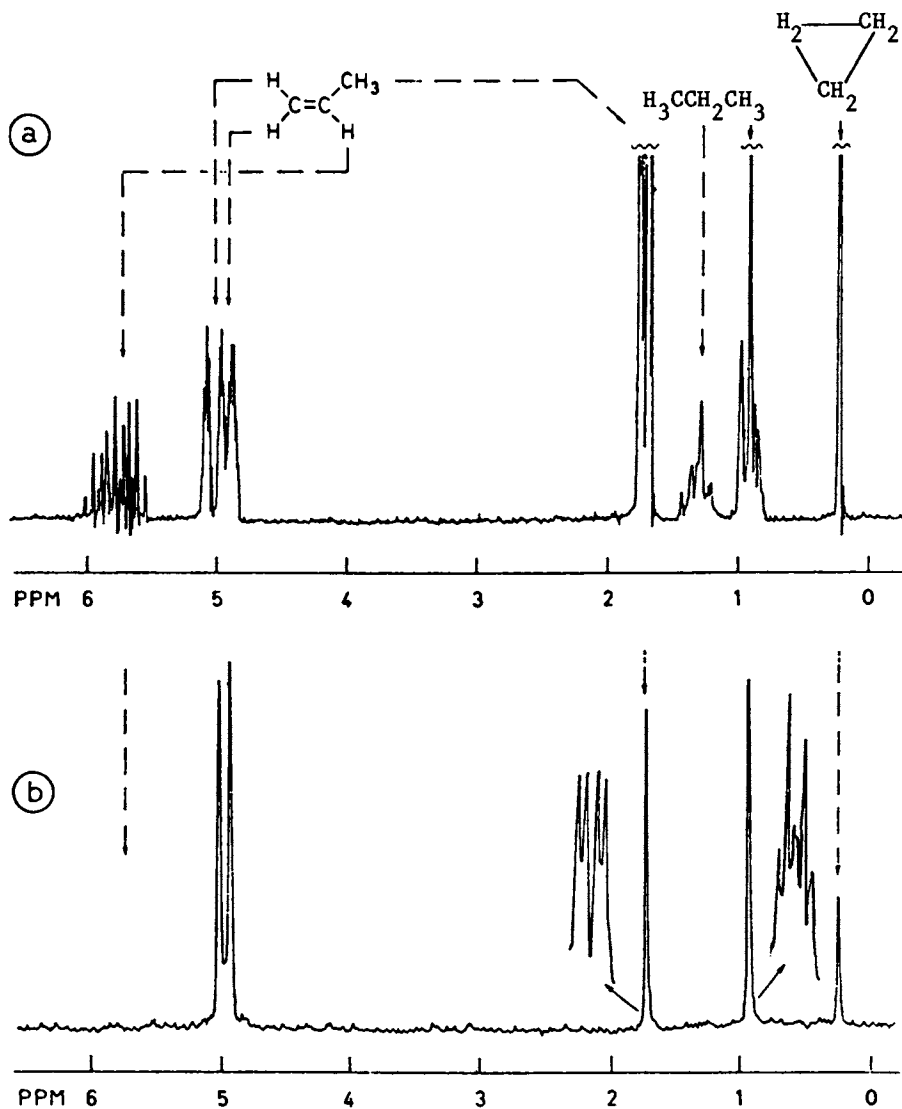
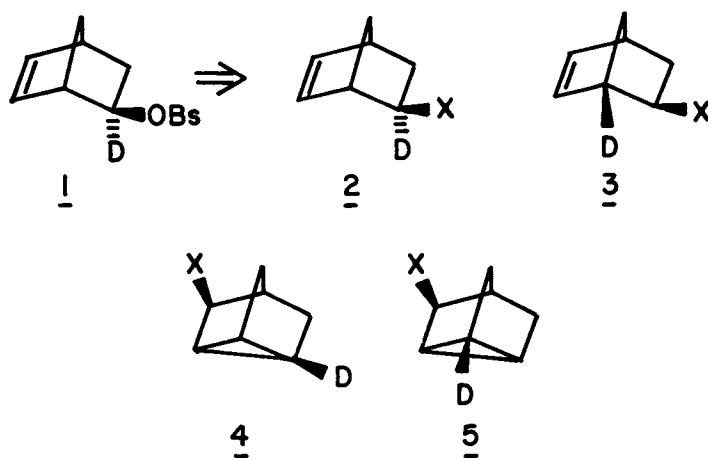


Figure 5. a,  $^1\text{H}$  NMR spectra (at 100 MHz, in  $\text{CCl}_4$  under pressure) of a mixture of gaseous propane, propene, and cyclopropane. b, Proton noise-decoupled  $^2\text{H}$  NMR spectra (at 15.4 MHz, in  $\text{CCl}_4$  under pressure) of some of the reaction products obtained from the electrolysis of the  $[2,2\text{-d}_2]$  butyrate ion: Expansion, proton-coupled deuterium resonances. (Reproduced from Ref. 6. Copyright 1980, American Chemical Society.)



Reaction mechanism of the solvolysis of norbornen-2-yl derivatives.

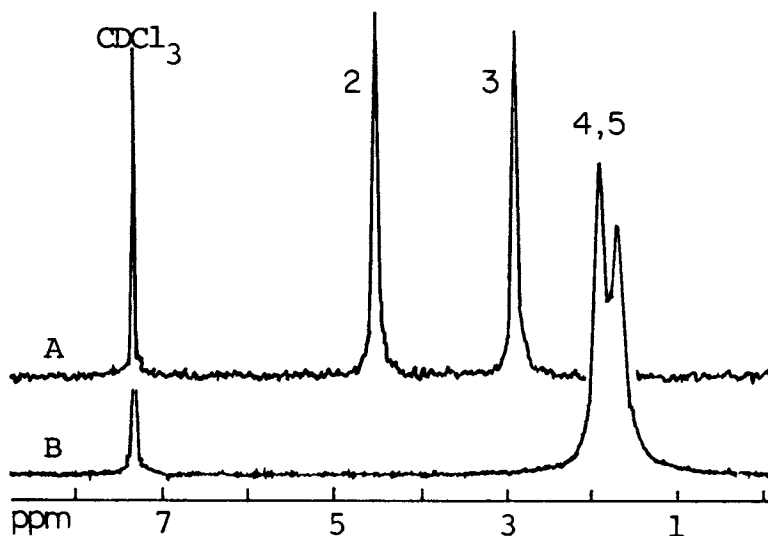


Figure 6. Proton noise-decoupled  $^2\text{H}$  NMR spectra (at 15.4 MHz) of the reaction products obtained from the acetolysis of [2-d]-exo-5-norbornen-2-yl brosylate in the absence (A) and presence (B) of  $\text{Eu}(\text{fod})_3$ . (Reproduced, with permission, from Ref. 7. Copyright 1980, Swiss Chemical Society.)

### Deuterium Nuclear Relaxation

As described earlier, the deuterium nucleus has a significant quadrupole moment which interacts with the electric field gradient at the nucleus. The interaction between the deuteron nuclear electric quadrupole moment and the electrostatic field gradient at the nucleus is at least an order of magnitude greater than either the deuteron dipole-dipole interaction or the spin-rotation interaction (2). Deuterium NMR relaxation thus results predominantly from the intramolecular quadrupole interaction, making deuterium an ideal nucleus for the study of intramolecular rotational motion (2,3). Due to the strength of this interaction, deuterium relaxation times are short relative to those of spin  $\frac{1}{2}$  nuclei reorienting with the same correlation time. In processes where a  $^2\text{H}$  nucleus is rapidly exchanging between two sites of different correlation times (for example a ligand exchanging between bulk solution and the binding site of a protein, the difference in correlation time between the free and the bound ligand is reflected in a greatly increased line width of the observed deuterium NMR signal relative to that of the free ligand (9).

A misconception often encountered among spectroscopists is that in high resolution deuterium NMR the resonances are so broadened by deuterium quadrupole relaxation as to be of little use. While this is certainly true for heavier quadrupole nuclei such as  $^{14}\text{N}$  or  $^{35}\text{Cl}$ , the line widths of deuterium resonances, particularly those of smaller molecules, are often small relative to the chemical shift separations of interest. In the case of  $\text{CDCl}_3$  the deuterium resonance has a width at half height of only 0.5 Hz (2), and the apparent width of such narrow signals is often determined by the inhomogeneity of the external magnetic field or by incomplete coalescence of multiplets arising from geminal or vicinal  $^1\text{H}$ - $^2\text{H}$  coupling. The most reliable way to determine the true line width of deuterium resonances is by measuring the spin-lattice ( $T_1$ ) or spin-spin ( $T_2$ ) relaxation time; under the conditions of extreme narrowing which are usually encountered for small molecules,  $\Delta\nu_{\frac{1}{2}} = 1/\pi T_1 = 1/\pi T_2$ . The  $T_1$  value of  $\text{CDCl}_3$  at  $30^\circ\text{C}$  is 1.6 s, corresponding to an intrinsic line width of 0.2 Hz.

Both direct and indirect methods have been used to measure deuterium relaxation (2); the inversion-recovery or partially relaxed Fourier transform method is most widely employed. Deuterium spin-lattice relaxation times for a variety of deuterated compounds have been reported in the literature (2,10,11). Deuterium atoms in highly mobile positions have long relaxation times while those in associated or very rigid systems have short relaxation times. The range of deuterium relaxation times reported in solution extends from very long (10), such as that of the methyl group in neat  $\text{CD}_3\text{Br}$  (7.43 s), to very short (11) such as in aqueous [3d] N-acetylglucosamine (0.017 s). In the limit

of rapid isotropic motion these correspond to deuterium resonances having line widths at half height of respectively 0.043 and 18.7 Hz. In rigid solids where relaxation is outside the motional narrowing range, deuterium  $T_1$  values can be very long.

Generally, molecular re-orientation in liquids can be described in a simple way by isotropic Brownian rotation, although this is rigorously applicable only to spherically-symmetric molecules. For the study of anisotropic molecular motion spin-lattice relaxation times of  $^{13}\text{C}$  have been used in the past as the standard technique, but spin-lattice relaxation of deuterium is becoming increasingly more important, since it is dominated by a single intramolecular quadrupole mechanism and does not require verification of the relaxation mechanism. Deuterium also has the advantage of short relaxation times and therefore  $T_1$  measurements involve considerably less instrument time. We have studied the stereochemical dependence of deuterium relaxation times for a wide range of deuterated compounds (12). In  $[\text{d}_5]$  pyridine for example, the deuterons at the  $\alpha$  (1.2 s),  $\beta$  (1.1 s) and  $\gamma$  (1.3 s) positions have almost identical  $T_1$  values, indicating that pyridine undergoes essentially isotropic motion. In  $[\text{d}_7-]$  dimethylformamide, on the other hand, the large difference between the relaxation times of the cis (3.0 s) and trans (1.6 s), deuteriomethyl groups indicates a preferred axis of rotation.

Equally informative are the deuterium spin-spin relaxation times  $T_2$  (usually obtained from line width measurements), especially when studying low deuterium concentrations. Due to the sensitivity of line widths to subtle changes in correlation times,  $^2\text{H}$  NMR can give a detailed picture of rotational motion of specifically deuterium-labeled reporter groups. This technique has, for instance, been used to study internal motions of deuterium-labeled molecules bound to proteins (2,9,11,13).

We have used this technique to delineate the molecular dynamics of sugars bound to a lectin (11). The binding to wheat germ agglutinin of N-acetylglucosamine deuterated specifically in the N-acetyl group and in the pyranoside ring (C3) was investigated via the line broadening of the deuterium resonances as a function of the total sugar concentration (Figure 7). Due to the short exchange rates (large dissociation rate constants) of N-acetylglucosamine with the lectin, this system was ideally suited for study by deuterium NMR. The correlation time of the bound  $[\text{3d}]$  N-acetylglucosamine ( $3 \times 10^{-8}$  s) was found to be identical to that of the protein, indicating that the six-membered ring has negligible motional freedom relative to the protein; the correlation time of the bound  $[\text{d}_3]$  N-acetylglucosamine ( $1.7 \times 10^{-9}$  s) indicates that the N-acetyl side chain is also immobilized, the only motion available being the rotation of the  $\text{CD}_3$  group around its threefold axis.

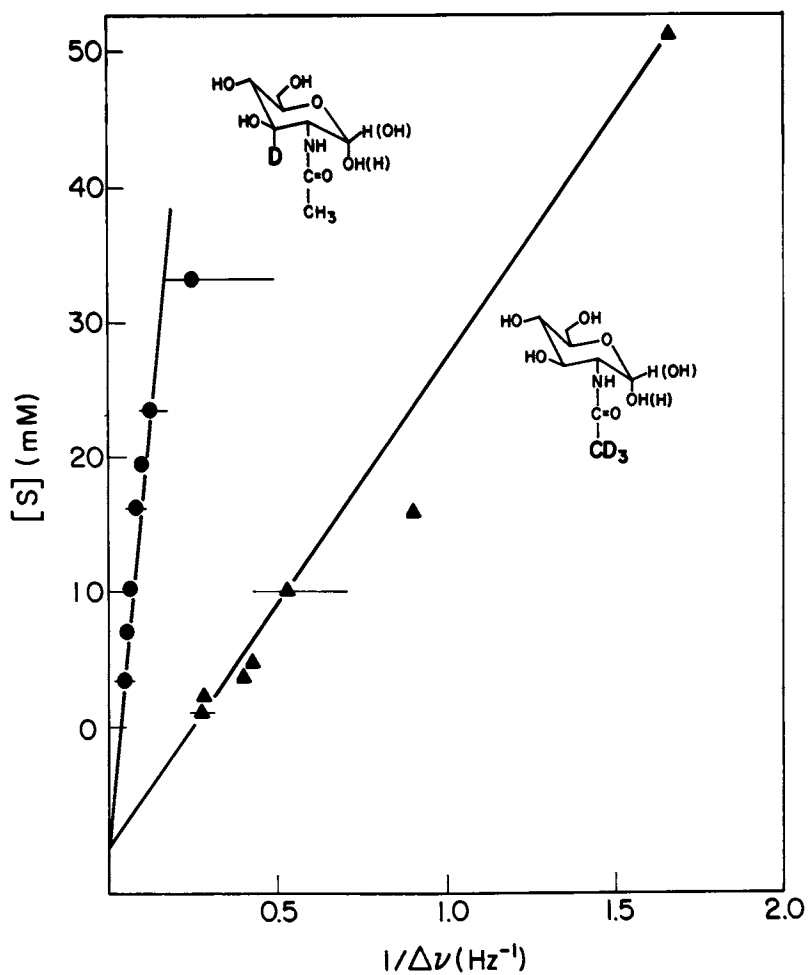


Figure 7. Binding of N-acetylglucosamine to wheat germ agglutinin. Plot of the total sugar concentration vs. the reciprocal linewidth of the indicated deuterated sites. The intercepts yield the dissociation constant and the slopes yield the linewidth of the bound species. (Reproduced, with permission, from Ref. 11. Copyright 1980, Biophysical Society.)

### Wide-line Deuterium NMR

Before the advent of Fourier transform spectrometers, wide-line  $^2\text{H}$  NMR was done by sweeping the magnetic field and observing the dispersion signal, or by pulsing the radiofrequency and observing the free induction decay without transformation. The very broad spectral widths have caused problems with baselines and faithful representations of the entire lineshapes. Various techniques, such as the quadrupole echo (14), progressive phase alternation of the excitation pulse and detector, short spectrometer dead times, and post-acquisition spectral correction (15) have circumvented most of these.

Wide-line spectra are observed for solids, or for systems in solution with very long (with respect to the inverse of the quadrupole splitting) correlation times for re-orientation. Examples of the latter are collagen fibres, membranes, and liquid crystals. As many examples of this type of study were given in our earlier review (2), we shall confine ourselves to collagen and membranes.

Single crystals give simple  $^2\text{H}$  NMR spectra whose quadrupole splittings depend on the angles between the applied magnetic field and the principal axes of the splitting tensor. Polycrystalline samples present all angles simultaneously, and therefore their spectra are superpositions of all those for the various angles (2,16). They are referred to as powder spectra; from their distinctive shapes the quadrupole splittings for two principal values of  $\theta$  ( $0^\circ$  and  $90^\circ$ , see Fig. 2 and reference (16)) can be easily obtained. Rapid anisotropic motion leads to reduction in the magnitudes of the principal splittings, and these reduced values lead to estimates of the degree of molecular order (3); this assumes that other motions are too slow to affect line shapes or apparent quadrupole splittings (16). Similar spectra arise for very large molecules, or molecular assemblies, which re-orient slowly in solution.

The synthetic polypeptide polybenzyl glutamic acid can be aligned in a magnetic field such that overall motion of the helical structure is very slow. Rapid anisotropic motion of the pendant side chains leads to reduced quadrupole splittings for these labeled positions, the magnitudes of which were used to derive information on the amplitudes of the anisotropic motions (17). A much more complex system is collagen, a triple polypeptide helix of dimensions  $1.5 \times 300$  nm and molecular weight 285,000. Jelinski *et al.* produced collagen containing either  $[3,3,3\text{-d}_3]$ alanine or  $[\text{d}_{10}]$ leucine via tissue culture in the presence of labeled amino acids (18, 19). Figure 8 shows both experimental and simulated  $^2\text{H}$  NMR spectra for this system containing  $[3,3,3\text{-d}_3]$ alanine. The top spectrum is that of the polycrystalline amino acid; it has a reduced quadrupole splitting of 38.8 kHz due to rapid rotation of the methyl group. Frozen collagen fibrils (Figure 8b), containing the same label

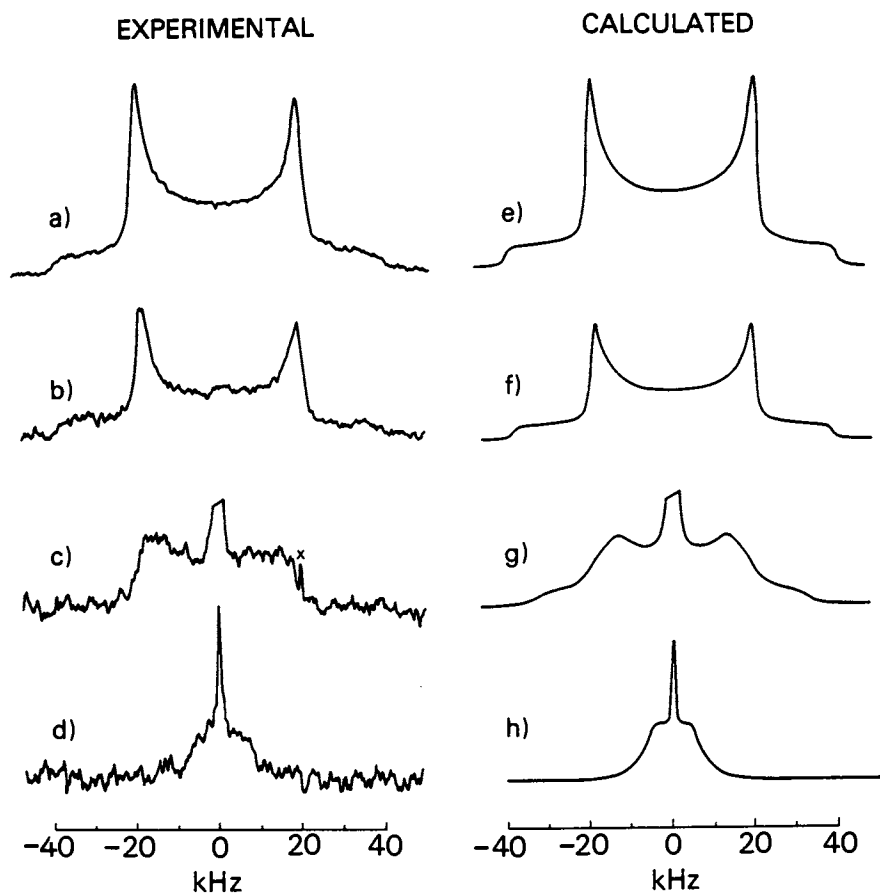


Figure 8.  $^2\text{H}$  NMR spectra (33.78 MHz) of  $[3,3,3\text{-d}_3]$  alanine and of collagen labeled with this amino acid. Key: a, polycrystalline  $[3,3,3\text{-d}_3]$  alanine; b, labeled collagen fibrils,  $-18^\circ\text{C}$ ; c, as in b, but  $18^\circ\text{C}$ ; d, labeled collagen in solution,  $18^\circ\text{C}$ ; and e-h, calculated spectra for a-d, respectively. (Reproduced, with permission, from Ref. 18. Copyright 1980, MacMillan Journals.)



acid, yield a very similar spectrum. However, the same fibrils at 18°C (Figure 8c) yielded a spectrum of reduced overall intensity with a reduced quadrupole splitting; this is due to the onset of sidechain motions other than rotation of the methyl group about its C<sub>3</sub> axis. Collagen in solution at 18°C yielded Fig. 8d, with a quadrupole splitting of only 10 kHz. This further reduction in quadrupole splitting was attributed to rotation of the collagen molecule about its long axis, with the angle between the CD<sub>3</sub>-CH bond of alanine and the long molecular axis having a value of roughly 70°. The shapes of the spectra were simulated (Figure 8, right side) in terms of a model where this bond jumps between two orientations. For the collagen fibrils it was concluded that the component collagen molecules undergo rapid (10<sup>7</sup> s<sup>-1</sup>) anisotropic motion with a range of azimuthal angles from 30-40°. Similar studies have been reported for artificially deuterated (deuteromethylation of methionine to its dimethyl sulfonium analog) heme protein crystals oriented in a magnetic field (20).

A field in which <sup>2</sup>H NMR has contributed extremely valuable information is biological membranes. Early studies concentrated on development of labeling methods, spectrometer techniques, and elucidation of the properties of lipids in model membranes (2,3,16). The experience gained with the models is now actively under application to intact biological membranes.

Early success in the study of biological membranes was attained by use of the relatively simple organism *Acholeplasma laidlawii* (21). It has a single membrane, the plasma membrane, and will accept labeled fatty acids from the growth medium without significant alteration. For some fatty acids enrichment of the membranes to greater than 95% can be achieved by use of the protein avidin in the growth medium (22). Figure 9 shows the <sup>2</sup>H NMR spectra of the membranes of this organism, enriched in either [12-d<sub>2</sub>]-oleic acid or [13-d<sub>2</sub>]-palmitic acid, at 37°C, the growth temperature. The narrow resonances at the centres of the quadrupolar patterns are due to <sup>2</sup>H at natural abundance in the surrounding water. This can be avoided by the use of deuterium-depleted water. The presence of the *cis* double bond in oleic acid leads to relatively fluid, liquid crystalline membranes at 37°. The quadrupole splitting is a measure of the degree of molecular ordering at the 12-position within the membrane. In contrast, the straight chain palmitic acid results in more ordered, less fluid membranes at this temperature (note the larger quadrupole splitting of the narrow pattern in the centre of the spectrum). Furthermore, the broad spectral components on the wings of the spectrum indicate the presence of a second lipid phase, the so-called gel phase, in which the acyl chains are essentially all-trans, and molecular motion is of lesser amplitude and rate than in the liquid crystalline phase. With both fatty acids the optimum growth temperature of *A. laidlawii* is 35 ± 1°, whereas the liquid crystal to gel transitions, T<sub>m</sub>, occur at widely

different temperatures. These spectra have been discussed in detail in earlier publications (23,24).

The variation of molecular order with position in the membranes of *A. laidlawii* has been studied in detail with both palmitic (25) and oleic (24) acids. For the saturated acid at temperatures above the phase transition, the order is of intermediate and constant magnitude for the first 10-12 carbon atoms from the carboxyl group, dropping rapidly thereafter to very low values for the terminal methyl group. The pattern for the unsaturated acid is shown in Figure 10; it is similar to that for the saturated acid except for a large drop near the *cis* double bond. This is largely a geometric factor; when the particular angles of the double bond are considered, it is shown to be also highly ordered (24). The circles in Figure 10 indicate the effect of incorporating 20 mole % cholesterol into the membranes. Note that this increases the quadrupole splitting (thus the order parameter) at all positions, with the largest increase coming for positions near the carboxyl group. A similar response to cholesterol addition was found for *A. laidlawii* membranes containing palmitic acid (26).

Figure 11 shows the temperature dependence of the  $^2\text{H}$  NMR spectra of *A. laidlawii* membranes enriched to 90% in the fourteen carbon saturated fatty acid labeled at the terminal methyl group. We see again the presence of a liquid crystal to gel phase transition for the membrane lipids, centered at  $40^\circ\text{C}$  as determined by scanning calorimetry. Note the large difference in quadrupole splittings, for even the terminal position of the chains, between the two states, indicating a high degree of ordering in the gel phase. A difficult problem with such two-component  $^2\text{H}$  NMR spectra is quantitating the relative proportions of the components. Recently Jarrell *et al.* have shown that the moments of the spectra can be used to derive reliable values for these fractions (27). Applications of their method to the data of Figure 11 yields the fraction of liquid crystalline liquid as a function of temperature, as shown in Figure 12. The parameter  $\Delta_2$ , which is a measure of the heterogeneity of the system (27), is also shown in Figure 12. It need not pass through a maximum at the midpoint of the transition; the temperature of the maximum depends upon the properties of the two component states (27).

Many of the properties of biological membranes, including those of *E. coli*, have been found to be very similar to those of model lipid systems. This, and a survey of other systems studied by NMR, has been discussed recently by Seelig and Seelig (28). The  $^2\text{H}$  NMR studies of model and biological membranes by Oldfield and co-workers have also been reviewed recently (29). The accomplishments of Bloom and co-workers have also been discussed in the recent reviews, and are exemplified by reference (30).

As a last example of  $^2\text{H}$  NMR of solids the recent work of Pines and co-workers must be mentioned. They have shown that use of multiple quantum transitions and cross-polarization, magic

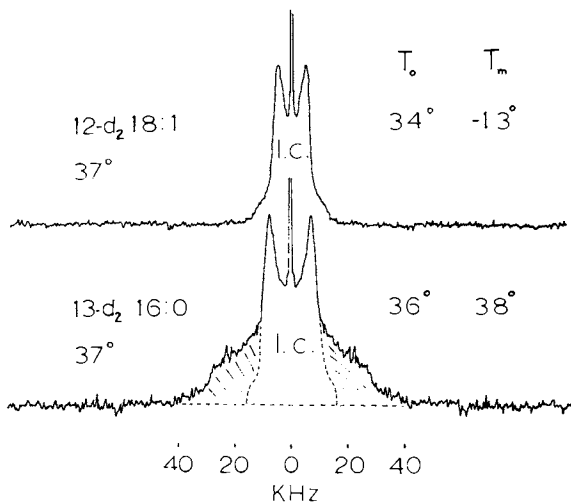


Figure 9.  $^2\text{H}$  NMR spectra of the plasma membranes of *Acholeplasma laidlawii* enriched in palmitic acid labeled at the 13-position ( $13\text{-d}_2$  16:0) and in oleic acid labeled at the 12-position ( $12\text{-d}_2$  18:1). Spectra were obtained at the growth temperature,  $37^\circ\text{C}$ . The temperatures of optimal growth,  $T_0$ , and the calorimetric gel to liquid crystal phase transition of the lipids in the membranes,  $T_m$ , are indicated. Details of sample preparation and spectral acquisition are given in Ref. 23 and 24.

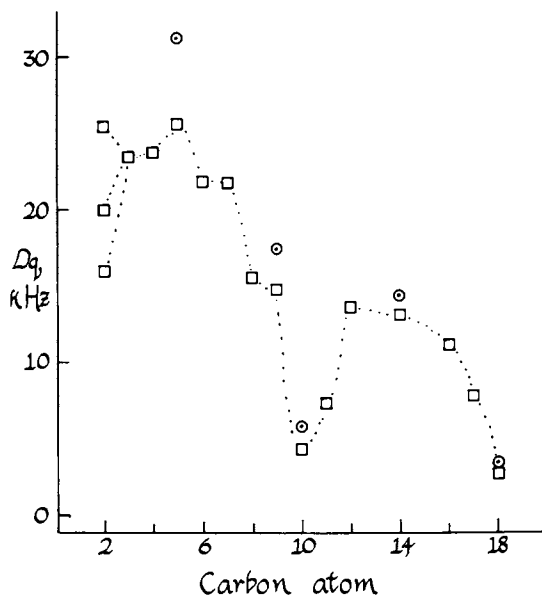


Figure 10. Variation of the quadrupole splitting ( $D_q$ , proportional to the order parameter) with position of labeling of the oleoyl chains in the membranes of *Acholeplasma laidlawii*, in the absence ( $\square$ ) and in the presence ( $\odot$ ) of 20 mol % cholesterol at  $25^\circ\text{C}$ . Data for membranes without cholesterol are from Ref. 24; those with cholesterol are the unpublished data of M. Rance, K. R. Jeffrey, A. P. Tulloch, K. W. Butler, and I. C. P. Smith.

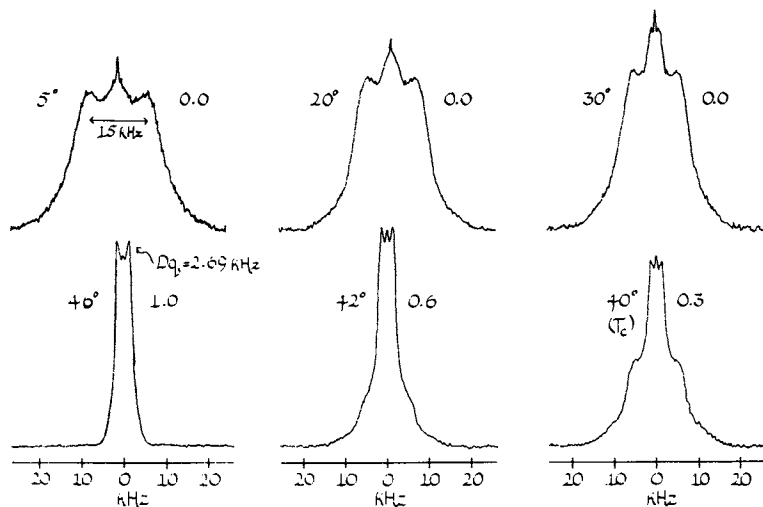


Figure 11.  $^2\text{H}$  NMR spectra (46.1 MHz) of the plasma membranes of *Acholeplasma laidlawii* enriched in myristic acid labeled at the terminal methyl group (C-14:0- $\omega$ - $\text{d}_3$  90%), at the indicated temperatures. The numbers to the right of each spectrum are the fractions of liquid-crystalline lipid calculated by the moment analysis of Ref. 27. (Unpublished data of H. C. Jarrell, R. Deslauriers, and I. C. P. Smith.)

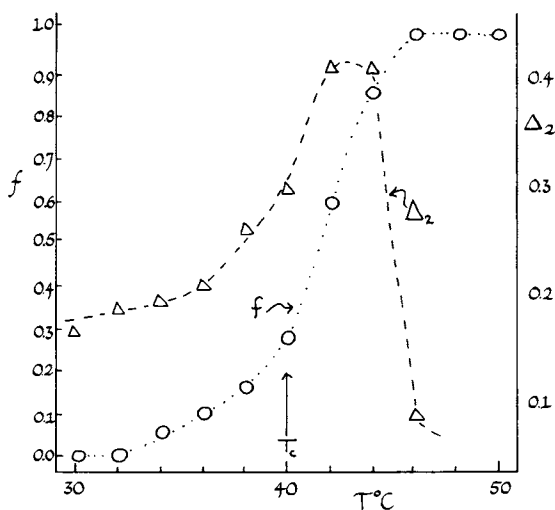


Figure 12. Temperature-dependence of the fraction of liquid crystalline lipid ( $f$ ) and the heterogeneity parameter ( $\Delta_2$ , proportional to the mean square deviation of the order parameter) for the  $^2\text{H}$  NMR spectra of *Acholeplasma laidlawii* membranes shown in Figure 11 (C-14:0- $\omega$ - $\text{d}_3$  90%). The calorimetric phase transition temperature is indicated by  $T_c$ . (Unpublished data of H. C. Jarrell, R. Deslauriers, and I. C. P. Smith.)

angle spinning techniques (31,32,33) can lead to very useful simplifications of spectra and to information previously unattainable. Figure 13 shows the  $^2\text{H}$  NMR spectra of solid deuterated dimethoxybenzene, with magic angle spinning at 1.07 kHz, in the presence and absence of cross-polarization to  $^1\text{H}$ . Note the enhancement of the methoxyl resonance due to cross-polarization. These techniques should be very useful in both chemical and biological applications of  $^2\text{H}$  NMR.

In closing, we must apologize for the lack of discussion of many excellent uses of  $^2\text{H}$  NMR in chemistry, physics and biology. This was necessitated by space restrictions.

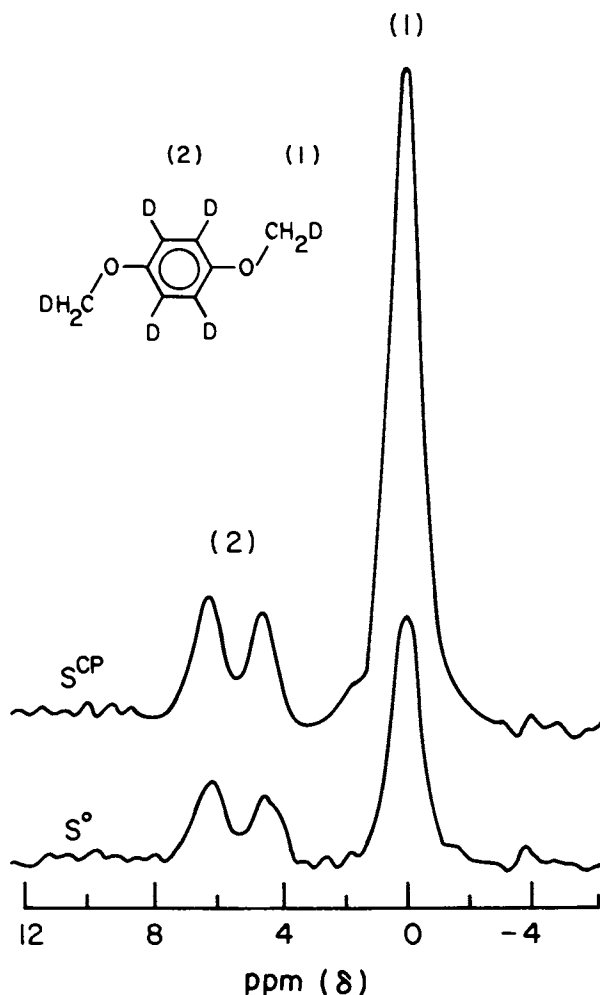


Figure 13.  $^2\text{H}$  NMR spectra (28 MHz) of polycrystalline deuterated dimethoxybenzene taken with magic angle spinning at 1.07 kHz, with ( $\text{S}^{\text{CP}}$ ) and without ( $\text{S}^{\circ}$ ) cross polarization from protons. (Reproduced, with permission, from Ref. 33. Copyright 1980, North-Holland Press.)

References

1. Diehl, P.; Leipert, Th. Helv. Chim. Acta 1964, 47, 545-557.
2. Mantsch, H.H.; Saitō, H.; Smith, I.C.P. Prog. NMR Spectr. 1977, 11, 211-272.
3. Seelig, J. Quart. Rev. Biophys. 1977, 10, 353-418.
4. Wehrli, F.W. Personal communication.
5. Pitner, T.P.; Edwards, W.B.; Bassfield, R.L.; Whidby, J.F. J. Am. Chem. Soc. 1978, 100, 246-251.
6. Laurent, E.; Thomalla, M.; Marquet, B.; Burger, U. J. Org. Chem. 1980, 45, 4193-4198.
7. Burger, U.; Sonney, J.-M.; Vogel, P. Helv. Chem. Acta. 1980, 63, 1006-1015.
8. Cox, S.J.; Styles, P. J. Mag. Res. 1980, 40, 209-217.
9. Zens, A.P.; Fogle, P.T.; Bryson, T.A.; Dunlap, R.B.; Fisher, R.R.; Ellis, P.D. J. Am. Chem. Soc. 1976, 98, 3760-3764.
10. Glasel, J.A. J. Am. Chem. Soc. 1969, 91, 4569-4571.
11. Neurohr, K.J.; Lacelle, N.; Mantsch, H.H.; Smith, I.C.P. Biophys. J. 1980, 32, 931-938.
12. Mantsch, H.H.; Saitō, H.; Leitch, L.C.; Smith, I.C.P. J. Am. Chem. Soc. 1974, 96, 256-258.
13. Wooten, J.B.; Cohen, J.S. Biochemistry 1980, 18, 4188-4191.
14. Davies, J.H.; Jeffrey, K.R.; Bloom, M.; Valic, M.I.; Higgs, T.P. Chem. Phys. Lett. 1976, 42, 390-394.
15. Bloom, M.; Davis, J.H.; Valic, M.I. Can. J. Phys. 1980, 58, 1510-1517.
16. Smith, I.C.P.; Stockton, G.W.; Tulloch, A.P.; Polnaszek, C.F.; Johnson, K.G. J. Colloid Interface Sci. 1977, 58, 439-451.
17. Samuelski, E.T. J. de Physique 1979, 40 (C3), 471-474.
18. Jelinski, L.W.; Sullivan, C.E.; Torchia, D.A. Nature 1980, 284, 531-534.
19. Jelinski, L.W.; Sullivan, C.E.; Batchelder, L.S.; Torchia, D.A. Biophys. J. 1980, 10, 515-529.
20. Rothgeb, T.M.; Oldfield, E. J. Biol. Chem. 1981, 256, 1432-1446.
21. Smith, I.C.P. Can. J. Biochem. 1979, 57, 1-14.
22. Silvius, J.R.; Mak, N.; McElhaney, R.N. Biochem. Biophys. Acta. 1980, 597, 199-215.
23. Smith, I.C.P.; Butler, K.W.; Tulloch, A.P.; Davis, J.H. FEBS Lett. 1979, 100, 57-61.
24. Rance, M.; Jeffrey, K.R.; Tulloch, A.P.; Butler, K.W.; Smith, I.C.P. Biochim. Biophys. Acta 1980, 600, 245-262.
25. Stockton, G.W.; Johnson, K.G.; Butler, K.W.; Tulloch, A.P.; Boulanger, Y.; Smith, I.C.P.; Davis, J.H. Nature 1977, 269, 267-268.
26. Davis, J.H.; Bloom, M.; Butler, K.W.; Smith, I.C.P. Biochim. Biophys. Acta. 1980, 597, 477-491.
27. Jarrell, H.C.; Byrd, R.A.; Smith, I.C.P. Biophys. J. 1981, 34, 451-463.
28. Seelig, J.; Seelig, A. Quart. Rev. Biophys. 1980, 13, 19-61.

29. Jacobs, R.E.; Oldfield, E. Prog. NMR Spectr. 1981, 14, 113-136.
30. Paddy, M.R.; Dahlquist, F.W.; Davis, J.H.; Bloom, M. Biochemistry 1981, 20, 3152-3162.
31. Eckman, R.; Alla, M.; Pines, A. J. Mag. Res. 1980, 41, 440-446.
32. Eckman, R.; Müller, L.; Pines, A. Chem. Phys. Lett. 1980, 74, 376-378.
33. Müller, L.; Eckman, R.; Pines, A. Chem. Phys. Lett. 1980, 76, 149-154.

RECEIVED March 18, 1982.

# NMR of $^{13}\text{C}$ Enriched Amino Acids and Peptides

ROBERT E. LONDON

University of California, Los Alamos National Laboratory, Los Alamos, NM 87545

The combination of isotopic enrichment and nuclear magnetic resonance spectroscopy provides an extremely powerful biochemical/biophysical probe. The magnetic properties (e.g. chemical shift, relaxation behavior) and the metabolic fates of individual nuclei can be studied in systems as complex as whole cells. Thus, the advantages of sensitivity gains, spectral simplification and spin labeling are the primary motivations for isotopic enrichment. In addition to these more obvious aspects of isotopic labeling, there are unique problems of interpretation and sources of information which require careful analysis and which represent important considerations in experimental design. Some of these aspects of the problem can be approached most directly by considering the spectral characteristics of relatively simple systems such as labeled amino acids and peptides. Such studies thus lay the groundwork for more sophisticated applications of isotopic labeling. The primary objective of the present article is to outline some of the characteristics of labeled systems, with particular emphasis on the relation of information content to labeling pattern.

## Spectral Characteristics of $^{13}\text{C}$ Enriched Amino Acids

The spectroscopic characteristics of  $^{13}\text{C}$  enriched amino acids are most conveniently discussed by considering separately the three categories of isotopic labeling: (1) Specific enrichment, usually of a single carbon position; (2) uniform enrichment with the labeling of each carbon statistically independent; (3) general enrichment with the carbon labeling non-random. The first type of labeling is typically obtained via organic synthesis and is of particular value for labeling studies of macromolecules in which spectral simplicity is a primary concern. The second category of labeled amino acids is most frequently obtained biosynthetically from algae grown for many

0097-6156/82/0191-0119\$10.25/0  
© 1982 American Chemical Society



generations on  $^{13}\text{CO}_2$  so that all carbons become equally enriched. The last category includes primarily molecules produced in biosynthetic studies in which the labeling pattern itself contains information of value for the elucidation of the biosynthetic pathways involved. The spectral characteristics of each type of labeled amino acid are considered below.

(a) Specifically Enriched Amino Acids. Specifically enriched amino acids are of use in metabolic studies and for macromolecular labeling studies, and a wide variety of isotopic isomers is now available commercially. The ready availability of these amino acids makes them attractive for NMR analysis, although relatively little work has been reported. Examination of the unenriched carbon resonances provides data on the  $^{13}\text{C}$  -  $^{13}\text{C}$  scalar coupling constants which are of use theoretically for the interpretation of the molecular orbital structure, as well as for assignment purposes. For example, we have recently studied the carbon-carbon couplings [ $90\%-3-^{13}\text{C}_1$ ]-L-tryptophan(1) which had been used for a labeling study of the enzyme, dihydrofolate reductase(2) (Fig. 1). The observed coupling pattern was used to help establish the  $^{13}\text{C}$  assignments.(1) In this case, the ring carbons were originally assigned correctly by Bradbury and Norton(3) but subsequent workers based the assignments on an incorrect indole assignment(4) leading to some confusion in the literature. Correct assignments of both the indole(5) and tryptophan(6) have since been made. Specific  $^{13}\text{C}$  enrichment combined with NMR analysis of the unlabeled carbons has also proven of value for the assignment of carbohydrate resonances.(7) We note further that although this coupling information is also available from the spectra of [U- $^{13}\text{C}$ ] enriched amino acids, the much greater complexity of the spectra occasionally obscures the information, particularly in the case of long range couplings. The availability of specifically enriched amino acids for coupling constant analysis represents an underutilized spectroscopic resource, and additional studies may be anticipated in the future.

(b) [U- $^{13}\text{C}$ ] Enriched Amino Acids. The spectra of [U- $^{13}\text{C}$ ] amino acids are in many respects analogous to typical  $^1\text{H}$  spectra. However, since enrichment levels are typically less than 100%, the spectra corresponding to a superposition of isotopic isomers are obtained. This characteristic is illustrated for the C-2 carbon of glycerol in Fig. 2(8) Although the large range of  $^{13}\text{C}$  shifts frequently justifies first order analysis of the spectrum, this is not always the case, as is apparent from the peak asymmetries in Fig. 2. An interesting aspect of this analysis which has been discussed by Bengsch and Ptak(9) is that the various sub-spectra may be of different order. Thus, some of the isotopic isomers will exhibit strong coupling and some may not. This complication can be utilized for spectral interpretation

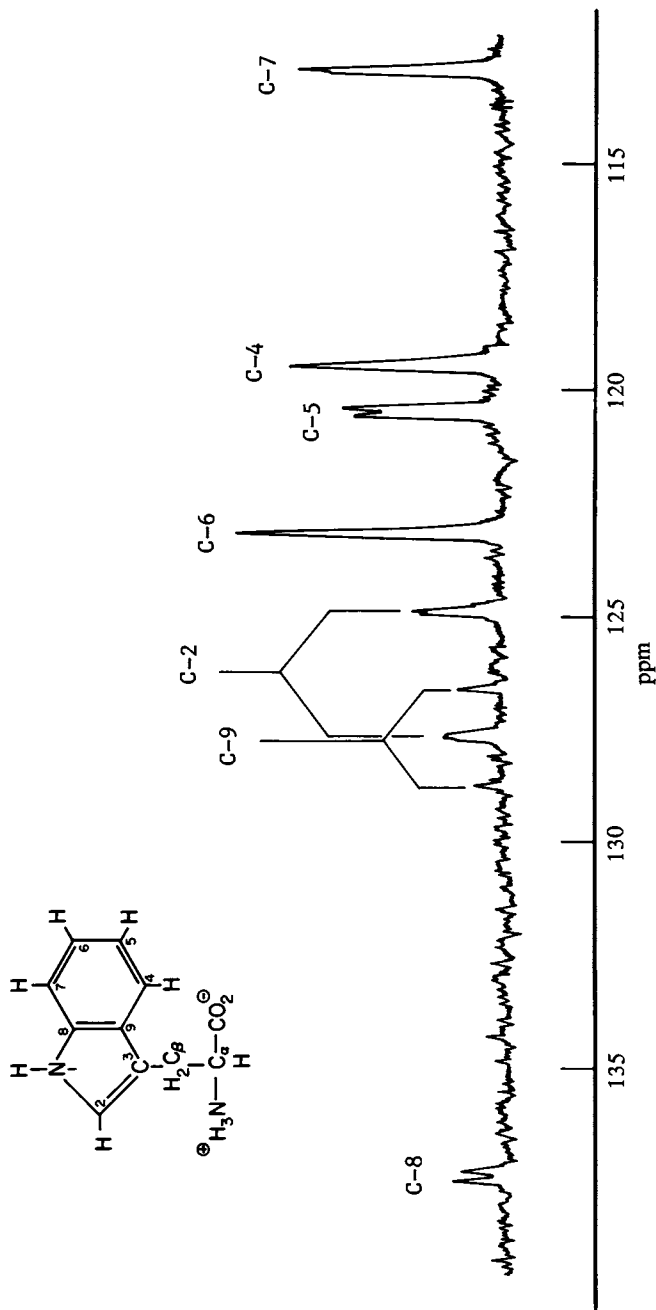


Figure 1. Unenriched ring carbon resonances of [90%- $\gamma$ -<sup>13</sup>C<sub>1</sub>] tryptophan, exhibiting scalar carbon-carbon coupling to the enriched nucleus. [Reproduced, with permission, from Ref. 1. Copyright 1981, Heyden (London).]

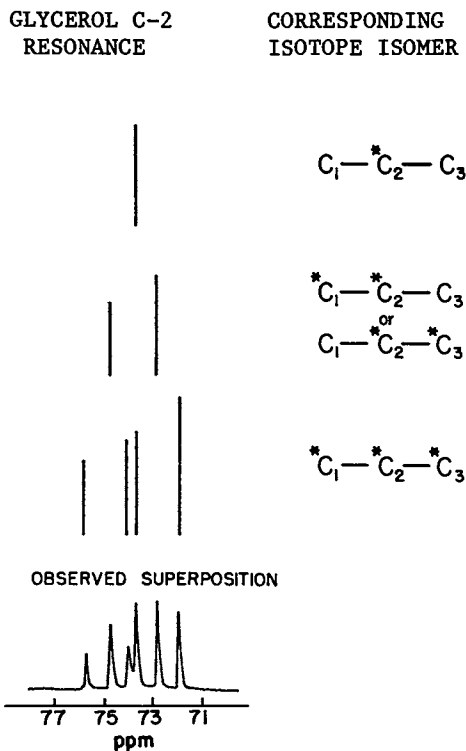


Figure 2. Proton decoupled C-2 resonances of  $[U-^{13}C_3]$  glycerol biosynthesized by a marine red alga. The observed resonances represent a superposition of singlet, doublet, and quartet corresponding to the isotope isomers illustrated in the figure. The relative intensities of the lines in each multiplet were calculated using the  $J$  and  $\Delta\nu$  values obtained from the spectrum. (Reproduced, with permission, from Ref. 8. Copyright 1979, John Wiley & Sons, Ltd.)

since the magnitude of some couplings can be deduced from first order sub-spectra, and used for the subsequent interpretation of higher order sub-spectra yielding additional couplings and signs of coupling constants.

Among the other consequences of the high order nature of some sub-spectra are: (1) <sup>13</sup>C - <sup>13</sup>C satellites will not be symmetrically disposed about the center resonances; and (2) small isotope effect contributions to the shift can be overwhelmed by shifts due to high order coupling. The simplest illustration of this effect can be observed in an AB system. The centers of the doublets corresponding to the [A,B-<sup>13</sup>C<sub>2</sub>] molecule will not coincide with the singlets arising from the [A-<sup>13</sup>C<sub>1</sub>] and [B-<sup>13</sup>C<sub>1</sub>] labeled molecules, but are shifted away from the signal of the adjacent carbon. Relative to the center of the AB pattern, the doublet/singlet shift differences will have magnitude =  $1/2[(\Delta\nu^2 + J^2)^{1/2} - \Delta\nu]$  where  $\Delta\nu = \nu_A - \nu_B$ . This situation is realized for the case of [1,2-<sup>13</sup>C<sub>2</sub>] taurine.(10) The observed doublet/singlet shift differences of 0.116 and 0.119 ppm for the S-methylene and N-methylene resonances, respectively, are in close agreement with the magnitude of 0.119 ppm due to the high order effects which can be calculated from the spectral parameters. Thus, there is a net 0.003 ppm upfield isotope shift of the S-methylene resonance produced by the N-methylene resonance, and no measurable isotope shift for the reverse case. In perhaps the most careful analysis carried out to date, Bangsch and Ptak(9) find no isotope shift for the carboxyl carbon resonances due to  $\alpha$ -carbon enrichment of several <sup>13</sup>C enriched amino acids and peptides, but an average 0.010 ppm upfield shift for the <sup>13</sup>C/<sup>12</sup>C substitution at other positions. In contrast, <sup>2</sup>H/<sup>1</sup>H and <sup>15</sup>N/<sup>14</sup>N produced larger isotope shifts of 0.25 ppm and 0.020 ppm, respectively.

Although high order analysis is clearly indicated for strongly coupled nuclei, the appropriate analysis of weakly coupled nuclei is more subtle and has frequently confused even experienced spectroscopists. The most thoroughly discussed example of the need for using high order analysis for the interpretation of resonances corresponding to weakly coupled nuclei has been labeled "virtual coupling".(11) This effect is most commonly considered for an ABX system in which the X resonances can appear as a 1:2:1 triplet despite the fact that  $J_{AX} \neq J_{BX}$ . Such spectra have been termed "deceptively simple" due to the likelihood of obtaining incorrect results based on a first order analysis which neglects the effect of strong AB coupling.

In observing the weakly coupled resonances of amino acids (most frequently carboxyl groups), we have frequently noted a marked asymmetry of resonances (Fig. 3).(12) This asymmetry is occasionally suggestive of a strong coupling interaction despite the obvious fact that the  $J_{X1}/(\nu_X - \nu_1)$  values for all coupling interactions involving X are small. Numerical simulation of the

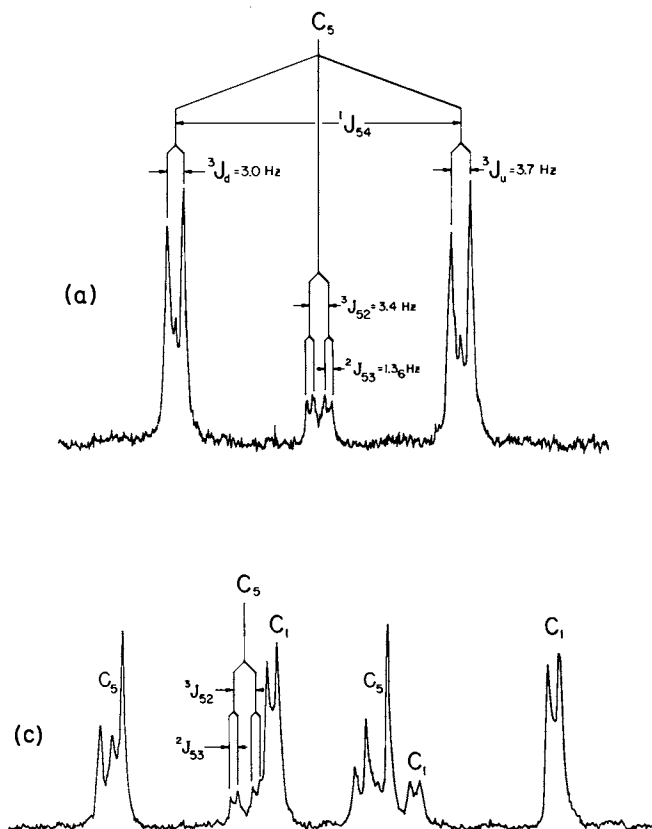


Figure 3. Proton decoupled  $^{13}\text{C}$  NMR spectra of the C-5 resonances of [90%-U- $^{13}\text{C}_5$ ] glutamic acid: a, pH 2.5; c, pH 10.6 (this pH is below the asymptotic value corresponding to essentially complete amino deprotonation, because under such conditions the C-1 and C-5 resonances overlap completely). (Continued on next page.)

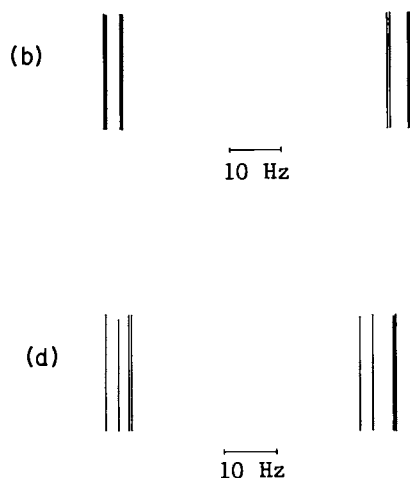
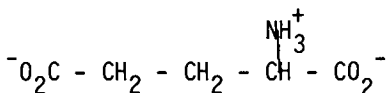


Figure 3. Continued. Theoretical transitions corresponding to the fully labeled molecule are illustrated in b and d. The coupling constants indicated in a are apparent first-order constants, which is substantially in error for  $^1J_{s_4}$ . The coupling constants used in the simulations are:  $^1J_{s_4} = 55.0$  Hz (pH 2.5) and 51.5 Hz (pH 10.6), and the remote coupling constants are given accurately from a first-order analysis of the center resonances corresponding to C-5, C-3, and C-2 but not C-4 labeled. The additional observable splitting at high pH reflects the increase in  $J_{s_4}/\Delta\nu_{s_4}$  from 0.31 to 0.43. The average observed coupling for the upfield and downfield doublets in a is equal to the actual  $^3J_{s_2}$  value [Reproduced, with permission, from Ref. 12. Copyright 1981, Heyden (London).]

spectra indicates that the observed spectral characteristics reflect the presence of unresolved transitions due to high order interactions in the spin system, with the apparent peak heights related to the separation of these unresolved transitions. Such effects are not observed in a three spin ABX system, but can arise in a four spin system with at least one strong coupling interaction, i.e., an ABMX system. The X resonances of an ABX system will never be asymmetric, however, the relative arrangements of the two ABX sub-spectra of the ABMX system can give rise to this apparent asymmetry.(12)

The C-5 carboxyl resonances of [90%-U-<sup>13</sup>C<sub>5</sub>]-glutamate:



provide a good illustration of these effects (Fig. 3). At low pH, the C-5 resonances include four center peaks corresponding to C-4 unlabeled, and two sets of satellites corresponding to C-4 labeled. It is apparent that these satellite resonances are structurally different than the center resonances, i.e., the introduction of a <sup>13</sup>C label at C-4 has two effects: (1) introduction of a large <sup>1</sup>J<sub>45</sub> coupling interaction; and (2) introduction of a moderately strong interaction between C-3 and C-4 ( $J_{34}/\Delta\nu_{34} = 0.31$ ) which indirectly alters the C-3 - C-5 and C-4 - C-5 interactions. It can be seen from Fig. 3a that the center resonances are first order and can be used to obtain the two small remote carbon-carbon coupling constants, <sup>2</sup>J<sub>53</sub> and <sup>3</sup>J<sub>52</sub>. The glutamate spectrum is actually an ABMRX system with only the one strong coupling interaction between C-3 and C-4, however the C-5 resonances can be interpreted neglecting C-1 since it is not coupled to C-5 and since it is only weakly coupled to the other nuclei. The theoretical spectrum shown in Fig. 3b illustrates the closely spaced component resonances which give rise to the apparent peak height asymmetries in Fig. 3a. At high pH, the shift difference between C-3 and C-4 decreases, enhancing the anomalous appearance of the C-5 resonances (Figs. 3c, 3d). In this case, some of the component resonances are sufficiently separated to appear as separate resonances.

Both the virtual coupling effect and the asymmetric appearance of weakly coupled nuclei are predicted directly from a high order analysis as can be carried out routinely by numerical solution of the Hamiltonian.(13) It is helpful, however, to have a general understanding that such effects exist and under what conditions they arise to facilitate spectral interpretation and to help avoid misinterpretation.

(c) Generally Labeled Amino Acids. The proton decoupled  $^{13}\text{C}$  spectrum of glutamate biosynthesized from a  $[90\%-1-^{13}\text{C}_1]$  glucose precursor by *M. ammoniaphilum*(14) is illustrated in Fig. 4. Analysis of the biosynthetic pathways involved indicates that the labeling occurs primarily at C-2 and C-4, with reduced enrichment at C-3 and C-1, and negligible C-5 enrichment. This pattern is consistent with the resonance intensities, subject to the usual caution required in comparing resonances with different  $T_1$  and NOE values. Absolute enrichment values may be obtained from the  $^1\text{H}$  NMR spectrum of the  $^{13}\text{C}$  enriched glutamate (Fig. 4a) subject to care not to overpulse the spectrum which can lead to considerable overestimation of the enrichment due to the shorter  $T_1$  values for the  $^1\text{H}$  satellites.

In contrast to the analysis of the  $^1\text{H}$  NMR spectra, intensities of the  $^{13}\text{C} - ^{13}\text{C}$  satellites arising from  $^{13}\text{C} - ^{13}\text{C}$  scalar coupling are generally not directly interpretable in terms of  $^{13}\text{C}$  enrichments if the labeling of the coupled carbons is not statistically independent.(15) In a typical biosynthetic study, the correlated nature of the  $^{13}\text{C}$  isotopic enrichment reflects the particular metabolic pathways involved. In the present case, the enrichment of glutamate C-3 inferred from the  $^1\text{H}$ -2 satellite/(center + satellite) intensity exceeds that inferred from  $^{13}\text{C}$ -1 splitting (Figs. 4a, 4b). This result suggests the contribution of a pathway in which the labeling of glutamate C-1 and C-2 will be negatively correlated. In the present case, synthesis via the Krebs cycle will produce such a negative correlation in which either C-1 or C-2 but not both are labeled. Thus, analysis of carbon-carbon multiplets can provide valuable insight on the biosynthetic paths involved in the synthesis of particular metabolites.

#### Conformational Interpretation of Scalar Carbon-Carbon Coupling Constants.

Scalar coupling constants extracted as described in the previous section can be used to probe the electronic structure and the conformation of  $^{13}\text{C}$  labeled amino acids and peptides. Studies of  $^1J_{\text{CC}}$  values have generally been consistent with expectations based on hybridization and substituents.(16-20)  $^1J_{\text{CC}}$  values for  $\text{C}' - \text{C}_\alpha$  for the free amino acids are sensitive to carboxyl protonation state with  $^1J_{\text{CC}}(\text{CO}_2) = 53.5 \pm 0.5$  Hz and  $^1J_{\text{CC}}(\text{COOH}) = 59.5$  Hz  $\pm$  0.5.(17,19,20) Values of  $\Delta J$  corresponding to titration of C-terminal amino acids of peptides are somewhat smaller,  $\sim 4.5 - 5$  Hz.(19) The side chain carboxyl groups of Asp and Glu show smaller  $^1J_{\text{CC}}$  values which also decrease upon deprotonation.(20) These effects are qualitatively predicted theoretically,(21) however the theoretical decrease in  $^1J_{\text{CC}}$  resulting from carboxyl deprotonation greatly exceeds the observed values, primarily as a result of neglect of hydrogen



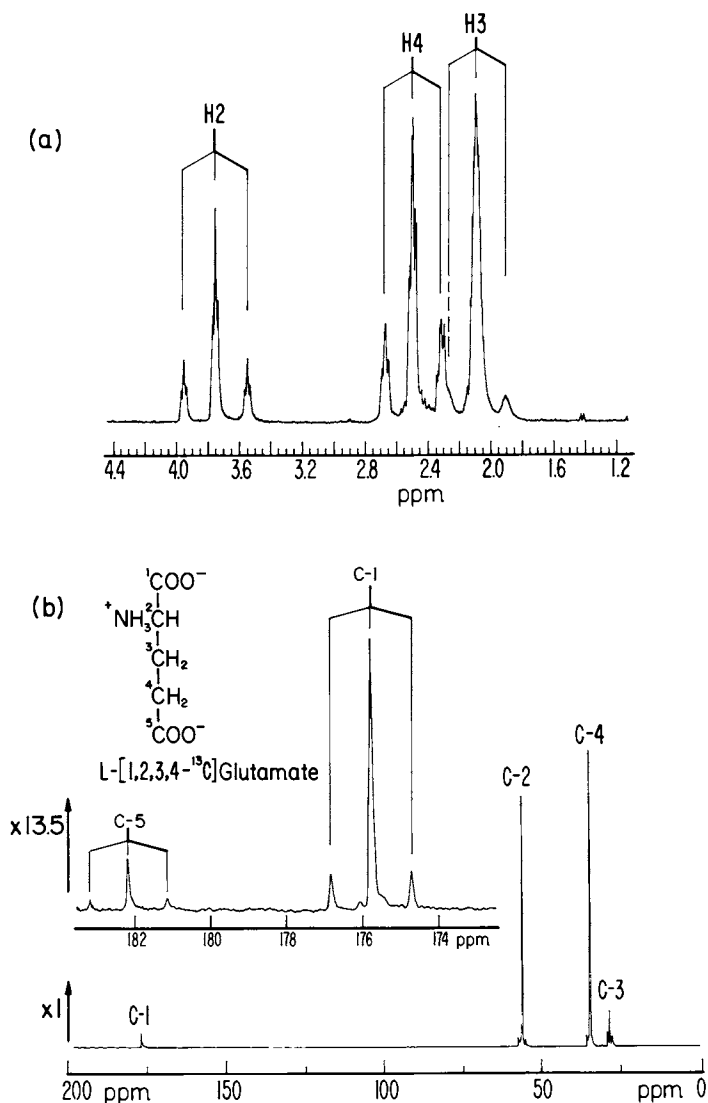


Figure 4. a,  $^1\text{H}$  NMR of  $^{13}\text{C}$  enriched glutamate biosynthesized from a  $[1-^{13}\text{C}_1]$  glucose precursor by *M. ammoniaphilum*, as described in Ref. 14. A pulse delay of 2 min was used to avoid erroneous overestimation of the satellites resulting from the shorter  $T_1$ , due to the  $^{13}\text{C}$ - $^1\text{H}$  dipolar interaction. b,  $^1\text{H}$  decoupled  $^{13}\text{C}$  NMR spectrum of  $^{13}\text{C}$  enriched glutamate. Note in particular the difference between the C-2 enrichment as reflected in the H-2 satellites, and the "apparent enrichment" as reflected in the C-1 satellites. (Reproduced, with permission, from Ref. 14. Copyright 1982, American Society of Biological Chemists.)

bonding interactions with the solvent.(21) As has been described by Maciel, et al.,(21) a comparison of experimental carbon-carbon couplings with theory can be used to evaluate these solvent interactions. A specific illustration is considered below.

In addition to sensitivity of the  $^1J_{CC}$  values to titration effects, differences in the  $^1J_{CC}$  values for the cis and trans conformations of peptide bonds formed to imino acids such as proline have also been observed. The Pro C' - C $_{\alpha}$  coupling is ~1 Hz smaller in cis than in trans Gly-Pro.(19) A smaller effect is observed for the Gly C' - C $_{\alpha}$  coupling in [90%-1,2-<sup>13</sup>C<sub>2</sub> Gly<sup>6</sup>]-bradykinin where the trans and cis values are 52.4 and 52.0 Hz, respectively.(22) As yet, there are no theoretical studies of this effect.

Vicinal scalar coupling constants have been of great value for the interpretation of the solution conformation of molecules. As discussed by Feeney,(23) this data can be used for defining dihedral angles in molecules of fixed conformation as well as for determining the fractional populations of conformers in a mixture of rapidly interconverting conformers. Such applications are based on the dihedral angle dependence of the vicinal couplings first described by Karplus.(24) The hallmark of this behavior is a dihedral angle dependence which is dominated by a  $\cos^2\phi$  term so that the coupling is large for  $\phi$  values near 0°, 180° and smaller for  $\phi$  near 90°.

Extension of this type of analysis to scalar coupling interactions involving other nuclei requires establishment of the dihedral angle dependence of the vicinal couplings. Three approaches have been used:(1) Measurement of coupling constants in conformationally constrained molecules; (2) correlation of observed couplings with rotamer distributions in flexible molecules deduced previously on the basis of  $^3J_{HH}$  values; (3) theoretical calculations. Studies of conformationally rigid structures have established the dominance of a  $\cos^2\phi$  dependence for  $^3J_{CC}$ .(25,26) with deviations for the  $\phi = 0^\circ$  case interpreted theoretically on the basis of non-bonded interactions.(27) In general, the  $^3J_{CC}$  analysis is more complex than the  $^3J_{HH}$  case, exhibiting a large variability related to the carbon substituents.(28) These features are illustrated for the case of [90%-1-<sup>13</sup>C<sub>1</sub>] enriched carbohydrates(7) in which  $^3J_{16}$  (trans) >  $^3J_{14}$  (gauche), however, the  $^3J_{16}$  values differ for the  $\alpha$  and  $\beta$  anomers despite the similar dihedral angles of 180°.

Initial applications of  $^3J_{CC}$  couplings to amino acid conformation analysis were based on the theoretical finite perturbation theory self consistent field molecular orbital theory at the INDO level of approximation for butanoic acid(25) (Table I). Ptak, et al.(29) noted in their studies of <sup>13</sup>C enriched threonine and aspartic acid that application of the butanoic acid couplings did not give agreement with the rotamer populations based on  $^3J_{HH}$  analysis and suggested different values (Table I). We have obtained theoretical results for aspartic

Table I.  $^{13}\text{C} - ^{13}\text{C}$  Scalar Coupling Constants used for Conformational Analysis

Molecule	$J(\text{cis})$	$J_t(\text{Hz})$	$J_g(\text{Hz})$	Method	Ref.	
Butane	5.79	4.27	1.97	Theory - INDO	25	
Butanoic Acid	1.76	5.87	1.24	Theory - INDO	27	
Aspartic Acid	3.97	4.46	0.99, 1.48	Theory - INDO	20	
		5.9	0.5	Comparison with $^1\text{H}$ Couplings	31	
		5.1	0.5	"	30	
		5.0	0.5	"	29	
Threonine		3.0	0.0	"	29	
Glutamic Acid		$^3J_{14}$	2.98	0.09, 1.05	Theory - INDO	20
		$^3J_{25}$	5.15	1.69, 0.98	Theory - INDO	20

and glutamic acids based on a finite perturbation theory self consistent field molecular orbital calculation at the INDO level of approximation.(20) The theoretical results differ significantly from those for butanoic acid and are generally in good agreement with those suggested by Ptak, et al.(29) and by Toma, et al.(30) The couplings show a clear dominance of the  $\cos^2 \phi$  dependence for  $^3J_{CC}$  (Fig. 5) as well as marked substituent effects which are reflected in the differences between Asp  $^3J_{14}$ , Glu  $^3J_{14}$ , and Glu  $^3J_{25}$ . Although these results suggest the need to look at each case separately, the agreement between  $J_t$  and  $J_g$  values for glutamate  $^3J_{14}$  and threonine  $^3J_{14}$ , and the applicability of the Asp couplings to conformational analysis of Phe(30) suggests that as a reasonable approximation the Asp results may be applied to  $^3J_{14}$  analysis where C-4 adopts  $sp^2$  hybridization and the Glu  $^3J_{14}$  results may be used in the analysis of cases in which C-4 adopts an  $sp^3$  hybridization. It is clear from these results that in many cases of interest in which the glutamate model couplings may apply, the  $^3J_{14}$  couplings will be very small, making rotamer population analysis difficult. This conclusion is reflected in the very small  $^3J_{14}$  couplings observed for many amino acids by Tran-Dinh, et al.(31)

On the basis of the  $\cos^2 \phi$  dependence of  $^3J_{CC}$ , observation of the increase in Asp  $^3J_{14}$  as a function of pH (Fig. 6) can be interpreted in terms of the increased population of the anti conformer,(20) consistent with interpretations on the basis of proton coupling analysis.(32) Dihedral angle analysis for glutamate about C-2 - C-3 is considerably more difficult due to the small magnitude of the couplings, however the changes in the dihedral angle about C-3 - C-4 as monitored by  $^3J_{25}$  can be determined, and reflect a large increase in the anti conformation resulting from deprotonation of the amino group (Fig. 7). A small decrease (0.2 Hz) in  $^3J_{25}$  as the pH is increased from 3.0 to 5.0 may reflect a change in the gauche/anti ratio, however, since the two gauche conformers are predicted to exhibit a significantly different coupling (Table I), this result might reflect a variation in the ratio of the gauche populations, or perhaps a change in electronic structure resulting from C-1 deprotonation which is essentially independent of conformation. Few conformational studies of glutamate based on  $^1H$  coupling analysis have appeared in the literature. We note finally that Toma, et al.(30) have concluded that different sets of coupling constants must be used to interpret the conformation of amino acid residues in peptides. This conclusion is consistent with the pronounced substituent effects noted above.

Experimental  $^3J_{CC}$  values for proline (Table II) are more easily interpreted on the basis of the conformational constraints introduced by the pyrrolidine ring, and show a clear  $\cos^2 \phi$  dominance.(19,31-36) The conformational variability reflects primarily the puckering of the 5-membered ring. The  $^3J_{14}$  values corresponding to dihedral angles in the range  $90^\circ$  (C-4 endo) to

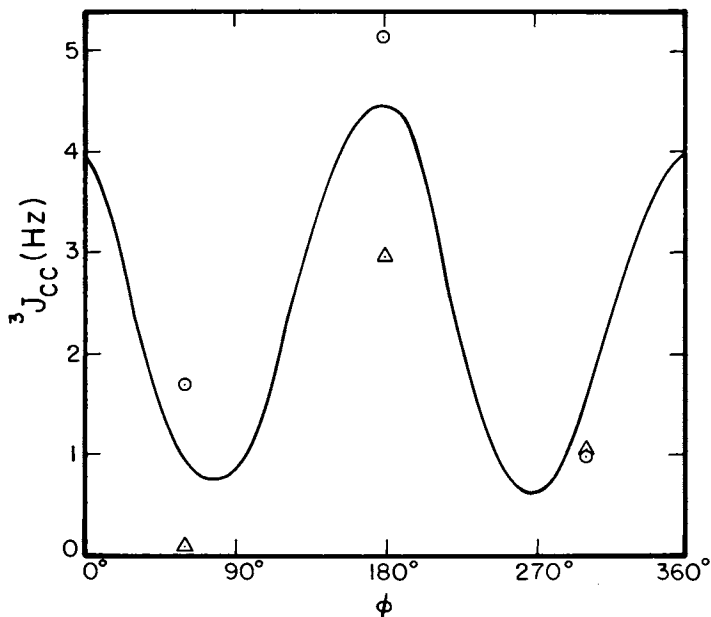


Figure 5. A plot of the theoretical dihedral angle dependence of  ${}^3J_{CC}$  for aspartic acid based on the numerical results given in Ref. 20. Theoretical results were based on a finite perturbation theory self-consistent field molecular orbital calculation at the INDO level of approximation. Data were calculated for the fully protonated molecule. Some theoretical values for glutamic acid  ${}^3J_{14}$  ( $\Delta$ ) and  ${}^3J_{25}$  ( $\odot$ ) also are included.

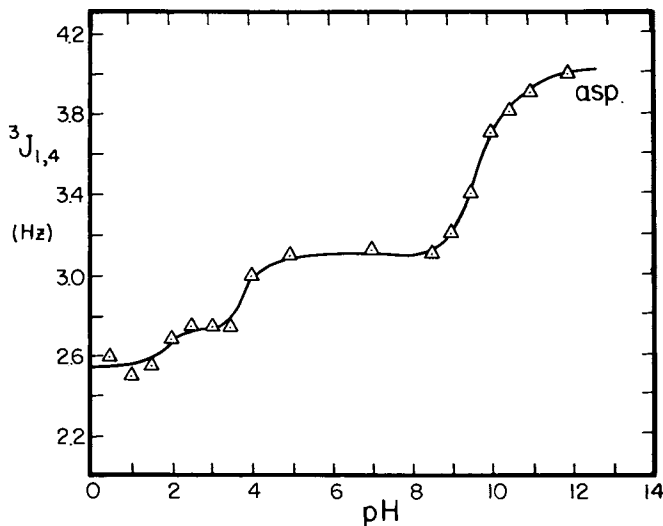


Figure 6. Observed dependence of  ${}^3J_{CC}$  for aspartic acid on pH. (Reproduced from Ref. 20. Copyright 1978, American Chemical Society.)

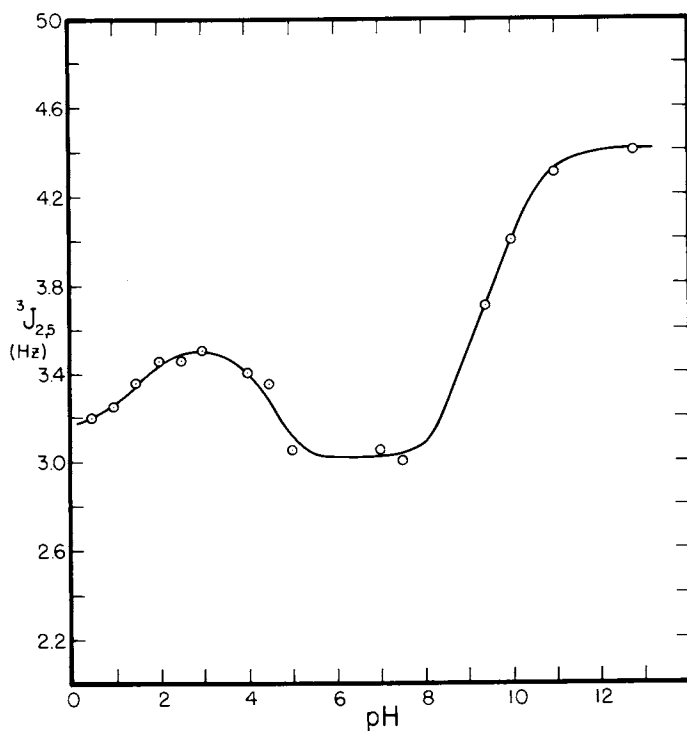


Figure 7. Observed dependence of  $^3J_{2,5}$  of glutamic acid on pH. (Reproduced from Ref. 20. Copyright 1978, American Chemical Society).

Table II. Vicinal  $^{13}\text{C} - ^{13}\text{C}$  Coupling Constants in Proline and Proline Containing Peptides.

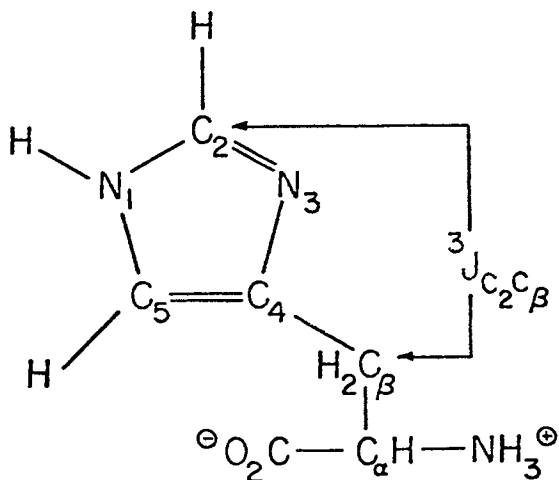
<u>Compound</u>	<u><math>^3J_{14}</math></u>	<u><math>^3J_{15}</math></u>	<u><math>^3J_{2,5}</math></u>	<u>Ref.</u>
Proline	1.5			19
	1.1			
Gly-Pro	<0.5		4.4	33
Gly-Pro-Gly	<0.5		4.3	33
[ $^{13}\text{C}$ -Pro]-TRF	<0.5		3.9	33
cyclo{Pro-Pro-[ $^{13}\text{C}$ -Pro]}	0.0	0.0	5.3, 4.9	34
[85%-U- $^{13}\text{C}$ -Pro <sup>7</sup> ] Angiotensin	0.0			
Pyroglutamic acid	1.1	-	7.5	31
[ $\gamma$ -S] Proline		1.4 (pH 1.3)		35
		2.4 (pH 6.1)		
		4.75 (pH 8.3)		
[85%- $^{13}\text{C}$ ] Pro <sup>7</sup> Angiotensin	0.0			36

150<sup>0</sup> (C-4 exo) are generally small. Since the geminal carbon-carbon couplings in saturated systems appear to be quite small,<sup>(31)</sup> the observed coupling between C-2 and C-5 presumably reflects an interaction via the three bond pathway and is thus related to the dihedral angle about the C-3 - C-4 bond. The <sup>3</sup>J<sub>14</sub> values are found to be reduced in several peptides, presumably reflecting an increased C<sup>γ</sup>-endo/C<sup>γ</sup>-exo ratio. This result may be related to the increased geminal C-2 - N - C-5 bond angle. <sup>1</sup>H coupling constant analyses for proline have shown an increased C<sup>γ</sup>-endo/C<sup>γ</sup>-exo ratio accompanies deprotonation of the nitrogen at high pH.<sup>(37)</sup> Studies of <sup>3</sup>J<sub>15</sub> in [γ-S] proline also show a pH dependence which has been interpreted on the basis of an increasing S-endo/S-exo ratio at high pH (Table II).<sup>(35)</sup> However, it is clear from <sup>13</sup>C relaxation data that the pyrrolidine ring of proline in both the free amino acid and in peptides undergoes rapid internal motion, and that appreciable forms of both puckered conformations must be present to explain the observed data.<sup>(38)</sup> A concerted coupling constant - relaxation analysis should be of great value in providing a more complete description of proline conformational dynamics. Pyroglutamic acid, a proline analog in which the C-5 methylene is replaced by a carbonyl, exhibits a larger <sup>3</sup>J<sub>25</sub> coupling, presumably reflecting the sp<sup>3</sup> → sp<sup>2</sup> hybridization difference<sup>(31)</sup> The <sup>3</sup>J<sub>14</sub> values are similar to those of proline.

Interresidue proton - proton couplings in peptides are not observable, however, interresidue <sup>3</sup>J<sub>CC</sub> values can, in principle, be obtained. Piriou, et al. have made such observations on cyclo([85%-U-<sup>13</sup>C] Asp-Pro).<sup>(39)</sup> The <sup>3</sup>J<sub>CC</sub> values for the Asp carbonyl and the Pro C-2 and C-5 carbons were obtained and allowed a determination of the dihedral angles φ and χ<sub>4</sub>, and a consequent determination of the pyrrolidine ring conformation as primarily in the C<sup>γ</sup>-endo form.

The agreement of rotamer populations based on theoretical coupling constants with those deduced from <sup>3</sup>J<sub>HH</sub> values suggests that this type of analysis can be extended to other situations of interest. The need for inclusion of solvent interactions to correctly predict <sup>1</sup>J<sub>CC</sub> values for deprotonated carboxyl groups suggests the possibility of using theoretical calculations to study intermolecular interactions or intramolecular interactions between remote groups. We have recently studied the <sup>3</sup>J(C-β, C-2) coupling in [90%-2-<sup>13</sup>C<sub>1</sub>] histidine.<sup>(40)</sup>





The results were compared with theoretical calculations for 4-methyl imidazole (Fig. 8). At low pH corresponding to the protonated imidazolium ion, the agreement between theory and experiment is remarkably good. At high pH corresponding to the neutral imidazole moiety, it becomes necessary to consider the two tautomeric forms of imidazole. The observed coupling constant is related to the fractional population of the N-1 protonated tautomer,  $f$ , by:

$${}^3J_{\text{CC}} = f \cdot ({}^3J_{\text{CC}}^{\text{c}}) + (1 - f) \cdot ({}^3J_{\text{CC}}^{\text{b}})$$

where superscripts b and c refer to Fig. 8. Application of this expression in combination with the observed coupling constant at pH 8.0 of 4.3 Hz gives a value of  $f = 50\%$ . This result is in poor agreement with other studies of histidine tautomerism which support a strong preference for the N-1 protonated tautomer. Data of Blomberg, et al.(41) and Alei, et al.(42) indicate a strong correlation between the preference for the N-1 tautomer and the protonation of the terminal amino group. Interactions with solvent  $\text{H}_2\text{O}$ , or with  $\text{NH}_3$  or  $\text{NH}_4^+$  to simulate the terminal amino group at high or neutral pH were modeled theoretically by introducing the molecules as illustrated in Fig. 8. The  $\text{H}_2\text{O}$  or  $\text{NH}_3$  interactions lead to small reduction of the predicted  ${}^3J_{\text{CC}}$  value, while  $\text{NH}_4^+$  has a more significant effect. This result suggests that at neutral pH, the tautomerism of histidine can be modeled theoretically with systems b and f, i.e.:

$${}^3J_{\text{CC}} = f \cdot ({}^3J_{\text{CC}}^{\text{f}}) + (1-f) \cdot ({}^3J_{\text{CC}}^{\text{b}})$$

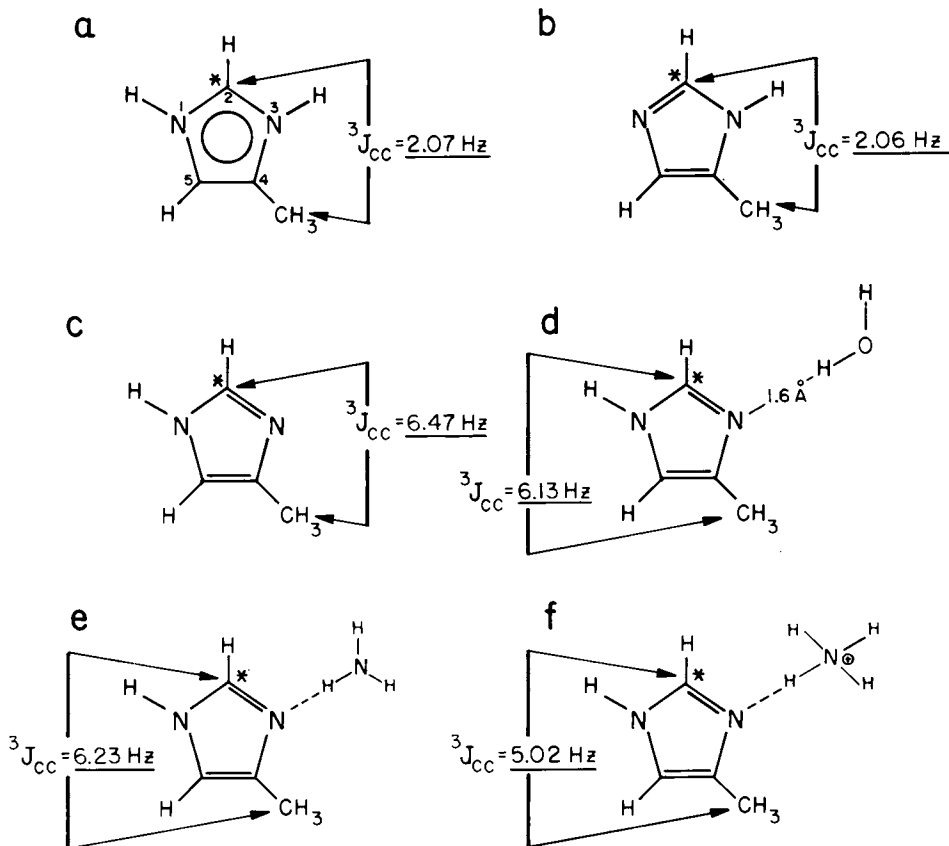


**Figure 8.** Theoretical  $^3J_{\text{CC}}$  values for 4-methylimidazole based on a finite perturbation theory self-consistent field molecular orbital calculation. a–c correspond to varied protonation states of the molecule; d–f include the effects of hydrogen bonding interactions with the solvent, and with the deprotonated and protonated amino group, respectively. (Based on calculations given in Ref. 40.)

The calculated N-1 tautomer probability,  $f = 76\%$ , is then in better agreement with the literature. This result is consistent with the intramolecular hydrogen bonding between the imidazole N-3 nitrogen and the terminal amino group as the primary determinant of the tautomeric asymmetry. At high pH, the use of systems d or e to model the tautomerism in combination with the observed coupling suggests a more equal tautomeric equilibrium. It is also possible to work backwards from the tautomeric distribution determined from other measurements to the coupling constants of the individual tautomers, however the results depend on the particular distribution used and are thus limited by the variability of the reported results.(42)

In addition to the application of  $^3J_{CC}$  analysis as a conformational probe, extensive use of  $^3J_{CH}$  values have been made recently to supplement the data available from  $^3J_{HH}$  analysis.(43-45) Most applications have involved the scalar coupling between the carboxyl carbon and the  $\beta$  protons. This approach frequently does not require isotopic labeling. The theoretical treatment used to obtain the  $^3J_{CC}$  values for aspartic acid gives mean values of  $J_t = 8.5$  Hz,  $J_g = 2.0$  Hz. These compare with literature values of approximately  $J_t = 10.0$  Hz,  $J_g = 1.2$  Hz.(45)

#### Relaxation Behavior of $^{13}C$ Enriched Amino Acids.

Specific  $^{13}C$  enrichment of individual carbon positions in amino acids facilitates relaxation measurements which are typically time consuming and enables studies to be carried out at reduced concentration. This is of particular value in view of the growing literature documenting intermolecular association of peptides.(46-48) Niccolai, et al.(49) have compared the rotational correlation times of N-acetyl alloisoleucine in  $H_2O$  as determined by  $^{13}C$  (high concentration) and  $^1H$  (lower concentration) studies, and suggest that intermolecular association may be responsible for the longer correlation time determined by the former method. In addition to the sensitivity advantage,  $^{13}C$  enrichment facilitates the measurement of  $^1H$  satellite relaxation and, in the case of multiple labeling, of  $^{13}C - ^{13}C$  dipolar interactions. Additionally, the short  $^{13}C$   $T_1$  values in peptides or proteins has important implications for the observation of scalar coupling interactions involving  $^{13}C$  which, as discussed in the previous section, are of importance for conformational analysis. These relaxation characteristics are the primary topic of the present discussion.

(a)  $^1H$  Relaxation in  $^{13}C$  Enriched Molecules. As a result of the  $^{13}C - ^1H$  dipolar interaction, protons bonded to  $^{13}C$  will typically exhibit shorter  $T_1$  values than protons bonded to  $^{12}C$ .(50-52) The relatively large effect of the  $^{13}C$  nucleus reflects the short  $^{13}C - ^1H$  bond length. For a typical methylene geometry with a  $^1H - ^1H$  internuclear distance of  $\sim 1.8$  Å and a  $^{13}C$

- <sup>1</sup>H bond length of 1.09 Å, the dipolar H - H and <sup>13</sup>C - H interactions are of similar magnitude. The <sup>1</sup>H inversion recovery experiment for an equal mixture of 1-<sup>13</sup>C and 2-<sup>13</sup>C glycine is illustrated in Fig. 9. For methine carbons, the T<sub>1</sub> value for the satellite proton resonances (corresponding to <sup>13</sup>C enrichment) can be several times shorter than the value for the center resonance. This result is illustrated, for example, for the case of the <sup>1</sup>H resonances of α-D-mannosamine in which the T<sub>1</sub> for the center resonance is 4.3 times that for the satellites.<sup>(52)</sup> It must be emphasized that homonuclear relaxation studies such as these <sup>1</sup>H measurements are generally more difficult to interpret than natural abundance <sup>13</sup>C studies due to the combination of pulse induced mixing of transitions in nonequilibrium systems,<sup>(53)</sup> cross relaxation<sup>(54,55)</sup> and cross correlation effects.<sup>(56)</sup> A combination of selective and non-selective pulsing has been used to sort out some of these problems.<sup>(49,54,57,58)</sup> The additional information which can be obtained from the <sup>1</sup>H satellites observable in <sup>13</sup>C enriched systems can be used to further define the motion by providing additional spectral density terms. Further, an appreciation of the <sup>13</sup>C - <sup>1</sup>H relaxation contributions is important in applications involving quantitation of <sup>13</sup>C labeling from <sup>1</sup>H spectra. Several practical applications of these effects are summarized below:

1. As noted in Section II(c), the intensity ratio of satellite/center proton resonances in <sup>13</sup>C enriched systems can be used to evaluate isotopic <sup>13</sup>C enrichment levels. However, if FT methods are used to obtain the <sup>1</sup>H spectra, a systematic error resulting in overestimation of the <sup>13</sup>C enrichment will be made if the system is overpulsed due to the shorter T<sub>1</sub> of the satellite resonances.
2. The <sup>13</sup>C - <sup>1</sup>H dipolar interaction is of value for the interpretation of molecular dynamics.<sup>(50-52)</sup> The satellite difference method can be used to obtain this information with high (proton) sensitivity. In this context, it is noted that the contribution monitored by the proton:

$$\frac{1}{T_1^H} = \frac{\gamma_C^2 \gamma_H^2 h^2}{10r_{CH}^6} \left[ \frac{\tau}{1+(\omega_C - \omega_H)^2 \tau^2} + \frac{3\tau}{1+\omega_H^2 \tau^2} + \frac{6\tau}{1+(\omega_C + \omega_H)^2 \tau^2} \right]$$

will differ from that measured by the carbon:

$$\frac{1}{T_1^C} = \frac{\gamma_C^2 \gamma_H^2 h^2}{10r_{CH}^6} \left[ \frac{\tau}{1+(\omega_C - \omega_H)^2 \tau^2} + \frac{3\tau}{1+\omega_C^2 \tau^2} + \frac{6\tau}{1+(\omega_C + \omega_H)^2 \tau^2} \right]$$

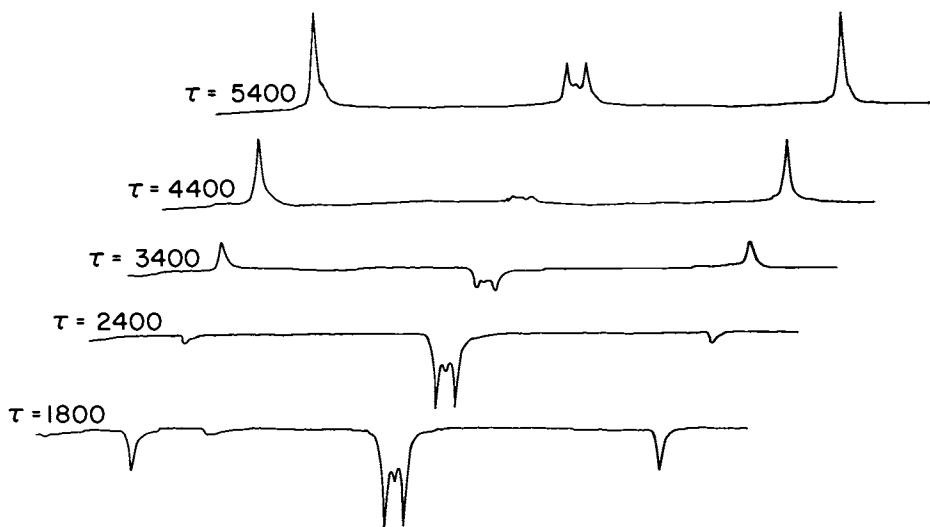


Figure 9. Partially relaxed  $^1\text{H}$  FT spectra of an equal mixture of  $[1-^{13}\text{C}_1]$  and  $[2-^{13}\text{C}_1]$  glycine. The C-1 labeling, which has a negligible effect on the proton relaxation, produces a small doublet ( $^2J_{\text{CH}} = 5.4$  Hz) at the center of the spectrum. A  $^1J_{\text{CH}} = 144$  Hz coupling corresponds to the large doublet. (Reproduced, with permission, from Ref. 52. Copyright 1977, Academic Press.)

in the second spectral density term. In the extreme narrowing limit, the <sup>13</sup>C NOE value can be obtained from this data:

$$\text{NOE} = 1 + \frac{1}{2} \frac{\gamma_H}{\gamma_C} \frac{T_1}{T_1^{\text{DD}}}$$

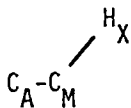
where  $T_1^{\text{DD}}$  is determined as:

$$\frac{1}{T_1^{\text{DD}}} = N_H \left[ \frac{1}{T_1^{\text{satellite}}} - \frac{1}{T_1^{\text{center}}} \right]$$

with  $N_H$  the number of protons directly bonded to the carbon.

3. <sup>1</sup>H relaxation in biological macromolecules tends to be dominated by spin diffusion processes.(59,60) A comparison of the observed and predicted ratio of the <sup>1</sup>H center and satellite resonances should be of value for evaluating the spin diffusion contribution to the <sup>1</sup>H relaxation.
4. Hill and Hall have used a combination of specific inversion experiments to obtain relative interproton distances in sugars.(57) A <sup>1</sup>H measurement on a <sup>13</sup>C enriched sugar could provide additional information which would allow absolute distances to be established. Of course, analogous information could, in principle, be obtained from <sup>13</sup>C  $T_1$  measurements.

(b) <sup>13</sup>C Relaxation in Multiply Enriched Systems. The relaxation contribution of <sup>13</sup>C - <sup>13</sup>C dipolar interactions in enriched systems was first demonstrated by Moreland and Carroll.(61) These interactions can be simply treated using an extended Solomon equation approach,(62,63) or using the full density matrix solution.(64,65) Calculations which have appeared thus far in the literature suggest that the differences between the two treatments are quantitatively quite small and can frequently, if not always, be neglected. The situation of most common interest can be approximated as an AM{X<sub>n</sub>} system, in which the A nucleus is an unprotonated carbon bonded to a protonated carbon M, and the X<sub>n</sub> are decoupled protons:



The coupled Solomon equations then become:

$$\frac{dA_z}{dt} = g_A(A_0 - A_z) + f_{AM}(M_0 - M_z) + f_{AX}X_0$$

$$\frac{dM_z}{dt} = g_M(M_0 - M_z) + f_{AM}(A_0 - A_z) + f_{MX}X_0$$

where  $A_0 = M_0 = \gamma_C H_0$ ,  $X_0 = \gamma_H H_0$ , and where

$$g_A = \frac{\gamma_C^2 \hbar^2}{10} \sum_i \frac{N_i \gamma_i^2}{r_{Ai}^6} \cdot \left[ \frac{\tau}{1 + (\omega_A - \omega_i)^2 \tau^2} + \frac{3\tau}{1 + \omega_A^2 \tau^2} + \frac{6\tau}{1 + (\omega_A + \omega_i)^2 \tau^2} \right]$$

$$f_{AM} = \frac{\gamma_A \gamma_M \hbar^2}{10 r_{AM}^6} \cdot \left[ \frac{-\tau}{1 + (\omega_A - \omega_M)^2 \tau^2} + \frac{6\tau}{1 + (\omega_A + \omega_M)^2 \tau^2} \right]$$

The response to an inversion recovery sequence for A (or M) is then biexponential having the form:

$$\frac{A_{eq} - 2A_z(t)}{2A_{eq}} = C_1 e^{-\lambda_1 t} + C_2 e^{-\lambda_2 t}$$

For a weakly coupled system, the observe pulse used to monitor the partially relaxed system will lead to mixing of intensities only within a given multiplet.<sup>(53)</sup> The expressions above correspond to the total magnetization of the A (or M) multiplets and are, therefore, not affected. Numerical solutions corresponding to isotropic motion, an M-X bond length of 1.09 Å and an A-M bond length of 1.53 Å are illustrated in Fig. 10. The  $T_1$  behavior for the unenriched (or singly enriched) systems exhibits the usual minimum as a function of correlation time. A corresponding  $T_1^{CC}$  curve which reflects the carbon-carbon interaction would apply if one of the carbons were saturated. In the absence of this procedure, the actual non-exponential decay is described by time constants  $\lambda_1^{-1}$  and  $\lambda_2^{-1}$ .

Neglecting the small inflection observed for the A coefficients (Fig. 10c), the relaxation is exponential and can be considered to fall into three regions. In the extreme narrowing limit the relaxation contributions of the  $^{13}\text{C}-^1\text{H}$  and  $^{13}\text{C}-^{13}\text{C}$  dipolar interactions are essentially additive. Below  $\sim 10^{-8}$  s, the rapid flip-flop interaction which reflects the first term in

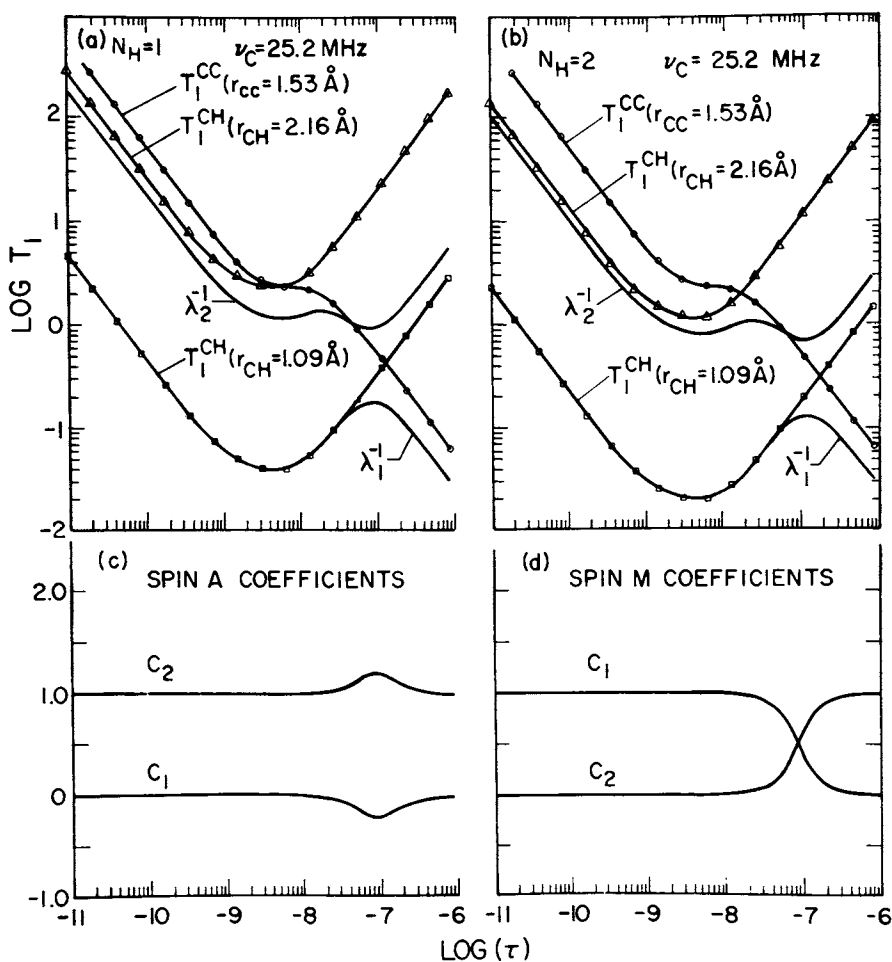


**Figure 10.** Spin-lattice relaxation behavior for an AM  $X_n$  system where A corresponds to a nonprotonated carbon for which  $r_{\text{CH}} = 2.16 \text{ \AA}$ , M corresponds to a protonated carbon with  $r_{\text{CH}} = 1.09 \text{ \AA}$ , and the proton(s) X are decoupled. (a)  $T_1$  behavior for A ( $\Delta$ ) and M ( $\square$ ) carbons in the absence of dipolar carbon-carbon interaction ( $N_{\text{H}} = 1$ );  $\nu_{\text{C}} = 25.2 \text{ MHz}$ ;  $T_1$  contribution ( $\circ$ ) corresponding to the carbon-carbon dipolar interaction with  $r_{\text{CC}} = 1.53 \text{ \AA}$ ; the two reciprocal time constants applicable for the cross relaxing system:  $\lambda_1^{-1}$  and  $\lambda_2^{-1}$  so that the relaxation is described by  $C_1 \exp(-\lambda_1 t) + C_2 \exp(-\lambda_2 t)$ . For long correlation times, the carbon-carbon interaction becomes equivalent to the cross relaxation term  $f_{\text{AM}}$ . b, The same calculation with two protons directly bonded to  $C_{\text{M}}$  ( $N_{\text{H}} = 2$ );  $\nu_{\text{C}} = 25.2 \text{ MHz}$ . c, Coefficients  $C_1$  and  $C_2$  for the A nucleus. As is apparent from the magnitudes of the coefficients, the relaxation is exponential over most of the range of correlation times considered. d, Coefficients corresponding to the M relaxation. As a result of the crossover near  $\tau = 10^{-7} \text{ s}$ , the relaxation behavior is transferred from the  $\lambda_1$  to the  $\lambda_2$  curve. (Reproduced from Ref. 63. Copyright 1982, American Chemical Society.)



Eq. 9 leads to spin diffusion with the flip-flop rate limiting the observed  $T_1$ . Below  $10^{-7}$  s, the relaxation for the A spin is limited by the relaxation sink, which corresponds to the bonded methylene carbon. The effect of the small deviation in the coefficients from 1.0 and 0.0 near  $\tau = 10^{-7}$  s is non-exponential recovery, with the negative coefficient leading to a curve which is concave downward. For the M spin, the decay jumps from the  $\lambda_1$  curve for correlation times  $<10^{-7}$  s to the  $\lambda_2$  curve for correlation times  $>10^{-7}$  s.

Based on the additivity of the  $^{13}\text{C} - ^1\text{H}$  and  $^{13}\text{C} - ^{13}\text{C}$  dipolar interactions in the extreme narrowing limit, subtraction of the rates for the center  $^{13}\text{C}$  and satellite  $^{13}\text{C}$  resonances has been used to determine a correlation time for the corresponding carbon-carbon bond,  $\tau_{\text{CC}}$ . Comparison of the values determined in this way with the correlation times for the C - H bonds of methylene carbons (Table III) indicates a significant difference which may reflect internal motion about the carbon-carbon bonds. Additional work in rigid systems is needed to explore these differences further. Extension of this technique to biologically interesting macromolecules should provide valuable information about the molecular dynamics.

Other relaxation parameters such as linewidth and Nuclear Overhauser Enhancement are also affected by carbon-carbon interactions. The Nuclear Overhauser Enhancement of spin A with and without the carbon-carbon dipolar interaction is illustrated in Fig. 11. Clearly, an evaluation of both the  $T_1$  effects and NOE effects resulting from the carbon-carbon interaction is important for the correct evaluation of  $^{13}\text{C}$  satellite intensities which are of use in biosynthetic studies as discussed above.

(c) Effects of Short Relaxation Times on Lineshapes and Couplings. The collapse of multiplet structures observed for spin 1/2 nuclei bonded to quadrupolar nuclei is well established.(66) In large biological molecules, the  $^{13}\text{C}$   $T_1$  values for protonated carbons can become sufficiently short so that this effect must be considered. This effect on multiplet structure has recently been observed in [90%-1,2- $^{13}\text{C}_2$  Gly<sup>6</sup>]-bradykinin.(63) In this case, the methylene  $T_1$  is sufficiently short ( $\sim 0.1$  s) to lead to noticeable broadening of the doublet structure observed for the carbonyl resonances (Fig. 12). Neglecting the intrinsic linewidth of the carbonyl resonance, the doublet structure will be described by:(63)

$$I(\omega) \sim \frac{1}{\left[ \frac{(2\pi J)^2}{4} + (\omega_0 - \omega)^2 \right]^2 + \left[ \frac{\omega_0 - \omega}{T_1 M} \right]^2}$$

Interestingly, the effect of short  $T_1$  on multiplet structure was

Table III. Rotational Correlation Times for <sup>13</sup>C Enriched Molecules.

Molecule	$T_1^{CC}$	$N_H T_1^{CC}$	$\tau_{CC}$	$\tau_{CH}$	Ratio
Diethylmalonate <sup>a</sup>	263	5.40	$2.1 \times 10^{-11}$	$8.6 \times 10^{-12}$	2.5
6-Phosphogluconate <sup>b</sup>	53.5	0.765	$1.05 \times 10^{-10}$	$6.1 \times 10^{-11}$	1.7
[85%-1,2- <sup>13</sup> C <sub>2</sub> , 97%-2,2- <sup>2</sup> H <sub>2</sub> ] Glycine <sup>c</sup>	e	41.0	$1.7 \times 10^{-11}$	$5.5 \times 10^{-12}$	3.1
[90%-1,2- <sup>13</sup> C <sub>2</sub> Gly <sup>6</sup> ]- bradykinin <sup>d</sup>	14.3	0.20	$3.9 \times 10^{-10}$	$2.3 \times 10^{-11}$	1.7

<sup>a</sup> Ref. 61

<sup>b</sup> Ref. 62

<sup>c</sup> Ref. 65

<sup>d</sup> Ref. 63

<sup>e</sup> Relaxation is non-exponential

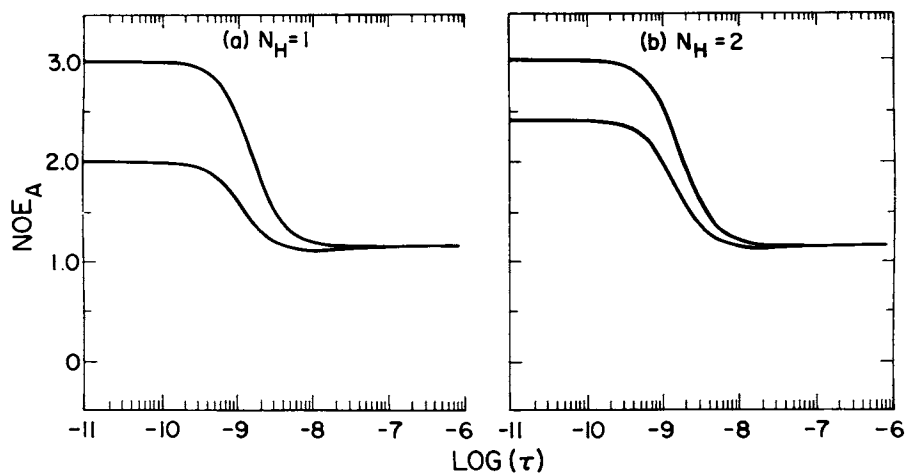
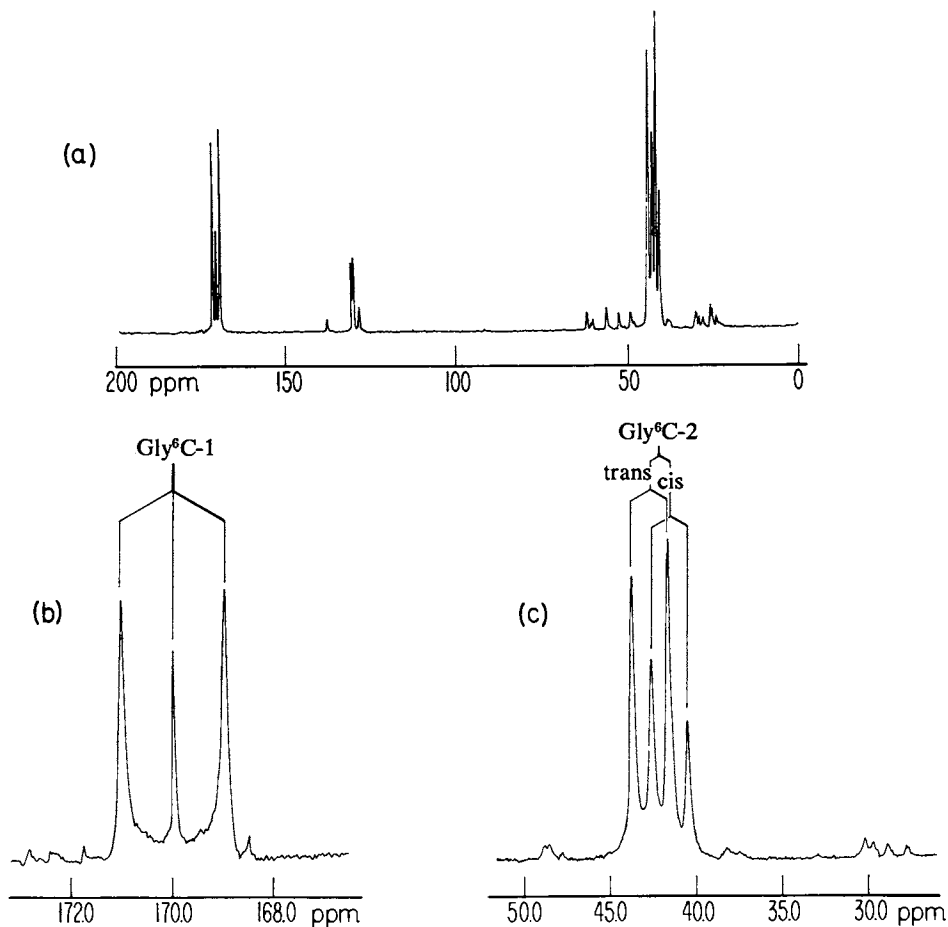


Figure 11. Nuclear Overhauser Enhancements for the A (nonprotonated) carbon in the presence and absence of the additional carbon-carbon dipolar interaction corresponding to  $N_H = 1$  (a) or  $N_H = 2$  (b). In either case, the  $NOE_A = 3.0$  in the extreme narrowing limit for the  $^{13}C-^{12}C-H$  systems because no relaxation mechanism other than the  $^{13}C-^1H$  dipolar mechanism is assumed. (Reproduced from Ref. 63. Copyright 1982, American Chemical Society.)



**Figure 12.** Proton decoupled  $^{13}\text{C}$  NMR spectrum of [90%-1,2- $^{13}\text{C}_2$ , Gly<sup>6</sup>] bradykinin: a, Full spectrum; b, Carbonyl resonance; c, Upfield resonances. The Gly<sup>6</sup> methylene resonances are doubled due to the slow cis/trans equilibrium with  $\delta(\text{cis-trans}) = 1.1$  ppm; This effect is not observed for the carbonyl resonances for which  $\delta(\text{cis-trans}) = 0.0$  ppm. (Reproduced from Ref. 63. Copyright 1982, American Chemical Society.)

American Chemical  
Society Library  
1155 16th St. N. W.

initially considered by Gutowsky, et al.(67) for two interacting spin 1/2 nuclei, rather than for the commonly observed quadrupolar case. The considerations noted here indicate that in favorable cases  $^{13}\text{C}$  (or  $^1\text{H}$ ) lineshapes can be used to monitor the  $T_1$  values of directly bonded carbons and care must be used in the evaluation of long range coupling constants for which the multiplet collapse effect may be sufficient to distort the apparent coupling.

### Biological Studies with Isotopically Labeled Amino Acids and Peptides

(a) Probes of Intracellular Properties. The combination of isotopic enrichment and NMR detection allows investigation of the intracellular properties of intact cells. The  $^{31}\text{P}$  NMR of inorganic phosphate to determine intracellular pH values has been extensively utilized.(68) Intracellular viscosities have been determined from the relaxation behavior of isotopically enriched molecules. Such applications are based on the dependence of the spin lattice relaxation behavior of protonated carbons on the rotational correlation time, which is in turn related via the Stokes Einstein relation to the viscosity of the medium. Studies of [2- $^{13}\text{C}$ ] glycine in frog muscle tissue indicated a small (50%) increase in rotational correlation time over that obtained in free solution.(69) Experiments with the labeled glycine largely confined to the extracellular space and the sarcoplasmic reticulum and studies with the glycine loaded in the cytoplasmic compartment gave similar results.(69) Qualitatively similar results have been obtained with macromolecules such as [2- $^{13}\text{C}$ ] histidine labeled hemoglobin, in which a 24% increase in viscosity of the hemoglobin in erythrocytes over that measured in solution was obtained.(70) Similar results for hemoglobin have also been obtained based on  $^1\text{H}$  NMR dispersion studies of water relaxation in red blood cells.(71) Studies with different reporter groups, including other labeled amino acids, which may be localized in different parts of the cell, should be of value in providing additional data on intracellular viscosity.

(b) Interactions of Peptides with Membranes and Proteins. A partial list of the biologically active peptides which have been isotopically enriched with  $^{13}\text{C}$  is given in Table IV.(72-86) From this table it is apparent that the  $^{13}\text{C}$  labeling/NMR analysis approach represents a rapidly increasing field of study. The objectives of these studies have been twofold: (1) To provide additional scalar coupling interactions which help define the molecular conformation; (2) to provide an enhanced, simplified signal in peptide complexes with membranes and proteins. Peptide - membrane interactions have been of particular interest in terms of the function of gramicidin A,(72,73) and in terms of opiate - receptor binding.(75) The oxytocin/neurophysin system provides a

Table IV. Biologically Active Peptides Isotopically Labeled with <sup>13</sup>C.

<u>Peptide</u>	<u><sup>13</sup>C Label</u>	<u>Ref.</u>
Gramicidin S/A	[10%-U- <sup>13</sup> C] Leu, Val, Phe, Pro	72
Gramicidin A	[20%-U- <sup>13</sup> C-formyl Val <sup>1</sup> ]; [90%-1- <sup>13</sup> C or 2- <sup>13</sup> C O-acetyl]	73,84
Thyrotropin Releasing Factor	[85%-U- <sup>13</sup> C] Pro	33
Leu-enkephalin	[94%-1- <sup>13</sup> C] Tyr <sup>1</sup> , Gly <sup>2</sup> , Gly <sup>3</sup> , Phe <sup>4</sup> , Leu <sup>5</sup>	97
Met-enkephalin, α-endorphin	[90%-2- <sup>13</sup> C] Gly <sup>2</sup> and Gly <sup>3</sup>	74-76
Oxytocin	[85%-U- <sup>13</sup> C] Gly <sup>9</sup>	77
	[ <sup>13</sup> C] Ile <sup>3</sup> , Leu <sup>3</sup>	78
	[90%-1-hemi[1- <sup>13</sup> C]] Cys <sup>1</sup>	79
	[90%-1-hemi[2- <sup>13</sup> C]] Cys <sup>1</sup>	80
	[90%-2- <sup>13</sup> C] Tyr <sup>2</sup>	81
	[85%-U- <sup>13</sup> C] Pro <sup>7</sup>	82
	[85%-U- <sup>13</sup> C] Leu <sup>8</sup>	82
Angiotensin	[85%-U- <sup>13</sup> C] Asp <sup>1</sup> , Val <sup>3</sup> , Tyr <sup>4</sup> , Val <sup>5</sup> , Pro <sup>7</sup> , Phe <sup>8</sup>	36
Human Enkephaligenic (EAE) Nonapeptide	[ <sup>13</sup> C] Gly <sup>4</sup> , Gly <sup>7</sup> ; [60%-3- <sup>13</sup> C] Ala <sup>5</sup>	83
ACTH	[85%-U- <sup>13</sup> C] Phe <sup>7</sup> , Tyr <sup>23</sup>	85
Bradykinin	[20%-1,2- <sup>13</sup> C <sub>2</sub> ] Gly <sup>6</sup> ; [90%-1,2- <sup>13</sup> C <sub>2</sub> ] Gly <sup>6</sup>	86,63

unique opportunity for study of peptide - protein interactions which are also presumably the basis of receptor interactions with peptide hormones. Specific  $^{13}\text{C}$  labeling studies have defined those regions of the peptide which interact directly with the protein, (77,82) have elucidated the exchange kinetics of the peptide protein complex, (81) demonstrated the trans conformation of the Cys-Pro bond, (82) demonstrated sensitivity of peptide resonances to a titrable protein group with a pK of 4.5, and shown that in the complex the pK<sub>a</sub> of the  $\alpha$ -amino group is increased from a value of 6.5 for the free peptide to at least 9.5 in the complex. (79,80) In  $^{13}\text{C}$  NMR studies of [90%-2- $^{13}\text{C}$  Gly<sup>3</sup>] methionine enkephalinamide in the presence of neuroblastoma x glioma hybrid cells (NG 108-15), extensive peptide degradation occurred despite treatment with puromycin and trypsin. (76) Future  $^{13}\text{C}$  NMR studies of peptide receptor interactions may generally require the use of metabolically stable analogs, as well as the simultaneous use of peptidase inhibitors.

### Future Developments

Most of the studies described here represent conventional NMR experiments with isotopically labeled compounds. The recent dramatic advances in both theoretical and experimental spin physics will have a strong impact on this area in two respects: (1) Information which previously has been attainable only by isotopic labeling can now be obtained by multiple quantum NMR studies. (87-89) In particular, the determination of scalar carbon-carbon coupling constants using multiple pulse techniques has been demonstrated by Freeman and co-workers. (90) The application of multiple quantum NMR to study  $^{13}\text{C}$  -  $^{13}\text{C}$  dipolar interactions is similarly feasible. The equivalence of multiple quantum NMR and isotopic labeling has recently been discussed by Warren and Pines. (89) (2) A second and perhaps more exciting prospect is the combined use of isotopic enrichment with the newly developed excitation and polarization techniques to enhance the utility of isotopic enrichment. For example, the use of cross polarization based on scalar coupling (91-93) in combination with isotopic labeling can lead to further increases in sensitivity, which represents the ultimate limit of applicability of the NMR technique. The use of multiple quantum NMR to isolate and quantitate the intensities of different isotopic isomers is of obvious utility in biosynthetic studies, as discussed here. Proton cross relaxation studies have proven of great value in the analysis of molecular conformation. As discussed here, for sufficiently slow motion  $^{13}\text{C}$  -  $^{13}\text{C}$  cross relaxation becomes significant and may provide analogous information. Recent applications of two dimensional NMR to study cross relaxation might be applied in  $^{13}\text{C}$  enriched systems. (94)

Another promising area which represents a combination of approaches is the utilization of sensitivity enhancement via

photo-CIDNP with isotopic labeling. This technique has recently been utilized in peptide studies.(95) The multiplicative enhancement resulting from the application of both techniques could push detection limits down to the micromolar range and possibly below. Factors of 40 for the <sup>19</sup>F resonance of o-fluorotyrosine have recently been reported by Wiener and Sykes.(96) In conclusion, it seems likely that the utility of isotopic labeling will continue to increase as this approach is combined with other experimental techniques, and the resulting sensitivity gains will have greatest significance for biological studies.

#### LITERATURE CITED

\*This work performed under the auspices of the U.S. Department of energy.

1. London, R. E. Org. Magn. Reson. 1981, 17, 134.
2. London, R. E.; Groff, J. P.; Blakley, R. L. Biochem. Biophys. Res. Commun. 1979, 86, 770.
3. Bradbury, J. H.; Norton, R. S. Biochem. Biophys. Acta 1973, 328, 10.
4. Parker, R. G.; Roberts, J. D. J. Org. Chem. 1970, 35, 996.
5. Gribble, G. W.; Nelson, R. B.; Johnson, J. L.; Levy, G. C. J. Org. Chem. 1975, 40, 3720.
6. Deslauriers, R.; Grzonka, Z.; Schaumburg, K.; Shiba, T.; Walter, R. J. Am. Chem. Soc. 1975, 97, 5093.
7. Walker, T. E.; London, R. E.; Whaley, T. W.; Barker, R.; Matwiyoff, N.A. J. Am. Chem. Soc. 1976, 98, 5807.
8. Kollman, V. H.; London, R. E.; Hanners, J. L.; Gregg, C. T.; Whaley, T. W.; J. Labelled Compds. and Radiopharm. 1979, 16, 833.
9. Bengsch, E.; Ptak, M. in "Stable Isotopes in the Life Sciences", IAEA Panel Proceedings Series, IAEA, Vienna (1977), p. 197.
10. Irving, C. S.; Hammer, B. E.; Danyluk, S. S.; Klein, P. D. J. Inorg. Biochem. 1980, 13, 137.
11. Musher, J. I.; Corey, E. J. Tetrahedron 1962, 18, 791.
12. London, R. E.; Walker, T. E. Org. Mag. Reson. 1981, 15, 333.
13. Castellano, S.; Bothner-By, A. A. J. Chem. Phys. 1974, 41, 3863.
14. Walker, T. E.; Han, C. H.; Kollman, V. H.; London, R. E.; Matwiyoff, N. A. J. Biol. Chem. (in press).
15. London, R. E.; Kollman, V. H.; Matwiyoff, N. A. J. Am. Chem. Soc. 1975, 97, 3565.
16. Sogn, J. A.; Craig, L. C.; Gibbons, W. A. J. Am. Chem. Soc. 1974, 96, 4694.
17. Tran-Dinh, S.; Fermandjian, S.; Sala, E.; Mermet-Bouvier, R.; Cohen, M.; Fromageot, P. J. Am. Chem. Soc. 1974, 96, 1484.



18. Hansen, P. E. Org. Magn. Reson. 1978, 11, 215.
19. Fermandjian, S.; Tran-Dinh, S.; Savrda, J.; Sala, E.; Mermet-Bouvier, R.; Bricas, E.; Fromageot, D. Biochim. Biophys. Acta 1975, 399, 313.
20. London, R. E.; Walker, T. E.; Kollman, V. H.; Matwiyoff, N. A. J. Am. Chem. Soc. 1978, 100, 3723.
21. Maciel, G. E.; McIver, J. W.; Ostlund Jr., N. S.; Pople, J. A. J. Am. Chem. Soc. 1970, 92, 1; Maciel, G. E.; McIver, J. W.; Ostlund Jr., N. S.; Pople, J. A. ibid. 1970, 92, 11.
22. London, R. E.; Phillippi, M. A.; Stewart, J. M.; Biochemistry (in press).
23. Feeney, J. Proc. Roy. Soc. London A 1975, 345, 61.
24. Karplus, M. J. Chem. Phys. 1959, 30, 11.
25. Doddrell, D.; Burfitt, I.; Grutzner, J. B.; Barfield, M. J. Am. Chem. Soc. 1974, 96, 1241.
26. Marshall, J. L.; Faehl, L. G.; Ihrig, A. M.; Barfield, M. J. Am. Chem. Soc. 1976, 98, 3406.
27. Barfield, M.; Burfitt, I.; Doddrell, D. J. Am. Chem. Soc. 1975 97, 2631; Barfield, M. ibid. 1980, 102, 1; Barfield, M.; Marshall, J. L.; Canada Jr., E. D. ibid. 1980, 102, 7.
28. Wray, V. J. Am. Chem. Soc. 1978, 100, 768.
29. Ptak, M.; Heitz A.; Dreux, M. Biopolymers 1978, 17, 1129.
30. Toma, F.; Monnot, M.; Piriou, F.; Savrda, J.; Fermandjian, S. Biochem. Biophys. Res. Commun. 1980, 97, 751.
31. Tran-Dinh, S.; Fermandjian, S.; Sala, E.; Mermet-Bouvier, R.; Fromageot, P. J. Am. Chem. Soc. 1975, 97, 1267.
32. Pachler, K. G. R. Fresenius' Z. Anal. Chem. 1967, 224, 211.
33. Haar, W.; Fermandjian, S.; Vicar, J.; Blaha, K.; Fromageot, P. Proc. Nat. Acad. Sci., U. S. A. 1975, 72, 4948.
34. Vicar, J.; Blaha, K.; Piriou, F.; Fromageot, P.; Fermandjian, S. Biopolymers 1979, 18, 1021.
35. Piriou, F.; Lintner, K.; Lam-Thanh, H.; Toma, F.; Fermandjian, S. Tetrahedron 1978, 34, 553.
36. Fermandjian, S.; Piriou, F.; Lintner, K.; Toma, F.; Lam-Thanh, H.; Fromageot, P.; Khosla, M. C.; Smeby, R. R.; Bumpus, F. M. in "Peptides: Structure and Biological Function"; Proc. 6th American Peptide Symposium (Eds: E. Gross and J. Meienhofer, Pierce Chemical Co., Rockford, Ill., 1979) p. 205.
37. Jankowski, K.; Soler, F.; Ellenberger, M. J. Mol. Structure 1978, 48, 63.
38. London, R. E. J. Am. Chem. Soc. 1978, 100, 2678.
39. Piriou, F.; Toma, F.; Savrda, J.; Fermandjian, S. Tetrahedron 1978, 35, 441.
40. London, R. E. J. Chem. Soc., Chem. Commun. 1978, 1070.
41. Blomberg, F.; Maurer, W.; Ruterjans, H. J. Am. Chem. Soc. 1977, 99, 8149.
42. Alei Jr., M.; Morgan, L. O.; Wageman, W. E.; Whaley, T. W. J. Am. Chem. Soc. 1980, 102, 2881.

43. Hansen, P. E.; Feeney, J.; Roberts, G. C. K. J. Magn. Reson. 1975, 17, 249.
44. Espersen, W. G.; Martin, R. B. J. Phys. Chem. 1976, 80, 741.
45. Martin, R. B. J. Phys. Chem. 1979, 83, 2404.
46. Khaled, M. A.; Long, M. M.; Thompson, W. D.; Bradley, R. J.; Brown, G. B.; Urry, D. W. Biochem. Biophys. Res. Commun. 1977, 76, 224.
47. Fossel, E. T.; Veatch, W. R.; Ovchinnikov, Y. A.; Blout, E. R. Biochemistry 1974, 13, 5264.
48. London, R. E.; Int. J. Peptide Protein Res. 1979, 14, 377.
49. Niccolai, N.; Miles, M. P.; Hehir, S. P.; Gibbons, W. A. J. Am. Chem. Soc. 1978, 100, 6528.
50. Ozawa, H.; Arata, Y.; Fujiwara, S. J. Chem. Phys. 1972, 57, 1613.
51. Briguet, A.; Duplan, J. C.; Erbeia, A. J. Phys. (Paris) 1971, 32, 23.
52. London, R. E.; Walker, T. E.; Kollman, V. H.; Matwiyoff, N. A. J. Magn. Reson. 1977, 26, 213.
53. Schaublin, S.; Hohener, A.; Ernst, R. R. J. Magn. Reson. 1974, 13, 196.
54. Freeman, R.; Hill, H. D.; Tomlinson, B. L.; Hall, L. D. J. Chem. Phys. 1974, 61, 4466.
55. Campbell, I. D.; Freeman, R. J. Magn. Reson. 1973, 11, 143.
56. Vold, R. L.; Vold, R. R. Progr. in NMR Spectrosc. 1978, 12, 79.
57. Hall, L. D.; Hill, H. D. W. J. Am. Chem. Soc. 1976, 98, 1269.
58. Jones, C. R.; Sikakana, C. T.; Hehir, S. P.; Gibbons, W. A. Biochem. Biophys. Res. Commun. 1978, 83, 1380.
59. Noack, F. in "NMR: Basic Principles and Progress" (Eds.: P. Diehl, E. Fluck, and R. Kosfeld, Springer-Verlag, New York, Vol. 3, 1971), pp. 83-144.
60. London, R. E. in "Magnetic Resonance in Biology" (Ed.: J. S. Cohen, Wiley-Interscience, 1980) pp. 1-69, and references therein.
61. Moreland, C. G.; Carroll, F. I. J. Magn. Reson. 1974, 15, 596.
62. London, R. E.; Matwiyoff, N. A.; Mueller, D. D. J. Chem. Phys. 1975, 63, 4442.
63. London, R. E.; Phillippi, M. A.; Stewart, J. M. Biochemistry (in press).
64. Canet, D.; Nery, H.; Brondeau, J. J. Chem. Phys. 70, 2098.
65. Nery, H.; Canet, D. J. Magn. Reson. 1981, 42, 370.
66. Pople, J. A. Mol. Phys. 1958, 1, 168.
67. Gutowsky, H. S.; McCall, D. W.; Slichter, C. P. J. Chem. Phys. 1953, 21, 279.
68. Moon, R. B.; Richards, J. H. J. Biol. Chem. 1973, 248, 7276; Burt, C. T.; Glonek, T.; Barany, M. J. Biol. Chem. 1976, 251, 2584; Ogawa, S.; Shulman, R. G.; Glynn, P.; Yamane, T.; Navon, G. Biochim. Biophys. Acta. 1978, 502, 45.

69. Neville, M. C.; Wyssbrod, H. R. Biophys. J. 1977, **17**, 259.
70. London, R. E.; Gregg, C. T.; Matwiyoff, N. A. Science 1975, **188**, 266.
71. Lindstrom, T. R.; Koenig, S. H. J. Magn. Reson. 1974, **15**, 344.
72. Sogn, J. A.; Craig, L. C.; Gibbons, W. A. J. Am. Chem. Soc. **96**, 3306.
73. Weinstein, S.; Wallace, B. A.; Morrow, J. S.; Veatch, W. R. J. Mol. Biol. 1980, **143**, 1.
74. Tancrede, P.; Deslauriers, R.; McGregor, W. H.; Ralston, E.; Sarantakis, D.; Somorjai, R. L.; Smith, I. C. P. Biochemistry 1978, **17**, 2905.
75. Jarrell, H. C.; Deslauriers, R.; McGregor, W. H.; Smith, I. C. P. Biochemistry 1980, **19**, 385.
76. Deslauriers, R.; Jarrell, H. C.; Griffith, D. W.; McGregor, W. H.; Smith, I. C. P. Int. J. Peptide Protein Res. 1980, **16**, 487.
77. Griffin, J. H.; Alazard, R.; DiBello, C.; Sala, E.; Mermet-Bouvier, R.; Cohen, P. FEBS Lett. 1975, **50**, 168.
78. Griffin, J. H.; DiBello, C.; Alazard, R.; Nicolas, P.; Cohen, P. Biochemistry 1977, **16**, 4194; Griffin, J. H.; DiBello, C.; Alazard, R.; Sala, E.; Cohen, P. in "Peptides: Chemistry, Structure and Biology", Proc. of 4th American Peptide Symposium, (Eds. R. Walter and J. Meienhofer, Ann Arbor Press, Ann Arbor, Mich. 1975) pp. 823-828.
79. Blumenstein, M.; Hruby, V. J.; Yamamoto, D.; Yang, Y. FEBS Lett. 1977, **81**, 347.
80. Hruby, V. J.; Yamamoto, D. M.; Yang, Y. C. S.; Blumenstein, M. in "Peptides": Proc. of the 5th American Peptide Symposium (Eds: M. Goodman and J. Meienhofer, Wiley, New York, 1977), pp. 179-182.
81. Blumenstein, M.; Hruby, V. J.; Viswanatha, V. Biochemistry 1979, **18**, 3552.
82. Convert, O.; Griffin, J. H.; DiBello, C.; Nicolas, P.; Cohen, P. Biochemistry 1977, **16**, 5062.
83. Deber, C. M.; Adawadkar, P. D.; Tom-Kun, J. in "Peptides": Proc. of the 5th American Peptide Symposium (Eds: M. Goodman and J. Meienhofer, Wiley, New York, 1977), pp. 357-360.
84. Veatch, W.; Weinstein, S.; Wallace, B. A.; Blout, E. R.; Morrow, J. in "Peptides: Structure and Biological Function"; Proceedings of the 6th American Peptide Symposium (Eds: E. Gross and J. Meienhofer, Pierce Chem. Co., Rockford, Ill. 1979) pp. 635-638.
85. Toma, R.; Fermanjian, S.; Low, M.; Kisfaludy, L. Biopolymers 1981, **20**, 901.
86. London, R. E.; Stewart, J. M.; Williams, R.; Cann, J. R.; Matwiyoff, N. A. J. Am. Chem. Soc. 1979, **101**, 2455.
87. Aue, W. P.; Bartholdi, E.; Ernst, R. R. J. Chem. Phys. 1976, **64**, 2229; Wokaun, A.; Ernst, R. R. Mol. Phys. 1978, **36**, 317.

88. Vega, S.; Shattuck, T. W.; Pines, A. Phys. Rev. Lett. 1976, 37, 43.
89. Warren, W. S.; Pines, A. J. Am. Chem. Soc. 1981, 103, 1613.
90. Niedermeyer, R.; Freeman, R.; J. Magn. Reson. 1978, 30, 617.
91. Bertrand, R. D.; Moniz, W. B.; Garroway, A. N.; Chingas, G. C. J. Magn. Reson. 1978, 32, 465.
92. Jakobsen, H. J.; Brey, W. S. J. Am. Chem. Soc. 1979, 101, 774.
93. Morris, G. A.; Freeman, R. J. Am. Chem. Soc. 1979, 101, 760.
94. Macura, S.; Ernst, R. R. Mol. Phys. 1980, 41, 95.
95. Hallenga, K.; Van Binst, G.; Scarso, A.; Michel, A.; Knappenberg, M.; Dremier, C.; Brison, J.; Dirx, J. FEBS Lett. 1980, 119, 47.
96. Sykes, B. D.; Weiner, J. H. in "Magnetic Resonance in Biology" (Ed: J. S. Cohen, Wiley-Interscience, New York, 1980), pp. 171-196.
97. Stimson, E. R.; Meinwald, Y. C.; Scheraga, H. A. Biochemistry, 1979, 18, 1661.

RECEIVED March 3, 1982.

# The Study of the Metabolism of $^{13}\text{C}$ Labeled Substrates by $^{13}\text{C}$ NMR Spectroscopy of Intact Cells, Tissues, and Organs

N. A. MATWIYOFF, R. E. LONDON, and J. Y. HUTSON

University of California, Los Alamos National Laboratory, Los Alamos, NM 87545

Carbon-13 nuclear magnetic resonance (nmr) spectroscopy, in conjunction with carbon-13 labeling, has become an important analytical technique for the study of biological systems and biologically important molecules. The growing list of its well established applications to isolated molecules in solution includes the investigation of: metabolic pathways; the microenvironments of ligands bound to proteins; the architecture and dynamics of macromolecules; the structures of coenzymes and other natural products; and the mechanisms of reactions. Recently interest has been reawakened in the use of the technique for the study of metabolic pathways and structural components in intact organelles, cells, and tissues. The promise and problems in the use of  $^{13}\text{C}$  nmr spectroscopy and  $^{13}\text{C}$  labeling in such investigations can be illustrated by the results of some early work on suspensions of the yeast, Candida utilis (1, 2).

Reproduced in Figure 1 is a set of  $^{13}\text{C}$  nmr spectra of a thick suspension of C. utilis cells to which  $[1-^{13}\text{C}]$  glucose had been added (1). These spectra show that, despite the high viscosity and heterogeneity of the suspension, the relaxation times of  $^{13}\text{C}$  are favorable enough to allow the time course to be traced for the anaerobic metabolism of the  $\alpha$  and  $\beta$  anomers of glucose ( $\cdot$ ) to the end product ethanol ( $\square$ ). In addition, the spectra revealed that an intermediate metabolite, later identified as trehalose (3), slowly accumulates and eventually is consumed. The  $^{13}\text{C}$  spectrum of the osmotically shocked C. utilis cells themselves shown in Figure 2b is also of remarkably high resolution, allowing the assignment of the major resonances to the fatty acid and choline residues of the lipids in the cell membranes and the glycoside residues of the cell wall (1). Later  $^{13}\text{C}$  relaxation time studies (2) of the membranes revealed a gradient of increased mobility from the glycerol backbone of the lipids toward the terminal methyl groups of the fatty acids and the choline head groups, and further that protein-lipid interactions make a negligible contribution to the mobility gradient.

0097-6156/82/0191-0157\$08.25/0

© 1982 American Chemical Society

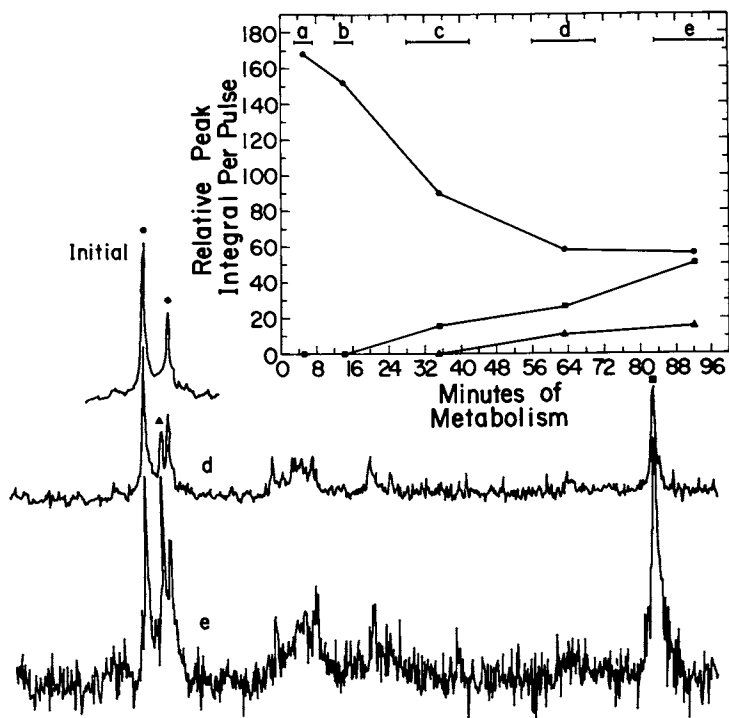


Figure 1. Proton noise decoupled, Fourier transform  $^{13}\text{C}$  NMR (25.2 MHz) spectra obtained during metabolism of the  $\beta$ - and  $\alpha$ -anomers of  $[1\text{-}^{13}\text{C}]$  glucose (●) to  $[2\text{-}^{13}\text{C}]$  ethanol (■) with the intermediate formation of  $[1,1'\text{-}^{13}\text{C}]$  trehalose (▲) by a suspension of *C. utilis* cells; and plots of the relative intensities of the labeled glucose, ethanol, and trehalose resonances as a function of time: a, 500 pulses, 3–7 min after initiation of metabolism; b, 500 pulses, 12–16 min; c, 1500 pulses, 28–42 min; d, 1500 pulses, 56–70 min; and e, 1500 pulses, 83–99 min. Spectra obtained during the initial time period exhibited only the resonances (●) corresponding to C-1 of the  $\beta$ - and  $\alpha$ -anomers of the substrate  $[1\text{-}^{13}\text{C}]$  glucose. Spectra obtained in the time periods d and e exhibited prominent resonances corresponding to C-1 of trehalose (▲) and C-2 of ethanol (■) together with natural abundance signals of glucose and *C. utilis* cells, and  $^{13}\text{C}$  enriched resonances of transient intermediates. Due to the low sensitivity, these could not be identified unequivocally.

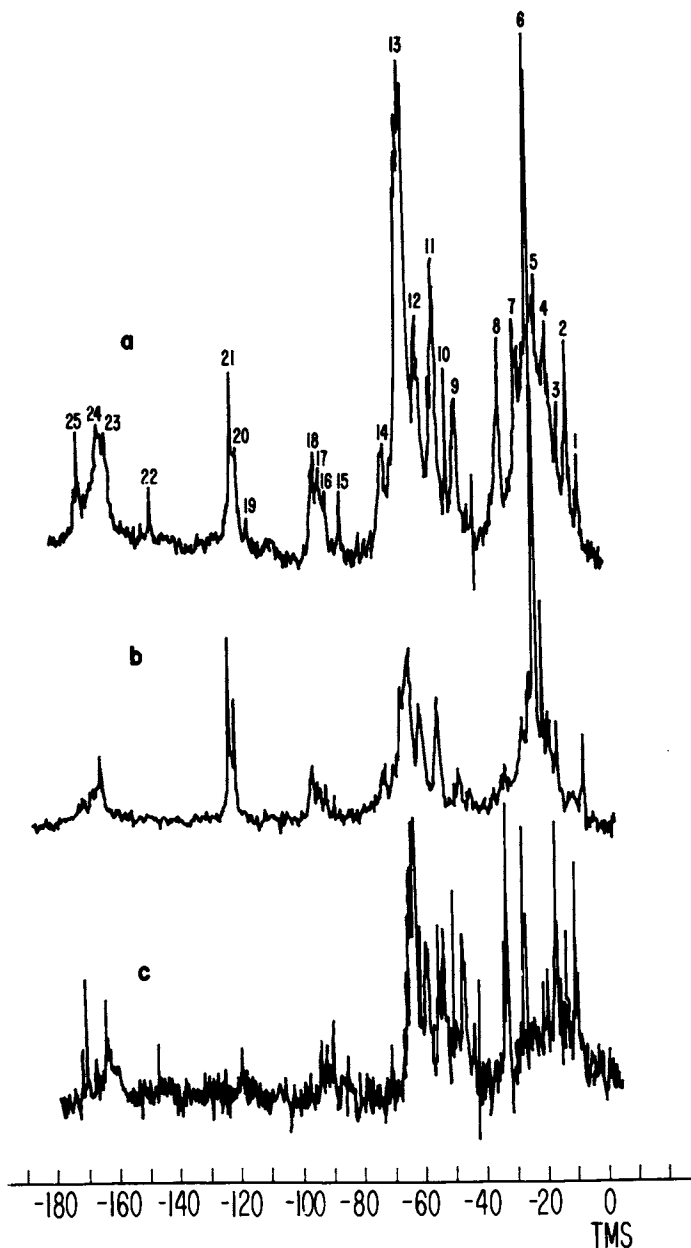


Figure 2. Proton noise decoupled Fourier transform  $^{13}\text{C}$  NMR (25.2 MHz) spectra of *C. utilis* cells enriched to the 20 atom % level with  $[1,2-^{13}\text{C}_2$  (20 atom %)] acetate: a, Cells suspended in  $\text{D}_2\text{O}$ , 995 pulses; b, Cellular components remaining after exhaustive extraction with  $\text{D}_2\text{O}$ , 10,000 pulses; and c, Water-soluble components released by the osmotic shock of b, 1082 pulses.

Despite the promise of the technique as revealed by these early studies, relatively little work on intact systems was done until quite recently. Figure 3, taken from a  $^{13}\text{C}$  nmr study (4) of in situ gluconeogenesis by mouse liver using  $[3-^{13}\text{C}]$  alanine as a substrate dramatically illustrates the progress now being made in this area. Progress has been equally rapid in the development of  $^{31}\text{P}$  nmr spectroscopy of intact biological systems, including man; but that topic has been the subject of a number of recent reviews (5-9) and will not be covered here.

### Methodology

The utility of  $^{13}\text{C}$  labeled substrates and  $^{13}\text{C}$  nmr spectroscopy for the non-destructive in situ analysis of metabolic pathways in intact cells, tissues, and organs, depends on the following considerations:

- (a) The natural background of  $^{13}\text{C}$  is low, 1.1 atom %, and is relatively constant in biological systems;
- (b) The  $^{13}\text{C}$  chemical shift dispersion is so large that each  $^{13}\text{C}$  atom at a distinct chemical site gives rise to a separate  $^{13}\text{C}$  resonance whose intensity is proportional to concentration at the site.
- (c) Favorable  $^{13}\text{C}$  relaxation times result in  $^{13}\text{C}$  spectra of cells and tissues having a high degree of resolution even for many protonated carbon atoms of macromolecules in viscous environments.
- (d) An increasing variety of specifically, selectively, and uniformly labeled  $^{13}\text{C}$  substrates in large quantities has become available in recent years.

Each of these considerations has been discussed in detail in a variety of reviews (10-16) and those discussions will not be repeated here. Instead, we should like to focus attention on two important but not generally appreciated, limitations on the methodology of evaluating the population of  $^{13}\text{C}$  at a particular site using the relative intensities of singlet to multiplet  $^{13}\text{C}$  resonances of multiply labeled  $^{13}\text{C}$  molecules which are usually encountered in metabolic studies. These limitations arise from: the non-statistical distribution of  $^{13}\text{C}$  labels that can result from the operation of certain metabolic pathways in biological systems and from "special" relaxation effects that can complicate intensity/population relationships in multiply labeled molecules. We stress this subject because as the following discussion will illustrate, the proper treatment of these relative intensities can provide information about metabolic pathways unobtainable with any other method.

Distribution of  $^{13}\text{C}$  in Multiply Labeled Compounds. To illustrate the effects of the non-statistical distribution of  $^{13}\text{C}$



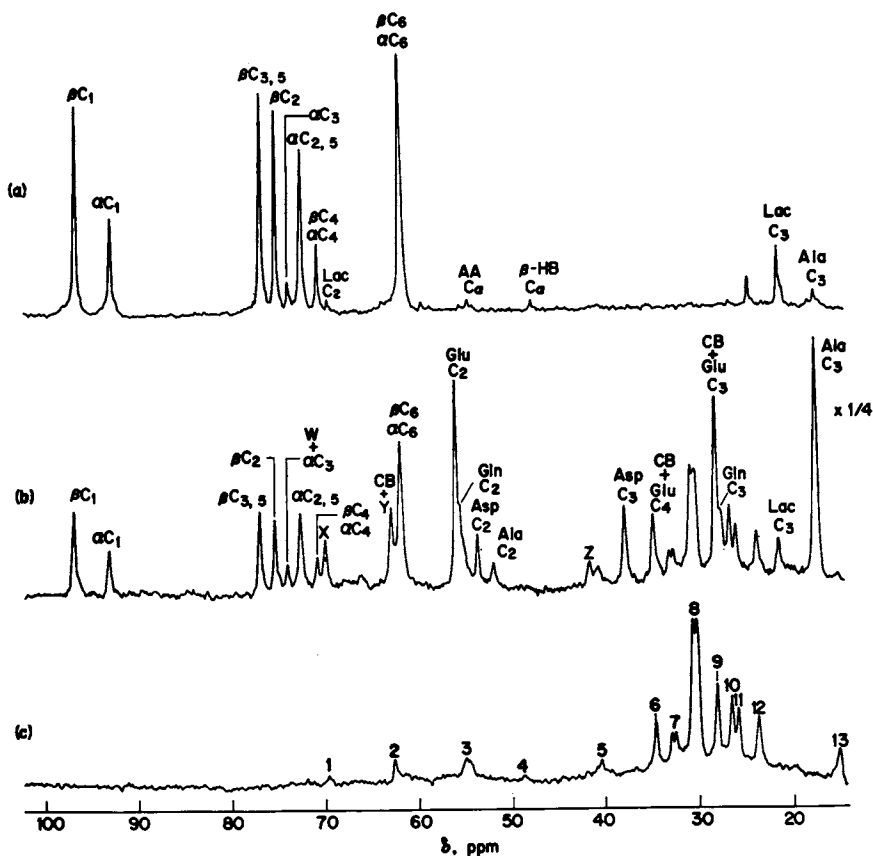


Figure 3.  $^{13}\text{C}$  NMR spectra from a perfused mouse liver at  $35^\circ\text{C}$ . c,  $^{13}\text{C}$  natural abundance background of this liver, accumulated before the substrate was added. The substrate, 8 mM  $[3\text{-}^{13}\text{C}]$  alanine and 20 mM unlabeled ethanol, was then added at 0 min and again at 120 min, and a series of  $^{13}\text{C}$  NMR spectra were taken. b, Spectrum measured during the period 150–180 min. a,  $^{13}\text{C}$  NMR spectrum of the perfusate after the perfusion was terminated, at 240 min; this spectrum consisted of 5000 scans. The pulse repetition times were 0.5 s for b and c and 2 s for a. The abbreviations used include:  $\beta\text{C}_1$ ,  $\alpha\text{C}_1$ ,  $\beta\text{C}_{3,5}$ ,  $\beta\text{C}_2$ ,  $\alpha\text{C}_3$ ,  $\alpha\text{C}_{2,5}$ ,  $\alpha\text{C}_1$ ,  $\beta\text{C}_6$ , and  $\alpha\text{C}_6$ , the carbons of glucose anomers; Glu C<sub>2</sub>, glutamate C2; Gln C<sub>3</sub>, glutamine C2; Asp C<sub>3</sub>, aspartate C2; Ala C<sub>2</sub>, alanine C2; Lac C<sub>3</sub>, lactate C3, cell background peak; w, x, y, and z, unknowns; AA C<sub>α</sub>, acetoacetate CH<sub>2</sub>; and β-HB C<sub>α</sub>, β-hydroxybutyrate CH<sub>2</sub>. (Reproduced, with permission, from Ref. 4.)

labels on the  $^{13}\text{C}$  nmr spectra of biological systems, we discuss in the following some work we have done recently on the biosynthesis of selectively labeled L-glutamic acid using the microorganism, *M. ammoniaphilum*, grown in media containing  $[1-^{13}\text{C}]$  glucose or  $[1-^{13}\text{C}]$  acetate as the predominant carbon source (17). The major metabolic pathways used by this bacterium to process these substrates are summarized in Figure 4. The organism accumulates L-glutamate because its Krebs cycle is partially blocked at the  $\alpha$ -ketoglutarate dehydrogenase step.

The processing of  $[1-^{13}\text{C}$  (70 atom %)] acetate is simplest and results in a  $[1,5-^{13}\text{C}_2]$  glutamate product whose  $^{13}\text{C}$  nmr spectrum (Figure 5) can be interpreted in a straightforward manner. The fractional populations of  $^{13}\text{C}$  at C-5 (70 atom %) and C-1 (35 atom %) derived from the intensities of the C-5 and C-1 resonance or from the ratio of the doublet: singlet intensities of the C-4 and C-2 resonances, suggest that  $[1-^{13}\text{C}]$  acetate is the dominant contributor to the acetate pool and that there is significant activity of the Krebs cycle when acetate is the predominant carbon source. The processing of  $[1-^{13}\text{C}$  (90 atom %)] glucose is more complicated. The  $^1\text{H}$  nmr spectrum, [Figure 6(a)] of L- $[1,2,3,4-^{13}\text{C}_4]$  glutamate derived from *M. ammoniaphilum* grown on  $[1-^{13}\text{C}]$  glucose clearly demonstrates a high degree of enrichment at C-2 (34 atom %), C-4 (39 atom %), and C-3 (14 atom %). Nonetheless, this high level of enrichment is not reflected in the  $^{13}\text{C}$ - $^{13}\text{C}$  multiplets of the  $^{13}\text{C}$  nmr spectrum [Figure 6(b)] of the glutamate. The apparent discrepancy arises from the presence of  $^{13}\text{C}$  isotope isomers (isotopomers; e.g.  $^{13}\text{C}_4$   $^{12}\text{C}_3$   $^{-13}\text{C}_2$  and  $^{12}\text{C}_4$   $^{13}\text{C}_3$   $^{13}\text{C}_2$ ) in which there is a high degree of negative correlation in the  $^{13}\text{C}$  labeling which does not affect the proton spectrum but which has a major influence on the appearance of  $^{13}\text{C}$  multiplets.

This problem is a general one. The  $^{13}\text{C}$  nmr spectrum of a multiply labeled metabolite or biosynthesized product is a superposition of subspectra corresponding to isotopomers consistent with the biosynthetic pathways involved. If the product contains  $n$  carbon atoms, there will be  $2^n$  isotopomers possible, with  $2^n - 1$  contributing to the  $^{13}\text{C}$  nmr spectrum. As illustrated above, a detailed analysis of the flux of  $^{13}\text{C}$  through the system cannot always be done using the  $^{13}\text{C}$  spectrum alone but frequently requires  $^1\text{H}$  nmr and mass spectrometric data as well. In the analysis of such data, one of several approaches can be taken.

In the most general, a variable can be assigned to each possible isotopomer in the mixture,  $p_i$ , with a normalization condition:

$$\sum_i p_i = 1$$

Determination of all of the  $2^n$  possible  $p_i$  values provides all of the information which can be obtained from the experiment. This can clearly represent a formidable task since, for example, a five carbon metabolite has 32 possible isotopomers. In some cases,

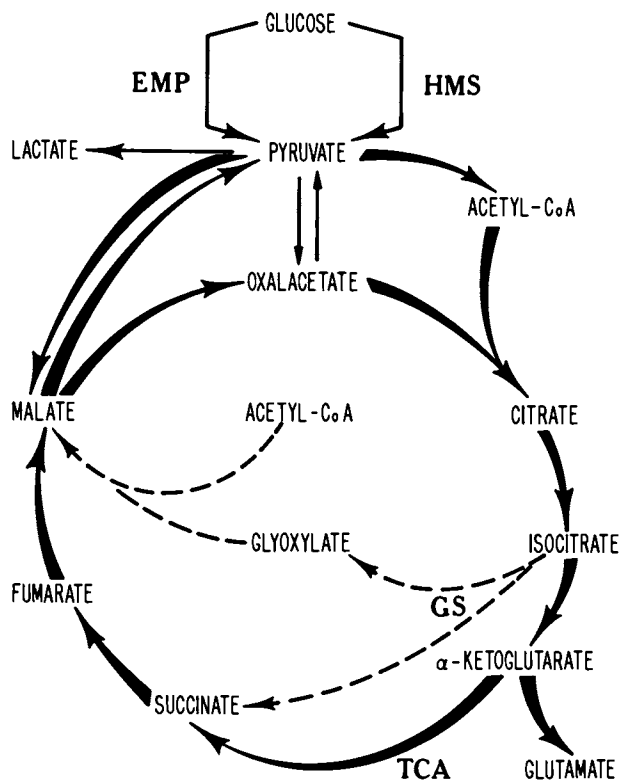


**Figure 4a.** Major metabolic pathways in *M. ammoniophilum* involving glucose, acetate, and glutamate. Glucose labeled at C-1 produces  $[3-^{13}\text{C}]$  pyruvate via the Embden-Meyerhof pathway (EMP) and unlabeled pyruvate via the hexose monophosphate shunt (HMS).  $[3-^{13}\text{C}]$  pyruvate enters the tricarboxylic acid (TCA) and glyoxylate shunt (GS) cycles as  $[3-^{13}\text{C}]$  oxaloacetate and/or  $[2-^{13}\text{C}]$  acetate and can result in the formation of  $[2-^{13}\text{C}]$  glutamate,  $[4-^{13}\text{C}]$  glutamate, and  $[2,4-^{13}\text{C}]$  glutamate via  $\alpha$ -ketoglutarate formed in 1/3 of a turn of the TCA cycle. Formation of glutamate after one or more turns of the TCA cycle will tend to randomize the label because of the formation of the symmetrical intermediates succinate and fumarate.

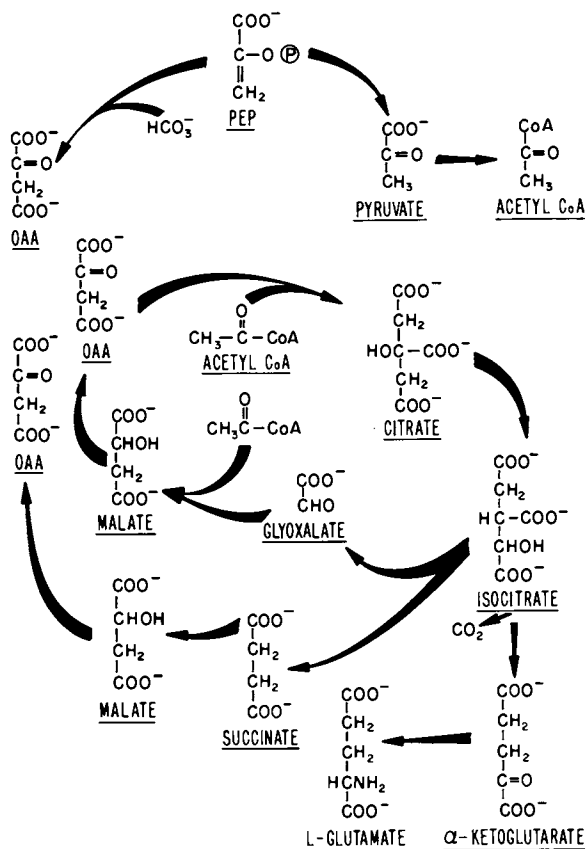
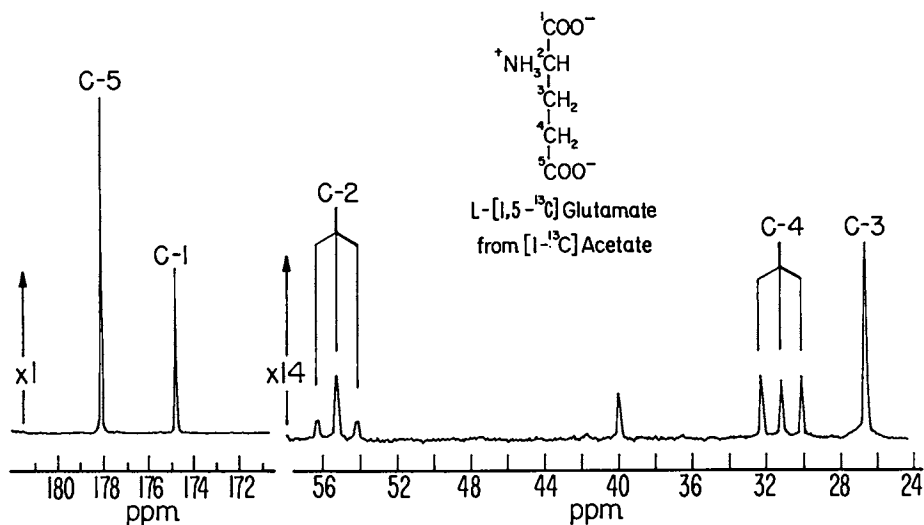


Figure 4b. Structure of the major intermediates involved in the metabolic pathways outlined in Figure 4a.



**Figure 5.** Proton decoupled  $^{13}\text{C}$  NMR (25.2 MHz) spectrum of [ $1,5\text{-}^{13}\text{C}_2$ ] glutamate obtained from *M. ammoniaphilum* grown on [ $^{13}\text{C}$  (70 atom %)] acetate. The cells were grown on natural abundance glucose for 24 h and then transferred to the medium containing [ $^{13}\text{C}$ ] acetate and cultured for an additional 96 h. Only C-1 and C-5 are labeled. From the multiplet to singlet intensities of C-4, the  $^{13}\text{C}$  enrichment at C-5 is calculated to be 70 atom %. From the corresponding intensities for the C-2 resonance, the  $^{13}\text{C}$  enrichment at C-1 is calculated to be 35 atom %. C-5 is labeled in 1/3 of a turn of the Krebs cycle by the initial condensation of [ $^{13}\text{C}$ ] acetyl CoA with oxaloacetate. Labeling of C-1 at half the level of C-5 occurs via the symmetrical intermediate succinate formed in one or more turns of the Krebs cycle.

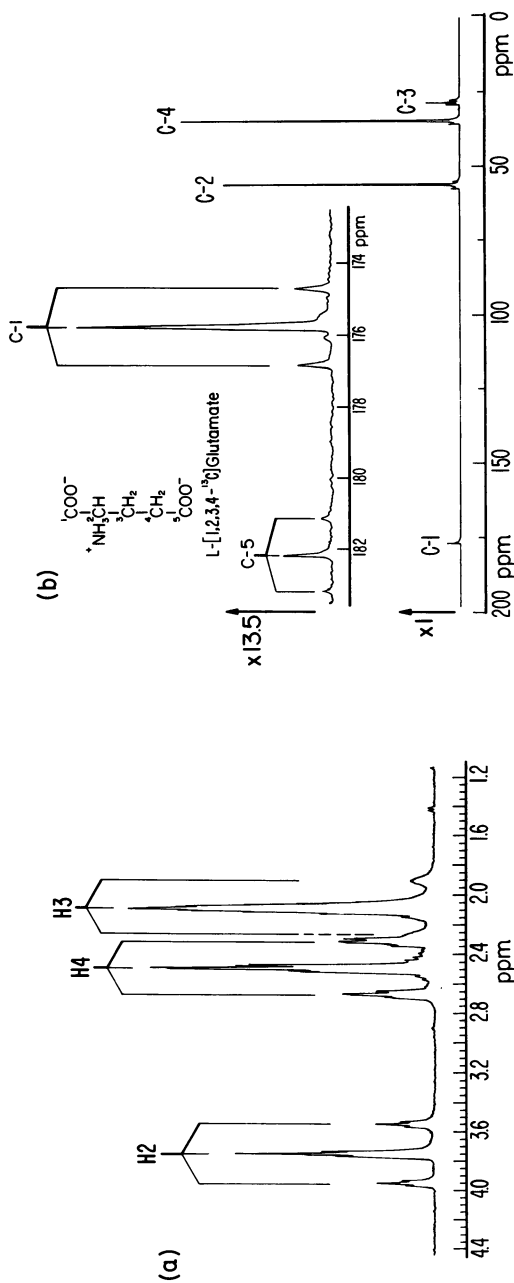


Figure 6. a, Proton NMR spectrum (360 MHz) of  $[1,2,3,4-^{13}\text{C}_4]$  glutamate derived from M. ammoniaphilum grown on  $[1-^{13}\text{C}$  (90 atom %)] glucose. For each proton, the center of the multiplet arises from  $^{12}\text{C}$ -H moieties with fine structure caused by H-H scalar interactions. The doublets with similar fine structure are due to the  $^{13}\text{C}$ -H splitting from moieties containing the  $^{13}\text{C}$  label. The  $^{13}\text{C}$  populations calculated from the ratio of the doublet to the singlet intensities are: C-2, 34%; C-4, 39%; and C-3, 14%. b, Proton decoupled  $^{13}\text{C}$  NMR spectrum (25.2 MHz) of  $[1,2,3,4-^{13}\text{C}_4]$  glutamate derived from M. ammoniaphilum grown on  $[1-^{13}\text{C}$  (90 atom %)] glucose. The spectrum illustrates the nonrandom distribution of the  $^{13}\text{C}$  label among the C-2, C-3, and C-4 sites. If the label were distributed randomly with the  $^{13}\text{C}$  abundances derived from the spectra in Figure 5 then, for example, the C-1 and C-2 signals should consist of approximate 1:2:1 multiplets.

particular carbons are not labeled and a more tractable subset of possibilities can be treated. Success of this approach is dependent on the size of the molecule, the degree of degeneracy of the chemical shifts and coupling constants, and on the mass fragmentation pattern. The primary advantage of this approach is that it requires no assumptions about the pathways or the nature of the labeling, but at the same time, a determination of all possible  $p_i$  values does not immediately provide information on the biosynthetic pathways, so that subsequent additional analysis is required to obtain meaningful biochemical conclusions.

A second approach, conceptually the simplest, is to treat the data in terms of a mixture problem (18). Specifically, the relevant biosynthetic pathways can be identified and assigned variables  $x_i$ , with the normalization condition

$$\sum_i x_i = 1$$

Based on knowledge of the biochemical transformations involved, the product labeling pattern can be determined from the known labeling of the precursor. An additional set of variables representing the labeling probabilities,  $\alpha_i$ , which may be different for the different carbons is thus introduced. A table describing the different pathways and labeling probabilities can then be constructed. From this table, the intensities and satellite probabilities of the mixture as a function of the variables  $x_i$  and  $\alpha_i$  can be determined by a fit of the model to the observed spectral parameters. We illustrate this approach in the following for the previous example of the biosynthesis of <sup>13</sup>C labeled L-glutamate from [1-<sup>13</sup>C] glucose.

Inspection of the major metabolic transformations (Figure 4) involved in the flux of carbon from glucose to glutamate indicates that [2-<sup>13</sup>C] acetate (as acetyl CoA derived from decarboxylation of [3-<sup>13</sup>C] pyruvate) will always be the immediate precursor for labeling C-4 of glutamate, even if cycling occurs via the glyoxylate shunt or the Krebs cycle. If we assume that all acetate is produced predominately via decarboxylation of pyruvate, then the relative contributions to the triose (pyruvate) pool of the Embden Meyerhoff (EM) pathway and the hexose monophosphate shunts can be evaluated from the <sup>13</sup>C enrichment at C-4 of glutamate--39 atom % derived from the <sup>1</sup>H nmr spectrum [Figure 6(a)]. Then letting  $\alpha_i$  represent the initial [1-<sup>13</sup>C (90 atom %)] glucose labeling, the fractional contribution of the EMP pathway can be related to the observed enrichment  $\alpha_0$

$$f \cdot \left( \frac{\alpha_1}{2} \right) + (1-f) \cdot 0 = \alpha_0$$

where the factor of 1/2 arises as a result of the formation of two triose molecules from a single [1-<sup>13</sup>C] glucose precursor, and the zero reflects loss of the label in the HMP shunt. The result of

87% activity for the EMP is consistent with analysis of pyruvate  $^{14}\text{C}$  enrichments in metabolically blocked cells (19).

Quantitation of the glyoxylate and Krebs cycle activities can be approached as above using a mixture analysis, although the case is somewhat more complex. Table I summarizes the important labeling pathways and the labeling patterns which result. As indicated in the table, several compromises have been made in the analysis since in some cases different labeling paths can result in identical labeling patterns and thus cannot be distinguished. In addition, a small quantity of the labeling patterns indicated under w and y can also be produced after additional turns of the Krebs and glyoxylate cycles. Nevertheless, the approach summarized represents a reasonable approximation for quantitative pathway analysis. Since spectral inspection [Figure 6(b)] indicates that the number of multiply enriched molecules (z) is small, these approximations are probably fairly good. As can be seen from the table, negative correlations of the labeling of C-2 and C-3 can result from the Krebs or glyoxylate cycle, or from back reactions which reach fumarase. Krebs cycle activity will also result in a negative correlation between C-1 and C-2 labeling. Analytical expressions for carbon labeling probabilities and relative multiplet probabilities can be derived in a straightforward manner and the results are summarized in Table II. Using these expressions and the value of  $\alpha_0$  (0.39) and the relative multiplet intensities in the  $^{13}\text{C}$  spectrum [Figure 6(b)], values of 58%, 26%, 10%, and 6% are obtained for x, y, z, and w, respectively. The relative contribution of these pathways should result in  $^{13}\text{C}$  populations at C-2 and C-3 of 33% and 10%, respectively, in good agreement with those obtained directly from the  $^1\text{H}$  nmr spectrum [Figure 6(a)]. Thus, the major metabolic routes involve the glycolytic degradation of glucose to pyruvate and phosphoenol-pyruvate, formation of acetyl CoA and oxalacetate via decarboxylation and carboxylation, respectively, and the first third of the Krebs cycle to yield  $\alpha$ -ketoglutarate and subsequently glutamate. Significant activity of the glyoxylate shunt is required to explain the C-3 labeling and reduced C-2 labeling of glutamate. The observed Krebs cycle activity was initially unexpected since this cycle is presumably shut down due to the reduction of  $\alpha$ -ketoglutarate dehydrogenase activity (19). Evidence for the activity of this cycle comes primarily from the observed negative correlation in the labeling of C-1 and C-2 of glutamate.

A somewhat different approach for the study of metabolic pathways involving mixtures of statistically enriched and unlabeled precursors has been proposed by Gagnaire and Taravel (20, 21). In this method, the variable of interest,  $P_{ij}$ , is defined as the joint probability of two adjacent carbon atoms in a product being derived from the same precursor molecule. If  $\alpha$  is the enrichment of the randomly labeled precursor,  $\beta$  the natural abundance  $^{13}\text{C}$  probability and  $f$  is the fraction of the enriched precursor incorporated into the product, then the observed probability of the  $i$ - $^{13}\text{C}$  having



Table I. Possible Labeling Patterns for [<sup>13</sup>C] Glutamate Derived from [1-<sup>13</sup>C] Glucose

Pathway Designation	Labeling Pattern	Source of Label
x	<sup>0</sup> C <sub>1</sub> - <sup>*</sup> C <sub>2</sub> -C <sub>3</sub> - <sup>*</sup> C <sub>4</sub>	Phosphoenolpyruvate carboxylase +1/3 turn of Krebs cycle
y	C <sub>1</sub> - <sup>*</sup> C <sub>2</sub> - <sup>*</sup> C <sub>3</sub> - <sup>*</sup> C <sub>4</sub> C <sub>1</sub> -C <sub>2</sub> - <sup>*</sup> C <sub>3</sub> - <sup>*</sup> C <sub>4</sub>	Fumarase activity plus single turn of glyoxylate cycle
z	<sup>*</sup> C <sub>1</sub> - <sup>*</sup> C <sub>2</sub> - <sup>*</sup> C <sub>3</sub> - <sup>*</sup> C <sub>4</sub>	Multiple turns of Krebs or or glyoxylate cycles
w	<sup>*</sup> C <sub>1</sub> -C <sub>2</sub> - <sup>*</sup> C <sub>3</sub> - <sup>*</sup> C <sub>4</sub> C <sub>1</sub> - <sup>*</sup> C <sub>2</sub> -C <sub>3</sub> - <sup>*</sup> C <sub>4</sub>	Single turn of Krebs cycle

(a) \* indicates a labeling probability  $\alpha$  derived from the enrichment of the acetyl CoA. <sup>0</sup> indicates a labeling probability  $\beta$  derived from the enrichment of the bicarbonate pool.

Table II. Glutamate Labeling and Multiplet Probabilities

I: Probability of <sup>13</sup>C Enrichment

$$\begin{aligned} \text{C-1} & \quad x\beta + (z + w/2) \cdot \alpha \\ \text{C-2} & \quad (x + y/2 + z + w/2) \cdot \alpha \\ \text{C-3} & \quad (y/2 + z + w/2) \cdot \alpha \\ \text{C-4} & \quad (x + y + z + w) \cdot \alpha = \alpha = \alpha_0 \end{aligned}$$

II: Relative <sup>13</sup>C-<sup>13</sup>C Multiplet Intensities

$$\begin{aligned} \text{C-1 (doublet/singlet)} & \quad : (x\alpha + z\alpha^2) / [(x\beta(1-\alpha) + z\alpha(1-\alpha) + \alpha w/2)] \\ \text{C-2}^{\text{a}} \text{ (doublet/singlet)} & \quad : [\alpha\beta + 2z\alpha^2(1-\alpha)] / [x\alpha(1-\beta) + \alpha(y+w)/2 + z\alpha(1-\alpha)^2] \\ \text{C-2}^{\text{b}} \text{ (quartet/singlet)} & \quad : z\alpha^3 / [x\alpha(1-\beta) + \alpha(y+w)/2 + z\alpha(1-\alpha)^2] \\ \text{C-3 (doublet/singlet)} & \quad : [2z\alpha^2(1-\alpha) + \alpha^2(y+w)/2] / [\alpha(1-\alpha)(y+w)/2 + z\alpha(1-\alpha)^2] \\ \text{C-4 (triplet/singlet)} & \quad : z\alpha^3 / [\alpha(1-\alpha)(w+y)/2 + z\alpha(1-\alpha)^2] \\ \text{C-4 (doublet/singlet)} & \quad : [z + (y+w)/2]\alpha^2 / [x\alpha + z\alpha(1-\alpha) + \alpha(1-\alpha/2)(y+w)] \end{aligned}$$

<sup>a</sup> Calculation represents the total doublet intensity although two separate doublets are resolvable due to different <sup>1</sup>J<sub>12</sub> and <sup>1</sup>J<sub>23</sub>.

<sup>b</sup> Quartet since <sup>1</sup>J<sub>12</sub> → <sup>1</sup>J<sub>23</sub>.

a  $j$ - $^{13}\text{C}$  as a neighbor,  $x_{ij}$ , will be given by

$$X_{ij} = P_{ij} \cdot \frac{f \alpha^2 + (1-f) \beta^2 - T^2}{T} + T$$

$T$  represents the fraction of labeling of carbons  $i$  and  $j$  with  $^{13}\text{C}$  and is assumed equal for both carbon atoms--a fairly restrictive assumption. For the cases where the natural 1 atom % abundance enrichment can be neglected the equation reduces to

$$X_{ij} \cong P_{ij} \alpha(1-f) + \alpha f$$

Gagnaire and Taravel (21) used this technique to study the synthesis of cellulose by Acetobacter xylinum from a 50:50 mixture of natural D-glucose and statistically enriched D-[ $^{13}\text{C}_6$  (87 atom %)] glucose. From an evaluation of the multiplet patterns in the  $^{13}\text{C}$  nmr spectra of derivatized monomers obtained from the enriched cellulose, the following joint probabilities were obtained:  $P_{1,2} = 0.89$ ,  $P_{2,3} = 0.6$ ,  $P_{3,4} = 0.25$ ,  $P_{4,5} = 0.95$  and  $P_{5,6} = 0.93$ . The high  $P_{4,5}$  and  $P_{5,6}$  values suggest that carbon atoms 4 and 5 and 5 and 6 are derived from a single precursor unit (e.g. glucose and/or pyruvate) whereas the low  $P_{3,4}$  value suggest that carbon atoms 3 and 4 have a high probability of being derived from different precursor units (e.g. a labeled and an unlabeled pyruvate via resynthesis of glucose). A detailed analysis of these joint probabilities in terms of the major biosynthetic pathways, allowed the following conclusions to be drawn: 23% of the glucose molecules in cellulose come from an unmodified molecule of glucose; 26% have been involved at least once in the hexose monophosphate shunt, and 10% at least twice; 30% of the glucose molecules come from triose recombination.

Relaxation Effects. As discussed in the foregoing, quantitation of the  $^{13}\text{C}$  population at specific sites in multiply labeled molecules requires the accurate evaluation of the ratios of singlet to multiplet intensities in both  $^1\text{H}$  and  $^{13}\text{C}$  nmr spectra. This is usually a straightforward task but it must be recognized that the satellite resonances can exhibit different  $T_1$  and/or NOE values than the center resonance. The differential  $T_1$  effect in  $^1\text{H}$  nmr spectra, can be quite significant. For example, a center band ( $^{12}\text{C-H}$ )/satellite ( $^{13}\text{C-H}$ )  $^1\text{H}$   $T_1$  ratio greater than 4 has been observed for a  $^{13}\text{C}$  enriched sugar methine proton (22). In such cases, the pulse delay must be sufficiently long that the center band is not overpulsed. A similar, but smaller, effect occurs in the  $^{13}\text{C}$  nmr spectra of enriched molecules. Although the  $^{13}\text{C}$ - $^{13}\text{C}$  dipolar interaction is negligible relative to the  $^{13}\text{C}$ -H dipolar interaction for proton bearing carbon atoms (23), the former interaction can be large for quaternary carbons and lead to significant differences in the satellite ( $^{13}\text{C}$ - $^{13}\text{C}$ ) and center band ( $^{13}\text{C}$ - $^{12}\text{C}$ )

$T_1$  values. Again if the pulse delay is not long enough, the intensity of the center band will be underestimated due to overpulsing. Another related potential source of error in the analysis of  $^{13}\text{C}$  multiplet intensities of quaternary carbon atoms is a reduction in the NOE due to  $^{13}\text{C}$ - $^{13}\text{C}$  dipolar interactions and which leads to a reduction in the satellite ( $^{13}\text{C}$ - $^{13}\text{C}$ )/center band ( $^{13}\text{C}$ - $^{12}\text{C}$ ) intensity ratio. A more general discussion of these phenomena and their theoretical basis appears elsewhere in this volume.

Another potential source of error in these measurements derives from the use by some workers of 10%  $\text{D}_2\text{O}$  as an internal lock. There are numerous metabolic pathways in biological systems which are accompanied by hydrogen exchange and hydrogen transfer. Thus, if certain metabolites become deuterated, their concentrations could be underestimated somewhat, because of undetected  $^{13}\text{C}$ -D coupling and/or loss of the NOE. Alternatively, in truly high resolution studies, the effect might be of some utility in defining metabolic pathways (24).

### Applications

Metabolic Studies. Summaries of the use of  $^{13}\text{C}$  labeled substrates and  $^{13}\text{C}$  nmr spectroscopy to study metabolism in suspensions of intact microorganisms and mammalian cells appear in Table III. Similar studies of intact organs are summarized in Table IV. These investigations address a number of interesting and important questions in metabolism but space will allow only a brief discussion of some illustrative examples. In the study of Deslaurier *et al.* (32) on the degradation of  $^{13}\text{C}$  labeled enkephalin and enkephalinamide by neuroblastoma X glioma hybrids, the intent was to analyze the conformation of those neuro-active peptides when bound to the opiate receptors of the cells. Instead, and despite reports of successful studies of the binding of enkephalins to neuroblastoma X glioma cells using other techniques, the  $^{13}\text{C}$  nmr studies of [3[2- $^{13}\text{C}$ ] glycine] methionine-enkephalinamide showed unequivocally that the peptide is extensively degraded to a number of metabolites including free glycine and peptides containing the [2- $^{13}\text{C}$ ] glycine in an N-terminal, a C-terminal and in a non-terminal position. The authors concluded that  $^{13}\text{C}$  nmr studies of opioid peptide-receptor interactions will require the use of metabolically stable analogs.

The study of Ogino *et al.* (30) on the metabolic regulations and pyruvate transport in anaerobic *E. coli* cells is of special interest because the [1- $^{13}\text{C}$ ] glucose metabolites were detected by proton correlation spectroscopy; and only signals from extracellular metabolites which had diffused through the cell membrane and accumulated in the medium were observed (acetate, lactate, ethanol, succinate, and pyruvate). This allowed the evaluation of perturbations to the cell on the influx and egress of pyruvate. In particular, a pulsed decrease in the pH of the external medium resulted in a transient rapid efflux from the cell of pyruvate

Table III.  $^{13}\text{C}$  Nuclear Magnetic Resonance Studies of Metabolism in Intact Cells and Tissues

System	$^{13}\text{C}$ Labeled Substrate	Observations	Ref.
Anacystis nidulans, Blue Green Alga	$^{13}\text{CO}_2$	Mixture analysis applied to $^{13}\text{C}$ - $^{13}\text{C}$ coupling patterns in extracts to show that significant respiration contributes to the $\text{CO}_2$ pool available for the synthesis of galactosyl glycerol.	18
Escherichia coli, bacterium; saccharomyces cerevisiae, yeast	[1- $^{13}\text{C}$ ] glucose and [6- $^{13}\text{C}$ ] glucose	Different rates for $\alpha$ and $\beta$ -glucose translocation; flux of carbon through most glycolysis intermediates to end products evaluated; $\alpha$ - and $\beta$ -fructose biphosphates are in anameric equilibrium; in yeast, but not in bacterium, aldolose-triose phosphate isomerase triangle is near equilibrium.	25,26
Rhodopseudomonas spheroides; propionibacterium shermanii	[5- $^{13}\text{C}$ ] aminolevulinic acid (ALA) [11- $^{13}\text{C}$ ] porphobilinogen (PBG)	Direct demonstration of porphyrinogen intermediates in porphyrin biosynthesis.	27
Rat hepatocytes, euthyroid and hyperthyroid	[2- $^{13}\text{C}$ ] glycerol, [1,3- $^{13}\text{C}_2$ ] glycerol and [3- $^{13}\text{C}$ ] alanine	Gluconeogenesis from alanine and glycerol; hyperthyroid rat cells show an increased activity of mitochondrial glycerol phosphate dehydrogenase resulting in enhanced gluconeogenesis. Mixture analysis applied to $^{13}\text{C}$ - $^{13}\text{C}$ coupling patterns in glucose from [1,3- $^{13}\text{C}_2$ ] glycerol to evaluate amount of triose from unlabeled fructose incorporated into glucose.	28,29

Table III (contd.)

System	$^{13}\text{C}$ Labeled Substrate	Observations	Ref.
Escherichia coli	[1- $^{13}\text{C}$ ] glucose	Uptake and efflux of pyruvate affected by pH of medium and will occur against osmotic gradient. Proton conductive uncouplers inhibit pyruvate uptake.	30
Erythrocytes	[1- $^{13}\text{C}$ ] glucose	Label from glucose incorporated into diposphoglycerate and lactate.	31
Neuroblastoma x glioma	[3[2- $^{13}\text{C}$ ]-Glycine] methionine-enkephalinamide	Cells degrade enkephalinamide to a mixture of peptides and free glycine.	32
Propionibacterium Shermanii; penicillium urticae	[3- $^{13}\text{C}$ ] propionate and [2- $^{13}\text{C}$ ] acetate	Methylmalonyl pathway in P. Shermanii rapidly equilibrates [3- $^{13}\text{C}$ ] propionate into [2,3- $^{13}\text{C}_2$ ] propionate and [2,2- $^{13}\text{C}_2$ ] succinate; P. urticae metabolizes [2- $^{13}\text{C}$ ] acetate to [4,6,7- $^{13}\text{C}_3$ ] gentis-alcohol and [1,5,7- $^{13}\text{C}$ ] patulin.	33
Pseudomonas putida; and in vivo cross-linked enzyme complexes	[ $\alpha$ - $^{13}\text{C}$ ] mandelate	[ $\alpha$ - $^{13}\text{C}$ ] mandelate is metabolized to [ $\alpha$ - $^{13}\text{C}$ ] benzaldehyde, [ $\alpha$ - $^{13}\text{C}$ ] benzoic acid, [ $\alpha$ - $^{13}\text{C}$ ] benzylformate, and [ $\alpha$ - $^{13}\text{C}$ ] benzyl alcohol.	34

Table IV.  $^{13}\text{C}$  NMR Studies of Metabolism in Intact Organs

System	$^{13}\text{C}$ Labeled Substrate	Observations	Ref.
Perfused mouse liver	[3- $^{13}\text{C}$ ] alanine and [2- $^{13}\text{C}$ ] ethanol	Enrichment at specific carbon atoms of glucose, glutamate, glutamine, aspartate, acetate, acetoacetate, $\beta$ -hydroxybutyrate and lactate measured. Alanine enters TCA cycle predominantly through pyruvate carboxylation in presence of ethanol which enters as acetyl CoA. Pentose cycle and fumarase activities estimated. Glutamine not in isotopic equilibrium with glutamate.	4
Perfused mouse liver and rat hepatocytes	[2- $^{13}\text{C}$ ], [1,3- $^{13}\text{C}_2$ ], [2- $^{14}\text{C}$ ], and [1,3- $^{14}\text{C}_2$ ] glycerol	Gluconeogenic flux from glycerol, synthesis of glycogen, recycling of triacylglycerol, and stimulation of pentose cycle by phenazine methosulfate followed. $^{14}\text{C}$ and $^{13}\text{C}$ gave same label distribution in newly synthesized glucose.	35
Perfused rat heart	[2- $^{13}\text{C}$ ] acetate	Perfused heart incorporates $^{13}\text{C}$ at high level into C-2, C-3, and C-4 of glutamate due to TCA cycle activity and activity of glutamate-oxalacetate transaminase. No label is incorporated into alanine (pyruvate). Some $^{13}\text{C}$ incorporation into aspartate if glucose is in the perfusion medium.	36

Table IV (contd.)  
System

$^{13}\text{C}$ Labeled Substrate	Observations	Ref.
Soybean $^{13}\text{CO}_2$	Early label appears in sugars and lipids; at later stages, sugar label is shuttled to lipids. $^{13}\text{C}$ - $^{13}\text{C}$ multiplet and singlet patterns in sugars and lipids shows partial randomization of label in original "pulse" labeled sugar due to recycling by the pentose cycle and transaldolase-transketolase reactions.	37

Table V. Illustrative  $^{13}\text{C}$  Nuclear Magnetic Resonance Studies of Biosynthetically  $^{13}\text{C}$  Labeled Cells and Reconstituted Macromolecular Assemblages

System	$^{13}\text{C}$ Labeled Precursor	Observations	Ref.
<u>Acholeplasma</u> membrane	[1- $^{13}\text{C}$ ] palmitic acid	Bulk membrane lipids behave as if in simple bilayer structures.	41
Vesicular stomatitis virions	[11- $^{13}\text{C}$ ] oleic acid [Me- $^{13}\text{C}$ ] choline	Motions of lipids in virion envelope are more restricted than those in liposomes.	42
Mouse erythrocytes	[2- $^{13}\text{C}$ ] histidine	Intracellular viscosity experienced by hemoglobin is only slightly higher than that of water.	43
<u>Aureobasidium pullulans</u>	[1- $^{13}\text{C}$ ] and [2- $^{13}\text{C}$ ] acetic acid	Dynamic behavior of membrane lipids similar to that in model membranes	44
Sarcoplasmic reticulum membranes	[Me- $^{13}\text{C}$ ] choline	Asymmetric distribution equilibrium of lysophosphatidyl choline between inner and outer sarcoplasmic reticulum membranes is established rapidly.	45
Frog muscle	[1- $^{13}\text{C}$ ] glycine	Motion of glycine provides no evidence for special organization of intracellular water.	46
Tobacco mosaic virus	$^{13}\text{CO}_2$	Significant rotational motion occurs for proteins within TMV and in protein oligomers.	47
Rat erythrocyte, endoplasmic, and sarcoplasmic reticulum membranes	[Me- $^{13}\text{C}_3$ ] choline	$^{13}\text{C}$ line widths of erythrocyte membrane lipids are typical for a lamellar arrangement but for endoplasmic reticulum membranes lipid line widths are small and characteristic of isotropic phases.	48



Table V (contd.)

System	$^{13}\text{C}$ Labeled Precursor	Observations	Ref.
<u>E. coli</u>	[1- $^{13}\text{C}$ ] oleate and diglycerides biosynthesized therefrom by <i>E. coli</i>	No incorporation of $^{13}\text{C}$ enriched diglycerides by growing cultures of <u><i>E. coli</i></u> . Fatty acid composition dictated by <u>De Novo</u> synthesis.	49
Chinese hamster ovary cells	[Me- $^{13}\text{C}$ ] choline	[Me- $^{13}\text{C}$ ] choline incorporated into phosphatidylcholine of cell membranes by phosphoryl choline transferase; motion of the polar headgroup is similar to that for sonicated lipid vesicles; large intracellular pool of phosphoryl [Me- $^{13}\text{C}$ ] choline exists. $T_1$ values of intracellular phosphorylcholine indicate that intracellular viscosity $\sim 1.2$ times that of water.	50
Chicken calvaria culture	[1- $^{13}\text{C}$ ] and [2- $^{13}\text{C}$ ] glycine	Labeled glycine incorporated into collagen. $T_1$ and NOE values of collagen in solution and reconstituted fibrils shows that rapid reorientation of helical backbone persists in fibrils.	51
Staphylococcus aureus	[1,2- $^{13}\text{C}_2$ ] glycine	Labeled glycine incorporated into cell walls of the bacterium. Rapid motion, highly correlated, occurs for pentaglycine bridges of cell wall peptidoglycan and appears dependent on degree of packing of glycan strands.	52

which was later taken up by the cells against a concentration gradient. The effect on pyruvate flux of the metabolic and physiological state of the cells and of proton conduction inhibitors led the authors (30) to suggest that the pH sensitive transport, which is selective to pyruvate, is mediated by a carrier protein which recognizes pyruvate with a high degree of specificity and translocates it and a proton across the membrane in a catalytic manner.

The fact that only the concentration of extracellular metabolites could be monitored in the latter study, raises questions about both the qualitative and quantitative significance of some of the fluxes measured with regard to the overall metabolism of the cell. For example, the unmeasured intracellular pyruvate concentration should be 10-20  $\mu\text{M}$ , whereas the maximum concentration measured outside the cell is  $\sim 2 \text{ mM}$ . This is illustrative of a general problem in the field, and one that others have not been as careful to address as Ogino and co-workers (30) — when one records the  $^{13}\text{C}$  spectrum of a cell or tissue suspension or a perfused organ, do the signals of the enriched metabolites originate from the extracellular fluids, from the cellular cytoplasm, and/or from special compartments (e.g. mitochondria) within the cells? How viable do the cells, tissues, and organs remain during the  $^{13}\text{C}$  experiments? Do they become leaky? Do they stop pumping substrates against a concentration gradient? These questions are becoming more critical as  $^{13}\text{C}$  nmr and  $^{13}\text{C}$  labeled substrates are applied more frequently to the study of metabolic control and compartmentation in "intact" biological systems.

In a series of reports, Shulman and co-workers (25, 26, 28, 29) have shown how high field  $^{13}\text{C}$  nmr (90.5 MHz) spectroscopy in conjunction with the use of  $^{13}\text{C}$  labeled substrates provides detailed information on glycolysis and gluconeogenesis in intact cells. The use of [1- $^{13}\text{C}$ ] and [6- $^{13}\text{C}$ ] glucose allowed an identification, and permitted an evaluation of the flux and its controls, of the principal intermediates in the glycolytic pathway of yeast and *E. coli* including [1, 6- $^{13}\text{C}_2$ ] fructose biphosphate (see Table III). Conversely the use of glucogenic precursors [2- $^{13}\text{C}$ ] glycerol, [1, 3- $^{13}\text{C}$ ] glycerol, and [3- $^{13}\text{C}$ ] alanine, permitted an evaluation of the major routes for the biosynthesis of "new" glucose (gluconeogenesis) by rat hepatocytes. A particularly interesting aspect of these studies is the new questions it has raised about the control and compartmentation of metabolism.

For example, the study (29) of gluconeogenesis by rat hepatocytes from a [3- $^{13}\text{C}$ ] alanine precursor revealed that the  $^{13}\text{C}$  label appeared not only in glucose but also in C-3 and C-2 of aspartate and glutamate. The C-3:C-2 intensity ratios in aspartate was consistently 2:1, whereas the equivalent C-2:C-3 ratio for glutamate was 1:1. The flow of  $^{13}\text{C}$  label into glutamate and aspartate occurs via a sequence of reactions involving transamination of [3- $^{13}\text{C}$ ] alanine to form [3- $^{13}\text{C}$ ] pyruvate which enters the mitochondrion and is carboxylated to [3- $^{13}\text{C}$ ] oxaloacetate. [3- $^{13}\text{C}$ ]

aspartate can be formed directly from oxaloacetate by transamination or [2-<sup>13</sup>C] glutamate can be formed via the tricarboxylic acid (Figure 4) and the action of glutamate dehydrogenase. In addition, the [3-<sup>13</sup>C] oxaloacetate can leave the mitochondrion via the malate pathway and in the cytoplasm serve as the substrate for gluconeogenesis (via [3-<sup>13</sup>C] phosphoenol pyruvate) and undergo C-2, C-3 label randomization due to cytosolic fumarase exchange. The fact that the aspartate label is not as completely randomized as that of glutamate seems to suggest not only that the mitochondrion is the site of aspartate synthesis but also that there is a favorable intramitochondrial location of aspartate amino transferase with respect to pyruvate carboxylase. In a related <sup>13</sup>C nmr study of gluconeogenesis by an intact mouse liver perfused with a solution containing [3-<sup>13</sup>C] alanine, the relative enrichments at C-2 and C-3 in both aspartate and glutamate were nonrandom, suggesting a reduced fumarase activity in intact mouse liver relative to rat hepatocyte suspensions (4). This might be due to a species difference or to a difference between cell suspensions and intact organs.

A more straightforward aspect of metabolic control revealed by studying the <sup>13</sup>C resonances of glutamate in this system is the competition between alanine and ethanol for entry into the TCA cycle (4). For mouse liver perfused with a medium containing [3-<sup>13</sup>C] alanine as the only carbon source, C-2, C-3, and C-4, were all found to be labeled appreciably; but when unlabeled ethanol and [3-<sup>13</sup>C] alanine were used, C-2 and C-3 were labeled but C-4 was not. Similarly a mixture of [2-<sup>13</sup>C] ethanol and [3-<sup>13</sup>C] alanine resulted in a labeling of C-2, C-3, and C-4 whereas a mixture of [2-<sup>13</sup>C] ethanol and unlabeled alanine resulted in an appreciable labeling only of C-4. The interpretation of these results is that ethanol enters the TCA cycle as acetyl CoA, is the dominant source of acetate when present in the medium, and is responsible for the presence ([2-<sup>13</sup>C] ethanol) or absence (unlabeled ethanol) of <sup>13</sup>C label at C-4 of glutamate (Figure 4). In the presence of ethanol alanine enters the TCA cycle as [3-<sup>13</sup>C] oxaloacetate via pyruvate and pyruvate carboxylase; but in its absence, uses the additional path of entry as [2-<sup>13</sup>C] acetyl CoA via pyruvate and pyruvate dehydrogenase. The authors (4) point out that two coordinate control mechanisms reasonably explain why the flux from alanine in the presence of ethanol is through pyruvate carboxylase and not pyruvate dehydrogenase. First, the production of acetate from alcohol by liver results in the formation of cytosolic and mitochondrial NADH, and both NADH and acetyl CoA facilitate conversion of the pyruvate dehydrogenase complex to its inactive form. Second, acetyl CoA activates pyruvate carboxylase (38).

Radda and co-workers (36) have studied the metabolism of [2-<sup>13</sup>C] acetate (5 mM) by perfused rat hearts. An increasing flux of <sup>13</sup>C from acetate via the TCA cycle into C-4, C-3, and C-2 of glutamate was observed to reach steady state after 30-40 minutes of perfusion. <sup>13</sup>C was incorporated into C-3 of glutamate at a

significantly slower rate than into C-4, providing a qualitative measure of the relative rates of cycling in the TCA cycle and synthesis of glutamate. Relatively little label was incorporated into aspartate when [2- $^{13}\text{C}$ ] acetate was the sole carbon source but labeled aspartate (C-2 and C-3) was formed in media containing [2- $^{13}\text{C}$ ] acetate and some glucose. Presumably this is related to the fall of oxaloacetate levels when acetate, rather than glucose, is the sole exogenous substrate (39). Surprisingly no  $^{13}\text{C}$  label was incorporated into alanine via pyruvate, even though alanine is present in high concentrations in heart which also is reported to have a high malic enzyme activity (40). The enzyme may be inhibited in this system or this may be another case of a high degree of enzyme compartmentation.

In concluding this section, we call attention to the spectrometer developed by Grathwohl *et al.* (31) for simultaneous binuclear nmr by alternate scan recording of  $^{31}\text{P}$  and  $^{13}\text{C}$  spectra. Its key features are: a wide bore 4.3T magnet; a probe containing a solenoidal receiving coil and tunable to four frequencies simultaneously,  $^{13}\text{C}$  (45.9 MHz),  $^{31}\text{P}$  (73.8 MHz),  $^1\text{H}$  (182.4 MHz), and  $^2\text{H}$  (28.0 MHz); and electronics and computer modifications allowing free induction decays of  $^{13}\text{C}$  and  $^{31}\text{P}$  to be generated alternately, and accumulated independently. The nearly simultaneous recording of  $^{31}\text{P}$  and  $^{13}\text{C}$  nmr spectra of erythrocytes suspended in a medium containing [1- $^{13}\text{C}$ ] glucose, allowed the simultaneous measurement of the flux of glucose, 2,3 diphosphoglycerate (DPG), lactate, inorganic phosphate, ADP, and ATP. In the simultaneous  $^{13}\text{C}$  and  $^{31}\text{P}$  measurements both the total level of DPG and the flux through the DPG pool could be measured accurately. Because measured metabolic fluxes in systems such as these are subject to wide variations among preparations, the correlations reported would be much more difficult, if not impossible, to establish by comparing the results of separate single nucleus nmr experiments. This multi-nucleus technique would offer special advantages when applied to scarce or unstable cell preparations.

Use of Metabolic Pathways to Label Specific Cellular Constituents. Although not the main theme of this article, we devote some space here to the subject of the use of  $^{13}\text{C}$  labeling and  $^{13}\text{C}$  nmr spectroscopy to the study of the architecture and dynamics of the constituents of intact cells and tissues. Certainly the kinds of studies suggested by the spectra in Figure 2 offer the promise of providing new insights into cellular structure and function. However, the  $^{13}\text{C}$  spectra of the uniformly  $^{13}\text{C}$  enriched *C. utilis* membranes shown in Figure 2 allows one to extract only the average chemical shift and relaxation data for a system which is markedly heterogeneous in its physical structure yet is redundant in its chemical composition. Considering these complexities and redundancies, we feel that significant progress in this field will be determined by the possibility of manipulating and making use of the metabolic machinery of the cell to direct  $^{13}\text{C}$  labeled substrates

to specific sites and structural elements. Recently there has been an increasing amount of work directed to that end, illustrative examples of which are summarized in Table V.

In an early study (43), mice were kept on a histidine deficient diet supplemented with [2-<sup>13</sup>C] histidine for a red blood cell lifetime with a consequent specific <sup>13</sup>C enrichment of the histidine residues of the red blood cell hemoglobin. Subsequent <sup>13</sup>C relaxation studies of the hemoglobin within the cell showed that the viscosity of the intracellular fluid is similar to that of water. A similar result was obtained in a related study of frog muscle labeled with <sup>13</sup>C enriched glycine (46) and Chinese hamster ovary cells loaded with phosphoryl [Me-<sup>13</sup>C] choline (50). These values are considerably less than that (>500 cp) obtained by Keith and Snipes (53) for chlamydomonas on the basis of an EPR spin label study. The validity of the latter result has been questioned by Finch and Harmon (54) who suggested that the correlation time of the spin label probe could be a weighted average of its predominant occupation of a "mobile" site and a small occupation of a highly immobilized one.

In an extensive series of studies, Van Deenen and co-workers (45) were able to highly label the phosphatidylcholine of red blood cell, liver microsome and sarcoplasmic reticulum membranes of rats fed a choline deficient diet supplemented with [Me<sub>3</sub>-<sup>13</sup>C] choline for a period of eight days. <sup>13</sup>C nmr studies of the muscle microsomes revealed an asymmetric distribution of phosphatidyl choline between the inner (60%) and outer (40%) surfaces of the membranes of the sarcoplasmic reticulum. This asymmetry is opposite to that found for erythrocytes and may be related to the fact that the former are endoplasmic membranes whose outer surface corresponds to the inner surface of plasma membranes. That same group has used reconstituted macromolecular assemblages to study the permeability barriers in large unilamellar glycoporphin containing vesicles of [Me<sub>3</sub>-<sup>13</sup>C] phosphatidyl choline and have found that the barrier properties of glycoporphin containing bilayers of phosphatidyl choline can be restored by 10 mol % phosphatidylethanolamine or lysophosphatidylcholine.

A final illustration of the broad range and great promise of the experiments being conducted in this area, even for uniformly enriched materials, is the study of de Wit and co-workers (47) who enriched tobacco mosaic virus and its proteins to the 12 atom % <sup>13</sup>C level using <sup>13</sup>CO<sub>2</sub> as the carbon source. In addition to developing some interesting conclusions about the interaction between RNA and protein, these workers observed that the double disks formed by the proteins in the absence of RNA contain mobile <sup>13</sup>C atoms at all sites within the disks which were formed in solutions of 0.1-0.2 ionic strengths. In contrast, X-ray data for crystals of stacks of double disks obtained from 0.8 ionic strength solutions indicate that the motion of the carbon atoms is highly restricted. Thus there are important structural differences between the crystals studied by X-ray and the disks formed in solution near the physiological ionic strength, a conclusion

strengthened by the nmr observation that there is an increasing degree of immobilization of the carbon atoms in the double disk-like oligomers as the ionic strength increases.

### Prospects for Future Developments

It is likely that the most informative and exciting future developments in the use of  $^{13}\text{C}$  nmr spectroscopy and  $^{13}\text{C}$  labeling in metabolic studies on intact cells and organs will be in the detailed investigation of control mechanisms and the compartmentation of metabolites. To achieve the full potential of the technique in this important area will require the improvement of the selectivity and sensitivity of the  $^{13}\text{C}$  nmr analysis. The use of higher field magnets obviously will improve both parameters but there are other possibilities as well.

Turning first to selectivity, we have illustrated how conventional nmr spectra of multiply  $^{13}\text{C}$  labeled molecules can provide unique information about metabolic pathways and control mechanisms. Nonetheless the interpretation of these conventional, one quantum spectra requires simplifying assumptions about the number of isotopomers present and metabolic pathways operational. Recently, multiple quantum nmr (55-57) has been applied to a study of the individual isotopomers (and their  $^{13}\text{C}$ - $^{13}\text{C}$  couplings) present in natural abundance piperidine (58). This double quantum coherence technique ought to find wide application in sorting out the many isotopomers resulting from the metabolism of multiply enriched substrates, because Freeman and co-workers have shown (58) that when there is optimum transfer into coherence, the spectrum from coupled  $^{13}\text{C}$ - $^{13}\text{C}$  molecules appears with the same sensitivity as the conventional spectrum. For the complicated  $^{13}\text{C}$  spectra exhibited by multiply labeled molecules, it may be necessary to use two dimensional FT methods to avoid overlap among different multiplets (59).

The continued improvement of magnet technology has had a profound influence on the development of biologically oriented nmr studies. In addition to the widespread use of high field superconducting magnets, the steadily increasing volume of high field homogeneity, permitting the use of larger sample tubes or of variable probe geometries, will lead to further improvements in sensitivity and to reductions in the concentrations of materials to values more representative of physiological conditions. The ultimate limitations on sample volume are physical: frequency dependent absorption of rf power leading to unacceptable sample heating in decoupled systems (60) and to rf losses (61, 62). The severity of these problems can be reduced using several techniques such as bilevel decoupling or shielding of the sample (63), however, the use of very large samples at lower field strengths may offer the greatest possibilities for metabolic studies in experiments which are not sample limited.

Future efforts toward additional sensitivity gains are likely to be focused on the probe where relatively inexpensive or simple modifications can have the greatest impact. As a result of the

poorer sensitivity characteristic of the Helmholtz coil geometry as compared with the solenoidal geometry (64), increased use has been made of transverse mounted solenoid coils in combination with sealed microcells (31, 65). The use of such cells is inconsistent with aeration of cell suspensions in vivo studies, however, modifications of these designs for non-spinning transverse mounted geometries would appear feasible. The use of low noise transistors (66) as well as the possibility of nitrogen cooling the receiver coil and preamplifier (67) have also been suggested. Although most of these improvements will lead to sensitivity increases in the range 2-4, the large savings in time, and the possibility of applying a combination of approaches could lead to very significant gains. Finally, the use of polarization transfer methods to improve the sensitivity of low  $\gamma$  nuclei such as <sup>13</sup>C and <sup>15</sup>N should prove of great value in nmr studies of metabolic processes (68-70).

#### Literature Cited

1. Eakin, R. T.; Morgan, L. O.; Gregg, C. T.; Matwiyoff, N. A. FEBS Letts 1973, 28, 259-263.
2. London, R. E.; Kollman, V. H.; Matwiyoff, N. A. Biochemistry 1975, 14, 5492-6000.
3. Kainosho, M.; Ajisaka, K.; Nakazawa, H. FEBS Letts. 1977, 80, 385-389.
4. Cohen, S. M.; Shulman, R. G.; McLaughlin, A.C. Proc. Nat. Acad. Sci. (USA) 1979, 76, 4808-4812.
5. Burt, C. T.; Cohen, S. M.; Barany, M. Am. Rev. Biophys. Bioeng. 1979, 8, 1-25.
6. O'Neill, I. K.; Richards, C. R. "Biological <sup>31</sup>P NMR Spectroscopy"; in Ann. Rep. NMR Spectrosc. 1980, 10A, 133-236.
7. Shulman, R. G.; Brown, T. R.; Ugurbil, K.; Ogawa, S.; Cohen, S. M.; den Hollander, J. A. Science 1979, 205, 160-166.
8. Gadian, D. G.; Radda, G. K.; Richards, R. E.; Seeley, P. J. "<sup>31</sup>P NMR in Living Tissue"; Shulman, R. G., Ed.; in Biological Applications of Magnetic Resonance; Academic Press, N.Y., 1979; pp 463-535.
9. Radda, G. K.; Seeley, P. J. Annu. Rev. Phys. 1979, 41, 749-769.
10. Monson, K. D.; Hayes, J. M. J. Biol. Chem. 1980, 255, 11435-11441.
11. Tanabe, M. Biosynthesis 1973, 2, 241-299.
12. Matwiyoff, N. A.; Ott, D. G. Science 1973, 181, 1125-1133.
13. Sequin, U.; Scott, A. E. Science 1974, 186, 101-107.
14. McInnes, A. G.; Walter, J. A.; Wright, J. L. C.; Vining, L. C. Top. Carbon-13 NMR Spectros. 1976, 2, 123-178.
15. Matwiyoff, N. A.; Walker, T. E. "Trends in the Use of Stable Isotopes in Biochemistry and Pharmacology"; in Stable Isotopes in the Life Sciences (Proc. Symp. Leipzig, 1977): IAEA, Vienna, 1977; pp 247-272.

16. Norton, R. S. Bull. Mag. Res., in press.
17. Walker, T. E.; Han, C. H.; Kollman, V. H.; London, R. E.; Matwiyoff, N. A. J. Biol. Chem., in press.
18. London, R. E.; Kollman, V. H.; Matwiyoff, N. A. J. Am. Chem. Soc. 1975, 97, 3565-3573.
19. Shio, I.; Otsuka, S.; Takahashi, M. J. Biochem. (Tokyo) 1961, 50, 164-165 and references therein.
20. Gagnaire, D.; Taravel, F. J. Am. Chem. Soc. 1979, 101, 1625-1626
21. Gagnaire, D.; Taravel, F. Eu. J. Biochem. 1980, 103, 133-143.
22. London, R. E.; Walker, T. E.; Kollman, V. H.; Matwiyoff, N. A. J. Magn. Res. 1977, 26, 213-218.
23. Moreland, C. G.; Carroll, F. I. J. Magn. Res. 1974, 15, 596-599.
24. Brown, F. F.; Campbell, I. D.; Kuchel, P. W.; Rabenstein, D. C. FEBS Lett. 1977, 82, 12-16.
25. Ugurbil, K.; Brown, T. R.; Den Hollander, J. A.; Glynn, P.; Schulman, R. G. Proc. Natl. Acad. Sci. (USA) 1978, 75, 3742-3746.
26. Den Hollander, J. A.; Brown, T. R.; Ugurbil, K.; Shulman, R. G. Proc. Natl. Acad. Sci. (USA) 1979, 76, 6096-6100.
27. Scott, A. I.; Burton, G.; Fagerness, P. E. J. Chem. Soc. (Chem. Commun.) 1979, 199-202.
28. Cohen, S. M.; Ogawa, S.; Schulman, R. G. Proc. Natl. Acad. Sci. (USA) 1979, 76, 1603-1607.
29. Cohen, S. M.; Glynn, P.; Shulman, R. G. Proc. Natl. Acad. Sci. (USA) 1981, 78, 60-64.
30. Ogino, T.; Arata, Y.; Fujiwara, S. Biochem. 1980, 19, 3684-3691.
31. Styles, P.; Grathwohl, C.; Brown, F. F. J. Magn. Res. 1979, 35, 329-336.
32. Deslaurier, R.; Jarrell, H. C.; Griffith, D. W.; McGregor, W. H.; Smith, I. C. P. Int. J. Peptide Protein Res. 1980, 16, 487-493.
33. Burton, G.; Baxter, R. L.; Gunn, J. M.; Sidebottom, P. J.; Fagerness, P. E.; Shishido, K.; Lee, J. Y.; Scott, A. I. Can. J. Chem. 1980, 58, 1839-1846.
34. Halpin, R. A.; Hegeman, G. D.; Kenyon, G. L. Biochemistry 1981, 20, 1525-1533.
35. Cohen, S. M.; Rogstad, R.; Shulman, R. G.; Katz, J. J. Biol. Chem. 1981, 256, 3428-3432.
36. Bailey, I. A.; Gadian, D. G.; Mathews, P. M.; Radda, G. K.; Seeley, P. J. FEBS Lett. 1981, 123, 315-318.
37. Schaefer, J.; Stejskal, E. O.; Beard, C. F. Plant Physiol. 1975, 55, 1048-1053.
38. In this context we might point out that both the rat hepatocyte and mouse liver systems were bathed in media containing high substrate loads, 28 mM alanine and 20 mM ethanol for the hepatocytes and 8 mM alanine and 20 mM ethanol for the mouse liver. These high loads might induce an enhanced differential activity of certain metabolic pathways in the two systems.



39. Randle, P. J.; Denton, R. M.; England, P. J. Biochemistry J. 1970, 117, 677-695.
40. Sato, T.; Tomika, K. Biochemistry J. (Tokyo) 1972, 73, 807-815.
41. Metcalfe, J. C.; Birdsall, N. J. M.; Lee, A. G. FEBS Lett. 1972, 21, 335-340.
42. Stoffel, W.; Bister, K. Biochemistry 1975, 14, 2841-2847.
43. London, R. E.; Gregg, C. T.; Matwiyoff, N. A. Science 1975, 188, 266-268.
44. Smith, I. C. P. Can. J. Biochem. 1979, 57, 1-14.
45. Van Den Besselaar, A. M. H. P.; DeKruijff, B.; Van Den Bosch, H.; Van Deenen, L. L. M. Biochem. Biophys. Acta 1979, 555, 193-199; De Kruijff, B.; Van Den Besselaar, A. M. H. P.; Van Den Bosch, A.; Van Deene, L. L. M. Biochem. Biophys. Acta 1979, 555, 181-192; Gerritsen, W. J.; Van Zoelen, E. J. J.; Verkley, A. J.; De Kruijff, B.; Van Deenen, L. L. M. Biochem. Biophys. Acta 1979, 551, 248-259.
46. Neville, M. C.; Wyssbrod, H. R. Biophys. J. 1977, 17, 255-267.
47. De Wit, J. L.; Alma-Zeestraten, N. C. M.; Hemmings, M. A.; Schaafsma, T. J. Biochemistry 1979, 18, 3973-3976.
48. De Kruijff, B.; Reitveld, A.; Van Echteld, C. J. A. Biochem. Biophys. Acta 1980, 600, 597-606.
49. Cronan, Jr., J. E.; Prestegard, J. H. Biochemistry 1977, 16, 4738-4742.
50. London, R. E.; Hildebrand, C. E.; Olson, E. S.; Matwiyoff, N. A. Biochemistry 1976, 15, 5480-5483.
51. Jelinsky, L. W.; Torchia, D. A. J. Mol. Biol. 1979, 133, 45-65.
52. Lapidot, A.; Irving, C. S. Biochemistry 1979, 79, 1788-1796.
53. Keith, A. D.; Snipes, W. Science 1974, 183, 666-668.
54. Finch, E. D.; Harmon, J. F. Science 1974, 186, 157-158.
55. Wokaun, A.; Ernst, R. R. Mol. Phys. 1978, 36, 317-341.
56. Vega, S.; Shattuck, T. W.; Pines, A. Phys. Rev. Lett. 1976, 37, 43-46.
57. Warren, W. S.; Pines, A. J. Am. Chem. Soc. 1981, 1103, 1613-1617.
58. Bax, A.; Freeman, R.; Kempell, S. P. J. Am. Chem. Soc. 1980, 102, 4849-4851.
59. Niedermeyer, R.; Freeman, R. J. Magn. Reson. 1978, 30, 617-620.
60. Led, J. J.; Petersen, S. B. J. Magn. Reson. 1978, 32, 1-17.
61. Hoult, D. I.; Richards, R. E. Proc. Royal Soc. Ser. 1975, A344, 311-340.
62. Gadian, D. G.; Robinson, F. N. H. J. Magn. Reson. 1979, 34, 449-455.
63. Alderman, D. W.; Grant, D. M. J. Magn. Reson. 1979, 36, 447-451.
64. Hoult, D. I.; Richards, R. E. J. Magn. Reson. 1976, 24, 71-85.
65. Oldfield, E.; Meadows, M. J. Magn. Reson. 1978, 31, 327-335.

66. Kipnich, H. D.; Esche, R.; Maurer, W. J. Magn. Reson. 1976, 22, 161-164.
67. Hoult, D. I. "Topics in Carbon-13 NMR Spectroscopy"; G. C. Levy, Ed.; Wiley-Interscience, New York, 1979, pp. 16-27.
68. Bertrand, R. D.; Moniz, W. B.; Garroway, A. N.; Chingas, G. C. J. Magn. Reson. 1978, 32, 465-467; Garroway, A. N.; Chingas, G. C. J. Magn. Reson. 1980, 38, 179-184.
69. Jakobsen, H. J.; Brey, W. S. J. Am. Chem. Soc. 1979, 101, 774-775.
70. Morris, G. A.; Freeman, R. J. Am. Chem. Soc. 1979, 101, 760-762.

RECEIVED January 21, 1982.

# Chemical Bond Labeling and Double Cross-Polarization NMR

JACOB SCHAEFER, E. O. STEJSKAL, and R. A. McKAY

Monsanto Company, Physical Sciences Center, St. Louis, MO 63166

Placing a radiolabel in a molecule is a popular method of following subsequent chemical or biochemical alterations of the tagged molecule (1). This procedure ultimately involves an indirect detection scheme. After separations and purifications, the distribution or radioactivity in products is compared with what might be expected from various kinetic models. Chemical or metabolic changes in the tagged molecule must then be inferred from labeling patterns.

By forming a pair of stable-isotope nuclear spin labels adjacent to one another in the same molecule, a particular chemical bond of that molecule is tagged. The rate of formation of the labeled bond, or subsequent chemical or metabolic changes to that chemical bond, can then be observed directly using nmr detection of the scalar or dipolar coupling between the pair of labels. For example, by pulse labeling intact soybean and corn leaves with  $^{13}\text{CO}_2$  for 5-45 minutes, the time dependence of the distribution of label among pairs of carbons in triose products of the Calvin cycle was interpreted in terms of the rates of photosynthetic and photorespiratory processes. The latter process generated  $^{12}\text{CO}_2$  from as yet unlabeled carbon sources and so affected the rate of formation of  $^{13}\text{C}$ - $^{13}\text{C}$  pairs (2). These pairs were detected by characteristic scalar spin-spin multiplet patterns in the solution  $^{13}\text{C}$  nmr spectrum of sucrose extracted from the leaves.

Often it is desirable to avoid extractions, purifications, or derivitizations in the detection of nuclear spin labels, especially in complex or fragile biological systems. This can be accomplished using solid-state cross-polarization rare-spin nmr. The combination of high-power resonant decoupling and high-speed mechanical sample spinning has been demonstrated to produce liquid-like high-resolution  $^{13}\text{C}$  nmr spectra of a wide variety of organic solids (3). Individual resonances from chemically different carbons can be observed. The high-resolution technique becomes a high sensitivity one when the rare-spin magnetization is obtained from a cross-polarization transfer from the abundant

0097-6156/82/0191-0187\$06.00/0  
© 1982 American Chemical Society

protons (4). These techniques work as well for  $^{15}\text{N}$  as for  $^{13}\text{C}$  (5).

Magic-angle cross-polarization  $^{15}\text{N}$  nmr of intact lyophilized *Neurospora crassa* mycelia grown in  $^{15}\text{N}$ -nitrate medium as a function of time showed the incorporation and subsequent metabolism of label (6), with individual nmr lines observed for nitrogen in lysine, arginine, and histidine residues, peptide nitrogen, and nitrogen in both nucleic acids and glutamine free amino acid. The time dependence of the intensity of each of these lines over an eight-hour period resulted in a detailed budget for nitrogen metabolism, impossible to achieve with a nitrogen radiolabel ( $^{13}\text{N}$  half-life of 10 minutes).

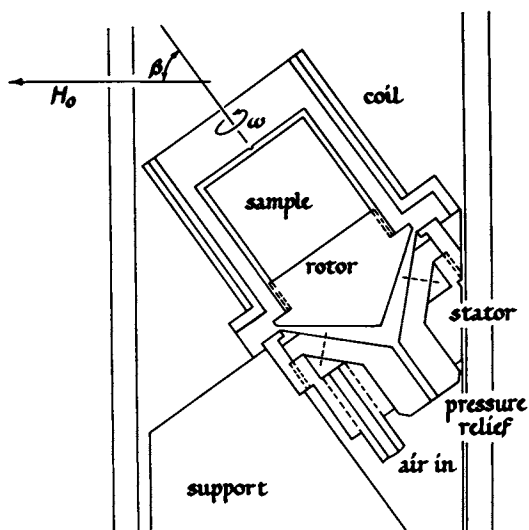
Double-cross polarization (7) combines the directness and specificity of chemical bond analysis for double-labeled materials mentioned above with the convenience of observing intact biological systems (8). Double-cross polarization is a serial extension of cross polarization to three-spin systems ( $^1\text{H}$ ,  $^{13}\text{C}$ , and  $^{15}\text{N}$ ). The experiment involves first a transfer of polarization from protons to either carbons or nitrogens, followed by removal of the proton radiofrequency (rf) together with a matched spin-lock contact of carbons and nitrogens. Either  $^{13}\text{C}$  or  $^{15}\text{N}$  spins can then be observed resulting in spectra which contain information about nitrogen-carbon dipolar coupling with high sensitivity (7,8).

In this paper we will illustrate the application of double-cross polarization techniques in experiments in which both specific and non-specific  $^{13}\text{C}$ - $^{15}\text{N}$  double labels are employed.

### NMR Apparatus

Magic-angle  $^{15}\text{N}$  nmr spectra were obtained at 9.12 MHz using matched spin-lock cross-polarization transfers with 1-msec single contacts and 26 kHz fields ( $H_1$ 's). The lyophilized samples were contained in a Beams-Andrew 420- $\mu\text{l}$  hollow rotor (Figure 1) spinning at 1.4 kHz. Technical details of the spinning and cross-polarization procedures have been reported before (9). Fast cross-polarization transfer rates for protonated nitrogens, long proton rotating-frame lifetimes, and high concentrations of protons in these biological samples ensure representative nmr intensities for all the nitrogens of interest in lyophilized samples (10).

Double-cross polarization  $^{15}\text{N}$  nmr spectra were obtained using consecutive matched spin-lock transfers (7), first from  $^1\text{H}$  to  $^{15}\text{N}$  and then from  $^{15}\text{N}$  to  $^{13}\text{C}$ . The pulse sequence employed in these experiments is shown in Figure 2. The first transfer is the same as used for  $^1\text{H}$ - $^{15}\text{N}$  cross polarization described above. (The  $^1\text{H}$  rf is adiabatically reduced from its maximum value of about 50 kHz used for spin locking and decoupling to the 26-kHz value needed to match the  $^{15}\text{N}$  rf field, the latter the most difficult to generate in a single triply-tuned coil.) The proton



$^{15}\text{N}$  magic-angle rotor

Figure 1. Schematic drawing of a magic-angle spinning device. The Kel-F sample holder screws into a rotor base that is then loaded through the top of the coil. The stator is fixed and the spacing between the pole faces of the iron magnet is 25 mm; other dimensions are to scale. Spinning speeds of 2 kHz can be achieved with 20 psi pressures and unfluted rotors, and over 3 kHz with fluted rotors. The sample volume is 420  $\mu\text{L}$ .

rf is turned off and the  $^{15}\text{N}$  magnetization held spin locked for a variable time,  $\tau$ , during which a  $^{13}\text{C}$  rf is turned on. If the  $^{13}\text{C}$  is on resonance and its amplitude satisfies a carbon-nitrogen Hartmann-Hahn condition (5), a matched spin-lock transfer from  $^{15}\text{N}$  to  $^{13}\text{C}$  drains polarization from the nitrogen spin system. The carbon rf is phase modulated to prevent an accumulation of carbon polarization thereby helping to ensure simple kinetics describing the  $^{15}\text{N}$  to  $^{13}\text{C}$  transfer (7). A direct difference experiment between single- and double-cross polarization procedures (Figure 2) results in the accumulation of a  $^{15}\text{N}$  signal arising exclusively from those nitrogens directly bonded to  $^{13}\text{C}$ . Data collection for difference spectra typically require 12-24 hours.

### Specific Double Labels: Soybean Organ Cultures

Single-Cross Polarization. A typical magic-angle  $^{15}\text{N}$  nmr spectrum of labeled soybean cotyledons is shown in Figure 3 (left). This spectrum was obtained from five intact lyophilized cotyledons, grown for 14 days on 4- $^{13}\text{C}$ - $^{15}\text{N}$  (amide)-asparagine. The mechanical sample spinning produced the spinning sidebands (SSB) which appear at the extremes of the spectrum. The major line (about 100 ppm downfield from solid ammonium sulfate as an external  $^{15}\text{N}$  nmr reference) is due to label in amide nitrogen, either in the form of peptide nitrogen or asparagine residue. The free asparagine concentration is low (10). The asparagine amide nitrogen is clearly metabolized to produce other functionality with label appearing, for example, in histidine (just to the low-field side of the 100-ppm line), arginine (just to the high-field side), and ammonium. The remaining two peaks are due to nitrogens in free glutamine and lysine residues. The appearance of the spectrum is changed considerably if the cotyledons are cultured on medium containing  $^{15}\text{N}$ -(amine)-asparagine as the only nitrogen source (Figure 3, right). No histidine peak is observed in this spectrum at all. This result illustrates that the two nitrogens of asparagine (the major translocation amino acid) are used with a degree of specificity. We have not observed the same specificity in the use of amine and amide nitrogens of glutamine in soybean cotyledon cultures (10).

Double-Cross Polarization. In the absence of a  $^{15}\text{N}$ - $^{13}\text{C}$  drain (Figure 2,  $^{13}\text{C}$  rf off resonance), the  $^{15}\text{N}$  magnetization,  $S_0$ , is a function of the rotating-frame hold time. In the simplest situation, this dependence is described by a single exponential relaxation time,  $T_{1\rho}(\text{N})$ , which may be related to either spin-spin or spin-lattice processes (11). In the presence of a drain, an additional decay process for the  $^{15}\text{N}$  magnetization is introduced to that

$$S = S_0 e^{-\tau/T_d} \quad (1)$$

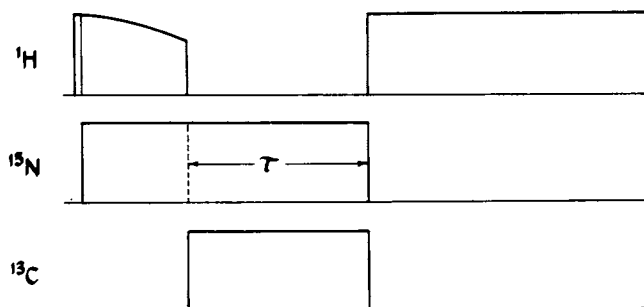


*Figure 2. Double cross-polarization pulse sequence. The y-axis shows radio-frequency field amplitude and x-axis time. A  $^{15}\text{N}$  direct difference signal can be accumulated by shifting the  $^{13}\text{C}$  radiofrequency off resonance for one scan and on resonance for the next. The second NMR signal is subtracted from the first. The time,  $\tau$ , during which the  $^1\text{H}$  is off is called the  $^{15}\text{N}$  hold time when the  $^{13}\text{C}$  radiofrequency is off resonance, and is called the drain time when the  $^{13}\text{C}$  is on resonance. Data acquisition occurs with the  $^1\text{H}$  radiofrequency field turned back on for dipolar decoupling. Pulse sequence: 1,  $^{15}\text{N}$  hold:  $^{13}\text{Crf}$  60 kHz off resonance; 2,  $^{15}\text{N} \rightarrow ^{13}\text{C}$  drain:  $^{13}\text{Crf}$  on resonance; 3, direct difference: 1 minus 2.*

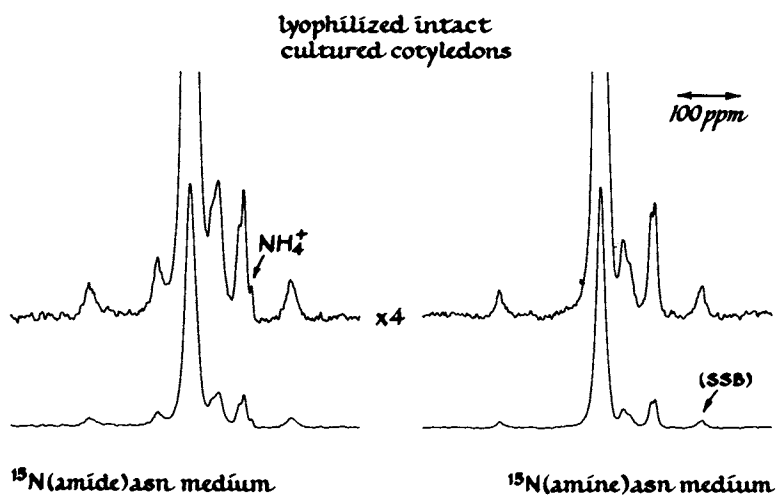


*Figure 3. Magic-angle cross-polarization <sup>15</sup>N NMR spectra of intact lyophilized soybean cotyledons grown in culture on media containing 4-<sup>13</sup>C-<sup>15</sup>N(amide)-asparagine (left) and <sup>15</sup>N(amine)-asparagine (right). The major resonance is due primarily to peptide nitrogen and occurs 100 ppm downfield from solid ammonium sulfate as an external reference.*



where we have assumed the drain process itself is adequately described by a single exponential time constant,  $T_d$ . Then, the relative difference signal arising from the difference experiment of Figure 2 is

$$\Delta S/S_0 = (S_0 - S)/S_0 = f(1 - e^{-\tau/T_d}) \quad (2)$$

and

$$1 - (\Delta S/S_0)/f = e^{-\tau/T_d} \quad (3)$$

where  $f$  is the fraction of carbons which are  $^{13}\text{C}$ s next to  $^{15}\text{N}$ s. Thus, a semi-log plot of  $1 - (\Delta S/S_0)/f$  against  $\tau$  yields a straight line whose slope is  $T_d$ . This time constant is the average matched spin-lock carbon-nitrogen cross-polarization transfer time, sometimes identified as  $T_{\text{CN}}(\text{SL})$  (4,7). Values of  $T_d$  for two solid double-labeled amino acids, glycine and 4- $^{13}\text{C}$ - $^{15}\text{N}$ -(amide)-asparagine have been measured as 10.9 and 3.64 msec, respectively (12). The drain process for both systems seems to be reasonably well represented as a single-exponential decay (Figure 4). The shorter relaxation time for asparagine is mostly, but not exclusively, the result of the shorter nitrogen-amide carbon bond length (relative to the nitrogen-aliphatic carbon bond for glycine), and the correspondingly stronger static dipolar coupling between  $^{15}\text{N}$  and  $^{13}\text{C}$  and faster cross-polarization transfer (12).

The fraction,  $f$ , of double label in the cultured cotyledons is, of course, not known. This number can be determined by a plot of  $\Delta S/S_0$  against  $(1 - e^{-\tau/T_d})$  which is a straight line with slope  $f$ . Since virtually all of the labeled carbon in these cotyledons is known to be carbonyl (10), an appropriate  $T_d$  is 3.64 msec. Values for  $f$  for sister cotyledons in a double-label dilution experiment are shown in Table I, and are reported as percent amide  $^{15}\text{N}$  (10).

Table I. Incorporation of  $^{15}\text{N}$ - $^{13}\text{C}$  in Cotyledon Protein

<u>Asparagine Nitrogen Source</u>	<u>Labeling, Days in Culture</u>	<u><math>^{15}\text{N}</math>, % Incorporated Nitrogen</u>	<u><math>^{15}\text{N}</math>-<math>^{13}\text{C}</math>, % Protein Amide <math>^{15}\text{N}</math></u>
60-mm 4- $^{13}\text{C}$ - $^{15}\text{N}$ (amide)	14	38	17
30-mm 4- $^{13}\text{C}$ - $^{15}\text{N}$ (amide) + 30-mM natural abundance	14	18	12

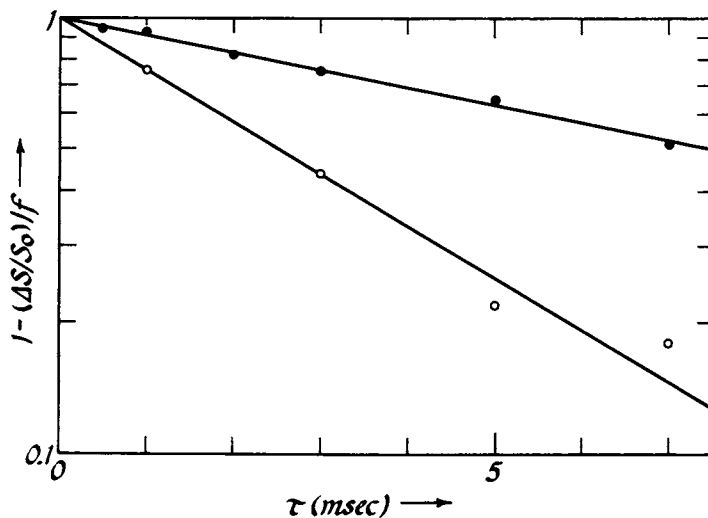


Figure 4. Determination of the C-N matched spin-lock cross-polarization transfer time constant for two solid double-labeled amino acids using double cross polarization.  $T_b$  is the time constant for the transfer from N to an aliphatic C, and  $T_a$  is for the transfer from N to an amide C. The  $^{13}\text{C}$  enrichment for both materials was 90 atom %. Key: ●,  $^{15}\text{NH}_2^{13}\text{CH}_2\text{COOH}$  ( $f = 0.9$ ) where  $T_b = 10.93$  ms; and ○,  $^{15}\text{NH}_2^{13}\text{COCH}_2\text{CH}(\text{NH}_2)\text{COOH}$  ( $f = 0.9$ ) where  $T_a = 3.64$  ms.

The ratio of  $f$  for the isotopically diluted system of Table I to that of the undiluted system is 0.7. That is, the concentration of double labels in the cotyledons grown on the medium isotopically diluted by 50% is more than one-half that of the cotyledons grown on the undiluted medium (Figure 5). However, the biological metabolism (and so  $T_{1\rho}$ s) in the undiluted and diluted double-label experiments can reasonably be assumed to be identical (all metabolites are chemically the same in the two experiments). Therefore, a large fraction of all asparagine residues in soybean protein produced in our experiments must have arisen from the direct incorporation of asparagine with no scrambling of label. This result establishes the operation of a regulatory metabolic system in soybeans for both asparagine incorporation and degradation in protein synthesis (10).

In the double-label dilution experiment described here, the specificity of a particular metabolic pathway was examined by monitoring the fate of an existing labeled chemical bond in a molecule entering that pathway. Naturally, the complementary experiment can also be performed in which the formation of a labeled chemical bond from two separate specific labels is observed directly using double-cross polarization nmr.

#### Non-Specific Double Labels: Protein Turnover in Soybean Leaves

During senescence, the protein in soybean leaves degrades and is transported to the maturing ovules, or seeds, where it is transformed into storage protein (13). Thus, a natural mechanism is in place in soybean leaves for protein degradation. A question arises as to whether prior to senescence, a mature, fully expanded leaf having a fixed concentration of protein (mostly carboxylase, the  $\text{CO}_2$ -fixing enzyme) undergoes rapid protein turnover, so that the steady-state carboxylase content of the mature leaf is, in fact, the result of a dynamic balance between continuous rapid protein synthesis and degradation.

The answer to this question can be obtained using  $^{13}\text{C}$  and  $^{15}\text{N}$  double labeling, together with double-cross polarization nmr (14). Fully expanded leaves of six-week old soybean plants (*Glycine max* L. cv. Elf) grown on  $^{15}\text{NH}_4^{15}\text{NO}_3$  were exposed to 90%  $^{13}\text{CO}_2$  (325 ppm, 21%  $\text{O}_2$ ) for seven days and then returned to normal conditions. Leaves were harvested over a 40-day period after the exposure to  $^{13}\text{CO}_2$ . N-15 double-cross polarization nmr spectra obtained from each lyophilized leaf were used to determine the percent of  $^{15}\text{N}$ - $^{13}\text{C}$  pairs in the peptide backbone. The former will be high if protein turnover in the leaves was fast during the labeling period and if the leaf was harvested soon after the completion of the  $^{13}\text{CO}_2$  labeling. A measure of the rate of protein turnover can be made both from the rate of incorporation of  $^{13}\text{C}$  into peptide linkages, as well as by comparison of its disappearance from comparable labeled leaves harvested at different times from different plants after their

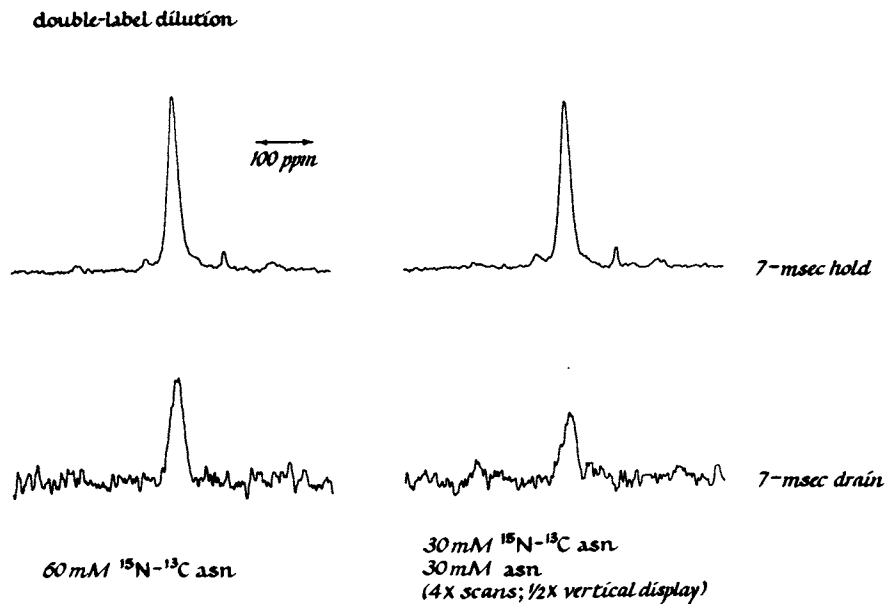


Figure 5. Magic-angle cross-polarization  $^{15}\text{N}$  nuclear magnetic resonance signal,  $S_0$ , of 5 ethanol-extracted lyophilized soybean cotyledon cultured for 14 days on media containing 60 mM  $4\text{-}^{13}\text{C}\text{-}^{15}\text{N}$ (amide)-asparagine (top left), or 30 mM natural-abundance asparagine plus 30 mM  $4\text{-}^{13}\text{C}\text{-}^{15}\text{N}$ (amide)-asparagine (top right). The corresponding difference signals,  $\Delta S$ , obtained as described in Figure caption 2, are shown bottom left and bottom right, respectively. The two spectra on the right involved  $4\times$  the data accumulation and are displayed at half the vertical scale of the two spectra on the left. (Each difference spectrum involved  $6\times$  the data accumulation and is displayed at twice the vertical scale of the spectrum shown immediately above it). The ratio of  $\Delta S/S_0$  for the isotopically diluted system (right) is more than half that of the undiluted system (left).

return to a natural abundance atmosphere. An example of the latter is shown in Table II. These measures are not confused by the kinetics of incorporation of label into sidechains.

Table II. Comparisons of Pairs of Leaves at Similar Developmental Stages Harvested at Different Times after  $^{13}\text{C}_2$  Labeling

<u>t<sub>1</sub></u> <u>(days)</u>	<u>t<sub>2</sub></u> <u>(days)</u>	<u>Main-Chain <math>^{13}\text{C}</math> Concentration</u>		<u>Protein Lifetime (days)</u>
		<u>c<sub>1</sub></u> <u>(%)</u>	<u>c<sub>2</sub></u> <u>(%)</u>	
6	16	6.1	4.2	21
6	21	8.2	5.9	38
6	21	10.6	5.2	18
11	26	6.9	4.3	25

The lifetimes were calculated assuming a constant completely  $^{15}\text{N}$ -labeled, homogeneous protein pool, and a simple first-order  $^{13}\text{C}$  labeling process described by  $dc/dt = -kc + kc_2$ , where  $c$  is the isotopic concentration of the protein carbon pool,  $c_2$  is the isotopic replacement concentration, and  $k$  is the turnover rate constant. From Table II, the lifetime of the protein of a mature, fully expanded leaf of soybean is fairly long, somewhere between 20 and 40 days. This result suggests that the synthesis of protein does not put a significant demand on the energy budget of expanded leaves (14).

### Conclusions and Projections

We have illustrated the use of double cross polarization  $^{15}\text{N}$  nmr to follow the formation or metabolism of particular chemical bonds of proteins in intact biological tissue. Neither the use of radioisotopes, nor the use of other means of detecting stable isotopes, has comparable directness and specificity.

All of the experiments reported here involve lyophilized tissue. Nevertheless, magic-angle spinning cross-polarization nmr experiments on in vivo functioning biological systems may also prove practical. With significant improvements in sensitivity available for  $^{15}\text{N}$  nmr experiments performed at 20 to 30 MHz (rather than 9 MHz) using 1-cc magic-angle rotors (instead of 0.4-cc rotors), monitoring metabolism in some plant and bacterial systems in real time is within reach. Simultaneous  $^{13}\text{C}$  and  $^{15}\text{N}$  detection in a double-cross polarization experiment is another possibility with the potential for rapid mapping of complicated biochemical pathways in actively metabolizing systems. Naturally,

solid-state single and double cross-polarization signals will arise only from those components of an in vivo system which are at least partially immobilized. These cross-polarization techniques therefore complement the use of Fourier transform  $^{13}\text{C}$  or  $^{15}\text{N}$  nmr which measures the flux of stable isotopes through the soluble pools of in vivo cellular systems (15-17).

#### Literature Cited

1. Chase, G. D. and Rabinowitz, J. L., Principles of Radioisotope Methodology, Burgess Publishing Co., Minneapolis, 1962.
2. Schaefer, J., Kier, L. D., and Stejskal, E. O. Plant Physiol. 1980, 65, 254.
3. Schaefer, J., and Stejskal, E. O., J. Amer. Chem. Soc. 1976, 98, 1030.
4. Pines, A., Gibby, M. G., and Waugh, J. S., J. Chem. Phys. 1973, 59, 569.
5. Gibby, M. G., Griffin, R. G., Pines, A. and Waugh, J. S. Chem. Phys. Letters 1972, 17, 80.
6. Jacob, G. S., Schaefer, J., Stejskal, E. O. and McKay, R. A. Biochem. Biophys. Res. Comm. 1980, 97, 1176.
7. Schaefer, J., McKay, R. A. and Stejskal, E. O. J. Mag. Reson. 1979, 34, 443.
8. Schaefer, J., Stejskal, E. O., and McKay, R. A. Biochem. and Biophys. Res. Comm. 1979, 88, 274.
9. Schaefer, J., and Stejskal, E. O. in Topics in Carbon-13 NMR Spectroscopy, Volume 3, (G. C. Levy, Editor), John Wiley, New York, 1979, 284-324.
10. Schaefer, J., Skokut, T. A., Stejskal, E. O., McKay, R.A. and Varner, J. E. Proc. Natl. Acad. Sci. USA, Oct., 1981.
11. Schaefer, J., Stejskal, E. O., Steger, T. R., Sefcik, M. D., and McKay, R. A. Macromolecules 1980, 13, 1121.
12. Schaefer, J., Stejskal, E. O., and McKay, R. A. J. Mag. Reson., in review.
13. Huffaker, R. C. and Peterson, L. W. Ann. Rev. Plant Physiol. 1974, 25.
14. Skokut, T. A., Varner, J. E., Schaefer, J., Stejskal, E. O., and McKay, R. A. Plant Physiol. (Suppl.) 1979, 63, 46.
15. Shulman, R. G., Brown, T. R., Ugurbil, K., Ogawa, S., Cohen, S. M., and den Hollander, J. A. Science 1979, 205, 160.
16. Llinas, M., Wüthrich, K., Schwotzer, W., and von Philipsborn, W. Nature 1975, 257, 817.
17. Lapidot, A. and Irving, C. S. Proc. Natl. Acad. Sci. USA 1977, 74, 1988.

RECEIVED February 19, 1982.

# NMR Spectroscopy at High Pressure

JIRI JONAS

University of Illinois, Department of Chemistry, Urbana, IL 61801

The field of NMR spectroscopy at high pressure has been discussed in several recent review articles.(1-4) It has been well documented that for providing rigorous experimental tests of current theoretical models of liquids, one has to use pressure as an experimental parameter and separate the effects of density and temperature on molecular motions and interactions. This article will discuss our recent developments in the field of NMR spectroscopy at high pressure and, in particular, will focus on multinuclear high resolution NMR FT spectroscopy at high pressure. Two illustrative examples of this specific technique are given. First, the  $^{13}\text{C}$  NMR experiments of rhodium carbonyl clusters under high pressures of  $\text{CO}/\text{H}_2$  illustrate the promising future of the high resolution, high pressure FT NMR in studies of homogeneous catalytic processes.(4) Second example deals with the investigation of the pressure effects on conformational inversion in cyclohexane. (5) This represents the first experiment which has shown conclusively the importance of the pressure dependent collisional contribution to isomerization reactions as predicted by recent stochastic models of isomerization dynamics in liquids.

In order to illustrate the scope and range of high pressure NMR experiments, the next part of the article discusses our recent results on relaxation and transport behavior of compressed supercritical water. The article finishes with a brief account of application of high pressure NMR to studies of the dynamic structure of various disordered systems.

## Multinuclear High Resolution FT NMR at High Pressure

High resolution NMR spectroscopy at high pressures represents one of the promising new areas of research at high pressure. Recent advances in magnet technology have resulted in the development of magnets capable of attaining a high homogeneity of the magnetic field over the sample volume so that even without sample spinning, one can achieve very high resolution. At the same time, the Fourier transform techniques make all these high

0097-6156/82/0191-0199\$06.00/0  
© 1982 American Chemical Society

resolution experiments much easier to be performed at high pressures than it was the case with classical CW techniques. We have recently described (6) a high resolution, high pressure NMR probe which is suitable for superconducting magnets and which has a number of features which are important for future applications of this specific NMR technique: i) wide pressure and temperature range; ii) high resolution ( $5 \times 10^{-9}$  for 6 mm samples); iii) contamination free sample cell.

In a collaborative effort with Dr. B. T. Heaton from the University of Kent at Canterbury, England, we have recently applied this technique (4) to measure  $^{13}\text{C}$  spectra of rhodium carbonyl clusters under high pressure of CO and  $\text{H}_2$ . In connection with the efforts by the petrochemical industry to find catalytic syntheses which use CO and  $\text{H}_2$  there is increasing evidence that transition metal carbonyl clusters are involved in the catalytic synthesis of ethylene glycol and in the Fischer Tropsch and related reactions.

These catalytic reactions require reasonably high pressures and temperatures and, so far, infrared spectroscopy has been the only spectroscopic technique used to monitor them. Although useful information has been obtained in this way, it is generally impossible to obtain unambiguous structural identification and mechanistic inter-/intra-exchange data which are of importance in establishing reactivity patterns of intermediates that are present under these conditions. These are a prerequisite for the basic understanding of the mechanism of these catalytic processes.

Multinuclear NMR studies at atmospheric pressure, i.e., under less extreme conditions, have yielded valuable structural and mechanistic information on transition metal carbonyl clusters and both the above limitations suffered by infrared spectroscopy have now been overcome by measuring high resolution NMR spectra at high pressure. Well-resolved  $^{13}\text{C}$  NMR spectra, with excellent signal/noise, have been obtained on the catalytic system involved in the formation of ethylene glycol.

The pentanuclear cluster,  $[\text{Rh}_5(\text{CO})_{15}]^-$ , has recently been isolated from the low pressure (ca. 10 bar) reaction of  $[\text{Rh}_{12}(\text{CO})_{30}]^{2-}$  with carbon monoxide. Because of the involvement of this cluster in the catalytic synthesis of ethylene glycol from synthesis gas, it was of interest to monitor this reaction by  $^{13}\text{C}$  n.m.r. spectroscopy at higher pressures of carbon monoxide and in the presence of hydrogen to see whether other species are formed.

The 45.2 MHz  $^{13}\text{C}$  n.m.r. spectrum of  $(\text{NMe}_3\text{Bz})_2[\text{Rh}_{12}(\text{CO})_{30}]$  in this high pressure cell, (Figure 1a, b), has good signal/noise (50:1) and resolution (ca. 25 Hz) and is similar to that obtained previously on a conventional high resolution spectrometer. Upon pressurizing with up to 575 bar of CO (13.7%  $^{13}\text{C}$ ) at  $-52^\circ\text{C}$ , there is a progressive transformation of  $[\text{Rh}_{12}(\text{CO})_{30}]^{2-}$  into  $[\text{Rh}_5(\text{CO})_{15}]^-$  but, even after ca. 24 h under 77 bar CO and 3 h under 575 bar CO, there is still evidence for unreacted



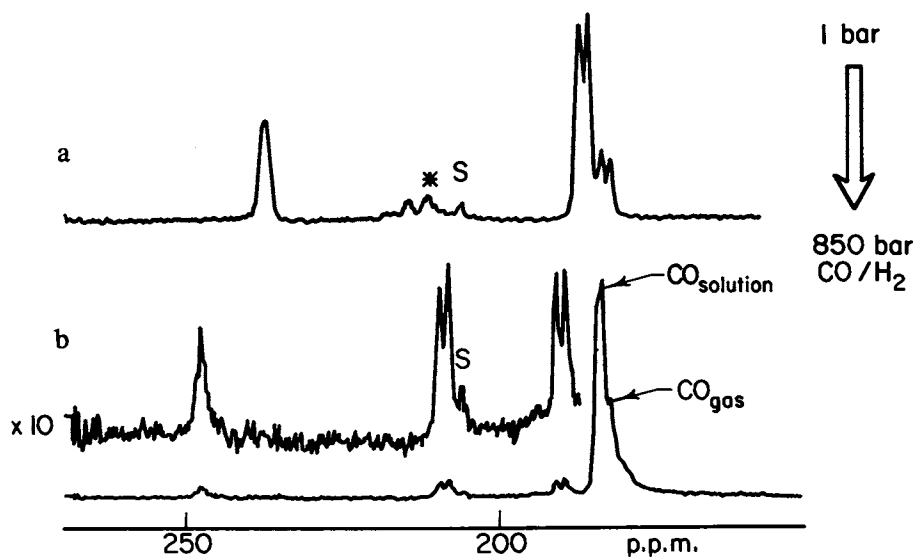


Figure 1. 45.2-MHz  $^{13}\text{C}$  NMR spectra in a high pressure probe a,  $(\text{NMe}_2\text{Bz})_2\text{-}[\text{Rh}_{12}(\text{CO})_{30}]$  at  $-40^\circ\text{C}$  in acetone- $\text{d}_6$ ; and b, after pressurizing (850 bar) with  $\text{CO}/\text{H}_2$  (2.1:1; 13.7%  $^{13}\text{C}$ ) at  $-32.8^\circ\text{C}$ . S = solvent; \* = impurity,  $[\text{Rh}_6(\text{CO})_{15}]^{2-}$ .

$[\text{Rh}_{12}(\text{CO})_{30}]^{2-}$ ; there is no change in the spectrum at this temperature on further pressurizing with  $\text{H}_2$  ( $P_{\text{total}} = 850$  bar;  $\text{CO}:\text{H}_2 = 2.1:1$ ). Warming to room temperature, followed by cooling to  $-32.8^\circ\text{C}$ , results in complete formation of  $[\text{Rh}_5(\text{CO})_{15}]^-$  (Figures 1a, b); this spectrum is similar to that obtained previously, but, in addition to the resonance due to CO at 184.3 p.p.m., there is a resonance due to CO at 182.0 p.p.m. At room temperature, the spectrum under 1000 bar  $\text{CO}/\text{H}_2$  (2.1:1) is similar to that obtained under 10 bar of CO and consists of a resonance at 247.5 p.p.m. due to the equatorial edge-bridging carbonyls and a broad resonance at ca. 200 p.p.m. due to the remaining carbonyls undergoing intra-molecular exchange.

It is significant that, even under such high pressures of CO, exchange of carbonyls with CO is not fast on the NMR time-scale at low temperatures. Thus, high pressure n.m.r. studies offer the possibility of structural identification of intermediates formed under extreme conditions of reactions of industrial interest and further studies of potential catalytic systems are underway.

The study of the pressure effects on the conformational inversion of cyclohexane in different solvents represents the second illustrative example of the application of high resolution, high pressure FT NMR.

A large number of studies employing different NMR techniques have been devoted to the investigation of the temperature dependence of the ring inversion of cyclohexane. This is not surprising in view of the fact that the problem of cyclohexane inversion represents the seminal problem in conformational analysis. What is surprising, however, that all previous studies have used a single solvent - carbon disulfide, and, that only a limited pressure study (up to 2 kbar) of cyclohexane in quaternary mixture has been performed by Lüdemann et al. (7)

There were two main motivations for our study. First, we wanted to follow the effects of pressure on the conformational inversion of cyclohexane in different solvents: acetone- $d_6$ , carbon disulfide and perdeuterated methylcyclohexane. Secondly, in view of recent theoretical research in the area of stochastic models for isomerization reactions as proposed by Montgomery, Chandler and Berne (8) and by Skinner and Wolynes (9) we attempted to provide the first experimental proof of the theoretical prediction of large pressure effects on the transmission coefficient, or otherwise stated, a large collisional contribution to the activation volume for an isomerization reaction. Our results show that we were successful in both aspects.

It is accepted that the lowest energy path for cyclohexane ring inversion proceeds via a half-chair transition state with the twist boat and its slightly (Figure 2) higher energy pseudo-rotation partner, the boat, as intermediates. When we completed the high pressure NMR measurements, we found that the ring

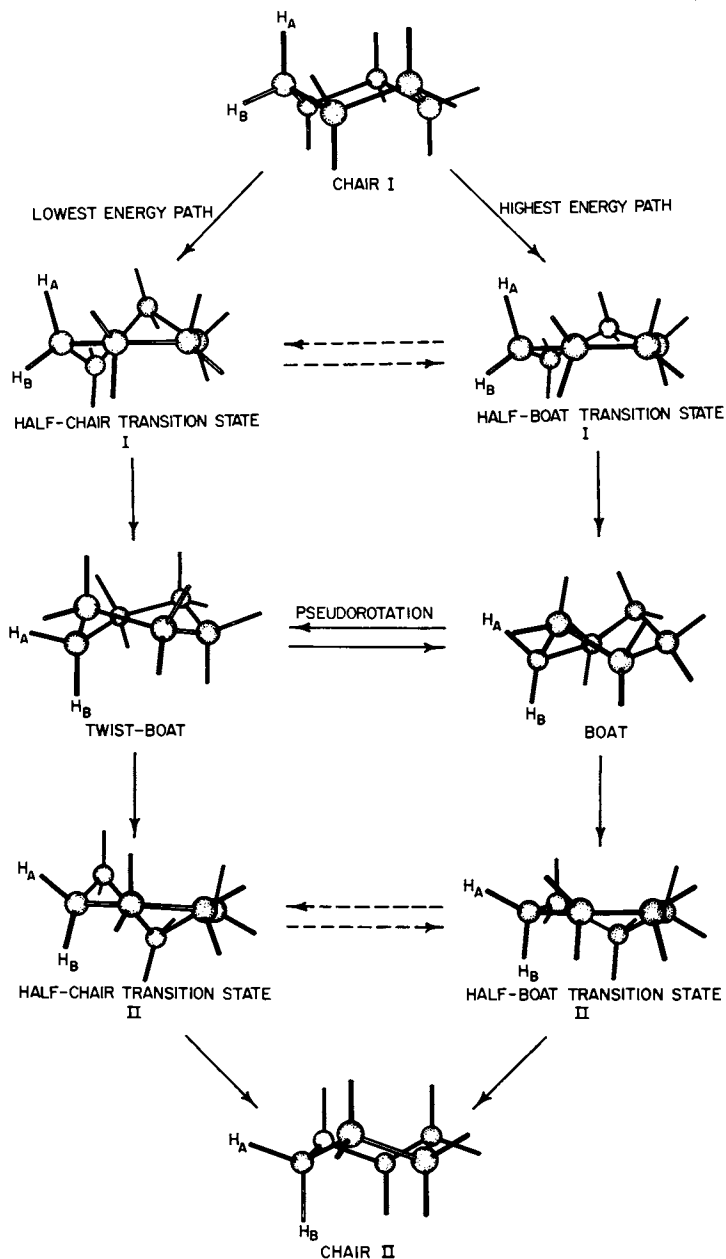


*Figure 2. Representation of the chair-to-chair interconversion process in cyclohexane showing the possible intermediates (boat and twist-boat) and transition states (half-chair and half-boat). The magnetically nonequivalent protons,  $H_A$  and  $H_B$ , undergo mutual exchange during ring inversion.*

inversion rate is accelerated with increasing pressure as can be seen in Figure 3.

It is clear from Figure 3 that the inversion rate exhibits the pressure dependence in the order: acetone- $d_6$ ,  $CS_2$ , and deuterated methylcyclohexane. It is important to emphasize that the slope of the logarithm of the inversion rate is strongly nonlinear with pressure.

In order to understand the results let us briefly outline the main features or better stated, the main results of the stochastic models (8, 9) for the isomerization dynamics. The details can be found in the original papers. (8, 9)

In this model it is proposed that there is a contribution to the activation volume from dynamical effects, because the reaction coordinate is coupled to the surrounding medium. This leads to the result that the transmission coefficient  $\kappa$  (usually assumed to be unity in the conventional transition state theory), is a function of the "collision frequency" which reflects the actual coupling to the surrounding medium. In our case of cyclohexane, which has no dipole moment, we may take the viscosity of the solvent as the measure of the reduced collision frequency. The theoretical calculations (8, 9) have shown that the transmission coefficient is strongly dependent on the collision frequency. This formalism allows us to calculate the collisional (dynamical) contribution to the activation volume. One may write

$$k(t) = \kappa k_{TST} \quad (1)$$

where  $k(t)$  is the observed isomerization rate,  $\kappa$  is the transmission coefficient and  $k_{TST}$  represents the classical rate in the transition state theory. The result of the calculation is that

$$\Delta V_{OBS}^\ddagger = \Delta V_{COLL}^\ddagger + \Delta V_{TST}^\ddagger \quad (2)$$

where  $\Delta V_{OBS}^\ddagger$  is the observed activation volume,  $\Delta V_{COLL}^\ddagger$  is the collisional contribution to the activation volume, and  $\Delta V_{TST}^\ddagger$  has its usual meaning. For cyclohexane one may estimate  $\Delta V_{TST}^\ddagger$  to be  $-1.5 \text{ cm}^3/\text{mole}$ .

According to the stochastic model the transmission coefficient is dependent on the collision frequency, i.e., on the strength of the coupling to the surrounding medium. The theory predicts that at weak coupling (inertial regime) the increase of pressure leads to the increase in collisional frequency with the subsequent increase in the inversion rate (or  $\kappa$ ). On the other hand, in the strong coupling limit (diffusive regime) the increase in pressure (collisional frequency) slows down the isomerization rate.

After analyzing our experimental data we were pleased to find results given in Figure 4. The observed activation volume  $\Delta V_{OBS}^\ddagger$  is strongly pressure dependent as is the collisional

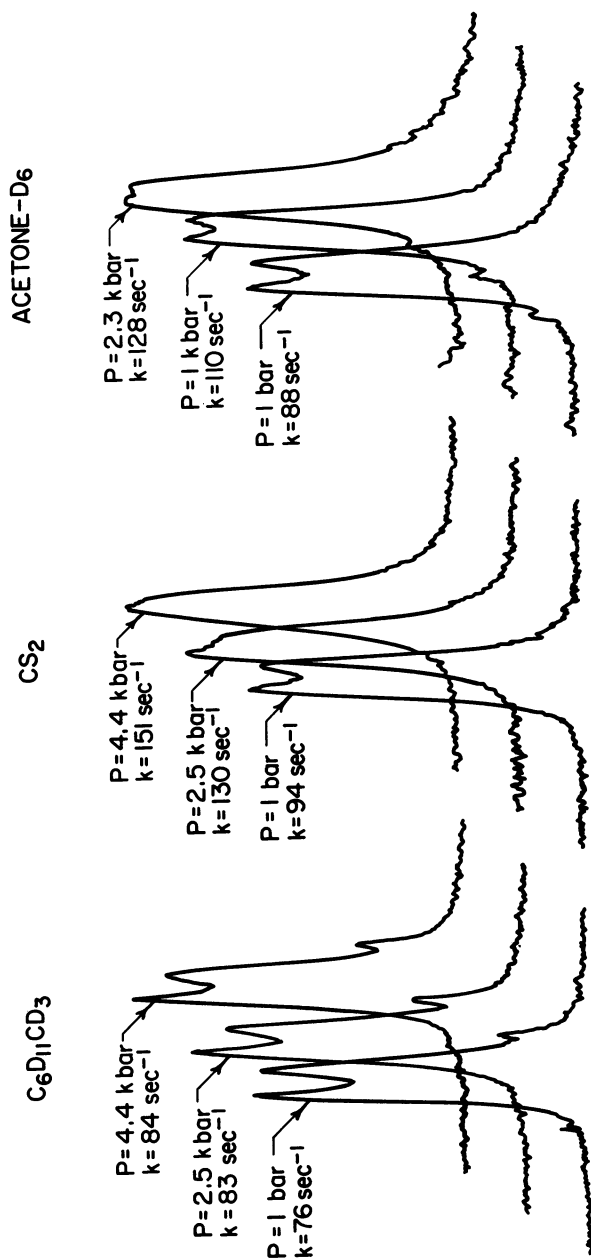


Figure 3. Experimental NMR spectra of cyclohexane at 218 K illustrating the effect of solvent and pressure on the ring-inversion process.

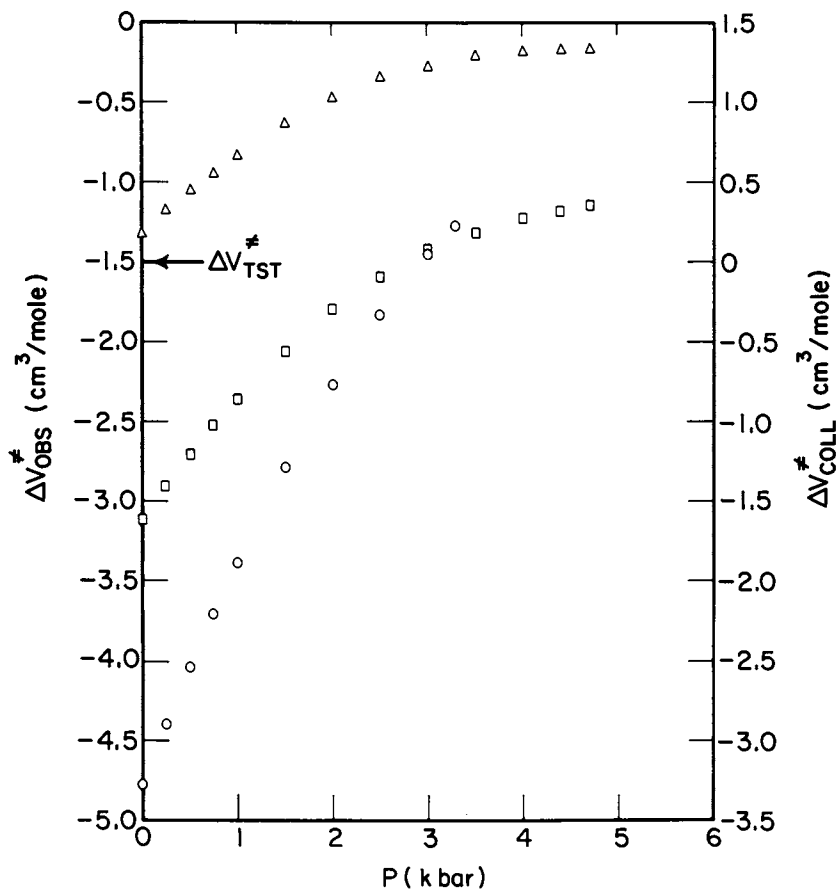


Figure 4. Pressure and solvent dependence of the volumes of activation at 225 K.  $\Delta V_{OBS}^{\ddagger}$  is obtained from a plot of the rate constant vs. pressure.  $\Delta V_{TST}^{\ddagger}$  is estimated to be  $-1.5 \text{ cm}^3/\text{mol}$ . (Ref. 5). Key:  $\Delta$ ,  $C_6D_{11}CD_3$ ;  $\square$ ,  $CS_2$ ; and  $\circ$ , acetone- $d_6$ .

contribution to the activation volume  $V_{\text{COLL}}^\ddagger$ . One realizes that our solvents are in the intermediate region between the weak coupling and strong coupling limits. Although the previous figure is convincing a better visual representation is accomplished by presenting Figure 5 where we plot the normalized transmission coefficient  $\kappa(P)/\kappa(1 \text{ bar})$  as a function of pressure for the three solvents studied. The acetone and  $\text{CS}_2$  solvents are still in the low coupling region whereas for deuterated methylcyclohexane (high viscosity) one deals already with the strong coupling limit and the  $\kappa$  decreases with the increasing pressure (collision frequency). We emphasize that our results (5) represent the first experimental proof of the theoretical predictions of the stochastic model for the isomerization reactions. Clearly, there is a large contribution to the activation volume from dynamical effects. The experimental data also indicate non-monotonic transition between the inertial and diffusive regimes of isomerization reactions.

#### Relaxation and Transport Behavior of Compressed Supercritical Water

The interesting findings (11) on the effects of pressure on the dynamic structure of water and heavy water in the temperature range up to  $200^\circ\text{C}$  prompted us to investigate the relaxation (12) and transport (13) behavior of compressed supercritical water. From the results obtained in our recent experiments, we shall mention only few experimental findings.

It was surprising to find that the  $T_1$  in supercritical water is a linear function of density up to relatively high densities ( $\rho \approx 1.5\rho_c$ ) (Figure 6). We are aware of a similar study of gaseous methane for which Gerritsma et al. (13) found that the proton  $T_1$  is proportional to  $\rho$  up to densities well above the critical density. What is even more important is that the  $T_1/\rho$  value obtained at these higher densities was in agreement with the  $T_1/\rho$  value obtained by Rajan et al. (14) for low density methane gas. Rajan et al. (14) have discussed in detail the analysis of the proton  $T_1$  data in methane and in methane mixtures with inert gases.

The fact that  $T_1$  is proportional to  $\rho$  offered an interesting opportunity to analyze the proton  $T_1$  data in supercritical water using the approach employed successfully to interpret the relaxation data of dilute gases. The  $T_1$  spin-rotation interaction mechanism dominates the observed proton relaxation rate in compressed supercritical water. The  $T_1^{\text{SR}}$  data were analyzed on the basis of the assumption that the collision modulated spin-rotation interactions can be described by a single correlation function which is an exponential function of time. In dilute gases composed of linear, spherical top and symmetric top molecules, the analysis of the  $T_1$  relaxation data has shown (15) that

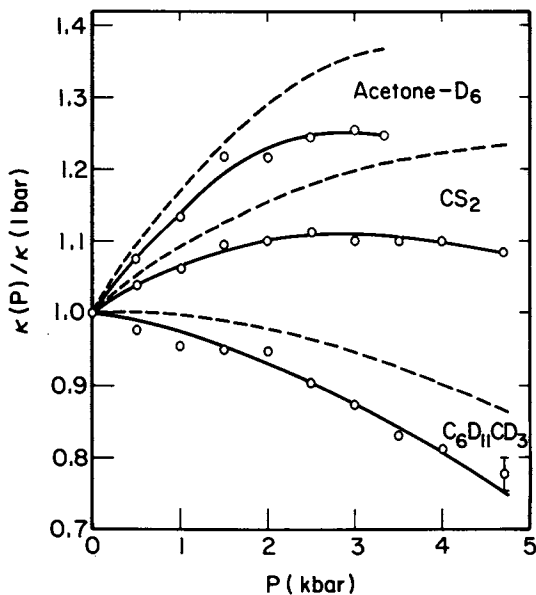


Figure 5. Reduced transmission coefficient as a function of pressure and solvent at 225 K. The circles are values calculated from experimental rate constants using  $\Delta V^{\ddagger}_{TST} = 1.5 \text{ cm}^3/\text{mol}$ . The lines represent values obtained from  $\Delta V^{\ddagger}_{OBS}$  in Figure 4 with  $\Delta V^{\ddagger}_{TST} = 1.5 \text{ cm}^3/\text{mol}$  (—) and  $\Delta V^{\ddagger}_{TST} = -1.0 \text{ cm}^3/\text{mol}$  (---).

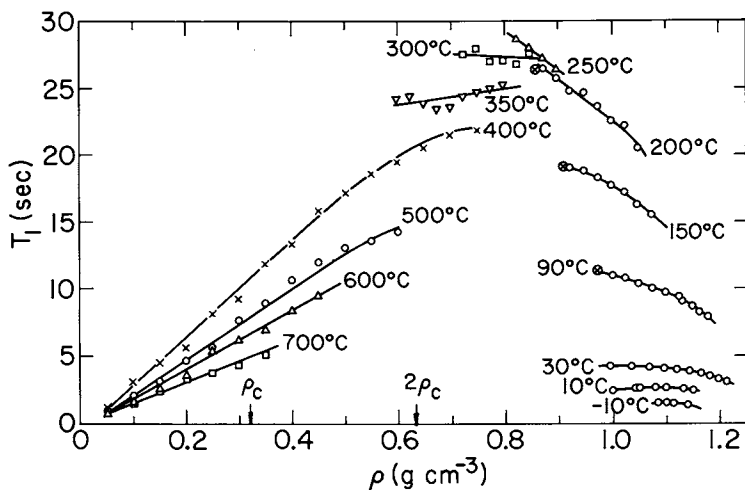


Figure 6. The proton spin-lattice time,  $T_1$ , in water as a function of temperature and density (Ref. 11). The supercritical values are at temperatures greater than  $T_c = 374^\circ\text{C}$ .



$1/T_1^{SR}/\rho \propto T^{-3/2}$ . A plot of  $\ln T_1^{SR}/\rho$  vs  $\ln T$  for supercritical water is given in Figure 7. The error bars represent plus and minus one standard deviation of the values of  $\ln T_1^{SR}/\rho$  at the various temperatures. The linearity of the plot shows that a relationship

$$T_1^{SR}/\rho = 1.14 \times 10^7 T^{-2.0} \quad (3)$$

with  $T_1^{SR}$  in sec.,  $\rho$  in  $\text{gcm}^{-3}$ , and  $T$  in  $^\circ\text{K}$ , holds over the temperature and density range studied. In comparison with other gases, the  $T_1^{SR}/\rho \propto T^{-2}$ . To the best of our knowledge, such a strong temperature of  $T_1^{SR}/\rho$  dependence has not been observed for other gases. In addition, we were able to calculate the effective cross section for the transfer of angular momentum,  $\sigma_{\text{eff}}$ , which show a strong temperature dependence ( $\sigma_{\text{eff}} \propto T^{-1.5}$ ), and which are several times larger than the kinetic cross section. This example clearly illustrates the high information content of high pressure NMR experiments on compressed supercritical fluids, even in the case of a complex fluid such as water.

The self-diffusion coefficients,  $D$ , of compressed supercritical water have been measured as a function of pressure in the temperature range  $400^\circ\text{C}$  to  $700^\circ\text{C}$  using the NMR spin-echo technique. (12) The experimental diffusion data were compared to theoretical predictions based on a dilute polar gas model using a Stockmayer potential for the evaluation of collision integrals and a temperature dependent hard sphere diameter. The empirical expression  $\rho D \propto T^n$  where  $n = 0.76$  fits the experimental data to within  $\pm 10\%$  over the entire density and temperature region studied. The value of the exponent  $n = 0.76$  agrees favorably with the  $n$  values found for diffusion of other gases. The product  $\rho D$  is density independent under isothermal conditions which indicates that two-body collisions dominate the diffusion behavior. This finding is in agreement with our earlier results for proton relaxation in compressed supercritical water which were analyzed using a binary collision approximation and a collision function which is an exponential function of time. The hydrodynamic Stokes-Einstein equation appears to hold at densities above  $\rho_c$ .

### Dynamic Structure of Disordered Materials

The versatility and range of applications of NMR high pressure techniques can further be illustrated on three specific studies dealing with the dynamic structure of various disordered materials. The high pressure experiments on three systems are briefly discussed: i) molecular motions in highly viscous liquid - glycerol; ii) lithium hopping motion in  $\text{Li}_{0.94}\text{TiS}_2$ ; the lithium intercalated compound of  $\text{TiS}_2$  and iii) temperature behavior of activation volumes for various NMR relaxation times in polybutadiene.

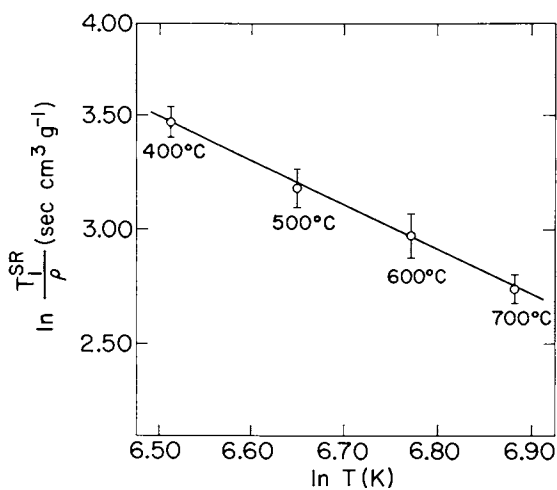


Figure 7. Plot of  $\ln T_1^{SR}/\rho$  vs.  $\ln T$  for supercritical water over the range of densities and temperatures studied. (Reproduced, with permission, from Ref. 11. Copyright 1981, American Institute of Physics.)

The main reason for including the few remarks on the NMR study of selectively deuterated glycerol (16) is to bring attention to the fact that in contrast to the number of experimental and theoretical studies of motions in low viscosity ( $\eta \approx 0.01\text{P}$ ) liquids very few investigations dealing with molecular dynamics in viscous fluids ( $\eta > 1\text{P}$ ) have been reported. In particular, the high pressure experiments offer great promise because the ability of varying viscosity over many orders of magnitude in viscous liquids should provide an advantage over nonviscous liquids in testing competing theories.

We have carried out deuteron magnetic resonance relaxation measurements in selectively deuterated glycerol over a wide range of temperature and pressure. Glycerol- $\text{d}_4$ ,  $(\text{D}_2\text{COH})_2\text{CHOH}$ , and glycerol- $\text{d}_3$  ( $\text{C}_3\text{H}_5(\text{OD})_3$ ) were studied. Glycerol was chosen for this study for several reasons: (1) it supercools readily; (2) the viscosity can be varied over many orders of magnitude ( $5\frac{1}{2}$  orders of magnitude over our temperature and pressure range), (3) although extensive hydrogen bonding is expected in glycerol, the molecule is small compared to most viscous liquids with few internal rotations; and (4) glycerol has been widely studied as a function of pressure and temperature using a number of different experimental techniques. At this point, let us focus on one specific question: What are the relative values of reorientational times for the deuterons on the carbon backbone compared to those of the hydroxyl group?

The temperature dependence of the deuteron  $T_1$  in glycerol- $\text{d}_4$  plotted at different pressures is given in Figure 8. An analogous dependence was found for glycerol- $\text{d}_3$  and it was found that the  $T_1$  minima for glycerol- $\text{d}_3$  and,  $\text{-d}_4$ , occur at the same temperatures and, in addition, along an isotherm, the  $T_1$  minima occur at the same pressure. Independent of the model of reorientation considered, this indicates that reorientation of the hydroxyl groups and the carbon backbone are strongly correlated. A possible physical picture is that internal reorientation about the C-C bond can only occur when a hydrogen bond is broken thus allowing reorientation of the hydroxyl group. Overall molecular tumbling of a molecule or cluster of molecules will be equally effective in causing decay of both the hydroxyl and C-D reorientational correlation functions. Many additional results which elucidated the details of motional dynamics in glycerol have been obtained and discussed in the original study.(16)

The next application deals with the investigation of high pressure effects (17) on the lithium motion in the  $\text{Li}_{0.94}\text{TiS}_2$ . The intercalation compound  $\text{Li TiS}_2$  is being examined as a potential cathode material in<sup>x</sup>reversible battery systems. Previous studies of the ionicity and transport properties of the guest Li cations indicated that Li is substantially ionized and highly mobile, with hopping among octahedral sites in the van der Waals gap region between  $\text{TiS}_2$  layers occurring at  $10^{-6}$  sec at

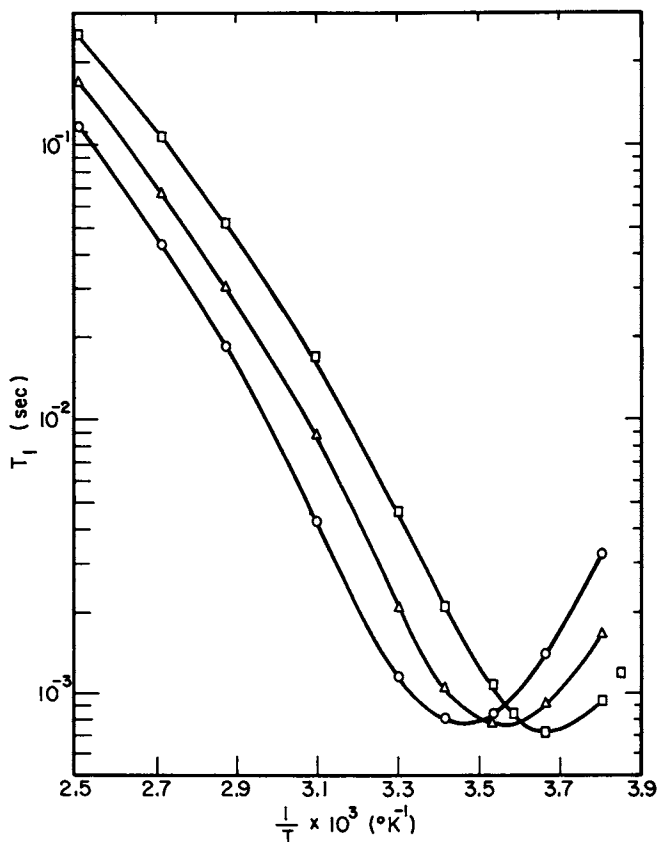


Figure 8. Temperature and pressure dependence of the deuteron spin-lattice relaxation time in glycerol- $d_4$ . Key:  $\square$ , 1 bar;  $\triangle$ , 2000 bar; and  $\circ$ , 4000 bar. (Reproduced, with permission, from Ref. 16. Copyright 1971, American Institute of Physics.)

300 K. Like other superionic conductors,  $\text{LiTiS}_2$  exhibits a prefactor anomaly in the NMR correlation time<sup>x</sup>,  $\tau_c^2$  applying a conventional activation energy model for the correlation time

$$\tau_c = \tau_0 \exp(E_a/k_B T) \quad (4)$$

where  $\tau_0$  is the prefactor and  $E_a$  is the activation energy for hopping,  $\tau_c$  values as long as  $10^{-7} - 10^{-9}$  sec were observed in a number of superionic conductors. (18, 19) These values contrast with  $\tau_0 10^{-12} - 10^{-13}$  sec expected if  $\tau_0$  were directly related to atomic vibrations. Two explanations for this anomaly have been proposed: a breakdown of absolute rate theory (18) and the effects of low dimensionality. (19) We reported the first observation of pressure effects on the  $^7\text{Li}$  NMR lineshape in  $\text{Li}_{0.94}\text{TiS}_2$ .

Figure 9 shows the typical spectra at 1 bar and 5 kbar which are slightly asymmetric because of the anisotropic magnetic response of  $\text{TiS}_2$  layers. The lineshapes correspond to the first order quadrupole powder pattern of an  $I = 3/2$  nucleus. The quadrupole coupling constant,  $e^2qQ/h = 31.7 \pm 0.7$  kHz, is estimated from the separation between the two satellite peaks.

The temperature dependence of the width of the central line is shown in Figure 10. Since  $e^2qQ/h$  is small, second order quadrupole shifts of the resonance line can be neglected and the linewidth of the central transition is expected to be mainly due to the dipole interaction between the Li nuclei. A constant linewidth of 3.1 G corresponding to the rigid lattice value of the linewidth is observed below  $0^\circ\text{C}$ . The motional narrowing between  $0^\circ\text{C}$  and  $140^\circ\text{C}$  is attributed to the reduction of the dipole interaction caused by the Li hopping motion. Above  $140^\circ\text{C}$ , the dipolar interaction is averaged and a residual linewidth of 0.9 G is observed. The difference value 2.2 G is almost exactly the width predicted from rigid lattice second moment calculations. Figure 10 reveals two important qualitative features of the pressure effects on Li ion motion. First, line narrowing occurs at higher temperatures under 5 kbar pressure, reflecting an inhibition of the diffusion process. Second, the broadening curve is steeper at 5 kbar than at atmospheric pressure, suggesting a higher activation energy for the diffusion process. These observations can be quantified by calculating the correlation time for Li motion employing the usual expression. The correlation times at each pressure lie on a straight line which can be represented by Equation 4. We calculated  $E_a = 4.7 \pm 0.5$  kcal/mole,  $\tau_c = 2.3 \times 10^{-8}$  sec at 1 bar and  $E_a = 7.6 \pm 0.5$  kcal/mole<sup>-1</sup>,  $\tau_0 = 4.9 \times 10^{-10}$  sec at 5 kbar.

It is interesting to point out that the barrier for the Li hopping increases with increasing pressure although the quadrupole coupling constant remains constant. The other important finding is the prefactor anomaly, i.e., an extremely long value

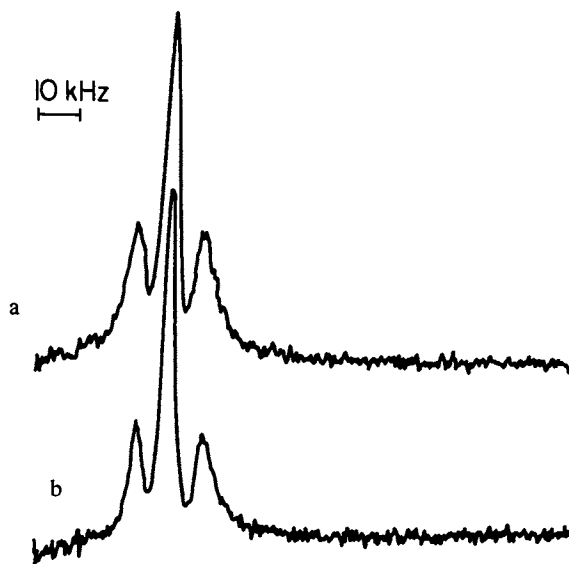


Figure 9.  ${}^7\text{Li}$  resonance spectra in  $\text{Li}_{0.94}\text{TiS}_2$  ( $52.1^\circ\text{C}$ ) at 70 MHz. Key: a,  $P = 5$  kbar; and b,  $P = 1$  bar. (Reproduced, with permission, from Ref. 17. Copyright 1981, Pergamon Press.)

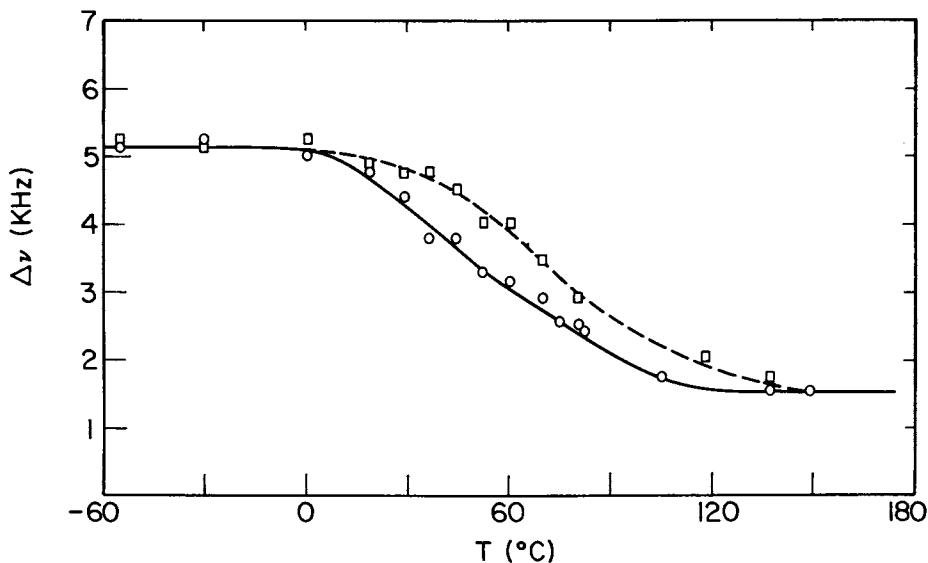


Figure 10. Temperature variation of the width of the central line at 1 bar (○) and at 5 kbar (□) in  $\text{Li}_{0.94}\text{TiS}_2$ . (Reproduced, with permission, from Ref. 17. Copyright 1981, Pergamon Press.)

of  $\tau_0$ , which decreases by a factor of fifty at 5 kbar pressure. The observed pressure effects on the prefactor favor the explanation by Huberman and Boyce (18) for the prefactor anomaly in terms of a breakdown of the absolute rate theory. Again, pressure as an experimental variable proved to be essential for providing information on the nature of the prefactor anomaly in lithium intercalated compounds. It is clear that analogous high pressure experiments on superionic conductors will help to elucidate the behavior of the highly interesting systems of potential practical interest.

Only one illustrative example of a NMR relaxation study of polymers at high pressure will be presented. In an earlier study of several elastomers Liu and Jonas (20) have found that the activation volume  $\Delta V^\ddagger$  exhibits a strong temperature dependence. The  $\Delta V^\ddagger$  for the proton  $T_1$  was found to increase with increasing temperature, while the opposite trend in  $\Delta V^\ddagger$  with temperature is observed for viscoelastic and dielectric measurements. (21) In our study of polybutadienes, (22) we were able to provide an explanation for this observation. The activation volume  $\Delta V^\ddagger$  for the various relaxation processes have been calculated and the results for high molecular weight polybutadiene are plotted in Figure 11. One can see that  $\Delta V^\ddagger$  for  $T_1$  increases with temperature whereas  $\Delta V^\ddagger$ 's for  $T_2$  and  $T_{10}$  are found to decrease with temperature in agreement with the reported  $\Delta V^\ddagger$  values obtained for viscoelastic and dielectric measurements. The reason why the temperature behavior of  $\Delta V^\ddagger$  for  $T_1$  is different from that obtained for  $T_2$ ,  $T_{10}$ , viscoelastic and dielectric measurements is related to the fact that  $T_1$  is determined by high frequency localized chain motions whereas the other relaxation parameters and techniques reflect low frequency motions, i.e., motions of larger segments of polymers.

The results of the various studies show convincingly the importance and scope of applications of NMR spectroscopy at high pressure. A variety of important problems in chemistry and physics can be solved by this specific technique.

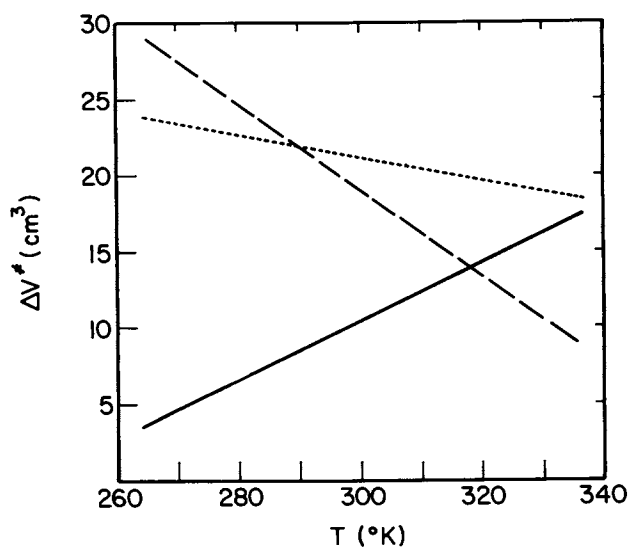


Figure 11. Temperature dependence of activation volumes for proton  $T_1$  (—),  $T_2$  (---), and  $T_{1\rho}$  (· · ·) in polybutadiene. (Ref. 22).



Acknowledgements

This research was partially supported by the National Science Foundation under Grant NSF CHE 79-12-8011420, by the Department of Energy under Contract DE-AC02-76ER01198, and by the Air Force Office of Scientific Research under Grant US AFOSR 81-0010.

Literature Cited

1. Jonas, J. Am. Rev. Phys. Chem. 1975, 26, 167.
2. Jonas, J.; Kelm, H., Ed.; "NATO ASI, on High Pressure Chemistry"; D. Reidel Publ. Co.: Dordrecht, Holland, 1978; p. 65.
3. Jonas, J. Rev. Phys. Chem. Japan 1980, 50, 19.
4. Heaton, B. T.; Jonas, J.; Eguchi, T.; and Hoffman, G. A. Chem. Commun. 1981, 331.
5. Hasha, D. L.; Eguchi, T.; and Jonas, J. J. Chem. Phys. 1981, 75, 1571.
6. Jonas, J.; Hasha, D. L.; Lamb, W. J.; Hoffman, G. A.; and Eguchi, T. J. Magn. Resonance 1981, 42, 169.
7. Lüdemann, H. D.; Rauchschalbe, R.; and Lang, E. Angew. Chem. Int. Ed. Engl. 1977, 16, 331.
8. Montgomery, J. A., Jr.; Chandler, D.; and Berne, B. J. J. Chem. Phys. 1979, 70, 4056.
9. Skinner, J. L. and Wolynes, P. G. J. Chem. Phys. 1978, 69, 2143.
10. Jonas, J. Comments Solid State Phys. 1977, 8, 29.
11. Lamb, W. J. and Jonas, J. J. Chem. Phys. 1981, 74, 913.
12. Lamb, W. J.; Hoffman, G. A.; and Jonas, J. J. Chem. Phys. 1981, 74, 6875.
13. Gerritsma, C. J.; Oosting, P. H.; and Trappeniers, N. J. Physica 1971, 51, 381.
14. Rajan, S.; Lalita, K.; and Babu, S.V. J. Magn. Resonance 1974, 16, 115.
15. Lalita, K. and Bloom, M. Chem. Phys. Lett. 1971, 8, 285.
16. Wolfe, M. and Jonas, J. J. Chem. Phys. 1979, 71, 3252.
17. Eguchi, T.; Marinos, C.; Jonas, J.; Silbernagel, B. G.; and Thompson, A. H. Solid State Comm. 1981, 48, 919.
18. Huberman, B. A. and Boyce, J. B. Solid State Commun. 1978, 25, 759.
19. Richards, P. M. Solid State Commun. 1978, 25, 843.
20. Liu, N. and Jonas, J. J. Magn. Resonance 1975, 18, 465.
21. Allen, G.; Gee, G.; Lanceley, H. A.; and Mandaraj, D. J. Polymer Sci. 1959, 34, 349.
22. Munie, G. C. Ph.D. Thesis, University of Illinois, Urbana, Illinois, 1980.
23. Smith, D. W. G. and Powles, J. G. Mol. Phys. 1966, 10, 451.

RECEIVED December 21, 1981.

## <sup>13</sup>C Cross-Polarization Magic-Angle

### Spinning NMR Study

#### Amines Adsorbed on $\gamma$ -Alumina Utilizing a Unique Spinner Design

WILLIAM H. DAWSON and STEVE W. KAISER

Union Carbide Corporation, Research and Development Department,  
South Charleston, WV 25303

RUTH R. INNERS, F. DAVID DOTY, and PAUL D. ELLIS

University of South Carolina, Department of Chemistry, Columbia, SC 29208

In recent years there has been an increasing interest in the application of spectroscopic techniques to problems involving the adsorption of molecules on catalytic surfaces. The primary objective of these experiments is centered around the nature of the "adsorbate-surface complex." To date, infrared(1) and nmr spectroscopy(2) have provided the most detailed information, the former being the easiest technique to apply to the problem. The nmr applications have suffered because the high resolution techniques normally used to study liquids cannot be applied with equal success to the study of surface adsorbed species. The exception to these studies has been the elegant partial tensor averaging experiments of Resing(3). In order to obtain a high resolution nmr spectrum of the adsorbate, most experimentalists have resorted to high sample temperatures (typically in excess of 400°K) and surfaces with high surface areas. The former requirement is necessitated by the strong dipolar processes that exist in the absence of rapid molecular motion and the latter condition is needed to observe an nmr resonance in a reasonable period of time.

*A priori*, <sup>13</sup>C NMR spectroscopy would seem to be ideally suited to study adsorbed species. Gay and co-workers(4a-d) recognized this fact several years ago in their pioneering experiments on the adsorption of amines to active surfaces. Olefins have also been the subject of a number of <sup>13</sup>C NMR investigations(4e-f).

The best spectra was obtained with weakly bonded molecules such as the  $\pi$ -bonded olefins that were in rapid equilibrium with the surface bonding sites. When strong bonding as in the case of pyridine bound to alumina was encountered(4a-d) it was necessary to resort to high temperature to provide the necessary line-narrowing. In all of these cases the averaging scheme precludes making a distinction between chemi- and physi- adsorbed species. Therefore one has lost a desirable feature of NMR spectroscopy, namely the ability to observe individual atomic sites in complicated system. Further, under these conditions the bound species undergo rapid transitional motion on the surface. Such a situation brings about a rapid exchange between surface sites and the observed spectrum

0097-6156/82/0191-0219\$06.00/0

© 1982 American Chemical Society

becomes the result of an average overall sites. In analyzing such a spectrum one is forced to apply only the simplest of models for chemisorption, the validity of which often rests upon data from other experimental techniques. To this extent one has also lost the ability to obtain from a NMR new information to complement other surface analysis techniques.

The present work details experiments that demonstrate the utility of natural abundance  $^{13}\text{C}$  nmr spectroscopy to study molecules adsorbed on active surfaces. These experiments are performed at ambient temperature and with low surface coverage on moderate surface areas,  $220\text{ m}^2/\text{g}$ . The cross-polarization technique of Pines, Gibby and Waugh(5) and the magic angle spinning(MAS) methods of Schaefer and Stejskal(6) have been discussed in detail elsewhere and will not be reviewed here. However, the development of a high sensitivity(7) and efficient MAS probe(8) is an essential feature of the success of the present approach, and therefore our own particular design for such a probe will be discussed. With these techniques in hand we will apply them to the study of two relatively simple systems: *n*-butylamine(9) and pyridine(10) adsorbed on  $\gamma$ -alumina. Finally, we will briefly discuss the possible extension of these techniques to more complicated systems.

## Experimental

**Magic Angle Spinning Probe.** A detailed analysis of the *rf* design features in a multinuclear solids probe has been published elsewhere(7) and will not be discussed here. However, the design of a high speed cylindrical nmr sample spinners will be briefly discussed. A detailed analysis of this design is given by Doty and Ellis(8). Basically, there have been two types of sample spinners employed for applications to solid state nmr spectroscopy; those after Andrew(11) employing a single conical surface for both the bearing and drive systems(12a-e) or a single bearing and drive surface(12f). The Andrews rotors have the principal advantage of simplicity of construction. However, it is impossible to optimize both the drive efficiency and the stability of such a rotor. The best compromise to date is the rotor design of Bartuska and Maciel (13), the so-called "Bullet design". The principal disadvantage of this approach is the difficulty of obtaining spinning stability with inhomogeneous samples at high speeds when high geometrical filling factors are desirable. For this reason, we have limited our investigation of sample spinner designs to those which employ separate bearing and drive systems. The first such methods was that of Lowe(12a), which consisted of spinning on small nylon axles. However, it appears that this approach is satisfactory only for solid rotors where the balance and concentricity can be maintained to within one part in ten thousand. The asymmetrical radial load produced even in carefully packed powder samples will destroy such a bearing very quickly. The "obvious" solution to this problem is

to use an air lubricated bearing. The first attempts at such a design were made by Alla(12b,c). Our own approach(8) differs from Alla's in several ways, i.e. the air bearing design, the number of drive jets and their location, and the design of the rotor and its associated end plugs. However, before we discuss our approach let's briefly review some of the ideas behind the design of an air bearing.

The radial load that the air bearing must support due to gravity and the impulse from the drive jets is negligibly small compared to the radial load,  $f_r$ , produced by asymmetrical packing of the sample. From Newton's second law we have

$$f_r = m_a \omega^2 r \quad [1]$$

where  $f_r$  is the radial force generated by the asymmetrical mass  $m_a$  at the radius  $r$  with angular velocity  $\omega$ . It is conceivable that  $m_a$  may be as much as 10% of the total sample mass for samples such as granules of polymers or biological gels, but it is more likely to be in the neighborhood of 1% of the total sample mass for carefully packed fine powders. The force produced by one gram sample in a 12 mm rotor with a 1% misbalance at an average radius of 0.4 cm amounts to  $1.6 \times 10^6$  dynes (about 3.6 pounds) at 3.2 kHz and four times that amount at 6.4 kHz. *The bearing must either have a load capacity at least equal to the unsymmetrical radial force, or else the ratio of the radial clearance to the rotor radius must be greater than the ratio of the asymmetrical mass to the total rotor mass.* The former condition implies rotation of the rotor about a *fixed axis*, whereas the latter situation results in the sample rotating about a precessing axis containing the center mass of the rotor plus sample. Clearly, spinning about a *fixed axis* is preferred when high speeds and efficient air utilization are necessary.

When one is forced to spin about a precessing axis containing the center of the mass rotor instabilities occur, which are manifested by an oscillatory movement of the rotor in the stator. When the rotor speed approaches these mechanical resonances there is insufficient drive energy to cross these high  $Q$  oscillations and an upper bound to stable spinning speeds is reached. Such a condition leads to a lower spinning frequency. These resonances are also present when one spins a sample about a *fixed axis*, however they occur at significantly higher frequencies, and therefore, one can spin at a faster rate.

Figure 1 depicts our approach to the design of a high speed cylindrical spinner. It basically consists of three parts: the cylindrical spinner and its associated end caps, the stator which has the drive and air bearing holes, and the stator housing which is coupled to the stator by four O-rings. The spinner is made of  $Al_2O_3$  that is either 8 mm or 12 mm in diameter (with an associated rotor wall thickness of 0.5 mm or 0.75 mm respectively). The end caps are made of either Delrin or Vespel and are sufficiently out of the coil region to present little problem with residual  $^{13}C$  signals

(see subsequent discussions). The drive end cap (we only drive from one end) consists of flutes which afford an efficient combination of impulse and reaction turbine design. The radial clearance between the rotor and the stator is 0.0024 cm for the 8 mm and 0.0027 cm for the 12 mm system. There are four tangential drive jets on the drive end of the stator. The stator contains two circles of 12 equally spaced pocketed air bearing holes. The several additional holes in the center of the stator provide a cooling mechanism for the rotor. The four O-rings on the outside of the stator fulfill several functions (see Figure 2). First, they center the stator within the housing. Further, they provide a mechanism by which one can easily separate the drive air from the source of air for the air bearing. Finally they act as a "suspension system" for the stator in the housing. This latter function provides the dissipative mechanism for the rotor to cross the natural resonance frequencies that the rotor has within the stator. Hence, the rotor can transfer momentum to the stator and the stator can in turn transfer this momentum to the housing via the O-rings. If high mechanical loss elastomers are selected for the O-rings they act analogously to a damping resistor in a high  $Q$  electrical circuit. The reader can convince himself of the validity of the model depicted in Figure 2 where  $m_r$ ,  $m_s$ ,  $m_h$  represent the masses of the rotor, stator and housing respectively. Further,  $k_a$ ,  $k_o$ , and  $k_h$  denote the "force constants" for the air-bearing, O-rings, and stator housing holder, respectively, to the probe body. The analysis of such a model clearly demonstrates the importance of the O-rings and how these natural resonance frequencies arise.

The performance of the system is self explanatory. In the 12 mm system, rotor speeds (packed) of 3.5 to 3.8 kHz can be obtained. In the 8 mm system, speeds in excess of 4 kHz and approaching 5 kHz (if the nerves are willing) can be obtained. The details of the construction of this design along with comments about rotor fatigue and extensions to other sizes of rotors can be found elsewhere(8).

Preparation of the Amine/Alumina Samples. The samples were prepared in the following way:  $\gamma$ -alumina (Norton 6173; 220 m<sup>2</sup>/g) was placed in a quartz u-tube, immersed in a fluidized sand and heated to 500°C. Dry helium was passed through the tube for two hours at which time the temperature was lowered to 300°C. The helium flow was diverted through a saturator containing the cold (0°C) amine. The helium/amine mixture was allowed to pass over the alumina until the surface was saturated as determined by the appearance of amine at the thermal conductivity detector of a gas chromatograph positioned on the downstream side of the u-tube. The saturator was then bypassed. The helium flow was maintained through the 300°C u-tube until the desorption of excess amine was no longer detected in the effluent. By calibrating the apparatus with the gas chromatograph it is possible to quantitate this amine/alumina titration. For the case of pyridine, the pyridine/alumina sample was found to have 0.47% pyridine by weight. Based on a

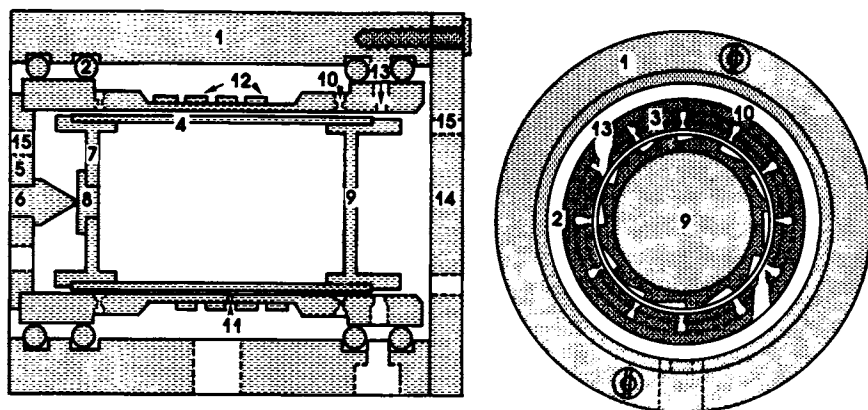


Figure 1. Side and end section views of the high speed cylindrical NMR sample spinner assembly. Key: 1, housing; 2, O-ring; 3, stator; 4, rotor; 5, lower end plate; 6, bearing point; 7, lower rotor end cap; 8, bearing button; 9, rotor drive end cap; 10, air bearing orifice and pocket; 11, cooling air hole; 12, NMR receiver coil; 13, turbine drive jet; 14, upper end plate; and 15, exhaust holes. (Reproduced, with permission, from Ref. 8.)

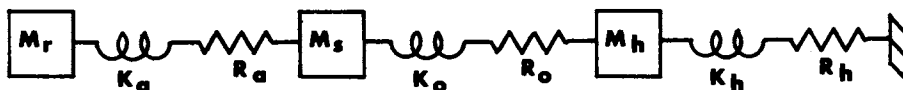


Figure 2. A model for obtaining cylindrical mode resonant frequencies of the rotor assembly is shown. The masses of the rotor, stator, and housing are  $m_r$ ,  $m_s$ , and  $m_h$ , respectively; and  $K_a$ ,  $K_o$ , and  $K_h$  are the stiffnesses of the air bearing, O-rings, and housing support structure. The suspension losses,  $R_a$ ,  $R_o$ , and  $R_h$ , are shown explicitly as mechanical resistances (force/velocity). Typically, the rotor mass is less than half the stator mass and about one-tenth the housing mass. The air bearing is about twice as stiff as the O-rings and about  $10\times$  stiffer than the housing support. The resistances of the air bearing and the housing support are small compared to the resistance of the O-rings. (Reproduced, with permission, from Ref. 8.)

specific area for pyridine of  $29 \text{ \AA}^2$  it can be estimated that the amount of surface covered by the pyridine is  $11 \text{ m}^2/\text{g}$  or 5% of a monolayer. Similar coverages exist for the n-butyl amine. Operating under a dry nitrogen atmosphere the granular sample was packed into an aluminum oxide NMR rotor.

### The $^{13}\text{C}$ NMR of Amines on $\gamma$ -Alumina

n-Butyl Amine. The question of surface acidity of aluminum oxides, silicates and mixed alumina-silicates is one of long standing interest(1,2,14). The problem is one of both practical and theoretical concern. Many industrially important catalytic reactions are based on these materials and their reactivity is determined to a large extent by the nature of surface acid sites(1,2,15). It is of prime interest to identify these catalytically active sites to ascertain whether they are of Brønsted or Lewis type and to determine their relative acidity.

Several methods have been used to study surface acidity, including the most straightforward approach of direct titration with acid-base indicators(16). Infrared spectroscopy has been extensively employed to examine those interactions involving surface hydroxyl groups(17). Widespread use of the IR method stems from its sensitivity and its adaptability to a variety of adsorbate-adsorbate systems. Proton NMR spectroscopy has similarly provided valuable information that is both quantitative and sensitive to the motions of the adsorbed species(2,18). More recently,  $^{13}\text{C}$  NMR has been used to advantage(4,19). For example, Gay and co-workers(4) have employed  $^{13}\text{C}$  nmr spectroscopy as a means of following the titration of surface acid sites with aromatic nitrogen bases. To date such studies have employed standard high resolution nmr techniques which are able to yield spectra with suitable resolution only in cases where the molecules are undergoing rapid motion on the surface. For the case of strongly adsorbed species it has been necessary to study the samples at elevated temperatures in order to induce enough motion to sharpen the resonances. This approach represents a serious limitation of investigating the nature of surface-adsorbate interactions by nmr. The recently developed technique of magic angle spinning in conjunction with high power decoupling provides an alternative method of narrowing the lines and avoids this limitation. We report here our CP-MAS results for n-butylamine adsorbed on  $\gamma$ -alumina(20).

The spectrum on n-butylamine on  $\gamma$ -alumina is shown in the Figure 3a(22). There are six prominent resonances, two of which are readily assigned to the  $\gamma$ -methylene and methyl carbons by direct comparison with the liquid phase spectrum. These resonances are only slightly shifted upon adsorption. The remaining four resonances arise from the two  $\alpha$  and  $\beta$  methylene carbons, from which we conclude that at least two types of chemically different butylamine species are present on the surface.

The existence of well resolved resonances demonstrates that if

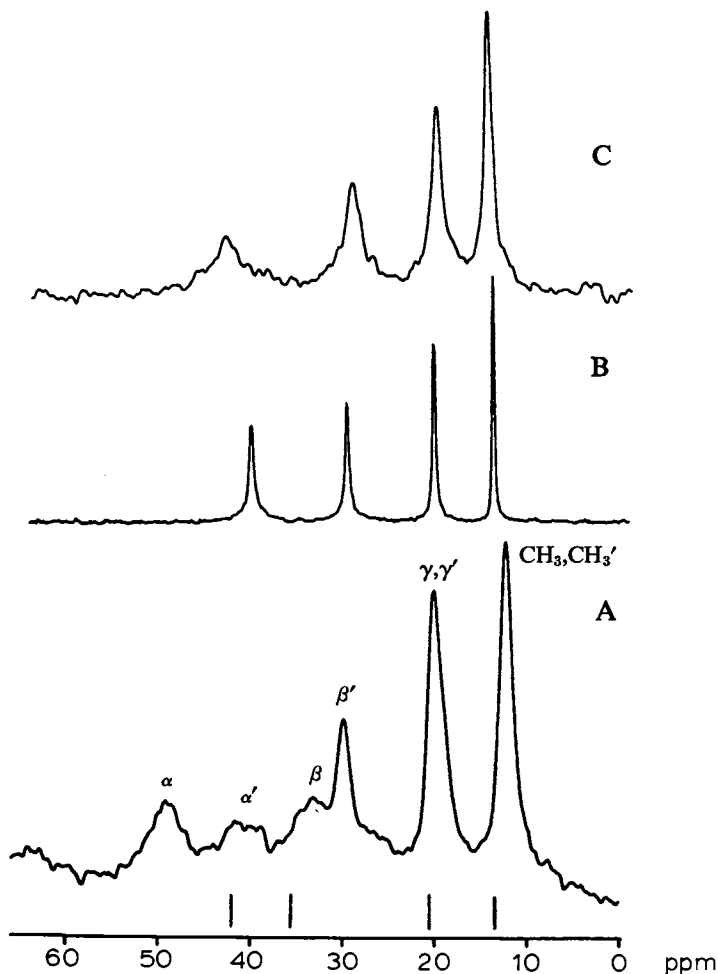


Figure 3. Carbon-13 CP-MAS spectra of *n*-butylamine. Key: A, adsorbed on  $\gamma$ -alumina (3800 accumulations), the vertical bars indicate  $^{13}\text{C}$  chemical shifts for liquid phase *n*-butylamine given in Ref. 25; B, the solid HCl adduct (146 accumulations); and C, the solid  $\text{BCl}_3$  adduct (212 accumulations).



surface diffusion is occurring, then the rate is not comparable to the spinning rate ( $\sim 3.2$  kHz) (23). Further, if site exchange is occurring then the rate must be slow compared to the chemical shift difference between the two species of the surface. Therefore, this spectrum is consistent with a picture whereby the nitrogen of the n-butylamine is firmly anchored to the surface. In all probability the system is executing rapid albeit limited angular diffusion about the bond axis connecting the surface to the nitrogen with the motion of the alkyl chains increasing as one moves away from the surface.

The appearance of four resonances in the region expected for the two  $\alpha$  and  $\beta$  carbons of the alkyl group is consistent with there being two quite different sites available to the amine. Two candidates are the classic Lewis and Bronsted sites. In order to check this possibility we obtained the CP-MAS  $^{13}\text{C}$  spectra of two solid adducts of n-butylamine (Figures 3b and 3c). Those resonances for the solid HCl adduct match closely to four of the resonances for the surface adsorbed species. The resonances corresponding to the  $\alpha$  and  $\beta$  carbons of the  $\text{BCl}_3$  adduct are shielded relative to the analogous carbons of the adsorbed amine. Hence, we conclude that the most deshielded set of resonances correspond to the n-butylamine which is attached to the surface via Lewis bonds to an aluminum atom. That the chemical shifts of this species are deshielded relative to those of the  $\text{BCl}_3$  adduct we attribute to the fact that the acid site in this surface is a stronger Lewis acid than  $\text{BCl}_3$ .

The breadth of the resonances for the  $\alpha$  and  $\beta$  carbons may arise from several factors. An important consideration is the presence of  $^{14}\text{N}$  dipolar coupling. The fact that we do not observe "well resolved" doublets for these carbons may be due in part to the diffusion of the molecule and/or the strength of the applied magnetic field relative to the  $^{14}\text{N}$  quadrupolar coupling constant(24). Perhaps of equal importance to the linewidth is a heterogeneity of the acid sites on the surface of the alumina. The presence of a distribution of site acidities would lead to a corresponding distribution of chemical shifts, and hence appear as a line broadening mechanism.

**Pyridine.** Gay and others have recently used pyridine and substituted aromatic bases in conjunction with wide-line nmr to probe the differences in variously treated aluminas and mixed alumino-silicates(4,19). Difficulties were encountered with bases that bound tightly to the surface since magnetic dipolar effects then broadened the lines causing overlap and loss of information. Pyridine gave a broad, ill-defined spectrum even at elevated temperatures and relatively high surface coverages(4). By contrast we have found that ambient temperature CP-MAS pyridine spectrum at 0.05 BET monolayer surface coverage is completely resolved with separate resonances for each of the three types of carbon present (Figure 4a). Within experimental error the line positions coincide with the values for liquid pyridine. The lines are noticeably broad

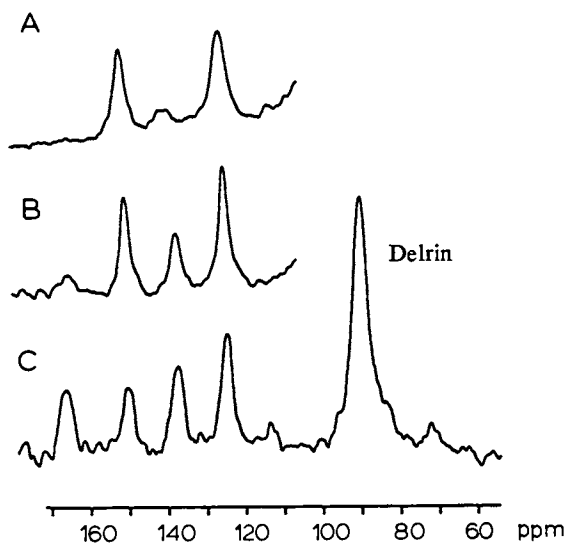


*Figure 4. Carbon-13 CP-MAS spectrum of  $^{15}\text{N}$ -pyridine (0.5 weight %) adsorbed on  $\gamma$ -alumina. Key: A, fresh sample (1 ms contact time); B, after exposure to air for 1 h (1 ms contact time); and C, spectrum d rerun using a 3 ms contact time. The Delrin background signal at 90 ppm is omitted from a and b for clarity. Each spectrum represents a 16 h accumulation using a 1s recycle time.*

(3-4 ppm). The use of  $^{15}\text{N}$  enriched (90%) material resulted in a partial reduction (ca 30%) in linewidth in the isotopically normal spectrum. The residual linewidths may be due to dipolar effects not removed by the level of decoupling power used(20), the presence of  $^{15}\text{N}$  scalar coupling, heterogeneity of the surface acid sites, or site diffusion between chemi-sites and/or physi-sites on the surface.

The intensities of the lines(Figure 4a) are in the approximate ratio 5:5:1 for  $\alpha$ ,  $\beta$ , and  $\gamma$  carbons respectively and do not reflect the true 2:2:1 ratio. This must arise from a difference in rotating frame relaxation times for the protons and/or carbons such that the cross-polarization dynamics of the  $\alpha$  and  $\beta$  carbons are not the same as for the  $\gamma$  carbon(5). Further, sidebands introduced by the sample rotation(2.8 kHz) appear to low field of the main resonances, indicating that the inherent chemical shift anisotropy of the planar molecules is not averaging by thermal motion. These data are consistent with restricted overall motion and perhaps a preferential rotation about the  $\text{C}_2$  symmetry axis of the pyridine.

Exposure of the sample to the atmosphere enables carbon dioxide and water to co-adsorb with the pyridine. The chemical shifts indicate that the carbon dioxide may have reacted to give a carbonate species(25, 26); whereas, the pyridine spectrum now resembles more closely that of liquid pyridine in that the linewidths are narrower ( $\sim 2$  ppm) and the intensities are nearly 2:2:1(Figure 4b). The water appears to have altered the surface in such a way as to cause the pyridine to be more loosely bound, or it may be competing with the pyridine for the chemisorbed sites on the surface. However, lengthening the cross-polarization contact time from 1 ms to 3 ms alters the line intensities in favor of the  $\gamma$  carbon(Figure 4c) implying that the pyridine maintains a preferential  $\text{C}_2$  rotation.

Our results for this sample differ from those of others who were able to observe by wide-line or carbon nmr protonated forms of alkyl-substituted pyridines adsorbed to alumina-silica surfaces(4). Significantly, there is no clear evidence in our spectra for other than a simple type of coordinate bonding between pyridine and the alumina. These differences may well reflect subtleties due to the additional presence of silica in their samples. Indeed, the marked changes that occurred upon exposing our sample to air underscore the way alumina surfaces can be made to vary with respect to the nature of the acid sites. Work to further develop the interesting points raised in this preliminary study is currently underway in our laboratories.

### Conclusions and Prospects for the Future Research

The preceding results clearly demonstrate that CP-MAS methods allow one to study, by natural abundance  $^{13}\text{C}$  nmr spectroscopy, small molecules adsorbed to active surfaces. Further, these experiments were performed at ambient temperature with 5% of a monolayer coverage on  $\text{Al}_2\text{O}_3$  with a moderate surface area(220  $\text{m}^2/\text{g}$ ). A typi-

cal experiment required approximately 12 hrs instrument time. Lower coverages and/or lower surface areas can be studied with moderate enrichment of the  $^{13}\text{C}$ . For example, the present studies could have been completed in  $\frac{1}{8}$  of the time if we had employed samples that were uniformly enriched by 10% in  $^{13}\text{C}$ .

The present design of our MAS probe is clearly amenable to variable temperature operation. Hence, one can study site exchange processes as a function of temperature and possibly separate rotational motion from translational motion of the molecule on the surface. Anisotropic rotational motion can be studied by  $^2\text{H}$  nmr, e.g. deuterated pyridine and n-butyl amine. The ease of the  $^{13}\text{C}$  experiment suggested that  $^{15}\text{N}$  nmr with enriched samples would be equally as straightforward. In the near future, the  $^{27}\text{Al}$ ,  $^{109}\text{Ag}$ ,  $^{103}\text{Rh}$  nmr spectroscopy of the surface acceptor can also be studied.

With the advent of the pulse Fourier transform technology, the field of nmr spectroscopy has undergone a major renaissance. One of the significant manifestations of this era is the recognition of the common and fertile ground between the "phenomenological practitioners" and the "high resolution" nmr spectroscopists. The ingenious rotating frame double resonance methods of Hahn and co-workers (27) and the incisive applications of these experiments to the "high resolution" nmr of solids by Waugh and associates (5,28) are excellent examples of how an entire field of research has been immeasurably broadened in its scope of application. The present work demonstrates that a similar situation exists between the nmr spectroscopists and the surface chemists. It is our hope that we and others can contribute to yet another level of understanding in this exciting area of chemistry.

#### Acknowledgements

The authors would like to thank Dr. R. C. Schoening for many helpful discussions. The encouragement and support of the management of Union Carbide Corporation is gratefully acknowledged. The use of the facilities at the South Carolina Nuclear Magnetic Resonance Spectroscopy Center, funded by the National Science Foundation Grant CHE78-18723, is acknowledged.

#### LITERATURE CITED

1. Basila, M.R. "Applied Spectroscopy Reviews", 1968, 1, 289; Little, L.H. "Infrared Spectra of Adsorbed Species"; Academic Press: New York, 1966.
2. Tabony, J. "Progress in NMR Spectroscopy", 1980, 14, 1.
3. Kaplin, S.; Resing, H.A.; Waugh, J.S. *J. Chem. Phys.* 1973 59, 5681; Slotfeidt-Ellingsen, D.; Resing, H.A. *J. Phys. Chem.* 1980, 84, 2204; Chang, J.J.; Pines, A.; Fripiat, J.J.; Resing, H.A. *Surf. Sci.* 1975, 47, 661.
4. (a) Gay, I.D.; Liang, S.H. *J. Catal.* 1976, 44, 306; (b) Gay,

- I.D. J. Catal. 1977, 48, 430; (c) Liang, S.H.; Gay, I.D. J. Catal. 1980, 66, 294; (d) Kriz, J.F.; Gay, I.D. J. Phys. Chem. 1976, 80, 2951; (e) Michel, D. Surf. Sci. 1974, 42, 453; (f) Nagy, J.B.; Guelton, M.; Derovane, E.G. J. Catal. 1978, 55, 43; (g) Michel, D.; Meiler, D.; Pfeifer, W. J. Mol. Catal. 1975, 1, 85.
5. Pines, A.; Gibby, M.G.; Waugh, J.S. J. Chem. Phys. 1973, 59, 569.
  6. Schaefer, J.; Stejskal, E.O. J. Am. Chem. Soc. 1976, 98, 1031.
  7. Doty, F.D.; Inners, R.R.; Ellis, P.D. J. Magn. Res. 1981, 43, 399.
  8. Doty, F.D.; Ellis, P.D. Rev. of Sci. Instr., in press.
  9. Dawson, W.H.; Kaiser, S.W.; Ellis, P.D.; Inners, R.R., J. Am. Chem. Soc., in press.
  10. Dawson, W.H.; Kaiser, S.W.; Ellis, P.D.; Inners, R.R., submitted to J. Am. Chem. Soc.
  11. Andrew, E.; Farnell, L.; Firth, M.; Gladhill, T.; Roberts, I. J. Magn. Res. 1969, 1, 27.
  12. (a) Lowe, I.J. Phys. Rev. Letter 1959, 2, 285; (b) Lippmaa, E.; Alla, M.; Tuherm, T. Proc. XIX Corq. Ampere, Eds. Brunner, H.; Hausser, K.H.; Schweitzer, D., 1976, pg. 113; (c) Eckman, R.; Alla, M.; Pines, A. J. Magn. Reson. 1980, 42, 440; (d) Van Kijk, P.A.S.; Schut, W.; VanOs, J.W.M.; Menger, E.M.; Veeman, W.S. J. Phys. E.: Sci. Instr. 1980, 13, 1309; (e) Schneider, B.; Doskocilova, D.; Babka, J.; Ruzicha, Z. J. Magn. Res. 1980, 27, 41; (f) Balimann, G.; Burgess, M.J.S.; Harris, R.K.; Cudby, M.E.A.; Eldrige, J.W. Chem. Phys. 1980, 46, 469.
  13. Bartuska, V.J.; Maciel, G.E. J. Magn. Res. 1981, 42, 213.
  14. Parry, E.P. J. Catal. 1963, 2, 317.
  15. Damon, J.P.; Delmon, B.; Bonnier, J.M. J. Chem. Soc. Faraday Trans., 1977, 73, 372.
  16. Akinson, D.; Curthorp, G. Chem. Soc. Rev. 1979, 8, 475.
  17. Basila, M.R.; Kantner, T.R. J. Phys. Chem. 1966, 70, 1681.
  18. Riviat, F.E.; Petrakis, L. J. Phys. Chem. 1973, 77, 1232.
  19. Rauscher, H.J.; Michel, D.; Deininger, D.; Geschke, D. J. Mol. Catal. 1980, 9, 369.
  20. The carbon-13 CP-MAS experiments were conducted at 50.3 MHz using a modified Bruker WP200-WP spectrometer(21). The single-contact pulse sequence used 50 kHz matching, a contact time (unoptimized) of 1 ms, and a recycle time of 1s.
  21. Inners, R.R.; Garber, A.R.; Doty, F.D.; Ellis, P.D., J. Magn. Res., in press.
  22. Operating under dry nitrogen atmosphere, the granular alumina sample was packed into Al<sub>2</sub>O<sub>3</sub> nmr rotors. An important experimental difficulty was overcome by the present rotor design, i.e. the carbon-13 background signal from the probe. These samples are relatively dilute (typically 40 mM in amine based upon total rotor value). The Delrin® end caps of the rotor leave a small signal of 90 ppm which we use for the reference.

23. Mariq, M.M.; Waugh, J.S. J. Chem. Phys. 1979, 70, 3300.
24. Hexem, J.G.; Frey, M.H.; Opella, S.J. J. Am. Chem. Soc. 1981, 103, 224; Frey, M.H.; Opella, S.J. J. Chem. Soc. Chem. Comm. 1980, 1980, 474.
25. Pertinent chemical shifts are  $\delta(\text{CO}_2) = 123.2$  ppm;  $\delta(\text{HCO}_3^-) = 160$  ppm;  $\delta(\text{CO}_3^{2-}) = 170$  ppm, from Stothers, J.B. "Carbon-13 NMR Spectroscopy"; Academic Press: New York, 1972, pg. 304.
26. Bowker, M.; Barteau, M.A.; Madix, R.J. Surf. Sci. 1980, 92, 528; Force, E.L.; Bell, A.T. J. Catal. 1975, 38, 440; Force, E.L.; Bell, A.T. J. Catal. 1975, 40, 356; Tascon, J.M.D.; Tejuca, L.G. J. Chem. Soc., Faraday Trans., 1981, 1, 77, 591.
27. Hartman, S.; Hahn, E.L. Phys. Rev. 1962, 128, 2042; MacArthur, D.A.; Hahn, E.L.; Walstedt, R.E. Phys. Rev. 1967, 188, 609.
28. Haeberlin, U. Advan. Magn. Res. supplement 1976; Mehring, M. "NMR Basic Principles and Progress", Eds.: Diehl, P.; Fluck, E.; Kosfeld, R. 1976, Vol. II, Springer-Verlag.

RECEIVED November 17, 1981.

## Solid State NMR of Linear and Cyclic Peptides

L. M. GIERASCH

University of Delaware, Department of Chemistry, Newark, DE 19711

M. H. FREY, J. G. HEXEM, and S. J. OPELLA

University of Pennsylvania, Department of Chemistry, Philadelphia, PA 19104

Studies of synthetic model peptides can contribute to the understanding of principles important in determining the structures of naturally occurring peptides and proteins. These tractable model systems also facilitate the development of methods for studying molecular structure and dynamics, since the methods can be verified and improved before being applied to more complex and often precious natural compounds.

High resolution NMR has proved to be a very powerful approach to the analysis of solution conformations of peptides (1). The capability of obtaining high resolution NMR spectra of solid samples extends the opportunity for analysis to crystalline peptides (2-5), therefore comparisons can be made of peptide conformations in different environments and physical states. In addition, some of the information obtained from the analysis of solid-state NMR spectra is unique and provides insight into both static and dynamic aspects of peptide conformation.

The experiments on peptides utilize high resolution dilute spin double resonance solid-state NMR (6, 7). In these experiments, magic angle sample spinning averages out chemical shift anisotropy and dipolar couplings, cross polarization enhances  $^{13}\text{C}$  sensitivity, and high power proton decoupling removes  $^1\text{H}$ - $^{13}\text{C}$  dipolar couplings. This combination of techniques gives spectra with sufficient resolution for analysis of chemical shifts as well as lineshapes of resonances.

Several of the model cyclic peptides used in these studies were designed to mimic regions of polypeptide chains where hydrogen bonded reverse turns are likely to occur (8, 9, 10). These peptides contain proline, an imino acid which has a high frequency of occurrence in turns (11), and which is intrinsically interesting

0097-6156/82/0191-0233\$06.00/0  
© 1982 American Chemical Society

because of the impact of its cyclic side chain on the local conformation of polypeptides. For example, various proline ring geometries are possible (12), and side chains of residues preceding prolines are allowed less conformational freedom than if they precede one of the amino acids (13). In addition, *cis* X-Pro bonds are energetically competitive with the *trans* configuration, in contrast to peptide bonds involving amino acids where the *trans* form is strongly favored (14).

Both cyclic and linear peptides have been studied by solid-state NMR. In some cases, comparisons can be made directly between solution and solid-state conformations and in others, direct comparisons between X-ray diffraction determined structures and NMR determined structures can be made. NMR data have also been used to describe the conformation of peptides in the solid-state in the absence of a prior diffraction analysis.

Three aspects of solid-state NMR have proved to be fruitful in our initial peptide studies. First, the isotropic  $^{13}\text{C}$  chemical shifts in the solid state have led to determination of conformations taken up in the solid (when the structure is not known), and to the correlation of expected chemical shifts with particular conformational features (when the structure is known from diffraction data).

Second, the positions and lineshapes of resonances arising from potentially mobile parts of the peptide (e.g. side chains) have revealed dynamical aspects of the solid-state structures of peptides. The analysis of molecular motions is simplified in the solid state by the absence of overall molecular tumbling, which modulates spin interactions and leads to complex frequency-dependent spectral responses. In particular, signals arising from aromatic ring side chains are well separated from other resonances, and may be interpreted in terms of reorientation models of these side chains. Such ring dynamics are of great importance in protein structures, and studies with model peptides can help elucidate fundamental aspects of these processes. The combined use of  $^{13}\text{C}$ ,  $^{15}\text{N}$ , and  $^2\text{H}$  spectral analysis enhances the utility of solid-state NMR analysis of ring dynamics.

Third, since magic angle sample spinning does not completely remove  $^{14}\text{N}$ - $^{13}\text{C}$  dipolar couplings (19), resonances from carbons directly bonded to nitrogens have an asymmetric doublet lineshape. Geometric information is available from the analysis of the  $^{14}\text{N}$  induced splittings of  $^{13}\text{C}$  resonances.

### Conformational Analysis of Isotropic Chemical Shifts

Three cyclic peptides designed to exemplify different features of peptide conformation have been studied by solid-state NMR (3), solution NMR (10, 18) and X-ray diffraction (16). The NMR results described here in brief form show a variety of interesting phenomena for these peptides. Cyclo(D-Phe-Pro-Gly-D-Ala-Pro) is a rigid cyclic pentapeptide which contains in solution



and in the solid (from X-ray diffraction analysis) both a  $\beta$ -turn (reverse turn stabilized by hydrogen-bonding between the carbonyl of residue  $i$  and the N-H of residue  $i+3$ ) and a  $\gamma$ -turn (reverse turn stabilized by hydrogen bonding between the carbonyl of residue  $i$  and the N-H of residue  $i+2$ ). The isotropic  $^{13}\text{C}$  chemical shifts for the aliphatic carbons of this crystalline peptide are essentially superimposable on the shifts in solution (Figure 1), thus confirming from NMR data that the peptide has the same conformation in solution and in the solid. Only the presence of the asymmetric doublets for the  $\alpha$  carbon, carbonyl, and Pro  $\text{C}_\delta$  resonances in the solid state spectrum yielded differences between the two spectra. Especially noteworthy is the appearance of an unusually high field proline  $\text{C}_\beta$  resonance in both spectra. This upfield position is due to an eclipsing of the Pro carbonyl and  $\beta$ -methylene group which results from a very low trans'  $\psi$  angle necessitated by the participation of this residue in a  $\gamma$ -turn (19). The close correspondence of chemical shifts in the solution and solid state spectra, especially the high field Pro  $\text{C}_\beta$  resonance, indicates that local intramolecular effects predominate on determining chemical shifts, and that spectra for solid samples may be correlated with peptide conformation.

The peptide cyclo(Gly-Pro-Gly)<sub>2</sub> presents a quite different situation. The analysis of its  $^{13}\text{C}$  NMR spectrum leads to the conclusion that it adopts a  $\text{C}_2$ -symmetric conformation in solution, at least on NMR timescales. The solution NMR spectrum (Figure 2B) shows the minimum number of resonances expected (one per carbon in the repeating tripeptide unit). By contrast, in the solid-state spectrum there is clear indication of asymmetry since there are two Pro  $\text{C}_\beta$  resonances in Figure 2A. X-ray diffraction analysis has revealed an asymmetric molecular conformation for the crystalline peptide (17), with two different types of  $\beta$ -turns, only one of which is intramolecularly hydrogen-bonded. Analysis of the solid state isotropic  $^{13}\text{C}$  chemical shifts in terms of local conformation yields a picture of the molecule which is consistent with the X-ray data.

A third cyclic peptide studied is cyclo(D-Phe-Gly-Ala-Gly-Pro). Figure 3 compares its solid state and solution  $^{13}\text{C}$  NMR spectra. Two aspects of this peptide have been studied. First, the isotropic chemical shift positions show that structure I is preferred in the solid state and both structures I and II exist in solution. The existence of a  $\gamma$ -turn with proline as the  $i+1$  residue in the solid state conformation is indicated by the high field position of the Pro  $\text{C}_\beta$  resonance. By contrast, the Pro  $\text{C}_\beta$  resonance position in solution supports an equilibrium between structures I and II, since it occurs midway between an unperturbed Pro and one in a  $\gamma$ -turn. Second, a striking feature of the solid state  $^{13}\text{C}$  spectrum of this peptide is in the aromatic region where a broad ill-defined resonance in the base line is all that is seen for the  $\delta$  and  $\epsilon$  carbons while the  $\gamma$

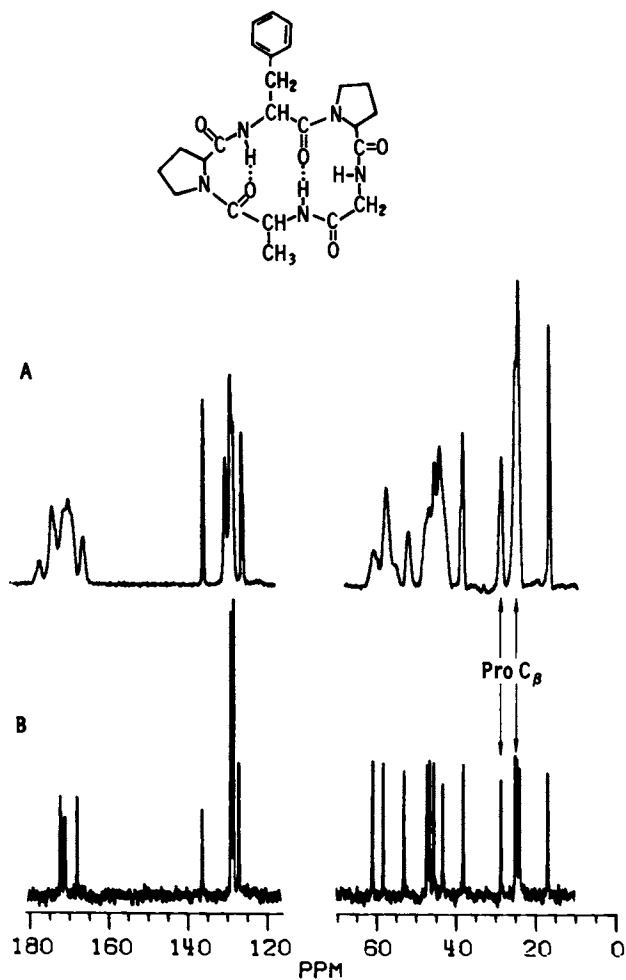


Figure 1.  $^{13}\text{C}$  NMR spectra of cyclo(D-Phe-Pro-Gly-D-Ala-Pro). Chemical shifts for all spectra are relative to external  $\text{Me}_4\text{Si}$  at 38 MHz resonance frequency. Key: A, polycrystalline sample; and B, solution ( $\text{CDCl}_3$ ) sample.

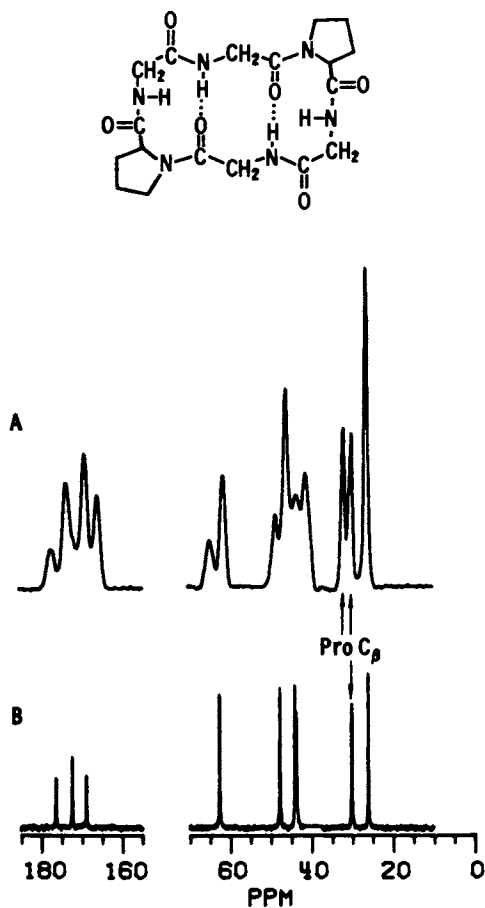


Figure 2. <sup>13</sup>C NMR spectra of cyclo(Gly-Pro-Gly)<sub>3</sub> at 38 MHz resonance frequency. Key: A, polycrystalline sample; and B, solution [(CD)<sub>3</sub>SO/H<sub>2</sub>O] sample.

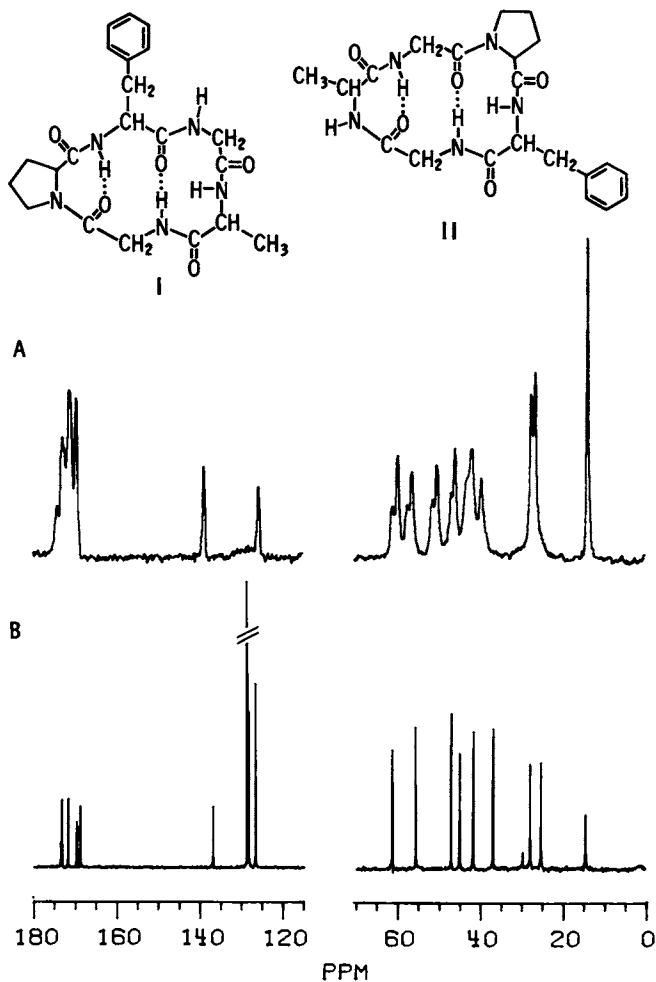


Figure 3.  $^{13}\text{C}$  NMR spectra of cyclo(D-Phe-Gly-Ala-Gly-Pro) at 63 MHz resonance frequency. Key: A, polycrystalline sample; and B, solution (CDCl<sub>3</sub>/MeOH) sample.

and  $\zeta$  resonances appear as sharp lines from the Phe residue. This will be analyzed in the next section in terms of dynamics.

The studies of these three cyclic peptides demonstrates the sensitivity of the proline chemical shifts of resonances to the geometry of the pyrrolidine ring. The observed variation in the resonance position of the Pro  $C_\beta$  appears to be correlated with the proline  $\Psi$  angle. Such a correlation has been proposed (19) and used in solution NMR of proline containing peptides (8, 9, 10, 20). The solid-state NMR spectra serve two purposes; since the  $^{13}\text{C}$  shifts in the solid can be directly compared to X-ray determined  $\Psi$  angles, and the shifts provide a means of assessing the preferred  $\Psi$  angle in peptides whose structures have not been determined by X-ray diffraction.

Table I lists the Pro  $C_\beta$  and  $C_\gamma$  chemical shifts for a variety of peptides. For those examples with known X-ray diffraction structures, the observed  $\phi, \Psi$  angles are cited. Important conclusions can be drawn from consideration of these data. The correlation of a small  $\Delta\beta\gamma$  with a low trans'  $\Psi$  angle leads to the conclusion that cyclo(D-Phe-Gly-Ala-Gly-Pro) takes up a conformation with the proline participating in a  $\gamma$ -turn in the solid state. This is in contrast to what would be inferred from examination of the solution spectrum (where the intermediate values of  $\Delta\beta\gamma$  (2.5 ppm) is consistent with conformational averaging. The data in Table I and the spectrum of solid Ala-Pro (Figure 4) that shows two distinct sets of proline resonances indicate that this dipeptide exist in forms with cis and trans Pro residues. According to resonance intensities, there is a 2:1 ratio of cis and trans conformers.

Spectra of solid peptides can be used to describe conformational features of the peptides. Of particular utility are the Pro  $C_\beta$  and  $C_\gamma$  chemical shifts, which can describe ring geometry or occurrence of cis or trans X-Pro bond conformation.

#### Dynamical Analysis of Lineshapes

Solid-state NMR spectroscopy is well suited for studies of intramolecular dynamics because side chain motions can be analyzed independent of overall molecular reorientation in crystalline samples. It is an alternative spectroscopic strategy to solution NMR because partial motional averaging of the anisotropic spin interactions occurs. Dipolar, chemical shift, and quadrupolar interactions can be used to describe the dynamics of aromatic rings of proteins and peptides.

TABLE I  
Proline C  $\beta$  and C  $\gamma$  Chemical Shifts<sup>a</sup>  
for Peptides in the Solid State

Compound	Pro C $\beta$	Pro C $\gamma$	$\Delta\beta_\gamma$	$\phi, \psi$ Dihedral Angles from X-ray
Proline	32.9	25.3	7.6	
<u>N</u> -Acetyl-Proline	29.6	24.7	4.9	
Ala-Pro	31.9	26.3	5.6	
_____, <u>trans</u> _____, <u>cis</u>	34.4	22.9	11.5	
Pro-Ala	33.2	26.8	6.4	
<u>t</u> -Boc-Gly-Pro-Gly-OBz	31.7	25.9	5.8	
H <sup>+</sup> Pro-Leu-Gly-NH <sub>2</sub>	30.7	26.9	3.8	--,152.9 <sup>b</sup>
<u>cyclo</u> (D-Phe-Pro-Gly- D-Ala-Pro)	26.2 29.8	25.5 25.5	0.7 4.3	-82,59 <sup>c</sup> -64,128 <sup>c</sup>
<u>cyclo</u> (Gly-Pro-Gly) <sub>2</sub>	29.0 30.8	25.3 25.3	3.7 5.5	{ -53,126 <sup>d</sup> -66,-36 <sup>d</sup>
<u>cyclo</u> (D-Phe-Gly-Ala-Gly- Pro)	27.3	26.6	0.7	

<sup>a</sup>Maximum uncertainty  $\pm 0.5$  ppm; typical uncertainty  $\pm 0.2$  ppm.

<sup>b</sup>reference 15

<sup>c</sup>reference 16

<sup>d</sup>reference 17

The ring dynamics of the two phenylalanine containing cyclic peptides have been studied. In solution, both of these peptides show  $^1\text{H}$  and  $^{13}\text{C}$  NMR spectra consistent with rapid reorientation of the aromatic rings about the  $\text{C}_\beta\text{-C}_\gamma$  bond axis. The aromatic regions of the solid state  $^{13}\text{C}$  NMR spectra of the two peptides are shown in Figure 5. The spectrum of cyclo (D-Phe-Pro-Gly-D-Ala-Pro) shows intensity from all six carbon sites of the ring. This indicates a long residence time in an asymmetric environment, and that on NMR timescales the ring is rigid. The spectrum of the aromatic ring carbons of crystalline cyclo (D-Phe-Gly-Ala-Gly-Pro) is much different. While the  $\gamma$  and  $\zeta$  carbon resonances are sharp lines there is only a very broad nondescript resonance for the other four carbons. Its very unusual appearance is retained at two field strengths and under a variety of experimental conditions. The most likely explanation is that the phenyl ring is in intermediate exchange, probably flipping at a rate around  $100\text{ sec}^{-1}$  about the  $\text{C}_\beta\text{-C}_\gamma$  bond axis. This rate was derived from the approximate chemical shift difference for the asymmetric environments based on our experience with linear and cyclic peptides. Additional evidence from other nuclei and other interactions supports these conclusions (5); therefore the peptide is a likely candidate for variable temperature studies.

There are large differences in the dynamics of the phenylalanine rings of the two cyclic peptides studied. The dramatic difference in the spectra shown in Figure 5 can only be due to intramolecular dynamics because all the aliphatic and carbonyl sites give narrow lines. The significant differences in phenylalanine ring dynamics may be a consequence of the Phe residue preceding proline in one case and glycine in the other.

#### Conformational Analysis of $^{14}\text{N}$ - $^{13}\text{C}$ Dipolar Couplings

The resonances from carbons directly bonded to nitrogen are asymmetric doublets in solid state NMR spectra (21). This unusual lineshape results from the failure of magic angle sample spinning to completely suppress the  $^{13}\text{C}$ - $^{14}\text{N}$  dipolar couplings, the success of which depends on the spins of interest being quantized along the applied magnetic field.  $^{14}\text{N}$  with spin  $S=1$ , has a quadrupole moment whose coupling with the nonspherically symmetric electric field gradient produces a quadrupole interaction with magnitude comparable to the  $^{14}\text{N}$  Zeeman interaction. Thus, the axis of quantization of the  $^{14}\text{N}$  spins is not along the applied magnetic field but is quantized along a resultant of the quadrupole and Zeeman interactions.

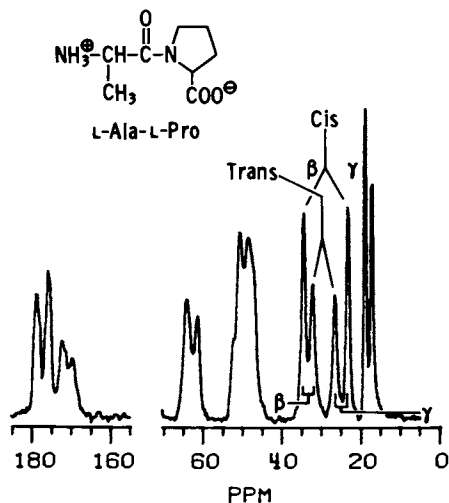


Figure 4. A  $^{13}\text{C}$  NMR spectrum of polycrystalline Ala-Pro at 38 MHz resonance frequency.

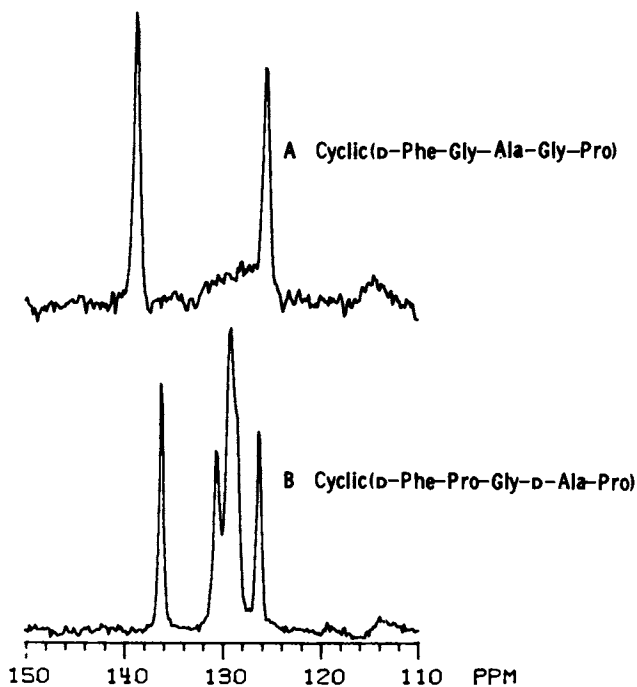


Figure 5. Aromatic regions of  $^{13}\text{C}$  NMR spectra of cyclic peptides containing phenylalanine. Key: A, expansion of Figure 3; and B, expansion of Figure 1.



When the presence of both these interactions is taken into account, it is found that the appropriate truncated dipolar Hamiltonian must be expanded to include additional terms whose angular dependence corresponds to the C and D terms of the classical dipolar Hamiltonian (22). These terms contain the Euler angles  $\alpha^D$  and  $\beta^D$  which orient the internuclear vector in the coordinate system, which determines the dipolar coupling for the specific  $^{14}\text{N}$ - $^{13}\text{C}$  sites of interest. This is the principle axis system of the electric field gradient, whose orientation with respect to the applied magnetic field determines the  $^{14}\text{N}$  spin states and hence their dipolar couplings.

The dependence of the dipolar couplings on the orientation of the internuclear vector in the principle axis system of the electric field gradient has inherent information about the molecular geometry of the relevant  $^{14}\text{N}$  and  $^{13}\text{C}$  sites. For example, in a peptide bond, where two carbons are bound to the same nitrogen, the dipolar coupling of each depends on the orientation of its respective internuclear vector with respect to the common coordinate system of the nitrogen electric field gradient principle axis system. Thus, the  $^{13}\text{C}$  NMR spectrum is analyzed in terms of the relative orientation of the internuclear vectors. In principle, this can lead to an independent determination of the conformation of the peptide bond.

As an example, the analysis of the dipeptide Ala-Ala is described. Figure 6 contains the solid-state  $^{13}\text{C}$  NMR spectrum of this compound, with expansions for the carbonyl and alpha carbon resonances illustrating their asymmetric doublet character. For the peptide bond, the Z-axis of the electric field gradient principle axis system is expected to be perpendicular to the plane of the bond (23) and although the location of the X-axis is unknown, by analogy with N-Acetyl Valine it is expected to lie along the N-H bond (24). These relationships are depicted in Figure 7. The dipolar interactions and the spectra can be calculated as described previously (4, 21). Using the quadrupole coupling constant and asymmetry determined for N-acetyl valine (24), the theoretical spectra are compared to the experimental spectra in Figure 6. Both the split between the peaks of the asymmetric doublet and the lineshape predicted from the theory agree well with the experimental spectrum. This close fit confirms the appropriateness of the conformational and spectroscopic parameters used in the calculation. These results indicate geometrical information is available from lineshape analysis of resonances from carbons bonded to nitrogen. This analysis is straightforward for planar peptide bonds, and significant spectral deviations are expected for non-planar peptide bonds.

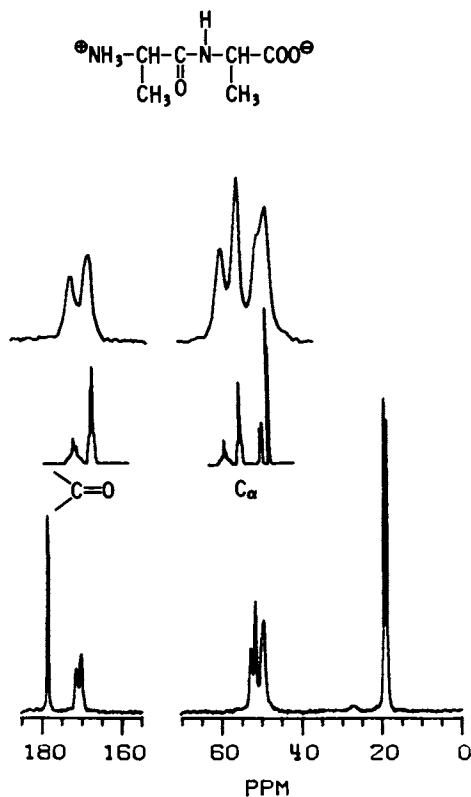


Figure 6.  $^{13}\text{NMR}$  spectrum of polycrystalline Ala-Ala at 63 MHz resonance frequency. Expansions are of peptide carbonyl, peptide  $\text{C}_\alpha$ , and terminal  $\text{C}_\alpha$  resonances from low to high field. Spectra were calculated as in Ref. 4. Theoretical spectra in applied field of 5.87 T. Parameters used: carbonyl carbon of peptide bond  $R_{\text{CN}} = 1.33 \text{ \AA}$ ;  $\alpha^{\text{D}} = 126.0^\circ$ ;  $\beta^{\text{D}} = 90.0^\circ$ ;  $e^2\text{Qq/h} = (-) 3.20 \text{ MHz}$ ; and  $\eta = 0.31$ ;  $\text{C}_\alpha$  of peptide bond  $R_{\text{CN}} = 1.445 \text{ \AA}$ ;  $\alpha^{\text{D}} = 112.0^\circ$ ;  $\beta^{\text{D}} = 90.0^\circ$ ;  $e^2\text{Qq/h} = (-) 3.20 \text{ MHz}$ , and  $\eta = 0.31$ ;  $\text{C}_\alpha$  of N-terminal L-ala  $R_{\text{CN}} = 1.49 \text{ \AA}$ ;  $\alpha^{\text{D}} = 0.0^\circ$ ;  $\beta^{\text{D}} = 3.9 \text{ \AA}$ ;  $e^2\text{Qq/h} = 1.1 \text{ MHz}$ , and  $\eta = 0.26$ .

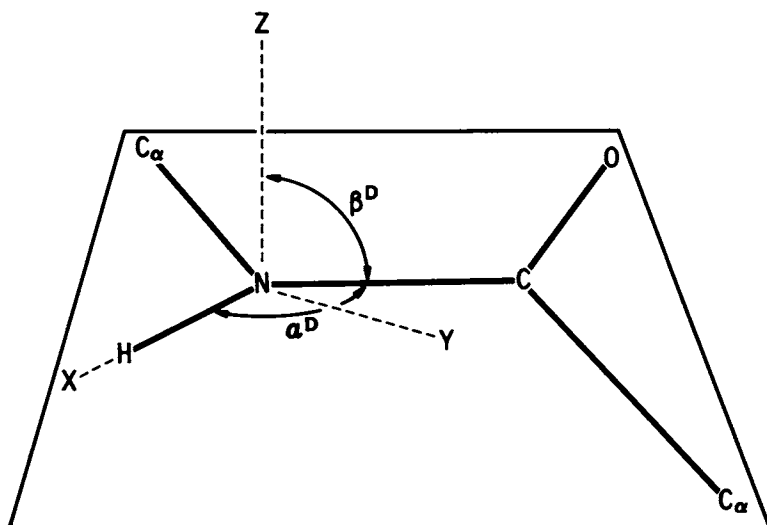


Figure 7. Drawing of peptide bond showing orientation of dipolar and quadrupolar vectors.

### Acknowledgements

We thank A. L. Rockwell for technical assistance. This work is supported by grants GM-24266 (S.J.O.) and GM-27616 (L.M.G.) from the National Institutes of Health and by grants from the American Chemical Society. M.H.F. is supported by a Cell and Molecular Biology Training Grant. J.G.H. is supported by the NIGMS graduate research training program (GM-07612) of the Department of Anesthesiology, University of Pennsylvania. S.J.O. is a Fellow of the A. P. Sloan Foundation (1980-1982).

### Literature Cited

1. Wuthrich, K., *NMR in Biological Research: Peptides and Proteins*, Elsevier, NY, 1976.
2. Frey, M. and Opella, S., *JCS Chem. Comm.* 1980, 474.
3. Pease, L.G., Frey, M.H., and Opella, S.J., *J. Am. Chem. Soc.* 1981, 103, 467.
4. Opella, S.J., Hexem, J.G., Frey, M.H., and Cross, T.A., *Phil Trans R. Soc. Lond. A*, 1981, 299, 665.
5. Gierasch, L.M., Opella, S. J., and Frey, M.H., *Proc. of Seventh Amer. Peptide Symp.* (Rich, D.H. and Gross, E., eds.) Pierce Chem. Co., Rockford, IL, in press.
6. Pines, A., Gibby, M., and Waugh, J., *J. Chem. Phys.*, 1973, 59, 569.
7. Schaefer, J. and Stejskal, E.O., *J. Am. Chem. Soc.* 1976, 98, 1030.
8. Pease, L.G. and Watson, C., *J. Am. Chem. Soc.*, 1978, 100, 1279.
9. Pease, L.G., Niu, C.-H., and Zimmermann, G., *J. Am. Chem. Soc.*, 1979, 101, 184.
10. Pease, L.G., in "Peptides: Structure and Biological Function, Proceedings of the Sixth American Peptide Symposium", E. Gross and J. Meienhofer, Eds., Pierce Chem. Co., Rockford, IL, 1979, 197.
11. Smith, J.A. and Pease, L.G., *CRC Crit. Rev. in Biochem.* 1980, 8, 315.
12. Balasubramanian, R., Lakshminarayanan, A.V., Sabesan, M.N., Tegoni, G., Kenkatesan, K., and Ramachandran, G.N., *Int. J. Protein Research* 1971, III, 25.
13. Ramachandran, G.N. and Sasiskharan, V., *Adv. Prot. Chem.* 1968, 23, 283.
14. Schimmel, P.R. and Flory, P.J., *J. Mol. Biol.* 1968, 34, 105.
15. Reed, L.L. and Johnson, P.L., *J. Am. Chem. Soc.* 1973, 95, 7523.
16. Karle, I.L., in "Perspectives in Peptide Symmetry", A. Eberle, R. Geiger, and T. Wieland, eds., S. Karger, Basel, 1981, 261.
17. Kostansek, E.C., Thiessen, W.E., Schomburg, D., and Lipscomb, W.N., *J. Am. Chem. Soc.* 1979, 101, 5811.

18. (b) Pease, L.G., Deber, C.M., and Blout, E.R., J. Am. Chem. Soc. 1973, 95, 258.
19. Siemion, T.Z., Wieland, T., and Pook, K.H., Angew. Chem. 1975, 87, 712.
20. Madison, V., Atreyi, M., Deber, C.M., and Blout, E.R., J. Am. Chem. Soc. 1974, 96, 6725.
21. Hexem, J.G., Frey, M.H., and Opella, S.J., J. Am. Chem. Soc., 1981, 103, 224.
22. Abragam, A. "The Principles of Nuclear Magnetism " 1961, Oxford Press.
23. Lucken, E.A.C., "Nuclear Quadrupole Coupling Constants", 1969, Academic Press, London.
24. Stark, R.E., Haberkorn, R.A., and Griffin, R.G. J. Chem. Phys. 1978, 68, 1996.

RECEIVED November 18, 1981.

American Chemical  
Society Library  
1155 16th St. N. W.

## <sup>31</sup>P NMR Studies of DNA Conformation and Dynamics

JACK S. COHEN and CHI-WAN CHEN

National Institutes of Health, National Institute of Child Health and Human Development, Developmental Pharmacology Branch, Bethesda, MD 20205

<sup>31</sup>P NMR is a valuable tool in elucidating the conformational and dynamic properties of DNA in solution. Recent work on natural DNA and synthetic polydeoxynucleotides of specific sequence are described. It is advantageous to study medium length DNA derived either from nucleosomes (145 base pairs) or from sonication of synthetic polymers, in order to resolve sharper signals. The <sup>31</sup>P NMR characteristics of alternating B-DNA and Z-DNA are delineated and compared.

Different conformations of DNA in fibers have been known for some time (1). However all of the models originally proposed had uniform backbone conformations with mononucleotide repeat units. Evidence for the existence of variant structures of DNA with non-uniform backbone conformations has become available only comparatively recently. This evidence has derived mainly from X-ray studies on oligonucleotide crystals (2,3), and from NMR studies of DNAs in solution (4,5,6). These variant structures have altered our view of double stranded DNA as a rigid rod in which only the base-sequence varies. While Watson-Crick base pairing is considered to be common to all these structures, the new features are not only the handedness, but the concept that the base sequence determines the conformation of the phosphodiester backbone.

The crystal structure of d(AT)<sub>2</sub> showed an alternating sugar-phosphate backbone conformation, although the molecules were not helically arranged (2). The crystal structures of d(CG)<sub>3</sub> (3) and d(CG)<sub>2</sub> (7,8) exhibited an alternating backbone conformation with a left-handed sense. These observations were made in the solid-state on small oligonucleotide crystals, and X-ray fiber diffraction patterns also indicate the formation of a left-handed variant structure for some sequences in DNA fibers (9). Observation of the transition of right- to left-handed DNA in solution, however, requires a spectroscopic technique. Circular dichroism (CD) is sensitive to the B- to Z-DNA transition, as originally observed by Pohl and Jovin in 1972 for poly(dGdC)\*poly(dGdC) in

This chapter not subject to U.S. copyright.  
Published 1982 American Chemical Society.

high salt concentrations (10).  $^{31}\text{P}$  NMR spectroscopy is emerging as an important technique for the elucidation of the structures and dynamics of these conformational variants of DNA in solution.

### Z-DNA

The transition from presumed right-handed B-DNA to presumed left-handed Z-DNA in solution has been monitored by  $^{31}\text{P}$  NMR for d(GC) in oligonucleotides (6), in 145 bp material derived from histone complexation and nuclease cleavage (11) and in sonicated polymeric material (12). This is shown in Fig. 1 (all  $^{31}\text{P}$  NMR spectra are proton decoupled), in which the Z-form is represented by the doublet of sharper peaks of approximately equal areas in high salt solution. These peaks represent the alternating nature of the GpC and CpG backbone conformations (Fig. 2). The DNAs were sonicated to provide sharper signals than in the polymeric synthetic starting materials (5). It was shown that these sonicated products gave the same salt-induced transition in CD spectra (12).

It is noteworthy that peaks broadened and signal intensity was lost in these spectra as a result of extensive aggregation at high salt concentrations. Attempts to follow this transition in high  $\text{Mg}^{2+}$  concentrations or in ethanol solutions resulted in precipitation of the polynucleotides at the high concentrations (ca 1 mg/ml) required for  $^{31}\text{P}$  NMR observation. By contrast CD spectra can be obtained on much lower concentrations of material.

This difficulty may be surmountable in view of the finding of Behe and Felsenfeld (13) that 5-methyl cytidine substituted for C in d(GC) causes the salt concentration of the midpoint of the B to Z transition to be greatly reduced. This has enabled us to follow this transition at low salt concentrations by  $^{31}\text{P}$  NMR, with no aggregation or precipitation (14). The lack of aggregation is shown by the absence of line broadening. Two signals of approximate area 1:2 were observed on addition of 0.8 M NaCl and three  $^{31}\text{P}$  NMR signals of approximately equal area were observed at 5mM  $\text{Mg}^{2+}$  concentration. The chemical shift of the central peak appears to be equivalent to that of the starting material, and this third component might have been present in the non-methylated copolymer but obscured by line broadening (12), although it was apparently absent in the other material in the Z-form (6,11). The complexation of  $\text{Mg}^{2+}$  with the phosphodiester in the Z' form described by Wang et al (15) might be expected to give rise to this shifted phosphodiester signal. We are currently attempting to clarify this phenomenon.

### Alternating B-DNA

The sharp transition of d(GC) and its derivatives from B to Z-DNA in high salt, and the large separation

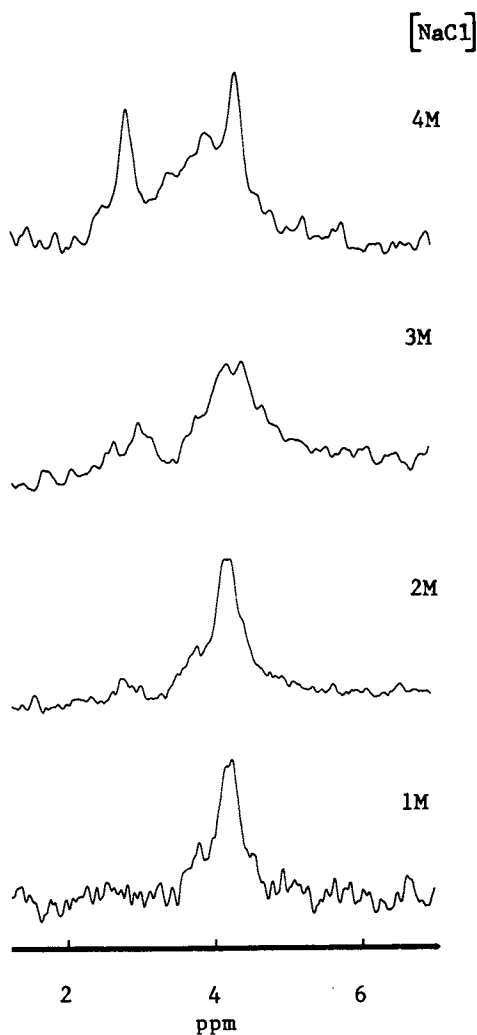


**Figure 1.** Salt dependence of  $^{31}\text{P}$  NMR spectra at 109.3 MHz of sonicated poly(dGdC) · poly(dGdC) at 22°C, pH 6.5. Salt concentration was increased by adding crystalline NaCl. The doublet in the high form arises from an alternating structure, presumed to be Z-DNA (12). The size distribution of sonicated samples was determined by gel electrophoresis.



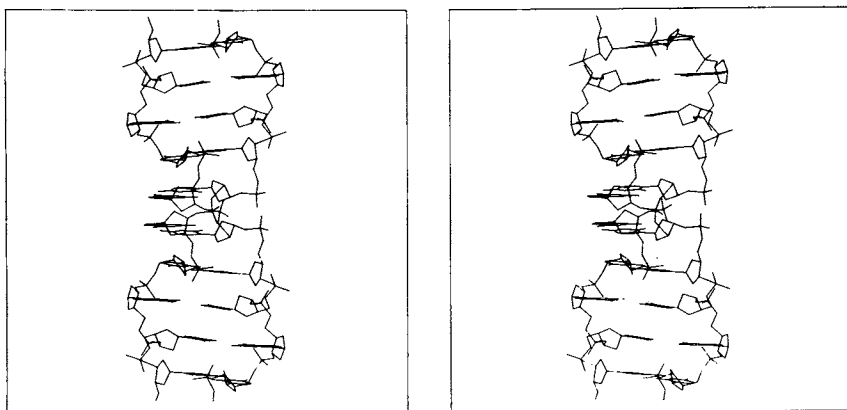


*Figure 2. Stereo view of the structure of Z-DNA (3). This structure is not necessarily the same as that present in solution.*

of the signals in the <sup>31</sup>P NMR spectra enable the Z-form to be readily characterized by <sup>31</sup>P NMR. Observation of alternating B-DNA is less easy.

The first evidence for the existence of two phosphodiester conformations in poly(dAdT)\*poly(dAdT) in solution was obtained with ca 145 bp material derived from histone complexation and nuclease digestion (Fig. 3) (5). However, the separation of the two components was only 22 Hz in this case. This separation could not be due to the simple effect of the differences in the adenine and thymine bases because of their distances from the phosphorus atoms (5). Consequently the two components were attributed to ApT and TpA alternating conformations (Fig. 4). In longer chain polymeric materials these two resonances could not be resolved due to broader NMR signals (5).

As mentioned earlier, the crystal structure of d(AT)<sub>2</sub> also exhibited alternating backbone conformations (2), which could be extended in the form of a double helix to so-called alternating B-DNA (16). Further evidence for the alternating structure in fibers of d(AT)\*d(AT) was obtained from solid state <sup>31</sup>P NMR spectra (17), which also showed a distinct doublet in the parallel orientation (Fig. 5).

Similarly poly(dAdT)\*poly(dAdT) prepared by sonication also exhibited the doublet spectrum in solution, as did sonicated poly(dAbr<sup>5</sup>U)\*poly(dAbr<sup>5</sup>U), although poly(dGdC)\*poly(dGdC) and poly(dAdU)\*poly(dAdU) did not do so (Fig. 6) (12). The <sup>31</sup>P NMR doublet was observed in unmelted sonicated samples as well as in 145 bp material. A further indication that the two peaks represent distinct conformations is that they give slightly different T<sub>1</sub> values (18).

That the formation of the alternating structure is completely reversible has been shown for d(AT) (12,19) and for d(Abr<sup>5</sup>U) (Fig. 7) (12). In the latter case the doublet also reversibly collapsed to a singlet at temperatures below ca 25°C. This may indicate the non-alternating B-form is preferentially stabilized at lower temperature. However, in the physiological temperature and salt concentration range d(AT) does exhibit the alternation.

The <sup>13</sup>C NMR spectrum of 145 bp d(AT), which exhibits doublets for the C<sub>2</sub>' and C<sub>3</sub>' carbons (Fig. 8) (20). This clearly extends the backbone alternation to the sugar components and indicates that the sugar alternation (C<sub>3</sub>' endo, C<sub>2</sub>' endo) seen in the crystal of d(AT)<sub>2</sub> (2), as well as that of d(GC)<sub>2,3</sub> (3,7,8), may be preserved in solution.

While poly(dAdT) does not convert into the Z-form in high salt, a systematic change did occur on addition of NaCl (Fig. 9) (12). An almost identical spectrum in 1 M tetramethylammonium chloride to that in 1 M NaCl has also been observed in an independent study (21). The reason that the doublet was not resolved in 1 M or lower NaCl concentrations in this study presumably results from the higher molecular weight material used, which gives broader signals. In

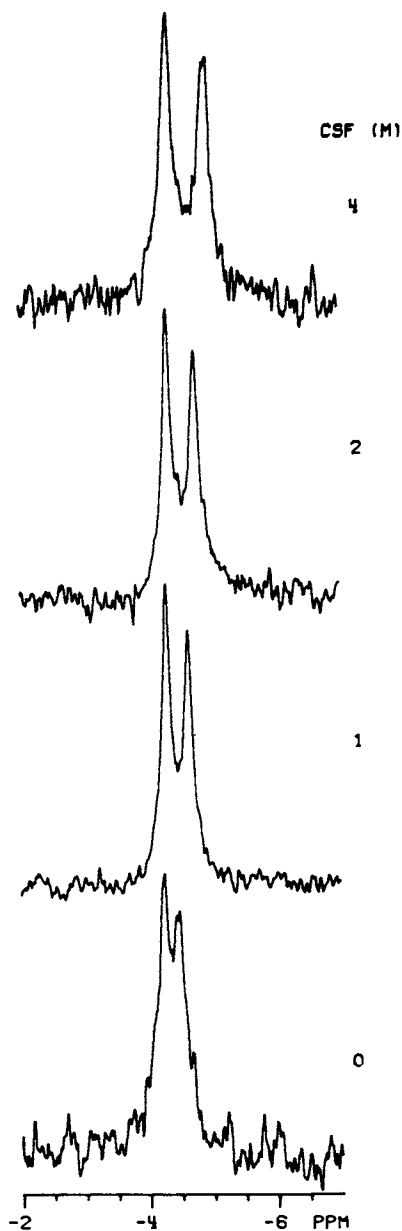


*Figure 3. Temperature dependence of the  $^{31}\text{P}$  NMR spectrum at 109.3 MHz of 145 bp poly(dAdT) hairpins in 10 mM tris-Cl (pH 8.0, 0.1 M NaCl, and 1 mM EDTA). (Reproduced, with permission, from Ref. 5. Copyright 1979, American Society of Biological Chemists.)*

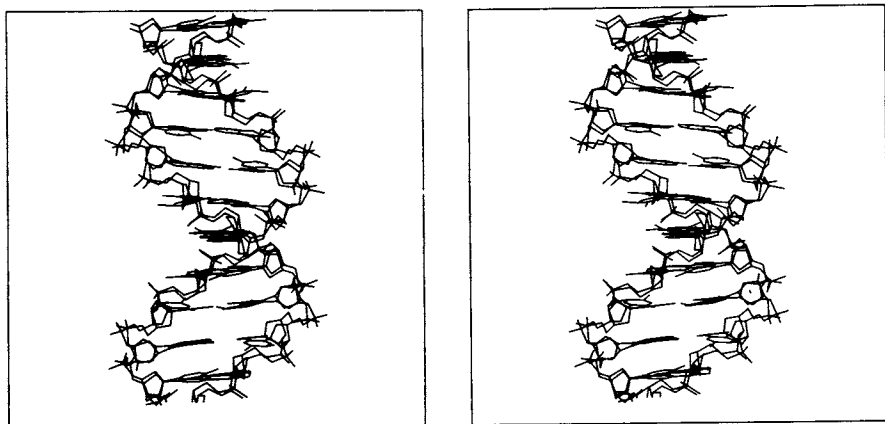


*Figure 4. Stereo view of structures of B-DNA and alternating B-DNA (16), superimposed as far as possible. The alternating structure is not necessarily the same as that present in solution.*

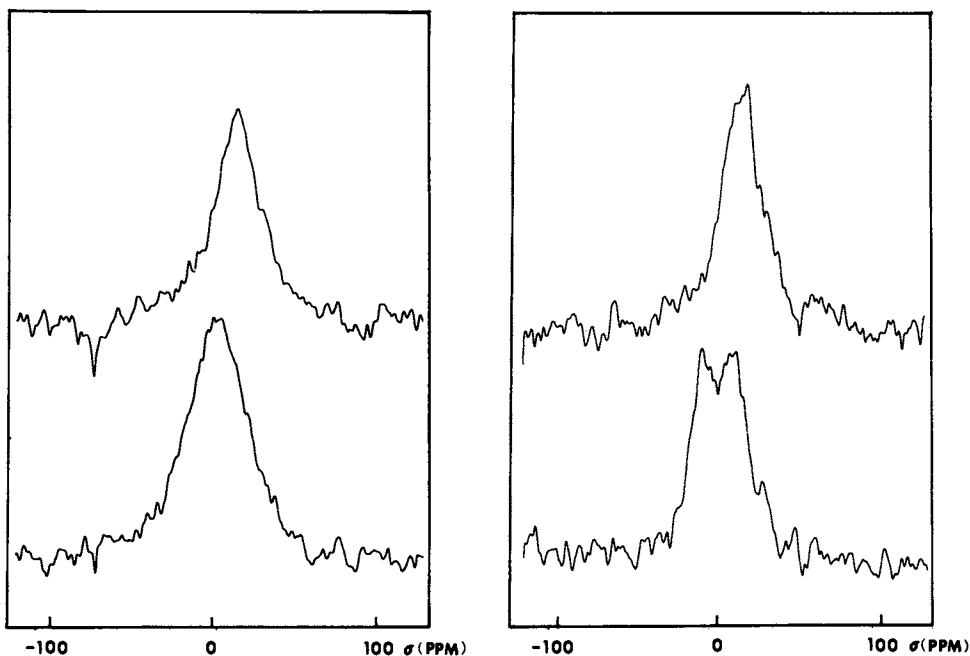


*Figure 5. Proton dipolar decoupled and cross polarized  $^{31}\text{P}$  NMR spectra (24.3 MHz) at 25°C of poly(dAdT) · poly(dAdT) fibers (right) and salmon sperm DNA fibers (left). The top spectra are from the fibers oriented perpendicular to the magnetic field in a teflon holder, and the bottom spectra are from the parallel orientation. Humidity was controlled. (Reproduced, with permission, from Ref. 17. Copyright 1980, Macmillan.)*

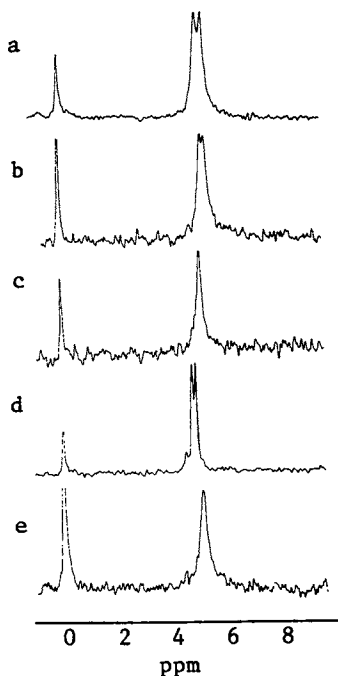


Figure 6.  $^{31}\text{P}$  NMR spectra at 109.3 MHz of sonicated alternating purine–pyrimidine hairpin duplexes. Key: a, poly(dAdT), 30°C; b, poly(dAdbr<sup>5</sup>U), 31°C; c, poly(dAdU), 31°C; d, poly(dIdC), 39°C; and e, poly(dGdC), 23°C; all in 0.1 M NaCl, 0.05 mM EDTA, pH 6–7 except b in 5 mM tris-Cl, 0.1 mM EDTA (12).

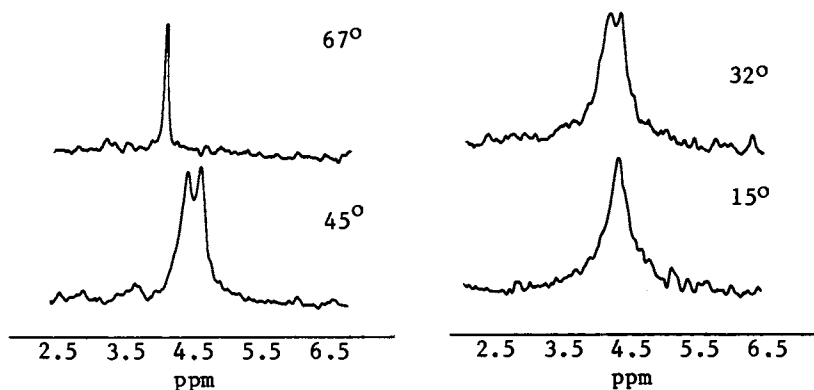


Figure 7. Temperature dependence of the  $^{31}\text{P}$  NMR spectra of sonicated (3 h) poly(dAdbr<sup>5</sup>U) in 5 mM tris-Cl, 0.1 mM EDTA, (pH 6.8) (12).

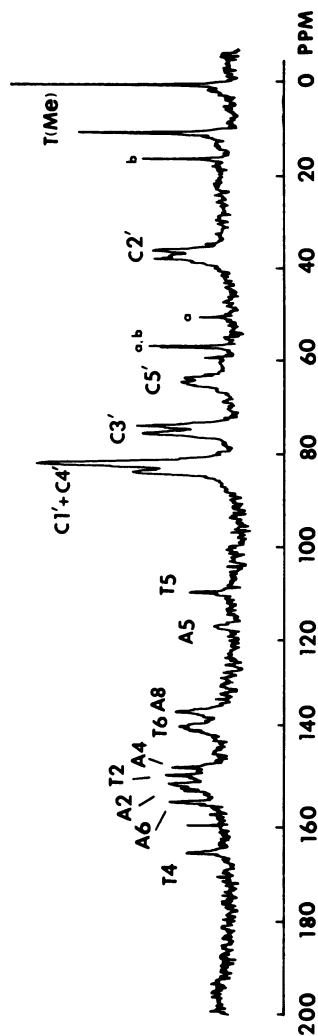


Figure 8. Proton decoupled  $^{13}\text{C}$  NMR spectra at 67.9 MHz of 145 bp hairpinned poly(dAdT) (12 mg in 1 mL) at 32°C. Peaks marked with a and b are from residual EDIA and ethanol. Total acquisition time, 62 h. Note the doubling of the C2' and C5' resonances (20).

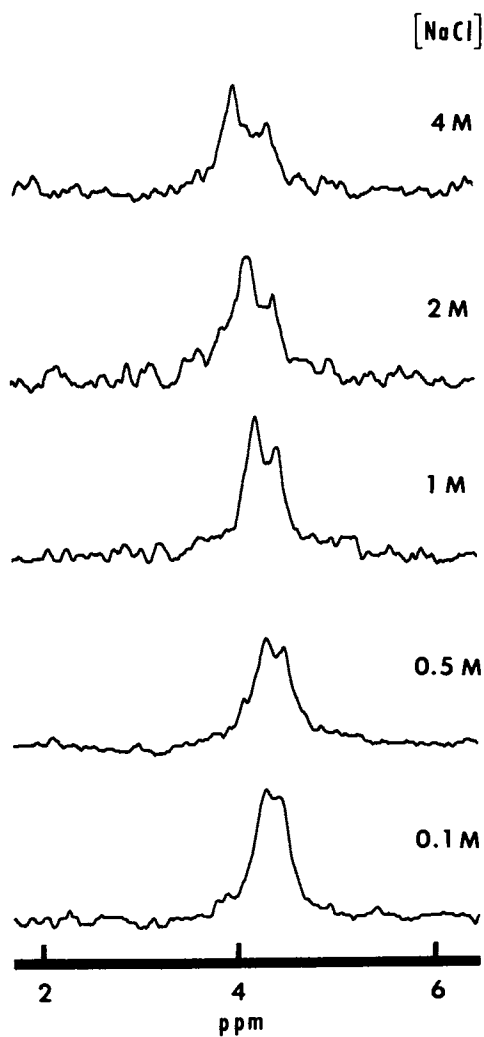


Figure 9. Salt dependence of  $^{31}\text{P}$  NMR spectra at 109.3 MHz of sonicated (3 h) poly(dAdT), 22°C, pH 6.8. Crystalline NaCl was added to the desired concentration (12).



our work on sonicated material it is clear that the smaller size and narrower distribution (22) give superior resolution (Fig. 10).

A new conformational variant of poly(dAdT)•poly(dAdT) has also been claimed in CsF solution from NMR (23) and CD results (24). Also, Patel *et al* (25) have interpreted the effects of CsF to indicate a fast non-cooperative transition between a low salt form having a singlet  $^{31}\text{P}$  resonance and a high salt form with a doublet. While we agree that there is such a transition, it is clear from our results that CsF increases the separation of the doublet (Fig. 11) which is resolved in low salt for smaller sized material (5,12,18). We also attribute this phenomenon to a gradual change in the degree of winding of the DNA double helix (26), and in the case of poly(dAdT).poly(dAdT) all forms are alternating or zig-zag structures (18). From the separation of the two components it is clear that interconversion between the two conformers represented by the doublet would be very slow (rate  $\ll 125 \text{ sec}^{-1}$  in low salt and  $\ll 336 \text{ sec}^{-1}$  in 4 M CsF), or nonexistent. The most likely conformations for the phosphodiester are *tt* and *tg*, with the latter shifted upfield (27), although at this juncture we cannot assign the resonances, nor can we be sure that the structure of poly(dAdT).poly(dAdT) (Fig. 4) really resembles that proposed by Klug *et al* (16).

### Dynamics

The fact that quite distinct  $^{31}\text{P}$  NMR signals are resolved for the alternating B- and Z-DNA forms indicates that these correspond to different phosphodiester conformations which are either not converting, or are interconverting very slowly. The lack of a doublet for d(GC) in low salt for example, might arise from a rapid interconversion of alternating conformations in this case (12). Poly d(GC) often gives broader signals than poly d(AT). The width of signals may be related, through the spin-spin relaxation time  $T_2$ , to the correlation time of the molecule in solution (28).

However, it is essential to carry out measurements at several frequencies to distinguish the contributions to the line width and the other relaxation parameters ( $T_1$  and NOE) which are related to mobility from those which are not. These include chemical shift anisotropy (CSA) and chemical shift dispersion (CSD). The linear dependence of the line widths observed for chicken erythrocyte DNA (4,28) indicated either or both could be contributing. A complete analysis, including best fits to the data at three frequencies indicated large contributions of both CSA and CSD. The presence of CSD is significant since it indicated the presence of many phosphodiester conformational environments in DNA (4,28,29), and was one of the first indications of such a phenomenon.

Thus, simple interpretations of line widths in terms of mobility should be avoided. Nevertheless, there are now many indications from NMR that DNA exhibits a high degree of local mobility (4,28-34)

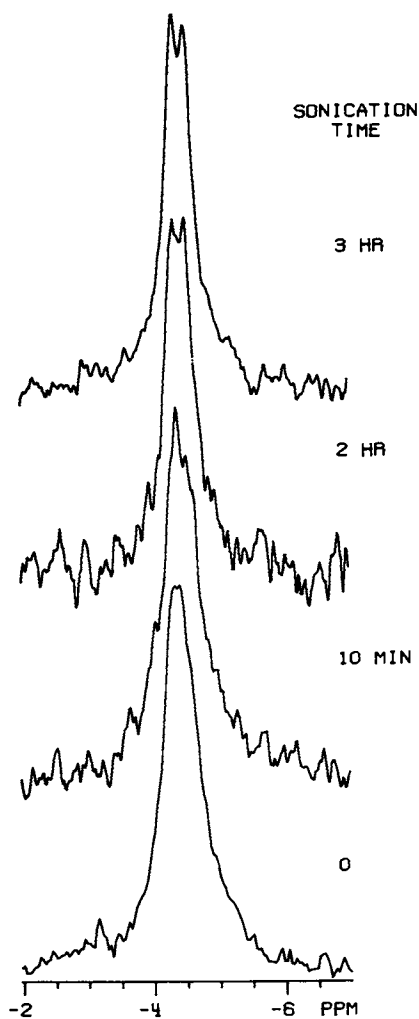


Figure 10. Effect of sonication time on  $^{31}\text{P}$  NMR signals of poly(dAdT) · poly(dAdT): 0 min, 31°C; 10 min, 26°C; 1 h, 28°C; and 3 h, 20°C, each with 3 Hz line broadening. The average chain lengths determined by gel electrophoresis were 690, 195, 116, and 84 bp, respectively (22).

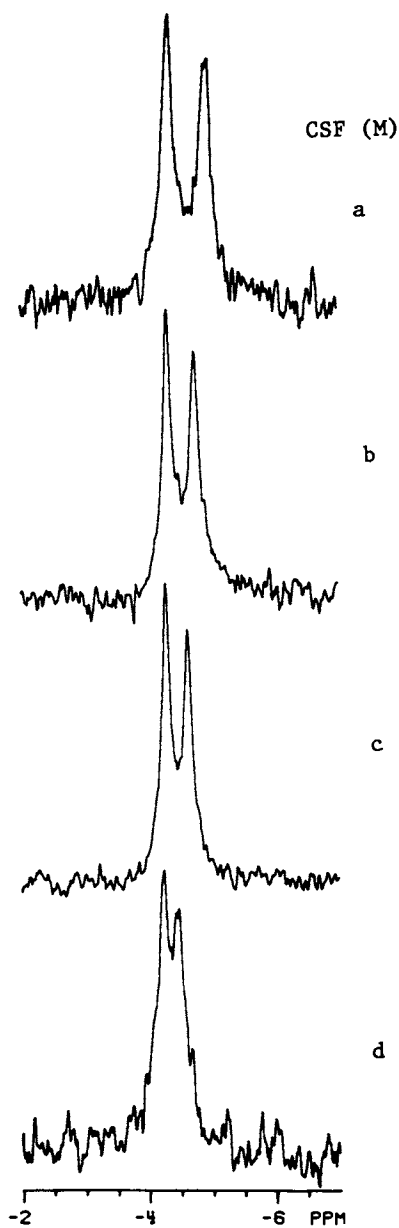


Figure 11. Dependence of  $^{31}\text{P}$  NMR spectra at 109.3 MHz of sonicated poly-(dAdT) on CsF concentration at 37°C. The increase in the separation of the two components is linear with CsF concentration (M): a, 4; b, 2; c, 1; and d, 0 (18).

with a component in the nanosecond range. However, the data currently available does not seem to be sufficient to obtain a physical picture of the internal motions (35). At the present time no generally satisfactory model for local backbone flexibility in DNA exists. A recent report questions this flexibility for DNA from <sup>31</sup>P NMR studies (36) on the basis of the broad linewidths of very long calf thymus DNA (reportedly 90 kilobases).

### Nucleosomes

Nucleosomes are DNA-protein (histone) complexes isolated from chromatin by treatment with nucleases, and nucleosomes constitute the main structural unit of the genetic material. There have been several <sup>31</sup>P NMR studies of DNA in intact nucleosome core particles (29,31,37,38). Several of these concluded that the DNA in the particles was quite mobile. In the study of Shindo et al (29), carried out at three frequencies (Fig. 12), it was concluded that the local mobility of the DNA in the particles was nearly as great as that of the naked DNA. In these studies there was no evidence for the presence of "kinks," i.e. distinct regions of abrupt local bending, although the analysis indicated multiple phosphodiester conformational environments (29).

A study of nucleosome core particles derived from poly(dAdT)•poly(dAdT) showed two clear stages in the thermal denaturation process (19,29). However, the doublet character of the naked d(AT)•d(AT) could not be resolved in the core particles (19).

The question of the degree of strong binding of DNA to the histone core particles was probed by <sup>31</sup>P NMR spectroscopy. The paramagnetic effect of Mn<sup>2+</sup> ions results in broadening of NMR signals (39). A comparison of nucleosome-bound DNA and naked DNA after removal of histones showed very little difference in the extent of <sup>31</sup>P line broadening by Mn<sup>2+</sup>; it appears that 95 ± 5% of the phosphates are readily accessible to solvent (40). This is consistent with other findings (41), including the fact that the periodic enzymatic cleavage of DNA adsorbed to flat surfaces mimics the cleavage of nucleosomes (42), and therefore primarily results from steric hindrance to the enzyme sites and not from inaccessibility of bound phosphates.

### Telestability

The concept of telestability in DNA is the propagation of a conformational change in one segment to neighboring segments along the DNA molecule (43). It is noteworthy that while d(GC)<sub>n</sub>, where n = 2 and 3, crystallized in the left-handed Z-form (7,8), an oligonucleotide containing d(AATT) flanked by two d(GC)<sub>2</sub> segments crystallized in a right-handed form (44). It is now possible to test how long a run of (GC) bases are required to convert into the Z-form in solution, and how effective such a run is in affecting adjacent non(GC) base sequences. It has been shown by

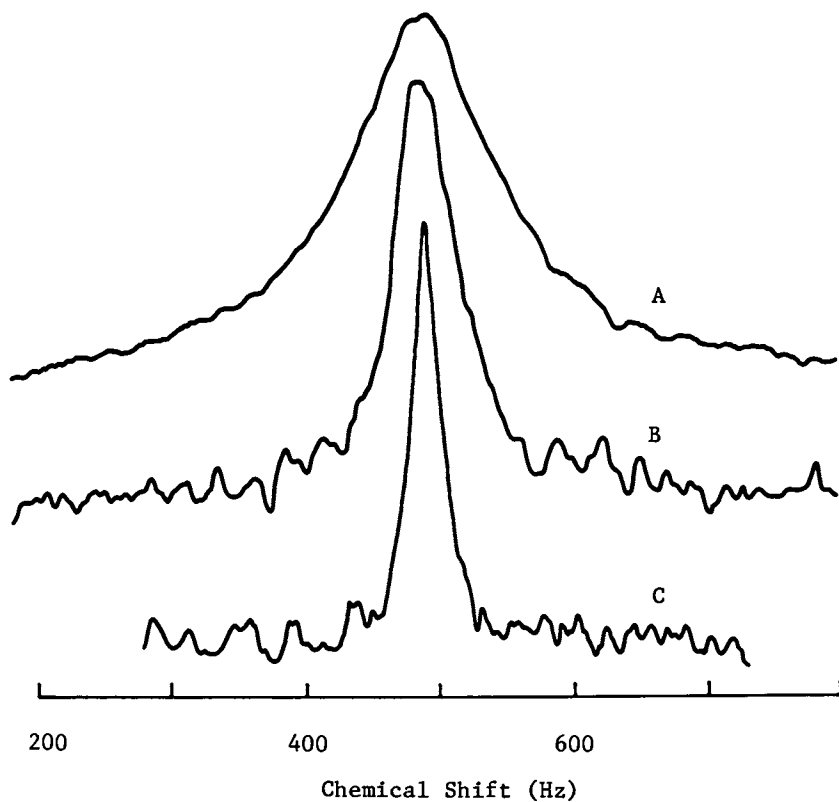


*Figure 12.  $^{31}\text{P}$  NMR spectra of nucleosome core particles (ca. 1 mg/mL) in 5 mM tris-Cl, 0.1 mM EDTA, pH 8, 19°C at three observing frequencies. The line widths are: A, 130 Hz; B, 45 Hz; and C, 25 Hz, with an approximately linear dependence on field strength A, 109.3 MHz; B, 40.3 MHz; and C, 24.3 MHz (29).*

CD that  $d(CG)_2$  does not convert in high salt to the Z-form while  $d(CG)_3$  does (45). These studies were carried out at low temperature where the oligonucleotides are double-stranded. Attempts to repeat these experiments with  $Mg^{2+}$  in  $^{31}P$  NMR studies have so far been unsuccessful due to the insolubility of the oligonucleotides at the high concentrations required for the NMR studies (46). The use of adjacent sequences of various lengths which are non-self-complementary but can form concatamers (45) should help to resolve the question of the extent of effectiveness of  $d(GC)$  segments.

### Genetic Significance

Alternating  $d(GC)$  segments embedded in longer DNA sequences have been interpreted to convert to left-handed Z-DNA in cloned and natural sequences (47). This requires relatively unphysiologically high salt concentrations, although the local environment of DNA in the cell might have an effectively high ionic strength, particularly in view of the presence of positively charged histones and spermidine, as well as mono- and di-valent metal ions.

The observation of the significant reduction of the ionic strength required to bring about the B to Z transition as a result of methylation on the 5-position of C may have direct genetic significance. Methylation of DNA bases is a common process and C is only methylated at the 5 position in eukaryotes (48). The possibility that the extent of methylation on C in CG sequences acts to facilitate conformational changes of DNA is very attractive. This effect could also be related to drug susceptibility (49). Variations in the backbone conformation of the B-form of DNA can be expected to be quite ubiquitous. Alternating AT sequences are quite uncommon in DNA, and one important region which is found to have this repeated sequence is the so-called (TATA) box in the promoter region of RNA polymerase (50). It is, of course, speculative to consider this a specific recognition site by virtue of its alternating DNA conformation. However, it is quite likely that local DNA conformations, resulting from specific base sequences and represented by particular constellations of phosphate charges and sugar hydroxyl groups, play significant roles in DNA-protein interactions.

### Acknowledgement

We thank James McGhee for helpful suggestions and Elmer Leininger for typing this manuscript.

Literature Cited

1. Arnott, S. Prog. Biophys. Mol. Biol., 1970, **21**, 265-319.
2. Viswamitra, M. A.; Kennard, O.; Jones, P. G.; Sheldrick, G. M.; Salisbury, S.; Farello, L. and Shakked, Z. Nature 1978, **273**, 687-8.
3. Wang, A. H. J.; Quigley, G. J.; Kolpak, F. J.; Crawford, J. L.; vanBoom, J. H.; van der Marel, G. and Rich, A. Nature 1979, **282**, 680-6.
4. Shindo, H.; McGhee, J. D. and Cohen, J. S. Proc. of the 8th Intl. Conf. on Mag. Res. in Biol., Nara, Japan, 1978.
5. Shindo, H.; Simpson, R. T. and Cohen, J. S. J. Biol. Chem., 1979, **254**, 8125-8.
6. Patel, D. J.; Canuel, L. L. and Pohl, F. P. Proc. Natl. Acad. Sci. USA 1979, **76**, 2508-11.
7. Crawford, J. L.; Kolpak, F. J.; Wang, A. H.-J.; Quigley, G. J.; vanBoom, J. H.; van der Marel, G. and Rich, A. Proc. Natl. Acad. Sci. USA 1980, **77**, 4016-20.
8. Drew, H.; Takano, T.; Tanaka, S.; Itakura, K. and Dickerson, R. E. Nature 1980, **286**, 567-73.
9. Arnott, S.; Chandrasekaran, R.; Birdsall, D. L.; Leslie, A. J. W. and Ratliff, R. L. Nature 1980, **283**, 743-5.
10. Pohl, F. M. and Jovin, T. M. J. Mol. Biol., 1972, **67**, 375-96.
11. Simpson, R. T. and Shindo, H. Nucleic Acids Res., 1980, **8**, 2093-103.
12. Cohen, J. S.; Wooten, J. B. and Chatterjee, C. L. Biochemistry 1981, **20**, 3049-55.
13. Behe, M. and Felsenfeld, G. Proc. Natl. Acad. Sci. USA 1981, **78**, 1619-23.
14. Cohen, J. S.; Chen, C.-W.; Behe, M. and Felsenfeld, G., unpublished results.
15. Wang, A. H. J.; Quigley, G. J.; Kolpak, F. J.; van der Marel, G.; vanBoom, J. H. and Rich, A. Science 1981, **211**, 171-6.
16. Klug, A.; Jack, A.; Viswamitra, M. A.; Kennard, O.; Shakked, Z. and Steitz, T. A. J. Mol. Biol., 1979, **131**, 669-80.
17. Shindo, H. and Zimmerman, S. B. Nature 1980, **283**, 690-1.
18. Chen, C.-W. and Cohen, J. S., unpublished results.
19. Simpson, R. T. and Shindo, H. Nuc. Acids Res., 1979, **7**, 481-92.
20. Shindo, H. and Simpson, R. T., unpublished results.
21. Marky, L. A.; Patel, D. and Breslauer, K. J. Biochemistry 1981, **20**, 1427-31.
22. Chen, C. W.; Cohen, J. S. and Zador, A. J. Biochem. Biophys. Methods, in press.
23. Kypr, J.; Vorlickova, M.; Budesinsky, M. and Sklenar, V. Biochem. Biophys. Res. Comm., 1981, **99**, 1257-64.
24. Vorlickova, M.; Kypr, J.; Kleinwachter, V. and Palecek, E. Nuc. Acids Res., 1980, **8**, 3965-73.
25. Patel, D. J.; Kozlowski, S. A.; Suggs, J. W. and Cox, S. D. Proc. Natl. Acad. Sci. USA 1981, **78**, 4063-67.
26. Zimmerman, S. B. and Pfeiffer, B. J. J. Mol. Biol., 1980, **315**, 1023-27.
27. Gorenstein, D. G. Ann. Rev. Biophys. Bioeng., 1981, **10**, 355-86.
28. Shindo, H. Biopolymers 1980, **19**, 509-22.
29. Shindo, H.; McGhee, J. D. and Cohen, J. S. Biopolymers 1980, **19**, 523-37.

30. Bolton, P.H. and James, T. L. J. Am. Chem. Soc., 1980, 102, 25-31.
31. Early, T. A. and Kearns, D. R. Proc. Natl. Acad. Sci. USA 1979, 76, 4165-9.
32. Klevan, L.; Armitage, I. M. and Crothers, D. M. Nuc. Acids Res., 1979, 6, 1607-16.
33. Hogan, M. E. and Jardetzky, O. (a) Proc. Natl. Acad. Sci. USA 1979, 76, 6341-5; (b) Biochem., 1980, 19, 3460-8.
34. Rill, R. L.; Hilliard, Jr., P. R.; Bailey, J. T. and Levy, J. C. J. Am. Chem. Soc., 1980, 102, 418-20.
35. Lipari, G. and Szabo, A. Biochemistry, in press.
36. Opella, S. J.; Wise, W. B. and DiVerdi, J. A. Biochem., 1981, 20, 284-90.
37. Cotter, R. I. and Lilley, D. M. J. F.E.B.S. Lett., 1977, 82, 63-8.
38. Kallenbach, N. R.; Appleby, D. W. and Bradbury, C. W. Nature 1978, 272, 134-8.
39. van Steenwinkel, R.; Campagnari, F. and Merlini, M. Biopolymers 1981, 20, 915-23.
40. Cohen, J. S.; Wooten, J. B.; McGhee, J. D. and Felsenfeld, G., unpublished results.
41. McGhee, J. D. and Felsenfeld, G. Nuc. Acids Res., 1980, 8, 2751-69.
42. Rhodes, D. and Klug, A. Nature 1980, 286, 573-8.
43. Wells, R. D.; Blakesley, R. W.; Hardies, S. C.; Horn, G. T.; Larson, J. E.; Burd, J. F.; Chan, H. W.; Dodgson, J. B.; Jensen, K. F.; Nes, I. F. and Wartell, R. M. CRC Crit. Revs. Biochem. 1977, 4, 305-40.
44. Wing, R.; Drew, H.; Takano, T.; Broka, C.; Tanaka, S.; Itakura, K. and Dickerson, R. E. Nature 1980, 287, 755-8.
45. Crea, R. and Quadrifoglio, F. Nuc. Acids Res., in press.
46. Cohen, J. S.; Chen, C.-W. and Crea, R., unpublished results.
47. Klysik, J.; Stirdivant, S. M.; Larson, J. E.; Hart, P. A. and Wells, R. D. Nature in press.
48. Razin, A. and Riggs, A. D. Science 1980, 210, 604-10.
49. Santella, R. M.; Grumberger, D.; Weinstein, I. B. and Rich, A. Proc. Natl. Acad. Sci. USA, 1981, 78, 1451-5.
50. Corden, J.; Wasyluk, B.; Buchwalder, A.; Sassone-Corsi, P.; Kedingen, C. and Chambon, P. Science 1980, 209, 1406-14.

RECEIVED February 2, 1982.



## Multiple Field Natural Abundance $^{13}\text{C}$ NMR Studies of DNA Dynamics

PETER R. HILLIARD and RANDOLPH L. RILL

Florida State University, Institute of Molecular Biophysics, Tallahassee, FL 32306

GEORGE C. LEVY and LINDA F. LEVY

Syracuse University, Syracuse, NY 13210

DNA is involved in several biological functions requiring substantial changes in conformation. For example, the intrinsically stiff DNA molecule is wrapped fairly tightly about histones in nucleosomes, and this entire complex must be partially unraveled during replication and transcription. The ability of DNA to assume several different conformational forms in response to its solid and solution environments has been evident for some time. Recent applications of spectroscopic methods sensitive to molecular dynamics have indicated that double stranded DNA can also undergo rapid local motions of significant amplitude.

Nuclear magnetic resonance spectroscopy seems well suited for characterizing fast local conformational changes and the rates at which they occur. Particularly attractive is the ability to probe the motions at many sites by observing different nuclei ( $^1\text{H}$ ,  $^{31}\text{P}$ ,  $^{13}\text{C}$  and  $^{15}\text{N}$ ). In the past, NMR spectra of solutions of large double stranded DNA could not be obtained. In principle this failure could be due to the extremely small overall motional correlation times predicted for long DNA, or to intermolecular interactions in the concentrated, extremely viscous solutions required for NMR measurements. Recent studies of the properties of highly concentrated solutions of DNA and other ionic polymers indicate that the latter effect dominates (see below). Use of micrococcal nuclease to digest calf thymus DNA, followed by size separation on agarose columns allows isolation of large quantities of double stranded DNA with a relatively small size dispersion, generally 80-90% within  $\pm 20\%$  size --e.g., 160 bp  $\pm 30$  bp. Size can be determined quite accurately using gel electrophoresis (isolation and characterization techniques described in detail Ref. 5). Several laboratories have now obtained proton,  $^{13}\text{C}$ , and  $^{31}\text{P}$  spectra of relatively small (ca. 120 to 300 bp), well fractionated and characterized double stranded DNA.(1-11) In many cases reasonably good values for  $T_1$  and NOE parameters have also been

0097-6156/82/0191-0269\$06.00/0

© 1982 American Chemical Society

obtained. These studies have led to a general consensus that double stranded DNA undergoes relatively rapid local or "internal" motions with correlation times of the order of a nanosecond.

Little is known about the exact nature of these local motions or the relative amplitudes and frequencies of motions at specific sites. Resolution of these questions requires data that is sufficiently accurate to differentiate the behavior at different sites, and to choose a model that appropriately describes the nature of these potentially complex motions. Despite low sensitivity at the natural abundance level,  $^{13}\text{C}$  NMR methods are probably most useful in this regard. The chemical shift range for  $^{13}\text{C}$  resonances is large and shift dispersion due to local variations in environment is modest. In practice this means that many DNA sites can be monitored, even though intrinsic linewidths are large compared to small molecule standards. In addition, the dominance of dipolar C-H coupling contributions to the relaxation of protonated carbons simplifies interpretation of  $^{13}\text{C}$   $T_1$  and NOE parameters.

For these reasons we have attempted to determine complete sets of linewidth,  $T_1$  and NOE data on several DNA sites obtained at several dispersed spectrometer frequencies (magnetic fields). Multiple field data is required to appropriately model DNA behavior (5,10). Improvements in instrumentation and methods of sample preparation have allowed us to discern modest differences in NMR parameters for several sugar and base carbons in double stranded DNA molecules, as functions of concentration and chain length. Less complete data have been obtained for single stranded DNA. In addition we have compared the NMR spectra of double stranded DNA in the presence and absence of mercury(II) to assess the usefulness of  $^{13}\text{C}$  NMR for studying DNA interactions with heavy metals.

Dependence of DNA  $^{13}\text{C}$  Linewidths on Chain Length. At high magnetic fields (corresponding for  $^{13}\text{C}$  NMR to 67.9 and 100.6 MHz) three of the five sugar carbon resonances of 160 bp DNA are fully resolved and many base resonances are partly resolved (Figure 1). Observation of these relatively narrow resonances is, in itself, highly suggestive of internal DNA motions. The correlation time for end-over-end tumbling of a rigid rod of this length (ca. 500 Å) is a few microseconds and would cause linewidths of a few thousand Hz if no other motions occur (7). Since the rotational correlation times of rigid rods of high axial ratios are proportional to length, DNA linewidths should decrease significantly if overall rotation made a major contribution. Very modest decreases in  $^{13}\text{C}$  linewidths were observed over the range from 160 to 34 bp (Table I). Early and Kearns (6,13) have also reported a small length dependence of proton linewidths for DNA smaller than 140 bp. Apparently contributions of overall tumbling to linewidths if present, are small.

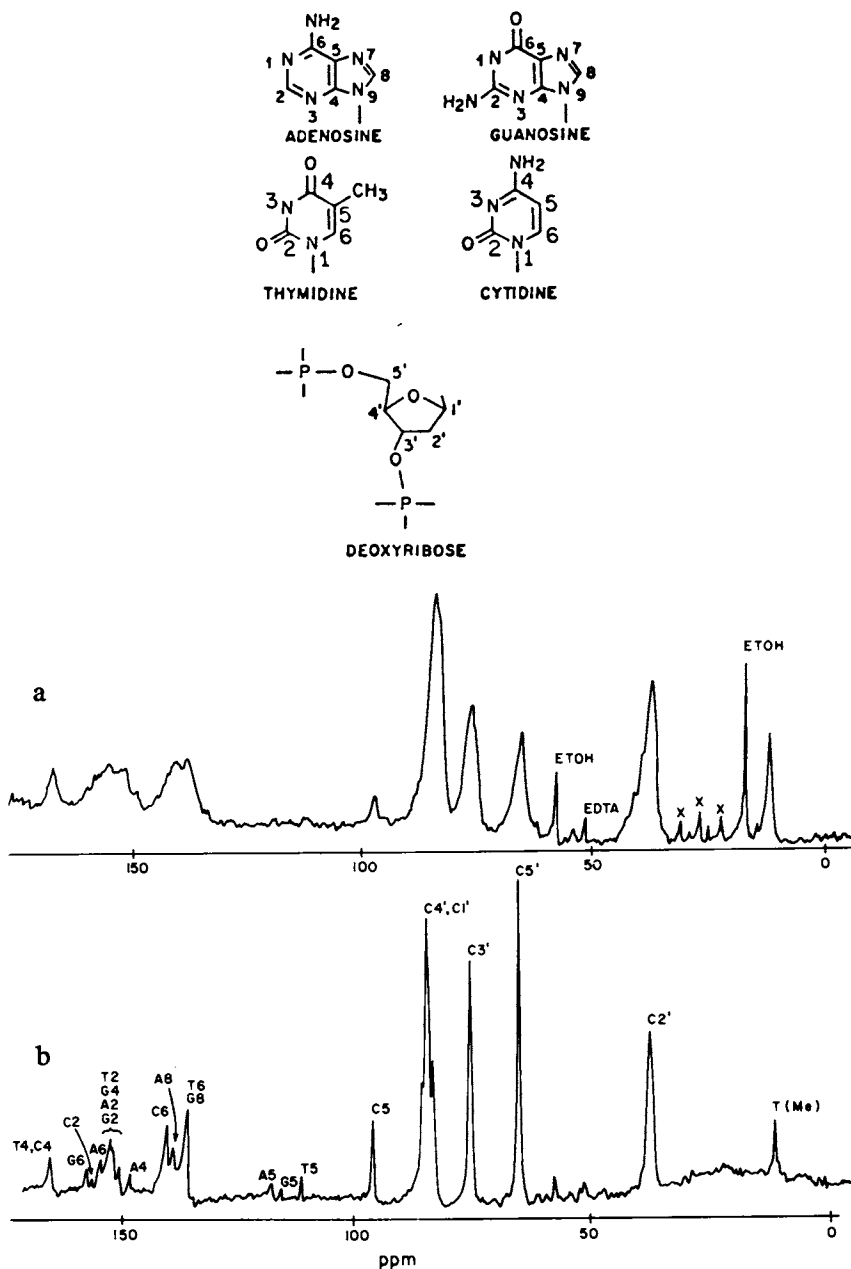


Figure 1.  $^{13}\text{C}$  NMR spectra of a, double-stranded and b, single-stranded 120 bp DNA, obtained at 100.6 MHz (scales approximately identical): a, 80 mg/mL, 32°C, 8000 scans, 20 Hz digital broadening, and scan interval 1 s; b, 80 mg/mL, 85°C, 3500 scans, 20 Hz digital broadening, and scan interval 1.5 s. (Reproduced, with permission, from Ref. 20. Copyright 1981, Adenine Press.)

Table I. Dependence of Sugar Carbon Resonance Linewidths on the Length of Double Stranded DNA.

Carbon	Linewidth ( $H_2$ ) for DNA of Length Indicated <sup>a</sup>					
	25-45 bp	110 bp	120 bp	160 bp <sup>b</sup>	236 bp <sup>c</sup>	800 bp <sup>d</sup>
C2'	176	219	279	262	344	No
C5'	152	---	179	154	---	spectrum
C3'	265	270	274	267	(328) <sup>e</sup>	observed
C4', C1'	254	230	270	266	351	
T(Me)	54	---	97	83	---	

<sup>a</sup>Measured at 32°C

<sup>b</sup>Average of 3-4 spectra, precision was ca. 10%

<sup>c</sup>Similar data has been obtained on 280 bp DNA contaminated with some mononucleosome length DNA

<sup>d</sup>Whole calf thymus DNA mechanically sheared and S1 nuclease treated, median size is given

In contrast, an increase in the DNA length from 160 bp to 230-280 bp caused significant increases in most linewidths. Linewidths of DNA averaging 800 bp long were too broad to allow acquisition of a useful spectrum under standard high resolution NMR conditions. Line broadening for long DNA probably reflects intramolecular ordering. Increases in the apparent molecular weight of concentrated DNA samples with time have been observed by light scattering methods (14), and recent sedimentation equilibrium measurements on highly concentrated DNA solutions have demonstrated the phase transition to an anisotropic state (15). Ordered solutions of sodium polyacrylate, another polyanion, have also been described (16). This ordering can be attributed to the requirement for minimization for strong repulsive electrostatic interactions at high polyanion concentrations and may reduce DNA motions due to the imposed intermolecular potentials. Of particular interest is the inverse relationship between the DNA length and the critical concentration required for transition to the ordered phase (15). We have observed a decrease in signal intensities accompanied by the appearance of turbidity in highly concentrated samples (> 200 mg/ml) of 160 bp length DNA. The failure to observe signals for 800 bp DNA at the concentration used (ca. 80 mg/ml) therefore may have been due to a lower critical concentration for ordering of this larger DNA. This can be tested using probes in widebore solenoids, which will allow samples to be run at less than 10 mg/ml. Such experiments are planned.

The Magnetic Field Dependence of DNA Linewidths. DNA linewidths are not controlled strictly by dynamics. There are many possible shielding environments due to ring current and other neighbor effects in random sequence DNA; thus a significant contribution of shift dispersion to linewidths is expected. Examination of the field dependence of selected resonance linewidths at four fields from 22.7 to 100.6 MHz confirms the importance of shielding dispersion (Figure 2). All sugar carbons exhibit similar shift dispersion calculated to be 1.4 to 1.9 ppm except for C2', for which the shift dispersion is somewhat less (ca. 1.0 ppm). Little dispersion was noted for the thymidine methyl shift. The linewidth of the C5' exocyclic sugar carbon is approximately 40% less than linewidths of other sugar carbons at low fields. Others have suggested that the similar linewidth represents a higher mobility at the C5' carbon (8,9), but NOE measurements do not support this conclusion (ref.5, see also below).

Spin-Lattice Relaxation Times and Nuclear Overhauser Enhancements of DNA Resonances.  $T_1$ 's and NOEF's are sensitive measures of molecular motions over a  $10^{-7}$  to  $10^{-12}$  second time scale (17). Linewidths are largely affected by dispersion and slower motions and thus  $T_1$ 's and NOEF's are better indicators of

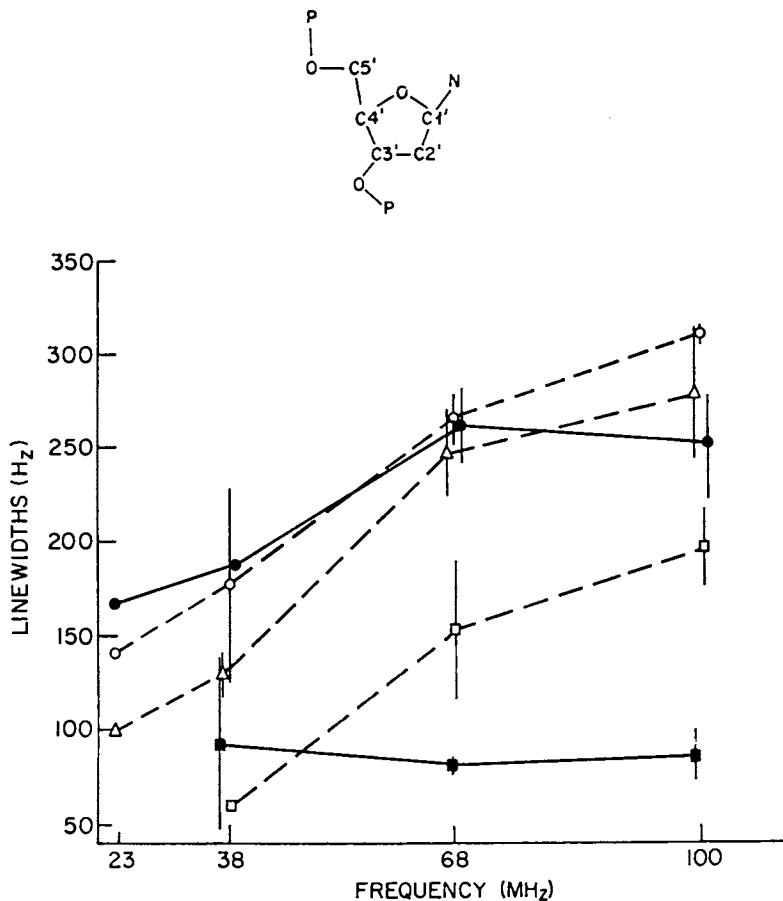


Figure 2. Line widths of double-stranded 160 bp (80 mg/mL) DNA as a function of magnetic field strength, 22.6 to 100.6 MHz: ○, C4', C1' band (unresolved); △, C3'; □, C5'; ●, C2'; and ■, thymidine methyl. Bars indicate the mean deviation of three different experiments at 37.7 and 100.6 MHz. (Reproduced, with permission, from Ref. 20. Copyright 1981, Adenine Press.)

rapid internal motions in polymers.  $T_1$ 's for protonated sugar carbons of native, 120 and 160 bp DNA are relatively small (ca. 0.5 sec at 67.9 MHz) and increase with increasing magnetic field (Table II), indicating that DNA motional rates are relatively fast, but slower than the extreme narrowing limit ( $< 10^{-10}$  sec). The few  $T_1$ 's measured for protonated base carbons were essentially identical to those of sugar carbons.

Reasonably large Overhauser Enhancements were observed for all sugar carbons (table III). These NOEF's are generally similar (ca. 0.5 to 0.7 at 67.7 MHz) and decrease modestly with increasing field, but the C2' NOEF's are consistently larger than NOEF's of other sugar carbons at all fields. Significant NOEF's averaging about 0.35 at 67.7 MHz were also observed for several protonated base carbons. Small NOEF's, probably reduced as a result of chemical shift anisotropy relaxation contributions, were observed for non-protonated base carbons.

These data can be compared to two other <sup>13</sup>C NMR studies of DNA. The  $T_1$ 's and NOE's measured at 50.3 MHz for sugar carbons of sonicated DNA of undefined length and degree of single strandedness by Bolton and James (8,9) are considerably smaller than we have found. No base resonances were observed in that study (8,9).  $T_1$ 's (0.13-0.16) and NOEF's (0.9-1.3) measured at 25.1 MHz for 260 bp DNA by Hogan and Jardetzky (3,7) are generally consistent with our data, although most individual resonances were unresolved at the lower field. As emphasized by Hogan and Jardetzky (3,7) the observation of significant NOE's provides the most unambiguous evidence for rapid internal motions in DNA. Although precise description of these motions requires choice of an appropriate model, the NOE's observed for DNA sugar carbons must be associated with motional correlation times of nanosecond order. We have observed a consistent pattern of small differences in  $T_1$ 's and particularly NOEF's of sugar and base carbons. These suggest two general features of the DNA motions. First, the motional dynamics of all sugar carbons are generally similar; however C2' (but not C5') appears to have slightly greater motional freedom than other carbons. Second, the DNA bases also undergo rapid motions that are presumably coupled with sugar motions, but exhibit slightly different dynamics. (Dynamics is used in a general sense here and may include frequency, amplitude, and geometric contributions to relaxation behavior.)

**Effects of Heat Denaturation.** We have also conducted <sup>13</sup>C NMR studies of heat denatured DNA to determine how much the intrinsic motional dynamics of the polynucleotide chain are influenced by formation of the double stranded structure. Heat denaturation of 160 bp DNA decreases sugar carbon linewidths by over 100 Hz at high fields (Figure 1b and Table IV). Protonated base carbon resonances sharpen to a similar degree, and at 100.6 MHz many resonances are resolved into site-specific lines. Sugar

Table II.  $^{13}\text{C}$  Spin Lattice Relaxation Times in DNA<sup>a</sup>

<u>Carbons</u>	<u>160 np DNA<sup>d</sup></u>			
	<u>Native<sup>b</sup></u>			<u>Denatured<sup>c</sup></u>
	<u>37.7 MHz</u>	<u>67.9 MHz</u>	<u>100.6 MHz</u>	<u>67.9 MHz</u>
C2'	0.20	0.27 $\pm$ .01	0.41 $\pm$ .01	0.28 $\pm$ .03
C5'	----	0.23 $\pm$ .01	0.37 $\pm$ .03	0.22 $\pm$ .01
C3'	0.21	0.48 $\pm$ .03	0.63 $\pm$ .06	0.50 $\pm$ .01
C4', C1'	0.21	0.54 $\pm$ .04	0.63 $\pm$ .08	0.41 $\pm$ .02
T(Me)	----	0.90	1.6 $\pm$ .02	----
C5	----	----	----	(0.55)

	<u>120 np DNA<sup>e</sup></u>				
	<u>Native<sup>b</sup></u>			<u>Denatured<sup>c</sup></u>	
C2'	----	0.28	0.45	0.34	0.24
C5'	0.12	0.24	0.33	0.29	0.24
C3'	0.21	0.47	0.57	0.63	0.52
C4', C1'	0.21	0.49	0.66	0.59	0.47
T(Me)	----	1.0	1.3	----	1.0
C5	----	----	0.65	----	0.65
T4, C4	1.7	----	----	----	----

<sup>a</sup> $T_{1s}$ , 10–20%. Mean deviations shown are from the average of 2 experiments

<sup>b</sup>Native DNA measurements at 32°C.

<sup>c</sup>Denatured DNA measurements at 85°C.

<sup>d</sup>160 nP DNA is essentially 100% double stranded by assays described in the text.

<sup>e</sup>120 nP DNA was 15% single stranded by assays described in reference 5.



Table III.  $^{13}\text{C}$  Nuclear Overhauser Enhancement Factors for  
120 bp double stranded DNA in  $\text{D}_2\text{O}^{\text{a}}$ .

<u>Carbons</u>		<u>Native<sup>b</sup></u>		<u>Denatured<sup>c</sup></u>
<u>Sugar</u>	<u>37.7 MHz<sup>d</sup></u>	<u>67.9 MHz<sup>d</sup></u>	<u>100.6 MHz<sup>d</sup></u>	<u>100.6 MHz</u>
C2'	0.81±0.04	0.72±0.06	0.58±0.03	1.2±0.06
C5'	0.79±0.02	0.58±0.03	0.40±0.04	1.3±0.02
C3'	0.58±0.05	0.65±0.01	0.43±0.04	1.3±0.05
C4',1'	0.62±0.02	0.55±0.02	0.37±0.05	1.3±0.06
<u>Bases</u>				
Th <sup>e</sup>	(0.81±0.11)	(0.65±0.02)	(0.48±0.09)	(0.64±0.07)
Nonprotonated (A5)	0.09	0.12±0.08	0.09±0.15	-
Protonated G8, T6, A8, C6)	0.30-0.45	0.30-0.40	0.24-0.36	-

<sup>a</sup> Measured in 19 mM  $\text{Na}_2\text{HPO}_4$ , 7 mM  $\text{NaH}_2\text{PO}_4$ , 50 mM  $(\text{CH}_3)_3\text{Si}(\text{CH}_2)_3\text{SO}_3\text{Na}$ , 2 mM  $\text{Na}_2\text{EDTA}$ , pH 7.25, and 3 mM  $\text{NaN}_3$ .

<sup>b</sup> Measured at 32°C.

<sup>c</sup> Measured at 85°C, estimated precision of two experiments ( $\pm$  mean deviation). An experiment in  $\text{H}_2\text{O}$  yielded NOEFs identical within experimental error.

<sup>d</sup> Estimated precision of two experiments ( $\pm$  mean deviation).

<sup>e</sup> NOEF is partly suppressed by delay time between pulses of less than 5 times  $T_1$ .

Table IV.  $^{13}\text{C}$  NMR Linewidths of Native and Denatured, 160 bp DNA at 67.9 MHz.

<u>Carbons</u>	<u>Linewidths<sup>a</sup></u>	
	<u>Native<sup>b</sup></u>	<u>Denatured<sup>c</sup></u>
<u>Sugar</u>		
C2'	262 ± 21	102 ± 11
C5'	154 ± 37	31 ± 8
C3'	248 ± 23	60 ± 17
C4', C1'	266 ± 14	125 ± 30
<u>Base</u>		
T(Me)	83 ± 3	42 ± 14
C5	-----	42 ± 14
T4, C4	-----	74 ± 14

<sup>a</sup>In Hz; estimated precision of three experiments ( $\pm$  mean deviation)

<sup>b</sup>Measured at 32°C

<sup>c</sup>Measured at 85°C; Measurements at 100.6 MHz resolve several of these bands into multiplets, with apparent "natural" linewidths near 10 Hz for C2', C3', C1' and C4'. C5' does not resolve into multiplet structure at 100.6 MHz.

carbon NOEF's increase significantly and more or less uniformly upon denaturation. These changes in linewidths and NOEF's are consistent with the macroscopically observable decrease in chain stiffness and increased mobility upon strand separation.

In contrast,  $NT_1$ 's of the native and denatured forms are quite similar (Table II). This unexpected equivalence of  $NT_1$ 's indicates that spin-lattice relaxation times may be insensitive to motional changes in these relatively short DNA chains. Three explanations may account for these results.

- i. The  $NT_1$ 's correspond to  $\tau_{eff}$  values more-or-less symmetrically disposed about the  $T_1$  minimum (Figure 3a).
- ii. The motional dynamics may reflect a non-exponential autocorrelation function, producing a decreased dependence of  $NT_1$  on the rate of molecular reorientation (Figure 3b) (18).
- iii. The  $NT_1$ 's may have a complex dependence on composite overall and internal motions, resulting in little change in the observed values.

At present a combination of (ii) and (iii) seem most plausible.

Effects of Mercury (II) on Double Stranded DNA. NMR methods may be particularly useful in the future for characterizing the mechanisms of binding of small molecules to DNA and their perturbations of the native DNA structure. Preliminary studies of the binding of mercury (II) to double stranded DNA support this view, but in a surprising way. Mercury binding to large DNA is accompanied by a release of protons, a hyperchromic shift in absorbance at 258 nm, and a substantial (nearly 10-fold) decrease in intrinsic viscosity (12). These effects indicate that mercury binds to DNA base sites normally involved in base pairing, causing partial strand separation. The properties of native, double stranded DNA are rapidly restored upon addition of chelating agents, hence some bound mercury must crosslink adjacent DNA strands.

Because of the strand separation and reduction in viscosity caused by mercury (II) we expected to observe significant decreases in resonance linewidths of DNA upon binding mercury. Instead we found that linewidths were essentially unchanged, even in the presence of nearly saturating amounts of mercury (Figure 4).  $T_1$ 's were also affected very little, with some lowering of observed NOEF's. Subsequent measurements have shown that the viscosity of 140-160 bp DNA decreases only by 15-20% upon binding equimolar amounts of mercury (per nucleotide), although the circular dichroism spectrum is drastically changed (L. Levy and P. Hilliard unpublished observations). The failure of high concentrations of mercury to significantly alter the viscosity or <sup>13</sup>C NMR parameters of DNA suggest that most bound mercury is involved in crosslinking DNA strands, and that rapid local chain

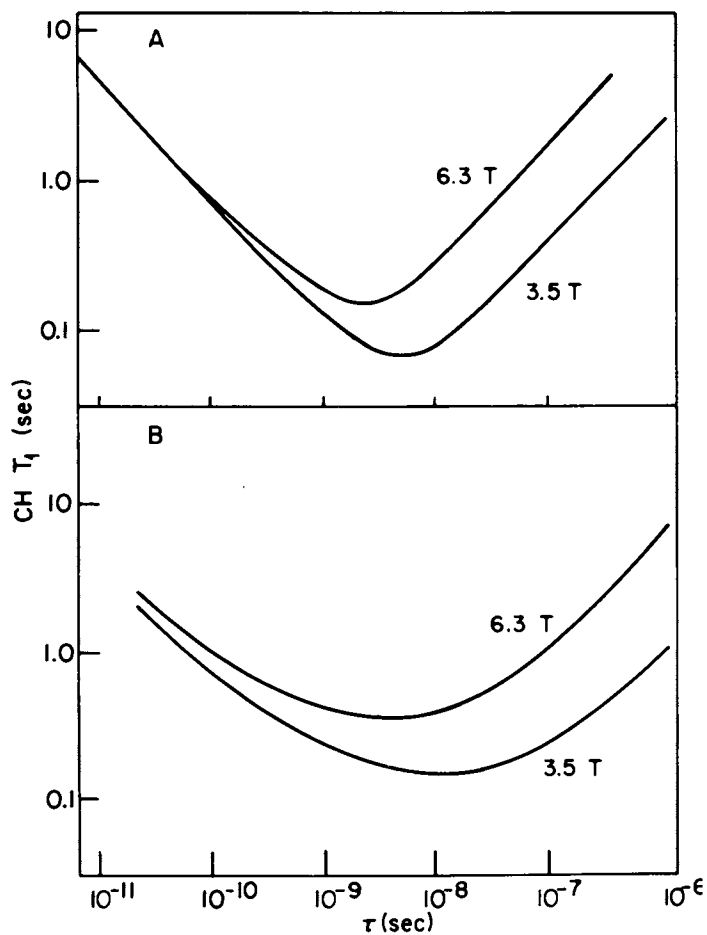


*Figure 3. Dipolar  $T_1$  for a CH carbon as a function of an effective correlation time for molecular tumbling,  $\tau$ . Key: A, isotropic or pseudoisotropic tumbling characterized by an exponential autocorrelation function  $G(\tau)$ ; and B, complex behavior resulting from a nonexponential decay of  $G(\tau)$ . This requires that motion be represented by a set of  $\tau$ 's, or a distribution around some mean. (Reproduced, with permission, from Ref. 20. Copyright 1981, Adenine Press.)*

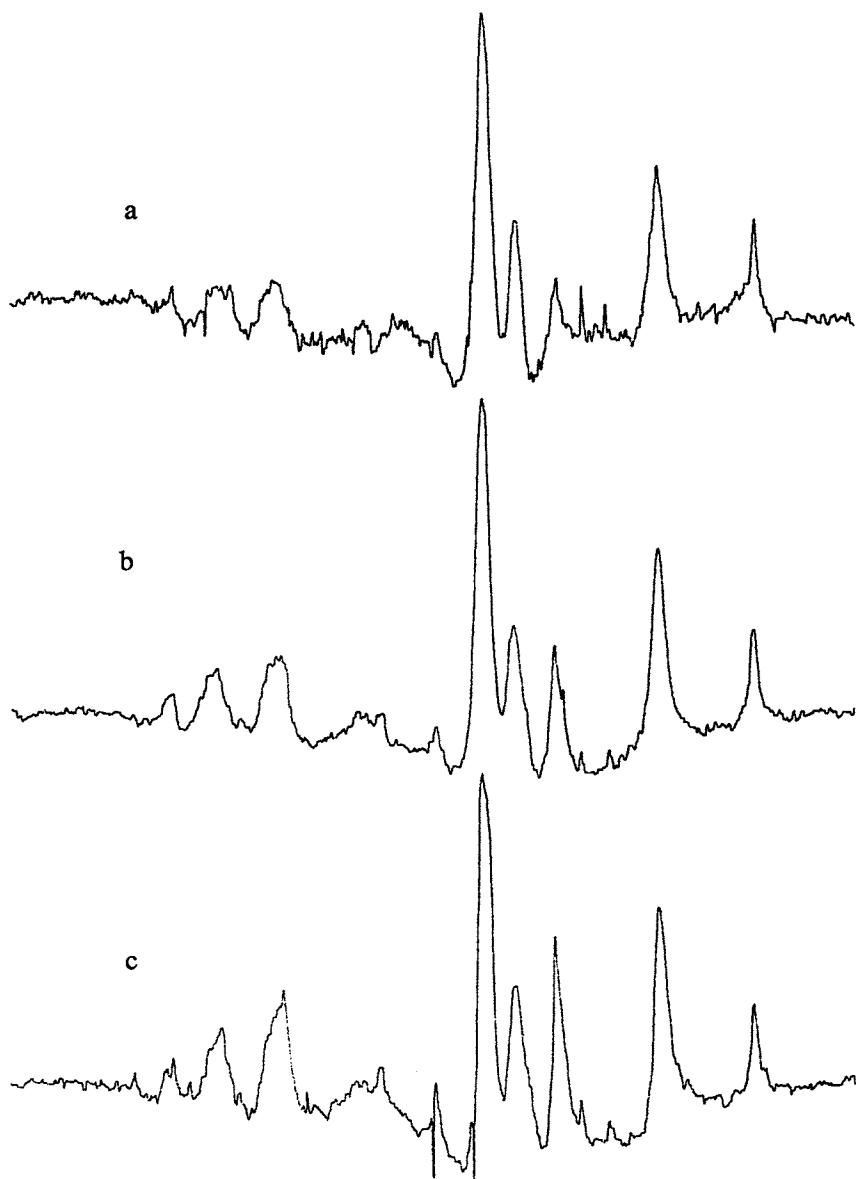


*Figure 4. Effects of Hg(II) binding to 120 bp double-stranded DNA: a, no Hg, b, 0.4 mole Hg(II) per mol of DNA base pairs, and c, 0.8 mol of Hg(II) per mol of base pairs; 72 mg/mL, 60,000 scans per spectrum, 32°C, 20 Hz digital broadening, and scan interval 1.2 s.*

dynamics are relatively unaffected by any partial strand separation.

Concluding Remarks. Carbon-13 NMR parameters clearly are sensitive to differences in motional dynamics at various sites in double and single stranded DNA and DNA complexes. Dynamics, as measured by NMR parameters, depend on the amplitudes and direction cosines, as well as the frequencies, of specific C-H vector motions. In general, local motions in double stranded DNA appear to occur with frequencies in the nanosecond range. These motions are probably superimposed on slower bending or wobbling of the chain as a whole (19). Interpretation of NMR data in terms of realistic amplitudes and frequencies of specific motions is not straightforward. Preliminary calculations based on a conical restricted diffusion model are consistent with an increase in both rate and amplitude of internal motions on denaturation of DNA. A description of this theory and a comparison to others currently in use are given in a forthcoming publication (19).

#### Literature Cited

1. Davanloo, P.; Armitage, I.M.; Crothers, D.M. Biopolymers 1979, **18**, 663-680.
2. Klevan, L.; Armitage, I.M.; Crothers, D.M. Nucleic Acid Research 1979, **6**, 1607-1616.
3. Hogan, M.E.; Jardetzky, O. Natl. Acad. Sci. USA 1979, **76**, 6341-6345.
4. Rill, R.L.; Hilliard Jr., P.R.; Bailey, J.T.; Levy, G.C. J. Amer. Chem. Soc. 1981, **102**, 418-420.
5. Levy, G.C.; Hilliard Jr., P.R.; Levy, L.F.; Rill, R.L.; Inners, R. J. Biol. Chem. 1981, **256**, 9986-9989.
6. Early, T.A.; Kearns, D.R. Proc. Natl. Acad. Sci. USA 1979, **76**, 4165-4169.
7. Hogan, M.E.; Jardetzky, O. Biochemistry 1980, **19**, 3460-3468.
8. Bolton, P.H.; James, T.L. J. Phys. Chem. 1979, **83**, 3359-3366.
9. Bolton, P.H.; James, T.L. Biochemistry 1980, **19**, 1388-1392.
10. Shindo, H. Biopolymers 1980, **19**, 509-522.
11. Simpson, R.T.; Shindo, H. Nucleic Acid Research 1979, **7**, 481-492.
12. Bloomfield, V.A.; Crothers, D.M.; Tinco, I. "Physical Chemistry of Nucleic Acids"; Harper and Row: New York, 1974; p 421-429.
13. Imino proton linewidths for the following lengths were observed: 192 Hz, 16 bp; 213 Hz, 53 bp; 260 Hz, 154 bp; 345 Hz, 200 bp; 445 Hz, 500 bp.
14. Reinert, K.E.; Geller, K. Stud. Biophys. 1974, **45**, 1-11.

15. Brian, A.A.; Firsch, H.L.; Lerman, L.S. Biopolymers 1981, 20, 1305-1328
16. Ise, N.; Okubo, T.; Yamamoto, K.; Kawai, H.; Hashimoto, T.; Fujimura, M.; Hiraga, Y. J. Amer. Chem. Soc. 1980, 102, 7901-7906.
17. Levy, G.C.; Lichter, R.L.; Nelson, G.L. "Carbon-13 Nuclear Magnetic Resonance Spectroscopy"; John Wiley and Sons: New York, 1980; p 229.
18. Schaefer, J. Macromolecules 1973, 6, 882-888.
19. London, R.L.; Craik, D.J.; Levy, G.C., to be submitted.
20. "Biomolecular Stereodynamics"; Edited by R. H. Sarma; Adenine Press, New York; 1981; Vol. I; pp 383-390.

RECEIVED February 1, 1982.

# Photochemically Induced Dynamic Nuclear Polarization (Photo-CIDNP) of Biological Molecules Using Continuous Wave and Time-Resolved Methods

P. J. HORE and R. KAPTEIN

University of Groningen, Physical Chemistry Laboratory,  
Nijenborgh 16, 9747 AG Groningen, Netherlands

NMR spectra of samples in which free radical reactions are taking place may show strongly perturbed intensities for lines belonging to reaction products. This effect is called chemically induced dynamic nuclear polarization or CIDNP. Over the past ten years CIDNP has become an established method for mechanistic investigations of reactions involving short-lived radical intermediates. Several reviews (1, 2, 3) and a monograph (4) have appeared on the theory and applications in organic chemistry.

Biochemical applications have been made more recently (5, 6). Here, cyclic photochemical reactions are employed to generate nuclear spin-polarization in biological macromolecules. The information obtained is of a structural nature rather than mechanistic. In the case of proteins aromatic amino acid residues (tyrosine, histidine and tryptophan) can be polarized by reversible hydrogen atom or electron transfer reactions with a photo-excited dye. These reactions require direct contact of the dye with the amino acid side-chains so that they only occur for residues lying at the surface of the protein. The method, therefore, affords a "surface probe" with the high intrinsic resolution of NMR. Furthermore, photo-CIDNP appears to be particularly useful in characterizing specific aromatic residues involved in interactions of proteins with ligands.

In this paper we shall first review the CIDNP phenomenon and give a simple account of the so-called radical pair mechanism, which is responsible for the effects in most cases. We then proceed to give a critical discussion of the special case of cyclic reactions, which are of paramount importance in biochemical applications. Due to the basic spin-sorting nature of the radical pair mechanism (partial) cancellation of polarization may occur in cyclic reactions where no net chemical change occurs. This obscures information and makes quantitative evaluation of CIDNP intensities difficult. Several sources of these cancellation effects will be discussed

0097-6156/82/0191-0285\$10.75/0  
© 1982 American Chemical Society



and the important role of nuclear spin-lattice relaxation in the radicals will be delineated.

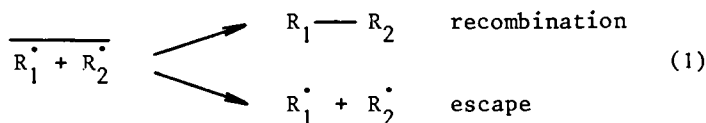
Photo-CIDNP spectra of amino acids are presented in the following section with the aim of establishing the ground rules for applications to protein systems. An illustrative example of protein CIDNP spectra is also given in this section.

The general method as applied to biological macromolecules makes use of photo-excitation by continuous wave argon laser irradiation in the NMR probe (in our laboratory of a 360 MHz spectrometer). In the last section we shall see, however, that as first demonstrated by Closs and Miller (7) pulsed lasers can be profitably employed in mechanistic photo-CIDNP studies. The resulting "flash photo-CIDNP" spectra allow monitoring of the build-up or decay of polarization with a time-resolution of a few microseconds (basically limited by the rf pulse). Particularly, in the case of cyclic reactions information that is lost in the more conventional experiment is regained in spectra taken in the short time regime.

#### The Radical Pair Mechanism of CIDNP

Spin-selective Radical Reactions. The CIDNP effect arises from magnetic interactions in pairs of free radicals.

The underlying principle is the fact that nuclear spins present in the radicals influence the chemical reaction of a radical pair, in particular whether the radicals will recombine during an encounter or escape back into solution:



Here, "recombination" stands for all types of radical pair collapse reactions, such as coupling, disproportionation, back electron transfer etc. This nuclear spin dependent reactivity is a consequence of two basic premises of the radical pair theory:

- (i) the reaction probability of a radical pair depends on its electronic spin state (usually recombination occurs only in the singlet state) and
- (ii) there are nuclear spin dependent interactions involved in interconverting singlet and triplet radical pair states (i.e. reactive and unreactive states).

We are quite familiar with the first assumption. For instance, in the prototype radical recombination reaction of two H-atoms to give a H<sub>2</sub> molecule it is well known that only a singlet pair of H-atoms would approach on an attractive potential energy curve, while the triplet pair would experience a repulsive force at short distances. A similar spin state

selectivity seems to be generally observed for more complex reactions, too. The only exceptions are some electron transfer reactions where the products have low lying triplet states, (8, 9) in which case products are formed preferentially in the triplet state.

The role of nuclear spins in chemical reactions does not seem to have been noted before the advent of CIDNP. It is easy to see, however, how (i) and (ii) can lead to a sorting mechanism for nuclear spins and therefore to strong polarizations in radical pair products. This is demonstrated in Figure 1, which shows a typical photo-induced radical reaction.

Vector Model. Now the question still remains how nuclei manage to change the spin-multiplicity of a radical pair and why this would depend on their spin state. This is most easily explained in terms of a vector representation for the unpaired electron spins. Let us consider a one proton radical pair  $R_1\dot{H} + R_2\dot{\phantom{H}}$  assuming  $g_2 > g_1$ . The resonance conditions for the electron spins in a magnetic field B are

$$\hbar\omega_1^\pm = g_1\beta B \pm \frac{1}{2}A \quad (2)$$

$$\hbar\omega_2 = g_2\beta B \quad (3)$$

expressed in terms of the angular frequency  $\omega = 2\pi\nu$ ; the + and - signs denote the  $\alpha$  and  $\beta$  nuclear spin state, respectively. A is the hyperfine coupling (hfc) constant of the proton. In a semiclassical picture the magnetic moments associated with the electron spins can be represented by vectors precessing about the direction of the effective magnetic field. The precession frequencies are then just given by  $\omega_1^\pm$  and  $\omega_2$  of equations (2) and (3). When a pair of radicals is formed from a common precursor, their spin vectors are initially correlated. For a singlet state precursor they are antiparallel, while for a pair formed in the triplet  $T_0$  state, as is assumed in Figure 2, there is a resulting component in the plane perpendicular to B. We need not consider the other triplet states,  $T_+$  and  $T_-$ , because in high magnetic fields there is no S-T mixing with these states. Figure 2 shows that, starting from the  $T_0$  state, unequal precession rates cause a transition from the triplet to the singlet state. For our radical pairs with  $\alpha$  and  $\beta$  protons these differences in precession rates are

$$\Delta\omega^+ = \omega_1^+ - \omega_2 = \hbar^{-1} [(g_1 - g_2)\beta B + \frac{1}{2}A] \quad (4)$$

$$\Delta\omega^- = \omega_1^- - \omega_2 = \hbar^{-1} [(g_1 - g_2)\beta B - \frac{1}{2}A] \quad (5)$$

The  $\Delta\omega$ 's (or rather their absolute magnitudes) determine the

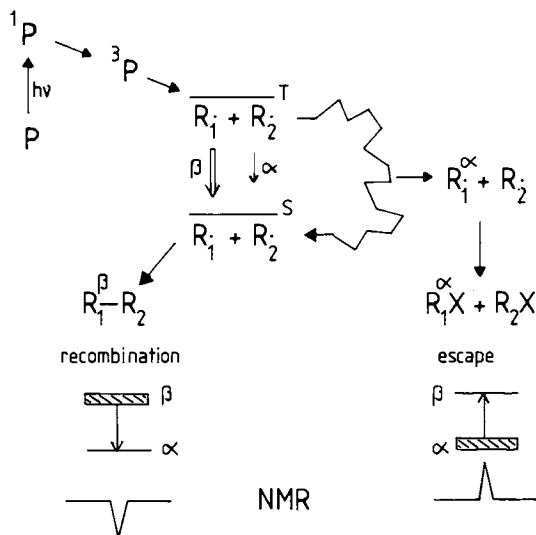


Figure 1. Schematic representation of the nuclear spin-sorting process in a photo-induced radical reaction;  $\alpha$  and  $\beta$  denote nuclear spin states. The following sequence of events is assumed to occur:

1. Compound P is photoexcited to a singlet state  $^1P$  which crosses over to a triplet state  $^3P$ .
2. A radical pair is formed from this state that will still be in a triplet (T) state initially (a pair of original partners with correlated electron spins is indicated by a bar)
3. Now a random-walk diffusion starts as indicated by the zig-zag path. Simultaneously, intersystem crossing ( $T \rightarrow S$ ) transitions may occur, induced by the coupling of the electron spins with nuclear spins (hyperfine coupling). The rate of this intersystem crossing depends on the nuclear spin state. Here it is assumed that it is faster for  $\beta$  nuclei than for  $\alpha$  nuclei.
4. Consequently, singlet pairs will be formed faster with  $\beta$  nuclei spins than with  $\alpha$  spins. During diffusive re-encounters, this excess of  $\beta$  spins is carried over to the recombination product because only singlet pairs recombine.
5. Thus, in the recombination product the  $\beta$  nuclear spin level, which is higher in energy, is overpopulated. This leads to an emissive NMR signal for this product.
6. Conversely, radicals with an excess of  $\alpha$  nuclear spins are left over in solution, leading to "escape" products for which the NMR spectrum shows enhanced absorption signals.

triplet to singlet interconversion rates and are indeed seen to be nuclear spin dependent. In the example chosen, with  $g_2 > g_1$  and  $A > 0$ , we have  $|\Delta\omega^-| > |\Delta\omega^+|$  and therefore inter-system crossing is faster for pairs with  $\beta$  protons than for those with  $\alpha$  protons conforming with the situation depicted in Figure 1.

The generation of CIDNP is seen to be a rather fast process. If a "CIDNP time-scale" can be defined, it is a combination of timescales of nuclear spin dependent inter-system-crossing ( $10^{-9}$ - $10^{-8}$  s) and of the re-encounter probability of a diffusing geminate radical pair, which is non-vanishing for times up to  $10^{-7}$  s. The polarization generated in times of  $10^{-9}$  -  $10^{-7}$  s, however, is stored in diamagnetic reaction products and decays with the much longer relaxation time  $T_1$ , which is typically 1 - 10 s for protons in small molecules (0.3 - 2 s for macromolecules). This slow decay allows the observation of CIDNP in a NMR experiment.

Sign Rules for CIDNP. In high magnetic fields there are two types of polarization: net polarization and multiplet effects, the latter being the occurrence of both absorption (A) and emission (E) in the J-coupled multiplet of a nucleus. Although multiplet effects occur seldom at the very high magnetic fields employed in biological applications we shall discuss them here for the sake of completeness. Both effects can be predicted qualitatively by multiplicative sign rules (10), when the chemistry and the magnetic parameters of the radical pair are known. Thus, the sign of the net polarization of nucleus  $i$  is given by a product of four signs:

$$\Gamma_n(i) = \mu \cdot \varepsilon \cdot \Delta g \cdot A_i \quad \begin{cases} + & A \\ - & E \end{cases} \quad (6)$$

Similarly the "phase" of the multiplet effect of the coupled nuclei  $i$  and  $j$  is given by

$$\Gamma_m(i,j) = \mu \cdot \varepsilon \cdot A_i \cdot A_j \cdot J_{ij} \cdot \sigma_{ij} \quad \begin{cases} + & EA \\ - & AE \end{cases} \quad (7)$$

where EA means E in the low field part and A in the high field part of the multiplet. The expressions contain the signs of the hfc constants  $A_i$  and  $A_j$  and of the spin-spin coupling constant  $J_{ij}$  in the  $i$  product;  $\Delta g$  is the sign of  $g_1 - g_2$  where  $g_1$  is the  $g$ -factor of the radical carrying nucleus  $i$ . The sign conventions for the other parameters are as follows:

$$\mu \begin{cases} + & \text{for a T precursor and random encounter pairs (F-pairs,} \\ & \text{see below)} \\ - & \text{for a S precursor} \end{cases}$$

$$\varepsilon \begin{cases} + & \text{for recombination products} \\ - & \text{for escape products} \end{cases}$$

$$\sigma_{ij} \begin{cases} + & \text{when nuclei } i \text{ and } j \text{ reside in the same radical} \\ - & \text{when nuclei } i \text{ and } j \text{ reside in different radicals} \end{cases}$$

Examples of the use of these rules will be given below.

### Cyclic Reactions and Cancellation

CIDNP in Cyclic Reactions. To facilitate the discussion of CIDNP intensities arising from cyclic reactions we consider the scheme in Figure 3 in which A and B are diamagnetic reactants and  $A^{*-}$  and  $B^{*+}$  are radicals derived from them by photolytically induced electron transfer. The geminate radical pair which is labelled G can be either singlet (S) or triplet (T). Escape polarization in  $A^{*-}$  and recombination polarization in A are denoted schematically by  $\downarrow$  and  $\uparrow$  respectively. The radicals which escape from the geminate radical pair eventually recombine in random encounters as shown; this is usually a much slower process than geminate recombination which is complete within about  $10^{-7}$  s. Although we consider the case of an electron transfer reaction, the following argument is general and recombination can be taken to imply any radical-radical reaction which re-forms the diamagnetic reactants.

Recalling the spin-sorting nature of the radical pair mechanism, we can anticipate that in the absence of nuclear spin relaxation, random recombination will eventually lead to exact cancellation of the  $\uparrow$  polarization when the  $\downarrow$  polarization in  $A^{*-}$  is transferred to A (making the usual assumption that chemical reaction preserves nuclear spin orientation). In such a situation, polarization in A could only be observed in a time-resolved experiment before all the radicals had recombined. Relaxation of the nuclei  $A^{*-}$ , however, allows some of the escape polarization to "leak away" preventing complete cancellation (11). Thus, unless the radical lifetime is very much smaller than the nuclear relaxation time in the radicals ( $T_1^R$ ), polarization may be observed even under steady state conditions (e.g. continuous photolysis).

Such a mechanism of cancellation leads one to expect that when relaxation is very slow, the initial polarization in A would fall, eventually to zero, with the same second order kinetics as the radical disappearance. Conversely for very fast relaxation we anticipate no time dependence whatsoever. At intermediate  $T_1^R$  values, a complicated time dependence is predicted with a non-zero final level.

In fact the situation is complicated slightly by the possibility of further polarization being generated in the so-called F-pairs that arise during the random recombination

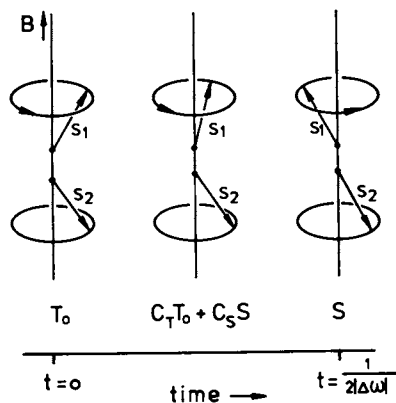


Figure 2. Precession of electron spin vectors  $S_1$  and  $S_2$  of a radical pair viewed in a frame rotating with  $S_2$ .

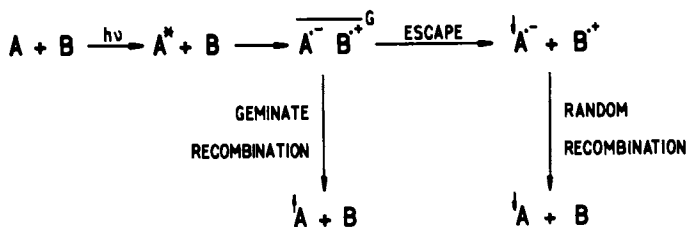


Figure 3. Cyclic reaction scheme. Arrows ( $\uparrow$ ) and ( $\downarrow$ ) denote recombination and escape type polarization, respectively. For simplicity, the polarizations of B and  $B^{\cdot+}$  are omitted.

reaction. In analogy with the geminate process, we can rewrite this reaction as in Figure 4.  $A^{\bullet-}$  and  $B^{\bullet+}$  radicals, having escaped from independently formed geminate pairs, diffuse together to form F-pairs which can either recombine or diffuse apart. At first sight it might appear that no CIDNP could arise from such a pair because of the random phase relationship of the two electron spins involved. Immediately after their formation, F-pairs have equal probabilities of being in S and  $T_0$  states (in contrast to geminate pairs which are initially spin-correlated in either pure singlet or pure triplet states) and this renders  $ST_0$  interconversion ineffective. However, when the radicals first encounter one another a fraction of the S pairs are able to react immediately leaving the remaining pairs with net triplet character which can then proceed to generate CIDNP in a manner qualitatively identical to triplet geminate pairs. Therefore, in addition to the cancellation arising from random recombination, there is also the possibility of F-pair polarization which either augments or opposes the geminate polarization depending on whether the latter arose from T or S spin correlated pairs respectively.

Recombination Cancellation and F-pair Polarization. To discuss more quantitatively the NMR time dependence arising from these processes the reaction scheme in Figure 5 is considered in which the polarization arrows have been omitted for convenience.

At this point, to keep the discussion general, we shall not specify whether the geminate pairs are S or T. The idealised case of B and  $B^{\bullet+}$  having no magnetic nuclei and of A and  $A^{\bullet-}$  each having a single proton will be treated.

Let  $\Pi_G$  and  $\Pi_F$  be the polarizations produced per mole of G and F-pairs respectively, where polarization is defined as the difference in the populations of  $\alpha$  and  $\beta$  nuclear spin states minus the population difference at thermal equilibrium. In addition let  $\Phi_G$  and  $\Phi_F$  be the corresponding reaction probabilities.  $\Pi$  and  $\Phi$  are quantities which include all effects of radical re-encounters and  $ST_0$  mixing and are simply related to the individual reaction probabilities of pairs containing the unique proton in  $\alpha$  and  $\beta$  states.

Suppose that geminate pairs at an initial concentration,  $C_R$  undergo the CIDNP process, diffuse apart, recombine etc. In this way we can treat a flash photo-CIDNP experiment in which G-pairs are formed very rapidly (within  $\sim 10^{-7}$  s of light absorption) by a light pulse of short duration ( $< 1 \mu s$ ). This argument can be generalized later to apply to the more conventional steady state experiment, for example with continuous photolysis.

From the above definitions, the geminate polarization at  $t = 0$  is  $C_R \Pi_G$  and the concentration of  $A^{\bullet-}$  radicals,

$C_R[1 - \phi_G]$ . An  $A^{\bullet-}$  radical, having escaped from its geminate pair, may encounter several different  $B^{\bullet+}$  radicals and thus form several F-pairs before finally reacting. We have therefore to sum the F-polarization over all these pairs to find the total contribution from the F-pair process. The polarization in A arising from the  $(n + 1)$ th F-pair formed by an  $A^{\bullet-}$  radical is simply  $\Pi_F$  multiplied by the probability that  $A^{\bullet-}$  has survived the previous  $n$  pairs, i.e.  $[1 - \phi_F]^n$ . The total polarization per mole of  $A^{\bullet-}$  is therefore given by the summation:

$$\sum_{n=0}^{\infty} \Pi_F [1 - \phi_F]^n = \Pi_F / \phi_F \quad (8)$$

and the total F-pair polarization from all radicals is:

$$C_R [1 - \phi_G] \Pi_F / \phi_F \quad (9)$$

The ratio of F- to geminate polarization,  $\gamma_G$  is:

$$\gamma_G = \frac{\Pi_F [1 - \phi_G]}{\Pi_G \phi_F} \quad (10)$$

This quantity may be evaluated for both S and T geminate pairs by the following simple arguments.

Consider firstly the T initial case. Since we assume that only the singlet state is reactive, recombination can only occur from a T pair if  $ST^0$  mixing occurs before the radicals finally diffuse apart. Except for radicals with very large hyperfine coupling, the  $ST^0$  interconversion is rather slow compared to the rate of diffusion in non-viscous solution so that the reaction probability  $\phi_T$  is generally small. This permits us to make the approximation that in equation (10)

$$1 - \phi_T \approx 1 \quad (11)$$

The polarization,  $\Pi_T$  is an average over the three triplet substates,  $T_0$ ,  $T_+$  and  $T_-$ :

$$\Pi_T = [\Pi_{T_+} + \Pi_{T_0} + \Pi_{T_-}] / 3 \quad (12)$$

where it is assumed that the initial populations of these states are equal, i.e. electron spin polarization (CIDEP) and the Boltzmann population differences are assumed negligible. In high fields for free radicals (i.e. not biradicals) the  $T_{\pm}$  states do not participate in the production of polarization so that



$$\Pi_T = \Pi_{T_0} / 3 \quad (13)$$

Now, we have already said that for F-pairs, polarization arises because singlet reactivity leads to net T character, allowing the random pairs to behave like initial  $T_0$  ones. The amount of T character is equal to the fraction of F-pairs that do react, i.e.  $\phi_F$  which leads to

$$\Pi_F = \phi_F \Pi_{T_0} \quad (14)$$

Substituting equations (11), (13) and (14) into equation (10) gives

$$\gamma_T = 3 \quad (15)$$

That is, the radicals which escape from a T pair generate three times more polarization than did the initial pair itself.

For S pairs, a similar line of reasoning can be used to find the value of  $\gamma_S$ . By the superposition principle,

$$\phi_F = [\phi_S + \phi_{T_+} + \phi_{T_0} + \phi_{T_-}] / 4 \quad (16)$$

and similarly for  $\Pi_F$ , since an F-pair has equal probability of being initially in each of the four radical pair states. As before,  $\phi_{T_{\pm}} = \Pi_{T_{\pm}} = 0$ , so that

$$\phi_F = \frac{1}{4} [\phi_S + \phi_{T_0}] \quad (17)$$

and similarly for  $\Pi_F$ . If  $\phi_{T_0} \ll \phi_S$  which will be true for radical pairs with slow  $ST_0$  mixing, then  $\phi_S \approx 4\phi_F$ . Using the expression for  $\Pi_F$  analogous to equation (17) and also equation (14) one obtains

$$\Pi_S = -[1 - \phi_S] \Pi_{T_0} \quad (18)$$

and therefore,

$$\gamma_S = -1 \quad (19)$$

So for an S pair, the initial polarization is equal but of opposite phase to that which is subsequently created by the escaping radicals.

This is consistent with the conclusion on general thermodynamics grounds that for a pair of radicals in thermal equilibrium with their diamagnetic dimer, no polarization is expected (12).

The values deduced above for  $\gamma_T$  and  $\gamma_S$  can, in fact,

be derived more rigorously from the exact relations of Pedersen and Freed (13, 14) for the spin dependent reaction probabilities of G and F radical pairs. Statistical factors of 1/2 and 1/3 which appeared naturally in the above argument must be included in the Pedersen-Freed relations to account for the  $T_{\pm}$  states (15).

**CIDNP Time Dependence.** We are now in a position to discuss the NMR time dependence expected from a cyclic reaction, such as in Figure 5 when initiated by a short light flash. Let  $R(t)$  be the total concentration of  $A^{\bullet-}$  radicals (with  $\alpha$  and  $\beta$  nuclear spins) and  $I_D(t)$  and  $I_R(t)$  the polarizations at time  $t$  of the single proton in the diamagnetic molecule, A, and in the radical,  $A^{\bullet-}$ , respectively. Suppose that  $A^{\bullet-}$  and  $B^{\bullet+}$  encounter one another and form F-pairs with a bimolecular rate  $k_2$ . The time derivatives of  $I_D$  and  $I_R$  are then: (15)

$$\dot{I}_D(t) = k_2 R [R I_F + I_R \phi_F] - I_D / T_1^D \quad (20a)$$

$$\dot{I}_R(t) = -k_2 R [R I_F + I_R \phi_F] - I_R / T_1^R \quad (20b)$$

where in the parentheses, the first term accounts for the production of  $F$ -polarization (the rate of formation of F-pairs =  $k_2 R^2 \text{ Ms}^{-1}$ ) while the second term allows for the transfer of polarization ( $I_R/R$  per mole) to A by the recombining radicals (rate,  $k_2 \phi_F R^2 \text{ Ms}^{-1}$ ).  $T_1^D$  and  $T_1^R$  are the nuclear spin lattice relaxation times.

The time dependence of  $R$  is given to a good approximation by (15)

$$\dot{R} = -k_2 \phi_F R^2 \quad (21)$$

so that

$$R(t) = \frac{R(0)}{1 + k_2 \phi_F R(0)t} = \frac{R(0)}{1 + xt} \quad (22)$$

Equations (20) must in general be solved numerically. Although this is quite straightforward, more physical insight is obtained by considering the two extreme cases of very fast and very slow relaxation of the  $A^{\bullet-}$  proton in which these expressions can be solved analytically. Until we consider steady state experiments, the nuclear relaxation in A will be neglected. This is valid since we shall be interested in times much shorter than one second.

(a) Slow relaxation ( $T_1^R \ll x$ )

In this limit,  $\dot{I}_D = -\dot{I}_R$  and, as required by the spin sorting radical pair mechanism,  $I_D(0) = -I_R(0)$ , so that

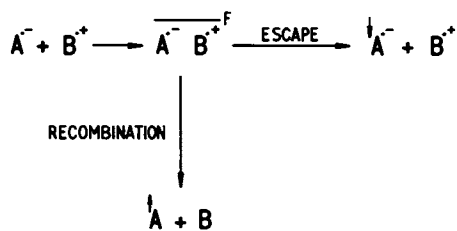


Figure 4. Scheme of the random recombination reaction via F-pairs.

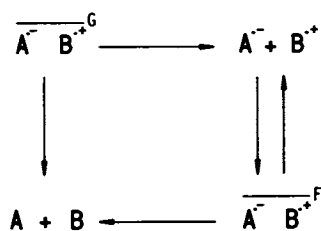


Figure 5. Cyclic reaction scheme including geminate (G) and F radical pairs.

$I_R(t) = -I_D(t)$ . Inserting this in equation (20a) and integrating, one obtains:

$$I_D(t) = \frac{I_D(0)}{1+xt} \left[ 1 + \frac{R(0)\Pi_F}{I_D(0)\phi_F} \ln(1+xt) \right] \quad (23)$$

But  $I_D(0) = C_R \Pi_F$  and  $R(0) = C_R [1 - \phi_F]$  so that:

$$\frac{I_D(t)}{I_D(0)} = \frac{1}{1+xt} [1 + \gamma_G \ln(1+xt)] \quad (24)$$

in which the first term arises from cancellation and the second from the production of F-polarization. This expression is plotted in Figure 6 for the S and T initial cases. For T, the maximum occurs at  $t_{\max} = 0.95/x$  and  $I_D(t_{\max}) = 1.54 I_D(0)$  while for S,  $t_{\min} = 6.397/x$  and  $I_D(t_{\min}) = -0.14 I_D(0)$ . Since the relaxation in A<sup>•</sup> is slow, both curves tend to zero eventually because of exact cancellation. The behaviour at shorter times reflects the F-polarization which causes  $I_D(t)$  to rise for T pairs and fall for S pairs as discussed above.

(b) Fast relaxation ( $T_1^R)^{-1} \gg x$   
If  $T_1^R$  is sufficiently small,  $I_R$  can be set equal to zero so that from equation (20)

$$\frac{I_D(t)}{I_D(0)} = 1 + \gamma_G \left[ 1 - \frac{1}{1+xt} \right] \quad (25)$$

which is shown in Figure 7 for S and T geminate pairs. In this limit, no cancellation of  $\uparrow$  and  $\downarrow$  polarization is possible and all the time dependence comes from the F-pair polarization.

In general the behaviour of  $I_D(t)$  is intermediate between these two extremes. For S geminate pairs  $I_D(t)$  always reaches zero at long times but depending on the value of  $xT_1^R$ , may not cross the  $I_D = 0$  axis. In the T geminate case,  $I_D(t)$  always rises initially as a result of the extra F-polarization. Then, again depending on  $xT_1^R$ , a point may be reached where the polarization cancelled per pair,  $I_R \phi_F / R$  exceeds that produced per pair,  $\Pi_F$ , in which case  $I_D(t)$  is at a maximum and subsequently falls.

(c) Steady state conditions

Continuous generation of radicals and therefore of geminate polarization can be included in equations (20) and (21) by the addition of zero-th order terms in which  $k_0$  moles of geminate radical pairs are formed per second, thus:

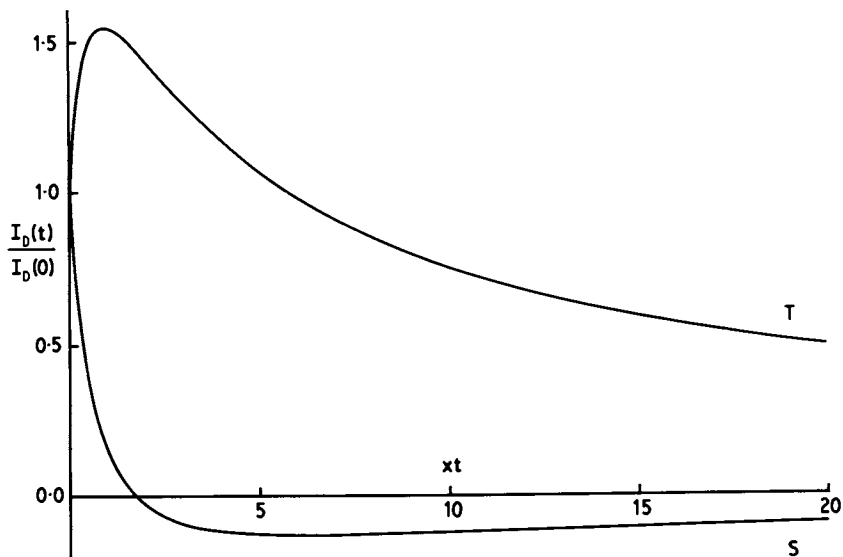


Figure 6. CIDNP time dependence arising from radical recombination for S and T geminate pairs. Slow relaxation, Equation 24.

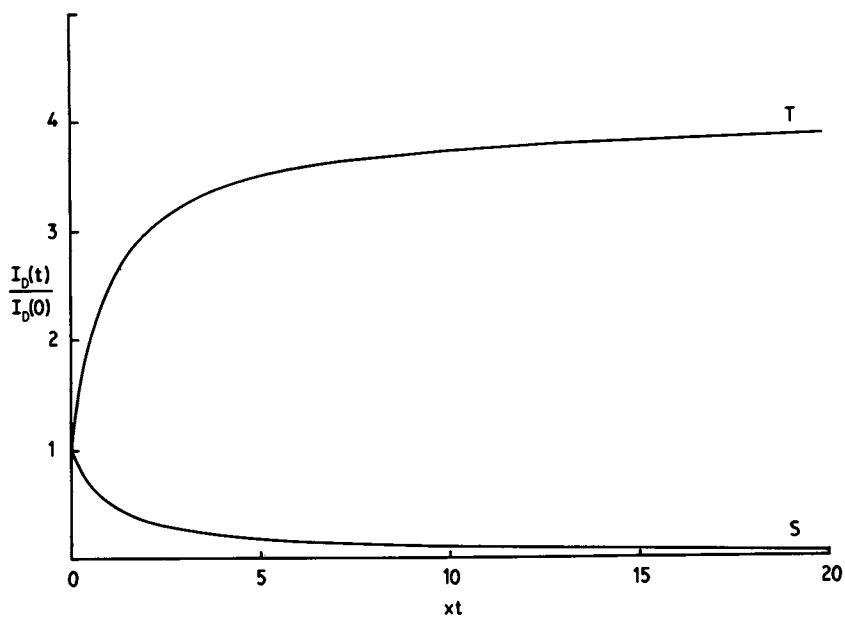


Figure 7. CIDNP time dependence arising from radical recombination for S and T geminate pairs. Fast relaxation, Equation 25.

$$\dot{I}_D = k_2 R [R \Pi_F + I_R \Phi_F] + k_o \Pi_G - I_D / T_1^D \quad (26a)$$

$$\dot{I}_R = -k_2 R [R \Pi_F + I_R \Phi_F] - k_o \Pi_G - I_R / T_1^R \quad (26b)$$

$$\dot{R} = -k_2 \Phi_F R^2 + k_o [1 - \Phi_G] \quad (27)$$

Solving these under steady state (ss) conditions ( $\dot{I}_D = \dot{I}_R = \dot{R} = 0$ ) gives:

$$I_D^{ss} = \frac{T_1^D}{T_1^R} \cdot \frac{k_o \Pi_G [1 + \gamma_G]}{x^{ss} + 1/T_1^R} \quad (28)$$

with

$$x^{ss} = k_2 \Phi_F R^{ss} \quad (29)$$

Therefore for S geminate pairs:

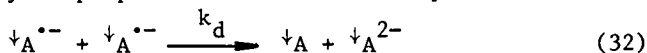
$$I_D^{ss} = 0 \quad (30)$$

irrespective of the relaxation rate, and for T-pairs:

$$I_D^{ss} = \frac{4T_1^D k_o \Pi_T}{T_1^R (x^{ss} + 1/T_1^R)} \quad (31)$$

When  $(T_1^R)^{-1} \ll x^{ss}$ , cancellation is very efficient and  $I_D^{ss} = 0$  while in the opposite extreme the polarization can be large.

Disproportionation Reactions. At this point it is interesting to discuss another type of recombination process, namely disproportionation. For example



in which one A molecule is produced for every two  $A^{\bullet-}$  radicals which react.

Although a reaction scheme involving disproportionation as a significant random recombination route is not strictly cyclic, it can lead to partial cancellation of the A polarization as indicated by the arrows in equation (32). In the limit of very slow relaxation, a maximum of half of the  $\uparrow$  polarization in A can be cancelled by the opposite phase  $\downarrow$  polarization in the radicals. The remainder of the escape polarization ends up in the other disproportionation product ( $A^{2-}$ ). This type of reaction leads to much simpler CIDNP time dependence than the  $A^{\bullet-} + B^{\bullet+}$  back reaction because no net polarization can arise in radical pairs consisting of identical free radicals.

To make equations (20) applicable to a disproportionation reaction (neglecting random radical back reaction) one can set  $\Pi_F$  equal to zero, replace  $k_2\Phi_F$  by  $k_d$  and insert a factor of  $\frac{1}{2}$  in the expression for  $\dot{I}_D$  to obtain:

$$\dot{I}_D = \frac{1}{2}k_d R I_R \quad (33a)$$

$$\dot{I}_R = -k_d R I_R - I_R/T_1^R \quad (33b)$$

$$R(t) = \frac{R(0)}{1+x't} \quad (34)$$

with  $x' = k_d R(0)$ . As before the  $T_1^D$  term has been dropped. Analytical solutions in two extreme cases can be found.

(a) Slow relaxation  $(T_1^R)^{-1} \ll x'$

In this case  $I_R(t) = I_D(0) - 2I_D(t)$   
so that

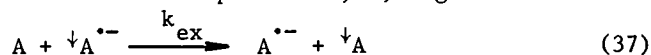
$$\frac{I_D(t)}{I_D(0)} = \frac{1}{2} \left[ 1 + \frac{1}{1+x't} \right] \quad (35)$$

(b) Fast relaxation  $(T_1^R)^{-1} \gg x'$   
i.e.  $I_R(t) \approx 0$ , so that

$$\frac{I_D(t)}{I_D(0)} = 1 \quad (36)$$

The time dependence predicted by these relations is shown in Figure 8 and agrees with the qualitative discussion of this mechanism given above.

Exchange reactions. Another process that can give rise to CIDNP cancellation, although not restricted to cyclic reactions, is a degenerate chemical exchange. Such a reaction between  $A^{*-}$  and its precursor, A, e.g.



is able to transfer escape polarization from radicals to molecules and in the absence of relaxation would again lead to complete destruction of initial polarization. As before, when the lifetime of  $A^{*-}$ , with respect to exchange, is not much less than  $T_1^R$ , cancellation is incomplete and steady state polarizations should be observable. When relaxation is very slow, cancellation should obey first order kinetics with a rate constant  $k_{ex}([A] + [A^{*-}])$  where the  $k_{ex}[A^{*-}]$  term accounts for the loss of polarization caused by

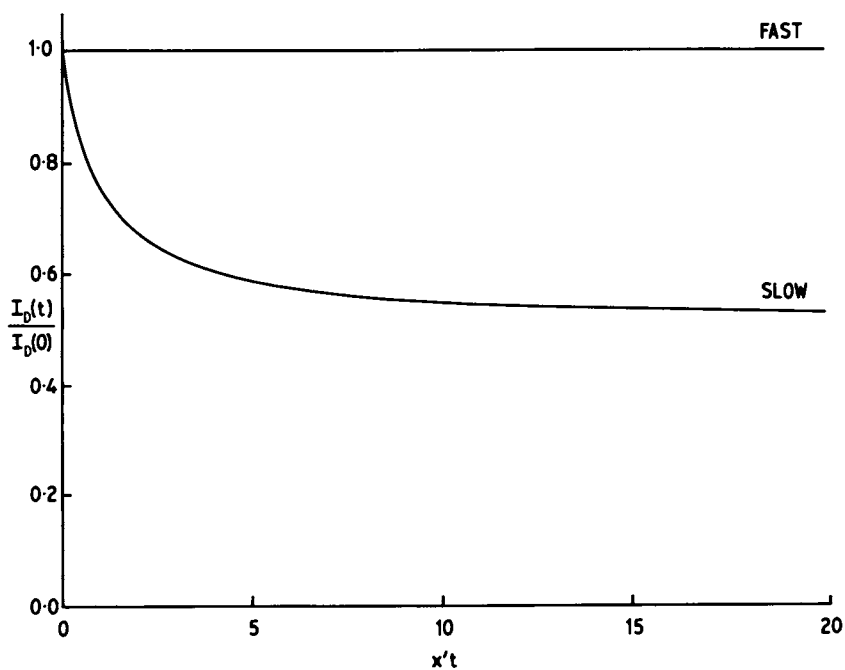


Figure 8. CIDNP time dependence arising from radical disproportionation for slow and fast relaxation, Equations 35 and 36, respectively.





However this is not the only source of CIDNP time dependence that can arise from such a reaction. Consider what happens in the limit of very fast nuclear relaxation in  $A^{\bullet-}$  (i.e. no cancellation). Exchange now transfers recombination polarization from A to unpolarized  $A^{\bullet-}$  where it is able to relax very rapidly. This may be called a "relaxation sink" mechanism, and should occur at a maximum rate of  $k_{ex}[A^{\bullet-}]$ , being most effective when the  $A^{\bullet-}$  radicals are able to relax completely prior to reconversion to A i.e.  $(T_1^R)^{-1} \gg k_{ex}[A]$ . In general, therefore we expect the evolution of CIDNP to be a biphasic decay to zero (in the absence of fast recombination reactions).

The time dependence of  $I_R$  and  $I_D$  arising from an exchange reaction such as equation (37) is given by (15):

$$\dot{I}_D = -k_{ex}RI_D + k_{ex}DI_R \quad (39a)$$

$$\dot{I}_R = k_{ex}RI_D - k_{ex}DI_R - I_R/T_1^R \quad (39b)$$

where D is the concentration of A molecules. That is, polarization in A ( $I_D$ ) is transferred to  $A^{\bullet-}$  at a rate  $k_{ex}R$  per second and at the same time polarization is received from  $A^{\bullet-}$  ( $I_R$ ) at a rate  $k_{ex}D$  per second. In the absence of recombination reactions,  $k_{ex}R$  and D are independent of time and these expressions may be solved easily, thus

$$I_D(t) = A_+ e^{\lambda_+ t} + A_- e^{\lambda_- t} \quad (40)$$

with

$$\lambda_{\pm} = -y/2 \pm \frac{1}{2}[y^2 - 4k_{ex}R/T_1^R]^{1/2} \quad (41)$$

$$y = k_{ex}(R + D) + 1/T_1^R \quad (42)$$

$$A_{\pm} = \mp I_D(0)[k_{ex}(R + D) + \lambda_{\mp}]/(\lambda_+ - \lambda_-) \quad (43)$$

Inspection of equations (41)-(43) reveals that  $\lambda_- < \lambda_+ < 0$  and  $A_+, A_- > 0$  so that  $I_D(t)$  consists of two exponentially decaying terms both with positive amplitude. In two limiting cases this behaviour becomes particularly simple.

(a) Slow relaxation  $(T_1^R)^{-1} \ll k_{ex}(R + D)$

$$I_D(t) = I_D(0)e^{-k_{ex}(R+D)t} \quad (44)$$

- "exchange cancellation".

$$(b) \text{Fast relaxation } (T_1^R)^{-1} \gg k_{ex}(R + D)$$

$$I_D(t) = I_D(0)e^{-k_{ex}t} \quad (45)$$

- "relaxation sink".

As anticipated in the foregoing discussion, relaxation via a radical sink is responsible for the time dependence at slow exchange rates whereas for faster rates, cancellation takes over as the predominant process.

Some solutions in intermediate cases are shown in Figure 9. In Figure 9a one sees that as the concentration of A is raised, cancellation becomes more extensive and occurs in a shorter time. Conversely the more slowly decaying component of  $I_D(t)$  which may be associated with the loss of polarization via the radicals, becomes faster as [A] is increased. This seems to arise because at the higher A concentrations, radicals are unable to relax before reconversion to A which reduces the efficiency of the relaxation sink.

Figure 9b shows that as the radical concentration is raised the degree and rate of cancellation remain approximately unchanged while the slower term becomes faster as expected.

#### Photo CIDNP of Biological Molecules

Nuclear spin polarization can be induced in a variety of biologically important molecules by laser irradiation of solutions in the presence of a dye. Initially we had found that using flavin dyes it is possible to polarize the amino acids tyrosine, histidine and tryptophan, both as free amino acids and as surface residues in proteins (5, 6). This occurs in cyclic reactions with a high degree of reversibility of the type discussed in the previous section. More recently, we found that the purine nucleotide bases can be polarized similarly (16). It appears that flavins are remarkable in that upon photo-excitation they react reversibly with several classes of compounds such as aromatic phenols, aromatic amines, and secondary and tertiary amines. In all these cases CIDNP can be observed. We shall now discuss the photo-CIDNP spectra of the amino acids in more detail.

Tryptophan. A typical photo-CIDNP experiment goes as follows. A solution of the substrate in the presence of 0.2 to 0.4 mM flavin is irradiated in the NMR probe by an argon ion laser (0.6 s, 5 W light pulses) prior to the rf pulse and acquisition of the free induction decay (FID). Alternating "light" and "dark" FID's are taken, which after

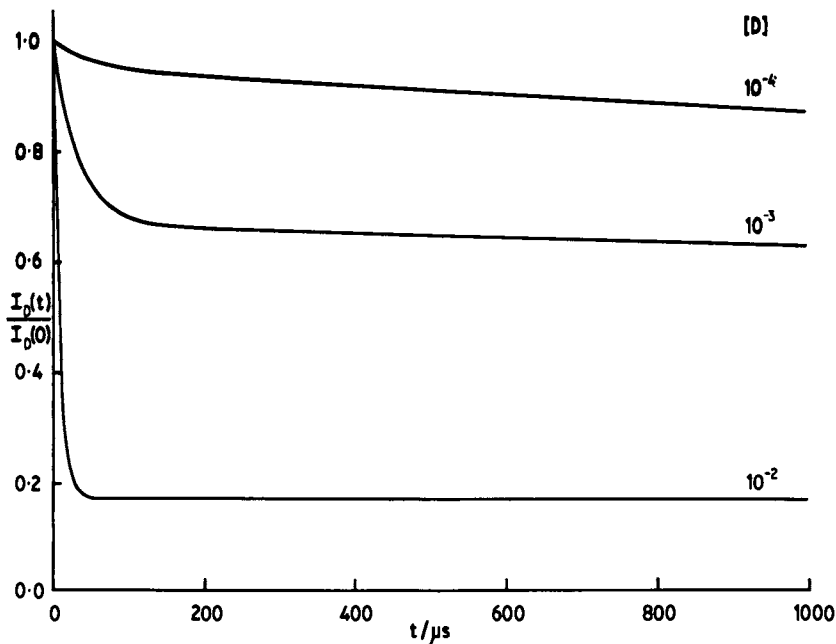
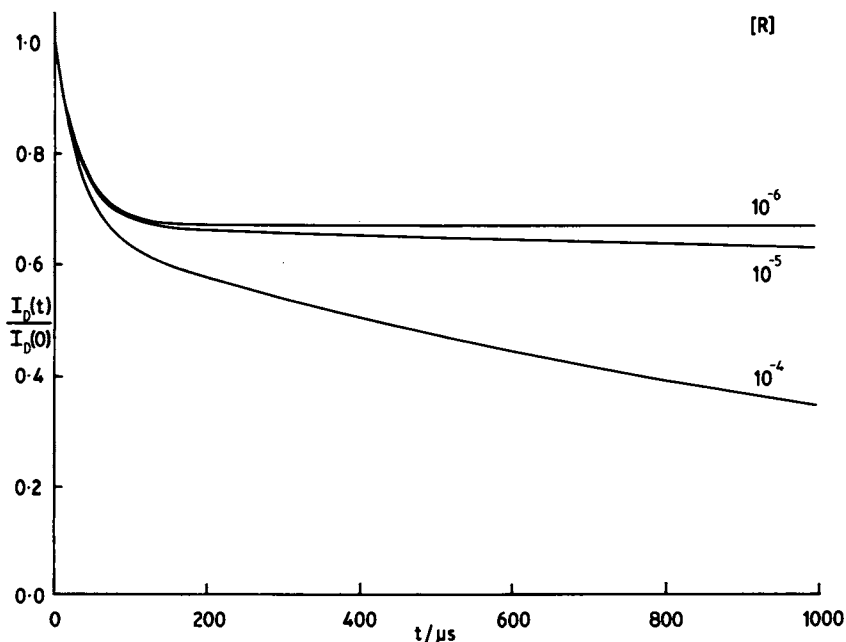


Figure 9a. CIDNP time dependence arising from an exchange reaction, as predicted by Equations 40-43.  $k_{ex} = 10^7 \text{ M}^{-1}\text{s}^{-1}$ ,  $T_1^R = 50 \mu\text{s}$ ,  $R = 10^{-5} \text{ M}$ ,  $D = 10^{-2}$  (a),  $10^{-3}$  (b), and  $10^{-4} \text{ M}$  (c).



Figures 9b. CIDNP time dependence arising from an exchange reaction.  $k_{ex} = 10^7 \text{ M}^{-1}\text{s}^{-1}$ ,  $T_1^R = 50 \mu\text{s}$ ,  $D = 10^{-3} \text{ M}$ ,  $R = 10^{-4}$  (a),  $10^{-5}$  (b), and  $10^{-6} \text{ M}$  (c).

Fourier transformation and subtraction yield the photo-CIDNP difference spectrum. Usually 10 to 20 FID's are accumulated. A waiting time of 5 s is included between scans to let the sample reach thermal equilibrium.

Figure 11 shows the result of this experiment on a solution of 5 mM N-acetyl tryptophan and 0.2 mM 3-N-carboxy-methyl lumiflavin, hereafter simply called flavin (see Figure 10). Positive enhancements can be observed for the aromatic C-2, C-4 and C-6 protons, while the CH<sub>2</sub> group shows emission. This polarization pattern corresponds with a tryptophyl radical in which the electron spin is delocalized over the aromatic ring. It can further be noted that almost no flavin polarization is present in the difference spectrum, Figure 11c (weak lines are present at 2.6 and 4.0 ppm). This is due to cancellation of recombination and escape polarization as will be discussed in Section 5. The mechanism of the photoreaction undoubtedly involves triplet flavin (17). Since 1-N-methyl tryptophan shows similar CIDNP effects, the primary step most probably is electron transfer to the photo-excited flavin. This is also supported by a flash photolysis study by Heelis and Phillips (18). The nature of the primary step in the photoreactions with amino acids is important in view of the interpretation of "accessibility" of an amino acid side chain in a protein as seen by the photo-CIDNP method. This question is therefore the subject of further study.

Tyrosine and Histidine. The flavin sensitized <sup>1</sup>H polarization patterns observed for the three polarizable aromatic amino acids are summarized in Figure 12. Histidine shows polarization similar to that of tryptophan i.e. absorption for the C-2 and C-4 protons in the aromatic region and emission for the CH<sub>2</sub> group. In practice, polarized His lines in a protein can be easily distinguished from those of Trp by pH variation, making use of the strong pH dependence of the chemical shift of the C-2 and C-4 protons of histidine around its pK<sub>a</sub> of 6 to 7.

Tyrosine shows predominantly strong emission for its C-3 and C-5 ring protons, opposite to that of His and Trp. This feature is extremely useful and makes so-called first stage assignments (as to type of residue) in protein CIDNP spectra a very simple matter. It is due to a change in sign of Δg and follows from the net effect rule of equation (6). Thus, inserting the correct signs we obtain for the 3,5 protons (A = -6.2 G), since g(tyr) = 2.0041 and g(flav) = 2.0030,

$$\Gamma_n(3,5) = + + + - = -, E$$

For the tryptophyl radical the g-factor is not known, but we

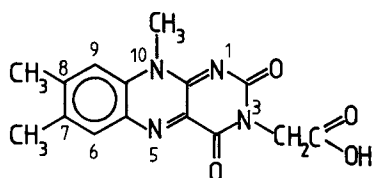


Figure 10. 3-N-Carboxymethylflavin with numbering scheme.

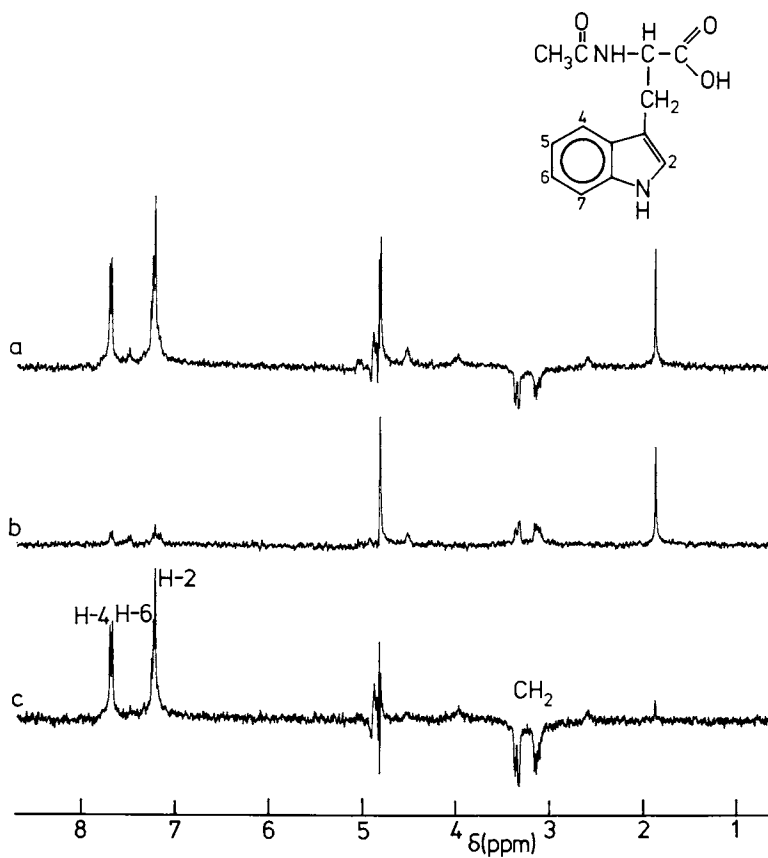


Figure 11. 360-MHz photo-CIDNP spectra of a solution of 5 mM N-acetyltryptophan and 0.2 mM flavin in  $D_2O$ , 10 scans. Key: a, light spectrum; b, dark spectrum; and c, difference  $a - b$ .

can conclude from the CIDNP spectrum that it must be lower than that of the flavosemiquinone:

$$\Gamma_n(2,4,6) = + + - - = +, A$$

In contrast to the case of tryptophan the photoreactions with tyrosine and histidine probably involve hydrogen atom transfer as the primary step. There are several indications for this. First, *O*-methylated tyrosine (*p*-methoxy phenylalanine) did not show any photo-CIDNP effect and its reactivity as a photo-reductant towards flavins is strongly reduced (19). Similarly, *l*-*N*-methyl histidine is not polarized at high pH (> 7.5), when no abstractable hydrogen is present. Secondly, in the protein ribonuclease A, which has a well known 3-dimensional structure, the residues Tyr 92 and His 105 have exposed rings, but their OH and NH protons are hydrogen bonded to backbone carbonyl groups. These residues do not show CIDNP, whereas several other residues do (Tyr 76, Tyr 115, His 119) (20). This strongly suggests that in the cases of tyrosine and histidine free phenolic OH and imidazole NH protons are required for the photoreaction with flavin in accordance with the hydrogen atom transfer mechanism.

The pH dependence of the CIDNP effect for the amino acids Trp, His and Tyr is shown in Figure 13. The tyrosine polarization is fairly constant over a wide pH range and decreases in the range where the phenolic OH-group is ionized ( $pK_a = 10.3$ ). This probably does not reflect lower activity towards the triplet flavin at pH > 10, however. Rather a change in mechanism from H-abstraction to electron transfer seems to be involved, since strong tyrosine polarizations have been observed for proteins at pH 11 (21). The reduction of CIDNP intensity for the amino acid could then be a consequence of cancellation effects due to an electron exchange reaction. This would be much faster for the tyrosine anion than for the neutral radical, while in the case of protein it would be slowed down by slower translational diffusion.

Histidine shows a larger CIDNP effect in the unprotonated form at high pH. Going to lower pH a decrease is observed corresponding with its  $pK_a$  of 7. A further decrease is observed in Figure 13 around pH 4, the origin of which is not known at present.

The pH dependence of tryptophan polarization is not easily interpretable. The increase between pH 4 and 5 could be related to the  $pK_a$  of 4.3 of the tryptophyl cation radical (22). At low pH the radical would not deprotonate and a fast exchange reaction with the parent molecule could lead to partial cancellation of polarization. Again, this cancellation is less effective in the case of proteins and

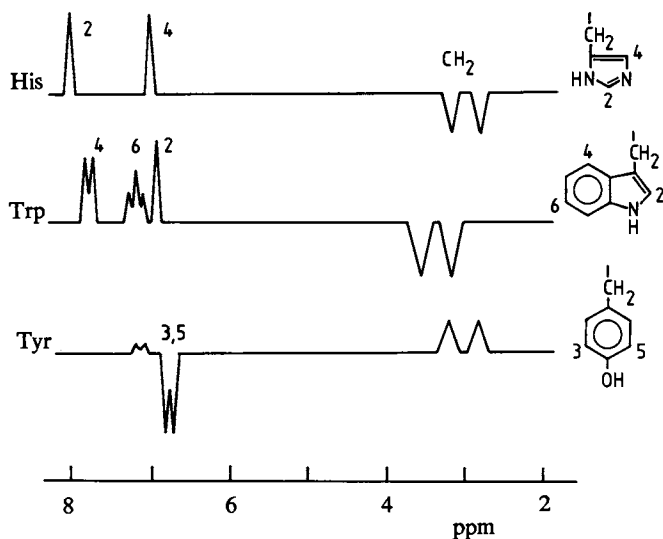


Figure 12. Schematic representation of the flavin induced  $^1\text{H}$  photo-CIDNP effects observed for the amino acids histidine, tryptophan, and tyrosine.

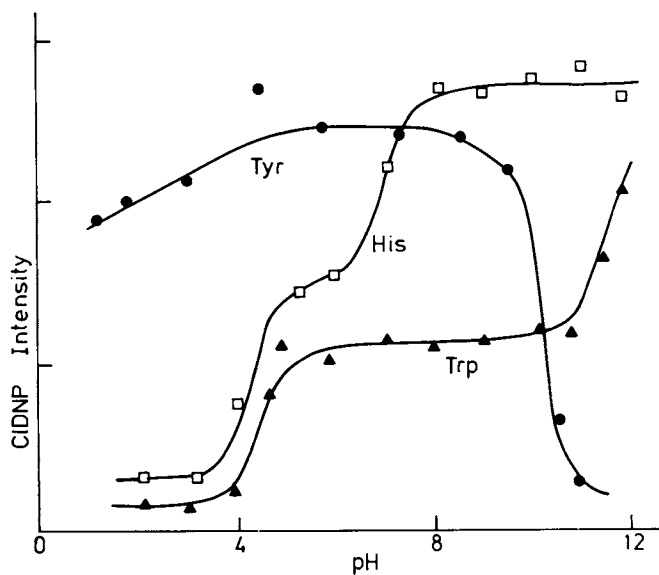


Figure 13. pH dependence of the photo-CIDNP effect of the amino acids tyrosine, histidine, and tryptophan.

therefore, the pH dependence for a Trp residue in a protein may be quite different. Indeed, strong polarization can be seen at pH 3.1 for Trp 3 in phospholipase A<sub>2</sub> (cf. Figure 14).

A Protein Example: Phospholipase A<sub>2</sub>. Pancreatic phospholipase A<sub>2</sub> is an enzyme of molecular weight 14,000, which catalyses the hydrolysis of 2-acyl ester bonds in a variety of naturally occurring phospholipids. The enzyme is secreted as a zymogen, which is activated by tryptic cleavage of the N-terminal heptapeptide. Both the enzyme and its precursor show catalytic activity towards monomeric lipids, but in contrast to the precursor the active enzyme shows a tremendous rate increase when it acts upon organized lipid structures such as micelles and bilayers (23).

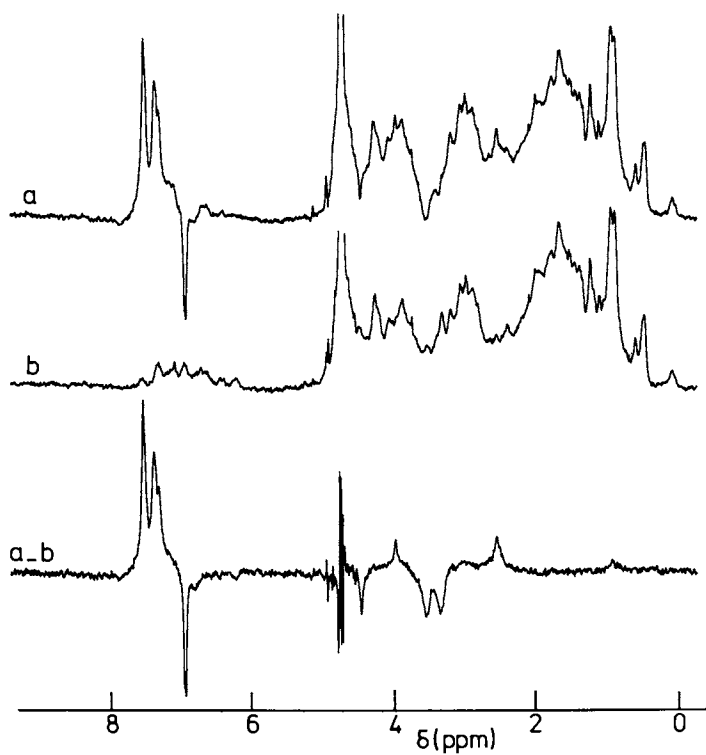
Recently an X-ray structure became available for the bovine enzyme (24). This, combined with the results from numerous studies on this enzyme by De Haas and his coworkers has led to a mechanistic model for the catalytic activity. Another problem is the mode of activation of the pro-enzyme and the nature of the interface recognition site. The photo-CIDNP method has shed some light on this latter problem.

Figure 14 shows the result of a photo-CIDNP experiment on the equine enzyme (25). The great simplification of the difference spectrum with respect to the dark spectrum allows complete assignments of the polarized lines. Absorption in the aromatic region and emission lines around 3.5 ppm belong to the single tryptophan (Trp 3). The strong emission at 7.0 ppm has been assigned to Tyr 69 by comparison with nitrated enzymes (26). A summary of photo-CIDNP work on phospholipases A<sub>2</sub> from different species is given in Table I. In all cases strong polarization is observed for Trp 3. In addition depending on the species, one or two tyrosines are observed of the seven to eight that are present. In general the polarization shows a pronounced pH dependence (25).

Upon tryptic activation of the enzyme the creation of the interface recognition site (IRS) is believed to occur via the formation of a saltbridge involving the N-terminal amino group of Ala 1, which, of course is only present after the N-terminal heptapeptide has been split off. In the photo-CIDNP difference spectrum it is possible to follow the chemical shifts of Trp 3, when the enzyme is going through a conformational change in the pH range 8 - 10 (27). This conformational change probably reflects the formation of the IRS, because it exactly correlates with the pK<sub>a</sub> of the α-amino group of Ala 1 (pK<sub>a</sub> = 8.9) measured by <sup>13</sup>C NMR (27).

<sup>a</sup> Evidence for the important role of Trp 3 in the IRS comes from fluorescence and UV difference spectroscopy (28) and is also supported by photo-CIDNP (25). As is shown in Figure 15 the addition of phospholipid micelles causes a reduction in the photo-CIDNP effect of both Trp 3 and Tyr 69.





**Figure 14.** 360-MHz  $^1\text{H}$  photo-CIDNP spectra of 1 mM equine phospholipase  $A_2$  in  $D_2O$ , pH 3.1 in the presence of 0.2 mM flavin. Key: a, light spectrum; b, dark spectrum; and a-b, difference spectrum; 20 scans were accumulated.

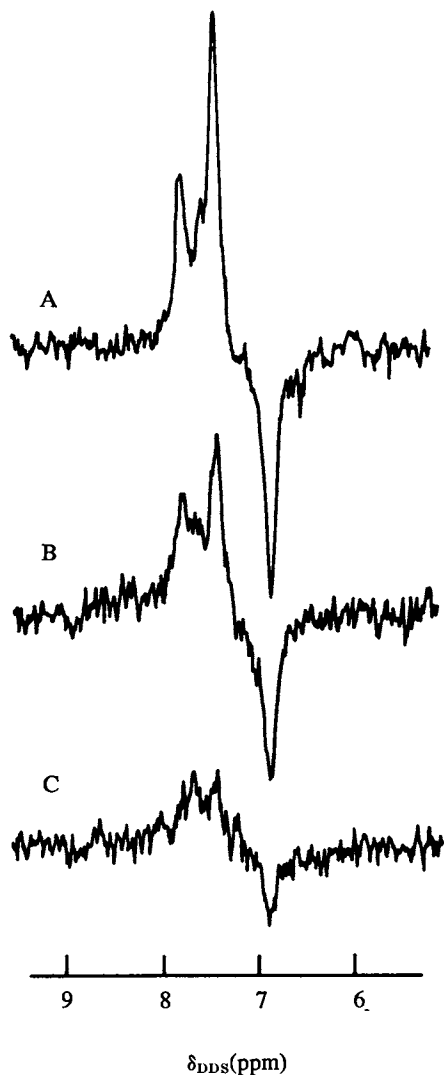


Figure 15. Photo-CIDNP difference spectra of equine phospholipase  $A_2$ . Key: A, enzyme alone; B, in the presence of micelles (24 mM phospholipid); and C, with 24 mM phospholipid + 10 mM  $Ca^{2+}$ . Experimental conditions: 1 mM protein, 5 mM Tris buffer, 100 mM NaCl, pH 8.3, 37°C.

Upon addition of  $\text{Ca}^{2+}$  ions, which are known to stabilize the enzyme-micelle complexes, a further reduction of the CIDNP signals is observed (Fig. 15c). In a control experiment with the pro-enzyme, in which the heptapeptide is still present, the same residues (Trp 3 and Tyr 69) are polarized but no reduction in the presence of micelles is observed. This demonstrates that dye inactivation is not the reason for the diminished CIDNP effects and we must conclude that the residues Trp 3 and Tyr 69 are rendered inaccessible to the dye by micelle binding. Therefore, they must belong to the IRS.

Summarizing the CIDNP results (see also Table I) it appears that Trp 3 and Trp 69 (and Tyr 19 in the equine enzyme but not Tyr 123 in the porcine enzyme) are part of the interface recognition site of pancreatic phospholipases  $A_2$ . These residues are equally accessible in the pro-enzymes, but apparently a change in conformation of the N-terminal region is necessary to establish the micelle binding properties.

Table I

Polarized Residues in Phospholipase  $A_2$  from Different Species<sup>a</sup>

	<u>ox</u>	<u>pig</u>	<u>horse</u>
low pH (< 4)	Trp 3;Tyr 69,73 <sup>b</sup>	Trp 3;Tyr 123	Trp 3;Tyr 69
high pH (> 6)	Trp 3;Tyr 69	Trp 3;Tyr 69,123	Trp 3;Tyr 19,69
enzyme micelle complex at pH 8	Trp 3 <sup>c</sup>	Tyr 69 <sup>c</sup> ,123	-

<sup>a</sup>Data taken from ref. 25 and 26.

<sup>b</sup>Tentative assignment

<sup>c</sup>weak polarization

Time Resolved Photo-CIDNP

Steady state CIDNP spectra are in general complicated functions of reaction rate constants, reactant concentrations, relaxation times etc. Moreover a lot of the information potentially available on cyclic reactions may be lost under steady state conditions due to partial or total cancellation effects. Many of these problems can be avoided by the use of flash photolysis instead of continuous illumination to obtain spectra with a time resolution of a few microseconds. The

fundamental idea is basically similar to conventional flash photolysis with the important difference that the probing light flash and optical detection are replaced respectively by a radio frequency pulse and NMR detection of the resulting free induction decay.

This technique was first used by Closs and Miller (7) who were able to distinguish geminate and F-pair polarizations from the time dependence of the latter.

Flash photo-CIDNP spectra have been obtained in the authors' laboratory using a dye laser (Phase-R 2100B), which delivers visible light flashes of  $\sim 0.5 \mu\text{s}$  duration and 1 - 3 J energy, in conjunction with the 360 MHz spectrometer (15).

A light flash is directed, by means of a mirror, lenses and a tapered quartz rod mounted along the axis of the cylindrical NMR probe onto the base of a flat bottomed sample tube. After a delay  $\tau_1$  an observing rf pulse is applied and the FID acquired immediately. To obtain a background or "dark" spectrum this sequence is repeated, after a waiting time  $\tau_2$  to allow all magnetizations to recover, but this time without a light flash. In addition rf pre-irradiation, usually for one second, prior to  $\tau_1$  delay is used for solvent peak suppression. The complete pulse sequence, as shown in Figure 16, is performed several times (typically 1 - 5) to obtain the desired signal-to-noise. As in the argon laser experiment, subtraction of light and dark spectra yields a photo-CIDNP difference spectrum at delay  $\tau_1$ .

The time resolution of this experiment, that is, the timescale of the fastest process that can be directly monitored, is limited in our case by the duration of the observing rf pulse, about  $10 \mu\text{s}$  for a  $90^\circ$  flip angle. Smaller flip angles can be used giving an improved time resolution but only at the expense of signal-to-noise.

The Photo-reaction of Flavin with Tryptophan. Typical spectra obtained from the flavin/N-acetyl tryptophan (Trp) system in  $\text{D}_2\text{O}$  are shown in Figure 17. At long delays (100 ms) the flavin peaks (labelled F) which were strong shortly after the laser flash have very nearly disappeared. In the corresponding spectrum obtained with c.w. laser illumination, (Figure 11) the flavin peaks are also very weak relative to those of tryptophan. Thus under steady state conditions a lot of information obtainable in a fast time resolved experiment is actually lost. As we shall see these effects are due to a rapid partial cancellation of geminate polarization.

Another interesting feature of the flavin enhancements visible at short delays in Figure 17, is the appearance of a line ( $F_7$ ) from the methyl protons at position 7 of the flavin ring. This peak had never been observed in the argon laser spectra even under conditions of pH and concentration where the flavin signals were rather strong. The very small

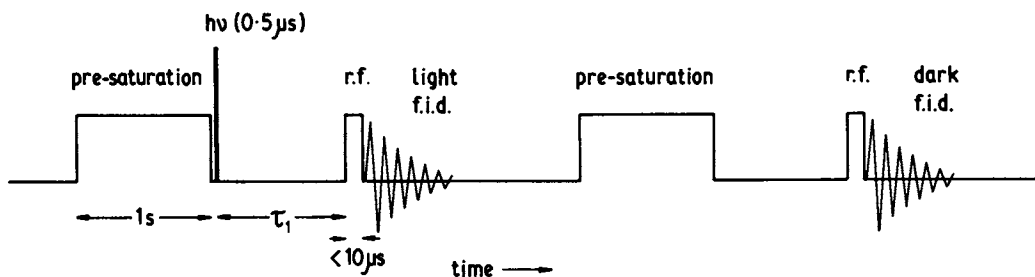


Figure 16. Pulse sequence for time resolved photo-CIDNP experiments.

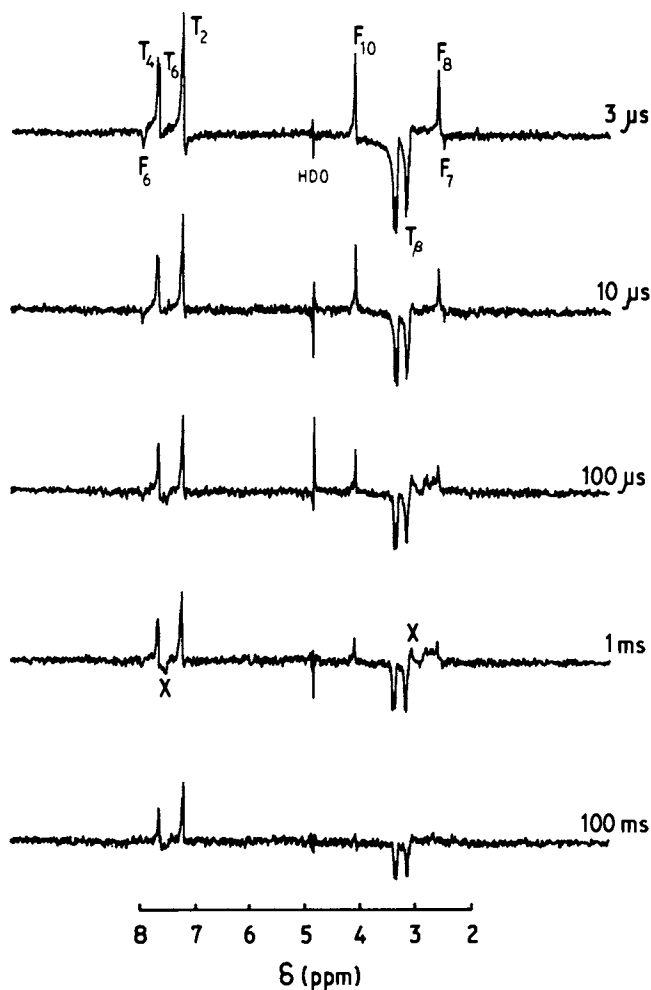


Figure 17. Photo-CIDNP spectra obtained by flash photolysis of a solution of 5 mM N-acetyltryptophan and 0.4 mM flavin in  $D_2O$  at pH 8.6 with  $\tau_1$  delays as indicated.

polarization of these protons had been attributed to a low hyperfine coupling in the flavin radical. The observation of the  $F_7$  peak in Figure 17, means that this conclusion cannot be completely correct. This distortion of relative CIDNP intensities illustrates the importance of nuclear spin relaxation in the radical intermediates of cyclic reactions (see Section 3). Thus clearly some cancellation process is responsible for the above observations and this will be most efficient for the nuclei with the longest  $T_1^R$ . It is reasonable that these relaxation times are determined mainly by the dipolar interaction with the unpaired electron spin density at the adjacent ring atom; this is known to be small for  $C_7$  of flavosemiquinones. More extensive cancellation for  $F_7$  than for its neighbour  $F_8$  which relaxes faster can therefore be rationalized.

The Mechanism of Cancellation. The time dependence of the  $F_8$  and  $F_{10}$  methyl peaks of flavin has been investigated in more detail. In Figure 18 the intensity of  $F_{10}$  is shown as a function of  $\tau_1$  in the region 0 - 100  $\mu$ s for several flavin concentrations. During this period the Trp intensities remain more or less constant while those of flavin decrease showing a greater relative reduction at higher flavin concentrations. Also, the enhancements immediately after the laser flash are approximately proportional to  $[F]$ .

The dependence on tryptophan concentration was also studied. As before the Trp lines showed only a weak time dependence whereas there is a much more pronounced fall of  $F_8$  with increasing  $\tau_1$  in the presence of 2 mM Trp than with 0.5 mM.

Furthermore, during the first 200  $\mu$ s little difference between  $F_8$  and  $F_{10}$  was observed. At longer delays, however, substantial differential effects were found, the  $F_{10}/F_8$  intensity ratio rising from about 1.8 at 10  $\mu$ s to more than 5 at 10 ms - 100 ms.

As discussed in Section 3, the cancellation of the flavin CIDNP signals just described could result from three types of radical reaction: (a) recombination, (b) exchange and (c) disproportionation. For the flavin/Trp system the possible reactions are set out in Figure 19 where as before cancellation of polarization is indicated by arrows.

The back reaction (a) could in principle explain the observed results but for the initial growth of  $I_D(t)$  expected from F-pair polarization. In addition this mechanism fails to explain the small time dependence of the tryptophan polarization. It is reasonable to expect that  $T_1^R$  for a ring proton in tryptophan would be somewhat smaller than for a ring-methyl proton in flavin simply because of the  $r^{-6}$  dependence of the electron-proton dipolar interaction. Therefore as shown in Figure 7 for short  $T_1^R$ , a predominantly increasing  $I_D(t)$  would be predicted for tryptophan in contrast to the observed results.

A degenerate exchange reaction between flavin radicals and

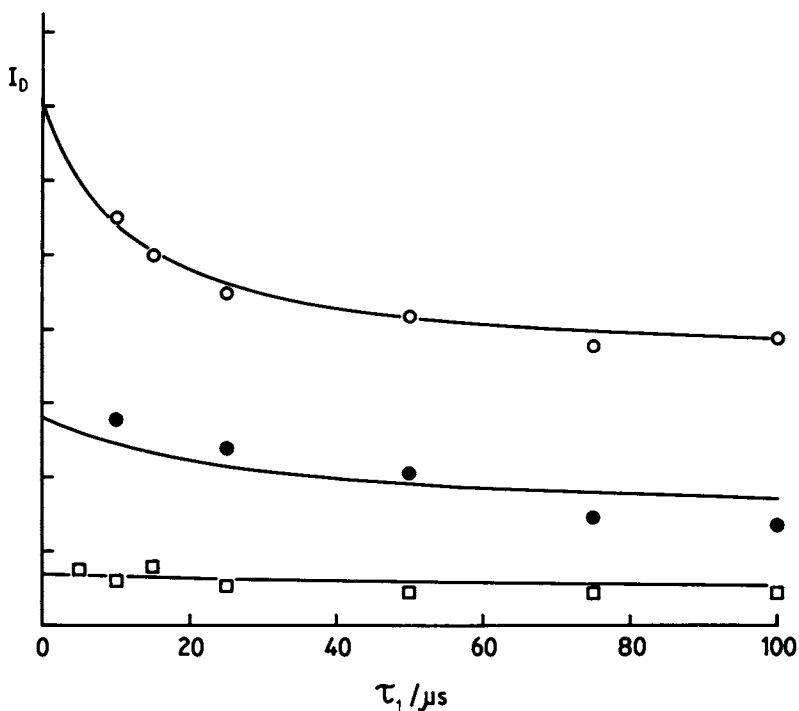


Figure 18. Time dependence of the photo-CIDNP difference intensity of  $F_{10}$  with 5 mM N-acetyltryptophan, 25 mM borate buffer, pH 8.0, and flavin concentrations: 1.0 mM (○), 0.4 mM (●), and 0.1 mM (□).

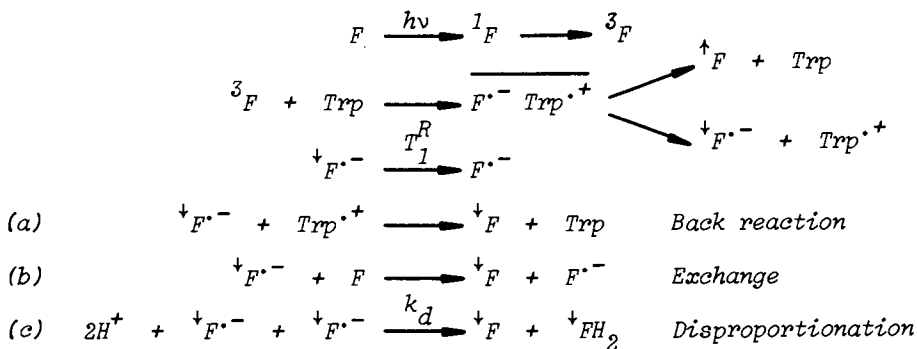


Figure 19. Possible reactions affecting CIDNP intensities in the flavin/tryptophan reaction.

flavin itself which, as discussed in Section 3, could result in cancellation is ruled out by the change in time dependence observed when the concentration of Trp was raised (15).

These results are, however, consistent with the model used to describe cancellation by disproportionation. The extent of cancellation is here sensitive to  $R(0)$  which in turn depends on the concentrations of both flavin and tryptophan.

As shown in Figure 18, the numerical solutions of eq. (33) can be fitted quite satisfactorily to the experimental data for the flavin enhancements. The three sets of results were fitted simultaneously assuming that the initial radical yield,  $R(0)$  is proportional to  $D(0)$ , the concentration of flavin present. This is reasonable as discussed above. Thus the optimum parameters were found to be  $k_d R(0)/D(0) = 8.8 \times 10^7 \text{ M}^{-1} \text{ s}^{-1}$  and  $T_1^R > 500 \mu\text{s}$ . So, even at the lowest  $D(0)$  studied (0.1 mM), the initial cancellation rate,  $k_d R(0)$  is faster than relaxation,  $(T_1^R)^{-1}$ . This very efficient cancellation is consistent with the similar time dependence of  $F_8$  and  $F_{10}$  observed during the first 100  $\mu\text{s}$ . The differential behaviour of these lines at longer delays however must reflect the different  $T_1^R$  of these two methyl groups. A value of 500  $\mu\text{s}$  for the relaxation time of a methyl group attached to an aromatic ring system is reasonable. For example, the ESR linewidth study of Leniart et al. (29) leads to a value between 300  $\mu\text{s}$  and 700  $\mu\text{s}$  for the protons of the tetramethyl-*p*-benzosemiquinone anion radical in ethanol at 0°C. Although the flavin radicals are larger than this species,  $D_2O$  at 20°C is less viscous as a solvent so that the rotational correlation times in the two cases should be approximately equal (the hyperfine couplings in the two radicals are comparable).

An independent determination of the radical yield  $R(0)$  is necessary to obtain a value for the disproportionation rate constant  $k_d$ . A value of 0.05 for  $R(0)/D(0)$  gives a rate comparable to those measured (17) for  $FH^{\cdot}$  at pH 5 ( $6.2 \times 10^9 \text{ M}^{-1} \text{ s}^{-1}$ ) and for  $F^{\cdot-}$  at pH 9 ( $1.1 \times 10^9 \text{ M}^{-1} \text{ s}^{-1}$ ).

The failure to observe the reduced flavin  $FH_2$  formed by the disproportionation may be due to severe linebroadening occasioned by the equilibrium between  $F$ ,  $FH_2$  and flavin radicals.

#### Literature cited

1. Closs, G.L. "Advances in Magnetic Resonance"; (Waugh, J.S., Ed.), Academic Press, New York, 1974; Vol. 7, p 157.
2. Kaptein, R. "Avances in Free Radical Chemistry"; (Williams, G.H., Ed.), Elek Science, London, 1975; Vol. 5, p 319.
3. Freed, J.H.; Pedersen, J.B. "Advances in Magnetic Resonance"; (Waugh, J.S., Ed.), Academic Press, New York, 1976; Vol. 8, p 1.



4. Muus, L.T.; Atkins, P.W.; McLauchlan, K.A.; Pederson, J.B., Eds.; "Chemically Induced Magnetic Polarization"; D. Reidel, Dordrecht, 1977.
5. Kaptein, R.; Dijkstra, K.; Nicolay, K. Nature 1978, 274, 293.
6. Kaptein, R. "NMR Spectroscopy in Molecular Biology"; (Pullman, B., Ed.), D. Reidel, Dordrecht, 1978; p 211.
7. Closs, G.L.; Miller, R.J. J. Amer. Chem. Soc. 1979, 101, 1639.
8. Roth, H.D. ref. 4; p 39.
9. Bargon, J. ref. 4; p 393.
10. Kaptein, R. Chem. Commun. 1971, 732.
11. Closs, G.L. Chem. Phys. Letters 1975, 32, 277.
12. Kaptein, R. J. Amer. Chem. Soc. 1972, 94, 6251.
13. Pedersen, J.B.; Freed, J.H. J. Chem. Phys. 1974, 61, 1517.
14. Pedersen, J.B. J. Chem. Phys. 1977, 67, 4097.
15. Hore, P.J.; Zuiderweg, E.R.P.; Kaptein, R.; Dijkstra, K. Chem. Phys. Letters 1981, 83, 376.
16. Kaptein, R.; Nicolay, K.; Dijkstra, K. Chem. Commun. 1979, 1092.
17. Vaish, S.P.; Tollin, G. Bioenergetics 1971, 2, 61.
18. Heelis, P.F.; Phillips, G.O. Photobiochem. Photobiophys. 1979, 1, 63.
19. McCormick, D.B.; Falk, M.C.; Rizzuto, F.; Tollin, G. Photochem. Photobiol. 1975, 22, 175.
20. Lenstra, J.A.; Bolscher, B.G.J.M.; Stob, S.; Beintema, J.J.; Kaptein, R. Eur. J. Biochem. 1979, 98, 385.
21. Canioni, P.; Cozzone, P.J.; Kaptein, R. FEBS Letters 1980, 111, 219.
22. Baugher, J.F.; Grossweiner, L.I. J. Phys. Chem. 1977, 81, 1349.
23. De Haas, G.H.; Bensen, P.P.M.; Pierson, W.A.; Van Deenen, L.L.M. Biochim. Biophys. Acta 1971, 239, 252.
24. Dijkstra, B.W.; Drenth, J.; Kalk, K.H.; Vandermaelen, P.J. J. Mol. Biol. 1978, 124, 53.
25. Jansen, E.H.J.M. Doctoral thesis, University of Utrecht, 1979.
26. Jansen, E.H.J.M.; Meyer, H.; De Haas, G.H.; Kaptein, R. J. Biol. Chem. 1978, 253, 6346.
27. Jansen, E.H.J.M.; Van Scharrenburg, G.J.M.; Slotboom, A.J.; De Haas, G.H.; Kaptein, R. J. Amer. Chem. Soc. 1979, 101, 7397.
28. Van Dam-Mieras, M.C.E.; Slotboom, A.J.; De Haas, G.H. Biochemistry 1975, 14, 5387.
29. Leniart, D.S.; Connor, H.D.; Freed, J.H. J. Chem. Phys. 1975, 63, 165.

RECEIVED February 8, 1982.

## **$^{13}\text{C}$ NMR Characterization of Solid Fossil Fuels Using Cross-Polarization and Magic-Angle Spinning**

GARY E. MACIEL and MARK J. SULLIVAN

Colorado State University, Department of Chemistry, Fort Collins, CO 80523

The development of high-resolution pulse Fourier transform (FT)  $^{13}\text{C}$  nmr as a routine analytical technique about 1970 constituted a major advance for the analysis of organic liquids, and was followed by important applications in the organic fuel areas. The characterization of such liquid materials as petroleum, coal liquids and shale oil became common during the 1970's. However, the chemical structural characterization of solid fossil fuels, coal and oil shale, did not benefit directly from these developments, because these kinds of samples could not be dissolved under conditions that would maintain their chemical structural integrity. In standard pulse FT  $^{13}\text{C}$  nmr approaches, such solid samples give only broad featureless resonances because of the line-broadening influences of  $^1\text{H}$ - $^{13}\text{C}$  dipole-dipole interactions and  $^{13}\text{C}$  chemical shift anisotropy. Pines, Gibby and Waugh<sup>1</sup> demonstrated that the  $^1\text{H}$ - $^{13}\text{C}$  dipolar broadening could be minimized by high-power  $^1\text{H}$  decoupling, while at the same time they circumvented via  $^1\text{H}$ - $^{13}\text{C}$  cross polarization any time bottleneck that could result from long  $^{13}\text{C}$   $T_1$  values. Schaefer and Stejskal<sup>2</sup> demonstrated that chemical shift anisotropy broadening could be eliminated by magic-angle spinning (MAS), i.e., rapidly spinning the sample about an axis that makes an angle,  $\beta$ , relative to  $H_0$  such that  $(1-3 \cos^2\beta) = 0$ . Figure 1 shows the timing diagram of a single-contact cross polarization experiment of the type typically employed in work on solid fossil fuels. Figure 2 gives a schematic diagram of the MAS technique.

Several spinner designs are in use for CP/MAS work.<sup>3</sup> Most of the studies of solid fossil fuels have used the mushroom<sup>3c</sup> and bullet types,<sup>3d</sup> made of Kel-F.<sup>4</sup>  $^1\text{H}$  decoupling fields of about 10-to-14 gauss are most common. In fossil fuel work cross polarization (contact) times of about 1 ms and repetition times of about 1s are typically used, although variations of these parameters have been made (see below). Spin-temperature alternation, in which one alternates by  $180^\circ$  the phase of the  $^1\text{H}$  spin-locking field and also alternates the

0097-6156/82/0191-0319\$07.25/0

© 1982 American Chemical Society

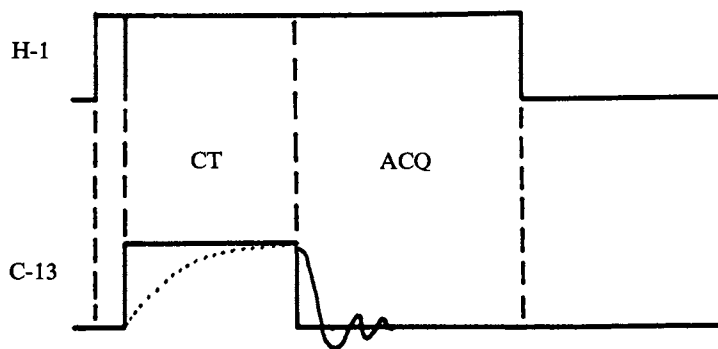


Figure 1. Pulse diagram of the single-contact cross-polarization experiment with a contact time, CT; and acquisition time ACQ.

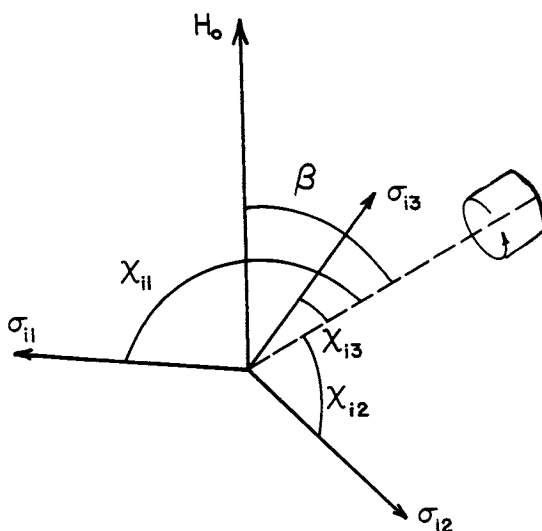


Figure 2. Magic-angle spinning, showing the orientation of the chemical shielding tensor,  $\sigma_i$ , with respect to the static field,  $H_0$ , and the spinning axis. Key:  $\sigma_{1,2,3}$ , principal elements of  $\sigma_i$ ;  $\chi_{1,2,3}$ , angles defining direction cosines between the principal axes of  $\sigma_i$  and the spinning axis; and  $\beta$ , angle between  $H_0$  and the spinning axis.

sign of the addition (or subtraction) of the free induction decay into memory, is helpful in obtaining spectra without artifacts.<sup>5</sup> If the data acquisition time, typically 30-to-100 ms, does not greatly exceed the proton  $T_{1\rho}$  value, then some advantage can be gained by a proton flipback technique,<sup>6</sup> in which the  $^1\text{H}$  magnetization remaining spin-locked at the end of the data acquisition period is flipped by a  $\pi/2$  pulse back to the  $H_0$  direction. This technique is especially advantageous for samples with long proton  $T_{1\rho}$  and  $T_1$  values, of which fossil fuels are not the most likely examples; nevertheless, there may be some advantage for certain fossil fuel systems that have especially long proton  $T_1$  values.<sup>7</sup> Since this kind of information on relaxation is typically not available a priori, this technique may sometimes be useful to avoid problems in case the proton spin lattice relaxation is inefficient.

A preeminent question in  $^{13}\text{C}$  CP/MAS work on fossil fuels, of course, concerns the analytical reliability of the results. That is, to what extent does the  $^{13}\text{C}$  magnetization generated and observed in a cross polarization experiment reflect the relative concentrations of different types of carbons in the sample? This question has been addressed in various ways in different laboratories during the past four years.

In one approach, VanderHart and Retcofsky<sup>8</sup> compared  $^{13}\text{C}$  results obtained by standard pulse FT experiments on a coal-derived liquid with data obtained by CP on a frozen sample of the same material; comparable results were obtained, implying that the CP approach was providing at least "representative" intensities. Maciel and coworkers have carried out studies in which the results of CP experiments at various contact times were compared with each other and with data obtained by solid-state experiments carried out with high-power  $^1\text{H}$  decoupling and MAS, but not CP.<sup>9</sup> These non-CP experiments generate observable  $^{13}\text{C}$  magnetization by  $^{13}\text{C}$  spin-lattice relaxation, a different process than cross polarization. Integration results that were comparable to within a few percent were obtained with CP (with contact times around 1 ms) and without CP; these results imply, albeit without definite proof, that both the CP and non-CP experiments sample the various carbon types representatively. However, one must acknowledge the possibility that there may be substantial numbers of  $^{13}\text{C}$  nuclei that are not being detected by either approach, and that neither of them provides analytically representative spectra. Gerstein has estimated on the basis of carbon counting experiments that between 60 and 100% of the carbon is accounted for in the CP/MAS experiment on typical coals.<sup>10</sup>

One reason why one might inquire about the possibility that some of the carbon atoms in a solid fossil fuel are not accounted for in a CP/MAS experiment is that there are large concentrations of unpaired electrons in such samples.

It is possible that the  $^{13}\text{C}$  resonances of a sufficient number of carbons are shifted and/or broadened by these paramagnetic centers to a degree that places them outside the detection limits of the usual CP/MAS experiment, thereby introducing significant intensity distortions in the  $^{13}\text{C}$  CP/MAS spectra. Perhaps the most promising approach for exploring the extent to which this possibility must be taken into account in  $^{13}\text{C}$  nmr analyses by CP/MAS is the electron-nuclear multiple-resonance approach introduced for coals by Wind and coworkers.<sup>11</sup> By systematically exploring the dependence of the observed spectra on microwave parameters of the experiment, it should be possible to elucidate the mechanism of nuclear polarization by the electrons and the effect that the paramagnetic centers have on the  $^{13}\text{C}$  spectra. Such studies are underway here and elsewhere. This electron-nuclear polarization approach also offers a major sensitivity enhancement factor that could extend the scope of  $^{13}\text{C}$  MAS studies of solids.

Examination of Figure 1 shows that the interpretation of  $^{13}\text{C}$  nmr integrations from CP/MAS experiments is most straightforward if the following conditions are satisfied:  $T_{\text{CH}} < \text{CT} < T_{1\rho\text{H}}$ ; and  $T_{1\text{H}} < T_{\text{rep}}$ . In this regime, the cross-polarization process (characterized by a relaxation time constant,  $T_{\text{CH}}$ ) is fast relative to the time scale of the Hartmann-Hahn contact time<sup>1,12</sup> (experimental contact time, CT), whereas the decay of spin-locked proton magnetization (characterized by a spin-lattice relaxation time in the rotating frame,  $T_{1\rho\text{H}}$ ) is slow on the scale of the contact time. The second condition insures that proton relaxation can occur between repetitions (characterized by a repetition time,  $T_{\text{rep}}$ ). Unfortunately, data on these relaxation parameters are usually not available on any specific fossil fuel sample of interest. Furthermore, relaxation behavior in complex systems like coal and oil shale are often more complex than what can be described by a single exponential. Nevertheless, some useful data are available.

Sullivan and Maciel<sup>9c,d</sup> have carried out detailed relaxation measurements on an eastern bituminous coal, Powhatan #5. An average value of about 100 ms was measured for the proton  $T_1$ , using an inversion recovery method in which the proton spin-lattice relaxation is monitored via  $^{13}\text{C}$  magnetization.<sup>9c,d</sup> This value is sufficiently smaller than the repetition time; thus the second constraint stated above is satisfied. An average proton  $T_{1\rho}$  value of about 4 ms was measured for the Powhatan #5 coal; this is roughly four times the value of the contact time typically used (1 ms), satisfying one part of the above constraint. However, this proton  $T_{1\rho}$  value is so much shorter than the data acquisition time that the proton flipback technique described above would not be useful for this kind of sample, at least

for the major components. An estimate of the cross polarization relaxation time,  $T_{\text{CH}}$ , of 0.1-to-1 ms was made for Powhatan #5 from experiments with the contact time, CT, as a variable parameter. Hence, the condition,  $T_{\text{CH}} < \text{CT}$ , is probably satisfied. Thus, focussing on the  $^{13}\text{C}_{\text{H}}$  signals that are observed in a CP/MAS experiment, it would appear that the data should be quantitatively useful, at least for coals of this type.

### Coals

Figure 3 is a collection of  $^{13}\text{C}$  CP/MAS spectra of coals of various rank.<sup>9b</sup> These spectra are representative of the appearances of most of the  $^{13}\text{C}$  CP/MAS spectra of coals that we have seen. They consist primarily of bands in two regions. These are the range from about 170 to about 90 ppm and from about 80 to about 0 ppm. The first band consists mainly of aromatic carbon resonances, and the latter is due mainly to aliphatic carbons. The "aromatic" and "aliphatic" bands are relatively featureless, but some reproducible shoulders can be discerned on some of the peaks, especially for the lower-rank coals. Indeed, some of the lignites show a considerable degree of fine structure, as exemplified by the spectrum of Byrd Stadium lignite shown in Figure 4.<sup>9d</sup> This additional fine structure can be attributed to specific structural features (e.g., a shoulder at about 155 ppm attributed to oxygen-substituted carbon in a phenolic system), and can often be accentuated by time-domain manipulations (see below).<sup>9d</sup> Somewhat surprisingly, the  $^{13}\text{C}$  CP/MAS spectra of coal macerals<sup>13</sup> do not generally exhibit more fine structure than the spectra of whole coals, and hence do not provide evidence of a dramatically simpler distribution of structural types than what is present in whole coals. Figure 5 displays spectra of three coal macerals.

The main parameter that can be derived directly from  $^{13}\text{C}$  CP/MAS spectra of coals is the apparent fraction ( $f'_a$ ) of the total integrated intensity that occurs in the "aromatic" band.<sup>14</sup> One should note that the "aromatic" region also encompasses the resonances of any olefinic carbons that may be present in the sample. From spectra of the type shown in Figure 3 one sees that there is a trend of increasing  $f'_a$  values with increasing coal rank. Values of 0.60 to 0.70 are found for lignites, 0.59 to 0.69 for subbituminous coals, 0.68 to 0.89 for bituminous coals and greater than 0.93 for anthracites.<sup>9b</sup> One also finds a trend toward narrower lines in the higher-rank coals. This may result from larger aromatic ring sizes, with less substitution and/or fewer heteroatoms in the higher-rank coals.

Other trends that have been explored in terms of  $^{13}\text{C}$  CP/MAS  $f'_a$  values of coals of various rank are heating values, atomic H/C ratios, fixed carbon, and temperature effects.<sup>9a,b,e</sup>

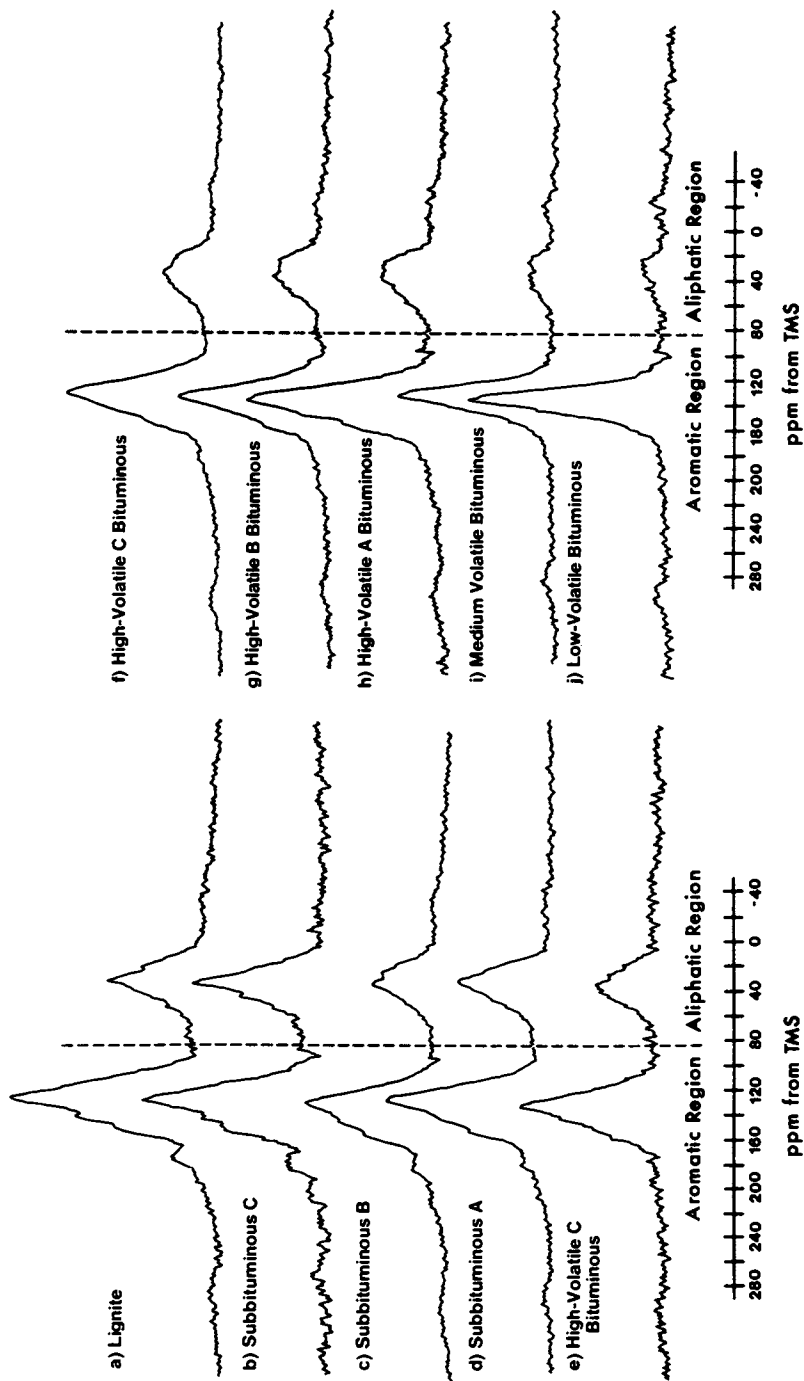


Figure 3.  $^{13}\text{C}$  CP/MAS spectra of coals of various rank. All spectra in this and other figures were obtained at 15 MHz, unless otherwise indicated. (Reproduced, with permission, from Ref. 9b. Copyright 1981, Pergamon Press.)

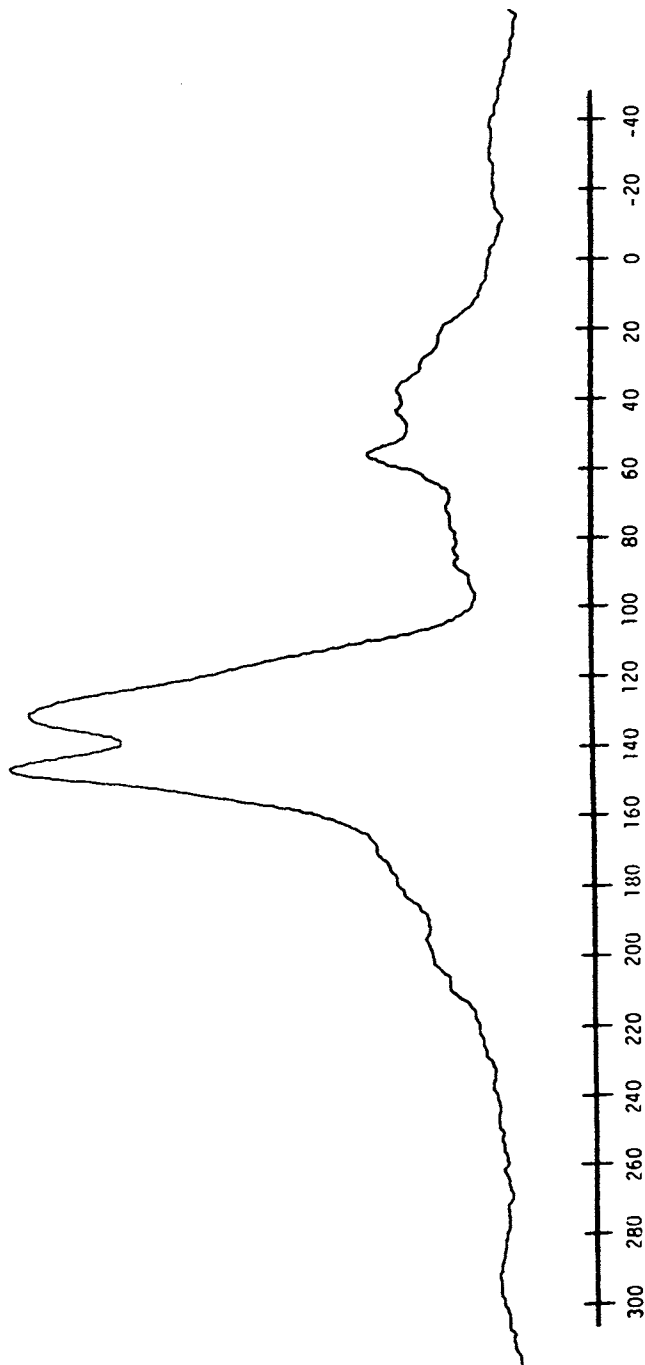


Figure 4. A  $^{13}\text{C}$  CP/MAS spectrum of Byrd Stadium lignite.



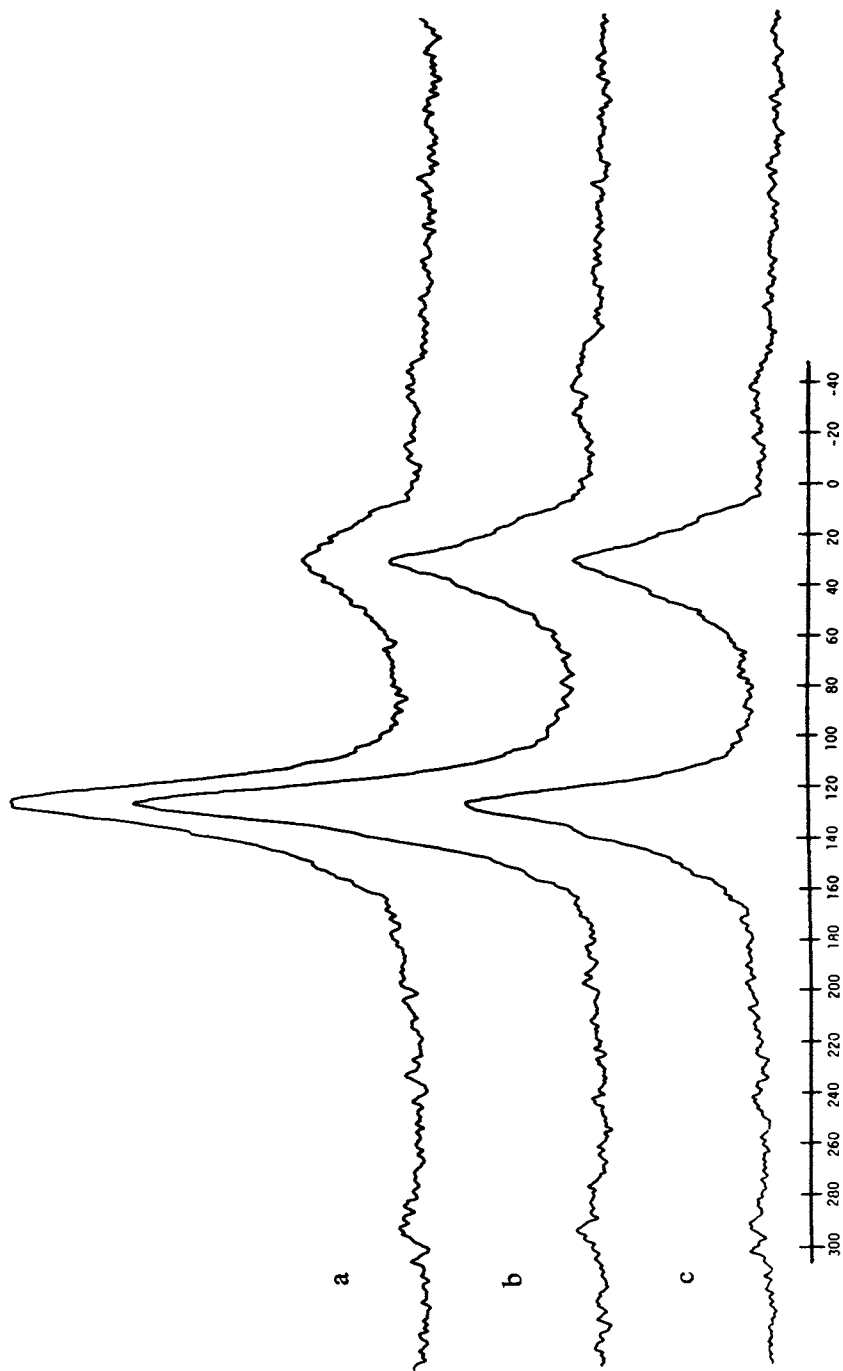


Figure 5.  $^{13}\text{C}$  CP/MAS spectra of coal macerals. Key: a, micrinite; b, atrites; and c, exinite. Reproduced, with permission, from Ref. 13a.

Figure 6 shows the selective depletion of aliphatic carbons in a coal sample that has been heated at  $450^\circ\text{C}$ .<sup>9e</sup> Similar aliphatic carbon depletions have been noted in  $^{13}\text{C}$  CP/MAS studies of reverse combustion and solvent refining processes,<sup>9e</sup> as seen in Figures 7 and 8. Zilm and coworkers have made extensive use of  $^{13}\text{C}$  CP/MAS nmr in a detailed study of a coal liquification process.<sup>15</sup>

Considerable effort has been directed to the use of  $^{13}\text{C}$  CP/MAS nmr in studying of the formation of coal. Hatcher, Breger and Earl have addressed the problem by examining various wood fragments buried in sediments under anaerobic conditions for variable lengths of time.<sup>16</sup> They concluded that coalification of wood tissues progresses from lignin to coal as the cellulose disappears. A later study followed the origin of coals from brown coal to bituminous coal.<sup>17</sup> Figure 9, taken from that work, shows the relationship between wood components, lignin and cellulose, and coal diagenesis. In progressing down the figure one sees the persistence of lignin patterns as the cellulose peaks diminish in relative intensity.

### Oil Shales

Although not studied as extensively as coals, oil shales and kerogens derived from them have received considerable attention in  $^{13}\text{C}$  CP/MAS work.<sup>18-21</sup> The spectra resemble those of coals, although for shales there is often a much larger aliphatic carbon fraction than for coals. Typical spectra of shales from around the world are given in Figure 10.<sup>18b</sup> One of the early developments in  $^{13}\text{C}$  CP/MAS work on oil shales was the recognition of a strong correlation of the oil yield obtained from retorting oil shales with the aliphatic carbon content determined in the  $^{13}\text{C}$  spectra.<sup>18a</sup> This correlation is shown in Figure 11.

Miknis and coworkers have explored the relationship between sample heating and  $^{13}\text{C}$  CP/MAS spectra in detail.<sup>21</sup> An example of the results of heating experiments is shown in Figure 12, which gives spectra of samples that have been heated to various temperatures. There it is clearly seen that the aliphatic carbons are depleted relative to aromatic carbons in high-temperature heating. It is suggested that the aromatic carbons originally present in the raw oil shales largely become the carbonaceous residue after retorting.<sup>21b</sup> Dennis and coworkers have studied an example of "retorting" in nature by  $^{13}\text{C}$  CP/MAS nmr.<sup>22</sup> They examined samples taken from a drilling core in the Eastern Atlantic in a region where the sediment was intruded by hot magma during the Miocene epoch. The retorting effects of the hot intrusion can be seen in the depletion of aliphatic intensity from the  $^{13}\text{C}$  CP/MAS spectra. Figure 13 shows representative spectra.

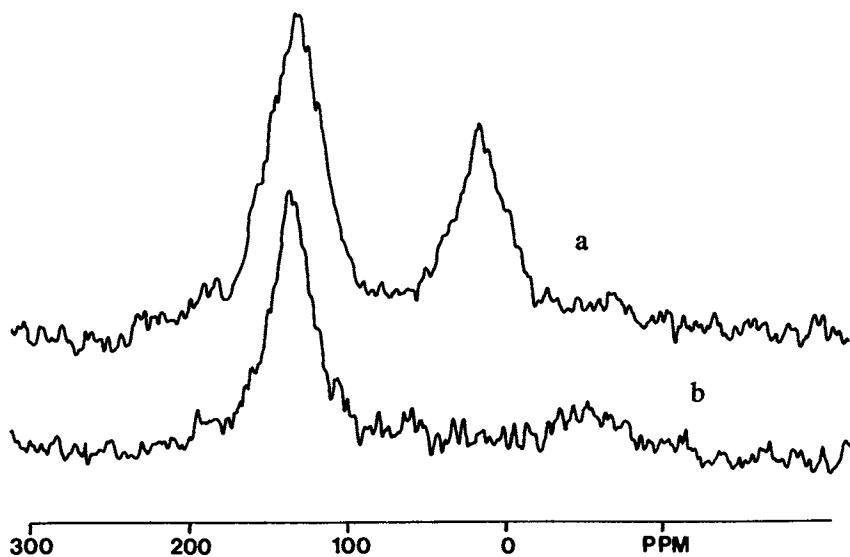


Figure 6.  $^{13}\text{C}$  CP/MAS spectra of heated and unheated Wyoming coal. Key: a, original coal ambient temperature; and b, coal heated to  $450^\circ\text{C}$ .

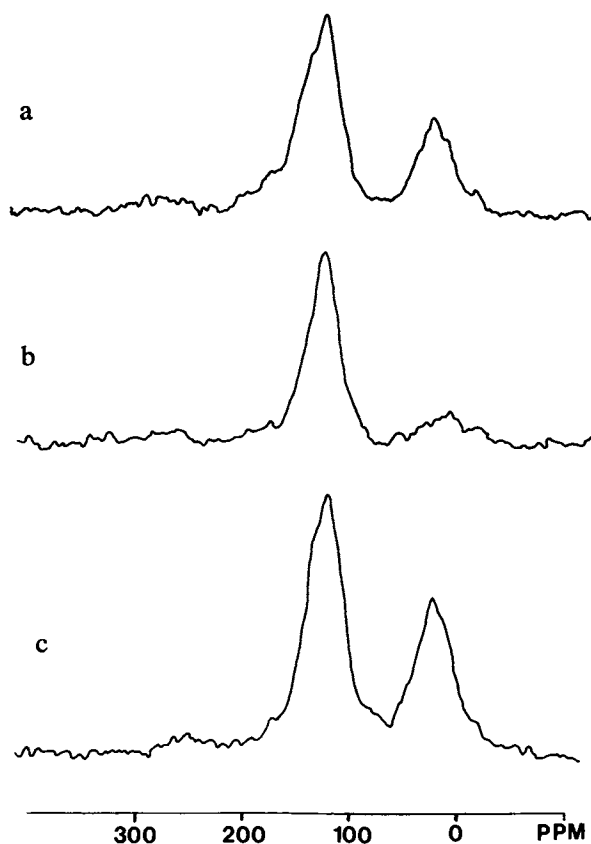


Figure 7.  $^{13}\text{C}$  CP/MAS spectra of Wyoming subbituminous coal before and after reverse combustion, and a cored (test) sample. Key: a, original coal; b, reverse-combusted coal; and c, cored sample. (Reproduced, with permission, from Ref. 9e. Copyright 1981, American Institute of Physics.)

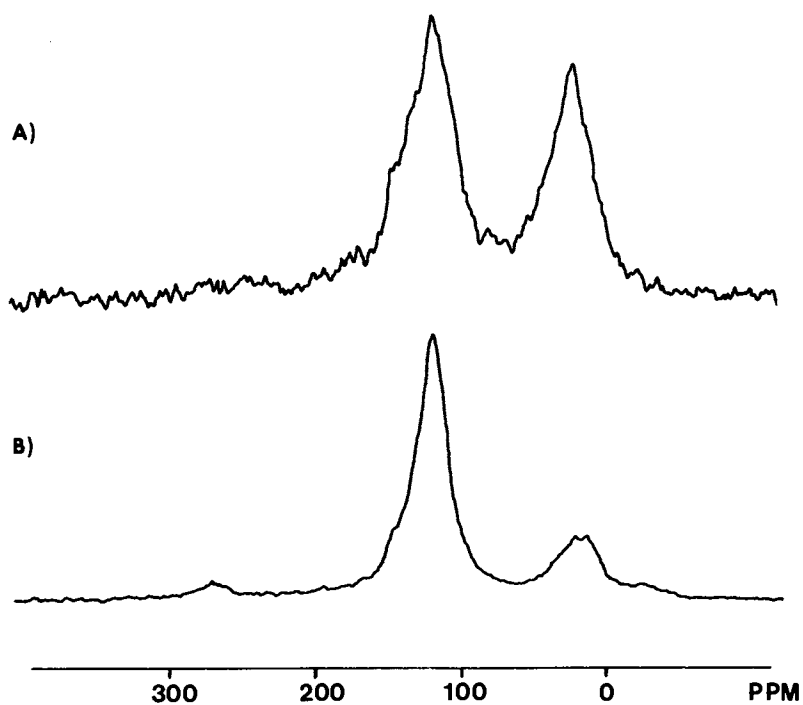


Figure 8.  $^{13}\text{C}$  CP/MAS spectra of Wyodak coal before (A) and after (B) solvent refining. (Reproduced, with permission, from Ref. 9e. Copyright 1981, American Institute of Physics.)

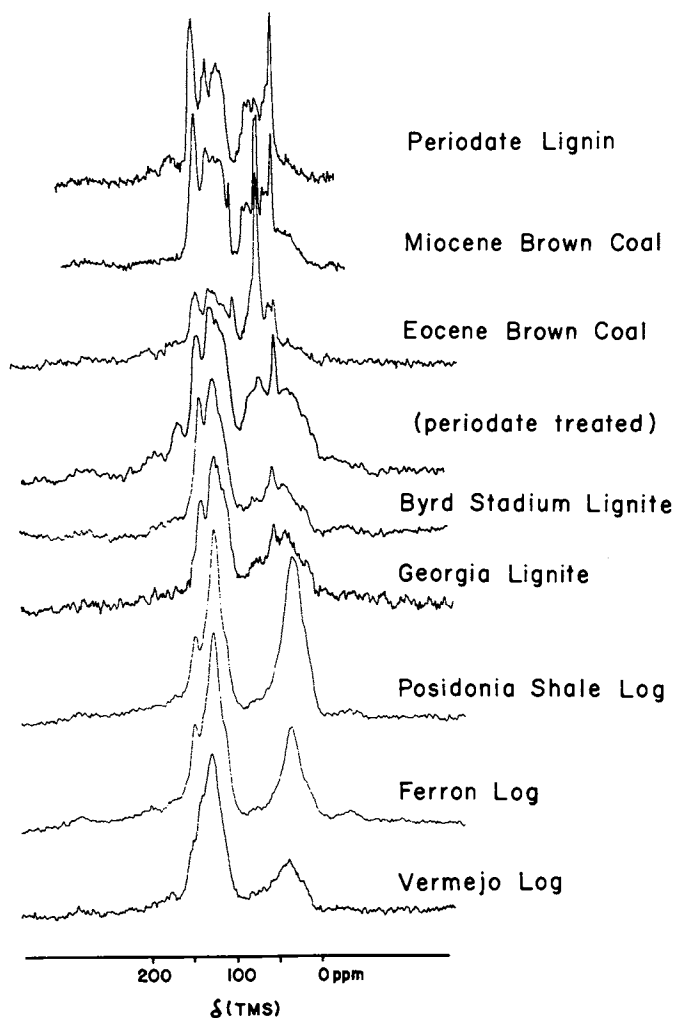


Figure 9.  $^{13}\text{C}$  CP/MAS spectra of coalified logs, lignin, and periodate Eocene brown coal (Reproduced, with permission, from Ref. 17).

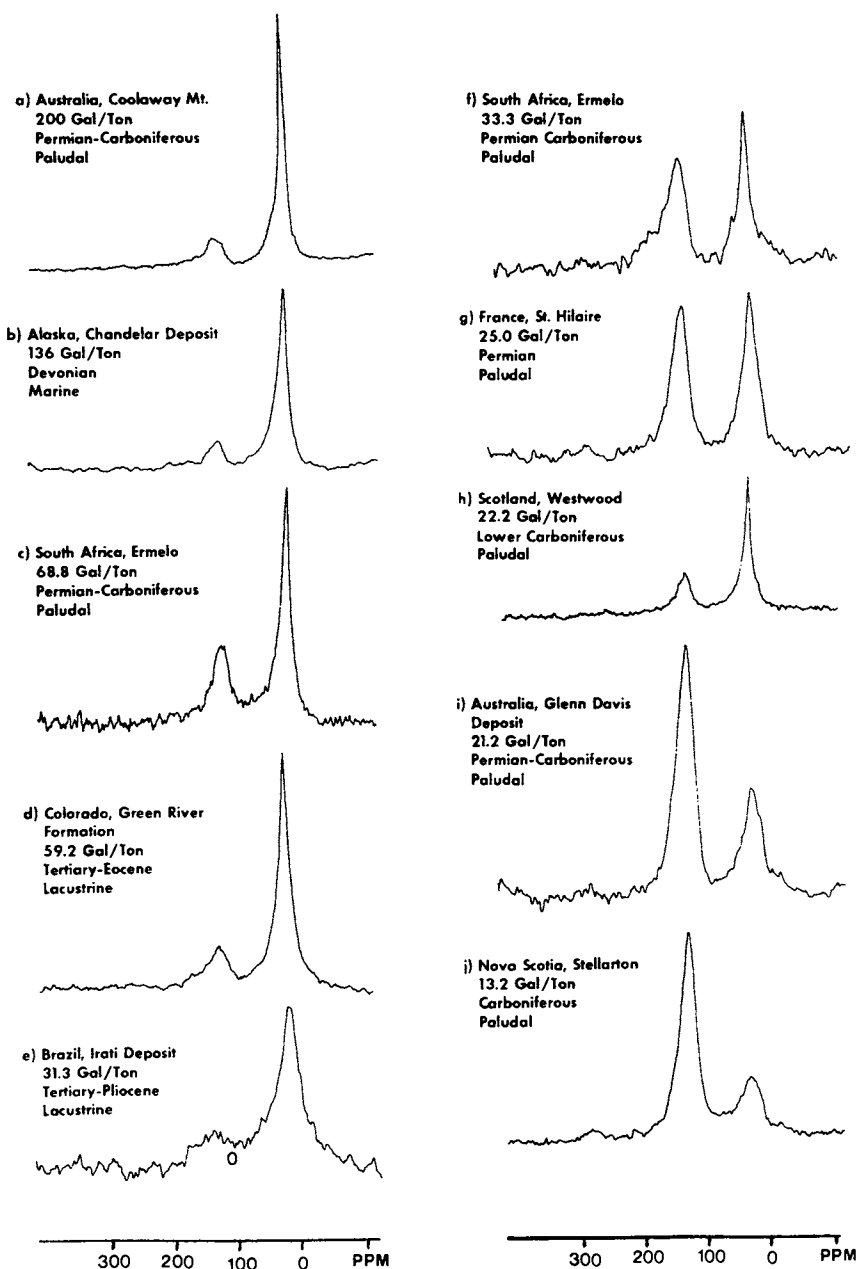


Figure 10.  $^{13}\text{C}$  CP/MAS spectra of oil shales from around the world. (Reproduced, with permission, from Ref. 18b. Copyright 1981, Pergamon Press.)

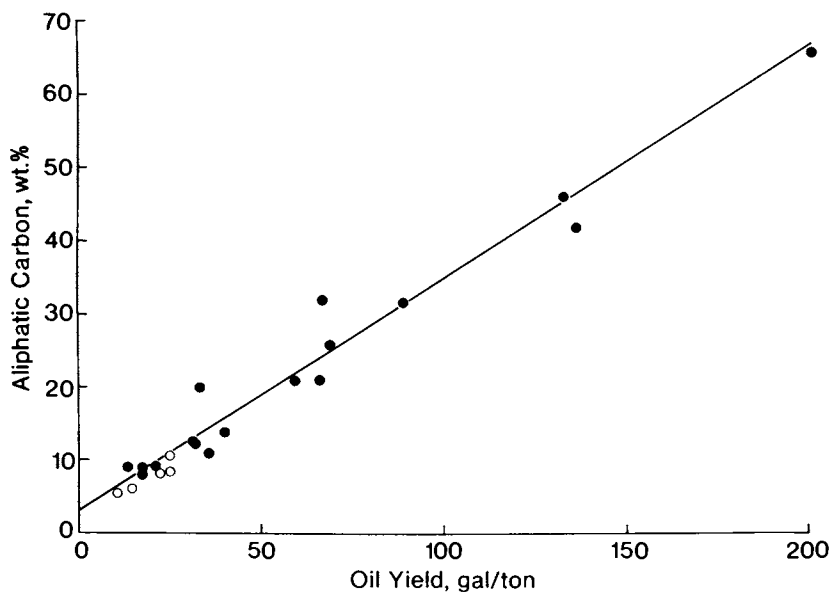


Figure 11. Plot of oil yields of shales vs. aliphatic carbon content determined by  $^{13}\text{C}$  CP/MAS NMR spectra. Key:  $\circ$ , kerogen concentrate; and  $\bullet$ , raw oil shale. (Reproduced, with permission, from Ref. 18a. Copyright 1979, IPC Bus Press.)



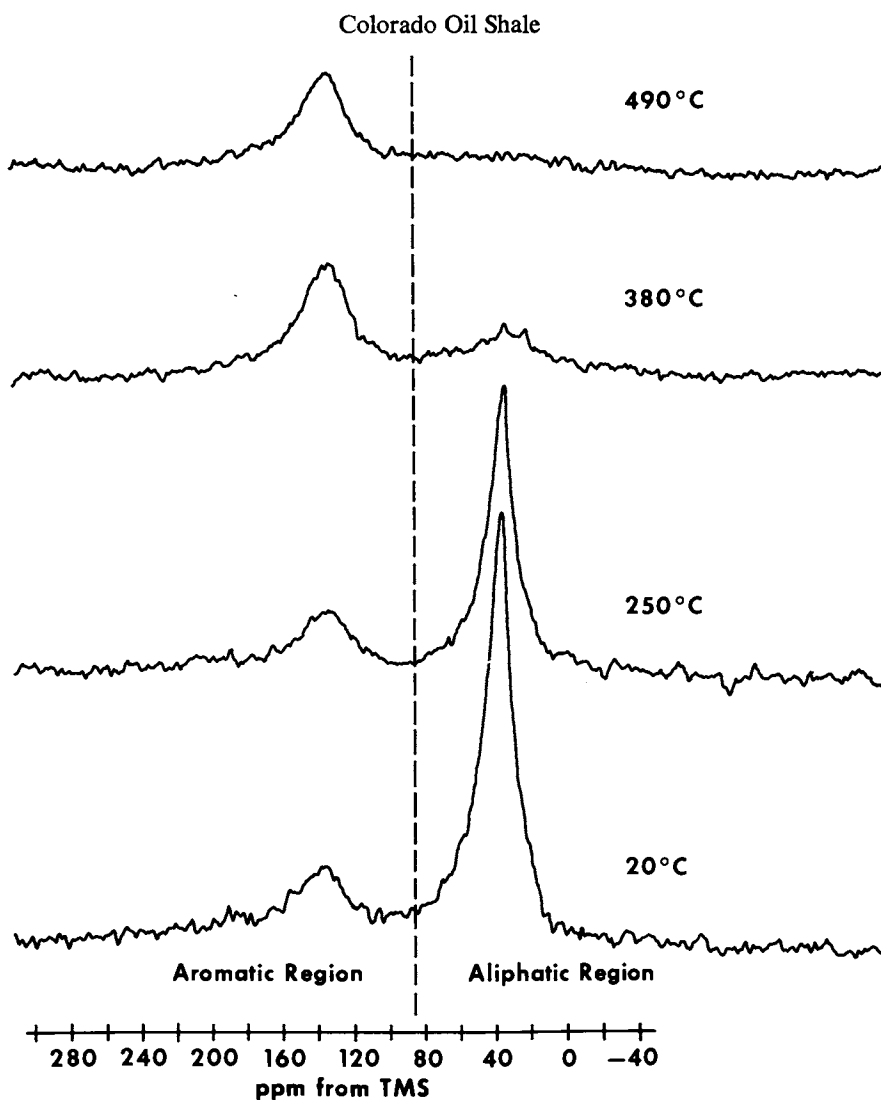


Figure 12.  $^{13}\text{C}$  CP/MAS spectra of oil shales heated to various temperatures. (Reproduced, with permission, from Ref. 21b. Copyright, IPC Bus Press.)

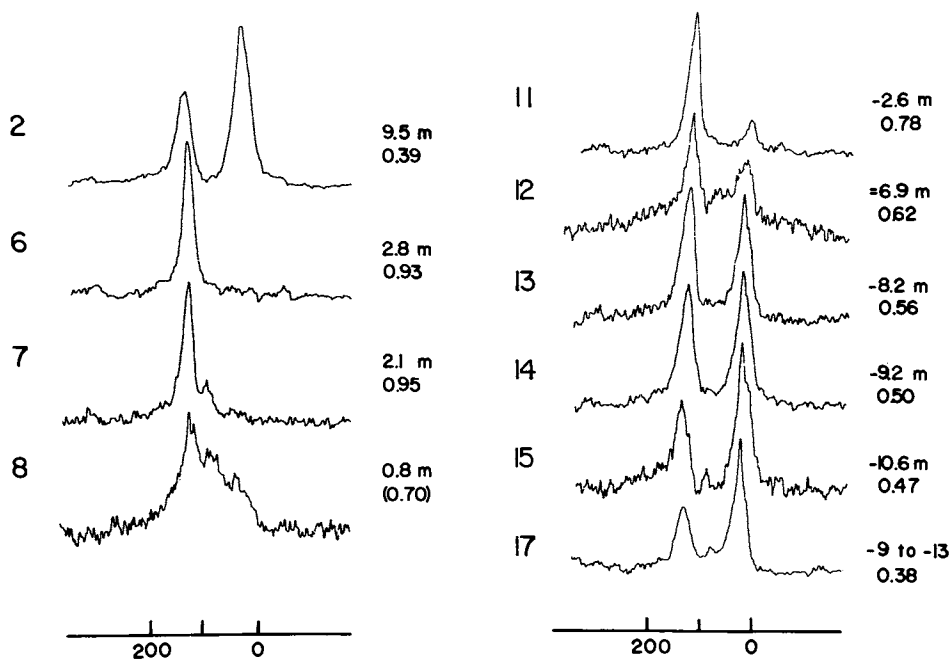


Figure 13.  $^{13}\text{C}$  CP/MAS spectra of organic matter taken at various distances (in meters) from the hot magma intrusion, showing depletion of the aliphatic content near the intrusion as measured by  $f'_a$  values. (Reproduced, with permission, from Ref. 22. Copyright, Pergamon Press.)

Because of the great difficulties involved in the characterization of organic matter in oil shale, there has been a tendency in some laboratories to study not the shale itself, but a kerogen concentrate isolated from it by procedures designed mainly to eliminate the inorganic matrix. The implied basis or goal of this approach is that the organic matter in oil shale is largely left intact in the conversion to kerogen concentrates. Maciel and Dennis have examined this point by comparing the  $^{13}\text{C}$  CP/MAS spectra of a series of shales and kerogen concentrates.<sup>23</sup> Figure 14 shows some of the results. It is found that the spectra of the kerogen concentrates are in general sharper, probably reflecting the removal of some paramagnetic centers, but that the  $f_a'$  values are nearly the same for a shale and its corresponding kerogen concentrate. Also, there is an indication of removal of some alkoxy-type carbons, e.g., carbohydrates, during kerogen isolation.

### Structural Resolution

One of the continuing efforts in  $^{13}\text{C}$  CP/MAS research on solid fossil fuels is to extend the structural resolution of the technique beyond what is obtained directly in spectra such as those given in Figures 3 and 10. One common approach in nmr for securing higher structural resolution is going to a higher applied magnetic field,  $H_0$ . That this is not usually productive in the case of a coal is seen in Figure 15, where  $^{13}\text{C}$  CP/MAS spectra of the Powhatan #5 coal are shown at three different  $^{13}\text{C}$  r.f. frequencies, 15 MHz, 25 MHz and 50 MHz. One sees no apparent resolution advantage in higher field in this case. In fact, there is considerable disadvantage at higher field, because of the spinning sideband problem.

At 15 MHz a 2.5-KHz spinning speed is sufficient to bring the spinning sidebands outside the main (centerband) spectrum. At 25 MHz, a 4.0-KHz spinning rate is just barely large enough to bring the right aromatic sideband to the higher-shielding side of the aliphatic carbon peak. A 4.0-KHz spinning rate in a 50-MHz experiment brings the right sideband of the aromatic peak into direct coincidence with the aliphatic peak. In order to avoid this kind of overlap in a 50-MHz experiment, spinning speeds in excess of 8 KHz are needed. It has not yet proved to be practical to spin large samples (needed for sensitivity reasons for many fossil fuel samples) at such speeds using spinner materials that are convenient to machine and devoid of interfering  $^{13}\text{C}$  nmr signals.

Thus it appears that currently the practical limit for most  $^{13}\text{C}$  CP/MAS studies of fossil fuels is about 25 MHz. This situation will change when methods become available for suppressing spinning sidebands without distorting the intensities of the spectrum obtained. In this regard there is considerable encouragement to be taken from the recent work of Dixon, who has developed

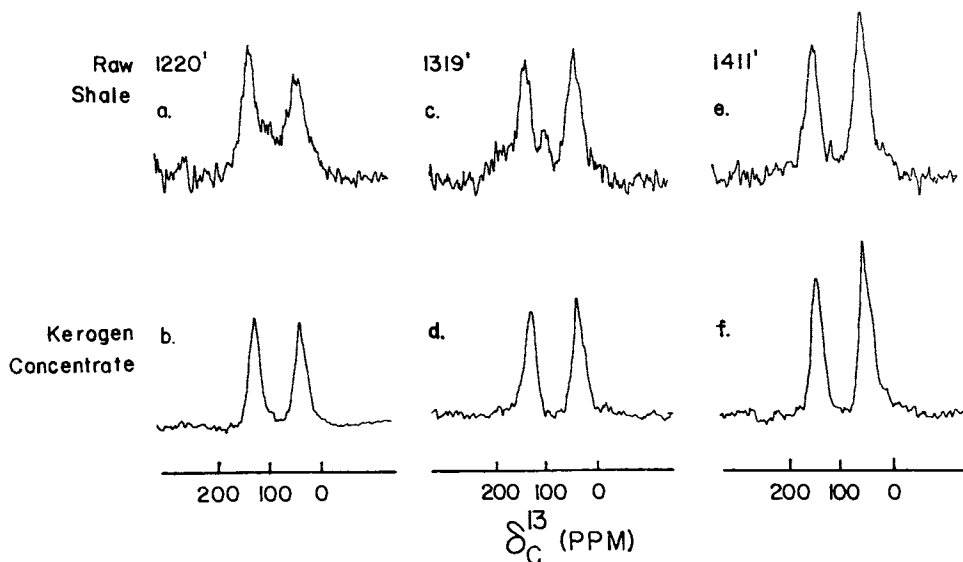


Figure 14.  $^{13}\text{C}$  CP/MAS spectra of oil shales (upper) and corresponding kerogen concentrates (lower).

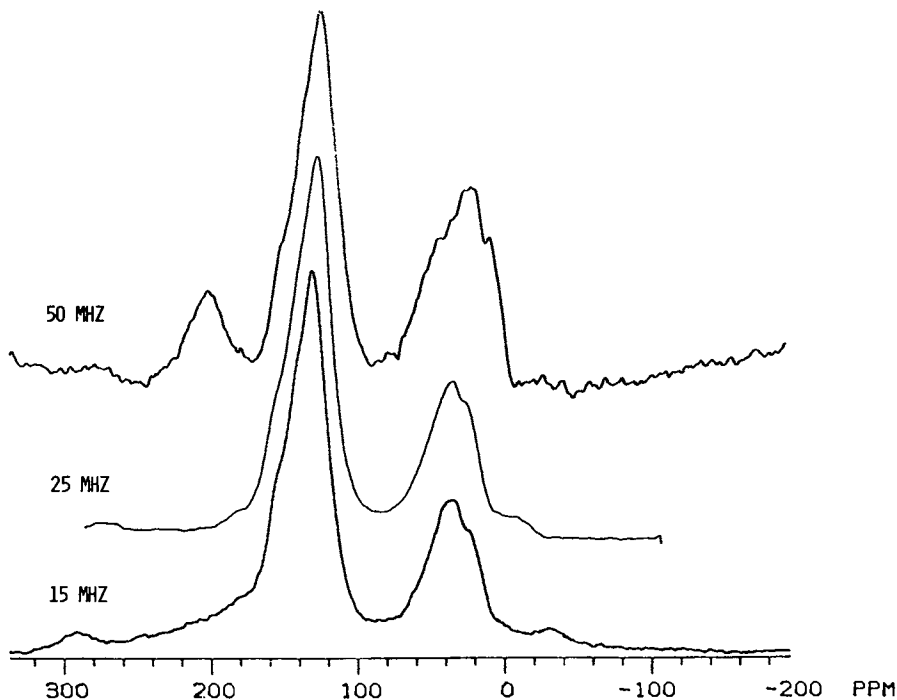


Figure 15.  $^{13}\text{C}$  CP/MAS spectra of Powhatan #5 coal at three magnetic field strengths (or  $^{13}\text{C}$  resonance frequencies).

a method that employs precisely-spaced  $\pi$  pulses to impart specific phases to sidebands of each order.<sup>24</sup> By suitable phase manipulation and combination of these spectra one can obtain separate spectra corresponding to the centerband and each sideband, and ultimately recombine these into the desired spectrum. This recombined spectrum is in the ideal case free of intensity distortions. It seems likely that an approach of this general type will make it possible to carry out  $^{13}\text{C}$  CP/MAS experiments on solid fossil fuels at high field in the future.

A pertinent question regarding the resolution issue is the origin of the broad aromatic and aliphatic peaks, or the natural linewidths, in fossil fuel samples. Sullivan and Maciel have carried out CP/MAS experiments incorporating the Hahn spin-echo approach for estimating  $^{13}\text{C}$   $T_2$  values in Powhatan #5 coal.<sup>9c,d</sup> In 15.1 MHz spectra an average value of 9.6 ms was obtained for the  $T_2$  of aromatic carbons (corresponding to a linewidth of 33 Hz); values of 8.6 ms (37 Hz) and 6.4 ms (49 Hz) were obtained for the low-shielding and high-shielding regions of the aliphatic band. These linewidths, ranging from 2.2 to 3.3 ppm, are much smaller than the widths of the bands obtained in the spectra. Hence, one can conclude that the primary reason for the broad bands in the  $^{13}\text{C}$  CP/MAS spectra of solid fossil fuels is a distribution of closely spaced chemical shifts, corresponding to a complex collection of individual structural types and resonances, each of which would alone exhibit a relatively narrow line.

Another approach to enhancing the amount of structural information one can extract from the  $^{13}\text{C}$  CP/MAS spectrum of a solid fossil fuel sample is to look for selective behavior in the time domain. Thus, one can try to capitalize on differences in relaxation properties of different carbon types in order to differentiate structural types for which distinct, separated peaks do not appear in the spectrum. An example of this approach is seen in Figure 16,<sup>9d</sup> which shows the results of using a variation of the interrupt time in the interrupted-decoupling experiment introduced by Opella and Frey.<sup>25</sup> In this experiment a variable time is introduced, during which the  $^1\text{H}$  decoupler is turned off, between the end of the contact period and the beginning of the data acquisition period in a CP experiment. During this interrupt time the  $^{13}\text{C}$  nuclear magnetic moments dephase at rates dependent on the strengths of the effective  $^1\text{H}$ - $^{13}\text{C}$  dipolar interactions. In Figure 16 one sees a dramatic difference between the dephasing rates of aromatic and aliphatic carbons, largely reflecting the higher abundance of directly-bonded hydrogens in aliphatic structures. More interesting, within the aliphatic band there is a faster dephasing on the lower-shielding relative to the higher-shielding side (compare interrupt times of 0 and 50  $\mu\text{s}$ ). This slower dephasing on the higher-shielding side is attributed to the fast rotation of methyl groups, which effectively attenuates the dipolar interaction. Sullivan and Maciel have explored

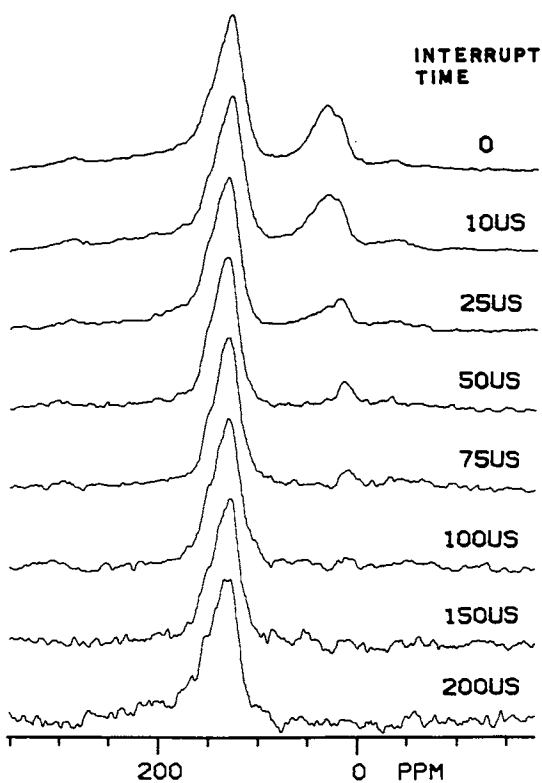


Figure 16. Stack plot of  $^{13}\text{C}$  CP/MAS interrupted decoupling spectra of Powhatan #5 coal. The tallest peak in each spectrum was scaled to a uniform height.

extensively the prospects for employing time-resolution of this general type for enhancing the structural information that can be extracted from coals by  $^{13}\text{C}$  CP/MAS nmr.<sup>9c,d</sup>

Another time-domain approach for enhancing resolution in an nmr experiment is to manipulate the free induction decay (FID) in ways that reduce the contributions of broad-line components and enhance the contributions of narrow-line components. One such approach that is commonly used in liquid-state nmr is convolution difference,<sup>26</sup> in which a spectrum (or FID) weighted exponentially with a larger line-width function is subtracted from one weighted with a smaller-linewidth function to give a resolution-enhanced spectrum. An example is presented in Figure 17, showing the technique applied to the Powhatan #5 coal. It is seen that the convolution difference spectra (at the top of the figure) greatly accentuate fine structure (hints of shoulders and peaks) that are barely detectable in the spectra ordinarily obtained (at the bottom of the figure). This permits one to confirm the existence of structural types that contribute to intensity in portions of the spectrum that would otherwise be unresolved.

#### Summary and Conclusions

$^{13}\text{C}$  CP/MAS nmr techniques have provided valuable new information on the nature of organic structures in solid fossil fuels. The activity in this field has progressed from simply obtaining spectra of various sample types to attacking specific practical problems and to addressing the detailed spin dynamics in representative systems. Additional work will be required to permit definitive conclusions on the analytical reliability of  $^{13}\text{C}$  CP/MAS integrations. One can expect major contributions from high-temperature experiments and from electron-nuclear polarization approaches. A variety of time-domain techniques are being explored to enhance the level of structural information one can extract from the spectra.

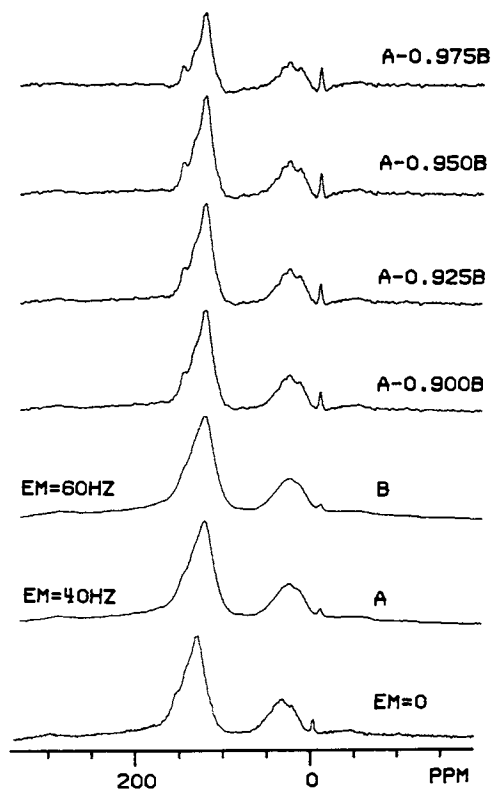


Figure 17. Convolution difference  $^{13}\text{C}$  CP/MAS spectra of Powhatan #5 coal. The sharp peak at  $-2$  ppm is due to an added external standard.



### Acknowledgements

The authors gratefully acknowledge support of this work by U.S. Department of Energy Contracts No. DE-AT20-81LC10652 (from the Laramie Energy Technology Center) and No. DE-AC22-79ET14940 (from the Pittsburgh Energy Technology Center) and the assistance of the Gulf Research and Development Company.

### References and Footnotes

1. Pines, A; Gibby, M.G.; Waugh, J.S. J. Chem. Phys. 1973, 59, 569.
2. Schaefer, J.; Stejskal, E.O. "Topics in Carbon-13 NMR Spectroscopy," Vol. 3, G.C. Levy, ed., Wiley-Interscience, New York, 1979; p 283.
- 3a. Lowe, I.J. Phys. Rev. Letters. 1959, 2, 285.
- b. Kessemeier, H.; Norberg, R.E. Phys. Rev. 1967, 155, 321.
- c. Andrew, E.R. Progr. Nucl. Magn. Reson. Spectrosc. 1971, 8, 1.
- d. Bartuska, V.J.; Maciel, G.E. J. Magn. Res. 1981, 42, 312.
- e. Zilm, K.W.; Alderman, D.W.; Grant, D.M.; J. Magn. Res. 1978, 30, 563.
- f. Burton, D.J.; Harris, R.K.; Mervin, L.H. J. Magn. Res. 1980, 39, 159.
- g. Opella, S.J.; Frey, M.H.; DeVerdi, J.A. J. Magn. Res. 1980, 37, 165.
- h. Doty, F.D.; Ellis, P.D. Rev. Sci. Inst., in press.
- i. Eckman, R.; Alla, M.; Pines, A. J. Magn. Res. 1980, 42, 440.
- j. vanDijk, P.A.S.; Schut, W.; vanOs, J.W.M.; Menger, E.M.; Veeman, W.S. J. Phys. E. Sci. Instrum. 1980, 13, 1309.
- k. Schneider, B.; Doskocilova, D.; Babka, J.; Ruzicka, Z. J. Magn. Res. 1980, 37, 41.
4. Kel-F is a trade name (Du Pont) for polytrifluoroethylene.
5. Stejskal, E.O.; Schaefer, J. J. Magn. Res. 1975, 18, 560.
6. Tegenfeldt, J.; Haeberlen, V. J. Magn. Res. 1979, 36, 453.
7. Maciel, G.E.; Sullivan, M.J.; Szeverenyi, N.M., unpublished results.
- 8a. VanderHart, D.L.; Retcofsky, H.L. Fuel 1976, 55, 202.
- b. Retcofsky, H.L.; VanderHart, D.L. Fuel 1978, 57, 421.
- 9a. Maciel, G.E.; Bartuska, V.J.; Miknis, F.P. Fuel 1979, 58, 391.
- b. Miknis, F.P.; Sullivan, M.; Bartuska, V.J.; Maciel, G.E. Org. Geochem. 1981, 3, 19.
- c. Maciel, G.E.; Sullivan, M.J., unpublished results.
- d. Sullivan, M.J., Ph.D. Thesis, Colorado State University, September, 1981.
- e. Maciel, G.E.; Sullivan, M.J.; Szeverenyi, N.M.; Miknis, F.P. in "Chemistry and Physics of Coal Utilization-1980," Cooper, B.R. and Petrakis, L., eds., Am. Inst. Phys., New York, 1981; pp. 66-81.

10. Balimann, G.E.; Groombridge, C.J.; Harris, R.K.; Packer, K.J.; Say, B.J.; Tanner, S.F. Phil. Trans. Soc. (London) A 1981, 299, 643.
11. Wind, R.A.; Trommel, J.; Smidt, J. Fuel 1979, 58, 900.
12. Hartman, S.R.; Hahn, E.L. Phys. Rev. 1952, 128, 2042.
- 13a. Maciel, G.E.; Sullivan, M.J.; Petrakis, L.; Grandy, D.W. Fuel, in press.
- b. Zilm, K.W.; Pugmire, R.J.; Larter, S.R.; Allan, J.; Grant, D.M. Fuel, 1981, 60, 717.
14. The word "apparent" is used to convey the uncertainties that remain regarding the analytical significance of integrated  $^{13}\text{C}$  CP/MAS intensities.
15. Zilm, K.W.; Pugmire, R.J.; Grant, D.M.; Wisner, W.H.; Wood, R.E. Fuel, 1979, 58, 11.
16. Hatcher, P.G.; Breger, I.A.; Earl, W.L. Org. Geochem. 1981, 3, 49.
17. Hatcher, P.G.; Breger, I.A.; Szeverenyi, N.M.; Maciel, G.E. Org. Geochem., in press.
- 18a. Maciel, G.E.; Bartuska, V.J.; Miknis, F.P. Fuel 1979, 58, 391.
- b. Miknis, F.P.; Maciel, G.E.; Bartuska, V.J. Org. Geochem. 1979, 1, 169.
- 19a. Vitorovic, D.; Vucelic, D.; Gasic, M.J.; Juranic, N.; Macura, S. Org. Geochem. 1978, 1, 89.
- b. Vucelic, D.; Juranic, N.; Vitorovic, D. Fuel 1979, 58, 759.
20. Resing, H.A.; Garroway, A.N.; Hazlett, R.N. Fuel 1978, 57, 450.
- 21a. Miknis, F.P.; Netzel, D.A.; Smith, J.W.; Mast, M.A.; Maciel, G.E. Geochim. Cosmochim. Acta, submitted.
- b. Miknis, F.P.; Szeverenyi, N.M.; Maciel, G.E. Fuel, submitted.
22. Dennis, L.W.; Maciel, G.E.; Hatcher, P.G.; Simoneit, B.R.T. Org. Geochem, submitted.
23. Maciel, G.E.; Dennis, L.W. Org. Geochem., in press.
24. Dixon, W.T. J. Magn. Res. 1981, 44, 220.
25. Opella, S.J.; Frey, M.H. J. Am. Chem. Soc. 1979, 101, 5854.
26. Campbell, I.D.; Dobson, C.M.; Williams, R.J.P.; Xavier, A.V. J. Magn. Res. 1973, 11, 172.

RECEIVED December 21, 1981.

# Solid State $^{13}\text{C}$ NMR Studies of Polyester Thermoplastic Elastomers

LYNN W. JELINSKI, JOSEPH J. DUMAIS, F. C. SCHILLING, and F. A. BOVEY  
Bell Laboratories, Murray Hill, NJ 07974

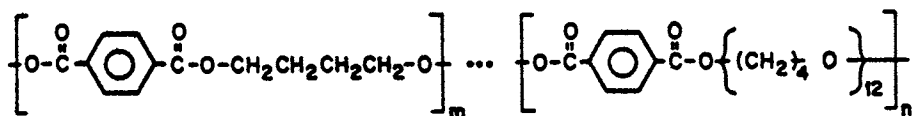
Solid state  $^{13}\text{C}$  NMR was used to study the molecular motions and domain structure of a series of Hytel thermoplastic elastomers. Hytel is a segmented block copolymer available in compositions ranging from 0.80 to 0.96 mole fraction poly(butylene terephthalate) "hard" segments, copolymerized with poly(tetramethyleneoxy) terephthalate "soft" segments. The mobile domains were observed selectively using low power proton decoupling (scalar decoupling;  $\gamma\text{H}_2/2\pi = 4$  kHz). The linewidths for the mobile aliphatic carbons are a linear function of the average hard block length of the polymer and are independent of temperature over a large ( $\sim 80^\circ\text{C}$ ) range in temperature. The  $T_1$  values are independent of the average hard block length of the polymer and increase with increasing temperature and increasing field strength.

The carbons comprising the rigid domains were studied by various combinations of dipolar decoupling ( $\gamma\text{H}_2/2\pi = 45$  kHz), cross polarization and magic angle spinning. The behavior of the signal intensity as a function of cross polarization contact time shows two-phase behavior. In addition, the principal values of the chemical shift tensors of the aromatic and carbonyl carbons were obtained from an analysis of the intensities of the sidebands from magic angle spinning experiments. The carbonyl carbons of dimethyl terephthalate, polybutylene terephthalate, and all Hytel samples have chemical shift tensors which are axially symmetric. The protonated aromatic carbon chemical shift anisotropy ( $|\sigma_{33} - \sigma_{11}|$ ) shows a reduced value for the Hytel sample which has the largest mole fraction of soft segments. This reduced anisotropy is attributed to small-angle excursions of the aromatic ring about the 1,4-phenylene axis.

These  $^{13}\text{C}$  NMR results, taken together, provide new insights into the structure and dynamics of this segmented copolymer system.

Hytel thermoplastic elastomer (1) is composed of  $m$  poly(butylene terephthalate) "hard" segments and  $n$  poly(tetramethyleneoxy) terephthalate "soft" segments. The hard and soft segments are assumed to be random in distribution. The ratio of  $m/n$  controls the mechanical properties of the copolymer (2).

0097-6156/82/0191-0345\$06.00/0  
© 1982 American Chemical Society



The morphology of Hytel has been studied by several physical techniques. Thermal analysis (3-7) and electron microscopy (3,8,9) have established that the Hytel copolymers exhibit a two-phase morphology. The rigid domains in Hytel form interpenetrating lamellar networks (3) (Figure 1), rather than the discrete domain structure seen for other segmented copolymers (10,11). Whether the lamellar networks are arranged in a random (3) or spherulitic (12) morphology is a matter of controversy; the exact morphology is probably related to the thermal history of the sample. Low angle fiber diffraction patterns of drawn Hytel samples are identical to those of drawn polybutylene terephthalate, with the exception of a halo due to amorphous material (3). This result has been taken to indicate that the structure of the rigid domains of Hytel is identical to that of the poly(butylene terephthalate) homopolymer.

Although the superstructural morphology of Hytel has been studied extensively, little molecular-level information is available in the solid state. In particular, we would like to characterize the domain boundaries and the nature of the phase separation. We would like to understand molecular motion in this polymer, both in the rigid domains and in the mobile regions. Also, we would like to clarify the relationships between molecular motion, chemical composition, and mechanical properties.

Solid state  $^{13}\text{C}$  NMR is a technique which is particularly well-suited for this investigation. Chemically distinct carbons in general have separate  $^{13}\text{C}$  NMR resonances. These resonances can be studied in terms of linewidth, chemical shift anisotropy, spin lattice relaxation times ( $T_1$ ), nuclear Overhauser enhancements (NOE),  $^{13}\text{C}$   $T_{1\rho}$  values,  $^1\text{H}$   $T_{1\rho}$  values, and cross polarization transfer rates. Hytel is an especially obliging polymer, as the mobile domains can be studied selectively using scalar (low power,  $\gamma\text{H}_2/2\pi \sim 4$  kHz) proton decoupling (13). (Sufficient motion exists in the mobile regions to partially average the dipole-dipole interactions and chemical shift anisotropy). Dipolar decoupling ( $\gamma\text{H}_2/2\pi \sim 45$  kHz), magic angle spinning, and cross polarization can be used in various combinations to resolve signals from the rigid domains.

We describe here the results of  $^{13}\text{C}$  NMR linewidth,  $T_1$ , and NOE measurements on the mobile domains of solid Hytel. For the rigid domains we present the results of cross polarization rate measurements and reconstructions of the chemical shift anisotropies (14). Taken together, these results provide us with new insights into the domain structure and molecular dynamics of a segmented copolymer which does not have a discrete domain structure.

### Experimental Section

**Samples.** Hytel types 7246, 6346, 5526 and 4056 were obtained in both powder and pellet form from the du Pont Company. The mole fraction and weight per cent of hard segments in these samples has been determined by solution state  $^{13}\text{C}$  NMR (13). The

results are summarized in Table I. Polyether glycol (Teracol 1000) was also obtained from du Pont. Eastman Chemicals provided the poly(butylene terephthalate) samples. All samples were employed as received.

TABLE I  
Mole Fraction and Weight Per Cent Hard  
Segments in Hytel Samples

<i>Hytel Sample</i>	<i>Mol Fraction Hard</i>	<i>Wt% Hard</i>	<i>Average Hard Block Length</i>
4056	0.80	44 wt%	6 units
5526	0.87	57	8
6356	0.94	75	17
7246	0.96	81	22

*Scalar Decoupled NMR Spectra.* Scalar decoupled  $^{13}\text{C}$  NMR spectra of polymer solutions and solids were recorded either at 21 kG on a Bruker WH-90 spectrometer (22.62 MHz for  $^{13}\text{C}$ ) or at 47 kG on a Varian XL-200 spectrometer (50.3 MHz for  $^{13}\text{C}$ ). The 90° pulse width for both probes was *ca.* 12  $\mu\text{s}$ . The solution state spectra were obtained on 15-20 wt% solutions of the polymers in hexafluoroisopropanol at 34°C or in *m*-cresol at 100°C using a 10 kHz spectral window and 16K time domain data points. An internal capillary of benzene- $\text{d}_6$  or ethylene glycol- $\text{d}_4$  was used for field frequency lock and reference purposes. Scalar decoupled spectra of solid polymer samples (powder or chopped pellets) were obtained on samples packed in 10 mm NMR tubes into which a capillary containing benzene- $\text{d}_6$ , ethylene glycol- $\text{d}_4$ , or acetone- $\text{d}_6$  (for reference and field frequency lock) was inserted. Some spectra were run in the unlocked mode on the XL-200 (estimated drift <0.01 ppm/hr). These spectra were recorded in a 12 kHz spectral window with 4K or 8K time domain data points. The strength of the proton decoupling field ( $\gamma\text{H}_2/2\pi$ ) was determined using either ethylene glycol or dioxane and was adjusted to 4 kHz (1 G).

Variable temperature was achieved using the standard spectrometer accessories. The temperature controller was calibrated using the proton shifts of ethylene glycol. The temperatures are considered accurate to  $\pm 2^\circ$ . The samples were generally equilibrated in the probe at the desired temperature for 30-60 minutes prior to data accumulation.

*Dipolar Decoupled NMR Spectra.* Dipolar decoupled  $^{13}\text{C}$  NMR spectra were recorded at 47 kG (50.3 MHz for  $^{13}\text{C}$ ) on a Varian XL-200 spectrometer equipped with an auxiliary high power amplifier and a solid state probe with magic angle spinning capability. The strength of the high power proton decoupling field ( $\gamma\text{H}_2/2\pi$ ) was  $\sim 45$  kHz (12 G).

American Chemical  
Society Library  
1155 16th St. N. W.

The Hartmann-Hahn condition (15) and the magic angle were adjusted using the aromatic signal from hexamethylbenzene. Polymer samples in the form of powder or pellets were packed into Kel-F rotors by hand or by a non-hydraulic pellet press. Each sample represents *ca.* 0.3 g of polymer. Probe tuning was optimized and the reflected power from the decoupler was minimized for each sample. All spectra were obtained at ambient temperature and in the unlocked mode (estimated drift  $<0.01$  ppm/hr). The static spectra were recorded in a 40 kHz spectral window with 2K time-domain data points; the spectra with magic angle sample spinning were obtained in a 20 kHz spectral window with 4K time-domain data points. The proton-enhanced spectra were obtained using proton spin temperature alternation (16). The free induction decays were zero-filled prior to transformation. The number of accumulations, the repetition rate, and the cross-polarization contact time for each spectrum are listed in the figure legends.

*T<sub>1</sub> Measurements.*  $T_1$  values for the mobile domain carbons were measured using a ( $180^\circ$ - $t$ - $90^\circ$ -T) inversion recovery pulse sequence (17) with continuous proton saturation. The optimum  $180^\circ$  pulse width was determined prior to each set of measurements. The time between pulse sequences was 2 s at 21 kG and 3 s at 47 kG. Measurements were generally made for 10-12 values of  $t$  which ranged from 0.005 s to  $T_1$ . Both integrated peak intensities and peak heights were used for the analysis of each  $T_1$  data set; equivalent results were obtained in both cases.

*Nuclear Overhauser Enhancements.* Nuclear Overhauser enhancements ( $1 + \eta$ ) of the mobile carbons were measured using the gated decoupling technique (18). The pulse repetition rate for both the Overhauser-suppressed and Overhauser-enhanced spectra was 8 s. Peak integrations were used to determine the NOE.

### Results — Mobile Domains

*General Description of Spectra.* All of the Hytrel samples studied contain carbons which are mobile enough to provide signals using only scalar decoupling, whereas the poly(butylene terephthalate) homopolymer does not (Figure 2). In this paper we shall use the term "scalar decoupling" to indicate a proton decoupling field strength ( $\gamma H_2/2\pi$ ) of 4 kHz, or 1 G. This is the field strength generally used in solution state NMR to remove the scalar  $J$  coupling. We will use the term "dipolar decoupling" to refer to the much stronger proton rf field ( $\gamma H_2/2\pi \sim 45$  kHz) which is necessary to remove static dipolar interactions in solids). The scalar decoupled spectra of Hytrel consist of a prominent peak at *ca.* 29 ppm, a broader peak at *ca.* 73 ppm, and a very broad distribution in the carbonyl/aromatic region (Figure 2). The peak at 29 ppm arises primarily from the soft segment  $-\text{CH}_2-$  carbons which are flanked on either side by  $-\text{CH}_2-$  carbons. The peak at 73 ppm is due to the  $-\text{OCH}_2-$  carbons of the soft segments. Quantification of the spins indicates that all of the soft segment carbons and at least 10% of the hard segment carbons contribute to the scalar decoupled  $^{13}\text{C}$  NMR signal intensity. The "extra" signal intensity arises primarily from the protonated aromatic carbons. In addition, spectra of Hytrel 4056 and Hytrel 7246 obtained with no decoupling retain  $>95\%$  and  $>80\%$ , respectively, of their original scalar decoupled signal intensity. Scalar decoupled and fully coupled spectra were obtained for Hytrel 4056, using magic angle sample spinning. Under these conditions the linewidths of the 29 and 73 ppm resonances (161 and 245 Hz, respectively) are reduced to respective values of 51 and 58 Hz.

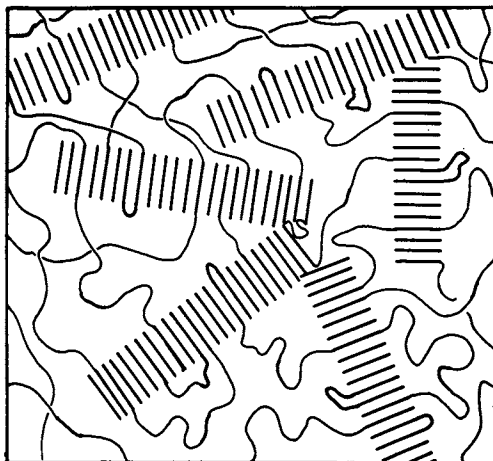


Figure 1. Schematic representation of Hytrel morphology (3). The heavy lines represent the hard segments of the copolymer.

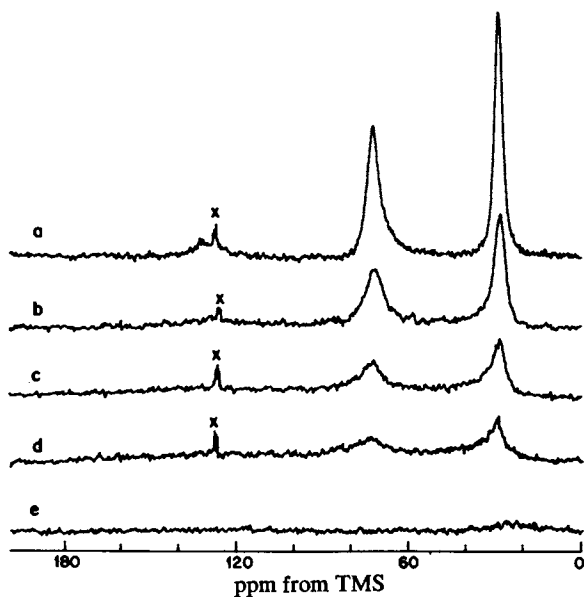


Figure 2. Scalar decoupled ( $\gamma H_z/2\pi = 4$  kHz) 50.3-MHz  $^{13}\text{C}$  NMR spectra of solid Hytrel and polybutylene terephthalate. Key: a, Hytrel 4056; b, Hytrel 5526; c, Hytrel 6346; d, Hytrel 7246; and e, polybutylene terephthalate. All spectra were obtained on the same amount of polymer and were recorded at  $34^\circ\text{C}$  with 1024 accumulations and a 3 s pulse repetition rate. Peaks marked with X arise from an internal capillary containing benzene- $d_6$ .

**Linewidths.** The scalar decoupled linewidths observed for the  $-\text{OCH}_2-$  and central  $-\text{CH}_2-$  carbons of the Hytel soft segments are a linear function of the average hard block length of the polymer (Figure 3). Scalar decoupled linewidths were also measured for these samples as a function of temperature. These linewidths are fairly temperature-independent over a large range ( $\sim 80^\circ\text{C}$ ) in temperature (Figure 4). Figure 4 also shows that the point at which the linewidth increases sharply is slightly different for both types of aliphatic carbons, and is different for each Hytel sample.

**Relaxation Measurements.** The  $T_1$  and NOE values for the central  $-\text{CH}_2-$  (29 ppm resonance) and the  $-\text{OCH}_2-$  (73 ppm resonance) are listed in Table II. The  $T_1$  values for both soft segment carbons for all samples are identical. The  $T_1$  values increase with increasing temperatures ( $T_1 = 0.43$  s at  $75^\circ\text{C}$ ) and are field strength-dependent ( $T_1$ 's for all carbons at 21 kG are  $\sim 0.12$  s).

Although the nuclear Overhauser enhancements for the 29 and 73 ppm resonances are not identical, they also appear to be independent of the average hard block length of the polymer.

TABLE II

$^{13}\text{C}$  NMR  $T_1$  and Nuclear Overhauser Enhancements for the Mobile Aliphatic Carbons of Hytel<sup>a/</sup>

Hytel Sample	$T_1^{b/}$		NOE <sup>c/</sup>	
	29 ppm	73 ppm	29 ppm	73 ppm
4056	0.21 s	0.22 s	2.3	2.1
5526	0.20	0.21	2.0	1.8
6346	0.20	0.24	2.3	1.9
7246	0.21	0.21	--	--

a/ Recorded at 47 kG (50.3 MHz for  $^{13}\text{C}$ ) and  $34^\circ\text{C}$ .

b/ Determined by inversion-recovery method; estimated uncertainty  $\pm 0.02$  s.

c/ Values are reported as  $1 + \eta$ ; estimated uncertainty  $\pm 0.2$ .



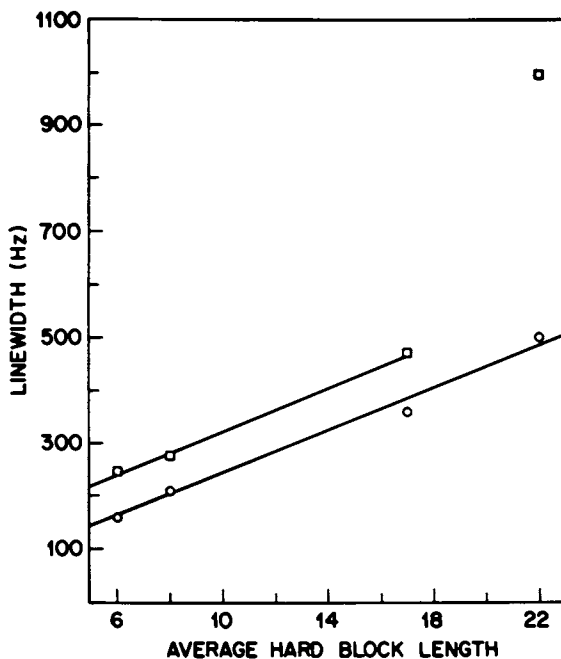


Figure 3. Line widths of the  $^{13}\text{C}$  NMR (50.3 MHz) solid Hytrel scalar decoupled 29 ppm (○) and 73 ppm resonance (□) as a function of average hard block length at 34°C. The temperature below which the line width increases due to dipolar broadening is slightly different for the two types of aliphatic carbons (see Figure 4). It also increases slightly as the hard segment content of the polymer increases. The  $-\text{OCH}_2-$  line width for the Hytrel 7246 sample was measured at a temperature below this point and therefore does not fall on this line.

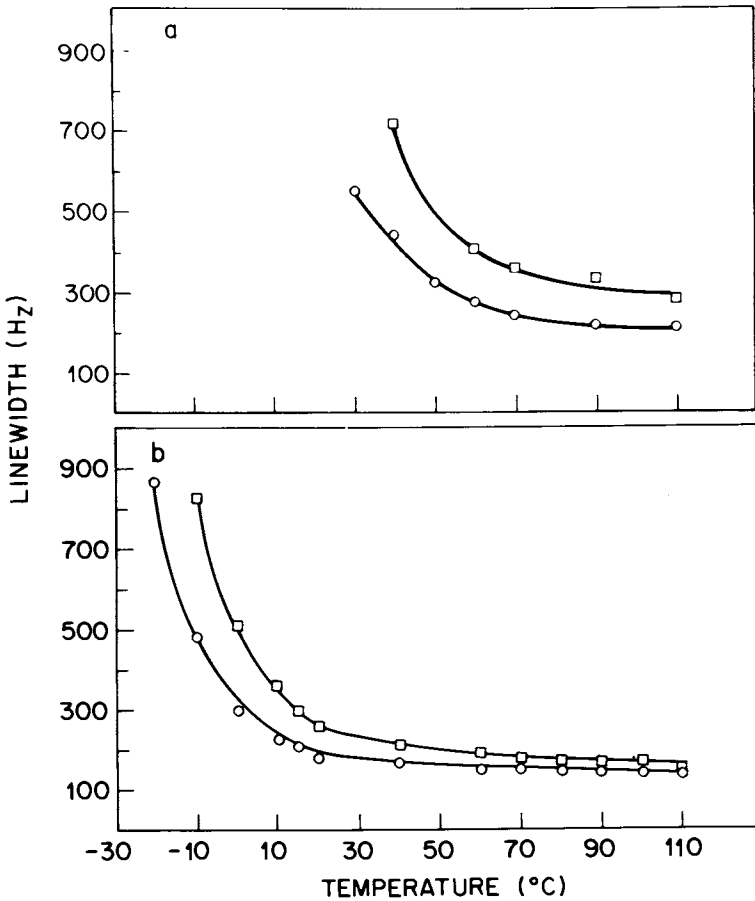


Figure 4. Scalar decoupled line width as a function of temperature for a, Hytrel 7246; and, b, Hytrel 4056. Key:  $\circ$ , central  $-\text{CH}_2-$  carbons; and  $\square$ ,  $-\text{OCH}_2-$  carbons.

### Results — Rigid Domains

**General Description of Spectra.** Figure 5(a-c) shows the static  $^{13}\text{C}$  NMR solid state spectra of Hytrel 4056, 7246, and poly(butylene terephthalate) obtained with cross polarization and dipolar decoupling. Each spectrum contains a broad carbonyl/aromatic resonance which extends from ca. 250 ppm upfield into the aliphatic region, an  $-\text{OCH}_2-$  peak centered at ca. 70 ppm, and a peak due to  $-\text{CH}_2\text{CH}_2\text{CH}_2-$  carbons at ca. 29 ppm. The intensity differences in the aliphatic region are due to relative differences in the amounts of hard and soft segments in the polymers. Other than these intensity differences, little information is available directly from these static powder spectra.

When magic angle sample spinning is used in conjunction with dipolar decoupling and cross polarization, the powder lineshape collapses into a pattern of isotropic resonances and sidebands (Figure 6). The carbonyl and aromatic carbons have spinning sidebands because the spinning rate (ca. 2.2 kHz) is less than the chemical shift anisotropies (8-10 kHz).

The isotropic chemical shifts in the solid state (Figure 6, (b) and (e)) can be assigned by analogy to the solution state spectra (Figure 6, (c) and (f)) and on the basis of other solution state  $^{13}\text{C}$  NMR work on poly(butylene terephthalate) (19). The isotropic chemical shifts are assigned as follows: 165 ppm, carbonyl carbons; 134 ppm, non-protonated aromatic carbons; 131 ppm, protonated aromatic carbons; 73 ppm,  $-\text{OCH}_2-$  carbons from the soft segments; 66 ppm,  $-\text{OCH}_2-$  carbons from the hard segments; and 29 ppm, overlapping peaks from both the hard and soft  $-\text{CH}_2\text{CH}_2\text{CH}_2-$  carbons.

**Cross Polarization Intensity as a Function of Contact Time.** Two-component decays are often seen in the proton NMR of solid block polymers (20,21,22), and have been associated with the presence of two phases with different mobilities. Shafer, *et. al.* (23) have pointed out that the decay of the cross polarization signal as a function of contact time (which reflects the proton  $T_{1\rho}$ ) can be used to characterize the polymer homogeneity. In the absence of phase separation the proton  $T_{1\rho}$  values for each carbon should be the same.

$^{13}\text{C}$  NMR spectra were obtained as a function of cross polarization contact time for Hytrel 4056 and Hytrel 7246. Figure 7 shows plots of the signal intensity against contact time for the aliphatic carbons of these two polymers. The strength of the spin lock field was  $\sim 20$  kHz.

**Reconstruction of Chemical Shift Anisotropies.** The principal values of the chemical shift tensors for the carbonyl, protonated aromatic, and non protonated aromatic carbons were determined by a Herzfeld-Berger analysis (24) of the intensities of the sidebands from magic angle spinning (14). Herzfeld and Berger have defined two parameters,  $\mu$  and  $\rho$ , which are related to the chemical shift tensor elements  $\sigma_{11}$ ,  $\sigma_{22}$ , and  $\sigma_{33}$  by:

$$\mu = \frac{\gamma H_0 (\sigma_{33} - \sigma_{11})}{\omega_{\text{rot}}}$$

$$\rho = \frac{(\sigma_{11} + \sigma_{33} - 2\sigma_{22})}{(\sigma_{33} - \sigma_{11})}$$

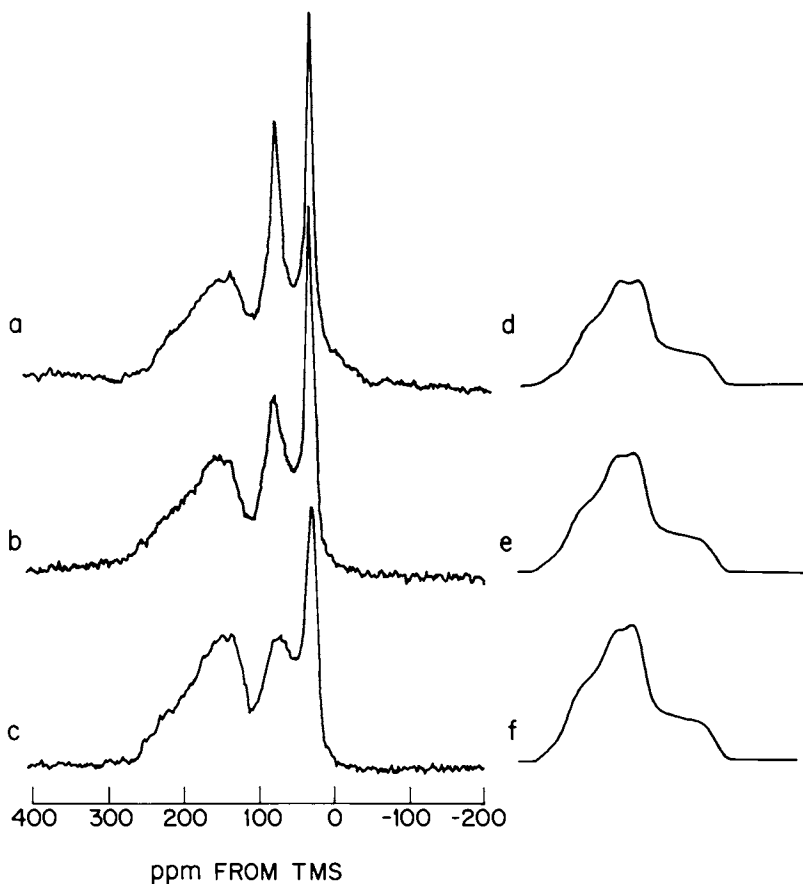


**Figure 5.** Proton-enhanced static powder spectra of a, Hytrel 4056; b, Hytrel 7246; and c, polybutylene terephthalate, compared with the respective calculated spectra of the carbonyl and aromatic regions (d-f). The experimental spectra were obtained at ambient temperature on 0.3 g of sample. Each spectrum represents 8192 accumulations using a 0.5 ms contact time and a 3 s recycle delay. The calculated spectra were obtained using the values listed in Table III.

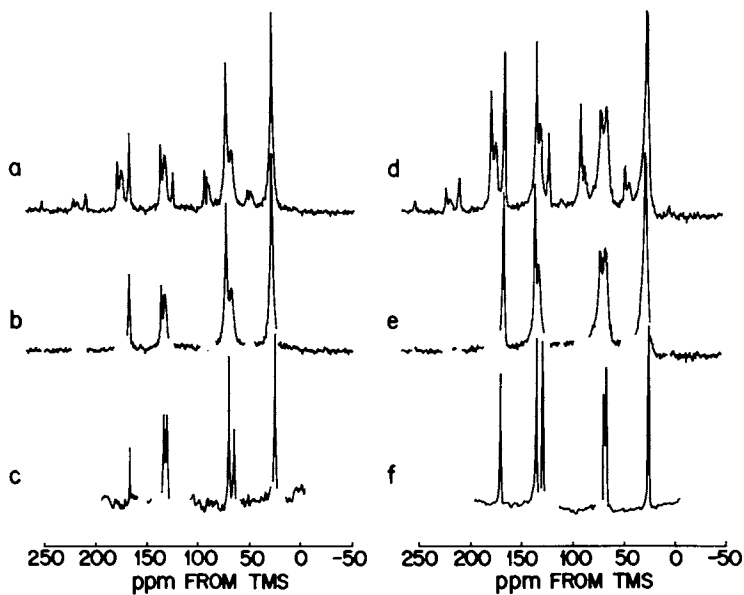


Figure 6.  $^{13}\text{C}$  NMR spectra of Hytrel 4056 (a-c) and Hytrel 7246 (d-f) obtained at 50.3 MHz. Key: a and d, solid state spectra obtained with magic-angle spinning at ca. 2.2 kHz, cross-polarization (0.5 ms contact time), and dipolar decoupling at ambient temperature; b and e, spectra a and d with sidebands removed (see text for line assignments). c, solution state spectrum in m-cresol at 100°C; f, solution-state spectrum in hexafluoroisopropanol at 34°C. The spectra in c and f were broadened artificially and the solvent lines were removed.

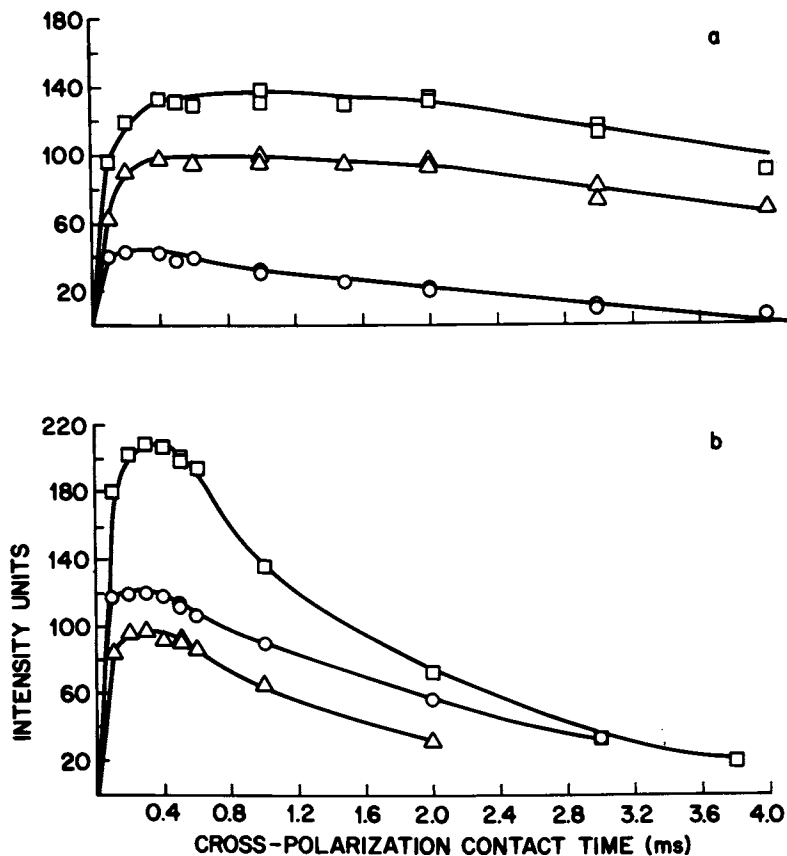


Figure 7. Plots of intensity vs. cross-polarization contact time for the aliphatic carbons of a, Hytrel 4056; and b, Hytrel 7246. Key:  $\square$ ,  $-\text{CH}_2\text{CH}_2\text{CH}_2-$  carbons;  $\circ$ , hard segment  $-\text{OCH}_2-$  carbons; and  $\triangle$ , soft segment  $-\text{OCH}_2-$  carbons. The curve corresponding to the hard segment  $-\text{OCH}_2-$  carbons in b was displaced vertically by +20 intensity units.

Here  $\sigma_{33} > \sigma_{22} > \sigma_{11}$ ,  $\gamma$  is the gyromagnetic ratio,  $H_0$  is the magnetic field strength, and  $\omega_{\text{rot}}$  is the rotor speed. In this method one measures the ratio of the intensity of each of the sidebands to the isotropic band. The possible values of  $\mu$  and  $\rho$  which correspond to each intensity ratio are determined graphically. Values for  $\mu$  and  $\rho$  for dimethyl terephthalate, poly(butylene terephthalate), and Hytrel samples 4056 and 7246 are listed in Table III. The lineshapes calculated for these principal elements are shown in Figure 5 (d)-(f).

TABLE III

Chemical Shift Parameters for Terephthalate Carbons

Sample	Carbonyl Carbon		Non-protonated Aromatic		Protonated Aromatic	
	$ \sigma_{33}-\sigma_{11} ^a/$	$\rho^b/$	$ \sigma_{33}-\sigma_{11} ^a/$	$\rho^b/$	$ \sigma_{33}-\sigma_{11} ^a/$	$\rho^b/$
dimethyl terephthalate	137 ± 4 ppm	+1.0 ± 0.1	201 ± 4 ppm	-0.24 ± 0.02	215 ± 4 ppm	-0.38 ± 0.03
polybutylene terephthalate	127 ± 5	+1.0 ± 0.1	202 ± 5	-0.20 ± 0.03	198 ± 5	-0.39 ± 0.02
Hytrel 7246	133 ± 7	+1.0 ± 0.1	198 ± 7	-0.23 ± 0.07	201 ± 4	-0.32 ± 0.02
Hytrel 4056	132 ± 3	+1.0 ± 0.1	203 ± 5	-0.25 ± 0.05	187 ± 3	-0.40 ± 0.02

$$a/ \quad |\sigma_{33}-\sigma_{11}| = \frac{\mu \omega_{\text{rot}}}{\gamma H_0}$$

$$b/ \quad \rho = \frac{(\sigma_{11} + \sigma_{33} - 2\sigma_{22})}{(\sigma_{33} - \sigma_{11})}; \quad \sigma_{33} > \sigma_{22} > \sigma_{11}$$

## Discussion

**Phase Separation.** Several lines of evidence suggest that phase separation exists in Hytrel.

First, the soft segment carbons of all Hytrel samples can be observed selectively using scalar decoupling (Figure 2). This indicates that the carbons in the mobile regions have dynamic properties which are different than those of the rigid carbons. In addition, the  $T_1$  data indicate that the rate of these motions is independent of the hard segment content of the polymer. If considerable mixed phase were present, one would expect that the number of spins observable with scalar decoupling would be a function of the average hard block length of the polymer.

Second, the soft segment aliphatic carbon linewidths are not a strong function of temperature over a large temperature range ( $\sim 80^\circ$ ; Figure 4). If a large amount of mixed phase were present, one would expect to see a continued decrease in linewidth associated with the continuous melting of a homogeneous phase.

Finally, plots of the signal intensity versus cross polarization contact time (Figure 7) indicate that two phases are present. As one increases the cross polarization contact time, one goes through a maximum, and then the signal begins to decrease (Figure 7). This decrease in intensity is due primarily to the proton  $T_{1\rho}$  (23). The presence of different proton  $T_{1\rho}$ 's for different carbons has been used previously to indicate phase separation (23). The data in Figure 7 indicate that the "hard" and the "soft"  $-\text{CH}_2-$  carbons in Hytel have different proton  $T_{1\rho}$  values, thus suggesting that these Hytel samples are phase separated. The  $^1\text{H}$   $T_{1\rho}$  evidence of phase separation presented here is not as distinct as that seen for polymers in which discrete phase separation is seen. This may be due to the large amount of motion present in the rigid domains (see below) or may indicate diffusive domain boundaries.

**Molecular Motion in the Mobile Domains.** Observation of all of the soft segment carbons with scalar decoupling (Figure 2) indicates that motion of these carbons is fast on the timescale of the dipolar interaction ( $\sim 10^5$  Hz). The linewidths observed by scalar decoupling can be further narrowed by magic angle spinning (using only scalar decoupling and a  $(90-\tau)$  pulse sequence). This indicates that the motions are anisotropic, and that residual dipole-dipole interactions and residual chemical shift anisotropy are the source of line broadening.

The  $T_1$  and NOE data (Table II) indicate that the rate of these thermal motions is independent of the hard segment content of the polymer. These  $T_1$  values increase with increasing field strength and increasing temperature, indicating that these motions are on the fast side of the  $T_1$  minimum but are not in the motional narrowing regime.

Although the  $T_1$  and NOE values are independent of the hard segment content of the polymer (Table II), the linewidths are not (Figure 3). Field-strength dependent line width measurements and scalar decoupled spectra obtained with magic angle spinning indicate that the linewidths arise from residual chemical shift anisotropy and unaveraged dipole-dipole interactions. The linewidths are a linear function of the average hard block length of the polymer. These results suggest that the presence of hard segment carbons restricts the angular range over which reorientation takes place. The linewidth data (Figure 3) and the  $T_1$  data (Table II) are consistent with a model for molecular motion in which the *rate* of motion is independent of the hard segment content of the polymer, but the *angular range* is not.

**Molecular Motion in the Rigid Domains.** The chemical shift anisotropy can be used to characterize molecular motion in the rigid domains. Figure 5 (c) shows that the two aliphatic carbons in the poly(butylene terephthalate) homopolymer have very different linewidths. We estimate that the  $-\text{OCH}_2-$  carbon anisotropy ( $|\sigma_{33}-\sigma_{11}|$ ) at ambient temperature is *ca.* 60 ppm, a value which is in agreement with rigid lattice anisotropies reported for other  $-\text{OCH}_2-$  carbons (27). However, the  $-\text{CH}_2\text{CH}_2\text{CH}_2-$  anisotropy (*ca.* 14 ppm) is significantly smaller than that reported for other aliphatic carbons (28,29). Slow speed magic angle spinning experiments (not shown) (14) gave sidebands for the  $-\text{OCH}_2-$  carbons but not for the  $-\text{CH}_2\text{CH}_2\text{CH}_2-$  carbons, indicating that the chemical shift anisotropies for these two types of carbons are significantly different. This result indicates that the central  $-\text{CH}_2\text{CH}_2\text{CH}_2-$  carbons of the poly(butylene terephthalate) homopolymer undergo motions which do not involve the  $-\text{OCH}_2-$  carbons to a large extent. X-ray fiber diffraction patterns of poly(butylene terephthalate) have shown that the aliphatic carbons of this polymer are not in an all-*trans* conformation (30,31). Therefore we attribute the line-narrowing we observe for the  $-\text{CH}_2\text{CH}_2\text{CH}_2-$  carbons to oscillations within the *gauche* conformation potential



energy well. Inspection of molecular models indicates that such oscillations do not require significant reorientation of the  $-\text{OCH}_2-$  groups.

The chemical shift anisotropies for the carbonyl and aromatic carbons of Hytel were reconstructed from a Herzfeld-Berger analysis (24) of the intensities of the sidebands from  $^{13}\text{C}$  NMR magic angle spinning experiments. The results in Table III indicate that the carbonyl carbon chemical shift anisotropy is axially symmetric for each terephthalate ester. We attribute this axial symmetry to a general property of terephthalate esters, rather than as a consequence of molecular motion, as the highly crystalline dimethyl terephthalate also has an axially symmetric carbonyl carbon chemical shift tensor.

The chemical shift anisotropies ( $|\sigma_{33} - \sigma_{11}|$ ) for the aromatic and carbonyl carbons are very similar for all samples, with the exception of the protonated aromatic carbon of Hytel 4056 (Table III). We feel that the reduced value for the shift anisotropy indicates that these carbons are involved in molecular motions which are rapid compared to the chemical shift anisotropy ( $\sim 10^3 - 10^4$  Hz). This conclusion is supported by auxiliary information. First, the  $T_1$  values for these carbons are short (26), indicating spectral density in the megahertz range. Second, scalar decoupled magic angle spinning experiments indicate that the scalar decoupled signal intensity observed in the carbonyl-aromatic region for Hytel 4056 arises primarily from the protonated aromatic carbons, suggesting that some motions are fast on the timescale of the dipolar interaction ( $\sim 10^5$  Hz). Taken together these data suggest that many, if not most, of the terephthalate groups in Hytel 4056 are in regions which are not highly crystalline. Presumably this is a consequence of an average hard block length (6 units) which is too short to form long-range crystalline order.

The principal elements of the chemical shift tensors for the carbonyl and aromatic carbons (Table III) have been used to produce the calculated spectra shown in Figure 5(d)-(f). The calculated spectra are in good agreement with the experimental spectra (Figures 5(a)-(c)).

### Summary

These data suggest a model for Hytel domain structure in which there is phase separation. Relaxation measurements indicate that the rates of molecular motions of the amorphous domains are independent of the hard segment content of the polymer, but that the angular range for reorientation of these soft segment carbons is a function of the average hard block length. The  $-\text{CH}_2\text{CH}_2\text{CH}_2-$  carbons of the poly(butylene terephthalate) homopolymer undergo motions which do not involve the  $-\text{OCH}_2-$  carbons. These same motions are observed qualitatively for the hard segment  $-\text{OCH}_2-$  carbons of Hytel. Molecular motion of the aromatic carbons in Hytel appears to be related to the average hard block length of the polymer. The motions of these protonated aromatic carbons are fast on the timescale of the chemical shift anisotropy, and probably involve torsional oscillations about the 1,4-phenylene axis.

### Literature Cited

1. Hytel is a registered trademark of the E. I. du Pont de Nemours Company, Inc.
2. Wolfe, J. R., Jr. *Polymer Preprints* 1978, 19 (1), 5.

3. Cella, R. J. *Encl. of Polym. Sci. and Technol.* 1977, *Suppl. V2*, 485.
4. Shen, M.; Mehra, V.; Niinomi, N.; Koberstein, J. T.; Cooper, S. L. *J. Appl. Phys.* 1974, *45*, 4182.
5. Hourston, D. J.; Hughes, I. D. *J. Appl. Polym. Sci.* 1977, *21*, 3093.
6. Nishi, T.; Kwei, T. K.; Wang, T. T. *J. Appl. Phys.* 1975, *46*, 4157.
7. Nishi, T.; Kwei, T. K. *J. Appl. Polym. Sci.* 1976, *20*, 1331.
8. Cella, R. J. *J. Polym. Sci. Symp.* 173, *C42*, 727.
9. Cella, R. J.; Buck, W. H. *Polymer Preprints* 1974, *15* (1), 159.
10. Morese-Séquela, B.; St-Jacques, M.; Renaud, J. M.; Prud'homme, J. *Macromolecules* 1980, *13*, 100.
11. Assink, R. A. *J. Polym. Sci., Polym. Phys. Ed.* 1977, *15*, 59.
12. Seymour, R. W.; Overton, J. R., Corley, L. S. *Macromolecules* 1975, *8*, 331.
13. Jelinski, L. W.; Schilling, F. C.; Bovey, F. A. *Macromolecules*, 1981, *14*, 581.
14. Jelinski, L. W. *Macromolecules*, in press.
15. Hartmann, S. R.; Hahn, E. L. *Phys. Rev.* 1962, *128*, 2042.
16. Stejskal, E. O.; Schaefer, J. *J. Magn. Reson.* 1975, *18*, 560.
17. Becker, E. D. "High Resolution NMR", 2nd ed.; Academic Press: New York, 1980; pp. 232-237.
18. Opella, S. J.; Nelson, D. J.; Jardetzky, O. *J. Chem. Phys.* 1976, *64*, 2533.
19. Komoroski, R. A. *J. Polym. Sci., Polym. Phys. Ed.* 1979, *17*, 45.
20. Lind, A. C. *J. Chem. Phys.* 1977, *66*, 3482.
21. Douglass, D. C.; McBrierty, V. J. *J. Chem. Phys.* 1971, *54*, 4085.
22. Wardell, G. E.; McBrierty, V. J.; Douglass, D. C. *J. Appl. Phys.* 1974, *45*, 3341.
23. Schaefer, J.; Sefcik, M. D., Stejskal, E. O.; McKay, R. A. *Macromolecules* 1981, *14*, 188.
24. Herzfeld, J.; Berger, A. E. *J. Chem. Phys.* 1980, *73*, 6021.
25. Pines, A.; Gibby, M. G.; Waugh, J. S.; *J. Chem. Phys.* 1973, *59*, 569.
26. Jelinski, L. W.; Dumais, J. J. *Polymer Preprints* 1981 (submitted for Fall ACS Meeting).
27. Pines A.; Gibby, M. G.; Waugh, J. S. *Chem. Phys. Lett.* 1972, *15*, 373.
28. VanderHart, D. L. *J. Chem. Phys.* 1976, *64*, 830.
29. Urbino, J.; Waugh, J. S. *Proc. Natl. Acad. Sci. USA* 1974, *71*, 5062.
30. Mencik, Z. *J. Polym. Sci., Polym. Phys. Ed.* 1975, *13*, 2173.
31. Alter, U.; Bonart, R. *Colloid and Polym. Sci.* 1976, *254*, 348.

RECEIVED December 21, 1981.

# INDEX

## A

- AB quartet, 44
- AB spectra of methyl  
pyropheophorbide a,  
43f
- Acetate metabolic pathways,  
162, 163f, 166
- Acetobacter xylinum,  
cellulose synthesis, 170
- N-Acetyl alloisoleucine, 138
- N-Acetyl tryptophan  
photo-CIDNP spectra, 306f
- N-Acetyl tryptophan/flavin  
system CIDNP difference  
intensity, 315, 316f
- N-Acetylglucosamine binding to  
wheat germ agglutinin,  
107, 108f
- Acholeplasma laidlawii,  
variation  
of molecular order, 111-114
- Acid --See Specific kinds
- Activation volumes, temperature  
dependence 213, 216f
- Activation volumes, pressure  
and solvent dependence,  
204, 206f
- Adsorption of molecules on  
catalytic surfaces 219-232
- Ala-Ala dipeptide,  $^{13}\text{C}$  NMR  
spectrum, 243, 244f
- Alanine,  $^2\text{H}$  NMR spectra, 110f
- Ala-Pro dipeptide,  $^{13}\text{C}$  NMR  
spectrum, 242f
- Aliphatic carbon content  
depletion, 327, 335f
- Aliphatic carbon content vs.  
oil yields of shales, 333f
- Aliphatic carbons dephasing  
rates, 339, 341f
- Alkylation by ethyl iodide of  
ambident anions, 70
- $^{27}\text{Al}$  NMR spectra of  $\text{AlCl}_3$ ,  
28f
- Alumina-amine samples  
preparation, 222, 224
- Aluminum chloride 28f
- Amines --See also specific  
names; e.g., n-butyl amine
- Amino acid(s)  
conformational analysis,  
129-138  
 $^{13}\text{C}$  enriched, 119-156  
relaxation behavior,  
138-148  
spectral characteristics,  
119-127  
isotopically labeled,  
biological studies, 148-150  
photo-CIDNP spectra, 303-309  
residue assignment 50, 52f  
resonances asymmetry, 123-125  
sequence, 31  
( $\text{U}^{13}\text{C}$ ) enriched, 120-127

- Amplitude, rf distribution,  
19, 20f
- AMX system of  
2-furancarboxylic acid  
methyl ester, 59f
- Analysis of line-shapes,  
239-241
- Analytical reliability of  
results  $^{13}\text{C}$  CP/MAS work  
on fossil fuels, 321-323
- Anisotropy of diamagnetic  
susceptibility, 26
- Antibiotics, ionophore, 76-79
- Antibiotics, and ion  
transport, gramicidin A, 78
- Applied magnetic field effect  
on resolution, 336
- Apparatus for double cross  
polarization of  $^{15}\text{C}$  NMR,  
188-190
- Aromatic amino acids,  
flavin-induced  $^1\text{H}$   
photo-CIDNP effects, 305,  
308f  
pH dependence of CIDNP  
effect, 307, 308f
- Aromatic  
carbon chemical shift  
anisotropy, 345  
carbons dephasing rate,  
339-341f  
compounds ordering  
determination, 40  
molecules susceptibility  
anisotropy and asymmetry, 38
- Aromatic regions, 323
- Aromatic regions of  $^{13}\text{C}$   
spectra of  
cyclic peptides, 241, 242f
- Array processors, 19
- Aspartic acid, pH dependence  
of  $^3\text{J}_{\text{CC}}$ , 132f
- Asymmetric doublets, 241
- Atmospheric condensation by  
polyelectrolytes, 71-76
- Attrites, 323, 326f
- Avidin, 111
- B
- Base sequence in DNA, 249
- Battery systems, 211
- B-DNA, 250, 253-260
- Binding --See specific kinds;  
e.g., cation binding, site  
binding, ion-binding
- Binding constants and  
derivation of  
stoichiometry, 67
- Binding of DNA, histone core  
particles, 263, 264f
- Binding and release, rate  
constants, 68-70
- Biologically active peptides  
labeled with  $^{13}\text{C}$ , 149t
- Biological membranes study  
with  $^2\text{H}$  NMR, 111
- Biological molecules  
photo-CIDNP, 285-318

- Biological molecules, proton spectroscopy, 19
- Biological studies with isotopically labeled amino acids and peptides, 148-150
- Biological systems,  $^{13}\text{C}$  NMR spectroscopy use for metabolic study, 157-186
- Biomolecular receptors,  $^{23}\text{Na}$  attachment, 67
- Biopolymers, determination of 3D structure, 56f
- Biopolymers glycosaminoglycans, 73
- Biosynthesis of  $^{13}\text{C}$  labeled L-glutamate, 163f, 167
- Biosynthetic pathways of glutamate, 127
- Biosynthetic pathways with labeled precursor, 157-183
- Bituminous coal relaxation measurements, 322
- Black mamba --See Dendroaspis polylepis polylepis
- Block copolymers, 345-360
- Bond labeling and double cross polarization, 187-198
- Bovine pancreatic trypsin inhibitor  $^1\text{H}$  NMR spectra, 51f
- Bradykinin, 31, 35f, 147f
- Bruker's HX-270 spectrometer, 9
- Bullet design, 220, 221
- Butanoic acid couplings, 129
- n-Butylamine, 224-226
- Butyrate ion anodic oxidation, 102, 104f
- Byrd Stadium lignite  $^{13}\text{C}$  CP/MAS spectrum, 323, 325f
- $^{13}\text{C}$  chemical shift dispersion, 160
- $^{13}\text{C}$  CP/MAS spectra of n-butylamines, 224-226
- Byrd Stadium lignite; 323, 325f
- coalified logs and Eocene brown coal, 331f
- coal marcerals, 326f
- coals, 323, 324f
- Hytrel, 355f
- oil shales, 332f, 334f, 337f
- organic matter, 335f
- pyridine, 226, 227f
- Wyodak coal, 330f
- Wyoming coal, 327, 328f
- Wyoming subbituminous coal, 329f
- $^{13}\text{C}$  CP/MAS work on fossil fuels, 321-323, 336
- $^{13}\text{C}$  distribution in multiply labeled compounds, 160, 162-170
- $^{13}\text{C}$  enriched amino acids and peptides, 119-156
- $^{13}\text{C}$  enriched bradykinin, 147f

- $^{13}\text{C}$  enriched molecules,  $^1\text{H}$  relaxation, 138-141
- $^{13}\text{C}$  enriched molecules, rotation correlation times, 145t
- $^{13}\text{C}$  enrichment probability, 169t
- $^{13}\text{C}$  FT NMR spectra of metabolism of glucose of anomers, 158f
- $^{13}\text{C}$  glutamate labeling patterns, 169t
- $^{13}\text{C}^1\text{H}$  and  $^{13}\text{C}$ - $^{13}\text{C}$  dipolar interactions, 142-144
- $^{13}\text{C}$  labeled substrates and  $^{13}\text{C}$  NMR spectroscopy, summaries, 171-180
- $^{13}\text{C}$  labeled substrates use in metabolic studies, 157-186
- $^{13}\text{C}$  labeling from  $^1\text{H}$  spectra, quantitation, 139, 141
- characterization of solid fossil fuels using CP/MAS, 319-343
- and labeling in metabolic studies, future developments, 182
- line widths of native and denatured DNA, 278t
- spectra -- See also specific compounds,  $^{13}\text{C}$  CP/MAS spectra
- $^{13}\text{C}$  labeling from  $^1\text{H}$  --continued
- spectra of
- Ala-Ala dipeptide, 243, 244f
- bradykinin, 147f
- cyclic peptides with phenylalanine, 241, 242
- DNA, 270, 271f
- glutamic acid, (90%-U- $^{13}\text{C}_5$ ), 124f, 125f
- cyclo(Gly-Pro-Gly), 237f
- hairpinned poly(dAdT), 253, 258f
- Hytrel, 354f, 355f
- MBBA, 48, 49f
- perfused mouse liver, 161f
- cyclo(D-Phe-Gly-Ala-Gly-Pro), 238f
- cyclo(D-Phe-Pro-Gly-D-Ala-Pro), 236f
- rhodium carbonylclusters, 200, 201f
- solids, 3
- spectroscopy and  $^{13}\text{C}$  labeled substrates, use to study metabolism, 171-180
- spectroscopy of intact cells, tissue, and organs, 157-186
- studies of amines, 224-226
- $^{13}\text{C}$  labeled cells and macromolecular assemblages, 176t, 177t

- $^{13}\text{C}$  labeling from  $^1\text{H}$   
  spectra of,--continued  
  DNA dynamics, 13,269-283,  
  metabolism, 172t, 175t  
  polyester thermoplastic  
  elastomer, 345-460  
  nuclear Overhauser  
  enhancements (NOE), 141  
  for double stranded DNA, 277t  
   $T_1$  for Hytrel mobile  
  aliphatic  
  carbons, 350t
- $^{13}\text{C}$  multiplet intensities,  
  169t
- $^{13}\text{C}$  relaxation time studies,  
  157, 160  
  of hemoglobin, 181  
  in multiply enriched  
  systems, 141-146
- $^{13}\text{C}$  satellites, 123, 127
- $^{13}\text{C}$  scalar coupling  
  constants, 120
- $^{13}\text{C}$  scalar coupling  
  constants, conformational  
  analysis, 130t
- $^{13}\text{C}$  spectra --See  $^{13}\text{C}$  NMR  
  spectra
- $^{13}\text{C}$  spin-lattice relaxation  
  times in DNA, 276t
- $^{13}\text{C}$  study of amines, 219, 232
- Calciproteins ellipsoidal  
  shape, 80f
- Calcium-binding protein, helix  
  conformation, 82f
- Calcium ions and proteins, 79
- Calmodulin, 79, 84f, 85
- Camphor,  $^1\text{H}$  NMR spectrum, 25f
- Cancellation of flavin CIDNP  
  signals, 315
- Cancellation of polarization  
  and cyclic reactions,  
  290-303
- Carbon-carbon  
  coupling constants,  
  conformational  
  interpretation, 127-138  
  couplings in proline, 134t  
  dipolar interaction, 146f
- Carbon-13 See  $^{13}\text{C}$
- Carbon content, aliphatic,  
  depletion, 327, 335f
- Carbon content, aliphatic, vs.  
  oil yields of shales, 333f
- Carbons, terephthalate,  
  chemical shift parameters,  
  357t
- Carbonyl clusters, transition  
  metal, 200-202
- Carboxylic polyethers, 77
- N-Carboxymethylflavin,  
  305, 306f
- Catalytic reactions using  $\text{SO}$   
  and  $\text{H}_2$ , 200
- Catalytic surfaces, adsorption  
  of molecules, 219-232
- Cation-binding muscular  
  proteins, 79

- Cation binding --See also  
specific cations; e.g.,  
 $N^+$
- Cation binding,  $^{23}Na$  NMR  
studies, 63-95
- Cation binding to  
phosphatidylserine  
vehicles,  
75, 76
- Cellular structure and  
function, 180
- Cellulose synthesis by  
Acetobacter xylinum, 170
- Cesium fluoride, 261, 262f
- Chair-to-chair interconversion  
process in cyclohexane,  
202, 203f
- Characterization of synthetic  
polymers, 21
- Charge fraction (f), 73
- C-H dipolar couplings, 48,  
49f, 13
- Chemical bond labeling and  
double cross polarization  
NMR, 187-198
- Chemically induced dynamic  
nuclear polarization  
(CIDNP), 4
- of biological molecules,  
303, 305-312  
phospholipase  $A^2$ , 309-312  
tryptophan, 303, 305  
tyrosine and histidine,  
305, 308-309  
in cyclic reactions, 290-292
- Chemically induced dynamic  
nuclear polarization  
(CIDNP), --continued  
intensities,  
flavin/tryptophan  
reaction, 315, 316f  
radical pair mechanism,  
286-240  
signal cancellation, 315-317  
sign rules, 289, 290  
time dependence, 295-299  
disproportionation  
reactions, 299-301  
from exchange reaction,  
303, 304f  
fast relaxation. 297, 298  
slow relaxation, 295, 297  
steady state conditions,  
297-299
- Chemical shielding tensor,  
319, 320f
- Chemical shift anisotropies,  
3, 260, 353, 357, 359
- Chemical shift anisotropy,  
aromatic carbon, 345
- Chemical shifts, isotropic,  
conformational analysis,  
234-239
- Chemical shifts, isotropic, in  
Hytre spectrum, 353
- Chemical shifts for peptides,  
239, 240t
- Chlorin ring, 44
- Chondroitin sulfate  $^{23}Na$  NMR  
study, 73, 74



- CH shielding, 21
- CIDNP --See Chemically induced  
dynamic nuclear  
polarization
- Coal(s), 323-331  
bituminous, relaxation  
measurements, 322  
 $^{13}\text{C}$  CP/MAS spectra, 323,  
324f  
macerals, 326f  
Powhatan #5, 338f, 341f  
Wyodak, 330f  
Wyoming, 327, 328f  
Wyoming subbituminous, 329f
- Collagen, 109-111
- Collision frequency, 204
- Common solvents,  $^2\text{H}$  NMR  
spectra, 101f
- Computer developments, 2
- Conformation of DNA,  $^{31}\text{P}$  NMR  
studies, 249-267
- Conformational analysis, 131  
 $^{13}\text{C}$ - $^{13}\text{C}$  scalar coupling  
constants, 130t  
 $^{14}\text{N}$ - $^{13}\text{C}$  dipolar  
coupling, 241-245  
isotropic chemical shifts,  
234-239  
proline, 131  
scalar C-C coupling  
constants, 127-138  
amino acid, 129-138
- Conformations, phosphodiester,  
253, 254f, 260, 263
- Constants --See individual  
type; e.g., binding
- Convolution difference,  $^{13}\text{C}$   
CP/MAS spectra of Powhatan  
#5 coal, 341f
- Copolymer hard segments, 346,  
349f
- Correlation times, C-H bonds  
of methylene carbons, 145t
- Cotyledon protein,  $^{15}\text{N}$ - $^{13}\text{C}$   
incorporation, 193t
- Coupling connectivities,  
50, 52f
- Coupling constant, 44  
for conformational analysis,  
130t  
quadrupolar, 74  
in proline, 134t  
scalar C-C, conformational  
interpretation, 127-138  
spin-spin, 21
- Couplings, short relaxation  
times effects, 144, 147,  
148
- CP --See Cross polarization  
(CP), 4
- CP/MAS, 4
- CP/MAS  $^{13}\text{C}$  spectra --See  
 $^{13}\text{C}$  CP/MAS spectra and  
 $^{13}\text{C}$  CP/MAS studies
- CP/MAS  $^{12}\text{C}$  studies, 319  
amines absorption, 219-232  
fossil fuels, 321-323, 336  
fossil fuels applied  
magnetic field, 339

- Critical density criterion of superconductors, 12
- Cross polarization (CP) --See also Single and Double cross-polarization
- Cross-polarization contact time for HytreI aliphatic carbons, 353, 355f
- magic angle spinning --See CP/MAS
- $^{15}\text{N}$  NMR spectra, soybean cotyledons, 190, 194f
- pulse diagram of experiment, 319, 320f
- transfer time, spin-lock C-N, 193, 194f
- Cross relaxation system --See also  $^{13}\text{C}$  Relaxation time studies
- Crown ethers,  $\text{Na}^+$  complexation, 70, 71
- Cryptand,  $\text{Na}^+$  complexation, 70, 71
- CSA --See Chemical shift anisotropy
- CSD --See Chemical shift dispersion
- Cyclic peptides, 234-241
- Cyclic reactions and cancellation of polarization, 240-303
- Cyclic reactions and CIDNP, 290-292
- Cyclohexane, pressure effects on conformational inversion, 202, 203f
- Cyclohexane spectra, 204, 205f
- Cylindrical spinner design, 221, 223f
- D
- 2D correlated  $^1\text{H}$  spectrum of Dendroaspis polylepis polylepis inhibitor K, 52f
- 2D correlated spectroscopy applications, 50
- 2D exchange spectroscopy, 54
- 2D exchange spectrum of heptamethylbenzenonium ion, 55f
- 2D experimental representation, 58f
- 2D FT NMR --See Two-dimensional Fourier transform NMR
- 2D J-resolved  $^1\text{H}$  spectroscopy, 48
- 2D J-resolved  $^1\text{H}$  spectrum of BPTI, 51f
- 2D NOE spectra of pancreatic trypsin inhibitor, 56
- 2D resolved spectroscopy, 3
- 2D spectroscopy, J-resolved, 3, 48, 51f
- 2D spectroscopic techniques, 48
- 2D spectrum of methyl formate powder, 53f

- Data memory, 14  
  computer, 4  
  requirements, 19t
- Deconvolution of experimental  
  line shape, 66
- Dendroaspis polylepis  
  polylepis, 52f
- Density effect on proton  
  spin-lattice time in  
  water, 207, 208
- Deoxyribonucleic acid (DNA)  
  transitions, 250, 251f,  
  263, 265
- Dephasing rates of carbons,  
  339, 341f
- Dermatan sulfate  $^{23}\text{N}$  NMR  
  study, 73, 74
- Detection sensitivity, 8
- Deuterated aromatic compounds,  
  quadrupole splitting, 38
- Deuterium  $^2\text{H}$  NMR  
  high resolution, 100-105  
  spectra, 25, 26  
    acholeplasma laidwii, 114f  
    alanine and collagen, 110f  
    bis[tolyl-tris(pyrozolyl)  
    borato]cobalt(II), 39f  
    camphor, 21, 25f  
    dimethoxybenzene, 115f  
    from electrolysis of  
    butyrate ion, 102, 104f  
    naphthalene, nitrobenzene,  
    41f  
    nitrobenzene, 27f  
    solvents, 101f
- Deuterium NMR  
  spectroscopy, 97-117  
    biological membranes,  
    111-115  
    high resolution  
    applications, 26  
    reaction mechanisms, 102  
    wide-line, 109-115
- Deuterium nuclear relaxation,  
  106-108
- Deuterium resonances line  
  width, 106-107
- Deuterium spectra --See  
  Deuterium NMR spectra
- Deuteron properties, 98t
- Deuteron spin-lattice  
  relaxation time in  
  glycerol- $\text{d}_4$ , 211, 212f
- Diamagnetic anisotropy, 40
- Diamagnetic susceptibility, 26
- Dichlorobenzene signal, 14, 16f
- Diffusion of gases, 209
- Dihedral angle dependence of  
   $^3\text{J}_{\text{CC}}$  for aspartic  
  acid, 132f
- Dihedral angle dependence,  
  vicinal couplings, 129
- Dimethoxybenzene  $^2\text{H}$  NMR  
  spectra, 115f
- Dipolar couplings,  
   $^{14}\text{N}$ - $^{13}\text{C}$ ,  
  conformational analysis,  
  241-245
- decoupled NMR spectra, 347,  
  355f

- Dipolar couplings,  
   $^{14}\text{N}$ - $^{13}\text{C}$ , --continued  
  decoupling, 348  
  decoupling high power proton  
  irradiation, 3, 4  
  interactions,  $^{13}\text{C}$ - $^1\text{H}$ ,  
  138-141  
  interactions,  $^{13}\text{C}$ - $^1\text{H}$ ,  
  and  $^{13}\text{C}$ - $^{13}\text{C}$ , 142-144  
  and quadrupolar vectors,  
  peptide bond drawing, 243,  
  254f  
  splittings, 40  
  vectors, drawing of peptide  
  bond with 243, 245f
- Disk storage capacities, 19
- Disk transfer rate, 14
- Disordered materials, dynamic  
  structure, 209-215
- Disproportionation reactions,  
  299-301
- Distribution of  $^{13}\text{C}$  in  
  multiply labeled  
  compounds, 160, 162-170
- DNA conformation and  
  dynamics,  
   $^{31}\text{P}$  NMR studies, 249-267  
  double-helical structure, 253  
  dynamic properties, 260-263  
  heat denaturation effects,  
  275  
  interaction with  $\text{Na}^+$ , 74,  
  75
- DNA conformation and  
  dynamics,  $^{31}\text{P}$  NMR  
  studies --continued  
  line widths dependence on  
  chain length, 270-274  
  protein (histone) complexes,  
  263, 264f  
  resonance, spin-lattice  
  relaxation, Overhauser  
  enhancements, 273, 275-277  
  telestability, 263-265  
  transformation from B-DNA to  
  Z-DNA 265
- Domains  
  mobile, 348-352  
  mobile, molecular motion,  
  358, 359  
  rigid, results, 353-357
- Double cross-polarization,  
  190, 191f
- Double-label dilution  
  experiment, 193, 194
- Double labels, soybean  
  leaves, 195, 197
- Double quantum transitions,  
  57, 59f
- Double resonance solid-state  
  NMR, 233
- Double and singlecross-  
  polarization difference  
  experiment, 190, 191f
- Double stranded DNA,  
  mercury(II) effects, 269,  
  281f, 282

Dual relaxation of spin 3/2  
particle, 64-66

Dwell time, 14

Dynamical analysis of line  
shapes, 239-241

Dynamic properties of DNA,  
260-263

Dynamic structure of  
disordered materials,  
209-215

## E

Electric field gradient  
tensor, 99f

Electronic spin state, 286

Electron spin vectors of  
radical pairs, 287, 291f

Electron-nuclear  
multiple-resonance  
approach,  
322

Emden-Meyerhof pathway (EMP),  
163f, 166

Energy of molecule, 38

Enkephalin degradation, 171

Enkephalinamide degradation,  
173t

Enrichment of randomly labeled  
precursor, 167, 168

Enzyme, hydrolytic, 309-312

Ethanol formation, 157, 158f

Ethyl iodide alkylation of  
ambident anions, 70

Ethylbenzene, 12, 14

Ethylbenzene spectra, 13f,  
17f, 18f

Exchange reactions, 300, 302,  
303

Exchange spectroscopy --See 2D  
spectroscopy

Exinite <sup>13</sup>C CP/MAS spectrum,  
323, 326f

## F

FID --See Free induction decay

Field focusing technique, 5

Field strength --See also  
specific type, e.g.,  
magnetic

Field strength increase and  
spectrum effects, 36

Field uniformity with  
superconducting magnet, 12

First-order quadrupole powder  
pattern, 213, 214f

Flash photo-CIDNP technique,  
313

Flavin CIDNP signals

cancellation, 315

Flavin induced <sup>1</sup>H  
photo-CIDNP effects for  
aromatic amino acids, 305,  
308f

Flavin/tryptophan reaction,  
315, 316f

- Flavosemiquinone, 307, 315
- Flavin, photoreaction in  
presence of, 306f, 310f,  
314f
- Fossil fuels characterization,  
319-343
- Fourier transform NMR (FT  
NMR), 2  
application to  
organometallic chemistry,  
63  
at high pressure,  
multinuclear high  
resolution, 199-207  
two-dimensional --See also  
2D FT NMR
- F-pair and recombination  
cancellation polarization,  
292-295
- F-pairs random recombination  
reactions, 290, 292, 296f
- F-polarization, 295, 297
- Free induction decay (FID),  
303, 305, 340
- Free radicals magnetic  
interactions, 286
- Frequencies, 600 MHz, 31-45
- Frequency ( $\omega$ ), 47
- FT NMR --See Fourier transform  
NMR
- Fuels, fossil,  
characterization, 319-343
- 2-Furancarboxylic acid methyl  
ester, AMX system, 59f
- Future developments in NMR  
spectroscopy, 150, 151
- G
- Gases, diffusion, 209
- Geminate polarization, 292, 297
- Geminate radical pair, 290,  
295, 296f
- Genetic significance of DNA  
conformational change, 265
- Globular proteins, 79, 80
- Gluconeogenesis, 178-180  
from alanine and glycerol,  
172t  
by mouse liver, 160
- Glucose metabolic pathways,  
162, 163f, 166
- Glucose metabolism, 157, 158f
- Glutamate  
biosynthesis, 162, 163f, 166  
conformational analysis, 131  
labeling and multiplet  
probabilities, 169f  
 $^1\text{H}$  NMR spectrum, 166f  
spectrum, 128f, 165f  
 $\text{U-}^{13}\text{C}$  enriched, high order  
interactions, 126
- Glutamic acid, pH dependence  
of  $^3\text{J}_{25}$ , 133f
- Glutamic acid,  $\text{U-}^{13}\text{C}$   
enriched, spectra, 124f,  
125f

- Glycerol, molecular motions,  
211, 212f
- Glycerol, U-<sup>13</sup>C enriched,  
spectra, 122f
- Glycine, <sup>13</sup>C enriched, <sup>1</sup>H  
FT spectra, 140f
- Glycosaminoglycans, 73, 74
- Glyoxylate shunt and  
tricarboxylic acid, 163f,  
167
- Gouy-Chapman shell, 75
- Gramicidin A, 78
- Guajol, <sup>1</sup>H NMR spectrum,  
22f, 23f
- H
- Hamiltonian (H), 47, 48
- Hard segments of copolymer,  
346, 349f
- Hard segments in Hytrel  
samples, 347t
- Heat denaturation effects on  
DNA, 275
- Helium consumption, 9t
- Helix conformation, Ca-binding  
protein, 82f
- Hemocyanin, 85
- Heparin binding strength, 74
- Heptamethylbenzenonium ion, 2D  
exchange spectrum, 55f
- Herzfeld-Berger analysis, 353
- Hexose monophosphate shunt  
(HMS), 163f, 166
- High field, instrumental  
requirements, 14-19
- High field magnets, 11
- High magnetic field, 19-28  
advantages, 31, 36  
applications, 19-28  
biological molecules, 19,  
31-45  
nucleic acid, 31-45
- High pressure NMR  
spectroscopy, 199-217  
application for study of  
cyclohexane  
conformational  
inversion, 202-207  
dynamic structure of  
disordered materials,  
209-215  
polymers relaxation study,  
215

- High pressure NMR  
  spectroscopy --continued  
  supercritical water,  
    207-209  
  transition metal carbonyl  
    clusters, 199-202
- High pressure probe  $^{13}\text{C}$  NMR  
  spectra, 200, 201f
- High resolution  $^2\text{H}$  NMR,  
  100-105
- High speed cylindrical spinner  
  design, 221, 223f
- $^1\text{H}$  inversion recovery  
  experiment, 139, 140f
- Histidine  
  pH dependence of photo-CIDNP  
    effect, 307, 308f  
  photoreaction with flavin,  
    304, 307-309  
  tautomerism, 136, 138
- Histone core particles,  
  binding of DNA, 263, 264f
- $^2\text{H}$  NMR --See Deuterium NMR
- $^1\text{H}$  NMR spectrum --See proton  
  NMR spectrum
- Homonuclear decoupled proton  
  spectrum, 3
- $^1\text{H}$  photo-CIDNP effects for  
  aromatic amino acids, 305,  
    308f
- $^1\text{H}$  photo-CIDNP spectra of  
  phospholipase, 309, 310f
- $^1\text{H}$  relaxation in biological  
  macromolecules, 141
- $^1\text{H}$  relaxation,  $^{13}\text{C}$   
  enriched molecules, 138-141
- $^2\text{H}$  spectra --See Deuterium  
  NMR spectra
- Hybrids cavity resonators, 14
- Hydrogen atom transfer, 307
- Hydrogen bonding interactions,  
  solvent effects, 137f
- Hydrolysis of 2-acyl ester  
  bonds, 309
- Hyperfine coupling, 288f, 289
- Hytrel thermoplastic  
  elastomers, 345-360
- I
- Imaging, NMR, 5
- Imidazole, tautomeric forms,  
  136
- INEPT, 4
- Inhibitor K, spectrum, 52f
- Ionophores, cation binding,  
  63-95
- Insensitive nuclei enhanced by  
  polarization transfer  
    (INEPT), 4
- Instrumentation, 1  
  improvements, 1, 2  
  requirements at very high  
    field, 14-19  
  resolving power, 8



- Intercellular properties,  
  probes, 148
- Interface recognition site,  
  (IRS), 309
- Interface recognition site of  
  pancreatic phospholipases  
   $A_2$ , 312
- Interrupted-decoupling  
  experiment, 339, 341f
- Intramolecular dynamics, 239
- Ion-binding, 76
- Ion complexation, 76, 77
- Ionophore antibiotics, 76-79
- Ionophores concentration  
  range, 67
- Ion transport, 76, 77
- IRS --See Interface  
  recognition site
- Isomerism, cis/trans, 29
- Isotope shift, 123
- Isotopically labeled amino  
  acids and peptides, 148-150
- Isotopic labeling, categories,  
  119, 120
- Isotopomers, 162
- Isotropic chemical shifts,  
  conformational analysis,  
  234-239
- Isotropic chemical shifts in  
  Hytrek spectrum, 353
- Isotropic motion, 142
- Isotropic tumbling, 280f
- J
- $^{3J}_{cc}$  analysis as  
  conformational probe,  
  129-138
- J-coupling connectivities, 50,  
  52f
- Joint probabilities, 168, 170
- Joint technology in a  
  superconducting magnet, 12
- K
- Kerogens, 327, 337f
- Ketoglutarate formation, 163f
- Kinetics,  $Na^+$  exchange, 68,  
  69
- Kinetics of Na-binding, 77
- Krebs cycle, 162-168
- L
- Labeling patterns for  
  glutamate from glucose,  
  169t
- Labels, soybean leaves, 195,  
  197
- Labels, soybean organ  
  cultures, 190-195
- Larmor frequency, 66
- Lasalocid, 77
- Lectin bound to sugars,  
  molecular dynamics, 107,  
  108
- Lifetime of  $Na^+$ , 68, 69
- Line broadening, equation, 36

- Line shapes, dynamical  
analysis, 239-241
- Line shapes, short relaxation  
times effects, 144, 147,  
148
- Line shape test spectra, 14-16
- Line width  
calculation, relaxation  
transition, 65  
contributions, 260, 263  
of deuterium resonances,  
106, 107  
of DNA, 270-274, 278t  
scalar decoupled, for  
HytreI, 350-352
- Lipid, enzymatic hydrolysis,  
309-312
- Lithium hopping motion, 211,  
213, 214f, 216f
- Lorentz-Gauss transformation,  
18f, 22f, 23f
- M
- Macerals, coal, spectra, 326f
- Magic angle cross-polarization  
--See also CP/MAS, 13C  
CP/MAS  
Neurospora crassa, 188  
soybean cotyledons, 192f,  
195, 196f
- Magic angle spinning (MAS), 3,  
4  
device, schematic drawing,  
189f  
probe, 220-222  
techniques, 115, 319, 320f
- Magnetic fields, 44  
advantages, 31  
applied, effect on  
resolution, 336  
dependence of DNA line  
widths on, 273, 274f  
equation, 38  
resonance conditions, 287  
strength, 1, 2, 7, 8  
strength and NMR  
spectrometers, 9, 10f
- Magnetic properties of  
deuterium, 97
- Magnetic techniques, detect  
ordering, 38
- Magnet technology, 9-14
- Magnetic technology,  
improvement, 182
- Magnetization of multiplets,  
142
- Magnetogyric ratios, 100
- Magnets, high field, 11
- Magnets, superconducting  
wide-bore, 1
- Manganese cation, paramagnetic  
effect, 263
- MAS/CP 13C NMR --See 13C  
CP/MAS

- MBBA --See 4'-Methoxy-  
benzylidene-4-n-  
butylaniline
- Metabolic pathways  
intact cells, tissues, and  
organs, 160  
in M. ammoniaphilum, 162-164  
use to label cellular  
constituents, 180-182
- Metabolic synthesis, 127
- Metabolism, <sup>13</sup>C NMR studies,  
157-186
- Mechanical properties of  
copolymer, 345
- Mechanism of cancellation,  
315-317
- Mechanistic investigations  
with CIDNp, 285-318
- Membranes studies with <sup>2</sup>H  
NMR, 111
- Membranes, Na-transport, 77
- Memory capability, 14
- Mercury(II) effects on  
double-stranded DNA, 279,  
281f, 282
- 4-Methoxybenzylidene-4-n-butyl-  
aniline (MBBA), <sup>13</sup>C  
spectrum, 19f, 48
- p-Methoxyphenylalanine, 30
- Methylation of DNA bases, 265
- Methylene carbons, C-H bonds  
correlation times, 145t
- Methyl formate powder, 2D  
spectrum, 53f
- Methyl pyropheophorbide a  
spectra, 43f
- 4-Methyl imidazole, 136, 137f
- Micelle-enzyme complexes, 311,  
312f
- Micelle formation, 78
- Micelles, 309, 311f
- Micrinite <sup>13</sup>C CP/MAS  
spectrum 323, 326f
- Multifilament Nb<sub>c</sub>Sn, 11
- Metallic nuclei, quadrupolar,  
63-95
- Mobile domains, 348-352
- Mobile domains, molecular  
motion, 358
- Molecular dynamics in viscous  
fluids, 211
- Molecular order variation  
with position, 111-114
- Molecular tumbling, 280f
- Monensin ionophore, 77
- Morphine, 36, 37
- Mouse liver gluconeogenesis,  
160
- Mucopolysaccharides --See  
Biopolymers
- Mucopolysaccharidosis, 73
- Multinuclear high resolution  
FT NMR at high pressure,  
199-207
- Multinuclear NMR, 2
- Multiple field natural  
abundance studies of DNA  
dynamics, 269-283

Multiple quantum NMR, 4, 5, 182

Multiplet

effects of coupled nuclei,  
289

intensities,  $^{13}\text{C}$ - $^{13}\text{C}$ ,  
169t

probabilities and glutamate  
labeling, 169t

structure, effect of short  
 $T_1$ , 146

Multiply enriched systems,

$^{13}\text{C}$  relaxation, 141-146

Multi-pulse techniques, 4

Muscular proteins,

cation-binding, 79

## N

$\text{Na}^+$  exchange kinetics, 68, 69

Napthalene  $^2\text{H}$  spectra, 41f

$^{23}\text{Na}$  attachment to

biomolecular receptors, 67

Natural abundance

$^{13}\text{C}$  NMR spectroscopy, 220

$^{13}\text{C}$  NMR studies of DNA  
dynamics, 269-283

$^{13}\text{C}$  probability, 168, 170  
samples, 5

$\text{Nb}_3\text{Sn}$ , 11, 12

$\text{NbTi}$ , 11

$^{14}\text{N}$ - $^{13}\text{C}$  dipolar couplings,

conformational analysis,  
241-245

$^{14}\text{N}$ - $^{13}\text{C}$  incorporation in  
cotyledon protein, 193t

$^{14}\text{N}$  dipolar coupling, 226

Neurospora crassa, 188

Nicotine  $^1\text{H}$  NMR spectrum,  
102, 103f

Nitrobenzene spectra, 27f, 41f

NMR --See also specific types

e.g.,  $^{13}\text{C}$  Deuterium,  
 $^{23}\text{Na}$ , 31p

NMR early use, 8

NMR new methods, 2

NMR spectrometers, field  
strength, 9, 10f

NMR spectrum --See individual  
compounds and types

$^{23}\text{Na}$  natural abundance  
studies, 66

$^{23}\text{Na}$  NMR applications to  
study of

structure correlations 70, 71  
whole tissue, 88-90

$^{23}\text{Na}$  NMR study of  
chondroitin and dermatan  
sulfate, 73

$^{15}\text{N}$  NMR future developments,  
197, 198

$^{15}\text{N}$  NMR studies of soybean  
cotyledons, 192f, 195, 196f

- $^{23}\text{Na}$  NMR studies of cation binding  
     $\text{Na}^+$  binding to 5'-GMP, 85, 88  
     $\text{Na}^+/\text{Ca}^{++}$  binding to muscular proteins, 78-85  
    by inophore antibiotics, 76-79
- NOE --See Nuclear Overhauser effect
- Nonquadrupolar nucleus  
    properties, 99f
- Norbornen-2-yl derivatives, 102, 105f
- $^{15}\text{N}$ -pyridine, of  $^{13}\text{C}$  CP/MAS  
    spectra, 226, 227f
- Nuclear magnetic resonance  
    --See NMR
- Nuclear Overhauser effect, 2D spectroscopy, 54
- Nuclear Overhauser enhancements of  
    DNA resonances, 273, 275-277  
    Hytrel, 346  
    spin A, 146f  
    thermoplastic elastomers, 348, 350t
- Nuclear spins, 48  
    role in reactions, 286-288  
    polarization, 303, 305-312  
    relaxation, 315  
    states, energy, 97, 99f
- Nuclei, quadrupolar metallic, 63-95
- Nucleosomes, 263, 264f
- Nucleotides, 85-88, 249-260
- O
- Oil shales, 327, 332, 336
- Oil yields of shales vs. aliphatic carbon content, 333f
- Oleic acid, 111
- One-dimensional vs. two-dimensional spectroscopy, 47, 48, 54, 57
- Opioid peptide-receptor interactions, 171
- Ordering determination, 40
- Ordering parameters, calculation, 38
- Organic matter  $^{13}\text{C}$  CP/MAS spectra, 335f
- P
- Pair interactions, 50
- Palmitic acid, 111, 112
- Palytoxin  
    gross structure, 32f  
    molecular formula, 31  
    spectrum, 32f, 33f
- Pancreatic hydrolysis of 2-acyl ester bonds, 309
- Pancreatic trypsin inhibitor, 55f

Parvalbumins, 79-83

Peptide

- bond drawing with vectors,  
253, 245f
- bonds, conformational effect  
on coupling constant, 129
- <sup>13</sup>C enriched, 119-156
- cyclic, 234-241
- interaction with membranes  
and proteins, 148-150
- proline chemical shifts,  
239, 240t
- solid state NMR, 233-247

Phase separation in Hytrel,  
357, 358

pH dependence of CIDNP effect  
for aromatic amino acids,  
307, 308f

Phenylalanine with cyclic  
peptides, 241, 242

Phosphatidylcholine, 177t, 181

Phosphatidylserine vesicles,  
cation binding, 75, 76

Phosphodiester conformations,  
253, 254f, 260, 263

Phospholipase A<sub>2</sub>, 309

Photo-CIDNP

- of biological molecules,  
303, 305-312
- pulse sequence, 314f
- spectra of N-acetyl-  
tryptophan and flavin,  
306f, 314f
- time resolved, 312-317

Photo-induced radical reaction

287, 288f

Photo-reaction of flavin with  
tryptophan, 313-315

Paramagnetic effect of MN<sup>2+</sup>,  
263

<sup>31</sup>P NMR spectra of

- nucleosome core particles,  
263, 264f
- poly(dAdbr<sup>5</sup>U), 253, 257f
- poly(dAdT), 253, 254f,  
258f, 259f, 262f
- poly(dAdT). poly(dAdT), 260,  
261f
- poly(dGdC) . poly(dGdC),  
250, 251f

<sup>31</sup>P NMR studies of DNA

- conformation and dynamics,  
249-267

Polarization --See also

- single cross and double  
cross-polarization

Polarization F-pair and

- recombination  
cancellation, 292-295

Polarization, tryptophan, 315

Polarized residues in

- phospholipase A<sub>2</sub>, 312t

Polybenzylglutamic acid, 109

Polybutadiene, NMR relaxation  
study, 215

Polybutylene terephthalate, 345

- conformational analysis, 358
- solid state spectra, 353,  
354f

- Poly(dAdbr<sup>5</sup>U), 253, 257f  
Poly(dAdT), 253, 254f, 258f,  
259f, 262f  
Polydeoxynucleotides, 249-267  
Poly(dGdC) . poly(dGdC), 250,  
251f  
Polyelectrolytes, 71-76  
Polyester thermoplastic  
elastomers, 345-360  
Polymers, NMR relaxation study  
at high pressure, 215  
Polypeptides and wide-line  
<sup>2</sup>H NMR, 109  
Polytetramethylene  
oxyterephthalate, 345  
Polyvinyl chloride, 24f  
Porphyrin biosynthesis, 172t  
Powder spectra, 109  
Powhatan #5 coal, 338f, 341f  
Pro-Aladipeptide <sup>13</sup>C NMR  
spectrum, 242f  
Precession rates of electron  
spin vectors, 287  
Probabilities, joint, 168, 170  
Probability of <sup>13</sup>C  
enrichment, 169t  
Probes of intercellular  
properties, 148  
Probe technology, 14  
Proline  
chemical shifts, 239, 240t  
conformational analysis, 131  
rings, Ramachandran A or B  
forms, 31  
vicinal <sup>13</sup>C-<sup>13</sup>C coupling  
constants. 134t  
Proteins  
muscular, cation-binding,  
79-85  
peptide interaction, 148-150  
RNA, 181  
spectra elucidation, 51f  
synthesis blockage, 76  
Protio-bis(tolyl-tris(pyrazolyl)  
borato)cobalt(II)  
spectrum, 42f  
Proton-enhanced spectra of  
HytreI, 354f  
Proton-enhanced spectra of  
polybutylene  
terephthalate, 354f  
Proton, activation volumes,  
temperature dependence,  
213, 216f  
Proton 2D NOE spectrum of  
pancreatic trypsin  
inhibitor, 56f  
Proton flipback technique, 321  
Proton FT spectra of <sup>13</sup>C  
enriched glycine, 140f  
Proton heteronuclear broadband  
decoupling, 14  
Proton NMR spectra of  
bovine pancreatic trypsin  
inhibitor, 51f  
camphor, 25f  
<sup>13</sup>C enriched glutamate, 128f  
ethylbenzene, 14, 17f, 18f  
glutamate, 166f

## Proton NMR spectra of

--continued

guajol, 22f, 23fnicotine, 102, 103f

propane, propene, and

cyclopropane, 102, 104f

## Proton spectroscopy of

biological molecules, 19

## Proton spectroscopy, 2D

J-resolved, 48

## Proton spin-lattice time,

water, 207, 208f

## Pulse power, 19

Pulse sequence, double cross-  
polarization, 191f

## Pulse sequence for time

resolved photo-CIDNP

experiments, 313, 314f

## Purine-pyrimidine hairpin

duplexes, 253, 257

## Pyridine, 226-228

Pyridine, <sup>13</sup>C CP/MASspectrum, 226, 227fPyridine, (d<sub>5</sub>), T<sub>1</sub>

measurements, 107

## Pyrrolidine ring geometry, 239

Pyruvate cell transport, 171,  
178

## Q

## Quadrupolar

coupling constant, 74

metallic nuclei, 63-95

nucleus properties, 99f

splitting variation with

Acholeplasma laidlawii,

113f

vectors, drawing of peptide

bond with, 243, 245f

## Quadrupole

interaction effect

on Zeeman energy levels,

99f

powder pattern, first-order,

213, 214fsplittings, 26, 27f, 30-41

## R

## Radical

disproportionation, 299-301

pair mechanism of CIDNP,  
286-240

pair theory, 286

disproportionation, 299-301

exchange, 300, 302, 303

photo-induces, 287, 288f

## Radical recombination, S and T

geminate pairs, 297, 298f

## Random recombination reaction

via F-pairs, 290, 292, 296f

## Rate constants for binding and

release, derivation, 68-70



- Rate constants for cation  
  binding, 83
- Reaction mechanisms, 102
- Reactions --See specific  
  types; e.g., cyclic, free  
  radical
- Receptor interactions with  
  peptide hormones, 150
- Recombination cancellation and  
  F-pair polarization,  
  292-295
- Recombination processes in  
  cyclic reactions, 290-292
- Recombination processes in  
  disproportionation  
  reactions, 299, 300
- Relaxation  
  behavior of compressed  
    supercritical water,  
    207-209  
  behavior,  $^{13}\text{C}$  enriched  
    amino acids, 138-148  
  deuterium nuclear, 106-108  
  ( $^1\text{H}$ ) in  $^{13}\text{C}$  enriched  
    molecules, 138-141  
  measurements on bituminous  
    coal, 322  
  parameters, 144, 322  
  properties differences, 339,  
    341f  
  sink mechanism, 302  
  time  
    asparagine, 193  
    in glycerol, 211, 212f
- Relaxation --continued  
  of methyl groups, 317  
  (short) effects on line  
  shapes and couplings, 144,  
  147, 148  
  studies,  $^{13}\text{C}$ , 157, 160  
  transition, line width  
    calculation, 65  
  transverse rate equation, 66
- Resolving power of  
  instruments, 8
- Resonance interpretation, 123
- Resonators, hybrid cavity, 14
- Retorting oil shales, 327
- rf amplitude distribution, 19,  
  20f
- Rhodium carbonyl clusters,  
  200-202
- Ribonuclease A, 307
- Rigid domains, molecular  
  motion, 358, 359
- Rigid domains, results, 353-357
- Rotor assembly, 222, 223f
- Rotational correlation times  
  for  $^{13}\text{C}$  enriched  
  molecules, 145t
- S
- Salt dependence of  $^{31}\text{P}$  NMR  
  spectra of  
  polynucleotides,  
  250, 251f, 259f
- Sample spinners design, 220

## Satellites

 $^{13}\text{C}$ - $^{13}\text{C}$ , 123, 127

probabilities, 167

proton resonances, 139

## Saturation fraction(s), 67

## Scalar C-C coupling constants,

conformational

interpretation, 127-138

## Scalar coupling constants, 3,

120

Scalar decoupled  $^{13}\text{C}$  NMR

spectra of Hytrel and

polybutylene-

terephthalate, 348, 349f

## Scalar decoupled line widths

for Hytrel, 350-352

## Scalar decoupling, 345, 348

## Sensitivity improvements for

 $^{15}\text{N}$  NMR experiments, 197

## Shielding, CH, 21

## Side-chain motions, 239

## Sign rules for CIDNP, 289, 290

## Single cross-polarization

 $^{154}\text{N}$  NMR spectra,

soybean cotyledone, 190,

192f

## Single and double cross-

polarization difference

experiment, 190, 191f

## Site binding by

polyelectrolytes, 71-76

DNA-cation interactions, 74, 75

## Site binding by poly-

electrolytes --continued

glycosaminoglycons, 73, 74

phosphatidylserine vesicles,

75, 76

schematic 72f

## Sodium-calcium cation binding

to proteins, 81, 83

## Sodium binding and 5' -OMP,

85-88

## Sodium binding kinetics, 77

## Sodium cation affinity for

DNA, 74, 75

## Sodium cation complexation

with crown ethers, 70, 71

## Sodium heparinate, 74

## Sodium ions as isoteric

probes, 81

## Sodium transport in membranes,

78

## Sodium, types of intracellular

bound, 88, 89

## Solid fossil fuels, 319-343

## Solids, NMR spectroscopy, 3, 4

Solids,  $^2\text{H}$  NMR, 111-115Solid state  $^{13}\text{C}$  NMR studies

of polyester thermoplastic

elastomers, 345-360

## Solid state NMR of linear and

cyclic peptides, 233-247

## Solomon equations, 141, 142

- Solvent and pressure effect on  
cyclohexane ring inversion  
process 204, 205f
- Sonication time effect on  
 $^{31}\text{P}$  NMR signals of  
poly(dAdT) . poly(dAdT),  
260, 261f
- Soybean cotyledons  $^{14}\text{N}$  NMR  
spectra, 192f
- Soybean leaves, protein  
turnover, nonspecific  
double labels, 195, 197
- Spectral density term, 141
- Spectral windows, 14
- Spectral windows, widened, 19
- Spectrometer for simultaneous  
binuclear NMR, 180
- Spectrometer, 600 MHz NMR, 31
- Spectrometer (NMR) commercial  
models, 9, 10f
- Spectrometers, 31
- Spermidine, 265
- Spin-echo technique, 89, 339
- Spin-lattice relaxation  
behavior for AM  $X_n$ , 143f
- Spin-lattice relaxation,  
effect on DNA resonances,  
273, 275-277
- Spin-lattice relaxation times  
for  
deuterium resonances, 106,  
107
- DNA, native and denatured  
279, 280f
- Hytrel, 348, 350t
- Spin-lock C-N cross-  
polarization transfer  
time, 193, 194f
- Spinner assembly model for  
obtaining resonant  
frequencies, 22, 223f
- Spinner design, 220, 221, 319
- Spinning assembly model, 221,  
223f
- Spinning device, magic-angle,  
schematic drawing, 189f
- Spinning sidebands, 336
- Spin-selective radical  
reactions, 286-287
- Spin-sorting process, 288f
- Spin-spin coupling --See also  
Coupling
- Spin-spin  
coupling constant, 21, 289  
relaxation time, 106, 107,  
260
- Spin number, 97-99
- Spin number (I) --See also  
Nuclear spins, 64, 65
- Spin 3/2 particle, dual  
relaxation, 64-66
- Spin quantum number, 64
- Splitting magnitude equation,  
40
- Splitting, methyl  
pryopheophobide a ring  $\nu$   
 $\text{CH}_2$  group, 43f, 44

- Spreading parameters, 3
- Stoichiometry, derivation and binding constants, 67
- Stokes-Einstein equation, 209
- Structural elucidation of polytoxin, 31
- Structure, dynamic, of disordered materials, 209, 215
- Structure reactivity correlations, 70, 71
- Sugar carbon resonance line widths, 272t
- Sugars bound to lectin, molecular dynamics, 107, 108
- Superconducting magnetic technology, 9-14
- Superconducting wide-bore magnets, 1
- Supercritical water, 207-210
- Susceptibility anisotropy, 38, 44
- Susceptibility asymmetry, 38
- Synthetic polymers, characterization, 21
- T
- Taurine, 123
- Tautomeric forms of imidazole, 136
- Tautomerism of hystidine, 136, 138
- Technology, magnet, 9-14
- Telestability in DNA, 263, 265
- Temperature dependence of activation volumes for proton, 213, 216f
- deuteron  $T_1$  in glycerol- $d_4$ , 211
- $^{31}\text{P}$  NMR spectra of polynucleotides, 254f, 257f
- Temperature effect on proton spin-lattice time in water, 207, 208
- Terephthalate carbons chemical shift parameters, 357t
- Tetracycline and protein synthesis inhibition, 76
- Tetramethyl- $p$ -benzosemiquinone anion radical, 317
- Thermoplastic elastomers, 345-360
- Time dependence CIDNP, 295-299
- Time dependence of  $F_{10}$  methyl peaks of flavin, 315, 316f
- Time-domain approach for enhancing resolution, 339, 340
- Time resolved photo-CIDNP, 312, 317
- Tissue, whole,  $^{23}\text{Na}$  NMR, 88
- Tabacco mosaic virus; enriched, 181
- Transfer time, spin-lock C-N cross-polarization, 193, 194f

- Transition metal carbonyl  
clusters, 200-202
- Transitions, zero and double  
quantum 57, 59f
- Transmission coefficient as  
function of pressure and  
solvent, 204, 208f
- Transport behavior of  
compressed supercritical  
water, 207-209
- Transverse relaxation rate  
equation, 66
- Trehalose, 157, 158f
- Tricarboxylic acid and  
glyoxylate shunt, 163f, 167
- Triplet-singlet  
interconversion 287,  
291-293
- Troponin-C, 79, 83-85
- Trypsin inhibitor, pancreatic,  
56f
- Trypsin inhibitor spectra, 51f
- Tryptic cleavage of  
N-terminal heptapeptide,  
309
- Tryptophan, 121f, 303, 305
- Tryptophan pH dependence of  
photo-CIDNP effect, 307,  
308f
- Tryptophan polarization, 315
- T<sub>1</sub> --See Spin-lattice  
relaxation time
- Tumbling, molecular, 280f
- Two-dimensional FT NMR  
spectroscopy (2D FT NMR),  
2, 3, 47-62
- Two-dimensional vs.  
one-dimensional  
spectroscopy, 47, 48, 54,  
57
- Types of polarization in high  
magnetic fields, 289
- Tyrosine pH dependence of  
photo-CIDNP effect, 307,  
308f
- Tyrosine photo reaction with  
flavin, 305, 307, 309
- U
- U-<sup>13</sup>C enriched amino  
acids, 120-127
- Ultra high field NMR 7-29
- Unsaturated acids, 111, 112
- V
- Vector model, 287, 289
- Vicinal <sup>13</sup>C-<sup>13</sup>C coupling  
constants in proline, 134t
- Vicinal couplings, dihedral  
angle dependence, 129
- Virtual coupling, 123
- Viscosity, effect of Hg<sup>2+</sup>  
binding to DNA, 279
- Viscous fluids, molecular  
dynamics, 211
- Volumes, activation, pressure  
and solvent dependence,  
204, 206f

## W

Water, proton spin-lattice  
time, 207, 208f  
Water, supercritical, 209, 210f  
Watson-Crick base pairing, 249  
Wheat germ agglutinin,  
N-acetylglucosamine  
binding, 107, 108f  
Wide-line deuterium NMR,  
109-115  
WM-500 spectrometer, 9  
Wyoming coal, 327-330, 331f

## Z

Z-DNA, 250, 252f  
Zeeman energy levels, 99f  
Zero quantum transition, 57,  
59f  
Zeugmatography imaging  
technique, 5  
Zymogen, 309